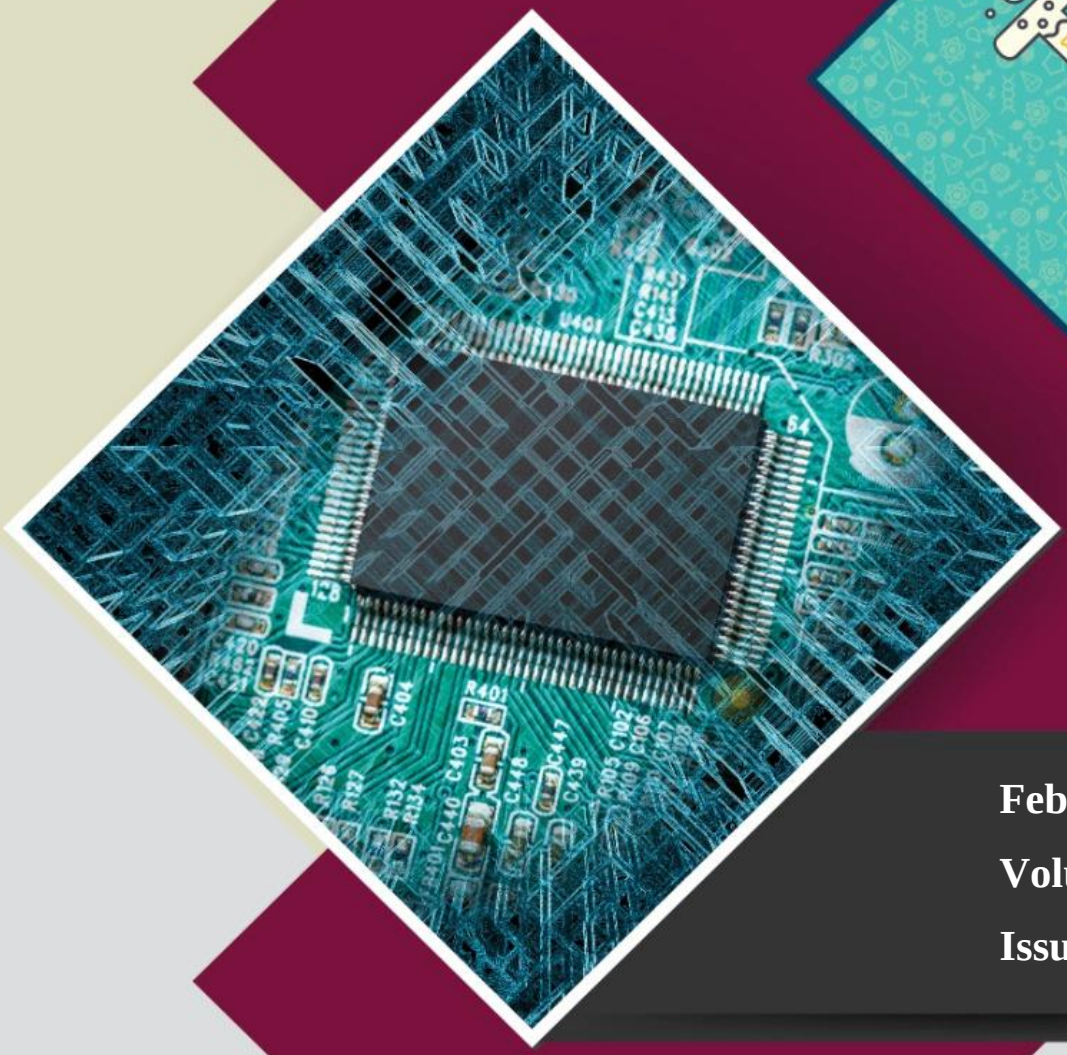
e-ISSN: 2822-2881

FUJECE

Firat University Journal of Experimental and Computational Engineering





February : 2026
Volume : 5
Issue : 1

https://dergipark.org.tr/tr/pub/fujece

Firat University Journal of Experimental and Computational Engineering

Fırat Üniversitesi Deneysel ve Hesaplamalı Mühendislik Dergisi

Volume: 5 Issues: 1 Year: 20226

Owner

On Behalf of Firat University

Rector

Prof. Dr. Fahrettin GÖKTAŞ (fgoktas@firat.edu.tr)

Editor-in-Chief

Prof. Dr. Mehmet YILMAZ, Firat University, Türkiye (mehmetyilmaz@firat.edu.tr)

Vice Editor-in-Chief

Prof. Dr. Ebru AKPINAR, Firat University, Türkiye (ebruakpinar@firat.edu.tr)

Prof. Dr. Ragıp İNCE, Firat University, Türkiye (rince@firat.edu.tr)

Prof. Dr. Mete Onur KAMAN, Firat University, Türkiye (mkaman@firat.edu.tr)

Assoc. Prof. Dr. Erkut YALÇIN, Firat University, Türkiye (erkutyalcin@firat.edu.tr)

Editorial Advisory Board

Prof. Dr. Yakup DEMİR, Firat University,Elazığ, Türkiye (ydemir@firat.edu.tr)

Prof. Dr. Levent TAŞÇI, Firat University, Elazığ, Türkiye (ltasci@firat.edu.tr)

Prof. Dr. Abdulkadir Cuneyt AYDIN, Atatürk University, Erzdurum,Türkiye (acaydin@atauni.edu.tr)

Prof. Dr. Fatih CETİŞLİ, Pamukkale University, Denizli, Türkiye (fcetisli@pau.edu.tr)

Assoc. Prof. Dr. Mustafa ULAŞ, Fırat University, Elazığ, Türkiye (mustafaulas@firat.edu.tr)

Prof. Dr. Bilal ALATAŞ, Firat University, Elazığ, Türkiye (balatas@firat.edu.tr)

Prof. Dr. Erhan AKIN, Firat University, Elazığ, Türkiye (eakin@firat.edu.tr)

Prof. Dr. Erkan KÖSE, Nuh Naci Yazgan University, Kayseri, Türkiye (ekose@nny.edu.tr)

Assoc. Prof. Dr. Filiz KAR, Firat University, Elazığ, Türkiye (fkar@firat.edu.tr)

Prof. Dr. Hasan SOFUOĞLU, Karadeniz Technical University, Trabzon, Türkiye (sofuoglu@ktu.edu.tr)

Prof. Dr. M. Şaban TANYILDIZI, Firat University, Elazığ, Türkiye (mtanyildizi@firat.edu.tr)

Prof. Dr. Özge HANAY, Firat University, Elazığ, Türkiye (ohanay@firat.edu.tr)

Prof. Dr. Oğuz YAKUT, Firat University, Elazığ, Türkiye (oyakut@firat.edu.tr)

Prof. Dr. Tacettin GEÇKİL, İnönü University, Malatya,Türkiye (tacettin.geckil@inonu.edu.tr)

Firat University Journal of Experimental and Computational Engineering

Fırat Üniversitesi Deneysel ve Hesaplamalı Mühendislik Dergisi

Volume: 5 Issues: 1 Year: 20226

Editorial Board

Prof. Dr. Ali TOPAL — Civil Engineering,Dokuz Eylül University, İzmir,Türkiye (ali.topal@deu.edu.tr)

Prof. Dr. Ayşe Vildan BEŞE — Chemical Engineering, Atatürk University, Ezdurum, Türkiye (avesis.atauni.edu.tr/vbese)

Asst. Prof. Dr. Ali BEHNOOD — Civil Engineering, University of Mississippi, Oxford, United of America, (abehnood@olemiss.edu)

Prof. Dr. Kadir TURAN — Mechanical Engineering, Dicle University, Diyarbakır, Türkiye (kturan@dicle.edu.tr)

Prof. Dr. H. Soner ALTUNDOĞAN — Bioengineering, Firat University, Elazığ, Türkiye (saltundogan@firat.edu.tr)

Prof. Dr. Mehmet Deniz TURAN — Metallurgy and Materials Engineering, Firat University, Elazığ, Türkiye, Elazığ, Türkiye (mdturan@firat.edu.tr)

Asst. Prof. Dr. Hasan ARSLANOĞLU — Chemical Engineering, Çanakkale Onsekiz Mart University, Çanakkale, Türkiye (hasan.arslanoglu@comu.edu.tr)

Dr. Nuno MENDES — Mechanical Engineering, University of Minho, Braga, Portugal (nunomendes@civil.uminho.pt)

Prof. Dr. Rashid NADİROV — Chemical, Al-Farabi Kazakh National University,Almaty, Kazakhstan (nadir.rashid@gmail.com)

Prof. Dr. Serdar Ethem HAMAMCI — Electrical-Electronics Engineering, İnönü University, Malatya,Türkiye (serdar.hamamci@inonu.edu.tr)

Prof. Dr. Selçuk ALEMDAĞ — Geological Engineering,Gümüşhane University, Gümüşhane, Türkiye (selcuk@gumushane.edu.tr)

Prof. Dr. Ömür GÖKKUŞ — Environmental Engineering, Sivas Cumhuriyet University, Sivas, Türkiye (omurgokkus@cumhuriyet.edu.tr)

Prof. Dr. Mehmet KARAKÖSE — Computer Engineering Firat University, Elazığ, Türkiye (mkarakose@firat.edu.tr)

Assoc. Prof. Dr. Fatih DEMİR — Software Engineering, Firat University, Elazığ, Türkiye (fatihdemir@firat.edu.tr)

Firat University Journal of Experimental and Computational Engineering

Fırat Üniversitesi Deneysel ve Hesaplamalı Mühendislik Dergisi

Volume: 5 Issues: 1 Year: 20226

Dr. Hamed SADEGHİ — Mechanical Engineering, Shanghai Jiao Tong University,Shanghai, China (hamedsadeghhi@gmail.com)

Prof. Dr. Muhammed Fatih TALU — Computer Engineering, İnönü University, Malatya, Türkiye (fatih.talu@inonu.edu.tr)

Asst. Prof. Dr. Batuhan SELVİ (Language Editor) — English Language Teaching,Yozgat Bozok University, Yozgat, Türkiye (batuhan.selvi@bozok.edu.tr)

Correspondence Address

Firat University Faculty of Engineering Journal of Experimental and Computational Engineering Publishing Coordinatorship

23119 Elazığ/TÜRKİYE

E-mail: fujece@firat.edu.tr

Web page: http://fujece.firat.edu.tr/

Firat University Journal of Experimental and Computational Engineering a peer-reviewed journal.

Firat University Journal of Experimental and Computational Engineering

Fırat Üniversitesi Deneysel ve Hesaplamalı Mühendislik Dergisi

Volume: 5 Issues: 1 Year: 20226

CONTENTS

Comparative Analysis of Digital Forensics Methods on Android Devices (Research Article)
Android Cihazlar Üzerinde Adli Bilişim Yöntemlerinin Karşılaştırmalı Analizi (Araştırma Makalesi)
Özge GÜNAY, Batuhan GÜL, Fatih ERTAM **1**

A Hybrid Deep Learning Approach for Image-based Malware Classification (Research Article)
Görüntü Tabanlı Kötü Amaçlı Yazılım Sınıflandırması için Hibrit Bir Derin Öğrenme Yaklaşımı (Araştırma Makalesi)
Zülfiye Beyza METİN, Fatih ÖZKAYNAK **26**

Smart Drone for Critical Missions: Development of a VTOL UAV with Real-Time Visual Intelligence (Research Article)
Kritik Görevler İçin Akıllı İnsansız Hava Aracı: Gerçek Zamanlı Görsel Zekâya Sahip Bir VTOL İHA'nın Geliştirilmesi (Araştırma Makalesi)
Bashar ALHAJAHMAD **44**

Time Frame Adaptive Arbitrage: Optimizing Pairs Trading Performance with Dynamic Signal Delays (Research Article)
Zaman Çerçevesine Uyarlanabilir Arbitraj: Dinamik Sinyal Gecikmeleri ile İkili İşlem Performansının Optimizasyonu (Araştırma Makalesi)
Mustafa Kanber, Yunus SANTUR **69**

Rheological Properties of Lightly Cemented Sodium Silicate Grouts (Research Article)
Sodyum Silikat ile Düşük Oranda Çimento İçeren Karışımların Reolojik Özellikleri (Araştırma Makalesi)
Emre DEVECİ, Eyübhan AVCI, Melih UYSAL **83**

Typical Damage Patterns In Masonry Structures After Various Major Earthquakes (Research Article)
Büyük Depremler Sonrasında Yığma Yapılarda Görülen Tipik Hasar Mekanizmaları (Araştırma Makalesi)
Alper ÖZMEN, Erkut SAYIN **94**

Comparative Analysis of U-Net and ResNet for MangaColorization: Consistency, Detail, and Computational Trade-offs (Research Article)
Manga için U-Net ve ResNet'in Karşılaştırmalı Analizi Renklendirme: Tutarlılık, Detay ve Hesaplamalı Ödünleşimler (Araştırma Makalesi)
Sami ÇAKIRAL, MD. Imran HOSEN, Tarkan AYDIN **119**

Auto-Tuning PID Control of a DC-DC Buck Converter for High-Precision Applications (Research Article)
Yüksek Hassasiyetli Uygulamalar için DC-DC Buck Dönüştürücünün Otomatik Ayarlamalı PID Kontrolü (Araştırma Makalesi)
Adile AKPUNAR BOZKURT **135**

Fault Detection in Electricity Transmission Lines: A Comparative Analysis of Ensemble Machine Learning and Convolutional Neural Network Methods (Research Article)
Elektrik İletim Hatlarında Arıza Tespiti: Topluluk Makine Öğrenmesi ve Evrişimsel Sinir Ağı Yöntemlerinin Karşılaştırmalı Analizi (Araştırma Makalesi)
Emrah ASLAN, Yıldırım ÖZÜPAK **150**

Simulation Based Decision Intelligence Model for Multicopter Charging Stations in Smart Cities (Research Article)
Akıllı Şehirlerdeki Multikopter Şarj İstasyonları için Simülasyon Tabanlı Karar Zekası Modeli (Araştırma Makalesi)
Kübra ÇELİK, Haluk EREN **169**

Effect of Source Parameter Variability on RVT-Based Site Response Analysis: A Case Study for the Aegean Region of Türkiye (Research Article)
Kaynak Parametrelerindeki Değişkenliğin RVT Tabanlı Zemin Tepkisi Analizine Etkisi: Türkiye Ege Bölgesi Örneği (Araştırma Makalesi)
Abdullah İÇEN **218**

Investigation of Local Scour at Classical Contracted Rectangular Weir Downstream using CFD (Research Article)
Klasik Dikdörtgen Büzülmeli Savakların Mansabında Oluşan Yerel Oyulmaların HAD Yöntemi Kullanılarak İncelenmesi (Araştırma Makalesi)
Erdinç İKİNCİOĞULLARI, Muhammet Emin EMİROĞLU, Mehmet Cihan AYDIN **231**

Numerical Investigation of Compression Behavior of Bio-Inspired Honeycomb Designs (Research Article)
Doğadan İlhamlı Bal Peteği Tasarımlarının Sıkıştırma Davranışının Sayısal Olarak İncelenmesi (Araştırma Makalesi)
Alparslan SOLAK **250**

Firat University Journal of Experimental and Computational Engineering

Fırat Üniversitesi Deneysel ve Hesaplamalı Mühendislik Dergisi

Volume: 5 Issues: 1 Year: 20226

Capturing Carbon Dioxide from Industrial Waste Gases (Research Article)
Endüstriyel Atık Gazlardan Karbon Dioksitin Yakalanması (Araştırma Makalesi)
Özcan BAŞARAN, Yavuz KIRIM **262**

Risk Averse Metaheuristic Hybrid Solution Approach to Vehicle Routing Problem of Hazardous Materials Through the Combination of Game Theory and Tabu Search (Research Article)
Oyun Teorisi ve Tabu Araması Yoluyla Tehlikeli Maddelerin Araç Rotalama Problemine Risk Kaçınımlı Metasezgisel Hibrit Çözüm Yaklaşımı (Araştırma Makalesi)
Hakan ASLAN, Michael G. H. BELL **270**

Comparative Analysis of Principle Component Analysis and Anova Feature Selection in Malware Detection (Research Article)
Kötü Amaçlı Yazılım Tespiti İçin Temel Bileşen Analizi ve Anova Özellik Seçiminin Karşılaştırmalı Analizi (Araştırma Makalesi)
Taha ETEM **299**

Latency and Resource Trade-off Analysis of AXI-DMA and BRAM Integration Approaches on SoC-FPGA (Research Article)
SoC-FPGA Ortamında AXI-DMA ve BRAM Tabanlı Entegrasyon Yöntemlerinde Gecikme ve Kaynak Tüketim Analizi (Araştırma Makalesi)
Güner TATAR **316**

Dynamic Pricing-Based Energy Management Model for Electric Vehicles Considering Real Traffic Information (Research Article)
Elektrikli Araçlar için Gerçek Trafik Bilgilerini Dikkate Alan Dinamik Fiyatlandırma Tabanlı Enerji Yönetim Modeli (Araştırma Makalesi)
Muhammed Sefa ÇETİN, Muhsin Tunay GENÇOĞLU, İlhan AYDIN, Ozan ERDİNÇ, Ayşe Kübra ERENOĞLU TATAR, Habip ŞAHİN **330**

Deep Steganography with U-Net: Hiding and Revealing Text in Video (Research Article)
U-Net ile Derin Steganografi: Video içerisine Metni Gizleme ve Yeniden Elde Etme (Araştırma Makalesi)
Mahmut SİNECEN **345**

Spatiotemporal Dynamics of Land Surface Temperature (LST) and Spectral Indices (NDVI, NDBI, NDBaI) in the Burdur Basin (Research Article)
Burdur Havzası'nda Kara Yüzey Sıcaklığı (LST) ve Spectral İndekslerin (NDVI, NDBI, NDBaI) Mekansal-Zamansal Dinamikleri (Araştırma Makalesi)
Erkan KARAKOYUN **363**

Fırat Üniversitesi Deneysel ve Hesaplamalı Mühendislik Dergisi

FUJECE

Android Cihazlar Üzerinde Adli Bilişim Yöntemlerinin Karşılaştırmalı Analizi

Özge GÜNAY[1], Batuhan GÜL[2*], Fatih ERTAM[3]

[1,2,3]Adli Bilişim Mühendisliği. Teknoloji Fakültesi, Fırat Üniversitesi, Elazığ, Türkiye.
[1]ozgegunay23@gmail.com, [2]b.gul@firat.edu.tr, [3]fatih.ertam@firat.edu.tr

Geliş Tarihi: 12.12.2024
Kabul Tarihi: 20.05.2025

Düzeltme Tarihi:05.2.2025

doi: https://doi.org/10.62520/fujece.1600312
Araştırma Makalesi

Alıntı: Ö. Günay, B. Gül ve F. Ertam,'' Android cihazlar üzerinde adli bilişim yöntemlerinin karşılaştırmalı analizi", Fırat Üni. Deny. ve Hes. Müh. Derg., vol. 5, no 1, pp. 01-25, Şubat 2026.

Öz

Android cihazların kullanımının artmasıyla birlikte, mobil kötü amaçlı yazılımlarla ilgili siber suçların ortaya çıkarılmasında adli bilişim incelemeleri büyük önem kazanmıştır. Android cihazlar, mobil cihaz türlerinden biri olarak, Android işletim sistemindeki zayıflıklar ve uygulama mağazasındaki güvenlik açıkları nedeniyle kolayca istismar edilebilmektedir. Mevcut çalışmaların çoğu, kötü amaçlı yazılım tespitine yönelik makine öğrenimi modellerine odaklanırken, zararlı uygulamaların analizinde kullanılan inceleme araçlarının etkinliğine dair literatürde bir boşluk bulunmaktadır. Bu çalışma, zararlı yazılımlarla enfekte olmuş Android cihazlardan dijital delil çıkarmak ve analiz etmek için kullanılan adli yöntemleri değerlendirmektedir. Dokuz temel delil özelliğini elde etme açısından manuel inceleme, mantıksal imaj ve fiziksel imaj yöntemleri karşılaştırılmıştır. Bulgularımız, manuel ve mantıksal imaj yöntemlerinin bu özelliklerin %55,56'sını geri kazandığını, fiziksel imaj yönteminin ise daha geniş erişim (%66,67) sağladığını ve özellikle silinmiş verilerin ve ayrılmamış alanlardaki verilerin kurtarılmasını kolaylaştırdığını göstermektedir. Magnet AXIOM aracı ve manuel analiz yöntemleri kullanılarak zararlı yazılımların statik ve dinamik analizleri gerçekleştirilmiştir. Sonuçlar, özel analiz araçlarının hem zararlı faaliyetlerin tespitinde hem de kritik bilgilerin kurtarılmasında değerli olduğunu ortaya koymakta ve Android ile ilgili adli bilişim incelemelerinde en etkili yaklaşımın seçilmesi konusunda çalışanlara rehberlik etmektedir.

Anahtar kelimeler: Mobil adli bilişim, Kötü amaçlı yazılım, Siber güvenlik

*Yazışılan yazar

İntihal Kontrol: Evet – Turnitin
Şikayet: fujece@firat.edu.tr
Telif Hakkı ve Lisans: Dergide yayın yapan yazarlar, CC BY-NC 4.0 kapsamında lisanslanan çalışmalarının telif hakkını saklı tutar.

Firat University Journal of Experimental and Computational Engineering

Comparative Analysis of Digital Forensics Methods on Android Devices

Özge GÜNAY[1], Batuhan GÜL[2]*, Fatih ERTAM[3]

[1,2,3]Digital Forensics Engineering Department, Faculty of Technology, Fırat University, Elazığ, Türkiye.
[1]ozgegunay23@gmail.com, [2]b.gul@firat.edu.tr, [3]fatih.ertam@firat.edu.tr

Received: 12.12.2024
Accepted: 20.05.2025
Revision: 05.2.2025
doi: https://doi.org/10.62520/fujece.1600312
Research Article

Citation: Ö. Günay, B. GÜL and F. Ertam, "Comparative analysis of digital forensics methods on android devices", Firat Univ. Jour.of Exper. and Comp. Eng., vol. 5, no 1, pp. 01-25, February 2026.

Abstract

With the increasing use of Android devices, forensic investigations have become crucial in uncovering cybercrimes involving mobile malware. Android devices, as one of the mobile device types, can be easily exploited due to weaknesses in the Android operating system and security vulnerabilities in the application store. While existing studies primarily focus on malware detection using machine learning models, there is a gap in the literature regarding the effectiveness of examination tools in analyzing harmful applications. This study evaluates forensic methods used to extract and analyze digital evidence from compromised Android devices. We compare manual inspection, logical imaging, and physical imaging in retrieving nine key evidentiary features. Our findings indicate that while manual and logical imaging recovered 55.56% of these indicators, physical imaging offered broader access (66.67%), particularly facilitating the recovery of deleted data and data from unallocated space. Using the Magnet AXIOM tool and manual analysis methods, we conducted static and dynamic analyses of malicious softwares. The results demonstrate the utility of specialized analysis tools in both identifying malicious activity and recovering critical information, offering guidance to practitioners in choosing the most effective approach for Android-related casework.

Keywords: Mobile forensics, Malware, Cyber security

*Corresponging author

Plagiarism Checks: Yes – Turnitin
Complaints: fujece@firat.edu.tr
Copyright & License: Authors publishing with the journal retain the copyright to their work licensed under the CC BY-NC 4.0

1. Introduction

Crimes committed today are carried out in digital environments through devices produced with the development of technology [1]. Crimes committed through information systems in electronic environments are called advanced technology, information, cyber and computer crimes. Any illegal, immoral and unauthorized behavior against the system that processes information automatically or causes data to be transferred is defined as 'Cyber Crime' [2]. The devices that cause crimes committed in digital environments and the data in these devices are called 'digital/electronic evidence'. The discipline of solving crimes committed in cyber environments using electronic evidence is called 'Computer Forensics' [3]. In forensic computer investigations are carried out to determine whether there is an element of crime in forensic crimes that occur in digital environments. Forensic computer investigations ensure the formation of the discipline of forensic computer investigations in forensic crimes involving digital/electronic devices and information systems [4]. The field of forensic computer investigations is growing rapidly with academic and technical studies as technology advances. As the field of computer forensics develops, the economic expenditures made in this field are also reflected in the statistics. The computer forensics market, valued at $4.5 billion in 2019, is projected to reach $9.453 billion by 2027 with a 10.8% annual growth rate [5]. As computer forensics evolves, it branches into areas like file system, network, mobile, social network, voice, and cloud forensics based on the device examined [6]. Crimes involving mobile devices within digital spaces have given rise to the field known as 'mobile forensics. Mobile devices have become one of the most important products preferred by users by being developed with all kinds of software, hardware and technology, and leading today's world called the information and communication age [7]. With the advancement of mobile technologies, it is seen that the use of mobile devices, especially smart phones and tablets, has become widespread. In its report on mobile and wireless network technologies, the famous research company Gartner predicts that the adoption of mobile devices is expected to continue rising steadily with the development of mobile technologies [8]. Mobile devices that have entered our lives, especially smart phones, tablets, portable computers, wearable devices; are used in all areas from communication to social life, from education to health. Users prefer mobile devices due to their ability to perform the desired operations. Mobile devices are generally classified in terms of their usage patterns, hardware and operating systems [9]. Operating systems created from software codes for these devices, which are found in the structure of different types of digital devices such as tablets and phones preferred by users today, are called 'mobile operating systems [10].

There are many mobile operating systems in mobile devices such as Apple iOS, Google Android, BlackBerry OS, Nokia's Symbian, Hewlett-Packard's webOS (formerly Palm OS) and Microsoft's Windows Phone OS [10]. According to the famous research company Gartner, Android operating system is preferred more by users on mobile phones, while iOS operating system is preferred more on tablets. When the market share rates of operating systems are examined, it is seen that Android and IOS operating systems are preferred more on mobile devices [11]. Smartphones, which are one of the mobile device types, are defined as a mobile device type that can connect to the internet and support some applications that can be downloaded by users. The number of smartphone users is increasing today due to the fact that smartphones are user-friendly, provide faster connections, support applications, increase in processing speed and develop their features. As technology advances, more features such as device encryption and creating privacy continue to be added to smartphones. With the advancement of technology, the applications supported by smartphones are also developing. Mobile forensics is defined as the recovery of digital evidence from mobile devices using appropriate scientific forensic conditions, which is envisaged as a branch of forensic computing. The increase in the number of users of mobile devices has caused the field of mobile forensics to become an increasingly complex discipline [12]. Mobile devices involved in crimes contain valuable forensic data such as search histories, messages, photos, videos, deleted files, social media apps, and storage areas [13]. Smartphones, widely used for communication and storing user data, play a key role in investigations as they can contain crime evidence and be used in committing crimes. [9]. Analysts, law enforcement officers, forensic computer experts; perform the process of obtaining and analyzing data from mobile devices used in committing forensic crimes. Reasons such as the diversity of technology used in mobile devices, accumulation of digital evidence, and the lack of standardized data extraction methodologies create difficulties for analysts to obtain digital evidence from mobile devices [12]. Because mobile devices hold various types of evidence that can be deleted, analysts must follow a structured process (protection, seizure, examination, and reporting) during

investigations. Analysts who will examine the mobile device are given the following; necessary training should be provided, necessary software (Encase, Oxygen Forensic, MOBILEdit, Paraben, Cellebrite, Salvationdata SPF etc.) [14] and hardware to be used in mobile investigation should be provided and they should have sufficient experience about mobile forensic process. Android devices with Android operating system, which is one of the mobile device operating systems, have been preferred by users and have a high market share rate. In this context, Android devices used by users are also the target focus of attackers today. There are many potential attack vectors where attackers try to gain unauthorized access to data stored and transferred on Android devices. Malware like ransomware, trojans, viruses, and worms can infect Android devices through vulnerabilities or social engineering, allowing attackers to control the device and perform malicious actions [15]. To ensure security, users should be aware of potential attacks, use antivirus software, avoid direct APK downloads, monitor app permissions, and regularly back up data [16]. Android devices used by users contain high-evidence data in crimes committed in digital environments. It is possible that malicious applications are installed on Android devices that are evidence in forensic cases and that attacks are carried out without the user's knowledge. For this reason, analysts and forensic computer experts need to know the types of malware and their behaviors, as well as have knowledge about techniques related to analyzing malicious applications infected with Android devices. Analysts and forensic computer experts greatly contribute to solving forensic crimes by performing malware analysis on Android devices in terms of forensic computer [17]. In the literature, there are very few studies that use both forensic tools and manual analysis when analyzing malware on a mobile device. Most research might focus either on forensic tools or manual analysis separately, but not a direct comparison of both. Furthermore, to the best of our knowledge, previous studies have not comprehensively demonstrated how different forensic methods, such as manual analysis, logical imaging, and physical imaging, perform in recovering malware-related evidence. By addressing these results, we aim to fill this gap in the literature.

Briefly, the main contributions of this review can be stated as follows:

- When previous studies in the literature are examined, it is seen that malware detection on mobile devices is mostly performed using machine learning techniques. And there is a gap in the literature regarding malware detection using forensic tools. In order to eliminate this problem, it is suggested to detect malware using forensic tools.
- To examine the device, physical image, logical image and manual examination methods were used to compare which one was more advantageous.
- Studies have shown that data belonging to deleted applications can be found with physical images, but cannot be detected with logical and manual examination methods. In addition, it has been observed that static and dynamic analysis of applications cannot be performed with logical and physical image methods, but can be performed with manual examination methods.
- Our work will help those working in the field of digital forensics to determine which digital forensics software and methods should be used when examining a mobile device with malware.

2. Literature Review

In the literature, various studies have been conducted on methods developed for analyzing malware on Android devices, approaches for malware detection, and protection systems. Some of these studies are summarized below:

Coşguner et al. [18] designed a sandbox for detecting malware using hybrid, static, and dynamic analysis methods. Android applications analyzed using the sandbox undergo steps of static analysis, dynamic analysis, and reporting. Findings from the analysis of potentially malicious Android applications are documented by analysts. To evaluate the capabilities of the sandbox, 100 applications were selected, half of which were malicious and the other half benign. Experimental results demonstrated that the proposed sandbox method achieved a 96% success rate. While their work emphasizes automated analysis accuracy within a sandbox setting, our study diverges by applying real-world penetration testing and emphasizing the forensic recovery of malware traces post-infection on an actual Android device.

In a study by F. Tong et al. [19], net_link technology was utilized to gather samples of malware and benign applications, adopting static and dynamic analysis methods to propose a new hybrid approach. The study

concluded that this hybrid approach was more effective in detecting malware compared to static and dynamic analyses alone. The authors initially collected system call data from malicious and benign applications and then compared the data to create a set of malicious and normal patterns. The proposed method achieved an 88% accuracy rate in detecting malware and over 92% accuracy in identifying benign applications. In contrast, our work does not primarily aim to improve detection rates but instead evaluates how well different forensic imaging methods can capture evidence after a malware infection has occurred.

P. Teulf et al. [16] conducted research on detecting and analyzing malware on Android platforms. They proposed a novel method to analyze metadata of applications available on app stores. Experimental results showed that the proposed method provided a high detection rate. The authors aim to improve the method's performance in future studies. While their approach emphasizes pre-emptive analysis based on application metadata, our research addresses forensic analysis after the malware has already been installed and executed. According to Ullah et al. [20], malware detection for Android phones was enhanced by using eXplainable AI (XAI) technology instead of traditional machine learning methods. Their approach was tested on datasets such as CIC-AAGM2017, CIC-AndMal2017, CIC-InvesAndMal2019, and CICMalDroid2020, achieving an average accuracy of 99.48%, which outperformed previous studies.

Researchers found that mobile malware detection approaches vary between machine learning and deep learning techniques, as detailed by Nawshin et al. [21]. They analyzed the challenges posed by mobile operating system architectures and their impact on user security and data privacy. The authors reviewed studies from 2019 to 2024 covering static analysis (14 studies), dynamic analysis (7 studies from 2017–2024), and hybrid analysis (10 studies from 2020–2024). Their study concluded with recommendations to build more comprehensive datasets and develop models suited to real-world conditions for effective machine learning-based malware detection systems.

Li et al. [22] conducted a literature review on static analysis techniques designed to protect Android phones from malware. They aimed to provide a clear overview of the state-of-the-art static analysis methods and their focal points. The study reviewed 124 research papers published up to 2015, comparing them based on techniques, accuracy, and evaluation scales. The authors found that the Soot framework and taint analysis were the most commonly used static analysis techniques. However, they also noted that most studies lacked contributions like publishing tools and datasets.

In today's cybersecurity landscape, malware is often developed to perform various operations on users' mobile devices. A review of the literature reveals that most studies focus on malware detection on mobile devices using machine learning and deep learning-based models. Also, while previous research has largely concentrated on improving malware detection accuracy through automated analysis or machine learning methods, this work focuses on malware detection in mobile devices using forensic tools. When detecting malware on Android devices plays a significant role in forensic investigations, it is crucial to use appropriate forensic software to acquire and analyze evidence, such as image capture and examination, without data loss or corruption. It's important to be careful during the image acquisition process. If the forensic tool runs into bad sectors or storage corruption, the copied image might end up incomplete or contain errors. Additionally, without proper write-blocking measures, the imaging process could accidentally change timestamps or metadata, which can compromise the integrity of the original evidence. In cases where sufficient evidence cannot be obtained, manual inspection of Android devices, despite the risks, can be carried out to conduct behavioral analysis of malware, contributing to clarifying the investigation. In this context, analyzing malware on Android devices requires sufficient knowledge about the performance of forensic tools and conducting examinations using the most appropriate tools.

3. Malware Analysis on Android Devices

The aim of this study is to conduct a forensic analysis of malware on devices running the Android operating system. To achieve this, various types of malicious software (e.g. ransomware and trojans) were developed and tested on an Android device as part of a penetration testing process. Ethical rules and legal regulations are of great importance when performing forensic investigations and malware analyses on mobile devices. Cybersecurity and forensic studies should be conducted only by authorized persons, within the legal

framework and in accordance with ethical values. This study was carried out considering ethical and legal limitations. The forensic tool used was used on the authorized device and an isolated test environment was established while creating the malware.

As part of the study, scenarios were created where Android users were deceived through different methods into downloading malicious Android applications onto their devices. These applications were then installed and executed, allowing for the simulation of real-world malware attacks. The purpose of these tests was to analyze the behavior, impact, and potential vulnerabilities associated with malware infections on Android devices, from a digital forensic perspective.

The research focuses on understanding the lifecycle of malware, identifying traces left by such software on the device, and evaluating the tools and techniques required for forensic analysis. This approach provides insights into the effectiveness of current forensic methodologies and contributes to the development of improved mechanisms for detecting, analyzing, and mitigating threats posed by malicious applications in Android environments.

3.1. Material

The experiments were conducted on a Huawei P7-L10 smartphone with 16 GB storage, running the Android 4.4.2 operating system. This device was used to install and analyze malicious Android applications. Additionally, the research utilized a Monster laptop equipped with Windows 10 Pro, a 64-bit processor, and 16 GB of RAM. To generate the malicious APK files, tools designed for Android malware were employed within a Kali Linux virtual environment set up on VMware. The Apktool was used for decompiling and recompiling applications, facilitating modifications for testing purposes.

The hardware and software resources utilized in the study are summarized in Table 1, detailing the technical setup that supported the research and experimentation.

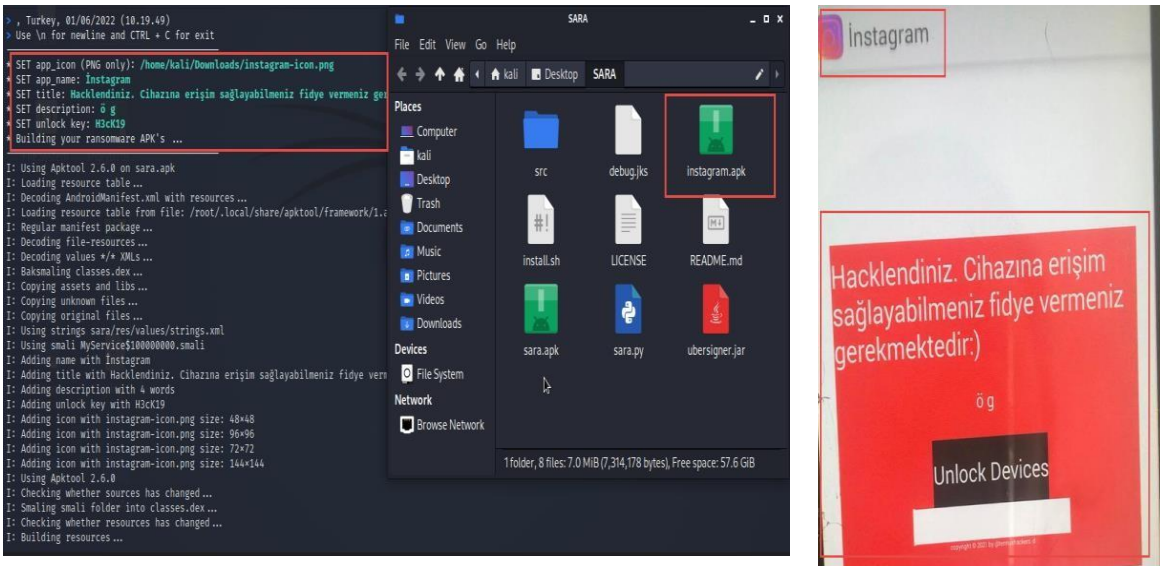
Table 1. Hardware and Software Used to Create Malware

Hardware and Software Used	Purpose of Use
Huawei P7-L10 16 GB Android 4.2.2	Device to be Examined
Windows 10 Pro, 64 bit processor, 16 GB RAM Monster Notebook	Workstation
TURKCELL SIM Card	SIM Card
Kali Linux	System to be Used for Penetration Testing
Apktool	Applications Creation Tool

3.1.1. Creating android ransomware malware and performing penetration testing

The SARA Ransomware tool, once installed on the Kali Linux operating system, can be used to generate malicious APK files [23]. In this study, a malicious APK named instagram.apk was created using the SARA tool and sent to an Android user via Google Drive. When the user downloaded and executed the instagram.apk file on their device, they were prompted to enter a password to regain access to their device. Without providing the password, the device became inoperable. To obtain the password, the user was asked to pay a ransom, successfully achieving the ransomware's malicious intent. As illustrated in Figure 1.a, the SARA ransomware tool setup process was completed. The app icon option was used to select an icon for the malicious application, while the app name option defined the name of the application. The title field specified the ransom message displayed to the victim upon launching the application, and the description option allowed for custom details to be added. The unlock key was used to set the password required to unlock the device. Finally, the malicious instagram.apk file was generated.

Figure 1.b demonstrates the result when the victim executed the malicious application, causing the device to lock. The screen shown to the victim says “you have been hacked, you must pay ransom to gain access to your device." The entire process, including the installation of the SARA tool, creation of the malicious APK, and execution of the penetration test, is detailed in Figure 1.

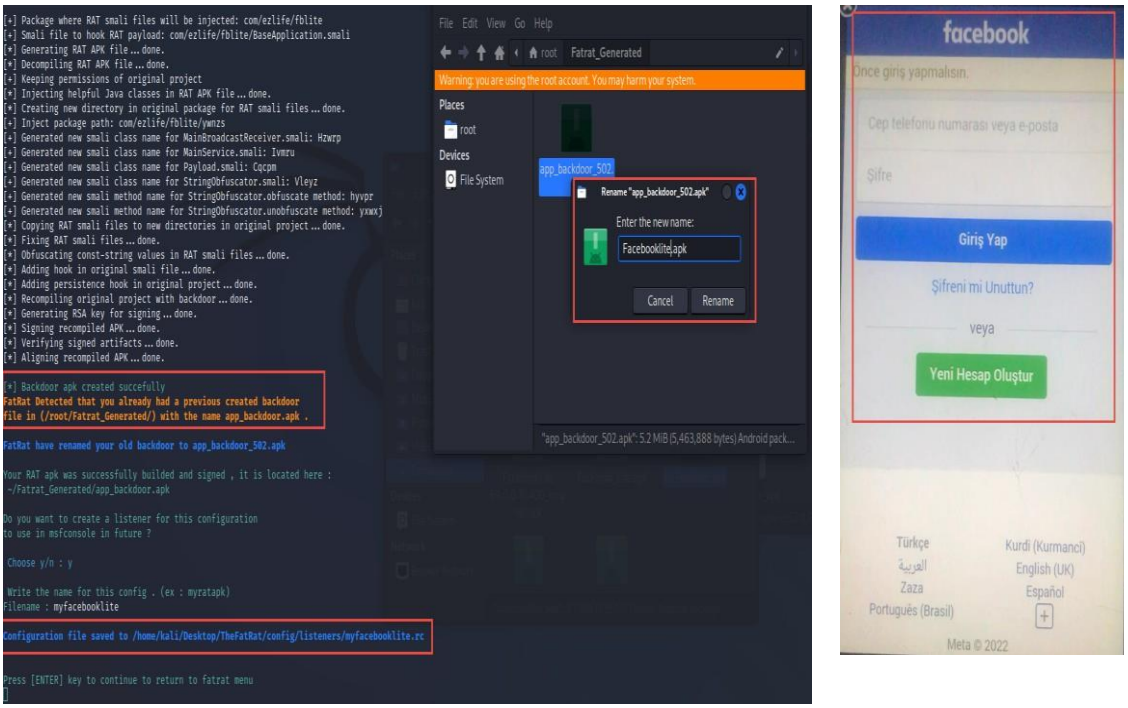


(a) (b)

Figure 1. Creating ransomware apk application. **(a)** Stages of creating the application **(b)** performing penetration testing

3.1.2. Creating malware and performing penetration testing by placing a backdoor in the original apk file

Malware can be created using the TheFatRat tool on the Kali Linux operating system [24]. This tool enables the generation of malicious Trojans and Remote Access Trojans (RATs) targeting Android, Windows, and macOS devices, allowing attacks on user systems. The malicious software generated with TheFatRat employs various payloads designed to evade antivirus scans. As part of the study, a backdoor was embedded into the original Facebook Lite APK file using TheFatRat, resulting in the creation of a malicious APK file. This modified APK was then shared with the target Android user via Google Drive. Once the file was downloaded and executed on the user's device, the attack phase was carried out. Figure 2.a demonstrates the installation of TheFatRat tool. After the backdooring process was applied to the original APK file and configurations were completed, the malicious FacebookLite.apk file was generated. In Figure 2.b, the penetration test is shown, where the user executed the malicious Facebook Lite application on their device. The full process, including the creation of the malicious APK file and its deployment during the penetration test, is detailed in Figure 2. This illustrates the steps from tool setup to the successful execution of the attack.



(a) (b)

Figure 2. Creating malware by placing a backdoor in the original apk file. **(a)** Stages of creating the application **(b)** performing penetration testing

3.1.3. Creating malware and performing penetration testing by manually injecting malicious payload into android application

Malware can also be created by manually injecting a malicious payload into an original Android application. This payload can be generated using msfvenom [25], a tool within the Metasploit framework. By manually injecting the payload into the original photo application, the APK file is modified and recompiled into a malicious version. The recompiled malicious APK file was then transferred to the target device via Bluetooth, infecting the Android device with the malware. Once installed and executed, a penetration test was conducted to analyze the impact and behavior of the malware. The step-by-step process of manually injecting a malicious payload into an original APK file is illustrated in Figure 3, showcasing the creation and deployment of the infected APK for testing purposes.

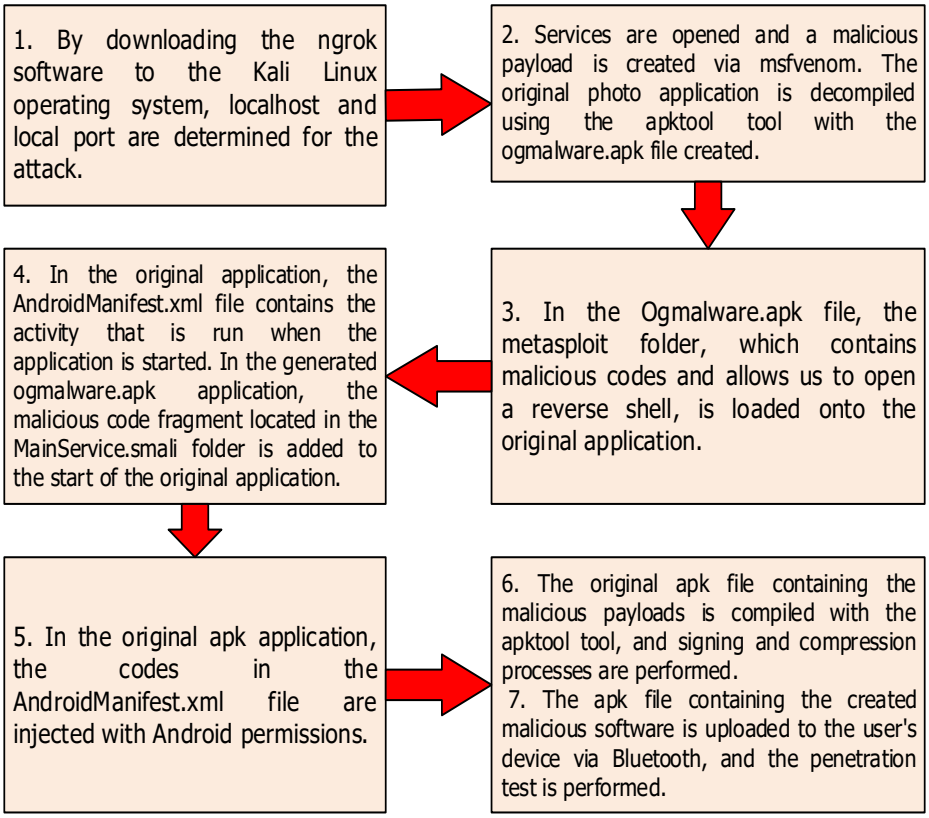


Figure 3. Creating malware and performing penetration testing by manually injecting malicious payload into android application

Examples of penetration testing with the photoeditor.apk file, which was manually injected with a malicious payload, are shown in Figure 4.

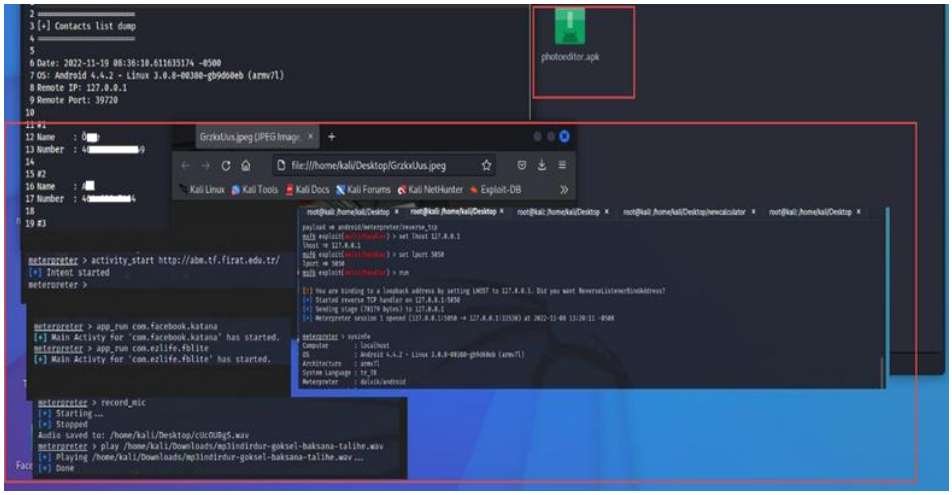


Figure 4. Penetration testing examples with photo editor.apk file

The successful and unsuccessful actions performed in the penetration test scenario performed by creating malicious applications are shown in Table 2.

Table 2. Success status of actions performed with penetration testing

Actions Performed in Penetration Testing	Success Status of Actions Performed with Penetration Testing
Obtaining System Information	+
Monitoring the User in Real Time	-
Obtain Application List on Device	+
Installing Apk File on Device	+
Deleting Apk File on Device	+
Running Application on Device	+
Viewing List of Webcams on Device	+
Taking Photos with Front Camera or Rear Camera	+
Taking Screenshot on Device	-
Viewing Local Date and Time of Device	+
Recording Audio	+
Running Music File on Device	+
Sending SMS	-
Reading SMS	+
Obtaining Call Log List	+
Saving Contact List	+
Obtaining Shell	+
Launching Any URL Address on Device	+
Hiding Application Icon in Launcher	+
Starting Video Chat	-
Locating Location	+
Running Post Module	-
Detecting Whether It Is Running as Root	+

3.2. Methodological analysis of malware on android devices in terms of digital forensics

To achieve the objectives of this study, malicious APK files were installed and executed on a Huawei P7-L10 smartphone with 16 GB storage, running the Android 4.2.2 operating system. The selected model was chosen because it is compatible with Magnet AXIOM and other forensic tools, it uses the ARM architecture that is commonly encountered in test scenarios, and the Huawei brand is widely used worldwide. Using different models together will expand the scope of the study, but each brand has its own security mechanisms and has different processors and chipsets, which can negatively affect the analysis process. The forensic examination of the Android device required the acquisition of both logical and physical images, enabling analysis to be conducted on forensic copies of the data. The analysis process was carried out using Magnet AXIOM, a forensic tool capable of acquiring images, extracting data, performing analysis, and generating reports. Both open-source and commercial software solutions were utilized. For manual examination, the Android device was connected to a computer via a USB cable for direct analysis. The APK files suspected of containing malicious payloads were analyzed using Apktool, which facilitated the decompilation and inspection of the application code. The most common methods used to analyze malware on mobile devices are logical image, physical image, and manual inspection. In order to compare the basic approaches used in mobile device analysis and to evaluate the strengths and weaknesses of each, these three methods were selected and the most powerful and widely used digital forensics tool, Magnet AXIOM, was used. In addition to Magnet AXIOM, there are other digital forensics tools such as UFED, Oxygen Forensics, and Autopsy. However, we decided not to use these tools because of the high license fee of UFED, the challenging user interface of Oxygen, and the fact that the Autopsy tool is not as comprehensive as Magnet AXIOM. A

detailed summary of the software used in the forensic analysis of the Android device is provided in Table 3. This setup ensured comprehensive examination and accurate reporting of findings.

Table 3. Softwares used in android device analysis

The Used Software	Purpose of Use
Apktool 2.6.0	Investigating Tool
Magnet AXIOM 3.0.0	Investigating Tool
Kingo ROOT	Tool for Rooting the Device

3.2.1. Performing forensic analysis of malicious applications with magnet axiom 3.0.0 tool

Magnet AXIOM is a forensic tool designed to collect relevant evidence from various data sources, including smartphones, computers, and cloud platforms. It offers advanced capabilities to visualize and analyze data intelligently, validate extracted information, and consolidate images acquired using other tools into a single case file for streamlined examination. The user interface of Magnet AXIOM allows investigators to select the device to be imaged. This feature facilitates the acquisition of data for forensic analysis while ensuring a systematic and organized workflow. Magnet AXIOM tool can perform logical and physical image acquisition operations. Logical image can capture only active and currently accessible data on a device. It cannot capture deleted data, unallocated space or system areas that are not normally visible to users. It is a better option than physical image for researchers who have time constraints or do not need all system data. Physical image is a process that allows you to take an exact copy of the device. It can also capture data such as unallocated space, deleted data and hidden partitions. It is a better option than logical image for researchers who need in-depth analysis of system artifacts.

The forensic analysis of the Huawei P7-L10 smartphone with 16 GB storage and running Android 4.2.2 began with the acquisition of a logical image using the Magnet AXIOM 3.0.0 forensic tool. Subsequently, the device was rooted using the Kingo ROOT tool, enabling the extraction of a physical image. Both logical and physical images were used to comprehensively analyze the Android device.

Evidence extracted from the browser.db file revealed records of Google Drive URLs accessed at specific dates and times. These URLs were further analyzed on platforms like VirusTotal, where they were identified as malicious. However, attempts to access the URLs resulted in error codes, as shown in Figure 5. This process highlights the steps taken to extract, verify, and analyze digital evidence, providing insights into potentially malicious activities on the device.

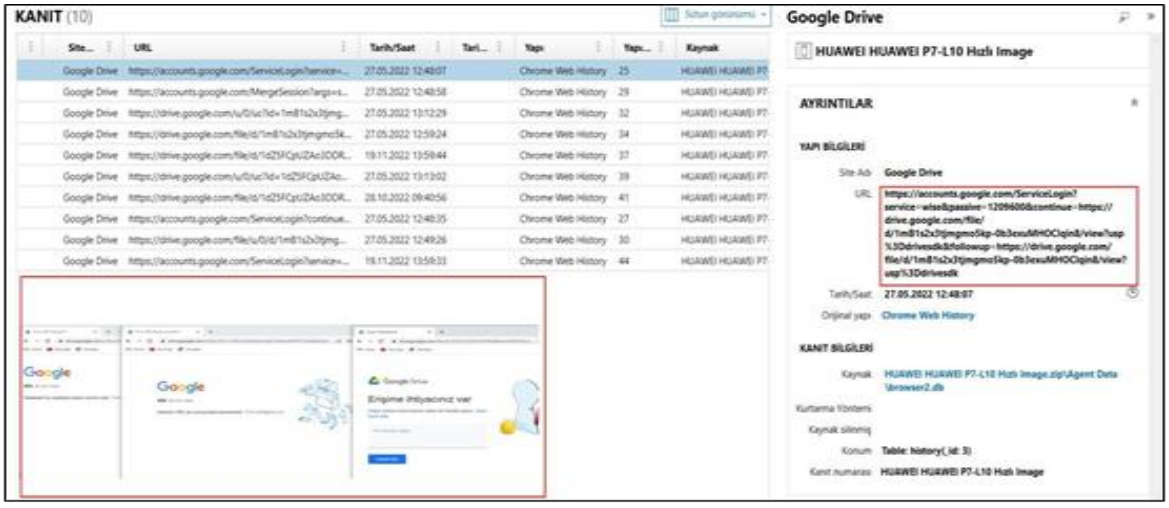
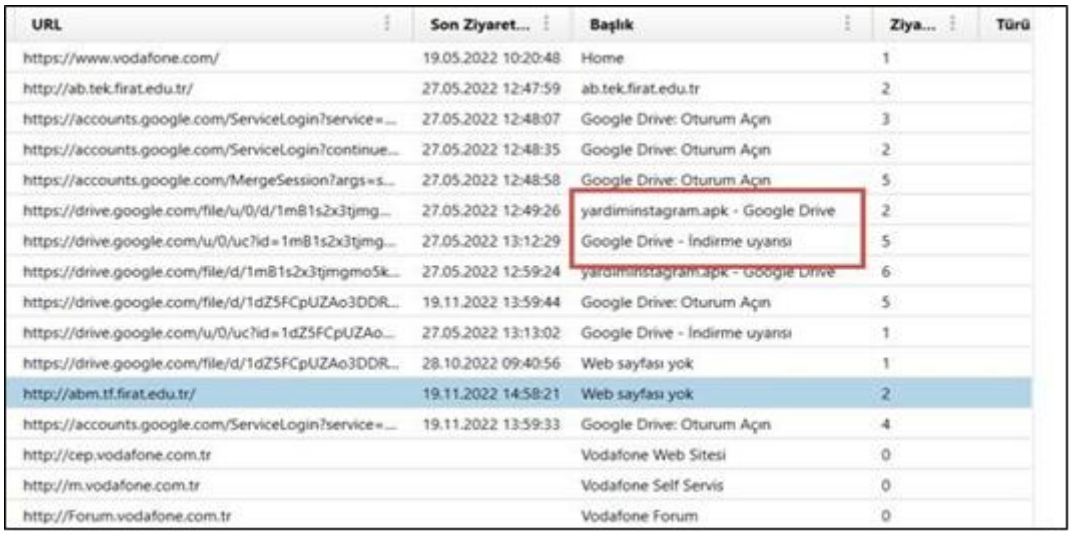


Figure 5. Google drive url addresses findings

Upon examining the evidence from the Chrome Web History, it was observed that while attempting to download the yardiminstagram.apk application from Google Drive, a download warning was displayed. This finding is illustrated in Figure 6, highlighting the browser's detection of potentially unsafe content during the download process.



URL	Son Ziyaret...	Başlık	Ziya...	Türü
https://www.vodafone.com/	19.05.2022 10:20:48	Home	1	
http://ab.tek.firat.edu.tr/	27.05.2022 12:47:59	ab.tek.firat.edu.tr	2	
https://accounts.google.com/ServiceLogin?service=...	27.05.2022 12:48:07	Google Drive: Oturum Açın	3	
https://accounts.google.com/ServiceLogin?continue...	27.05.2022 12:48:35	Google Drive: Oturum Açın	2	
https://accounts.google.com/MergeSession?args=s...	27.05.2022 12:48:58	Google Drive: Oturum Açın	5	
https://drive.google.com/file/u/0/d/1m81s2x3tjmg...	27.05.2022 12:49:26	yardiminstagram.apk - Google Drive	2	
https://drive.google.com/u/0/uc?id=1m81s2x3tjmg...	27.05.2022 13:12:29	Google Drive - İndirme uyarısı	5	
https://drive.google.com/file/d/1m81s2x3tjmgmo5k...	27.05.2022 12:59:24	yardiminstagram.apk - Google Drive	6	
https://drive.google.com/file/d/1dZ5FCpUZAo3DDR...	19.11.2022 13:59:44	Google Drive: Oturum Açın	5	
https://drive.google.com/u/0/uc?id=1dZ5FCpUZAo...	27.05.2022 13:13:02	Google Drive - İndirme uyarısı	1	
https://drive.google.com/file/d/1dZ5FCpUZAo3DDR...	28.10.2022 09:40:56	Web sayfası yok	1	
http://abm.tf.firat.edu.tr/	19.11.2022 14:58:21	Web sayfası yok	2	
https://accounts.google.com/ServiceLogin?service=...	19.11.2022 13:59:33	Google Drive: Oturum Açın	4	
http://cep.vodafone.com.tr		Vodafone Web Sitesi	0	
http://m.vodafone.com.tr		Vodafone Self Servis	0	
http://Forum.vodafone.com.tr		Vodafone Forum	0	

Figure 6. Google drive download warning

Analysis of the findings in the Usage.txt file revealed that after the FacebookLite and PhotoEditor applications were used, the Metasploit framework was executed. This activity is shown in Figure 7, indicating a possible link between the use of these applications and the initiation of malicious actions through Metasploit.

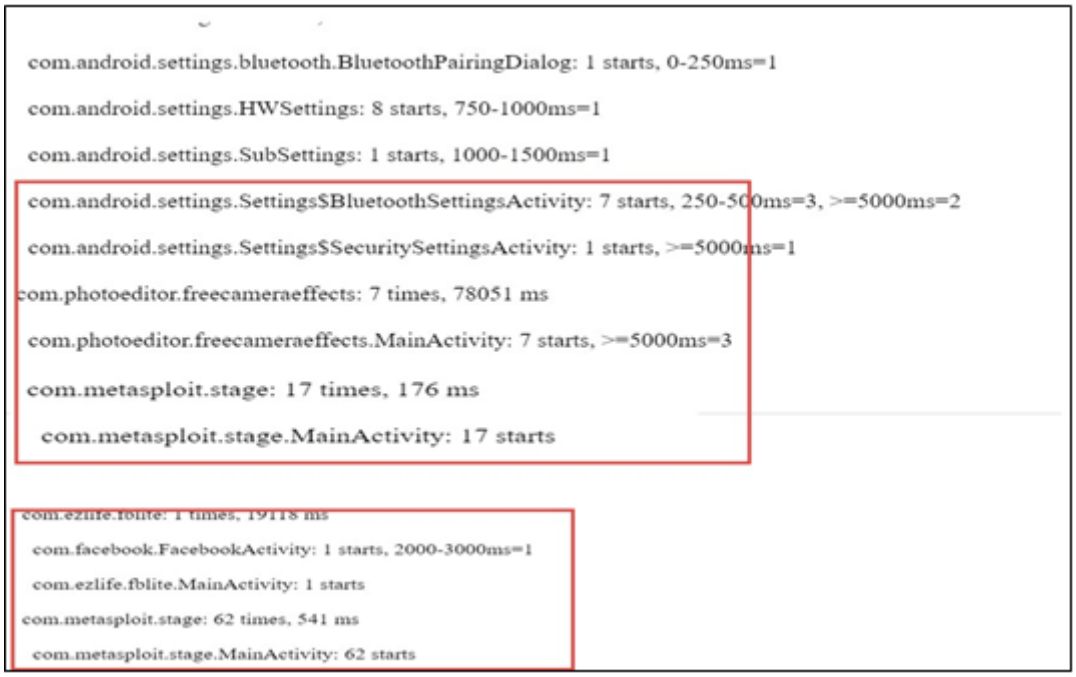


Figure 7. Finding that metasploit was run after applications

Upon examining the carved archived files, it was determined that the instagram.apk and Facebooklite.apk files were downloaded, as shown in Figure 8. This discovery highlights the presence of these malicious APK files on the device, which were likely part of the attack vector used to compromise the system.

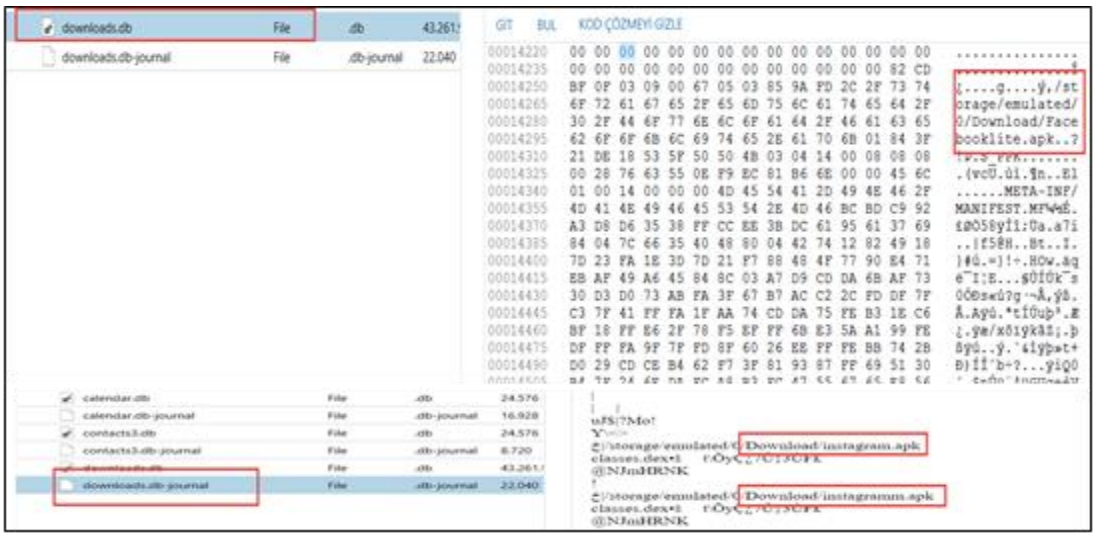


Figure 8. Evidence of downloaded archived apps

The results of the logical and physical image examination conducted with Magnet AXIOM revealed evidence related to the malicious software. These findings are presented in Table 5, which summarizes the key forensic evidence gathered during the analysis.

3.2.2. Performing forensic analysis with manual investigation

The Huawei P7-L10 smartphone with Android 4.4.2 was transferred to a computer via USB cable. The folders in the device's internal storage were manually examined. In the Bluetooth folder, the photoeditor.apk file was found, as shown in Figure 9. This file was uploaded to VirusTotal, where it was identified as malicious by several antivirus engines. The folder containing the photoeditor.apk file and the results of the antivirus analysis are displayed in the figure, confirming the presence of the malicious file on the device.

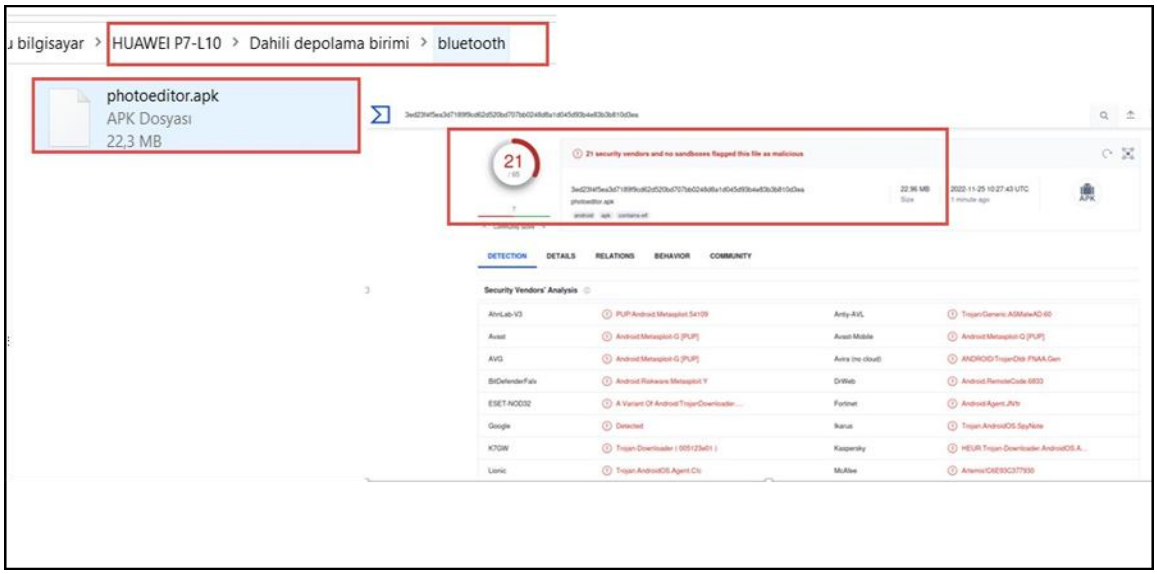


Figure 9. Application installed via bluetooth device with manual investigation

The photoeditor.apk file was decompiled using the Apktool tool for further analysis. The META-INF folder, which contains the signature and metadata of the APK file, was examined. Upon inspection, it was found that the APK file was created by Debian 11.0.6 and was not signed by Google Play, as shown in Figure 10. This indicates that the application is not an official Google Play app, which could be a potential security concern.

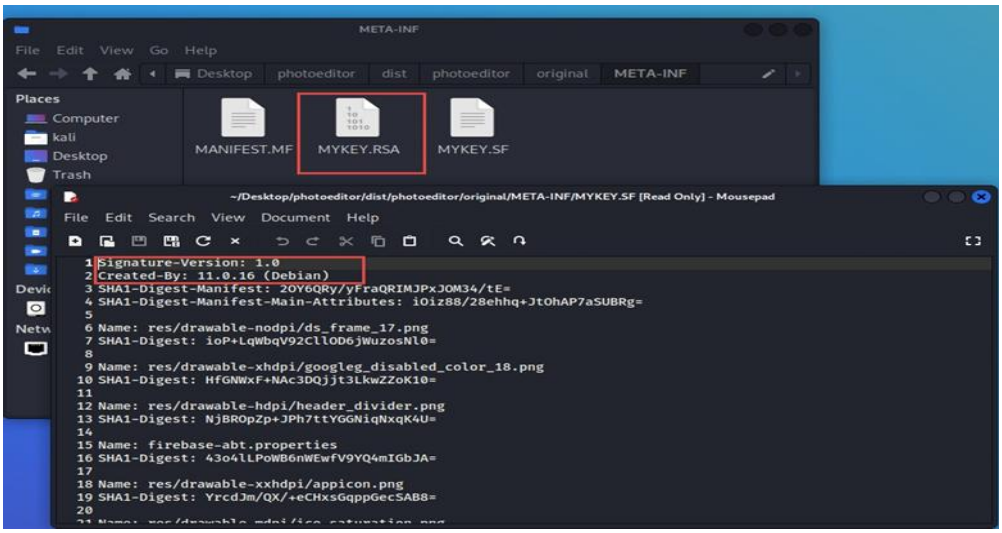


Figure 10. Photoeditor.apk meta-inf file analysis

The decompiled photoeditor.apk file contains a smali folder, which is used by developers to recompile the executable dex files stored within Android application archives. Within the smali folder, a metasploit folder was found, as shown in Figure 11. This folder contains payload.smali, which includes shell code designed to establish a reverse shell. It was determined that these files were included in the original photoeditor.apk, suggesting that the application was crafted with malicious intent, likely to facilitate unauthorized access to the device.

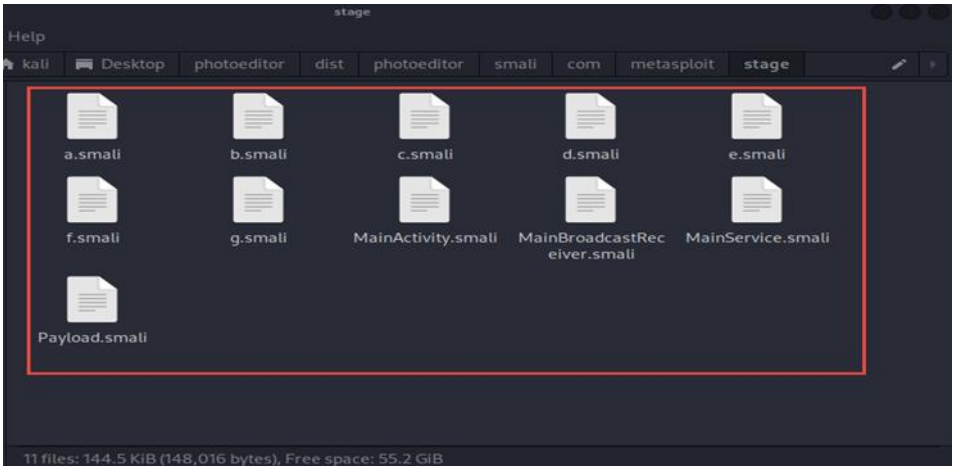


Figure 11. Photoeditor.apk smali folder analysis

The Mainservice.smali file contains commands related to a public method that is accessible by all applications. Figure 12 demonstrates that the analyzed command is designed to execute the payload, as confirmed through method inspection. This indicates that the malicious code within the photoeditor.apk is designed to trigger the payload and potentially compromise the device by running the reverse shell or other malicious actions.

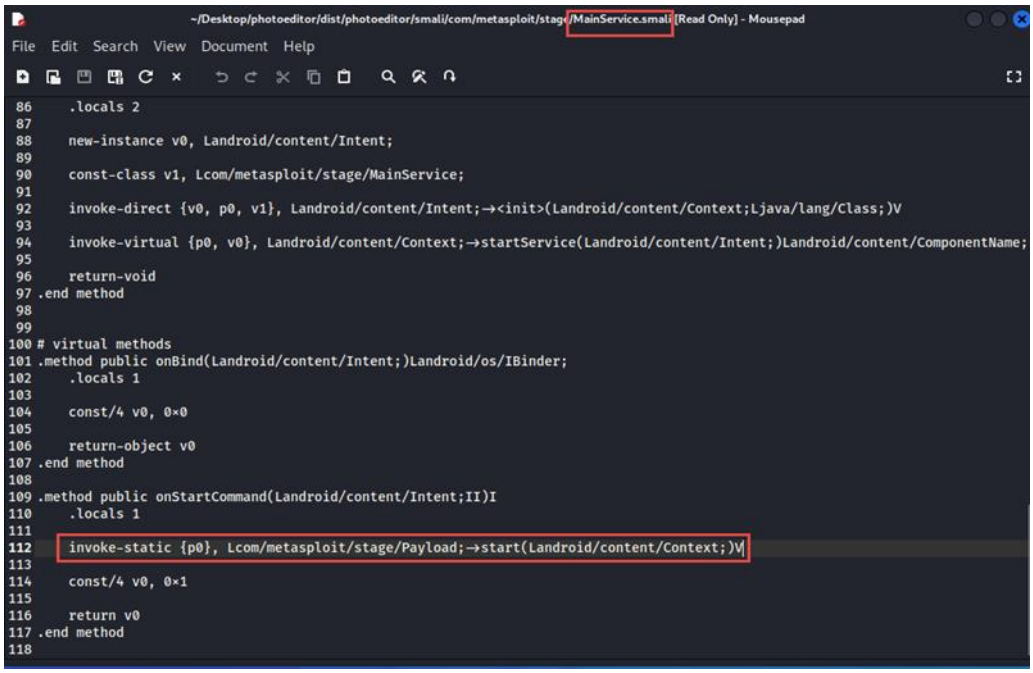


Figure 12. Detection of commands running photoeditor.apk payload

In the AndroidManifest.xml file, the path containing the package name was traced, leading to the MyApplication.smali file. As depicted in Figure 13, the analysis revealed that a command intended to execute the payload had been embedded into the application's startup routine. This indicates that the malicious payload is triggered when the application is launched, allowing it to run as soon as the user interacts with the app.

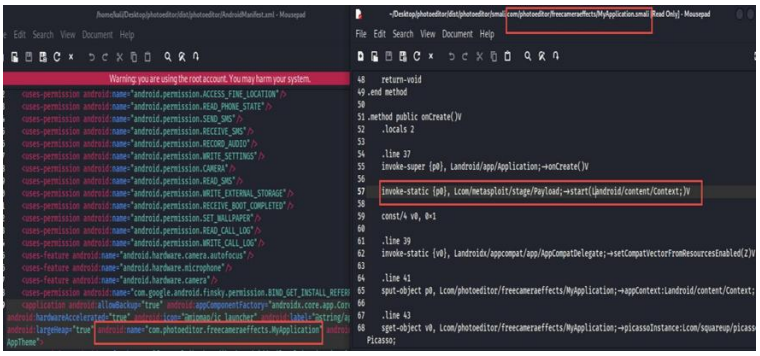


Figure 13. Findings that the photoeditor.apk command was added to the startup of the application

When the application is installed, the AndroidManifest.xml file reveals, as shown in Figure 14, that the app requests a wide range of permissions on the device. These permissions include the ability to read the phone's status/identity, receive/read/send SMS messages, capture images, record audio, access GPS and network-based location, read/write the call log, read messages, read/write/modify/delete the contents of the SD card, view network connections, access the internet, execute on startup, prevent the phone from sleeping, set wallpaper, and modify system settings. These extensive permissions suggest that the application has the potential to perform a variety of intrusive and malicious actions on the device.

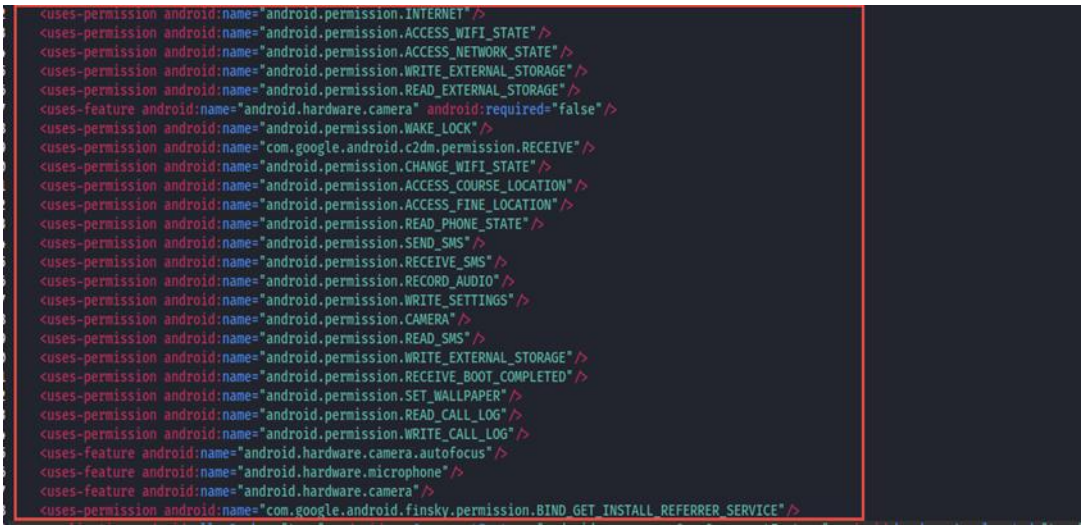


Figure 14. Photoeditor.apk permissions on the device

During the manual examination of the device, multiple APK files were identified within the Downloads directory. These APK files, located within the Downloads folder, are shown in Figure 15. This finding indicates that additional potentially malicious applications may have been downloaded to the device, which could be part of the attack vector used to compromise the system.

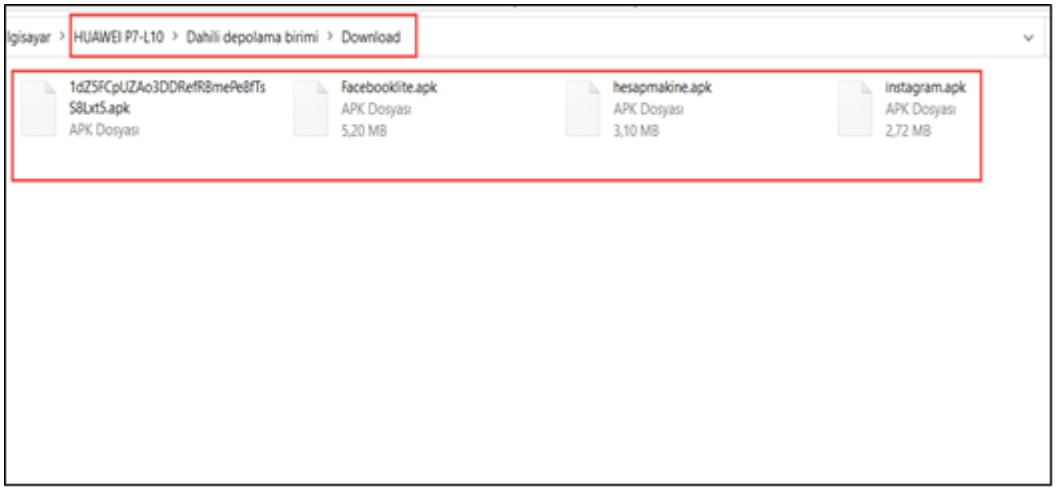


Figure 15. Applications detected in download folder by manual investigation

The instagram.apk file found in the Downloads folder was analyzed by antivirus engines, and as shown in Figure 16, it was identified as malicious. This indicates that the file poses a security threat to the device, potentially containing harmful code designed to exploit vulnerabilities or compromise the device's functionality.

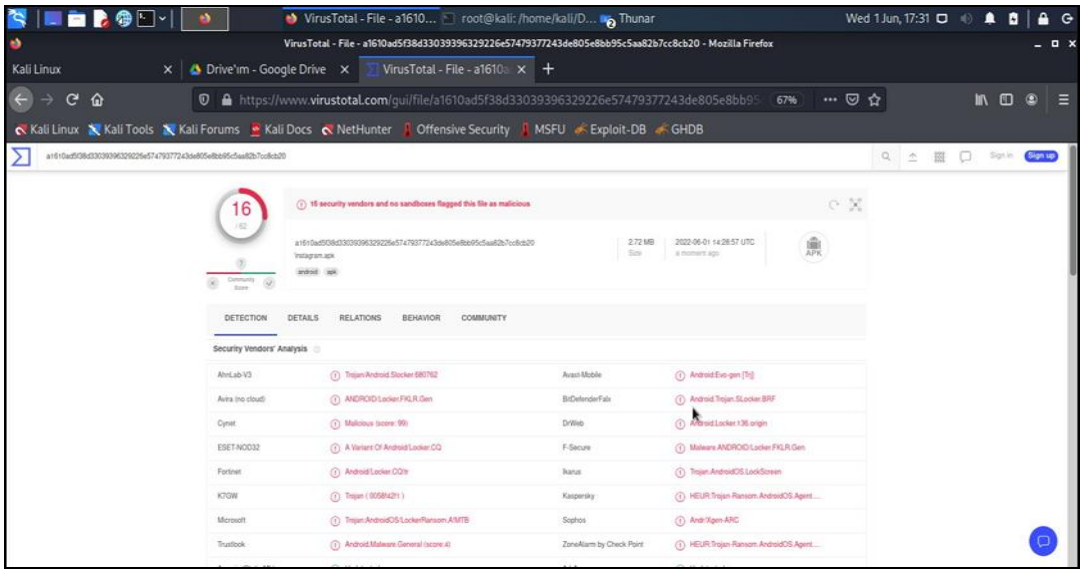


Figure 16. Instagram.apk virustotal analysis

The instagram.apk file was decompiled using the Apktool tool. Analysis of the META-INF directory revealed that the instagram.apk file was generated using Android version 1.0, but the application lacked a valid Google Play signature, as shown in Figure 17. This suggests that the app is unofficial and likely contains malicious code, as it was not verified by Google Play's security processes.

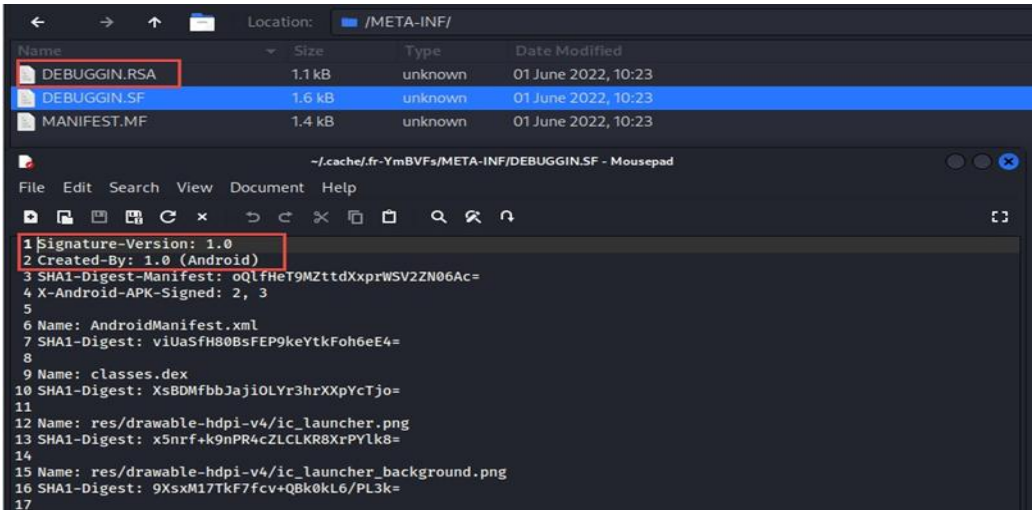


Figure 17. Instagram.apk meta-inf folder analysis

Examination of the AndroidManifest.xml file revealed that the application's package name is 'com.termuxhackers.id', as illustrated in Figure 18. This package name suggests that the application might be related to the Termux environment, which is often used for running command-line utilities on Android. However, given the context, this package name may also indicate a potentially malicious app designed to carry out unauthorized activities on the device.



Figure 18. Instagram.apk application package name

When the application is installed, the AndroidManifest.xml file reveals, as shown in Figure 19, that the app requests several permissions on the device. These permissions include reading messages, capturing images, saving images, accessing location data, reading contacts, reading/modifying/deleting SD card contents, accessing the network, launching applications, executing on startup, and preventing the phone from going into sleep mode. These extensive permissions suggest that the application could perform various intrusive actions on the device, potentially compromising the user's privacy and security.

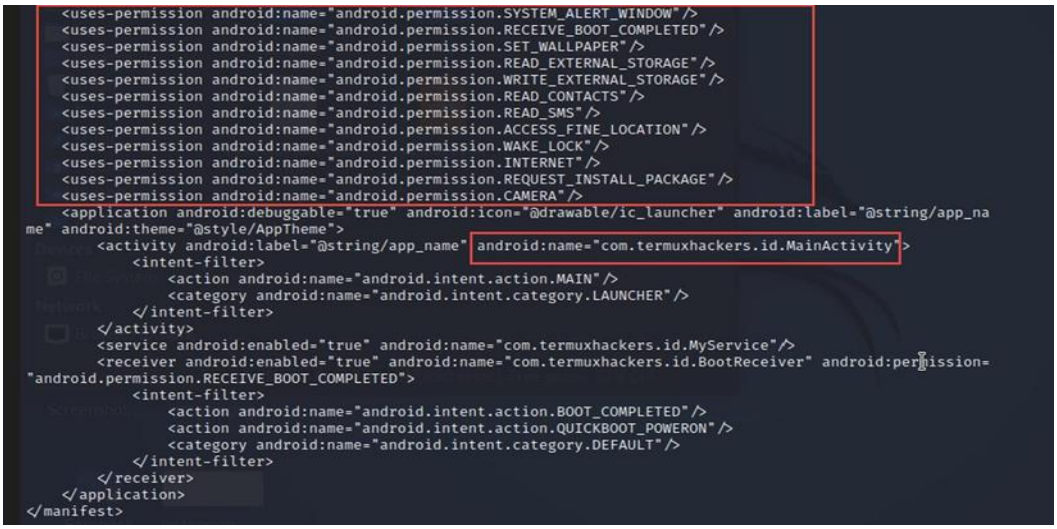


Figure 19. Permissions of instagram.apk application on the device

The Facebooklite.apk file found in the Downloads folder was analyzed by antivirus engines, and as shown in Figure 20, it was identified as malicious. This indicates that the file poses a security risk to the device, potentially containing harmful code designed to compromise the device or steal sensitive information.

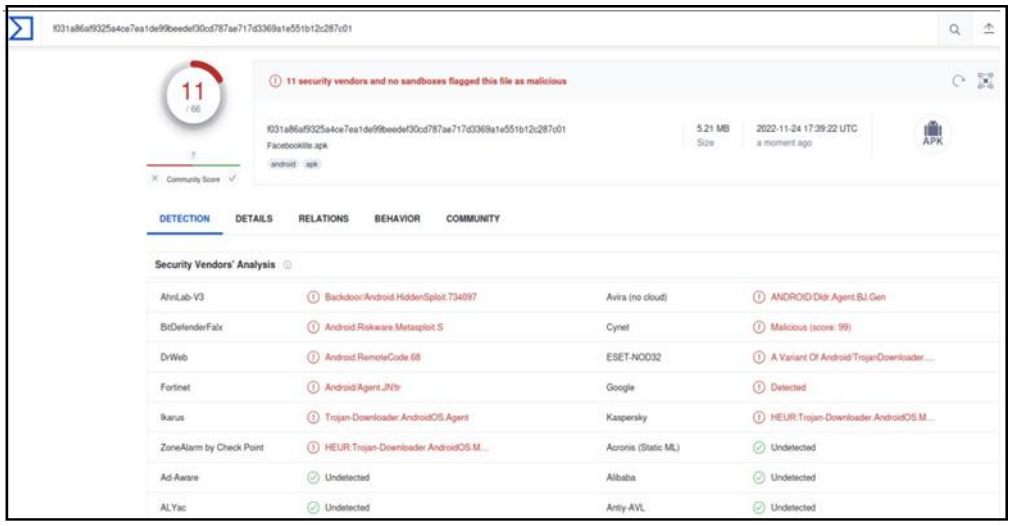


Figure 20. Facebook lite.apk virustotal analysis results

The Facebooklite.apk file was decompiled using the Apktool tool. The META-INF folder, which contains the signature and metadata of the APK file, was examined. Analysis revealed that the Facebooklite.apk file was generated using the Debian 11.0.6 operating system and Google Play did not sign the application, as shown in Figure 21. This suggests that the application is not officially verified and could potentially contain malicious code or other security risks.

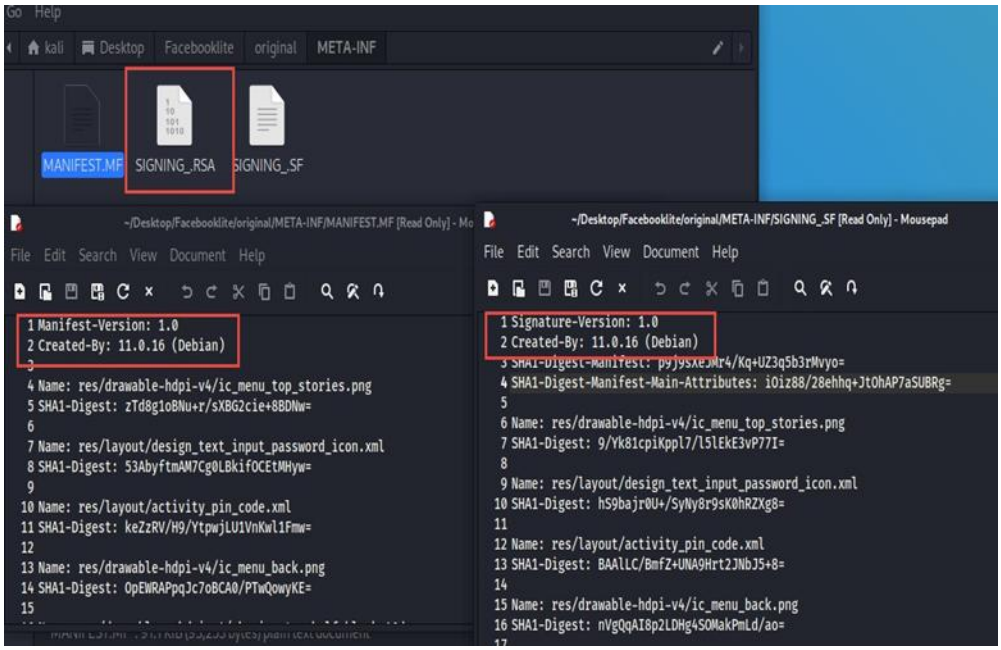


Figure 21. Facebook lite.apk meta-inf folder analysis

Upon tracing the relevant path under the Activity section, a folder named 'dhczs' was found, containing smali files created by the Metasploit tool. Analysis of the smali files revealed the presence of shellcode intended to establish a reverse shell connection. The command responsible for executing the payload was identified, as shown in Figure 22. This confirms that the application is engineered to execute malicious actions, likely allowing unauthorized access to the device or network.

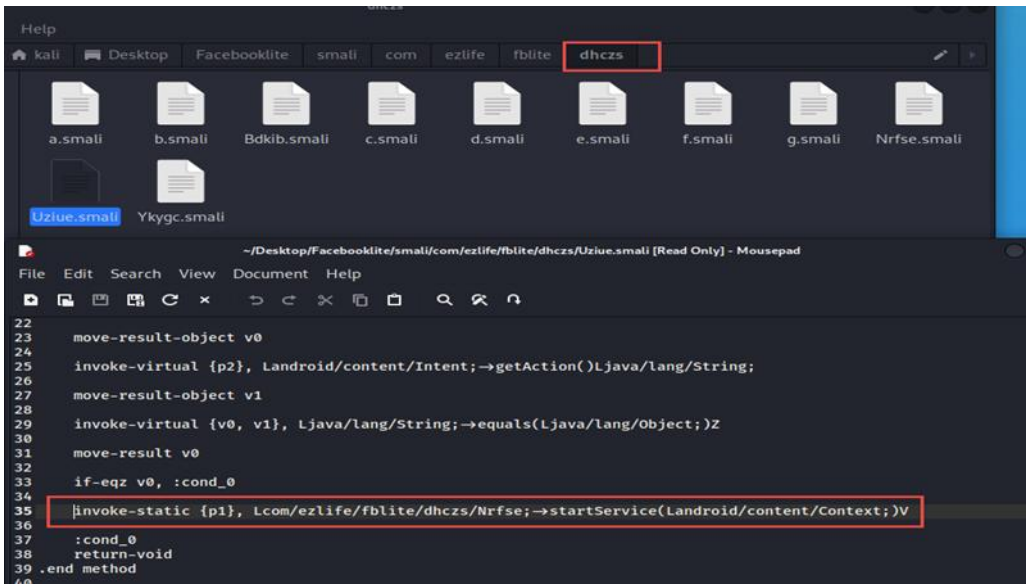


Figure 22. Facebook lite.apk payload running command

Analysis of the AndroidManifest.xml file revealed that the application, upon installation, requests multiple permissions on the device, as illustrated in Figure 23. These permissions include accessing GPS and network-based location, reading/modifying/deleting SD card contents, accessing the network, viewing network connections, retrieving data from the internet, executing on startup, controlling vibration, and preventing the phone from entering sleep mode. These permissions suggest that the application can perform a variety of potentially invasive actions, raising concerns about privacy and security.

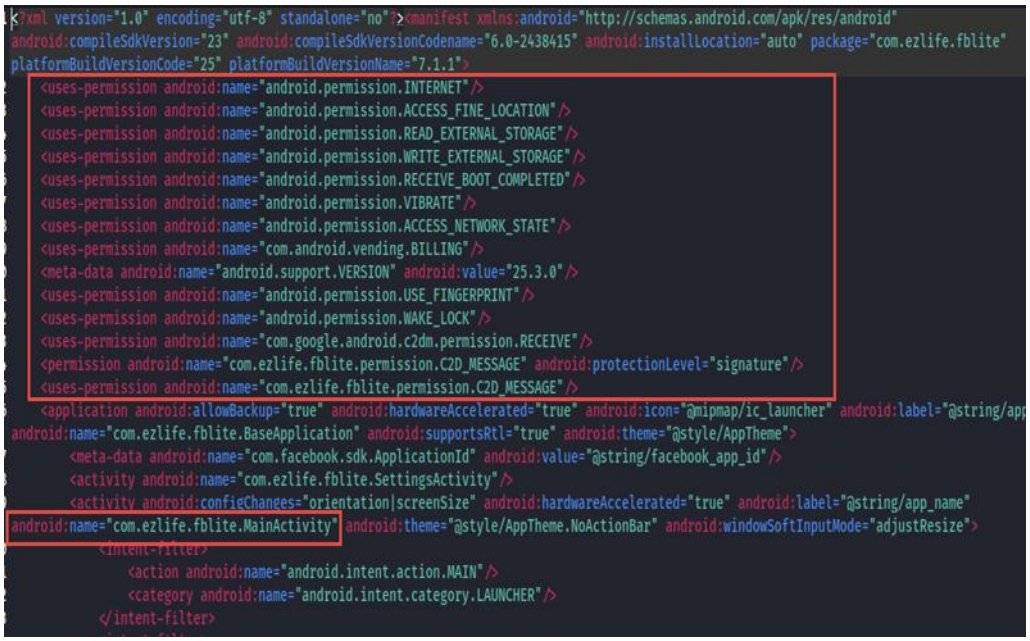


Figure 23. Facebook lite.apk permissions on device

The results of the manual examination, along with the evidence related to the malicious software, are presented in Table 4. This table summarizes the findings from the manual analysis of the device, which helped identify indicators of compromise and the presence of harmful applications on the device.

Table 4. Data obtained on malicious applications as a result of manual review

Evidence Obtained Regarding Malicious Apps	Manuel Investigation
Google Drive Links	+
Apps Installed via Bluetooth	+
Indication of Malicious App Running	-
Deleted Apps	-
Indication of Who Sent the App	-
Indication of Where Metasploit Was Run	-
Web Browser History	+
File of the App Itself	+
Indication of Ransonware App	+
Analysis of Apps	+

4. Findings and Discussions

In this study, the malicious applications created on Android devices running the Android operating system were examined using digital forensics tools. To maintain the integrity of the evidence on the Android device, a forensic copy (image) of the device was first taken, and all analyses were conducted on the image file. Forensic tools were initially used to capture logical images. In the logical imaging process, mobile operating systems allow access to some of the data. The evidence obtained from a logical image typically includes data such as call logs, SMS messages, photos, videos, and audio files. In contrast to logical images, a physical image captures an exact replica of the entire memory of the Android device. With a physical image, it is possible to retrieve data from both the areas the user has access to and from unallocated space, as well as deleted data. Evidence obtained from a physical image includes call logs, SMS messages, photos, videos, deleted messages, deleted call logs, emails, application data, and more. By using a physical image, a more comprehensive investigation can be conducted, allowing access to deleted data and unallocated space that cannot be accessed through logical imaging.

When adequate evidence could not be obtained from the malicious software analysis using logical and physical images, a manual examination could be performed. However, there are risks of data loss in manual examination. Despite this, static and dynamic analysis of APK files that can not be extracted using logical and physical images can be performed through manual methods. Manual examination methods also have limitations in accessing deleted data or all data on the device.

The forensic copies were analyzed using the Magnet AXIOM mobile forensics tool. Based on the analysis, it was determined that the performance of forensic tools used for examining Android devices may vary depending on factors such as the version of the forensic tools, the device's operating system, model, brand, and the version of the applications installed. In the analysis of malicious software on the Android device, detailed findings for these applications could not be obtained. Additionally, it was concluded that the software interfaces of the mobile forensic tools were user-friendly and easy to use.

The analysis results indicated that, in order to access more comprehensive data (such as deleted data or data from unallocated space), a physical image should be created and analyzed. In cases where creating a physical image is not possible (e.g., if root access cannot be granted to the device), logical imaging can be used for further investigations. For static and dynamic analysis of malicious applications on Android devices, manual examination methods can be used.

In conclusion, as shown in Table 5, when examining the performance of logical imaging, physical imaging, and manual examination methods for investigating malicious software on Android devices, the presence of malicious applications was detected in all three methods. However, findings regarding the actions performed by the attacker were not identified using any of the methods. While the logical and physical image methods revealed details about the execution of Metasploit during the installation and execution of the malicious applications, the manual examination method did not uncover how often Metasploit was executed. Evidence of deleted applications was accessible only through the physical image method, and could not be detected through logical or manual examination. While the static and dynamic analysis of applications could not be performed using logical or physical image methods, it was successfully conducted through manual examination.

Table 5. Comparison of malware findings with mobile forensic tools

Evidence Obtained Regarding Malicious Apps	Manual Investigation	Physical Image	Logical Image
Google Drive Links	+	+	+
Apps Installed via Bluetooth	+	+	+
Indication of Malicious App Running	-	+	+
Deleted Apps	-	+	-
Indication of Who Sent the App	-	-	-
Indication of Where Metasploit Was Run	-	-	-
Web Browser History	+	+	+
Analysis of Apps	+	-	-
Indication of Ransomware App	+	+	+

5. Conclusions and Suggestions

In this study, a trojan virus was created by manually injecting payload into the Android device and placing a backdoor into the original apk file using a tool. We created malicious APK files and uploaded them to the Android device via Google Drive and Bluetooth, then performed a penetration testing scenario. TheFatRat and SARA were used in creating malware. These tools are quite powerful in generating malicious files, making them valuable for penetration testing and cybersecurity research. However, they present several limitations that can limit their effectiveness, especially in more advanced or real-world scenarios.

For example, the SARA tool has a complex and user-unfriendly interface, which can be challenging for new users who are not familiar with its operation. Unlike more user-friendly malware creation tools, SARA requires a deeper understanding of its functionality, making it less accessible for beginners. Additionally, SARA is limited to creating only certain types of malware, which means it may not be sufficient for broader research purposes. It lacks the flexibility needed to generate highly customized payloads, which can be a drawback for security professionals looking to test a wide range of threats.

On the other hand, TheFatRat has its own set of disadvantages. One of its biggest weaknesses is that it can now be easily detected by modern antivirus and EDR (Endpoint Detection & Response) solutions. As cybersecurity technologies advance, many signature-based and behavioral-based detection systems have been updated to recognize TheFatRat-generated malware, making it less effective for stealthy operations. Additionally, TheFatRat is not updated frequently enough, which puts it at a disadvantage compared to constantly evolving antivirus software. This lack of regular updates means that newly implemented security measures in operating systems and antivirus programs can quickly render TheFatRat's payloads ineffective. Moreover, both tools lack advanced evasion techniques found in more sophisticated malware creation frameworks. For example, modern penetration testing tools incorporate obfuscation, encryption, and polymorphic techniques to bypass detection. In contrast, TheFatRat and SARA offer limited capabilities in this regard, making them easier targets for security solutions.

A comparison of mobile forensic tools (manual examination, physical image, logical image) was made in terms of performing malware analysis on Android devices in terms of forensic computing. With the advancement of technology, the use of mobile devices is increasing day by day. With the increase in the number of mobile device users, mobile operating systems are updated and devices with different operating systems are released to the market. For this reason, mobile devices play a major role in committing cybercrimes. The importance of evidence obtained from mobile devices in a forensic investigation in clarifying the investigation was mentioned. With the increase in cybercrimes, crimes committed using informatics have brought about the concept of forensic computing. A general definition of digital forensics was made and the stages of identification, protection, examination, analysis and reporting used in digital forensics processes were mentioned, and it was mentioned that digital forensics is divided into different sub-branches due to the variety of devices and their different features. In order to perform the forensic examination of mobile devices correctly; mobile device types (smartphones, tablets, wearable devices etc.), operating systems of mobile devices (Palm OS, Windows Mobile OS, IOS, Android OS etc.), stages of digital forensics process of mobile devices, types of data collection from mobile devices (physical acquisition, logical acquisition, manual acquisition), digital forensics software that examines mobile devices (Cellebrite, Oxygen Forensic, Paraben, Magnet AXIOM, MOBILEdit Forensic, SAFT etc.) and the problems that may be encountered in the forensic examination of mobile devices were mentioned.

Nowadays, mobile devices used by users are the target focus of attackers. Android devices, which have a high market share among mobile device types, have many potential attack vectors where the attacker tries to gain unauthorized access to the data stored on the device and transferred by the device. The types of malware that are attack vectors (Ransonware, trojan, scareware, virus, worm, etc.) are mentioned and information is given about malware analysis techniques (static analysis, dynamic analysis, hybrid analysis). The precautions that can be taken to protect against malware on mobile devices are mentioned.

Finally, a penetration test scenario was performed by creating malicious applications containing Ransonware and trojan for the Android device with the Android operating system. After the penetration test process was completed, 49 examinations of malware analysis on the Android device were carried out in terms of forensic computing. Analysis of malware on the Android device was performed using Magnet AXIOM forensic computing software on logical and physical image files. Static and dynamic analysis of malicious applications was performed with the manual examination method. As a result of the examinations, when the logical image, physical image and manual examination performances were examined for malware examination on the Android device, the presence of malicious applications was detected in three examination methods. No findings were found with the three examination methods regarding the actions taken by the attacker. The number of times Metasploit was executed could be determined through logical and physical imaging, while this detail was not recoverable using manual inspection. Deleted applications were only

recoverable through physical imaging, not through logical or manual methods. Static and dynamic analyses were achievable only through manual inspection, as logical and physical methods lacked access to the necessary runtime data. Thus, logical and physical imaging, when used with appropriate forensic tools, can jointly support a reliable malware analysis process on Android devices. It has been observed that at the point where the findings of malicious applications are detected, the manual examination method should be preferred and the static and dynamic analysis of the applications should be performed.

The performances of manual image, logical image and physical image methods are compared with their performances in obtaining 9 specially selected statements such as Indication of Where Metasploit Was Run, Indication of Who Sent the App. At the end of the comparison, manual examination managed to obtain 55.56% of the features we selected. This rate is 66.67% in physical image and 55.56% in logical image, which is the same rate as manual examination. In our future work, we aim to incorporate a greater variety of mobile devices and utilize a wider range of forensic tools to enhance the depth and scope of our research. By analyzing multiple devices with different operating systems, hardware configurations, and security features, we will be able to assess how various forensic methods perform across diverse environments. Additionally, integrating multiple forensic tools will allow us to compare their efficiency, accuracy, and effectiveness in extracting and analyzing digital evidence. This comparative approach will help identify the strengths and limitations of each tool, ultimately leading to more reliable and validated forensic methodologies. By expanding our research in this way, we aim to provide valuable insights for future researchers by offering a more comprehensive dataset, identifying best practices, and uncovering potential forensic challenges. The findings from our future studies will not only contribute to the field of digital forensics but also serve as a reference for investigators, law enforcement agencies, and cybersecurity professionals working on similar scopes.

This study contributes to the field of mobile forensics by presenting a realistic penetration testing scenario using custom Android malware and evaluating forensic analysis methods (logical, physical, and manual) for their effectiveness in detecting malicious applications. It also highlights the limitations of popular malware tools and the strengths of manual analysis in uncovering hidden evidence. Additionally, it emphasizes the need for continuously updated forensic tools due to frequent Android updates and recommends the use of at least two forensic tools for reliable evidence collection. The study further underlines the importance of hands-on training, sharing of forensic experiences, and establishing a general framework, especially considering the challenges posed by licensed forensic tools that limit widespread expert training.

6. Acknowledgments

This study was supported by Fırat University Scientific Research Projects Coordination Unit (FÜBAP) with the project protocol number TEKF.21.36.

7. Author Contribution Statement

Author 1 contributed to the writing of the original draft and experiments. Author 2 was involved in writing, reviewing and editing. Author 3 conceptualized the study and was involved in editing and reviewing.

8. Ethics Committee Approval and Conflict of Interest

“There is no conflict of interest with any person/institution in the prepared article”

9. Ethical Statement Regarding the Use of Artificial Intelligence

No artificial intelligence-based tools or applications were used in the preparation of this study. The entire content of the study was produced by the author in accordance with scientific research methods and academic ethical principles.

10. References

[1] Y. Korkmaz and A. Boyacı, "Audio analysis in terms of digital forensics," Sci. Eng. J. Fırat Univ., vol. 30, no. 1, pp. 329–343, 2018.
[2] C. Aliusta and R. Benzer, "The Council of Europe's Convention on Cybercrime and Turkey's inclusion process," Int. J. Inf. Secur. E., vol. 4, no. 2, pp. 35–42, 2018.
[3] H. Arshad, A. B. Jantan, and O. I. Abiodun, "Digital forensics: Review of issues in scientific validation of digital evidence," J. Inf. Process. Syst., vol. 14, no. 2, pp. 346–376, 2018.
[4] B. Önel and E. Irmak, "Computer forensics and examination of digital evidence on Windows operating system," J. Polytech., vol. 24, no. 3, pp. 1187–1196, 2021.
[5] J. N. D. Gupta, E. Kalaimannan, and S. M. Yoo, "A heuristic for maximizing investigation effectiveness of digital forensic cases involving multiple investigators," Comput. Oper. Res., vol. 69, pp. 1–9, 2016.
[6] A. Almuqren, H. Alsuwaelim, M. M. H. Rahman, and A. A. Ibrahim, "A systematic literature review on digital forensic investigation on Android devices," Procedia Comput. Sci., vol. 235, pp. 1332–1352, 2024.
[7] K. Gözde, A. Akhan, and Z. Abdül Halim, "Security in mobile devices—Threats and basic strategies," Istanbul Commer. Univ. J. Sci., vol. 15, no. 30, pp. 55–75, 2016.
[8] Y. Bal and N. Arıcı, "Mobile-based learning materials preparation," J. Inf. Technol., vol. 4, no. 1, pp. 7–12, 2011.
[9] K. D. Lutes and R. P. Mislan, "Challenges in mobile phone forensics," in Proc. IICS IMETI, Florida, USA, vol. 1, pp. 348–352, 2008.
[10] V. Rao and A. S., "Survey on Android forensic tools and methodologies," Int. J. Comput. Appl., vol. 154, no. 8, pp. 17–21, 2016.
[11] A. Adekotujo, A. Odumabo, A. Adedokun, and O. Aiyeniko, "A comparative study of operating systems: Case of Windows, UNIX, Linux, Mac, Android, and iOS," Int. J. Comput. Appl., vol. 176, no. 39, pp. 16–23, 2020.
[12] C. M. da Silveira et al., "Methodology for forensics data reconstruction on mobile devices with Android operating system applying in-system programming and combination firmware," Appl. Sci., vol. 10, no. 12, 2020.
[13] S. G. Punja and R. Mislan, "Mobile device analysis," Small Scale Digit. Device Forensics, vol. 2, no. 1, pp. 1–16, 2008.
[14] O. Osho and S. O. Ohida, "Comparative evaluation of mobile forensic tools," Int. J. Inf. Technol. Comput. Sci., vol. 8, no. 1, pp. 74–83, 2016.
[15] H. Abualola, H. Alhawai, M. Kadadha, H. Otrok, and A. Mourad, "An Android-based Trojan spyware to study the NotificationListener service vulnerability," Procedia Comput. Sci., vol. 83, pp. 465–471, 2016.
[16] P. Teufl, M. Ferk, A. Fitzek, D. Hein, S. Kraxberger, and C. Orthacker, "Malware detection by applying knowledge discovery processes to application metadata on the Android Market (Google Play)," Secur. Commun. Netw., vol. 9, pp. 389–419, 2016.
[17] D. Kasiaras, T. Zafeiropoulos, N. Clarke, and G. Kambourakis, "Android forensic data analyzer (AFDA): An open-source tool to automatize event correlation analysis on Android devices," Int. J. Inf. Secur. Res., vol. 4, no. 4, pp. 501–509, 2014.
[18] M. C. Coşguner, "Implementing hybrid Android sandbox for malware analysis on Android platform," M.S. thesis, Sakarya Univ., Inst. Nat. Sci., Sakarya, Türkiye, 2019.
[19] F. Tong and Z. Yan, "A hybrid approach of mobile malware detection in Android," J. Parallel Distrib. Comput., vol. 103, pp. 22–31, 2017.
[20] S. Ullah et al., "The revolution and vision of explainable AI for Android malware detection and protection," Internet Things, vol. 27, p. 101320, Aug. 2024.
[21] F. Nawshin, R. Gad, D. Ünal, A. K. Al-Ali, and P. N. Suganthan, "Malware detection for mobile computing using secure and privacy-preserving machine learning approaches: A comprehensive survey," Comput. Electr. Eng., vol. 117, 2024.
[22] L. Li et al., "Static analysis of Android apps: A systematic literature review," Inf. Softw. Technol., vol. 88, pp. 67–95, 2017.

[23] E. Dushku, M. M. Rabbani, M. Conti, L. V. Mancini, and S. Ranise, "SARA: Secure asynchronous remote attestation for IoT systems," IEEE Trans. Inf. Forensics Secur., vol. 15, pp. 3123–3136, 2020.
[24] D. Samociuk, "Antivirus evasion methods in modern operating systems," Appl. Sci., vol. 13, no. 8, 2023.
[25] S. Raj and N. K. Walia, "A study on Metasploit framework: A pen-testing tool," in Proc. Int. Conf. Comput. Perform. Eval. (ComPE), Meghalaya, India, Jul. 2–4, pp. 296–302, 2020.

Fırat Üniversitesi Deneysel ve Hesaplamalı Mühendislik Dergisi

FUJECE

Görüntü Tabanlı Kötü Amaçlı Yazılım Sınıflandırması için Hibrit Bir Derin Öğrenme Yaklaşımı

Zülfiye Beyza METİN [1*], Fatih ÖZKAYNAK [2]

[1,2]Yazılım Mühendisliği Bölümü, Teknoloji Fakültesi, Fırat Üniversitesi, Elazığ, Türkiye.
[1]zbmetin@firat.edu.tr, [2]ozkaynak@firat.edu.tr

Geliş Tarihi: 10.11.2024
Kabul Tarihi: 9.08.2025

Düzeltme Tarihi:30.12.2024

doi: https://doi.org/10.62520/fujece.1582676
Araştırma Makalesi

Alıntı: Z. B. Metin ve F. Özkaynak,'' Görüntü tabanlı kötü amaçlı yazılım sınıflandırması için hibrit bir derin öğrenme yaklaşımı", Fırat Üni. Deny. ve Hes. Müh. Derg., vol. 5, no 1, pp. 26-43, Şubat 2026.

Öz

Kötü amaçlı içeriklerin çeşitliliği ve karmaşıklığı, Bilgi ve İletişim Teknolojilerinin son kullanıcılarını önemli ölçüde etkilemiştir. Kötü amaçlı içeriklerin etkisini azaltmak için, kullanıcı sistemlerini kötü amaçlı yazılımlara karşı proaktif olarak korumak üzere otomatikleştirilmiş derin öğrenme tabanlı teknikler geliştirilmiştir. Bu çalışmada, MaleVis veri setini kullanarak kötü amaçlı yazılımların tespiti ve sınıflandırılması için hibrit bir model uyguluyoruz. İlk olarak, veri setinden özellik çıkarma işlemi DenseNet-121, EfficientNet-B0 ve ResNet-50 modelleri kullanılarak gerçekleştirilmiştir. Bu modeller, büyük veri setleri üzerinde eğitilmiş ve güçlü özellik çıkarma yetenekleriyle bilinen derin öğrenme mimarileridir. Her model, Malevis veri setindeki görüntülerden özellik vektörleri çıkarmak için kullanılmıştır. Bu özellik vektörleri daha sonra birleştirilmiştir. Birleştirilen özellik vektörleri, güçlü bir sınıflandırma algoritması olan XGBoost kullanılarak sınıflandırma için kullanılmıştır. Bu hibrit model yaklaşımı, kötü amaçlı yazılımları tespit etmek için derin öğrenme modellerinin özellik çıkarma yeteneklerini XGBoost'un sınıflandırma yeteneği ile birleştirir. Deney sonuçları, önerilen hibrit modelin MaleVis veri setinde yüksek doğruluk oranları elde ettiğini göstermektedir. Çalışma, farklı derin öğrenme modellerinin özellik çıkarma yeteneklerini birleştirmenin ve bu özellikleri XGBoost gibi bir sınıflandırıcıyla kullanmanın kötü amaçlı yazılımların algılanması ve sınıflandırılmasında önemli iyileştirmeler sağlayabileceğini göstermektedir. Sonuçlar, modelin gerçek dünyadaki tehdit algılama sistemlerine entegre edilme potansiyelini ortaya koymaktadır.

Anahtar kelimeler: Kötü amaçlı yazılım, Derin öğrenme, Bilgi ve iletişim teknolojileri, Malevis veri seti

[*]Yazışılan yazar

İntihal Kontrol: Evet – Turnitin
Şikayet: fujece@firat.edu.tr
Telif Hakkı ve Lisans: Dergide yayın yapan yazarlar, CC BY-NC 4.0 kapsamında lisanslanan çalışmalarının telif hakkını saklı tutar.

Firat University Journal of Experimental and Computational Engineering

A Hybrid Deep Learning Approach for Image-based Malware Classification

Zülfiye Beyza METİN [1*], Fatih ÖZKAYNAK [2]

[1,2]Software Engineering, Faculty of Technology, Firat University, Elazığ, Türkiye.
[1]zbmetin@firat.edu.tr, [2]ozkaynak@firat.edu.tr

Received: 10.11.2024
Revision:30.12.2024
doi: https://doi.org/10.62520/fujece.1582676
Accepted: 9.08.2025
Research Article

Citation: Z. B. Metin and F. Özkaynak, "A hybrid deep learning approach for ımage-based malware classification", Firat Univ. Jour.of Exper. and Comp. Eng., vol. 5, no 1, pp. 26-43, February 2026.

Abstract

The diversity and sophistication of malicious content has significantly impacted end-users of Information and Communication Technologies. In order to mitigate the impact of malicious content, automated deep learning-based techniques have been developed to proactively defend user systems against malware. In this study, we implement a hybrid model for malware detection and classification using the MaleVis dataset. First, feature extraction from the dataset is performed using DenseNet-121, EfficientNet-B0 and ResNet-50 models. These models are deep learning architectures that have been trained on large datasets and are known for their powerful feature extraction capabilities. Each model was used to extract feature vectors from the images in the Malevis dataset. These feature vectors were then merged. The combined feature vectors were used for classification using XGBoost, a powerful classification algorithm. This hybrid model approach combines the feature extraction capabilities of deep learning models with the classification capability of XGBoost to detect malware. Experimental results show that the proposed hybrid model achieves high accuracy rates on the MaleVis dataset. The study shows that combining the feature extraction capabilities of different deep learning models and using these features with a classifier such as XGBoost can provide significant improvements in malware detection and classification.The results demonstrate the model's potential for integration into real-world threat detection systems.

Keywords: Malware, Deep learning, Information and communication technologies, Malevis dataset

[*]Corresponging author

Plagiarism Checks: Yes – Turnitin
Complaints: fujece@firat.edu.tr
Copyright & License: Authors publishing with the journal retain the copyright to their work licensed under the CC BY-NC 4.0

1. Introduction

In recent years, the internet has become an integral part of everyday life for almost every member of society. Activities such as social interactions, online banking, health-related transactions, and marketing are almost impossible to carry out without the internet. As the internet has developed rapidly, criminals have increasingly turned to committing crimes online rather than in the physical world [1]. These cybercriminals use malicious software, commonly known as malware, to launch attacks on targeted machines [2]. Any software designed to intentionally execute malicious payloads on devices such as computers, smartphones, and networks is classified as malware [3]. There are several types of malware, including viruses, worms, Trojans, rootkits, and ransomware, each designed to infect the compromised system in different ways, such as damaging the system, enabling remote code execution, or stealing confidential data [4].

The classification of malware has become increasingly difficult due to the emergence of malware that exhibits characteristics of more than one type simultaneously. In the early days, malware was created for simpler purposes and was therefore easier to detect, often referred to as traditional or simple malware. Today, however, malware has evolved into more destructive and harder-to-detect forms, known as next-generation malware [5]. This new generation of malware can run in kernel mode and bypass protection software such as firewalls and antivirus programs. Unlike traditional malware, which usually consists of a single process and uses simple techniques, next-generation malware employs multiple processes and obfuscation techniques to hide and persist in the system [6]. These advanced malware strains can launch unprecedented and more devastating attacks, often involving multiple malware strains simultaneously [7].

Detecting these malicious programs is essential to protect users and organizations from malware [8]. Malware detection is the process of determining whether a particular program is malicious. Initially, signature-based detection approaches were widely used, but they have limitations, especially in detecting unknown and next-generation malware. Over time, researchers have developed new approaches such as behavioral, heuristic, and model-checking based detection. Data mining and machine learning (ML) algorithms are also increasingly applied in malware detection [9]. Recently, advanced techniques based on deep learning have emerged [10], showing promise in detecting both known and unknown malware [11]. Several studies have explored image-based malware classification. Nataraj et al. [12] visualized malware binaries as grayscale images and used similarity calculations to classify malware into families, achieving 98% classification accuracy. Similarly, Makandar et al. [13] applied Support Vector Machines (SVM) for malware classification, reaching 98.88% accuracy. Ni et al. [14] converted malware opcodes into grayscale images and achieved 99.26% accuracy. Qiao et al. [15] visualized malware binaries as multi-channel images and employed the LeNet5 model, obtaining 98.76% accuracy. Xiao et al. achieved 99.7% accuracy using deep learning-based feature extraction methods. Vu et al. [16] proposed pixel encoding and byte arrangement from binaries into images using space-filling curves, combining entropy coding and a character class scheme over the Hilbert curve, and achieved 93.01% accuracy. Vasan et al. [17] transformed malware binaries into colored images for multi-class classification using an ESA architecture, transfer learning, and data augmentation, achieving 98.82% accuracy on the Malimg dataset and 97.35% on an IoT Android dataset, noting that colored images outperformed grayscale. Khan et al. [18] classified malware on MMCC datasets using ESA architectures (Inceptionv4, ResNet18, ResNet34, ResNet50, ResNet101, ResNet152) and found that ResNet152 achieved the best test accuracy of 88.36%.

Machine learning and deep learning-based methods have proven effective in detecting malware, especially in large datasets [19]. However, each method has limitations. Therefore, hybrid approaches that combine different methods can enhance detection. Hybrid models leverage the feature extraction capabilities of deep learning models with robust classifiers such as XGBoost, providing higher accuracy in malware detection. In this study, we propose a hybrid model for malware detection using pre-trained deep learning models, including ResNet-50, EfficientNet-B0, and DenseNet-121. Features extracted by these models are combined with an XGBoost classifier to classify malware. The aim of the study is to enhance existing detection methods and achieve higher accuracy in malware detection.

2. Material and Methods

This paper proposes a deep learning-based hybrid method for the automatic and effective detection of malware. In the proposed method, we process input data using state-of-the-art and popular deep learning models such as ResNet-50, EfficientNet-B0, and DenseNet-121. These models are selected primarily for their image-based and generalizable feature extraction capabilities, which demonstrate high performance across different datasets. Each network extracts meaningful and abstract features from the input data and represents them as high-dimensional feature vectors. However, a summarization step is required to make these features directly usable for classification. For this purpose, we employ a Global Average Pooling layer to summarize feature maps.

We then combine the summarized feature vectors during the feature fusion stage, allowing the strengths of each deep learning model to be utilized, resulting in a rich, unified feature vector. This step enables the capture of more meaningful and discriminative features by consolidating the inference power of different networks under a single representation. As a result, the classification performance is significantly improved. In the final stage, we train the combined feature vector using XGBoost, a powerful gradient boosting algorithm. XGBoost demonstrates superior performance compared to other traditional machine learning algorithms due to its high discriminative capacity and ability to model complex data relationships. This computationally efficient algorithm effectively handles noise in the dataset, enabling more accurate classifications.A block diagram of the proposed hybrid method is presented in Figure 1.

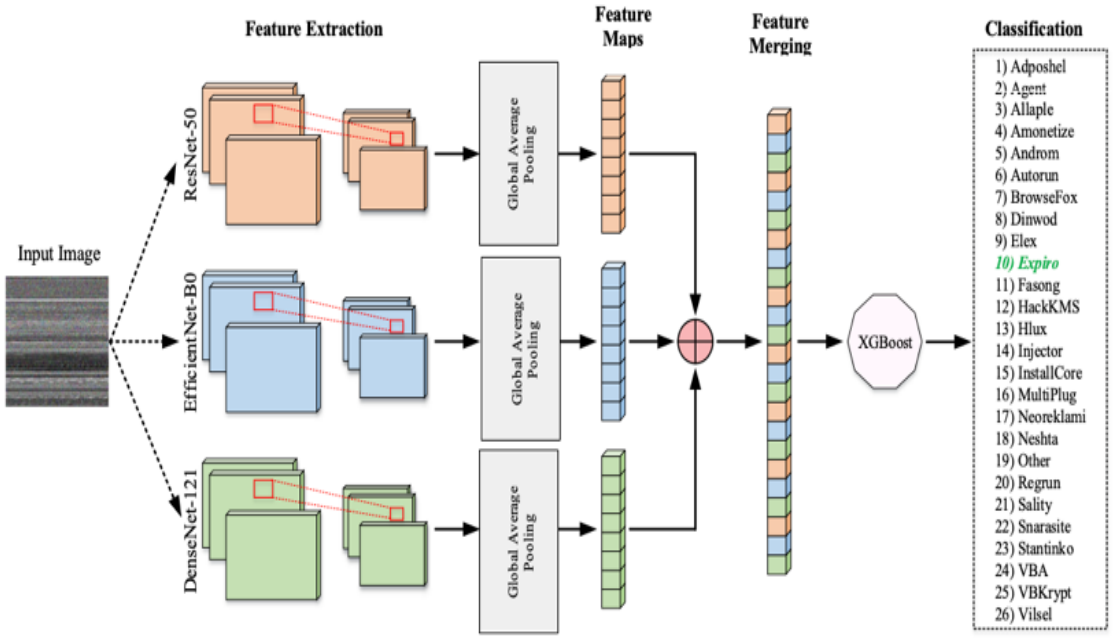


Figure 1. Proposed hybrid method

2.1. Dataset

In this study uses the Malware Evaluation with Vision (Malevis) dataset. The Malevis dataset is a pioneering resource developed for researchers focusing on the detection of multi-class malware through image-based approaches. It provides an RGB-based real data set specifically designed to facilitate the evaluation of various malware detection efforts. The Malevis dataset contains images from 26 different classes, where one class represents “legitimate” samples and the remaining 25 classes correspond to various types of malware. The dataset was converted to RGB images using the Bin2png library as described in [20]. The steps taken to create the Malevis dataset are summarized in Figure 2.

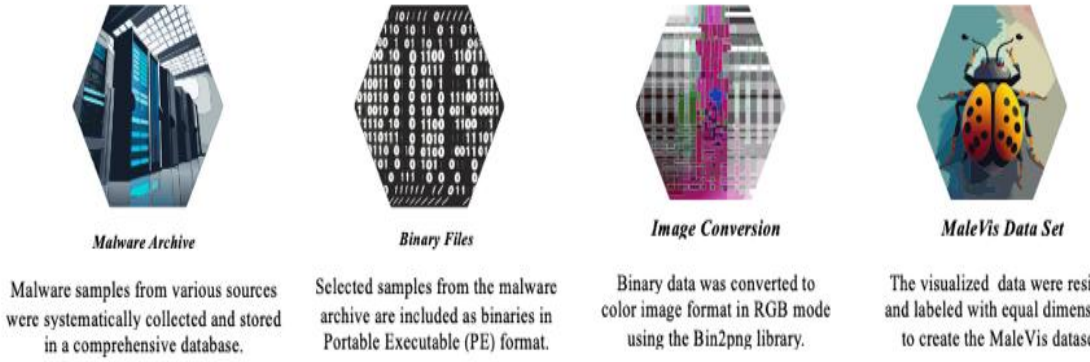


Figure 2. Steps in creating the malevis dataset

The Malevis dataset has a balanced distribution with 500 or close to 500 samples for each class. Randomly selected examples among the Malevis dataset classes are presented in Figure 3.

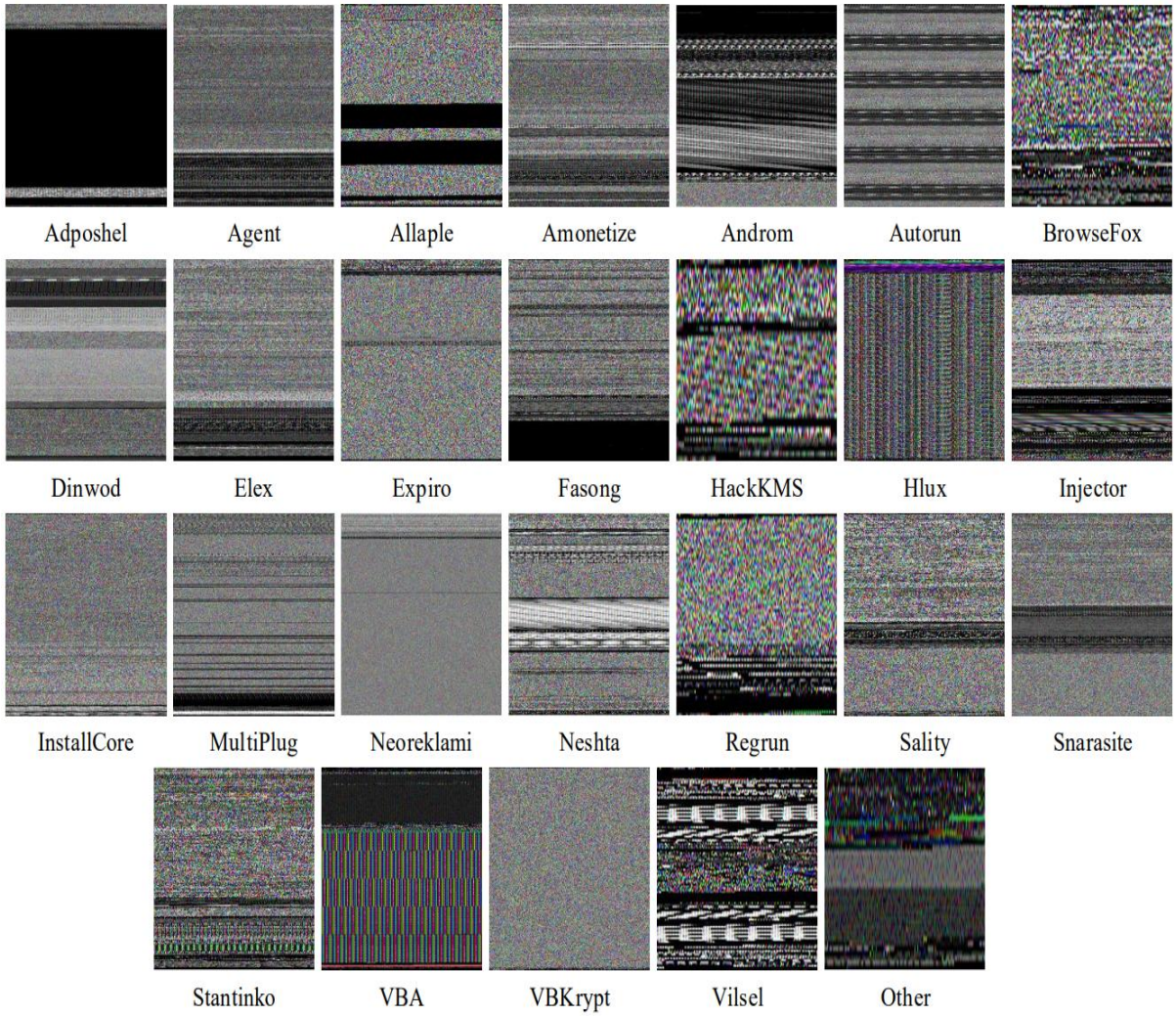


Figure 3. Malevis dataset samples

Table 1. Distribution of data set samples

Category	Class Name	Number of Samples
Adware	Adposhel	494
	Amonetize	497
	BrowseFox	493
	InstallCore	500
	MultiPlug	499
	Neoreklami	500
Trojan	Agent	470
	Dinwod	499
	Elex	500
	HackKMS	499
	Injector	495
	Regrun	485
	Snarasite	500
	VBKrypt	496
	Vilsel	496
Worm	Allaple	478
	Autorun	496
	Fasong	500
	Hlux	500
Backdoor	Androm	500
	Stantinko	500
Virus	Expiro	501
	Neshta	497
	Sality	499
	VBA	500
Normal	Other	1832

The dataset contains a total of 9100 training images and 5126 validation images. Each training class contains 350 image samples, while the validation set contains various numbers of images per class. The class-based distribution of the Malevis dataset samples is given in Table 1.

2.2. Pretrained models

Pretrained models have become a major focus of interest in the fields of artificial intelligence and machine learning in recent years. These models are systems that are pre-trained on large datasets and then adapted for a specific task. This process is called transfer learning and is widely used, especially in deep learning applications. The main advantage of pre-trained models is that they eliminate the need to restart the training process, which requires large amounts of data and high computational power. These models are usually trained on large and diverse datasets, which allows them to have a large knowledge base. Furthermore, pre-trained models allow for better performance with less data. This is a big advantage, especially in areas where data collection is difficult or costly. Thanks to transfer learning, a pre-trained model can be retrained on a small dataset to achieve high performance on a given task [21]. Popular representatives of pre-trained models include architectures such as ResNet, EfficientNet and DenseNet [22].

2.2.1. ResNet architecture

In traditional neural network architectures, the output of each layer is directly used as input for the next layer. In this approach, as the network depth increases, problems such as vanishing gradients may occur. To address these issues, the ResNet architecture was developed in 2015 by Kaiming and his colleagues. In the ResNet architecture, residual blocks are formed by connecting two layers. The second layer directly receives the output of the first layer and adds it to the input from the initial layer. This allows errors occurring at any layer of the network to propagate back to the input layer, thereby preventing issues such as vanishing gradients [23].

2.2.2. EfficientNet architecture

ESAs are typically developed with an initial fixed resource cost, and as more resources become available, the number of layers is increased to achieve better accuracy. In addition to increasing the number of layers, enhancing the model's depth or width and using higher input resolution for training and evaluation can improve accuracy. However, these methods may still be insufficient in terms of performance, even if they enhance accuracy. Tan and colleagues proposed a novel model scaling method that uses a compound coefficient to systematically scale ESAs. Instead of independently increasing depth, width, or input resolution, this method adjusts these dimensions using a fixed scaling factor [24]. With this new scaling method, the EfficientNet model family, which is smaller and faster compared to other models, was developed. The EfficientNet family consists of eight models named sequentially from EfficientNet-B0 to EfficientNet-B7. EfficientNet-B0 was designed as the base model, and all other models are scaled versions of it [25].

2.2.3. DenseNet architecture

The DenseNet architecture, proposed by Huang and colleagues, features an innovative structure where layers are densely connected. In this architecture, each layer receives the outputs of all preceding layers as input. This densely connected structure facilitates better gradient propagation and enhances feature reusability, thereby significantly improving the model's accuracy and efficiency. The DenseNet architecture has been further optimized through various scaling methods. Adjusting dimensions such as depth, width, and input resolution using a fixed scaling factor improves the model's performance and accuracy [26]. Different variants of DenseNet are sequentially named from DenseNet-121 to DenseNet-201, each representing a scaled version of the base model. This scaling strategy ensures that DenseNet models are smaller and more efficient, offering superiority in terms of both accuracy and performance [27].

2.3. Evaluation metrics

A frequently used method to evaluate the performance of deep learning models on classification tasks is the confusion matrix. The confusion matrix reveals the correspondence between the class label predicted by the model for a given input image and the actual class label of that image. In AI-based classification studies, various results can be obtained at the output layer of the model. These results can be summarized in four basic metrics: The areas represented by the relevant metrics of a randomly selected class used in this study are shown in Figure 4 on the confusion matrix.

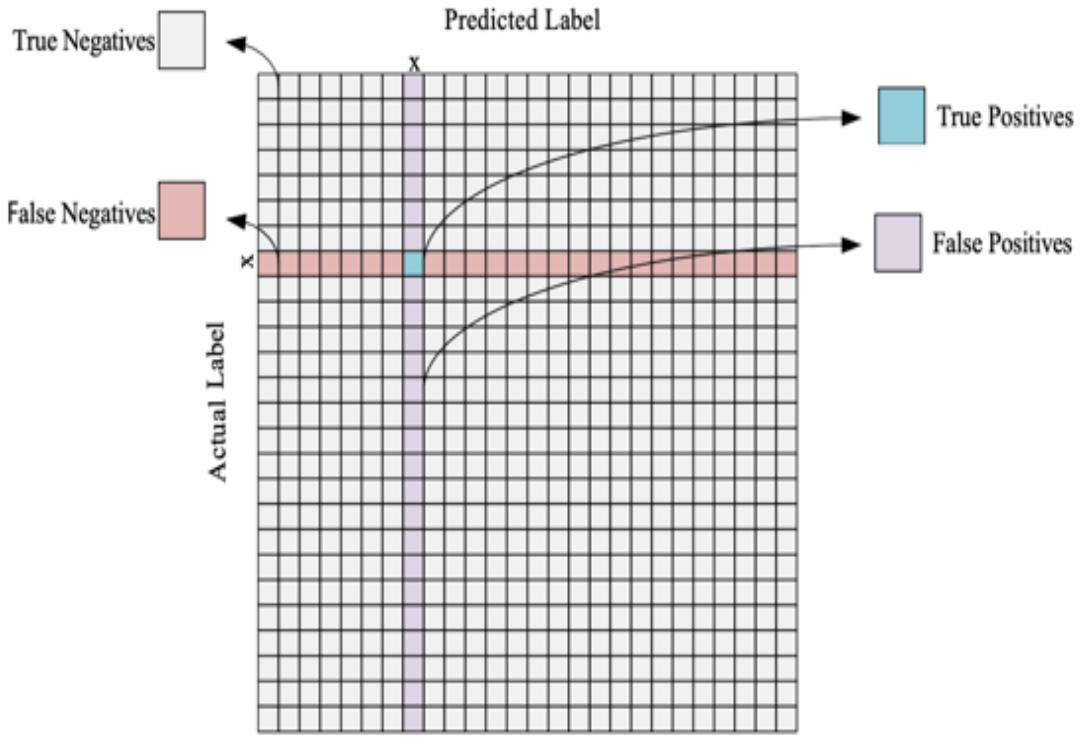


Figure 4. Confusion matrix

Various metrics such as accuracy, precision, sensitivity and F-1 score can be used to evaluate the performance of an image classification deep learning model. Accuracy refers to the rate at which the model makes correct predictions and is calculated as the ratio of correct predictions to total predictions. It is calculated using Equation 1. Recall measures the capacity of the model to accurately detect all positive cases and is calculated as the ratio of true positive predictions to total true positive cases. It is calculated using Equation 2. Precision measures the proportion of cases that the model correctly identifies as positive and is calculated as the ratio of true positive predictions to total true positive predictions. It is calculated using Equation 3. The F-1 score, the harmonic mean of sensitivity and precision, balances these two metrics and provides a useful measure in cases of overlap. It is calculated using Equation 4. The mathematical formulas for these performance metrics are presented below.

$$\text{Accuracy} = \left(\frac{\text{TP+TN}}{\text{TP+FP+TN+FN}}\right) \quad (1)$$

$$\text{Recall} = \left(\frac{\text{TP}}{\text{TP+FN}}\right) \quad (2)$$

$$\text{Precision} = \left(\frac{\text{TP}}{\text{TP+FP}}\right) \quad (3)$$

$$\text{F1 Score} = \left(\frac{2 \times \text{Pre} \times \text{Rec}}{\text{Pre+Rec}}\right) \quad (4)$$

3. Experiments

The experiments carried out to evaluate the performance of the hybrid model are detailed in this section. Furthermore, the following sections present the analysis of the experimental results and the evaluation of the performance metrics.

3.1. Experimental setup

The dataset samples can be randomly separated using 70% training, 20% working and 10% testing methods. Then, pre-trained ResNet-50, EfficientNet-B0 and DenseNet-121 models with ImageNet weights were included in the Python environment. It was shown that each model was classified and validated with its default layers and hyperparameters for a maximum of 100 steps. However, the properties of the early termination functions and the accuracy value obtained by combining them were monitored. If there is no decrease in accuracy during the five consecutive steps, the early termination function is activated and the model's training is terminated. In this way, the weights of the step with the lowest accuracy values exposed to excessive explosions are recorded. The detailed layout for this study is given in Figure 5. The hyperparameters for the XGBoost based classifier were determined through a systematic evaluation process in order to increase the generalization capability of the model and prevent overlearning; different parameter combinations were compared through multiple trials and the configuration that provided the highest accuracy performance was preferred.

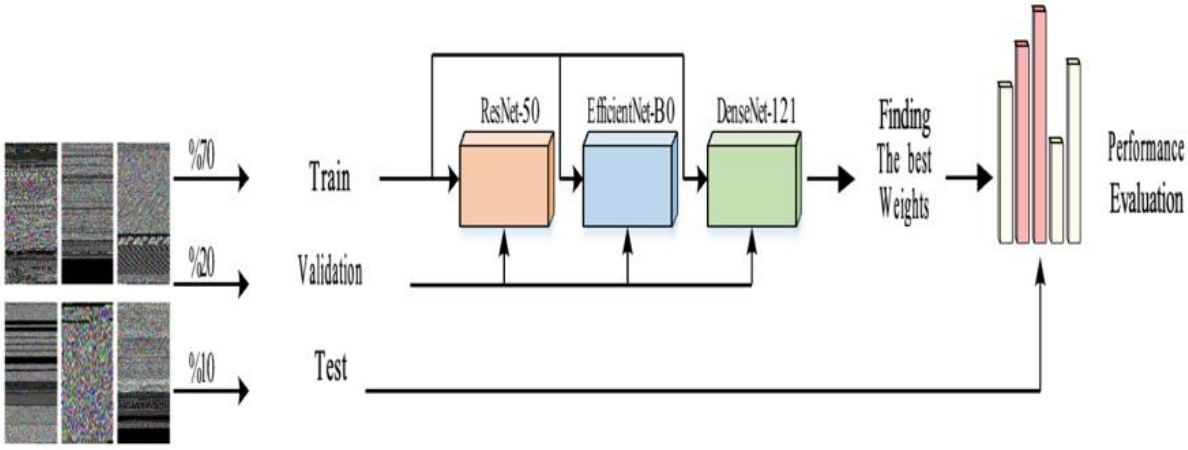


Figure 5. Experimental layout steps

3.2. Results

ResNet-50, EfficientNet-B0 and DenseNet-121 deep learning models were trained for a maximum of 100 rounds with the help of an early termination function. The weights at the end of the round are recorded andthe resulting loss and accuracy graphs are given in Figure 6. The loss and accuracy graphs in Figure 6 clearly show how the ResNet-50, EfficientNet-B0 and DenseNet-121 models performed during the training period and in which rounds their performance improved or stagnated. Through these graphs, critical points such as which model learns faster, which one achieves higher accuracy rates, and how their losses change during training can be analyzed.

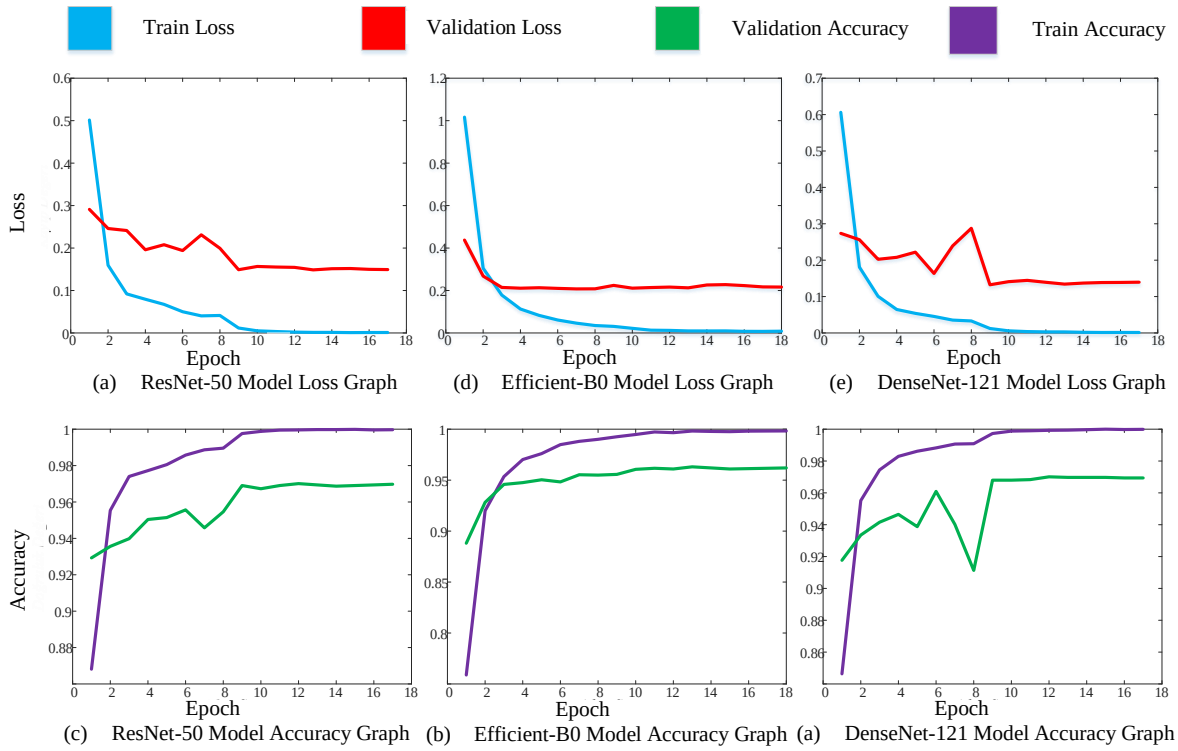


Figure 6. Loss and accuracy graph of ResNet-50, DenseNet-121 and EfficientNet-B0

Only the images allocated for the test phase were given as input to the ResNet-50 model. The confusion matrix created with reference to the model's predictions for these test images is given in Figure 7.

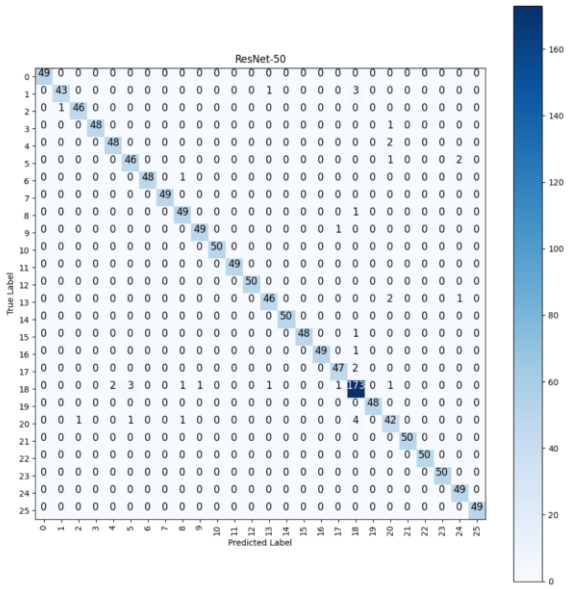


Figure 7. Confusion matrix of ResNet-50

Table 2 shows the values of the performance metrics achieved by the ResNet-50 model during testing. The ResNet-50 model achieved the highest verification accuracy rate of 97.32%.

Table 2. Performance values of the ResNet-50

Class (Label)	Precision	Recall	F-1 Score
Adposhel (0)	1	1	1
Agent (1)	0.977273	0.914894	0.945055
Allaple (2)	0.978723	0.978723	0.978723
Amonetize (3)	1	0.979592	0.989691
Androm (4)	0.96	0.96	0.96
Autorun (5)	0.92	0.938776	0.929293
BrowseFox (6)	1	0.979592	0.989691
Dinwod (7)	1	1	1
Elex (8)	0.942308	0.98	0.960784
Expiro (9)	0.98	0.98	0.98
Fasong (10)	1	1	1
HackKMS (11)	1	1	1
Hlux (12)	1	1	1
Injector (13)	0.958333	0.938776	0.948454
InstallCore (14)	1	1	1
MultiPlug (15)	1	0.979592	0.989691
Neoreklami (16)	1	0.98	0.989899
Neshta (17)	0.959184	0.959184	0.959184
Other (18)	0.935135	0.945355	0.940217
Regrun (19)	1	1	1
Sality (20)	0.857143	0.857143	0.857143
Snarasite (21)	1	1	1
Stantinko (22)	1	1	1
VBA (23)	1	1	1
VBKrypt (24)	0.942308	1	0.970297
Vilsel (25)	1	1	1

Only the images allocated for the test phase are given as input to the EfficientNet-B0 model. The confusion matrix created with reference to the model's predictions for these test images is given in Figure 8.

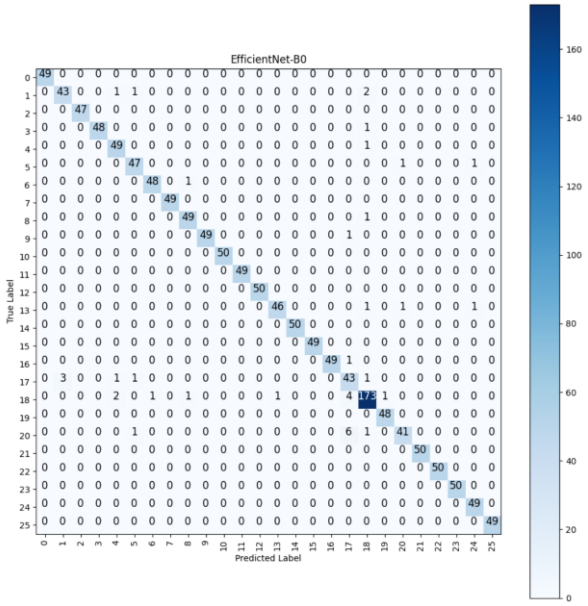


Figure 8. Confusion matrix of EfficientNet-B0

Table 3 shows the values of the performance metrics achieved by the EfficientNet-B0 model during testing. The EfficientNet-B0 model achieved the highest verification accuracy rate with 97.24%.

Table 3. Performance values of the EfficientNet-B0

Class (Label)	Precision	Recall	F-1 Score
Adposhel (0)	1	1	1
Agent (1)	0.934783	0.914894	0.924731
Allaple (2)	1	1	1
Amonetize (3)	1	0.979592	0.989691
Androm (4)	0.924528	0.98	0.951456
Autorun (5)	0.94	0.959184	0.949495
BrowseFox (6)	0.979592	0.979592	0.979592
Dinwod (7)	1	1	1
Elex (8)	0.960784	0.98	0.970297
Expiro (9)	1	0.98	0.989899
Fasong (10)	1	1	1
HackKMS (11)	1	1	1
Hlux (12)	1	1	1
Injector (13)	0.978723	0.938776	0.958333
InstallCore (14)	1	1	1
MultiPlug (15)	1	1	1
Neoreklami (16)	1	0.98	0.989899
Neshta (17)	0.781818	0.877551	0.826923

Table 3. (Contineu) Performance values of the EfficientNet-B0

Class (Label)	Precision	Recall	F-1 Score
Other (18)	0.955801	0.945355	0.950549
Regrun (19)	0.979592	1	0.989691
Sality (20)	0.953488	0.836735	0.891304
Snarasite (21)	1	1	1
Stantinko (22)	1	1	1
VBA (23)	1	1	1
VBKrypt (24)	0.960784	1	0.98
Vilsel (25)	1	1	1

Only the images allocated for the test phase were given as input to the DenseNet-121 model. The confusion matrix created with reference to the model's predictions for these test images is given in Figure 9.

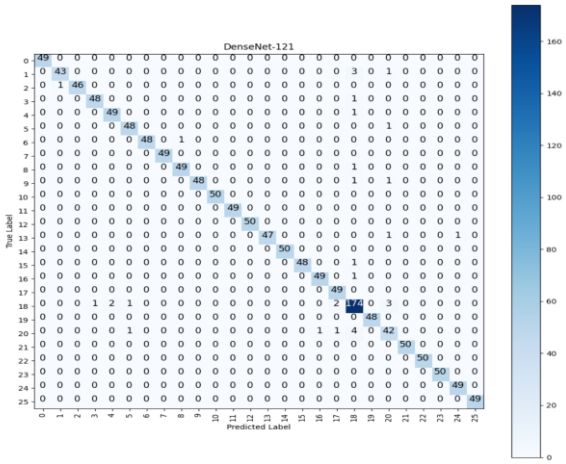


Figure 9. Confusion matrix of DenseNet-121

Table 4 shows the values of the performance metrics achieved by the DenseNet-121 model during testing. The DenseNet-121 model achieved the highest verification accuracy rate with 97.74%.

Table 4. Performance values of the DenseNet-121

Class (Label)	Precision	Recall	F-1 Score
Adposhel (0)	1	1	1
Agent (1)	0.977273	0.914894	0.945055
Allaple (2)	1	0.978723	0.989247
Amonetize (3)	0.979592	0.979592	0.979592
Androm (4)	0.960784	0.98	0.970297
Autorun (5)	0.96	0.979592	0.969697
BrowseFox (6)	1	0.979592	0.989691
Dinwod (7)	1	1	1

Table 4. (Continue) Performance values of the DenseNet-121

Class (Label)	Precision	Recall	F-1 Score
Elex (8)	0.98	0.98	0.98
Expiro (9)	1	0.96	0.979592
Fasong (10)	1	1	1
HackKMS (11)	1	1	1
Hlux (12)	1	1	1
Injector (13)	1	0.959184	0.979167
InstallCore (14)	1	1	1
MultiPlug (15)	1	0.979592	0.989691
Neoreklami (16)	0.98	0.98	0.98
Neshta (17)	0.942308	1	0.970297
Other (18)	0.930481	0.95082	0.940541
Regrun (19)	1	1	1
Sality (20)	0.857143	0.857143	0.857143
Snarasite (21)	1	1	1
Stantinko (22)	1	1	1
VBA (23)	1	1	1
VBKrypt (24)	0.98	1	0.989899
Vilsel (25)	1	1	1

Only the images allocated for the test phase are given as input to the proposed hybrid model. The confusion matrix based on the model's predictions for these test images is given in Figure 10.

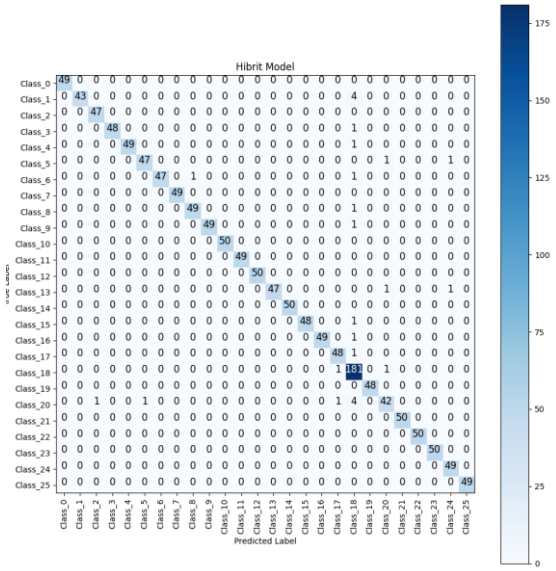


Figure 10. Confusion matrix of the proposed hybrid model

Table 5. Performance values of the proposed hybrid model

Class (Label)	Precision	Recall	F-1 Score
Adposhel (0)	1	1	1
Agent (1)	1	0.914894	0.955556
Allaple (2)	0.979167	1	0.989474
Amonetize (3)	1	0.979592	0.989691
Androm (4)	1	0.98	0.989899
Autorun (5)	0.979167	0.959184	0.969072
BrowseFox (6)	1	0.959184	0.979167
Dinwod (7)	1	1	1
Elex (8)	0.98	0.98	0.98
Expiro (9)	1	0.98	0.989899
Fasong (10)	1	1	1
HackKMS (11)	1	1	1
Hlux (12)	1	1	1
Injector (13)	1	0.959184	0.979167
InstallCore (14)	1	1	1
MultiPlug (15)	1	0.979592	0.989691
Neoreklami (16)	1	0.98	0.989899
Neshta (17)	0.96	0.979592	0.969697
Other (18)	0.918782	0.989071	0.952632
Regrun (19)	1	1	1
Sality (20)	0.933333	0.857143	0.893617
Snarasite (21)	1	1	1
Stantinko (22)	1	1	1
VBA (23)	1	1	1
VBKrypt (24)	0.960784	1	0.98
Vilsel (25)	1	1	1

Table 5 shows the values of the performance metrics achieved by the proposed hybrid model during testing. The proposed hybrid model achieved the highest verification accuracy rate of 98.16%.

4. Discussion

In recent years, malware classification has become a critical concern in the field of cybersecurity. Traditional detection methods often fall short in addressing the rapidly evolving and increasingly sophisticated nature of malware. Consequently, the adoption of machine learning and deep learning techniques has gained significant momentum, as these methods offer enhanced accuracy and adaptability in threat detection.

This study introduces a hybrid deep learning approach for malware classification. The proposed model integrates feature extraction from three pre-trained CNN architectures DenseNet-121, EfficientNet-B0, and ResNet-50 and employs XGBoost as the final classifier. This combination enables the extraction of complementary and high-level feature representations, while leveraging the discriminative capability of XGBoost for robust decision making. The effectiveness of the proposed approach is evidenced by a test accuracy of 98.16%, which demonstrates a performance gain over earlier studies. For instance, Tuncer et al. [28] proposed a byte-code-based malware recognition method utilizing Local Neighborhood Binary Pattern (LNBP), achieving 89.40% accuracy. In another study, they employed Local Binary Pattern (LBP), Singular Value Decomposition (SVD), and a Local Ternary Pattern Network (LTPNet), reaching 88.08% accuracy [29]. Compared to these prior approaches, the hybrid model proposed in this work achieves higher classification accuracy and improved robustness, making it more suitable for practical cybersecurity applications. However, potential limitations should be noted: the MaleVis dataset may not fully capture the diversity of real-world malware, which could introduce dataset bias; scalability to larger or streaming data environments may require additional optimization; and real-world deployment would necessitate considerations of latency and resource constraints.

5. Conclusion

In this study, a deep learning-based hybrid model for automatic malware detection is proposed. The proposed model is applied on the MaleVis dataset. In the proposed method, we extract features from input images using ResNet-50, EfficientNet-B0, and DenseNet-121 models, and these features are summarized by global mean pooling. The resulting feature maps are combined in the feature fusion stage to create a richer feature vector. Finally, this fused feature vector is trained and classified using the XGBoost algorithm to accurately identify different types of malware. As a result of the experimental evaluation, the proposed hybrid model achieved a test accuracy of 98.16%. The results demonstrate that integrating the features obtained by deep learning models with a powerful classifier such as XGBoost is an effective strategy for detecting next-generation threats in cybersecurity. Moreover, the findings indicate that the proposed model shows strong potential for deployment in real-time malware detection frameworks, while also being adaptable for larger datasets and broader application domains in future research.

6. Acknowledgements

This paper is supported by Fırat University Scientific Research Projects Coordination Unit (FUBAP) with project number TEKF 24.27 and Scientific and Technological Research Council of Turkey (TUBITAK) with project number 122E337. Also, the authors sincerely thank the editor(s) and the anonymous reviewers contributed positively to this paper's academic development with their constructive and quick feedback.

7. Author Contribution Statement

Author 1 contributed to the preparation of the original draft of the study, methodology development, visualization and experimentation stages. Author 2 conceptualized the study and participated in the writing, revising and editing processes.

8. Ethics Committee Approval and Conflict of Interest

Ethics committee permission is not required for the prepared article. There is no conflict of interest with any person/institution in the prepared article.

9. Ethical Statement Regarding the Use of Artificial Intelligence

No artificial intelligence-based tools or applications were used in the preparation of this study. The entire content of the study was produced by the authors in accordance with scientific research methods and academic ethical principles.

10. References

[1] A. Di Nicola, "Towards digital organized crime and digital sociology of organized crime," Trends Organ. Crime, pp. 1–20, 2022.
[2] Y. Zhang, Y. Xiao, K. Ghaboosi, J. Zhang, and H. Deng, "A survey of cyber crimes," Secur. Commun. Netw., vol. 5, no. 4, pp. 422–437, 2012.
[3] A. Chakraborty, A. Biswas, and A. K. Khan, "Artificial intelligence for cybersecurity: Threats, attacks and mitigation," in Artificial Intelligence for Societal Issues. Cham, Switzerland: Springer, 2023, pp. 3–25.
[4] Ö. Aslan, S. S. Aktuğ, M. Ozkan-Okay, A. A. Yilmaz, and E. Akin, "A comprehensive review of cyber security vulnerabilities, threats, attacks, and solutions," Electron., vol. 12, no. 6, p. 1333, 2023.
[5] E. M. Rudd, A. Rozsa, M. Günther, and T. E. Boult, "A survey of stealth malware attacks, mitigation measures, and steps toward autonomous open world solutions," IEEE Commun. Surv. Tutor., vol. 19, no. 2, pp. 1145–1172, 2016.
[6] S. S. Chakkaravarthy, D. Sangeetha, and V. Vaidehi, "A survey on malware analysis and mitigation techniques," Comput. Sci. Rev., vol. 32, pp. 1–23, 2019.
[7] J. G. Heiser, "Understanding today's malware," Inf. Secur. Tech. Rep., vol. 9, no. 2, pp. 47–64, 2004.
[8] F. A. Aboaoja, A. Zainal, F. A. Ghaleb, B. A. S. Al-Rimy, T. A. E. Eisa, and A. A. H. Elnour, "Malware detection issues, challenges, and future directions: A survey," Appl. Sci., vol. 12, no. 17, p. 8482, 2022.
[9] M. I. Malik, A. Ibrahim, P. Hannay, and L. F. Sikos, "Developing resilient cyber-physical systems: A review of state-of-the-art malware detection approaches, gaps, and future directions," Computers, vol. 12, no. 4, p. 79, 2023.
[10] A. Thakkar and R. Lohiya, "A review on machine learning and deep learning perspectives of IDS for IoT: Recent updates, security issues, and challenges," Arch. Comput. Methods Eng., vol. 28, no. 4, pp. 3211–3243, 2021.
[11] Z. Chen et al., "Machine learning-enabled IoT security: Open issues and challenges under advanced persistent threats," ACM Comput. Surv., vol. 55, no. 5, pp. 1–37, 2022.
[12] L. Nataraj, S. Karthikeyan, G. Jacob, and B. S. Manjunath, "Malware images: Visualization and automatic classification," in Proc. 8th Int. Symp. Visualization Cyber Secur., 2011, pp. 1–7.
[13] M. Goyal and R. Kumar, "IVMCT: Image visualization based multiclass malware classification using transfer learning," Math. Stat. Eng. Appl., vol. 71, no. 2, pp. 42–50, 2022.
[14] S. Jang, S. Li, and Y. Sung, "FastText-based local feature visualization algorithm for merged image-based malware classification framework for cyber security and cyber defense," Mathematics, vol. 8, no. 3, p. 460, 2020.
[15] Y. Qiao, Q. Jiang, Z. Jiang, and L. Gu, "A multi-channel visualization method for malware classification based on deep learning," in Proc. IEEE Int. Conf. Trust, Secur. Privacy Comput. Commun. (TrustCom), 2019, pp. 757–762.
[16] D. L. Vu, T. K. Nguyen, T. V. Nguyen, T. N. Nguyen, F. Massacci, and P. H. Phung, "HIT4Mal: Hybrid image transformation for malware classification," Trans. Emerg. Telecommun. Technol., vol. 31, no. 11, p. e3789, 2020.
[17] D. Vasan, M. Alazab, S. Wassan, H. Naeem, B. Safaei, and Q. Zheng, "IMCFN: Image-based malware classification using fine-tuned convolutional neural network architecture," Comput. Netw., vol. 171, p. 107138, 2020.
[18] R. U. Khan, X. Zhang, and R. Kumar, "Analysis of ResNet and GoogLeNet models for malware detection," J. Comput. Virol. Hack. Tech., vol. 15, no. 1, pp. 29–37, 2019.
[19] U.-H. Tayyab, F. B. Khan, M. H. Durad, A. Khan, and Y. S. Lee, "A survey of the recent trends in deep learning based malware detection," J. Cybersecur. Priv., vol. 2, no. 4, pp. 800–829, 2022.
[20] O. Katar and Ö. Yıldırım, "Classification of malware images using fine-tuned ViT," Sakarya Univ. J. Comput. Inf. Sci., vol. 7, no. 1, pp. 22–35, 2024.
[21] A. Hosna, E. Merry, J. Gyalmo, Z. Alom, Z. Aung, and M. A. Azim, "Transfer learning: A friendly introduction," J. Big Data, vol. 9, no. 1, p. 102, 2022.

[22] A. Ait Nasser and M. A. Akhloufi, "A review of recent advances in deep learning models for chest disease detection using radiography," Diagnostics, vol. 13, no. 1, p. 159, 2023.
[23] B. Koonce, "ResNet-50," in Convolutional Neural Networks with Swift for TensorFlow: Image Recognition and Dataset Categorization. Berkeley, CA, USA: Apress, 2021, pp. 63–72.
[24] B. Koonce, "EfficientNet," in Convolutional Neural Networks with Swift for TensorFlow: Image Recognition and Dataset Categorization. Berkeley, CA, USA: Apress, 2021, pp. 109–123.
[25] H. Garg, B. Sharma, S. Shekhar, and R. Agarwal, "Spoofing detection system for e-health digital twin using EfficientNet convolutional neural network," Multimedia Tools Appl., vol. 81, no. 19, pp. 26873–26888, 2022.
[26] J. Hemalatha, S. A. Roseline, S. Geetha, S. Kadry, and R. Damaševičius, "An efficient DenseNet-based deep learning model for malware detection," Entropy, vol. 23, no. 3, p. 344, 2021.
[27] H. A. Sanghvi, R. H. Patel, A. Agarwal, S. Gupta, V. Sawhney, and A. S. Pandya, "A deep learning approach for classification of COVID and pneumonia using DenseNet-201," Int. J. Imaging Syst. Technol., vol. 33, no. 1, pp. 18–38, 2023.
[28] T. Tuncer, F. Ertam, and S. Doğan, "Automated malware recognition method based on local neighborhood binary pattern," Multimedia Tools Appl., vol. 79, no. 37, pp. 27815–27832, 2020.
[29] T. Tuncer, F. Ertam, and S. Doğan, "Automated malware identification method using image descriptors and singular value decomposition," Multimedia Tools Appl., vol. 80, no. 7, pp. 10881–10900, 2021.

Fırat Üniversitesi Deneysel ve Hesaplamalı Mühendislik Dergisi

FUJECE

Kritik Görevler İçin Akıllı İnsansız Hava Aracı: Gerçek Zamanlı Görsel Zekâya Sahip Bir VTOL İHA'nın Geliştirilmesi

Bashar ALHAJAHMAD [1*]

[1]Bilgisayar Mühendisliği Bölümü, Mühendislik Fakültesi, Siirt Üniversitesi, Siirt, Türkiye.
[1]bashar.ahmad@siirt.edu.tr

Geliş Tarihi: 14.5.2025
Kabul Tarihi: 8.9.2025

Düzeltme Tarihi: 24.6.2025

doi: https://doi.org/10.62520/fujece.1698945
Araştırma Makalesi

Alıntı: B. Alhajahmad, "Kritik görevler için akıllı insansız hava aracı: gerçek zamanlı görsel zekâya sahip bir VTOL iha'nın geliştirilmesi" Fırat Üni. Deny. ve Hes. Müh. Derg., vol. 5, no 1, pp. 44-68, Şubat 2026.

Öz

Bu çalışma, arama-kurtarma, gözetleme ve hassas tarım gibi kritik görevler için optimize edilmiş, yerleşik gerçek zamanlı görsel zekâ sistemine sahip sabit kanatlı bir Dikey Kalkış ve İniş (VTOL) insansız hava aracının (İHA) tasarımını, üretimini ve değerlendirmesini sunmaktadır. İHA, hafif ve düşük maliyetli malzemeler ile 3B baskı bileşenleri kullanılarak üretilmiş, bu sayede geliştirme maliyetleri önemli ölçüde azaltılmış ve sistemin hem akademik araştırmalarda hem de saha uygulamalarında erişilebilirliği artırılmıştır. Bu çalışmanın temel katkısı, tamamen açık kaynaklı bir mimari içerisinde VTOL işlevselliğinin, gömülü donanım üzerinde gerçek zamanlı derin öğrenme çıkarımıyla bütünleştirilmesidir. Mevcut İHA'ların çoğu hacimli veya pahalı donanımlara bağımlı iken, önerilen sistem nesne tespitini (YOLOv5s) doğrudan Raspberry Pi 4B üzerinde gerçekleştirerek harici hesaplamaya gerek duymadan verimli yerleşik işlem yapabilmektedir. Üç farklı algılama modeli- YOLOv5s, Tiny-YOLOv4 ve MobileNet-SSD-özel olarak oluşturulmuş bir hava veri kümesi üzerinde eğitilmiş ve gerçek zamanlı performans açısından değerlendirilmiştir. YOLOv5s modeli, %82,4 ortalama hassasiyet (mAP@0.5) ve 4,2 FPS değerleriyle en yüksek doğruluğu elde etmiştir. Modüler ve ölçeklenebilir tasarımı sayesinde, önerilen İHA platformu, gerçek dünya koşullarında akıllı hava sistemlerinin uygulanması için pratik ve ekonomik bir çözüm sunmaktadır.

Anahtar kelimeler: Sabit kanatlı insansız hava aracı, Döner kanatlı hava aracı, Gerçek zamanlı hava gözetimi, Gömülü yapay zekâ, VTOL İHA

*Yazışılan yazar

İntihal Kontrol:Evet – Turnitin
Şikayet: fujece@firat.edu.tr
Telif Hakkı ve Lisans: Dergide yayın yapan yazarlar, CC BY-NC 4.0 kapsamında lisanslanan çalışmalarının telif hakkını saklı tutar.

Firat University Journal of Experimental and Computational Engineering

Smart Drone for Critical Missions: Development of a VTOL UAV with Real-Time Visual Intelligence

Bashar ALHAJAHMAD [1*]

[1]Computer Engineering Department, Engineering Faculty, Siirt University, Siirt, Türkiye.
[1]bashar.ahmad@siirt.edu.tr

Received: 14.5.2025
Accepted: 8.9.2025
Revision: 24.6.2025
doi: https://doi.org/10.62520/fujece.1698945
Research Article

Citation: B. Alhajahmad, "Smart drone for critical missions: development of a VTOL UAV with real-time visual intelligence" Fırat Üni. Deny. ve Hes. Müh. Derg., vol. 5, no 1, pp. 44-68, February 2026.

Abstract

This study presents the design, construction, and evaluation of a fixed-wing Vertical Take-Off and Landing (VTOL) unmanned aerial vehicle (UAV) equipped with an onboard real-time visual-intelligence system optimized for critical missions such as search and rescue, surveillance, and precision agriculture. The UAV was built using lightweight, cost-effective materials and 3D-printed components, which considerably reduced development costs and improved accessibility for both academic research and field applications. A central contribution of this work is the integration of VTOL functionality with real-time deep-learning inference on embedded hardware within a fully open-source architecture. Unlike most existing UAVs that depend on bulky or expensive hardware, the proposed system performs efficient object detection (YOLOv5s) directly on a Raspberry Pi 4B, enabling onboard processing without external computation. Three detection models-YOLOv5s, Tiny-YOLOv4, and MobileNet-SSD—were trained on a custom aerial dataset and evaluated for real-time performance. YOLOv5s achieved the highest accuracy, with a mean Average Precision (mAP@0.5) of 82.4 % at 4.2 FPS. Owing to its modular and scalable design, the proposed UAV platform offers a practical and affordable solution for implementing intelligent aerial systems in real-world critical-mission environments.

Keywords: Fixed-wing drone, Rotating-wing aircraft, Real-time aerial surveillance, Embedded AI, VTOL UAV

*Corresponging author

Plagiarism Checks: Yes – Turnitin
Complaints: fujece@firat.edu.tr
Copyright & License: Authors publishing with the journal retain the copyright to their work licensed under the CC BY-NC 4.0

1. Introduction

Drone technologies are rapidly advancing and have been increasingly adopted across sectors such as defense, healthcare, and agriculture in Turkey. This study focuses on the practical development of unmanned aerial vehicles (UAVs), addressing key aspects of their design, construction, and application. UAVs can be categorized into four main types according to their structural configuration: fixed-wing, rotorcraft, flapping-wing, and unconventional designs [1]. The chronological evolution of fixed-wing UAVs has progressed through nine main stages, as shown in Figure 1.

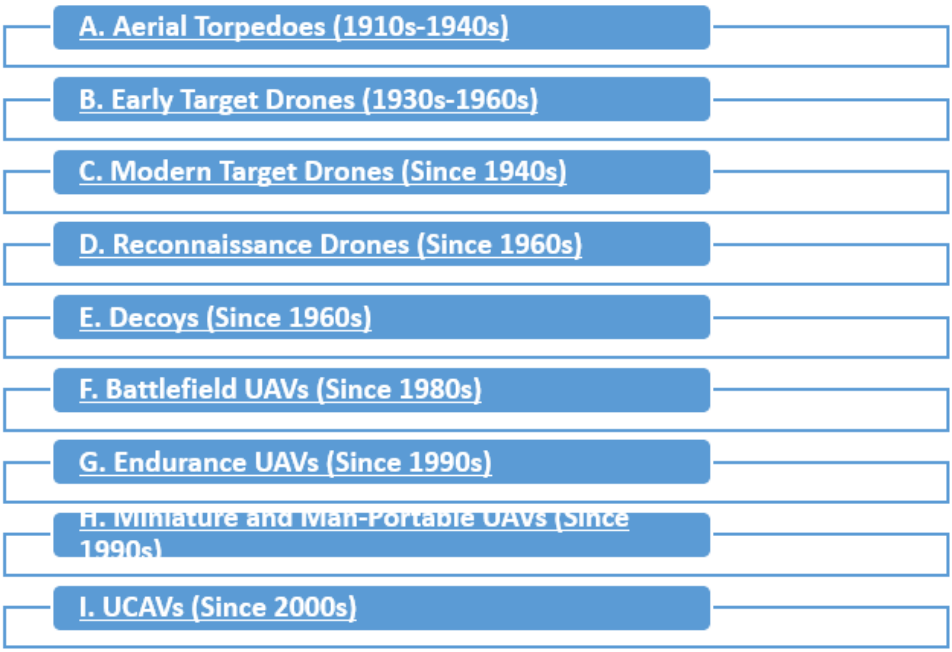


Figure 1. History of fixed-wing UAV

Figure 2 shows the commercial UAV market growth from 2010 to 2025. A substantial increase occurred between 2012 and 2017 for communication-related applications. UAV-based inspections have also expanded rapidly since 2010, particularly in assessing infrastructure such as power lines, solar panels, bridges, and wind turbines [2, 3].

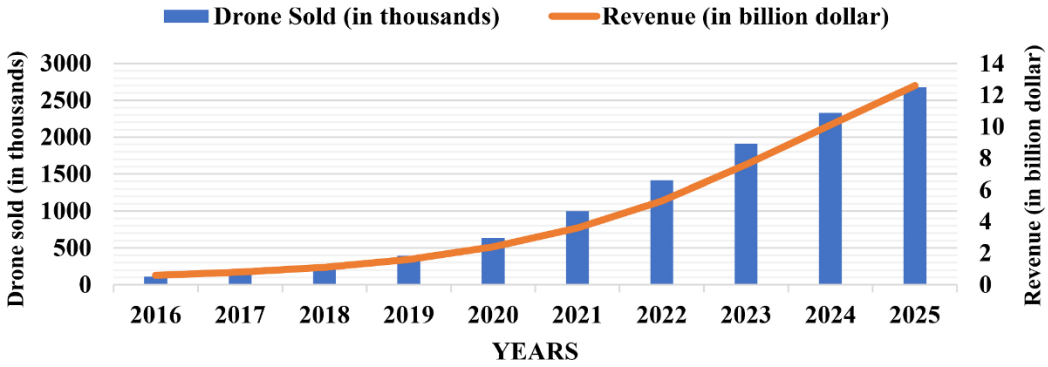


Figure 2. The forecasted global market growth for commercial drones (Buchholz, 2019)

For visual inspection tasks, UAVs are generally classified as rotary-wing or fixed-wing. Fixed-wing UAVs provide longer flight ranges and are suitable for wide-area surveillance and monitoring. Their ability to capture images over large distances is advantageous, although they require more space to change direction

and have slower response times. Rotary-wing UAVs, by contrast, are better suited for confined environments such as cities or construction sites. They can take off and land vertically and maintain stable hovering, making them effective for short-distance missions and aerial imaging [4, 5]. However, vibrations caused by rotor movement may reduce image stability in some cases.

Compared with fixed-wing aircraft, rotary-wing UAVs provide greater maneuverability and are well-suited for capturing horizontal imagery over medium-sized areas [6]. The main advantages and disadvantages of both types are summarized in Figure 3 [7].

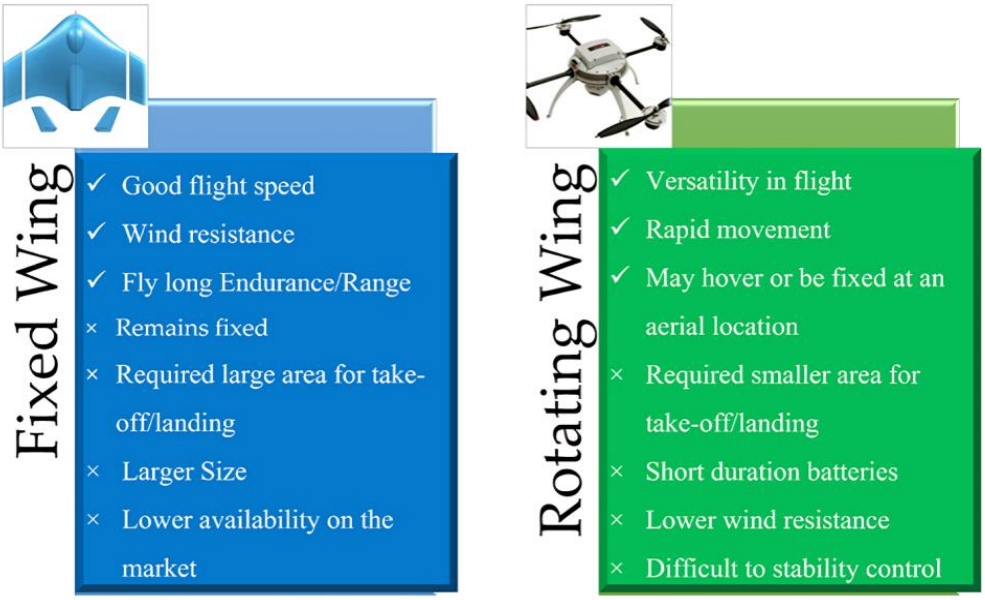


Figure 3. Main Different Between Fixed and Rotating Wing Airplane (Advantages '✓' and disadvantages '×')

UAVs are now used widely in defense, disaster management, environmental monitoring, and logistics. Their autonomous operation across different terrains makes them valuable for missions such as search and rescue, aerial surveillance, and payload transport. Fixed-wing VTOL drones combine long-range efficiency with vertical take-off and landing capability, removing the need for runways while retaining the endurance benefits of fixed-wing designs [5, 8]. Despite these strengths, research on cost-effective UAVs equipped with onboard artificial intelligence remains limited. Many commercial systems depend only on basic sensors, highlighting the need for affordable UAVs that can perform real-time inference to support situational awareness and autonomous control [9, 10].

This study adopts a dual focus: (1) the design and construction of a low-cost fixed-wing VTOL UAV and (2) the integration of real-time object detection using deep-learning models on embedded hardware. The UAV was developed around the FY-41AP flight controller and inspired by the Titan Cobra VT airframe, a 2 m-wingspan quad-plane known for efficient VTOL performance. The onboard vision system employed a YOLOv5s model on a Raspberry Pi 4B, trained on the COCO dataset and an additional custom aerial dataset to enhance detection accuracy. The system achieved a 5.5-kg payload capacity and supported surveillance operations at altitudes between 30 and 60 m. Comparative evaluation of YOLOv5s, MobileNet-SSD, and Tiny-YOLOv4 demonstrated the feasibility of real-time, low-power AI detection. Future enhancements will include thermal imaging, autonomous mission planning, and multi-UAV coordination. By combining practical UAV fabrication with onboard intelligence, this work provides a scalable and adaptable platform for security, search-and-rescue, environmental monitoring, and precision agriculture.

Unlike prior works that focused separately on UAV flight performance or AI model development, this study contributes a systems-level innovation. It demonstrates the integration of real-time object detection on a low-cost, fixed-wing VTOL UAV using only open-source hardware and software. The novelty lies not in proposing a new theoretical model but in the applied deployment, optimization, and real-world validation of

AI-powered UAV systems under resource constraints. This approach lowers barriers for research and humanitarian applications by providing a replicable, scalable, and affordable platform.

1.1. Literature Review

Numerous studies have investigated UAV applications across specific domains. For example, one study developed and tested a UAV for the 2022 AIAA Design/Build/Fly competition, targeting vaccine delivery and humanitarian operations during the COVID-19 period [11]. Another experimental work verified the feasibility of UAV-based building inspections in areas that are difficult to access [12].

Studies on UAV noise perception have identified gaps in psychoacoustic evaluation and regulation, highlighting the importance of systems that balance technical efficiency with public acceptance [4]. In robotics, UAVs have been applied to autonomous wall-building tasks using RGB-D sensing and cooperative path planning. Research on tilt-rotor platforms such as TURAC has advanced understanding of low-cost prototyping and flight validation but mainly addressed mechanical performance rather than onboard AI integration. Overall, few investigations have examined affordable, AI-enabled fixed-wing UAVs that perform real-time inference in flight using open-source hardware and modular design [13].

The integration of YOLO algorithms with UAVs has recently gained momentum, enabling real-time object detection across many fields. A comprehensive review describes the evolution of YOLO-based UAV technology (YBUT) and its applications in engineering, agriculture, automation, and transportation. The review also suggests future directions for interdisciplinary development [14].

Another important research area in UAV systems is Simultaneous Localization and Mapping (SLAM), which supports autonomous navigation. Recent studies have examined SLAM and data-fusion techniques such as Kalman filters and visual odometry, emphasizing sensor fusion for accurate perception and object detection. These findings highlight continuing challenges and research opportunities in SLAM-based UAV navigation [15].

Mobile object-detection systems face similar performance constraints when UAVs operate in limited environments. A comparative study evaluated 22 lightweight CNN models from the MobileNet and EfficientDet families on seven mobile devices, showing trade-offs between detection accuracy and latency. The results underline the need for further optimization of CNNs in embedded applications [16].

Within Intelligent Transportation Systems (ITS), UAVs serve as valuable mobile data-collection platforms. Recent surveys group existing contributions into Functionality, Application, and Planning categories, highlighting UAV roles as aerial base stations and emergency responders. The studies also summarize common simulation environments and datasets used for testing and identify key challenges for integrating UAVs into ITS infrastructure [17].

The deployment of advanced object-detection models such as YOLOv4-Tiny on edge devices has become a major focus area. Recent research demonstrated that a quantized YOLOv4-Tiny model on Raspberry Pi 5 achieves fast inference and low power consumption for aerial emergency detection, confirming the feasibility of energy-efficient AI systems for real-time safety-critical applications [18].

UAVs have also shown strong potential in early forest-fire detection through multisensor fusion. A recent study introduced the FFDM-F model, which combines visible and infrared imagery to improve fire-detection precision by over 10 % and reduce false alarms. This approach demonstrates the benefits of multisource image fusion for environmental monitoring using UAVs [19].

Unlike earlier studies that addressed either flight performance or AI model development separately, the present research combines both aspects in a practical methodology. It integrates real-time onboard object detection with a VTOL-capable fixed-wing UAV using open-source components. This approach targets cost-sensitive and mission-critical applications that require both endurance and edge-intelligence capabilities.

2. Materials and Methods

2.1. Main components

2.1.1. Airplane 3D printed model

The fuselage forms the central structure of a fixed-wing aircraft, providing balance and ensuring aerodynamic stability during flight. To meet these design requirements, a commercially available 3D model was obtained from an online vendor. The selected airframe, Titan Cobra VT (Figure 4), is a quad-plane with a 2-m wingspan designed for smooth takeoff and landing, even under challenging conditions. The A-tail configuration enhances roll and pitch control during forward flight. The design files and assembly instructions are publicly available on the Titan Dynamics website [10].

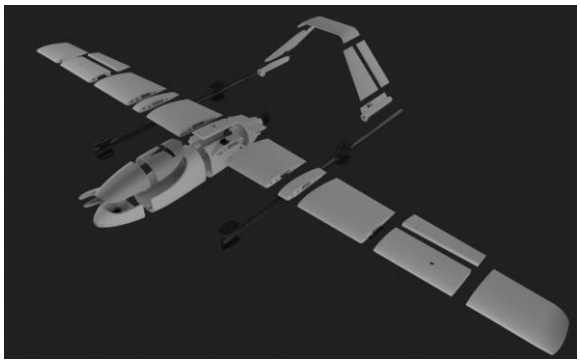


Figure 4. Titan cobra design from titan dynamics

2.1.2. 3D printer

Utilizing a 3D printer involves the transformation of digital designs into tangible objects through the sequential addition, fusion, and solidification of multiple layers of material. For this study, the Creality Ender 3 Pro printer was employed.

2.1.3. Flight ontroller

As shown in Figure 5, the FY-41AP flight controller was utilized in this study. Designed for FPV flight on both fixed-wing and multi-rotor aircraft, the FY-41AP serves as an inertial attitude measurement instrument. Equipped with an integrated OSD video overlay system, it offers crucial flight data such as power management, airspeed, altitude, and flight direction through an electronic compass, ensuring clear visual guidance while keeping essential information readily visible. The latest iteration of the FY-41AP features enhanced altitude control and a GPS module, enabling improved pinpoint inertial navigation and automated piloting capabilities. Flight stabilization is achieved through a combination of integrated sensors including a 3-axis gyro, 3-axis accelerometer, 3-axis magnetometer, and a barometric pressure sensor. For seamless installation, detailed instructions are provided on the manufacturer's official website [20].



Figure 5. FY-41AP Autopilot module

2.1.4. ESC (Electronic speed controller)

The Electronic Speed Controller (ESC) regulates motor speed and ensures reliable propulsion performance [21]. In this study, an 80-A Skywalker ESC was used to control motor operation, as shown in Figure 6.



Figure 6. ESC circuit used in project

2.1.5. Brushless motor

A brushless DC motor operates using three-phase AC input and replaces the mechanical commutator of brushed motors with an electronic controller [22]. The Sunnysky X3520-KV520 motor (Figure 7) was selected based on its performance specifications and suitability for UAV propulsion.



Figure 7. Sunnysky x3520 kv520 motor

2.1.6. Electric propeller

The chosen electric propeller is a two-bladed fan tailored for specific applications within our field. Each fan is identified by a four-digit code, with the first two digits denoting its length and the latter two indicating the

blade inclination. Our selection, the APC12*6 fan, was made following careful consideration and consultation of the engine efficiency table (Figure 8).



Figure 8. APC 12 x 6 electric propeller

2.1.7. Servo motors

Servo motors are precision electric motors renowned for their ability to rotate machine parts with exceptional accuracy. Equipped with a control circuit providing real-time feedback on the motor shaft's position, these motors ensure precise rotational movements. In our project, we require four units of the Emax ES08MAII servo motor (Figure 9) to facilitate controlled movements over various distances and angles.



Figure 9. Emax ES08MAII servo motor

2.1.8. RC 2.4Ghz transmitter

The RC transmitter, operating wirelessly on the 2.4GHz spectrum and depicted in Figure 10, serves as a pivotal device through which the aircraft pilot transmits control commands directly to the receiver. This communication mechanism enables manual control over the aircraft, allowing for seamless maneuvering during flight operations.



Figure 10. Flysky FS-i6 FS I6 2.4G 6ch RC transmitter controller

2.1.9. Receiver

The receiver plays a critical role in establishing wireless communication between the controller and other aircraft components. Utilizing a 2.4GHz WiFi connection, the receiver (such as the Flysky RC FS-iA6B

Receiver shown in Figure 11) ensures efficient data transmission, directly interfacing with the controller to facilitate precise control over the aircraft.



Figure 11. Flysky RC FS-iA6B receiver

2.1.10. Li-po battery

Rechargeable lithium-polymer (Li-Po) batteries are widely used in electric aircraft due to their high energy density. As shown in Figure 12, this project used eighteen 18650-type cells (3.7 V, 2200 mAh, 20 C discharge rate) to supply consistent power for flight operations [23, 24].



Figure 12. 18650 Battery

2.1.11. MS battery management system

The definition of BMS varies from application to application. In general, BMS refers to a management scheme that monitors, controls, and optimizes an individual's performance or multiple battery modules in an energy storage system. The BMS, depicted in Figure 13, or Battery Management System, plays a crucial role in optimizing the performance and safety of the battery system. This intelligent management scheme monitors, controls, and safeguards individual or multiple battery modules within the energy storage system. In our application, the BMS ensures optimal battery performance while implementing safety protocols to mitigate risks during operation [25].

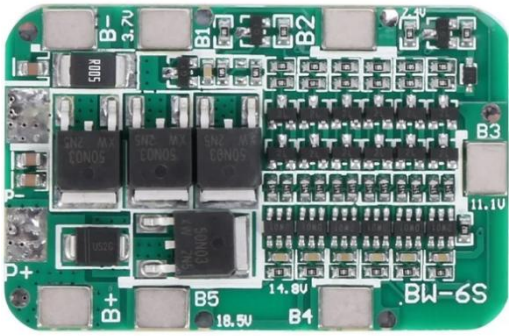


Figure 13. The 6s bms circuit capable of charging 6 cells in series

2.1.12. Carbon fiber rods

Carbon fiber rods were selected for their high strength-to-weight ratio and flexibility. Each rod consists of carbon fibers embedded in a resin matrix to provide stiffness and durability. In this project, the rods were installed within the wing structure to increase rigidity and resistance to stress during flight, as illustrated in Figure 14 [26].

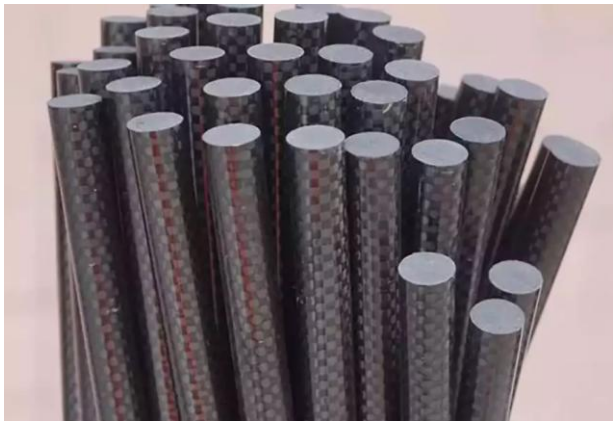


Figure 14. Carbon fiber rods

2.1.13. Raspberry Pi 4B as the edge ai processor

The Raspberry Pi 4B was used as the onboard computing unit for real-time object detection. It features a quad-core Cortex-A72 (1.5 GHz) processor, 4 GB RAM, integrated Wi-Fi/Bluetooth, and dual-display outputs (Figure 15). The board processed aerial images during flight and executed deep-learning inference tasks. It also interfaced with the camera module for image capture and data transfer [27].



Figure 15. Raspberry Pi 4B used for onboard AI processing

2.1.14. Camera module-raspberry pi camera V2

For aerial image acquisition, the UAV utilizes the Raspberry Pi Camera Module V2, a lightweight and high-definition imaging unit capable of recording 1080p video and capturing 8-megapixel still images. It connects

to the Raspberry Pi via the Camera Serial Interface (CSI) port and enables low-latency, high-resolution video capture in real time (Figure 16). This module was selected based on its compact size, proven compatibility with the Raspberry Pi ecosystem, and minimal power consumption, making it well-suited for embedded UAV applications [28].

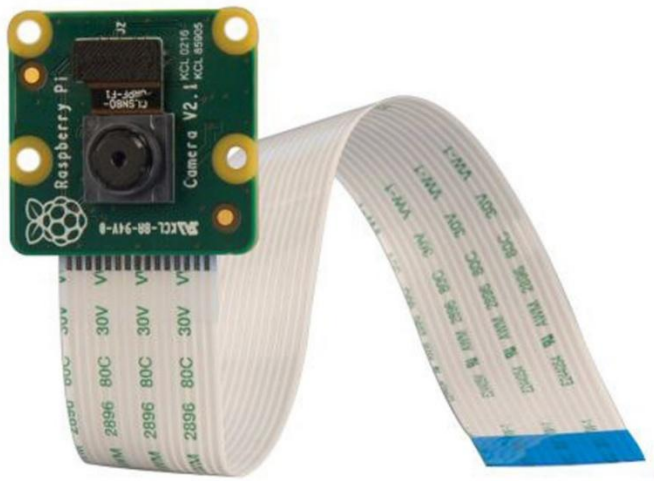


Figure 16. Raspberry Pi Camera V2 module used for capturing real-time video feed

2.1.15. Object detection model and deployment framework

The YOLOv5s (You Only Look Once v5 – small variant) model was adopted for onboard object detection due to its optimal balance between inference speed and detection accuracy. Initially pre-trained on the COCO dataset, the model was subsequently fine-tuned using a custom aerial dataset comprising 300 images collected during UAV test flights. For deployment on the Raspberry Pi, the trained YOLOv5s model was converted to the ONNX format and executed using PyTorch Mobile, ensuring compatibility with resource-constrained edge environments [29].

2.1.16. Custom Dataset and Annotation Workflow

To tailor the detection model for aerial perspectives, a domain-specific dataset was developed using imagery captured at altitudes of 30 to 60 meters during UAV missions. The collected images were manually annotated using the Roboflow platform, with bounding boxes applied to key object classes such as person, car, and truck [30]. This annotated dataset was then used for transfer learning, allowing the YOLOv5s model to adapt to the specific visual characteristics and viewpoints encountered in UAV-based surveillance tasks [31].

2.2 Design and development

2.2.1 UAV body design

The pinnacle of any product's journey lies in its design phase. In the case of this UAV body, meticulous attention was given to crafting its form and function using Ultimaker Cura software, showcased in Figure 17. The printing and assembly instructions, pivotal for bringing this design to life, were sourced from the Titan Dynamics website. The final assembly stage resulted in a functional UAV that integrates all structural and electronic components into a ready-to-fly platform.

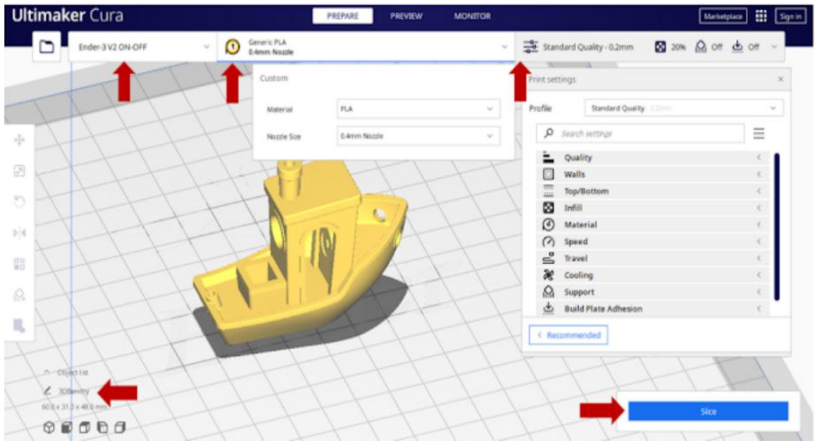


Figure 17. Ultimaker cura main interface

To execute the printing process, the Creality Ender 3 Pro Printer was selected for its precision and reliability. It served as the cornerstone in materializing the various components of the airplane body, as illustrated in Figure 18.

Upon completion of the printing and assembly stages, our UAV reached its final state, exemplified in Figure 19. This culmination represents the culmination of meticulous planning, precise execution, and unwavering dedication to crafting a functional and formidable aerial vehicle.



Figure 18. The creality ender 3 pro printer used in making parts of fixed-wing aircraft

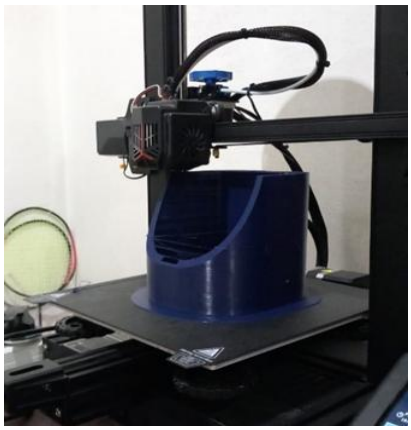


Figure 19. AUV parts assembly process

2.2.2. Electrical connection

The electrical system comprises key components including the FY-41AP flight controller circuit, LiPo battery, GPS module, ESCs (Electronic Speed Controllers), brushless motors, receiver, and four servo motors. Power from the battery is efficiently distributed to both the FY-41AP controller board and ESCs. Each ESC is individually linked to its respective brushless DC motor, ensuring precise control over propulsion. The GPS module and receiver interface directly with the FY-41AP controller board. Upon receiving signals from the transmitter, the receiver relays this information to the FY-41AP controller, which acts as the central hub for processing commands. This control board then disseminates control signals to all interconnected components, orchestrating seamless operation.

The GPS module serves a critical role in navigation, facilitating path-finding capabilities for the UAV. ESCs, on the other hand, regulate the speed of brushless motors, optimizing performance and maneuverability. The comprehensive electrical connection setup is depicted in Figure 20, showcasing the culmination of meticulous wiring and integration efforts

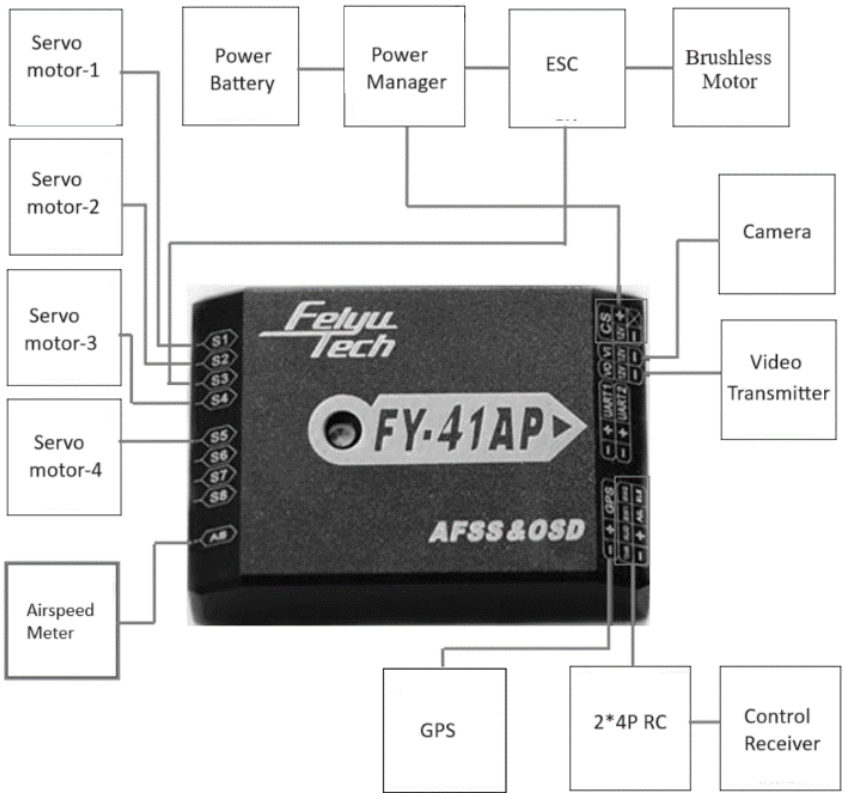


Figure 20. Electrical connection for AUV

2.2.3. Flight controller configuration

The configuration process for the flight controller involved the utilization of the FYGCS 5.11 application, illustrated in Figure 21. This specialized application is tailored specifically for the FY-41AP flight controller, offering unparalleled efficiency and user-friendly adjustment capabilities. Renowned for its intuitive interface and streamlined functionality, the FYGCS 5.11 application simplifies the configuration process, distinguishing it from other controllers in terms of ease of use and efficiency.

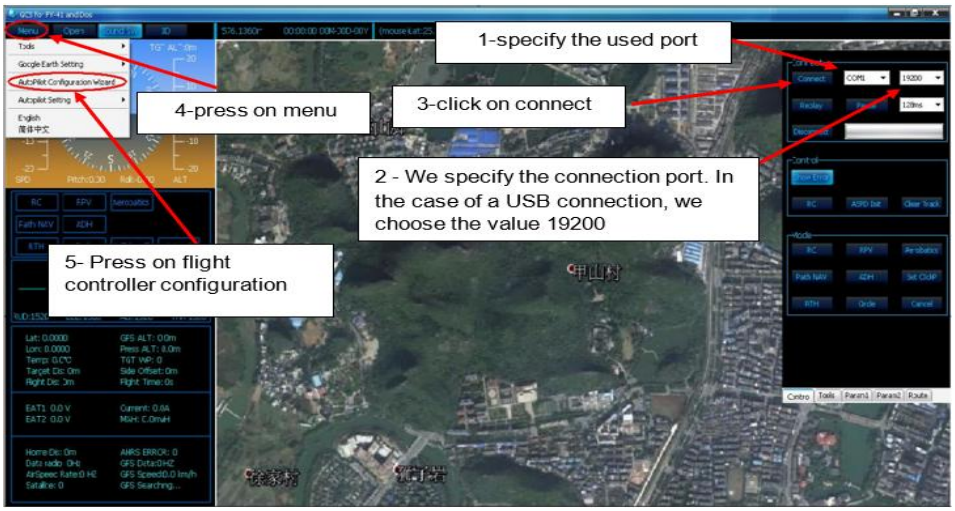


Figure 21. Fygcs 5.11 main interface

To finalize the configuration process, we must follow the six steps outlined in Figure 22:

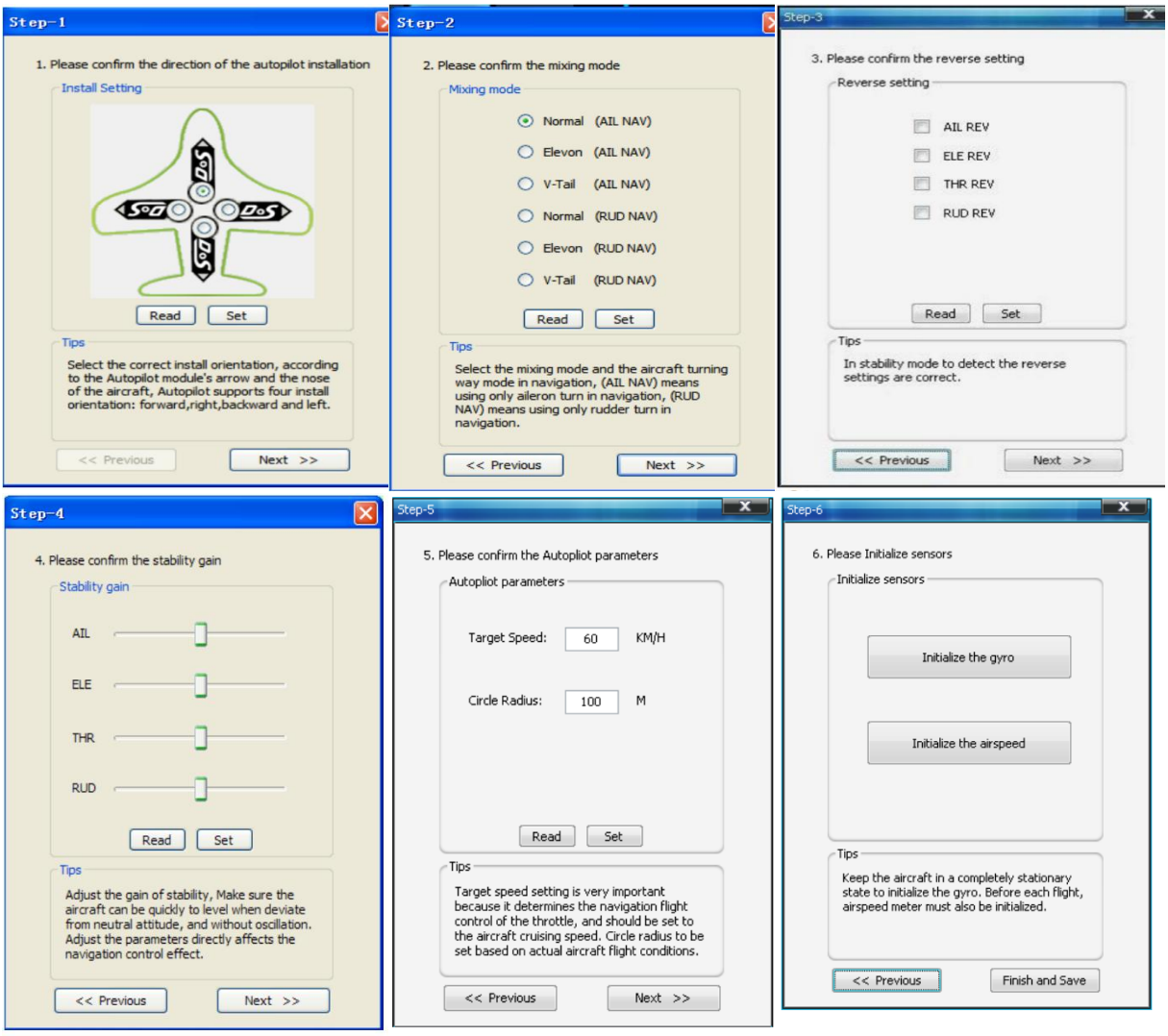


Figure 22. The main flight controller configuration steps

Following meticulous adjustments within the application, the stabilizer settings of the fixed-wing drone were finely tuned, ensuring optimal performance and stability during flight operations. This comprehensive configuration process represents a critical step in the preparation of the UAV for successful deployment and mission execution.

2.2.4. Selecting batteries

To ensure our ESCs and brushless motors receive the optimal voltage of 26V for peak performance, we've selected Samsung INR18650 LiPo batteries for our study. These batteries boast a nominal voltage of 3.7V and a maximum voltage of 4.2V when fully charged.

To achieve the required 26 V output, six 4.2 V batteries were connected in series, resulting in a total maximum voltage of 25.2 V. In series configurations, voltage adds while capacity remains constant; in parallel configurations, capacity adds while voltage remains the same (Figure 23). This setup ensured stable and efficient power delivery to the propulsion system [32].

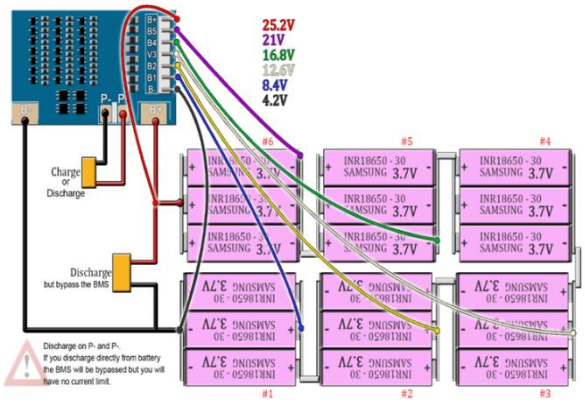
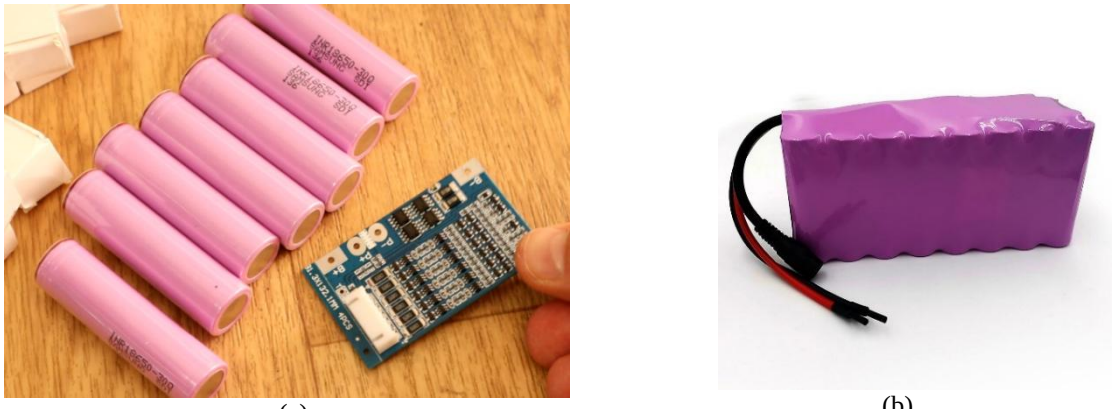


Figure 23. 6S BMS connection

As depicted in Figure 24, during the battery assembly process, it's crucial to consider the utilization of connectors capable of effectively transmitting high currents. This ensures that the battery operates with the requisite efficiency needed to power the engine optimally. Additionally, it's imperative to verify the circuit output values using a multimeter to validate the accuracy of the connections. By adhering to these procedures, we guarantee a reliable and robust electrical system, essential for the smooth operation of our UAV.



(a) (b)

Figure 24. BMS circuit and batteries (a) before assembly (b) after assembly

2.2.5. Movement mechanism and function of the moving parts in the fuselage

Before flight, it is essential to perform automatic movement checks on the aileron, elevator, and rudder servos to verify proper functionality, following the manufacturer's instructions [33]. For the aileron servo, when rolling the plane to the right, the right aileron should move downward while the left moves upward; the opposite occurs when rolling left. If movement is incorrect, adjust using the AIL dial (Figure 25).

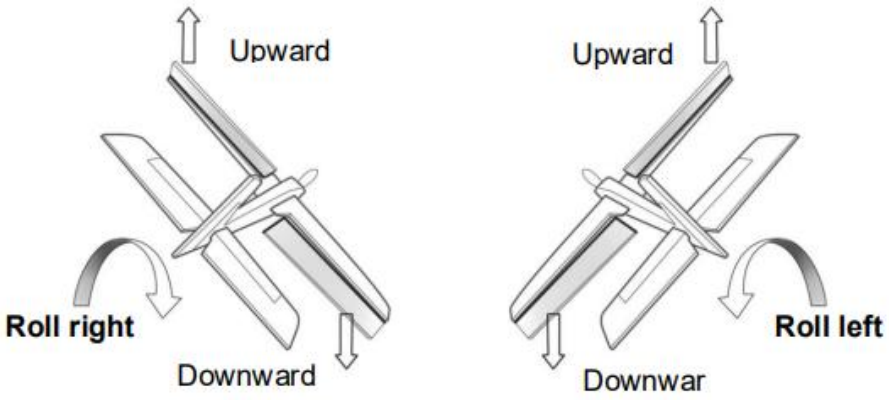


Figure 25. Aileron servo auto movement configuration

For the elevator servo, tilting the nose upward should cause the elevator to move downward, and vice versa when tilting the nose downward; incorrect movement can be corrected via the ELE dial (Figure 26).

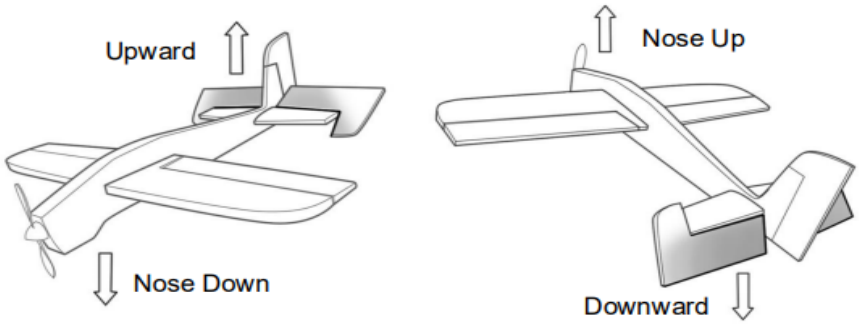


Figure 26. Elevator servo auto movement configuration

For the rudder servo, rotating the plane clockwise should result in the rudder moving left, while a counterclockwise rotation should cause it to move right; use the RUD dial if adjustments are needed (Figure 27). Correct servo response to control inputs is required to maintain flight stability and maneuverability.

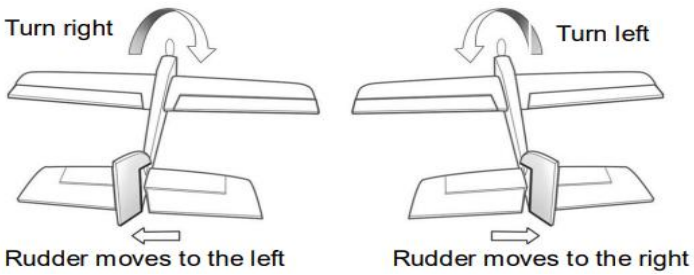


Figure 27. Rudder Servo Auto Movement Configuration

2.2.6. Integration of AI-Based object detection for surveillance

A lightweight object-detection module was integrated to enable real-time aerial surveillance. The onboard Raspberry Pi 4B processed image data captured by a 5 MP camera using a pre-trained YOLOv5s model optimized for edge devices. The model detected objects such as people and vehicles directly during flight. Three detection models-YOLOv5s, MobileNet-SSD, and Tiny-YOLOv4-were compared, with YOLOv5s showing the best balance between accuracy and efficiency.

The model achieved a mean Average Precision (mAP@0.5) of 82.4 % on the test set and an average frame rate of 3–5 FPS, which was sufficient for low-altitude UAV missions. Figures 28–30 illustrate the system architecture and example detections.

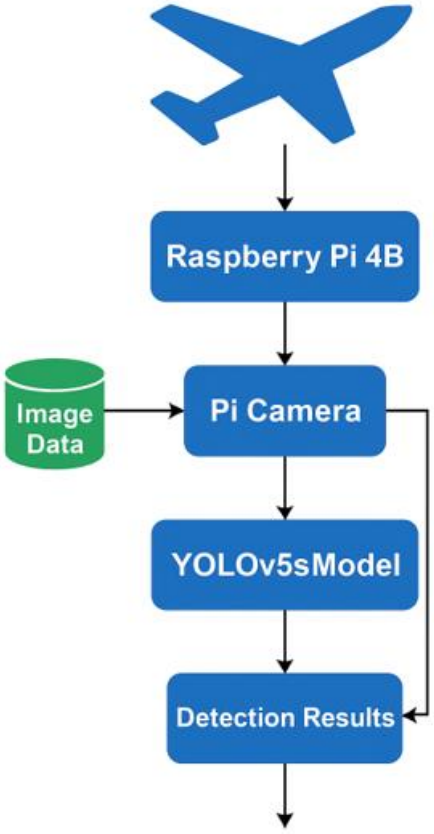


Figure 28. System architecture showing AI-powered object detection integration onboard the UAV

2.2.7. Dataset used for object detection

The COCO (Common Objects in Context) dataset was used to train and fine-tune the object detection model employed onboard the UAV. COCO is a large-scale object detection, segmentation, and captioning dataset containing over 330,000 images, more than 1.5 million object instances, and 80 object categories, including humans, vehicles, animals, and everyday objects [27].

For this work, a subset of the COCO dataset relevant to aerial surveillance was utilized, focusing on object classes such as "person", "car", "truck", and "bicycle". The dataset includes diverse contexts and labeling, which supports training models for outdoor and aerial surveillance tasks. The use of COCO allowed for effective transfer learning, where the pre-trained weights from COCO were fine-tuned with 300 aerial images collected using the UAV itself to improve domain-specific accuracy. This hybrid training strategy helped achieve a balance between general object detection performance and specific optimization for aerial views captured at altitudes between 30 and 40 meters.

3. Results and Discussions

3.1. Testing the aircraft functionality

During installation, all electronic components were positioned to maintain the aircraft's balance. The flight controller was aligned with the center of gravity, and the battery was secured for stability. The aircraft was then suspended under the wings to verify the center-of-mass alignment, which confirmed acceptable balance for stable flight. Ground tests (Figures 29 and 30) verified onboard system functionality and airworthiness.



Figure 29. The fuselage after final assembly and painting



Figure 30. Balance test showing the aircraft suspended from a single wing point

The development process also involved two failed experiments, which led to structural damage:

- In the first trial, the original engine was underpowered and was replaced with a larger motor (Figure 31, left). However, this introduced excess torque, causing uncontrollable rotation and a crash.
- The second failure resulted from a malfunction in the right aileron's servo motor (Figure 31, right), causing the aircraft to spin and crash.



Figure 31. Failed prototypes during pre-takeoff tests

3.2. Successful flight test and payload evaluation

After two unsuccessful trials, the third prototype achieved a stable and controlled flight (Figure 32). Following calibration of all systems, the UAV successfully carried a payload of 5.5 kg, comparable to that of commercial-class platforms. This capacity allows integration of additional mission modules such as sensors, delivery containers, or onboard AI units.



Figure 32. Aircraft used in successful test prior to takeoff

In addition to descriptive observations, the flight performance results were systematically documented to provide clearer insight into endurance, payload capacity, and environmental conditions during testing. Table 1 summarizes the outcomes of all flight trials, including failed attempts and successful missions, along with relevant contextual factors such as wind conditions and payload weights. This structured overview highlights both the challenges encountered during early tests and the stability achieved in the final prototype.

Table 1. Summary of flight test results

Test No.	Flight Duration (min)	Distance Covered (km)	Payload (kg)	Weather/Wind Conditions	Notes
1	0 (failed takeoff)	-	-	Calm	Underpowered motor
2	<1 (crash)	-	-	Light wind (~5 km/h)	Servo malfunction
3	18	12.5	3.0	Calm	Stable flight
4	22	15.2	5.5	Moderate wind (~10 km/h)	Successful, max payload

3.3. Cost analysis

As shown in Table 2, the total component cost was 29.637 TL (≈ 985 USD), which is considerably lower than comparable commercial VTOL UAVs priced between 3.000 and 35.000 USD on online marketplaces [35]. This demonstrates the cost-effectiveness of the developed platform.

Table 2. Component Costs in Turkish Lira

Part	Qty	Unit Price (TL)	Total (TL)
Emax ES08MAII servos	4	400.00	1.600.00
Sunnysky X3520-520KV motor	1	2.031.00	2.031.00
Propeller 12×8	1	100.00	100.00
ESC 60A Skywalker	1	1.800.00	1.800.00
Remote Control (Skydroid T12)	1	6.897.00	6.897.00
18650 Battery	20	120.00	2.400.00
SpeedyBee F405	1	1.400.00	1.400.00
BMS 6S	1	350.00	350.00
Matek M8Q-5883 GPS	1	1.280.00	1.280.00
Polymaker PolyLite LW-PLA (spools)	2	1.800.00	3.600.00
Carbon Fiber Rods	1	3.000.00	3.000.00
Raspberry Pi Compute Module CM5, 4GB RAM	1	3.482.87	3.482.87
Raspberry Pi Kamera Modül V2	1	1.669.42	1.669.42
Total Cost			29.637.29

3.4. Real time performance metrics

A flight mission was conducted to evaluate real-world detection performance. The onboard system identified vehicles and people from aerial video streams. During live operation, the detection model achieved an average rate of 4.2 frames per second (FPS) and a latency of 230 ms on the Raspberry Pi 4B. The AI module consumed less than 4 W of power, producing minimal impact on flight endurance.

A custom aerial dataset was created from images captured during test flights and annotated with Roboflow and LabelImg for object classes (person, car, motorbike). The dataset, combined with COCO images, was used for fine-tuning.

To assess real-time behavior under realistic conditions, test flights were carried out in campus and urban environments containing dynamic objects.

Each scenario included at least 10 test flights, during which the UAV flew at altitudes ranging from 30 to 60 meters. The onboard system was tasked with detecting three target classes: person, car, and motorcycle. The UAV successfully identified all categories across scenarios, demonstrating robustness in diverse conditions.

3.5. Model Selection and comparison

YOLOv5s was selected for its balance of computational efficiency and detection accuracy. The model was compared against MobileNet-SSD and TinyYOLOv4 on the aerial test dataset. In addition to the commonly used mAP@0.5 metric, precision, recall, and F1-score were calculated to provide a more comprehensive evaluation of detection reliability. As shown in Table 3, YOLOv5s not only achieved the highest mAP but also outperformed the other models in terms of accuracy metrics, including mAP@0.5, precision, recall, and F1-score, confirming its suitability for real-time UAV-based surveillance. While MobileNet-SSD exhibited faster inference speed, it lagged in accuracy and overall detection balance.

The evaluation of object detection models was conducted using a curated aerial dataset collected during UAV test flights. As shown in Table 3, YOLOv5s achieved superior performance across all key metrics, including mean Average Precision (mAP@0.5), precision, recall, and F1-score. Specifically, YOLOv5s obtained an mAP@0.5 of 82.4%, outperforming MobileNet-SSD (72.1%) and TinyYOLOv4 (74.6%). In terms of detection reliability, YOLOv5s reached 83.1% precision and 81.6% recall, resulting in an overall F1-score of 82.3%. These results highlight YOLOv5s as the most balanced model, capable of maintaining both accuracy and consistency in real-time aerial surveillance.

Although MobileNet-SSD had the fastest inference speed (≈ 5 FPS), its lower precision (70.4 %) and recall (71.2 %) reduced its suitability for safety-critical missions. Tiny-YOLOv4 offered moderate accuracy but performed below YOLOv5s in all metrics. Overall, YOLOv5s provided the best balance between computational demand and accuracy, confirming its suitability for resource-constrained embedded platforms. This evaluation validates the feasibility of deploying deep-learning-based detection within low-cost UAV systems for real-world applications.

Table 3. Object detection model accuracy metrics on UAV aerial dataset

Model	mAP@0.5	Precision (%)	Recall (%)	F1-Score (%)	Inference Speed (FPS)	Power Draw (W)
YOLOv5s	82.4%	83.1	81.6	82.3	~4.2	<4W
MobileNet-SSD	72.1%	70.4	71.2	70.8	~5.0	<3.5W
TinyYOLOv4	74.6%	73.0	72.1	72.5	~3.8	~4W

3.6. Evaluation and comparative model performance

The object detection module was tested during real-time, low-altitude flight missions (30–40 meters). The YOLOv5s model achieved 4.2 FPS with a latency of 230 ms on a Raspberry Pi 4B, confirming the feasibility of embedded edge-AI for lightweight surveillance tasks in small UAV platforms. Table 4 summarizes runtime metrics such as inference speed, latency, power draw, and edge suitability.

Table 4. Object Detection Model Runtime and Deployment Performance on UAV Aerial Dataset

Model	mAP@0.5	Avg FPS	Latency	Power Draw (W)	Edge Suitability
YOLOv5s	82.4%	4.2	230 ms	<4W	Excellent
MobileNet-SSD	72.1%	5.0	190 ms	<3.5W	Good
TinyYOLOv4	74.6%	3.8	260 ms	~4W	Moderate

While MobileNet-SSD offered marginally better speed, YOLOv5s provided superior accuracy and robustness, making it the optimal choice for this UAV system.

To put the contributions of this work in context, Table 5 compares the developed UAV system against recently related works. In contrast to prior works that adopted multirotor-based platforms or performed offline object recognition, the presented approach makes use of a complete open-source fixed-wing VTOL UAV system with onboard real-time inference. In addition, the developed system supports higher payload capacity and improved energy efficiency while relying on accessible and low-cost hardware components.

Table 5. Comparison of the Proposed UAV with Related Studies

Study	UAV Type	AI Model	Hardware	Real-Time?	Payload Capacity	Open Source	Novelty
Wu et al. [1]	Multirotor	YOLOv3	Jetson TX2	✓	Not specified	✗	Precision agriculture use case
Zhou et al. [5]	Multirotor	YOLOv4-tiny	Jetson Nano	✓	Low	✗	Aerial surveillance, no VTOL
Guerra et al. [4]	VTOL Fixed-wing	–	PX4	✗	4 kg	✗	Terrain mapping only
This Study	VTOL Fixed-wing	YOLOv5s	Raspberry Pi 4B	✓	5.5 kg	✓	Real-time AI on low-cost, modular platform

Note: Reported values represent averages across 10 test runs. Standard deviations for detection accuracy metrics were within ±1.2%, and latency variations were within ±15 ms.

4. Limitations and Future Work

Despite the satisfactory performance of the UAV during testing, several limitations were identified:

- **Altitude constraint:** Detection accuracy decreased at higher altitudes because smaller image scales made objects harder to identify.
- **Lighting sensitivity:** Detection performance declined under low-light or high-glare conditions, limiting operation in certain environments.
- **Computational limits:** The current onboard hardware restricted the deployment of larger models or multi-camera configurations, reducing the potential for complex detection tasks.

Although this study did not propose a new detection algorithm, it demonstrated the practical feasibility of deploying existing deep-learning models on a modular, low-cost UAV platform. The emphasis remained on applied deployment and system-level integration for real-time intelligence in the field.

To overcome these limitations, future research will focus on the following improvements:

- **AI-functionality expansion:** Adding object-tracking capability, thermal-imaging support for night operations, and anomaly-detection features to widen application areas.
- **Flight-autonomy enhancement:** Incorporating AI-based path-planning and obstacle-avoidance algorithms to increase operational safety and independence in dynamic environments.
- **Extended endurance:** Investigating higher-capacity or solar-assisted batteries to lengthen flight time and range.

These developments are expected to improve the UAV system's adaptability and efficiency for use in diverse fields such as security, environmental monitoring, disaster response, precision agriculture, and humanitarian logistics. While initial flight tests confirmed technical feasibility, the sample size was limited. Additional experiments under varied environmental conditions—including wind, temperature, and longer missions—will be required to verify long-term endurance and reliability.

5. Conclusion

This study presents a practical and systematic approach to the design, construction, and testing of a cost-effective VTOL (Vertical Take-Off and Landing) fixed-wing UAV platform. The results demonstrate that advanced aerial systems can be developed with affordable, commercially available components and 3D-printed structures, making the technology accessible to small research groups and institutions with limited resources.

A major contribution of this work is the successful integration of an onboard AI-based object-detection system using the YOLOv5s model on a Raspberry Pi 4B. The UAV performed real-time inference during flight, achieving a mean Average Precision (mAP@0.5) of 82.4 % and an average processing speed of 4.2 FPS at altitudes between 30 and 60 m. These findings demonstrate the feasibility of deploying deep-learning models on low-power edge devices for aerial-surveillance tasks.

The developed UAV also exhibited stable flight behavior, efficient energy consumption (≈ 2.1 Wh per km), and the ability to carry payloads of up to 5.5 kg. With a 4S4P 16800 mAh battery configuration, it achieved an estimated range of 120 km and more than 2 hours of continuous flight, making it suitable for extended missions such as monitoring, inspection, and logistics.

From an economic perspective, the total system cost (≈ 985 USD) is considerably lower than that of comparable commercial UAVs, positioning the platform as a scalable solution for applications in disaster response, security surveillance, environmental monitoring, agriculture, and humanitarian operations. Although performance decreased under low-light or high-altitude conditions, these limitations suggest directions for future work, including the integration of thermal imaging, advanced sensors, and coordinated multi-UAV systems.

In summary, this research indicates that low-cost, AI-enabled UAV systems can be effectively designed for mission-critical applications. The findings provide a foundation for future advancements in autonomous navigation, enhanced sensing, and multi-agent coordination in aerial robotics.

6. Acknowledgment

We sincerely thank Mahmoud Engineering & Electronics Company, led by Mr. Mahmoud Al-Habbal, for their generous sponsorship and support. Their provision of essential components and testing facilities was vital to the successful development, deployment, and validation of the UAV system.

7. Author Contribution Statement

In the study, Author 1 contributed to conceptualization, data curation, formal analysis, investigation, methodology, validation, visualization, writing – original draft, writing - review and editing.

8. Ethics Committee Approval and Conflict of Interest Statement

Ethics committee approval is not needed for preparing the article. There is no conflict of interest for this article.

9. Ethical Statement Regarding the Use of Artificial Intelligence

During the preparation of this manuscript, the artificial intelligence tool ChatGPT (developed by OpenAI) was used solely for limited purposes such as language editing and translation. All scientific content, analyses, interpretations, and results are the sole responsibility of the authors.

10. References

[1] G. Cai, K. Y. Lum, B. M. Chen, and T. H. Lee, "A brief overview on miniature fixed-wing unmanned aerial vehicles," in Proc. IEEE Int. Conf. Control Autom. (ICCA), 2010, pp. 285–290.
[2] F. Ahmed, J. C. Mohanta, A. Keshari, and P. S. Yadav, "Recent advances in unmanned aerial vehicles: A review," Arab. J. Sci. Eng., vol. 47, no. 7, pp. 7963–7984, 2022.
[3] K. Buchholz, "Commercial drones projected growth," Statista, Mar. 3, 2019. [Online]. Available: https://www.statista.com/chart/17201/commercial-drones-projected-growth/.
[4] T. Baca, R. Penicka, P. Stepan, M. Petrlik, V. Spurny, D. Hert, and M. Saska, "Autonomous cooperative wall building by a team of unmanned aerial vehicles in the MBZIRC 2020 competition," Robot. Auton. Syst., vol. 166, p. 104482, 2023.
[5] A. Puri, "A survey of unmanned aerial vehicles (UAV) for traffic surveillance," Dept. Comput. Sci. Eng., Univ. South Florida, pp. 1–29, 2005.
[6] E. J. V. Rozo, "Medición de contaminación mediante UAV (Vehículo Aéreo no Tripulado)," Mundo Fesc, vol. 6, no. 11, pp. 16–26, 2016.
[7] R. D. B. Ruiz, A. C. Lordsleem Júnior, and J. H. A. Rocha, "Inspeção de fachadas com veículos aéreos não tripulados (VANT): estudo exploratório," Rev. ALCONPAT, vol. 11, no. 1, pp. 88–104, 2021.
[8] A. Aabid, B. Parveez, N. Parveen, S. A. Khan, J. M. Zayan, and O. Shabbir, "Reviews on design and development of unmanned aerial vehicle (drone) for different applications," J. Mech. Eng. Res. Dev., vol. 45, no. 2, pp. 53–69, 2022.
[9] A. J. Torija and C. Clark, "A psychoacoustic approach to building knowledge about human response to UAV noise," Int. J. Environ. Res. Public Health, vol. 18, no. 2, p. 682, 2021.
[10] Titan Dynamics, "Cobra VTOL: Build & User Manual," Rev. 1.1, 2024. [Online]. Available: https://www.titandynamics.org/s/Titan-Cobra-User-Manual.pdf.
[11] C. Davenport, J. Jonas, J. Martin, H. Mazur, S. Vinson, and B. Wirtz, "Aircraft design for AIAA Design Build Fly Competition," Worcester Polytechnic Institute, 2022.
[12] M. Y. Narkevich, O. S. Logunova, P. I. Kalandarov, A. N. Kalitaev, G. V. Tokmazov, P. Y. Romanov, and O. Alimov, "Results of a pilot experiment on monitoring the condition of buildings and structures using UAVs," IOP Conf. Ser.: Earth Environ. Sci., vol. 939, no. 1, p. 012030, 2021.
[13] Y. O. Aktaş et al., "A low-cost prototyping approach for design analysis and flight testing of the Turac VTOL UAV," in Proc. Int. Conf. Unmanned Aircr. Syst. (ICUAS), 2014, pp. 1029–1039.
[14] C. Chen, Z. Zheng, T. Xu, S. Guo, S. Feng, W. Yao, and Y. Lan, "YOLO-based UAV technology: A review of research and applications," Drones, vol. 7, no. 3, p. 190, 2023.
[15] A. Gupta and X. Fernando, "Simultaneous localization and mapping (SLAM) and data fusion in unmanned aerial vehicles: Recent advances and challenges," Drones, vol. 6, no. 4, p. 85, 2022.
[16] J. Łęcki, M. Hering, M. Jabłoński, and A. Karpus, "An analysis of the performance of lightweight CNNs for object detection on mobile devices," Sensors, vol. 24, no. 6, p. 1234, 2024.
[17] A. Telikani et al., "Unmanned aerial vehicle–aided intelligent transportation systems: Vision, challenges, and opportunities," IEEE Commun. Surveys Tuts., vol. 27, no. 1, pp. 45–78, 2025.
[18] S. Boddu and A. Mukherjee, "Efficient edge deployment of quantized YOLOv4-Tiny for aerial emergency object detection on Raspberry Pi 5," arXiv preprint arXiv:2506.09300, 2025.
[19] K. Niu, C. Wang, J. Xu, J. Liang, X. Zhou, K. Wen, and C. Yang, "Early forest fire detection with UAV image fusion: A deep learning method using visible and infrared sensors," IEEE J. Sel. Top. Appl. Earth Obs. Remote Sens., vol. 18, no. 5, pp. 1234–1245, 2025.
[20] Feiyu Technology, "FY-41AP AutoPilot & OSD System Installation and Operation Manual," 2024. [Online]. Available: https://cdn1.feiyu-tech.com/download/20190926/58574a74bea0d.pdf
[21] N. Nithyavathy, S. Pavithra, M. Naveen, B. Logesh, and T. James, "Design and development of a drone for healthcare," Int. J. Sci. Technol. Res., vol. 9, no. 1, pp. 2676–2680, 2020.
[22] A. Üzel, D. C. Zuidervliet, and P. J. van Duijsen, "Educational setup for brushless motor drives," in Proc. 17th Conf. Electr. Mach., Drives Power Syst. (ELMA), 2021, pp. 1–6.
[23] S. Sripad, A. Bills, and V. Viswanathan, "A review of safety considerations for batteries in electric aircraft," MRS Bull., vol. 46, no. 5, pp. 435–442, 2021.

[24] T. Placke, R. Kloepsch, S. Dühnen, and M. Winter, "Lithium-ion, lithium-metal, and alternative rechargeable battery technologies: The odyssey for high energy density," J. Solid State Electrochem., vol. 21, pp. 1939–1964, 2017.
[25] H. A. Gabbar, A. M. Othman, and M. R. Abdussami, "Review of battery management systems (BMS) development and industrial standards," Technologies, vol. 9, no. 2, p. 28, 2021.
[26] CFRP-Tstar, "Carbon fiber rods – the best choice for your projects," 2024. [Online]. Available: https://www.cfrp-tstar.com/high-quality-carbon-fiber-rods/.
[27] C. J. Swinney and J. C. Woods, "Low-cost Raspberry Pi–based UAS detection and classification system using machine learning," Aerospace, vol. 9, no. 12, p. 738, 2022.
[28] M. Pagnutti, R. E. Ryan, G. Cazenavette, M. Gold, R. Harlan, E. Leggett, and J. Pagnutti, "Laying the foundation to use Raspberry Pi 3 V2 camera module imagery for scientific and engineering purposes," J. Electron. Imag., vol. 26, no. 1, p. 013014, 2017.
[29] M. H. Hamzenejadi and H. Mohseni, "Fine-tuned YOLOv5 for real-time vehicle detection in UAV imagery: Architectural improvements and performance boost," Expert Syst. Appl., vol. 231, p. 120845, 2023.
[30] Roboflow, "Roboflow: Annotate and preprocess tool." [Online]. Available: https://roboflow.com
[31] Z. Chen, L. Cao, and Q. Wang, "YOLOv5-based vehicle detection method for high-resolution UAV images," Mobile Inf. Syst., vol. 2022, Art. no. 1828848, 2022.
[32] Electronoobs, "6S & BMS Battery Pack," 2024. [Online]. Available: https://electronoobs.com/eng_circuitos_tut27.php.
[33] Feiyu Technology, "FY-40A Flight Stabilization System Installation & Operation Manual," 2024. [Online]. Available: http://www.feiyu-uav.net/data/upload/admin/20181124/5bf915baf02ff.pdf.
[34] T. Y. Lin et al., "Microsoft COCO: Common objects in context," in Comput. Vis. – ECCV 2014, Cham, Switzerland: Springer, 2014, pp. 740–755.
[35] Made-in-China, "Fixed Wing Drone," 2024. [Online]. Available: https://www.made-in-china.com/products-search/hot-china-products/Fixed_Wing_Drone.html.

Fırat Üniversitesi Deneysel ve Hesaplamalı Mühendislik Dergisi

FUJECE

Zaman Çerçevesine Uyarlanabilir Arbitraj: Dinamik Sinyal Gecikmeleri ile İkili İşlem Performansının Optimizasyonu

Mustafa KANBER[1]*, Yunus SANTUR [2]

[1]Yazılım Mühendisliği, Fen Bilimleri Enstitüsü, Fırat Üniversitesi, Elazığ, Türkiye.
[2]Yapay Zeka ve Veri Mühendisliği, Mühendislik Fakültesi, Fırat Üniversitesi, Elazığ, Türkiye.
[1]mkanber@firat.edu.tr, [2]ysantur@firat.edu.tr

Geliş Tarihi: 08.7.2025
Kabul Tarihi: 10.9.2025

Düzeltme Tarihi:11.8.2025

doi: https://doi.org/10.62520/fujece.1737324
Araştırma Makalesi

Alıntı: M. Kanber ve Y. Santur,'' Zaman çerçevesine uyarlanabilir arbitraj: dinamik sinyal gecikmeleri ile ikili işlem performansının optimizasyonu '', Fırat Üni. Deny. ve Hes. Müh. Derg., vol. 5, no 1, pp. 69-82, Şubat 2026.

Öz

Bu çalışma, klasik z-score tabanlı çiftli işlem (pairs trading) stratejisini dinamik sinyal gecikme mekanizmalarıyla geliştirerek istatistiksel arbitraja zaman uyarlamalı bir yaklaşım sunmaktadır. Apple Inc. (AAPL) referans alınarak, Dow Jones Industrial Average (DJIA) endeksindeki 29 hisse çifti üzerinde *t+1*'den *t+5*'e kadar farklı işlem gecikmelerinin performansa etkisi analiz edilmiştir. İşlemler, günlük kapanış fiyatlarından türetilen z-score sinyallerine göre açılıp kapatılmış; gecikmeli yürütme yaklaşımı kısa vadeli piyasa gürültüsünü azaltarak işlem zamanlamasını optimize etmeyi hedeflemiştir. Ampirik bulgular, önerilen stratejinin yüksek performans sergilediğini göstermektedir. Çiftlerin %93.8'i pozitif getiri, %89.7'si ise 1.0'ın üzerinde Sharpe Oranı elde etmiştir. Ortalama olarak *t+3* gecikme penceresi en etkili risk-getiri dengesini sağlamış; 2.371 Sharpe Oranı ve %192.98 toplam getiri ile en iyi performansı göstermiştir. Yalnızca %24.1 oranındaki çiftlerde anlık (*t+0*) işlemler en iyi sonucu vermiştir; bu da arbitrajda uyarlanabilir zamanlamanın avantajını ortaya koymaktadır. Sonuçlar, işlem zamanlamasının optimizasyonunun arbitraj modellerinin kârlılık ve istikrarını önemli ölçüde artırdığını doğrulamaktadır. Bulgular, zaman uyarlamalı yürütme yaklaşımının geleneksel çiftli işlem çerçevelerine değerli bir katkı sunduğunu güçlü biçimde ortaya koymaktadır.

Anahtar kelimeler: Finansal teknolojiler, İstatistiksel arbitraj, Finansal hesaplama, Çiftli arbitraj

*Yazışılan yazar

İntihal Kontrol: Evet – Turnitin
Şikayet: fujece@firat.edu.tr
Telif Hakkı ve Lisans: Dergide yayın yapan yazarlar, CC BY-NC 4.0 kapsamında lisanslanan çalışmalarının telif hakkını saklı tutar.

Firat University Journal of Experimental and Computational Engineering

Time Frame Adaptive Arbitrage: Optimizing Pairs Trading Performance with Dynamic Signal Delays

Mustafa KANBER[1]*, Yunus SANTUR [2]

[1]Software Engineering, Graduate School of Natural and Applied Sciences, Firat University, Elazig, Türkiye.
[2]Artificial Intelligence and Data Engineering, Faculty of Engineering, Firat University, Elazig, Türkiye.
[1]mkanber@firat.edu.tr, [2]ysantur@firat.edu.tr

Received: 08.07.2025
Revision: 11.8.2025
Accepted: 10.9.2025
doi: https://doi.org/10.62520/fujece.1737324
Research Article

Citation: M. Kanber and Y. Santur, "Time frame adaptive arbitrage: optimizing pairs trading performance with dynamic signal delays", Firat Univ. Jour.of Exper. and Comp. Eng., vol. 5, no 1, pp. 69-82, February 2026.

Abstract

This study enhances the classical z-score-based pairs trading strategy by introducing dynamic signal delay mechanisms to develop a time-adaptive approach to statistical arbitrage. Using Apple Inc. (AAPL) as a benchmark, 29 stock pairs from the Dow Jones Industrial Average (DJIA) index were analyzed to assess the impact of execution delays ranging from *t+1* to *t+5* on trading performance. Positions were opened and closed based on z-score signals derived from daily closing prices, where delayed execution aimed to reduce short-term market noise and optimize trade timing. Empirical results demonstrate that the proposed strategy achieved favorable performance, with 93.8% of the pairs generating positive returns and 89.7% attaining a Sharpe Ratio greater than 1.0. On average, the *t+3* delay window yielded the most effective balance between risk and return, achieving a Sharpe Ratio of 2.371 and a cumulative return of 192.98%. Only 24.1% of the pairs performed best under immediate execution (*t+0*), highlighting the advantages of adaptive timing in arbitrage. Overall, the findings confirm that optimizing trade timing significantly enhances the profitability and stability of arbitrage models. The results provide empirical evidence supporting the potential of time-adaptive execution as a valuable improvement to traditional pairs trading frameworks.

Keywords: Fintech, Statistical arbitrage, Financial calculation, Pairs trading

*Corresponging author

Plagiarism Checks: Yes – Turnitin
Complaints: fujece@firat.edu.tr
Copyright & License: Authors publishing with the journal retain the copyright to their work licensed under the CC BY-NC 4.0

1. Introduction

Temporary price deviations between assets in financial markets present exploitable opportunities through statistical arbitrage strategies [1]. These strategies rely on the fundamental assumption that when long-term equilibrium relationships between price series are disrupted, deviations tend to revert to the mean over time [2]. Within this framework, the pairs trading approach generates buy and sell signals by analyzing the price spread between two assets assumed to be correlated or cointegrated [3].

This study develops a z-score-based arbitrage strategy for selected asset pairs in the U.S. equity market, specifically between Apple Inc. (AAPL) and the components of the DOW30 index. The z-score, a simple yet effective indicator, measures how far the price spread between two stocks deviates in terms of standard deviations [4]. Trading positions are initiated when the z-score exceeds the ±1 thresholds and are closed once it returns to a convergence band between –0.25 and +0.25. Unlike conventional approaches that execute trades immediately at threshold crossings (t), this study applies delayed execution intervals ($t+1$ to $t+5$) to reduce short-term market noise and identify optimal delay periods (n) for more robust signal generation. This design enhances consistency in response to price deviations and improves the overall performance of the strategy.

Traditional z-score models typically assume stationary relationships between price series [5]. However, classical cointegration tests were intentionally omitted in this study because short-term arbitrage strategies are better captured by high-frequency correlations that reflect the market's dynamic structure [6]. Accordingly, pair selection is based on instantaneous correlation and volatility-normalized spread values. This approach eliminates the rigid requirement of cointegration, allowing greater flexibility and adaptability in real-world applications.

The proposed framework systematically tests all delay windows from $t+1$ to $t+5$, evaluating performance metrics separately for each. The objective is to determine which delayed signal window achieves the highest return, lowest risk, and greatest consistency, thereby identifying the most effective delay interval. This approach produces a model that is more responsive and better aligned with market dynamics compared to conventional z-score strategies that operate with fixed parameters.

The performance of the strategy is evaluated using well-established metrics such as the Sharpe Ratio, Sortino Ratio, Profit Factor, and Maximum Drawdown. Additionally, each arbitrage pair's results are compared to the classical buy-and-hold performance of the corresponding stocks, enabling a detailed assessment of absolute and risk-adjusted returns.

While traditional pairs trading models rely solely on statistical threshold breaches to trigger trades [7], this study introduces timing optimization, making the execution of signals dynamically adaptive. Consequently, the proposed approach optimizes not only the trading direction but also the timing of position entry. This represents a novel contribution to the field of time-adaptive arbitrage and underscores the critical role of execution timing in trading performance.

A review of the literature reveals that most pairs trading studies employ z-score-based threshold mechanisms but often overlook systematic evaluations of delayed signal triggering, optimal threshold selection, and decision deferral windows. This study addresses these gaps by developing a dynamic, time-adaptive version of z-score-based pairs trading. Recent empirical findings reinforce the continuing relevance of pairs trading; for instance, Zhu [8] replicated classical methodologies and found that pairs trading consistently generated statistically and economically significant returns, with an average annual excess return of 6.2% and a Sharpe Ratio of 1.35, confirming its enduring effectiveness in modern financial markets.

2. Materials and Methods

This section provides a detailed description of the dataset used in the study, the implementation procedure of the pairs trading strategy, the performance evaluation metrics, and the overall analysis process. Additionally,

the technological infrastructure employed, the assumptions made during computations, and the data preprocessing steps are explained. To ensure the reproducibility of the study, the algorithmic framework is expressed through equations, and the tools utilized are explicitly specified.

2.1. Dataset

In this study, Apple Inc. (AAPL) was selected as the reference stock from among the 30 constituents of the Dow Jones Industrial Average (DJIA), and pairs trading analysis was conducted with the remaining 29 stocks [9]. The analysis period spans from January 1, 2023, to December 1, 2024, using daily closing prices obtained via the Yahoo Finance API. In summary, AAPL was designated as the reference asset, and the arbitrage strategy was tested against the other 29 DJIA stocks.

2.2. Pairs trading strategy methodology

2.2.1. Spread and z-score calculation

A spread value has been calculated for each stock pair. The spread represents the fundamental metric for the price difference between two stocks in pairs trading strategies [10]. The two stocks are typically selected as correlated assets that co-move over the long term. The spread is utilized to detect arbitrage opportunities when the relationship between these two stocks temporarily deviates. The calculation of the spread value is shown in Equation 1 as follows [11].

$$Spread_t = P_t^{AAPL} - \beta_t \cdot P_t^{(i)} \tag{1}$$

In Equation. 1, P_t^{AAPL} denotes the closing price of Apple stock on day t, $P_t^{(i)}$ represents the closing price of the compared test stock, and β_t ignifies the regression coefficient calculated for the relevant period. A 60-day rolling window was applied to the spread time series, and the mean and standard deviation were calculated as shown in Equation 2.

$$\mu_t = \frac{1}{N}\sum_{k=t-N+1}^{t} Spread_k, \quad \sigma_t = \sqrt{\frac{1}{N}\sum_{k=t-N+1}^{t}(Spread_k - \mu_t)^2} \tag{2}$$

Using the values from Equation 2, the standardized spread (i.e., Z-score) is calculated as shown in Equation 3 [12].

$$z_t = \frac{Spread_t - \mu_t}{\sigma_t} \tag{3}$$

2.2.2. Signal generation criteria

Trading signals are generated based on the Z-score value according to the threshold values specified in Equation 4. A sample position strategy based on the Z-score is illustrated in Figure 1.

$$\begin{aligned} &\text{Buy}: z_t < -1.0 \\ &\text{Sell}: z_t > 1.0 \\ &\text{Close}: -0.25 < z_t < 0.25 \end{aligned} \tag{4}$$

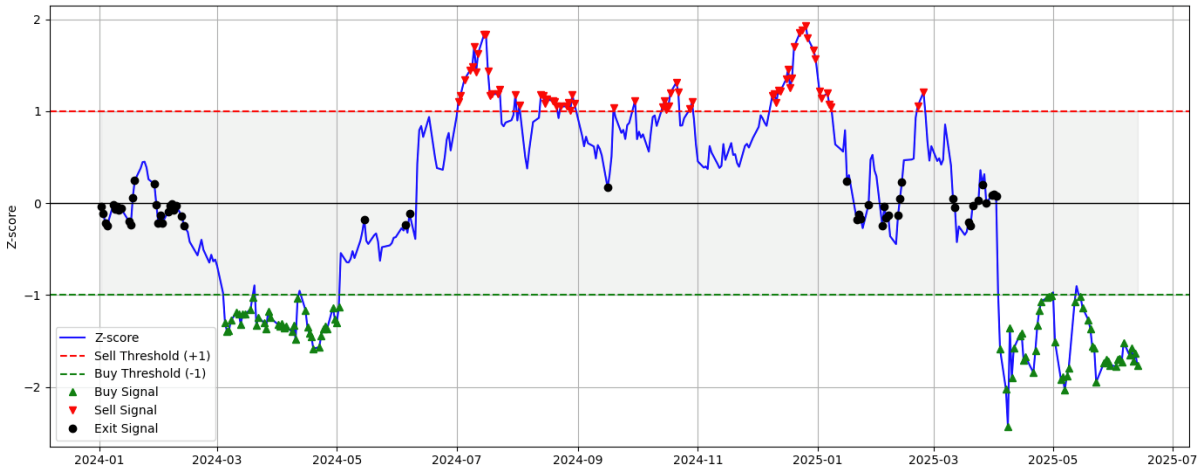


Figure 1. Z-Score position opening behavior

To model transaction delays under real market conditions, delayed strategies were tested based on the execution day relative to signal generation. In this context, *t+1*, *t+2*, *t+3*, *t+4*, and *t+5* delays were analyzed.

2.3. Performance measurement and analysis methods

In this study, the efficacy and risk profile of the pairs trading strategy were comprehensively evaluated using diverse performance metrics. These performance measures were selected to reveal the strategy's robustness and adaptability to market conditions, while accounting for the risk-return trade-off.

2.3.1. Risk-adjusted return metrics

To evaluate the performance of the implemented strategy from a risk-balanced perspective, widely accepted performance criteria were utilized. Within this scope, the Sharpe Ratio – which measures the excess return per unit of total risk – and the Sortino Ratio – which provides a more refined measurement by considering only downside risk (negative volatility) – were calculated.

- **Sharpe Ratio:** This metric quantifies the return per unit of risk, where risk is defined as volatility (standard deviation) [13]. While the Sharpe Ratio reveals the overall risk-return trade-off, it can sometimes be misleading because it treats both positive and negative volatility equally [14]. The calculation of the Sharpe Ratio is shown in Equation 5.

$$S = \frac{R_p - R_f}{\sigma_p} \times \sqrt{252} \tag{5}$$

In Equation 5, R_p denotes the mean daily return of the portfolio (or strategy), R_f represents the risk-free rate of return, and σ_p is the standard deviation of daily returns. The term $\sqrt{252}$ annualizes the ratio under the assumption of 252 trading days in a year.

- **Sortino Ratio**: An enhanced version of the Sharpe Ratio. Here, only downside volatility is considered risk. This metric offers a more realistic risk assessment by focusing on losses, which are investors' primary concern [15]. The calculation of the Sortino Ratio is given in Equation 6 [16].

$$SoR = \frac{R_p - R_f}{\sigma_d} \times \sqrt{252} \tag{6}$$

In Equation 6, R_p denotes the mean daily return of the portfolio (or strategy), R_f represents the risk-free rate of return, and σ_d is the standard deviation of negative returns (downside deviation). The term $\sqrt{252}$ annualizes the ratio under the assumption of 252 trading days in a year.

2.3.2. Risk metrics

As a risk metric, the Maximum Drawdown (Max Drawdown) value is calculated in this study. Max Drawdown measures the peak-to-trough decline of the strategy [17], representing the largest potential loss an investor could face. It serves as a critical indicator for assessing outcomes during sudden market collapses and detecting strategy failures. The calculation of the Max Drawdown value is shown in Equation 7 [18].

$$\text{MaxDrawdown} = \min\left(\frac{C(t)}{C_{max}(t)} - 1\right) \tag{7}$$

In Equation 7, $C(t)$ denotes the current cumulative return, while $C_{max}(t)$ represents the maximum cumulative return value up to that date.

2.3.3. Transaction-based performance metrics

To measure the success of trades executed in this study, the Profit Factor and Win Rate were employed.

- **Profit Factor:** Measures trade-level efficiency by ratio of gross profit to gross loss. Values > 1 indicate a profitable strategy. The calculation is shown in Equation 8 [19].

$$\text{ProfitFactor} = \frac{\sum \text{Profit}}{|\sum \text{Loss}|} \tag{8}$$

- **Win Rate:** Represents the percentage of profitable trades relative to total trades executed. The calculation is shown in Equation 9 [20].

$$\text{Win Rate} = \frac{Number\ of\ Profitable\ Trades}{\text{Total Trades}} \times 100 \tag{9}$$

2.4. Analytical approach

2.4.. Optimization process

Among the 5 delay periods tested for each stock pair, the delay period yielding the highest Sharpe ratio was designated as 'optimal'.

2.4.2. Statistical analysis

Statistical analysis was conducted in this study. The performed analyses are as follows:

- Comparison of mean performance across delay periods
- Distribution of optimal delay periods by stock pair
- Risk-return profile visualizations"

3. Experimental Results

In this study, AAPL was selected as the benchmark stock, and the pairs trading strategy was analyzed with the other 29 stocks in the Dow Jones Industrial Average index. The impact of delay periods from *t+1* to *t+5* on performance was comprehensively examined. The key findings are as follows:

- Total Analyzed Pairs: 29 stock pairs (in AAPL-X format)
- Tested Delay Periods: t+1, t+2, t+3, t+4, t+5
- Total Strategy Combinations: 145 distinct strategy tests
- Success Rate: 98.6% with positive Sharpe Ratio, 93.8% with positive return
- Analysis Period: January 1, 2023 – December 1, 2024 (≈2 years)

3.1. Top-performing stock pairs and performance metrics

The 10 most successful arbitrage pairs with AAPL, ranked by Sharpe ratio, are shown in Table 1. For each stock pair, different trade execution delays from *t+1* to *t+5* were tested, and the delay period yielding the highest Sharpe Ratio was designated as optimal.

Table 1. Performance metrics of stock pairs by optimal delay period

Rank	Stock Pair	Optimal Delay	Sharpe Ratio	Return (%)	Max Drawdown (%)	Win Rate (%)
1	AAPL-MMM	*t+3*	2.371	192.98	-12.14	61.23
2	AAPL-V	*t+4*	1.988	88.40	-13.88	53.91
3	AAPL-AMGN	*t+1*	1.972	112.42	-17.92	56.14
4	AAPL-WMT	*t+2*	1.957	96.10	-10.52	55.15
5	AAPL-UNH	*t+1*	1.927	138.92	-18.10	57.74
6	AAPL-HON	*t+1*	1.909	80.25	-10.21	56.71
7	AAPL-TRV	*t+5*	1.795	120.26	-14.39	54.32
8	AAPL-IBM	*t+1*	1.773	91.81	-17.70	53.60
9	AAPL-DIS	*t+5*	1.768	98.66	-12.57	57.60
10	AAPL-JNJ	*t+2*	1.666	73.47	-15.53	53.74

When Table 1 is examined, the AAPL-MMM pair achieves the highest Sharpe Ratio of 2.371 with a *t+3* delay period. This pair is also notable for its total return of 192.98% and Maximum Drawdown of 12.14%. The win rate was measured at 61.23%, suggesting highly successful trade execution.

Sharpe Ratio values generally range between 1.6 and 2.4, indicating consistently favorable risk-adjusted returns across pairs. Maximum Drawdown values fluctuate between -10% and -18%, demonstrating that the strategy may experience periodic significant declines.

These performance metrics reveal that the pairs trading strategy is viable and profitable, particularly between AAPL as the benchmark stock and selected constituents of the Dow Jones index. The selection of optimal delay periods plays a critical role in enhancing the strategy's risk-return balance.

3.2. Average performance by delay period

The 10 highest-performing arbitrage pairs with AAPL, ranked by Sharpe ratio, are presented in Table 2. For each stock pair, trade execution delays ranging from *t+1* to *t+5* were tested, with the delay period yielding the maximum Sharpe ratio designated as optimal.

Table 2. Average performance metrics across delay periods

Delay	Avg Sharpe	Avg Return %	Avg MaxDD %	Avg Win %
t+1	1.895	105.85	-15.98	56.05
t+2	1.812	84.78	-13.03	54.45
t+3	2.371	192.98	-12.14	61.23
t+4	1.988	88.40	-13.88	53.91
t+5	1.782	109.46	-13.48	55.96

The highest average Sharpe Ratio value of 2.371 was observed at the *t+3* delay period. This indicates that executing trades three days after signal generation provides the most favorable risk-adjusted returns. In parallel, the *t+3* delay also yielded the highest average return rate of 192.98%, further reinforcing its effectiveness. Conversely, the lowest average Maximum Drawdown (-12.14%) was likewise recorded at *t+3*, suggesting that this execution window is the most efficient in limiting potential losses.

The highest win rate (61.23%) was also achieved with a *t+3* delay, demonstrating strong consistency across multiple performance metrics. Overall, the *t+3* delay stands out as the optimal timing for trade execution in pairs trading strategies, highlighting the critical impact of delay selection on trading performance. Results are visually summarized in Figure 2.

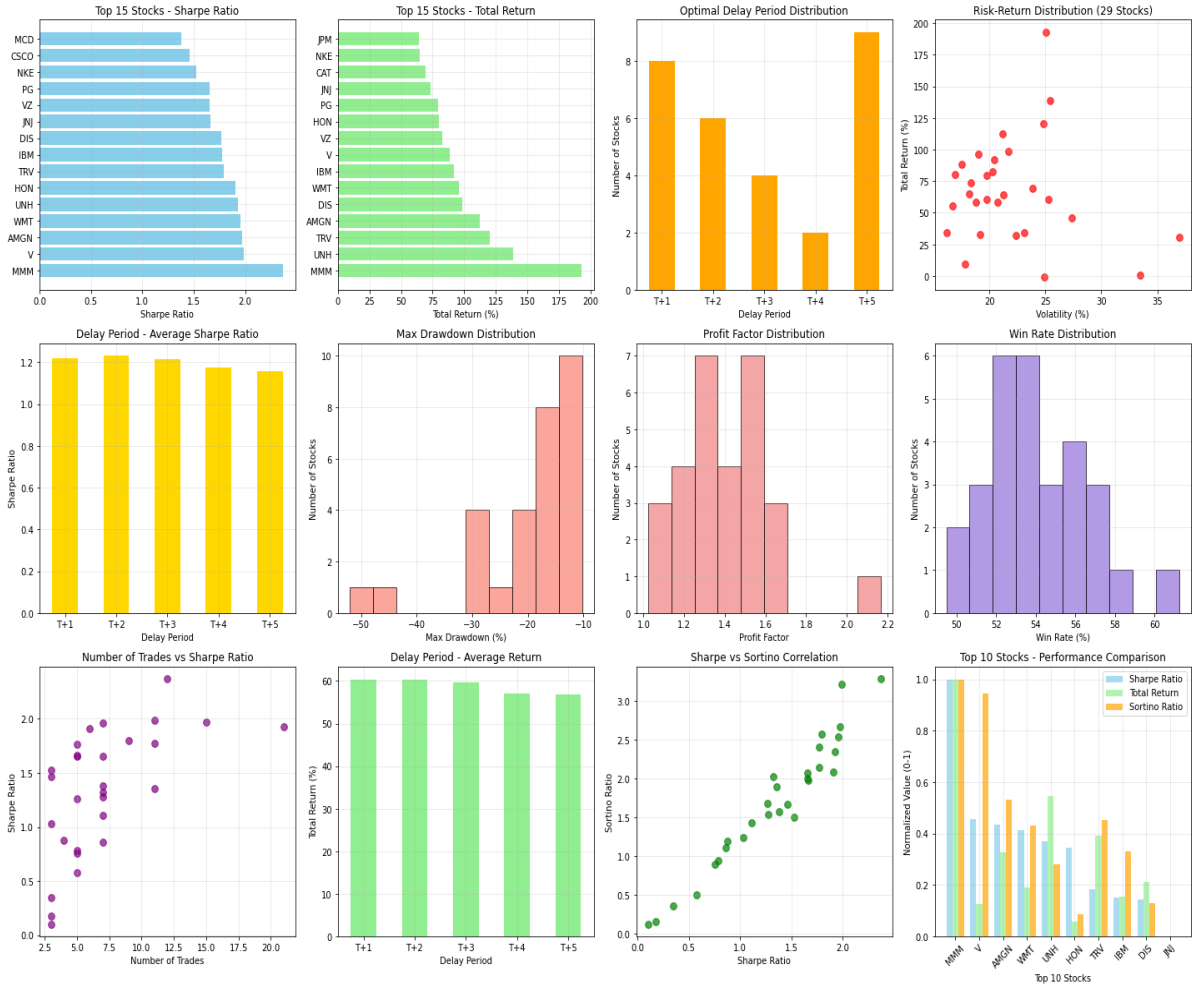


Figure 2. Comparative performance analysis of *t+n* periods

3.3. Distribution of optimal delay periods

The distribution of optimal delay periods across individual stock pairs is presented in Table 3. Analytical results indicate that the most frequently selected optimal trade execution delay is *t+1*, accounting for 31% of all stock pairs. This is followed by the *t+5* delay period at 24.1%. Medium-term delays (*t+3* and *t+4*) were adopted less frequently. This distribution underscores the critical importance of both short-term and long-term transaction delays for enhancing strategy performance.

Table 3. Distribution of stock pairs by optimal delay period

Delay	Number of Stock Pairs	Percentage Distribution
t+1	9	31,0%
t+2	6	20,7%
t+3	4	13,8%
t+4	3	10,3%
t+5	7	24,1%

3.4. Risk-return analysis

The study analyzed volatility, return, and risk metrics across stock pairs. The AAPL-HON pair exhibited the lowest volatility at 16.96%, while AAPL-INTC showed the highest volatility at 36.95%. The average portfolio volatility stood at 21.15%. From a risk management perspective, 55.2% (16/29) of pairs maintained a Maximum Drawdown below 15%. The majority of pairs (89.7% or 26/29) achieved Sharpe ratios exceeding 1.0. Furthermore, 96.6% (28/29) of pairs generated positive returns within the optimal time-series framework. Conversely, only 41.4% (12/29) maintained win rates > 55%. These results collectively demonstrate the strategy's overall success in delivering high return potential while operating at moderate risk levels.

3.5. Sectoral performance analysis

The sector-based performance of stock pairs is summarized in Table 4. Within the technology sector, AAPL-IBM (Sharpe: 1.773; Return: 91.81%; Delay: *t+1*) delivered the highest performance. In financials, AAPL-JPM (Sharpe: 1.325; Return: 63.86%; *t+3*) outperformed peers while AAPL-GS generated negative returns. The healthcare sector exhibited remarkably high performance with AAPL-UNH (Sharpe: 1.927; Return: 138.92%; *t+1*) and AAPL-AMGN (Sharpe: 1.972; Return: 112.42%; *t+1*). For consumer goods, AAPL-WMT (Sharpe: 1.957; Return: 96.10%; *t+2*) emerged as the leader. These findings demonstrate that sector-specific characteristics significantly influence strategy efficacy, with healthcare and technology sectors yielding superior risk-adjusted returns.

Table 4. Sectoral performance analysis

Sector	Stock Pair	Sharpe Ratio	Total Return (%)	Optimal Delay
Technology	AAPL-MSFT	0.876	33.02	*t+5*
Technology	AAPL-INTC	0.575	30.71	*t+2*
Technology	AAPL-IBM	1.773	91.81	*t+1*
Financials	AAPL-JPM	1.325	63.86	*t+3*
Financials	AAPL-GS	0.102	-1.09	*t+5*
Financials	AAPL-AXP	0.757	31.73	*t+1*
Healthcare	AAPL-UNH	1.927	138.92	*t+1*
Healthcare	AAPL-JNJ	1.666	73.47	*t+2*
Healthcare	AAPL-AMGN	1.972	112.42	*t+1*
Consumer Staples	AAPL-WMT	1.957	96.10	*t+2*
Consumer Staples	AAPL-PG	1.654	79.47	*t+5*
Consumer Staples	AAPL-KO	1.033	34.04	*t+1*

3.6. Statistical significance and reliability

When examining the statistical distribution of performance metrics, the average Sharpe ratio was calculated as 1.333 with a standard deviation of 0.612. The mean return was 67.75% ($\sigma = 44.23$), while the average Maximum Drawdown was -19.83% ($\sigma = 9.54$). The average number of trades was found to be 7.1 ($\sigma = 4.2$). In terms of reliability, the Profit Factor was > 1.0 for all stock pairs (100%), and exceeded 1.5 for 55.2% of

them (16 out of 29). Additionally, the Sortino Ratio was greater than 1.0 for 82.8% of the stock pairs (24 out of 29). These indicators support the conclusion that the strategy delivers a consistent and stable performance.

3.7. Performance comparison with the buy-and-hold strategy

This study compares the performance of the pairs trading strategy with the classical buy-and-hold strategy for both the reference stock (AAPL) and the corresponding paired stocks. The results of this comparison are presented in Figure 3.

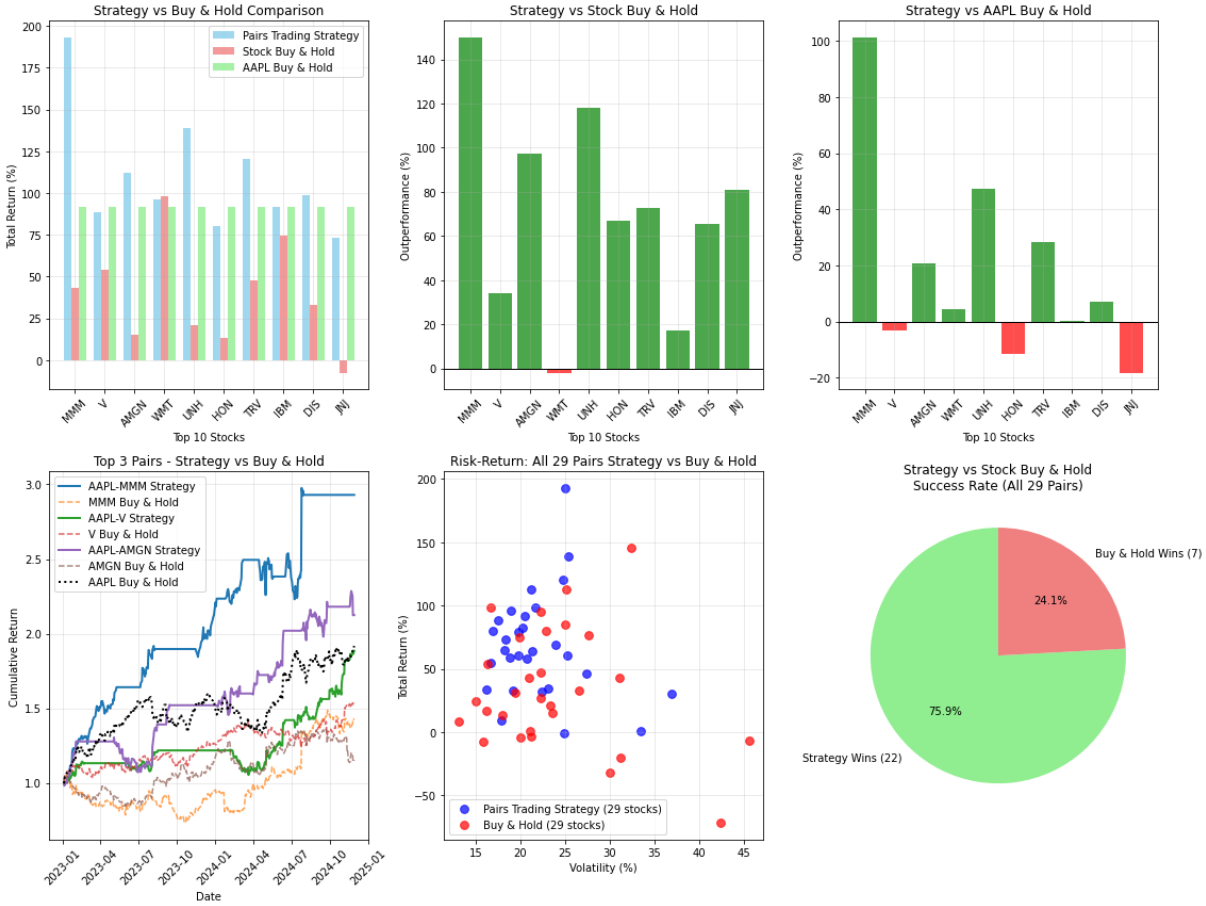


Figure 3. Performance comparison of the buy-and-hold and arbitrage strategies

As can be seen, the strategy outperforms both the individual stock's buy-and-hold (B&H) return and the AAPL B&H return for the majority of stock pairs. For instance, the strategy yielded notably high returns in the MMM and AMGN pairs, with gains of 192.98% and 112.42%, respectively. Although in certain cases (e.g., V and HON stocks) the strategy underperformed compared to AAPL's buy-and-hold return, the overall trend indicates that it offers superior risk-adjusted returns. These results suggest that, compared to the classical B&H approach, the pairs trading strategy may provide a more flexible and profitable alternative in the face of market fluctuations.

3.8. Performance comparison of ımmediate and delayed order execution

In real-world arbitrage strategies, immediate market orders are commonly utilized. In this study, dynamic time delays were applied to arbitrage strategies in an effort to optimize performance. This section compares the performance of trades executed immediately upon signal generation with those using dynamically selected delay periods.

In tests conducted on 29 stock pairs, the dynamic delayed position opening method achieved higher Sharpe ratios in 22 pairs compared to the instant trading strategy. This indicates that dynamic delay selection

improves the Sharpe ratio in equity pair arbitrage strategies by 75.86%. The findings demonstrate that the proposed algorithm enhances risk-adjusted return performance and generates more stable and reliable trading signals. A pairwise comparison of Sharpe ratios is presented in Figure 4.

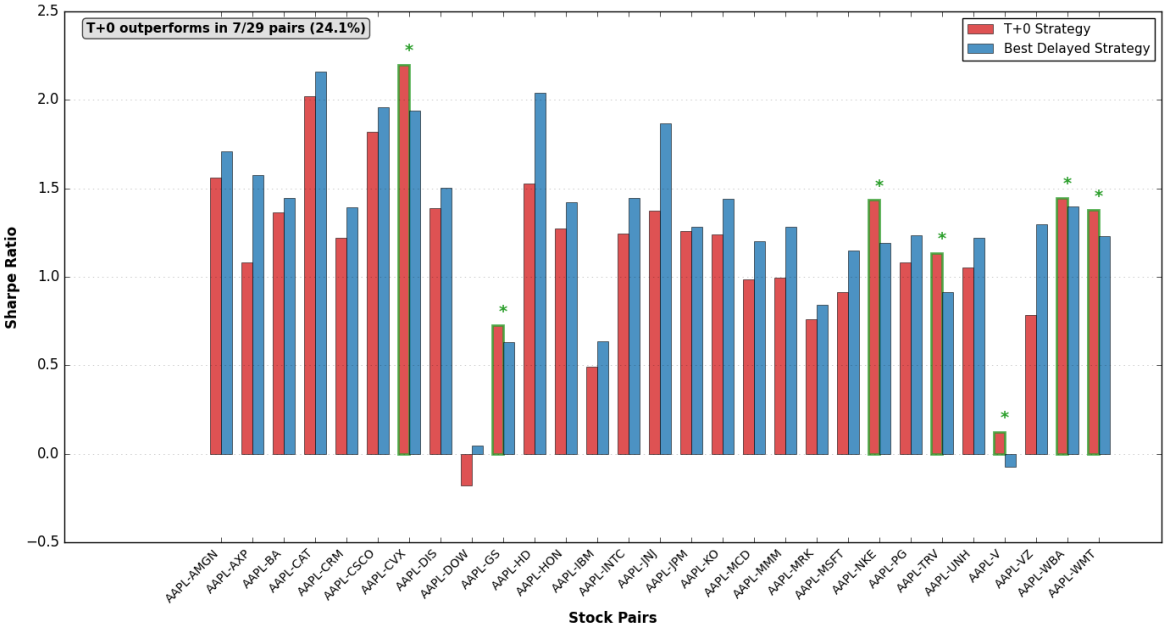


Figure 4. Pairwise performance comparsion: *t+0* vs optimal delay strategy

When applying the optimal delay selection strategy, the real-time execution method (*t+0*) was selected as optimal in only 24.1% of cases, as shown in Figure 4. The distribution of optimal delay values across all pairs is presented in Figure 5, which demonstrates the dominance of deferred execution windows.

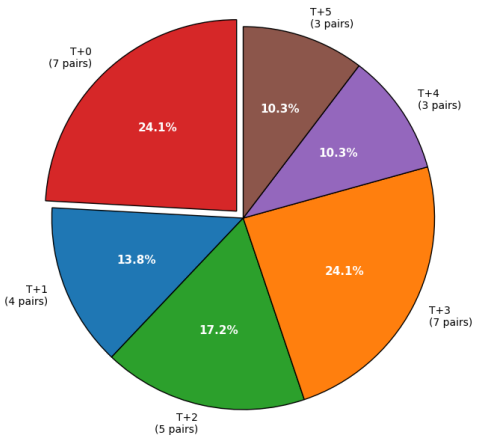


Figure 5. Distribution of optimal delay strategies across stock pairs

4. Discussion

The pairs trading strategy developed in this study was tested on 29 stock pairs constructed using AAPL as the reference asset and generally achieved superior results compared to the classical buy-and-hold strategy. Performance evaluation based on the Sharpe Ratio, Sortino Ratio, and Maximum Drawdown indicated substantial advantages, particularly in optimizing low-risk returns. The strongest results were observed for the AAPL-MMM and AAPL-AMGN pairs, and with few exceptions, the strategy generated positive returns across all analyzed pairs.

In the sensitivity analysis of execution delays, trades executed with a *t+3* day lag achieved the highest average Sharpe Ratio. This outcome suggests that allowing a short lag after signal generation enables the market to absorb information more effectively, thereby enhancing trading performance. From a sectoral perspective, the technology and healthcare sectors demonstrated the highest efficiency and consistency in pairs trading outcomes.

These findings are consistent with those reported in prior studies employing classical cointegration-based or Hurst exponent-based approaches [21]. However, the present z-score-based framework with delayed execution mechanisms achieved comparable results with substantially lower computational complexity, underscoring its practical advantages.

The key strengths of the proposed strategy include high Sharpe Ratios, low Maximum Drawdowns, and a broad generation of positive returns. Nevertheless, several limitations must be acknowledged. Transaction costs, slippage, and liquidity constraints were not incorporated, potentially leading to an overestimation of real-world profitability. Moreover, the absence of classical cointegration testing constitutes a methodological limitation that may weaken the theoretical basis of the mean-reversion assumption underpinning statistical arbitrage. Although short-term correlations often produce more practical and adaptive signals in dynamic markets, future research could integrate correlation-based pair selection with cointegration validation to enhance robustness.

Another consideration concerns the risk of overfitting in backtesting. The strategy's performance may vary across different time horizons; thus, testing under multiple market regimes would strengthen generalizability. Additionally, the superior performance of the *t+3* and *t+4* delays may reflect underlying market microstructure effects—such as information diffusion, investor reaction lags, or gradual signal absorption—which merit deeper investigation. Finally, although this analysis was limited to DJIA constituents, extending the framework to other equity indices, commodities, or forex markets could further validate its applicability.

Overall, while the proposed model demonstrates strong empirical performance, additional testing under real-world trading conditions is required before practical deployment.

5. Conclusion

In this study, a z-score-based pairs trading strategy using AAPL as the reference stock was tested with 29 stocks listed in the Dow Jones Index and comprehensively evaluated in terms of risk-adjusted performance. The strategy, incorporating dynamic execution delays, consistently outperformed both the individual stock buy-and-hold strategies and AAPL itself, demonstrating the advantages of adaptive timing in statistical arbitrage.

The results indicate that the proposed approach offers a viable alternative for investors seeking low-volatility and high risk-adjusted returns. The finding that 93.8% of the stock pairs generated positive returns and 89.7% achieved a Sharpe Ratio greater than 1.0 supports the model's potential applicability in real-world financial markets.

Future studies could further improve the strategy's accuracy and robustness by incorporating transaction costs and slippage effects, employing machine learning techniques for pair selection, and integrating time-series forecasting algorithms to enhance predictive capabilities.

6. Acknowledgments

This work was supported by the TUBITAK (The Scientific and Technological Research Council of Turkey) under Grant No: 7230972.

7. Author Contributions

Author 2 primarily developed the conceptual framework and research idea. Author 1 carried out data collection, coding, analysis, and manuscript preparation. Both authors contributed to the manuscript review and approved the final version.

8. Ethics Committee Approval and Conflict of Interest Statement

Ethics committee permission is not required for the prepared article.
There is no conflict of interest with any person/institution in the prepared article

9. Ethical Statement Regarding the Use of Artificial Intelligence

Ethical Statement Regarding the Use of Artificial IntelligenceDuring the preparation of this manuscript, the writing assistance tool ‘Gemini’ was used solely forlimited linguistic editing; all scientific content, analyses, and conclusions remain entirely theresponsibility of the authors.

10. References

[1] T. A. Hanson and J. Hall, "Statistical arbitrage trading strategies and high frequency trading," SSRN, Art. no. 2147012, 2012.
[2] B. Zhan, S. Zhang, H. S. Du and X. Yang, "Exploring statistical arbitrage opportunities using machine learning strategy," *Comput. Econ.*, vol. 60, no. 3, pp. 861–882, 2022.
[3] E. Gatev, W. N. Goetzmann and K. G. Rouwenhorst, "Pairs trading: Performance of a relative-value arbitrage rule," *Rev. Financ. Stud.*, vol. 19, no. 3, pp. 797–827, 2006.
[4] C. Krauss, "Statistical arbitrage pairs trading strategies: Review and outlook," *J. Econ. Surv.*, vol. 31, no. 2, pp. 513–545, 2017.
[5] Y. W. Ti, T. S. Dai, K. L. Wang, H. H. Chang and Y. J. Sun, "Improving cointegration-based pairs trading strategy with asymptotic analyses and convergence rate filters," *Comput. Econ.*, vol. 64, no. 5, pp. 2717–2745, 2024.
[6] G. J. Miao, "High frequency and dynamic pairs trading based on statistical arbitrage using a two-stage correlation and cointegration approach," *Int. J. Econ. Finance*, vol. 6, no. 3, pp. 96–110, 2014.
[7] S. M. Sarmento and N. Horta, *A Machine Learning Based Pairs Trading Investment Strategy*. Berlin, Germany: Springer, 2020.
[8] X. Zhu, "Examining pairs trading profitability," Yale Univ., New Haven, CT, USA, Senior Essay, 2024. [Online]. Available: https://economics.yale.edu/sites/default/files/2024-05/Zhu_Pairs_Trading.pdf. [Accessed: Aug. 26, 2025].
[9] S&P Dow Jones Indices, "Dow Jones Industrial Average," 2025. [Online]. Available: https://www.spglobal.com/spdji/en/. [Accessed: Jul. 3, 2025].
[10] T. Bogomolov, "Pairs trading based on statistical variability of the spread process," *Quant. Finance*, vol. 13, no. 9, pp. 1411–1430, 2013.
[11] M. Avellaneda and J. H. Lee, "Statistical arbitrage in the US equities market," *Quant. Finance*, vol. 10, no. 7, pp. 761–782, 2010.
[12] F. Rotondi and F. Russo, "Machine learning for pairs trading: A clustering-based approach," SSRN, Art. no. 5080998, 2024.
[13] W. F. Sharpe, "The Sharpe ratio," *J. Portfolio Manage.*, vol. 21, no. 1, pp. 49–58, 1994.
[14] S. E. Pav, *The Sharpe Ratio: Statistics and Applications*. Boca Raton, FL, USA: Chapman & Hall/CRC, 2021.
[15] T. N. Rollinger and S. T. Hoffman, "Sortino: A 'sharper' ratio," Red Rock Capital, Chicago, IL, USA, 2013.
[16] F. A. Sortino and L. N. Price, "Performance measurement in a downside risk framework," *J. Invest.*, vol. 3, no. 3, pp. 59–64, 1994.
[17] A. Chekhlov, S. Uryasev and M. Zabarankin, "Drawdown measure in portfolio optimization," *Int. J. Theor. Appl. Finance*, vol. 8, no. 1, pp. 13–58, 2005.
[18] B. V. de Melo Mendes and R. C. Lavrado, "Implementing and testing the maximum drawdown at risk," *Finance Res. Lett.*, vol. 22, pp. 95–100, 2017.
[19] Z. Huang and F. Martin, "Pairs trading strategies in a cointegration framework: Back-tested on CFD and optimized by profit factor," *Appl. Econ.*, vol. 51, no. 22, pp. 2436–2452, 2019.
[20] S. Andrade, V. Di Pietro and M. Seasholes, "Understanding the profitability of pairs trading," Univ. California, Berkeley, CA, USA, Tech. Rep., 2005.
[21] I. P. Fernandes, *Pair Trading: Strategies and Performance*, Ph.D. dissertation, Univ. Coimbra, Coimbra, Portugal, 2024. [Online]. Available: https://estudogeral.uc.pt/retrieve/275337/Dissertation_Ines_Fernandes.pdf. [Accessed: Aug. 26, 2025].

Fırat Üniversitesi Deneysel ve Hesaplamalı Mühendislik Dergisi

FUJECE

Sodyum Silikat ile Düşük Oranda Çimento İçeren Karışımların Reolojik Özellikleri

Emre DEVECI [1], Eyübhan AVCI[2], Melih UYSAL[3*]
[1,2,3]İnşaat Mühendisliği, Mühendislik ve Doğa Bilimleri Fakültesi, Bursa Teknik Üniversitesi, Bursa, Türkiye.
[1]emre.deveci@btu.edu.tr, [2]eyubhanavci@gmail.com, [3]melih.uysal@btu.edu.tr

Geliş Tarihi: 10.6.2025
Kabul Tarihi: 13.10.2025
Düzeltme Tarihi: 07.8.2025
doi: https://doi.org/10.62520/fujece.1714622
Araştırma Makalesi

Alıntı: E. Deveci, E. Avcı ve M. Uysal, "Sodyum silikat ile düşük oranda çimento içeren karışımların reolojik özellikleri" Fırat Üni. Deny. ve Hes. Müh. Derg., vol. 5, no 1, pp. 83-93, Şubat 2026.

Öz

Bu deneysel çalışmada, farklı oranlarda hazırlanmış çimento–sodyum silikat (C-SS) karışımlarının reolojik özellikleri araştırılmıştır. Deneyler, 25 °C sıcaklıkta, toplam hacim üzerinden kütlece %3 ile %6 oranında çimento ilave edilerek, hacimce %30, %50 ve %70 sodyum silikat/çözelti (SS/S) oranlarına sahip karışımlar için gerçekleştirilmiştir. Reolojik özelliklerin belirlenmesine yönelik hazırlanan numuneler sabit hızda (100 rpm) karıştırılmıştır. Jelleşme deneylerinde reaktör olarak iki farklı çimento türü, Normal Portland Çimentosu (OPC) ve Ultra İnce Taneli Çimento (UFC) kullanılmıştır. Deneylerde kullanılan ve su camı olarak da bilinen sodyum silikat sıvı formdadır ve modülü 3'tür. OPC' nin Blaine değeri 350 m²/kg iken, UFC' nin Blaine değeri 900 m²/kg'dır. Daha yüksek Blaine değerine sahip olması nedeniyle, UFC-sodyum silikat karışımları, OPC-sodyum silikat karışımlarına kıyasla daha kısa jelleşme süresine sahiptir. Her iki çimento türü için de çimento oranı arttıkça jelleşme süresi azalmış; sodyum silikat oranı arttıkça ise jelleşme süresi artmıştır. Sinerez yüzdeleri, çimento oranı arttıkça azalmış; sodyum silikat oranının %50'ye kadar artmasıyla sinerez artmıştır ancak %50'den sonra azalma göstermiştir. Viskozite değerleri hem sodyum silikat oranının hem de çimento miktarının artmasıyla birlikte artmıştır. Bu deneysel çalışmada, literatüre kıyasla daha düşük çimento oranları kullanılarak sodyum silikat-çimento reaksiyonları sonucunda jelleşmenin gerçekleşebileceği gözlemlenmiştir. Çalışmanın bir diğer özgün yönü, silikat esaslı enjeksiyon karışımlarında reaktör olarak çimentonun da kullanılabilmesidir. Alternatif enjeksiyon malzemesi olarak kullanılabilecek bu karışımların reolojik özellikleri belirlenmiştir.

Anahtar kelimeler: Ultra ince taneli çimento, Enjeksiyon, Jelleşme süresi, Viskozite, Sinerez

*Yazışılan yazar

İntihal Kontrol: Evet – Turnitin
Şikayet: fujece@firat.edu.tr
Telif Hakkı ve Lisans: Dergide yayın yapan yazarlar, CC BY-NC 4.0 kapsamında lisanslanan çalışmalarının telif hakkını saklı tutar.

Firat University Journal of Experimental and Computational Engineering

Rheological Properties of Lightly Cemented Sodium Silicate Grouts

Emre DEVECI[1], Eyübhan AVCI[2], Melih UYSAL[3*]
[1,2,3]Department of Civil Engineering, Faculty of Engineering and Natural Sciences, Bursa Technical University, Bursa, Türkiye.
[1]emre.deveci@btu.edu.tr, [2]eyubhan.avci@btu.edu.tr, [3]melih.uysal@btu.edu.tr

Received: 10.6.2025
Revision:07.8.2025
Accepted:13.10.2025
doi: https://doi.org/10.62520/fujece.1714622
Research Article

Citation: E. Deveci, E. Avcı and M. Uysal "Rheological properties of lightly cemented sodium silicate grouts", Firat Univ. Jour.of Exper. and Comp. Eng., vol. 5, no 1, pp. 83-93, February 2026.

Abstract
In this experimental study, the rheological properties of cement-sodium silicate (C-SS) mixtures prepared at different ratios were investigated. The experiments were carried out by adding 3% to 6% cement by mass of the total volume to 30%, 50%, and 70% sodium silicate/solution (SS/S) mixing at 25 °C. The samples prepared for the rheological property determination experiments were mixed at a constant speed of 100 rpm. In the gelation experiments, two different cements, ordinary Portland cement (OPC) and ultra-fine cement (UFC) were used as reactants. Sodium silicate, also known as water glass, was used in the experiments in liquid form, and its modulus was 3. The Blaine value of OPC was 350 m^2/kg, whereas that of UFC was 900 m^2/kg. UFC-sodium silicate mixtures have faster gelation times than OPC-sodium silicate mixtures due to their high Blaine values. For both cements, the gelation time was shortened as the cement ratio increased, and the gelation time was extended as the sodium silicate ratio increased. The syneresis percentages decreased as the cement ratio increased, whereas the sodium silicate ratio increased up to 50% and decreased after 50%. Viscosity values increased with increasing sodium silicate ratio and cement amount. In this experimental study, gelation reactions could be achieved as a result of sodium silicate-cement reactions using lower cement ratios than those reported in the literature. Another unique aspect of the study is that cement can also be used as a reactant to prepare silicate grouts. The rheological properties of these mixtures, which can be used as alternative grout materials were determined.

Keywords: Ultrafine cement, Grouting, Gelation time, Viscosity, Syneresis

*Corresponging author

Plagiarism Checks: Yes – Turnitin
Complaints: fujece@firat.edu.tr
Copyright & License: Authors publishing with the journal retain the copyright to their work licensed under the CC BY-NC 4.0

1. Introduction

Soil improvement is one of the most important geotechnical engineering applications. Recent academic studies have widely preferred chemical injections because of their ease of application and effectiveness in fine-grained and low-permeability soils. Low-viscosity mixtures are injected into the ground, reducing its permeability and increasing its strength and carrying capacity [1].

Sodium silicate is frequently preferred as a chemical injection material because of its low viscosity, easy gelation control and economy [2]. The use of sodium silicate alone can cause negative effects, such as insufficient strength and early gelation [3]. For this reason, various reactants have been used in the literature to control the gelation of sodium silicate grouts. Cement derivatives are frequently used as reactants. Kazemian et al. investigated effect of the amount of cement on the viscosity and gelation time in cement-sodium silicate mixtures [3, 4]. They observed rapid gelation at high cement ratios. Avcı et al. examined the permeability and strength properties of cement-sodium silicate grouts, emphasized that the cement ratio is an important parameter for gel stability [5].

The use of high-rate cement can lead to a rapid increase in the viscosity and failure to control the gelation time in field applications [6, 7]. Therefore, the study aimed to delay gelation time and control injection time by using low cement rates between 3% and 6% in sodium silicate grouts. The Blaine value of the ultrafine cement (UFC) was 900 m^2/kg. Thus, even when used at a low rate, it can initiate a reaction because of the high pH effect [8, 9]. In addition, the effect of specific surface factors on the rheological properties were investigated using OPC in addition to UFC.

Not all cement particles are water-soluble. One of the most significant problems encountered in cement injection is the difficulty encountered in injecting into low-permeability soils such as fine sand and silt due to the large particle sizes. In this context, the most significant advantage of fine-grained cement over conventional Portland cement is its approximately ten-fold smaller particle size.

In this experimental study, sodium silicate/water ratios were determined as 30%, 50%, and 70% by volume. The cement was added by mass at a rate of 3% to 6% of the solution mixture volume. The rheological properties such as viscosity, gelation time, and syneresis of the grout systems were determined and evaluated. As a result of experimental studies, as an alternative to grout materials with high cement ratios in the literature; sodium silicate-UFC and sodium silicate-OPC mixtures provide a unique contribution in terms of having sufficient and controllable application time, low viscosity, and more economical and environmentally sustainable properties. In addition, in most studies in the literature, sodium silicate has been added to cement-water mixtures, and its performance has been evaluated. The use of cement as a reactant material is another unique aspect of this study.

2. Literature Review

Some prominent studies in the literature evaluating the engineering and gelation control of sodium silicate mixtures with cement and different reactant materials can be listed as follows:

Kazemian et al. conducted viscometer tests on mixtures prepared with different cement, sodium silicate, kaolinite, and water ratios. It was found that cement and sodium silicate were the most important determinants of viscosity. It has also been reported that high cement ratios cause rapid gelation [4]. Kazemian et al. investigated the effect of sodium silicate on cement-based mortar systems. In the study, viscosity and strength tests were performed on mixtures with different ratios. As the sodium silicate ratio increased, gel time decreased and viscosity increased [3]. Avci determined the rheological properties of sodium silicate-formamide mixtures such as gelation time, viscosity, and syneresis. The gelation time decreased with increasing the amount of reactant [9]. Zhang et al. tested the injection performance of cement/sodium silicate mortars at 1:1 and 1:2 ratios on rock cracks. They emphasized that the injection performance depends on the viscosity and crack aperture [2]. Zhu et al. studied the time-dependent viscosity behavior of cement-sodium silicate mixtures at different temperatures. Gelation times are shortened at high temperatures and viscosity

control becomes difficult at high temperatures [10]. Avci et al. performed injection applications on sandy soils using sodium silicate and fine-grained cement with different proportions. The strength and permeability decreased with the addition of sodium silicate to cement mixtures. Viscosity values increased with the increase in the sodium silicate additive ratio [5].

As a result, the cement ratio was generally kept between 10% and 55%, but this situation caused high viscosity and rapid gelation problems in field applications [2-5, 8, 11-15]. In this experimental study, mixtures with low viscosity and controllable gelation rates that can be used as soil injection materials were obtained using low cement content.

Studies in the literature generally initiate the C-S-H reaction using cement as the main binder injectable. In this context, sodium silicate was added to the mixtures, and its effects on strength and rheological properties were primarily investigated on samples. However, high viscosity and the inability to control gelation time pose significant obstacles to the effective use of such mixtures as injection materials.

In the experimental study, sodium silicate was selected as the main injection material, and cement types were used as reactants to initiate the chemical reactions. This approach constitutes one of the most important and unique aspects that distinguishes our study from existing studies. Furthermore, the low viscosity and controllable gelation time of the mixtures with determined rheological properties demonstrates their potential as injection materials compared to other studies.

3. Materials and Methods

3.1. Sodium silicate

Sodium silicate, also known as water glass, is a chemical material widely used in the construction industry and underground applications. The product coded EGENAT 3203, produced by Ege Kimya A.Ş. in Turkey, was used in the experimental study. The physical and chemical properties of sodium silicate are summarized in Table 1.

Table 1. Physical and chemical properties of sodium silicate (data from manufacturer)

Properties	Values
General Formula	Na_2SiO_3
Appearance	Clear liquid, colorless
Weight Ratio, SiO_2/Na_2O	3-3.3
Molar Ratio, SiO_2/Na_2O	3.1-3.4
Bome (at 20°C)	39-41
Density (at 20°C, gr/cm^3)	1.37-1.39
Na_2O (%)	8.5-9.5
SiO_2 (%)	26-28
Viscosity (at 20°C, cp)	75-300
pH (at 20°C)	11.0-12.5

3.2. Ordinary portland cement and ultrafine cement

In the experiments, CEM-I 42.5 R normal Portland cement (hereinafter referred to as OPC) produced by Bursa Cement Inc. (TR) and MasterRoc MP900 fine-grained cement (hereinafter referred to as UFC) supplied by BASF were used. The physical and chemical properties of the cement are summarized in Table 2.

Table 2. Physical and chemical properties of cements (data from manufacturer)

Properties		Values
SO_3 (%)	Ordinary Portland Cement (CEM-I 42.5R)	<4
MgO (%)		<4
CaO (%)		<3
SiO_2 (%)		<1
Cl^- (%)		<0.1
Density (g/cm^3)		3.10-3.15
Blaine (m^2/kg)		350-370
Insoluble Residue (%)		<5
LOI (%)		<5
Appearance	Ultrafine Cement (MasterRoc	Powder
Colour		Gray
CaO (%)		<3
$CaCO_3$ (%)		<3

Table 2. (Continue) Physical and chemical properties of cements (data from manufacturer)

Properties		Values
MgO (%)	Ultrafine Cement (MasterRoc	<3
$CaSO_4$ (%)		<5
pH (at 20 °C)		12-13
Density (g/cm^3)		3.05
Blaine (m^2/kg)		>900

3.3. Rheological properties

3.3.1. Gelation time

Gel time is used to express the time until the injection mixtures transition from liquid to gel (semi-solid) state. Parameters such as reactant ratio, sodium silicate content, and ambient temperature affect gel time.

Meng et al. reported that high water/cement ratios prolonged gel times in their study on gel times with different water/cement ratios [15]. Similarly, Lee and Jeon stated that gel times were shortened with increasing cement amount in their study on sodium silicate mixtures with recycled material additives [16]. Govindan showed that gel times were sensitive to the test method and initial temperature of the mixture [17].

3.3.2. Syneresis

Syneresis is defined as the volume contraction that occurs when a mixture in gel form expels water as a result of reactions over time. Shrinkage and water accumulation on the surface occur with volume contraction. It is an important parameter in terms of gel stability and long-term durability.

Syneresis is the main indicator of the physical stability of the mixture. As the sodium silicate ratio increases, the tendency for syneresis increases and decreases as the cement ratio increases [7].

3.3.3. Viscosity

The viscosity is a measure of the resistance of a liquid to flow. The value is expressed in Pa.s or cp (centipoise) units in different unit systems. Viscosity is an important parameter in terms of ease of injection, spreading and gel time control in injection applications. Although low viscosity provides an advantage in filling ground voids, high viscosity has a spreading-reducing effect. In these aspects, viscosity is one of the basic rheological parameters affecting the success of injection [2, 4].

3.4. The chemical reaction

As a result of mixing cement with water, a hydration reaction occurs and calcium hydroxide is produced (Eq. 1). Due to the small amount of cement, there is limited C-S-H production. A small amount of calcium hydroxide is formed.

The sodium silicate ions are dissociated into sodium silicate ions when sodium silicate is mixed with water. (Eq. 2). By adding cement to sodium silicate-water solutions that are basic and stable, the pH of the environment increases and excess silicate ions undergo a polycondensation reaction within themselves and gelation occurs. This reaction produces an amorphous silica gel is formed (Eq. 3). Some water is also released by the reaction [18]. The low cement ratio ensured a slow increase in the pH and controlled gelation.

$C_3S + H_2O \rightarrow C\text{-}S\text{-}H + Ca(OH)_2$ (Eq. 1)
$Na_2SiO_3 + H_2O \rightarrow 2Na^+ + 2OH^- + Si(OH)_4$ (Eq. 2)
$Si(OH)_4 + Si(OH)_4 \rightarrow Si(OH)_3\text{–}O\text{–}Si(OH)_3 + H_2O$ (Eq. 3)

4. Results and Discussions

In the experimental studies, 3 different sodium silicate-water solution ratios were used. The solution mixtures were mixed according to the percentages specified by volume in Table 3. The rheological properties of the ratios formed by mixing 3%, 4%, and 5% Ultrafine Cement (UFC) and 4%, 5%, and 6% OPC for the total solution volume were determined. The test procedure was as follows:

The cement was mixed in the specified proportions at 100 rpm for 3 minutes. The relevant amount of sodium silicate was added to the solutions and the mixture was mixed at a constant speed until gelation began. The gelation time is defined as the interval between the moment the mixture turns from liquid to semi-solid (gel). At this moment, the viscosity of the mixture begins to increase and it resists flow. Completed gelation samples were kept in closed containers to determine the percentage of syneresis. In the viscosity tests, the initial viscosities of the samples mixed in the specified ratios were measured using a rheometer device during the gelation period. The measurements were completed before gelation.

Table 3. Rheological properties of different sodium silicate-cement mixtures

Water (%)	Sodium Silicate (%)	Cement Type	Cement content (%)	Gelation Time (sec)	Syneresis (%)	Initial Viscosity (cp)
70	30	Ultrafine Cement (MasterRoc MP900)	3	352	11.06	1.87
50	50			942	14.19	4.45
30	70			4120	12.72	6.65
70	30		4	200	8.50	2.01
50	50			451	10.74	4.73
30	70			1037	9.95	6.83
70	30		5	146	6.81	2.44
50	50			176	8.77	4.83
30	70			715	8.33	7.09
70	30	Ordinary Portland Cement (CEM-I)	4	644	6.39	1.96
50	50			1005	9.01	4.44
30	70			3532	7.63	6.7
70	30		5	476	5.21	2.21
50	50			620	6.91	4.69
30	70			1666	6.60	6.89
70	30		6	365	3.63	2.55
50	50			530	5.24	4.89
30	70			1213	5.28	7.05

4.1. Gelation time

Gelation times were determined by continuously mixing with a mechanical mixer at 100 rpm to prevent cement particles from settling into the solution. The experiments were performed on 100 ml mixtures. In preliminary experiments, it was observed that if continuous mixing was not performed, the cement particles would settle over time and the bottom of the container would gel earlier. In laboratory and field applications, injection applications should not exceed 100 rpm. Otherwise, early gelation problems and strength losses are anticipated.

In the experiments, two types of reactants (cement) were used: OPC and UFC. The most important difference between these two types of cement is the specific surface. UFC has a higher specific surface area compared to OPC. This allows the gelation time to be more controllable. In addition, it is possible to start the same chemical reaction and gelation process using less material.

The gelation times of the mixtures prepared with UFC varied between 146 seconds and 4120 seconds, and those prepared with OPC varied between 365 and 3532 seconds (Figures 1 and 2). As the amount of cement increases, the gelation time decreases as an exponential function. With increasing sodium silicate percentage at the same UFC and OPC concentrations, the gelation time increases as an exponential function. The R^2 values of the trend lines in Figure 1 and Figure 2 are greater than 0.93. The gelation times of the UFC mixtures at the same ratios are shorter compared to OPC.

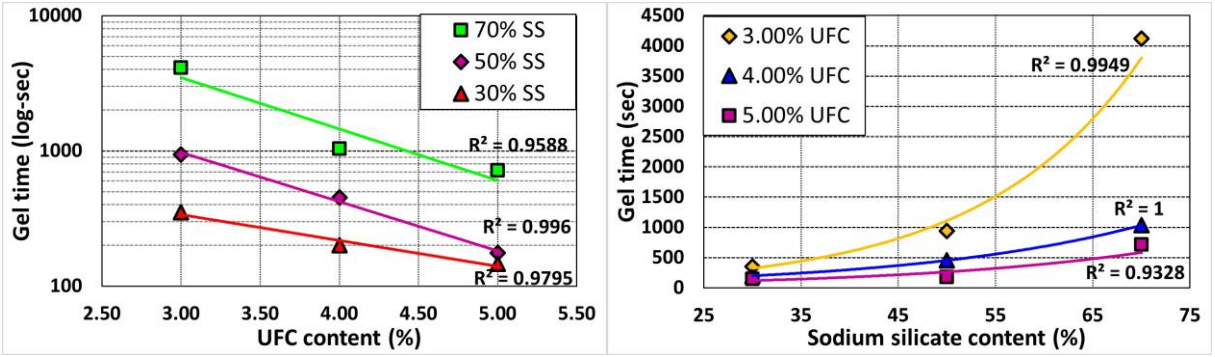


Figure 1. Variation in gel time at different cement (UFC) and sodium silicate ratios

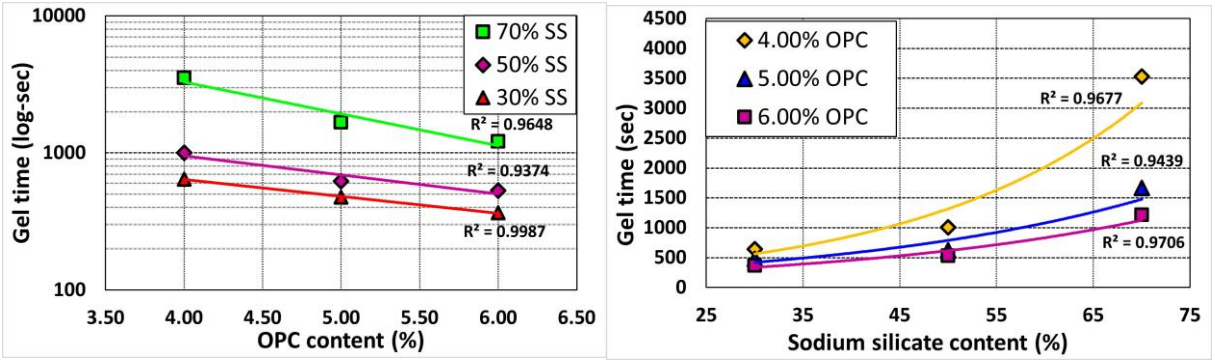


Figure 2. Variation in gel time at different cement (OPC) and sodium silicate ratios

4.2. Syneresis

The mixtures that completed the gelation period were kept in closed containers for 180 days and syneresis measurements were performed. The final measurement results for the different mixtures are shown in Figure 3 and Figure 4, respectively. The percentage of syneresis was calculated by dividing the volume of water released by the shrinkage of the samples by the initial volume of the sample.

The syneresis percentages of mixtures containing UFC varied between 6.81% and 14.19%, whereas that of mixtures containing OPC varied between 3.63% and 9.01%. The syneresis percentages decrease exponentially with the increase in the amount of UFC and OPC content. The syneresis percentages of both the UFC and OPC mixtures used at the same rate increased up to 50% sodium silicate and then decrease. The R^2 values of these trend lines expressed by polynomial equations are equal to 1 for all rates in both graphs.

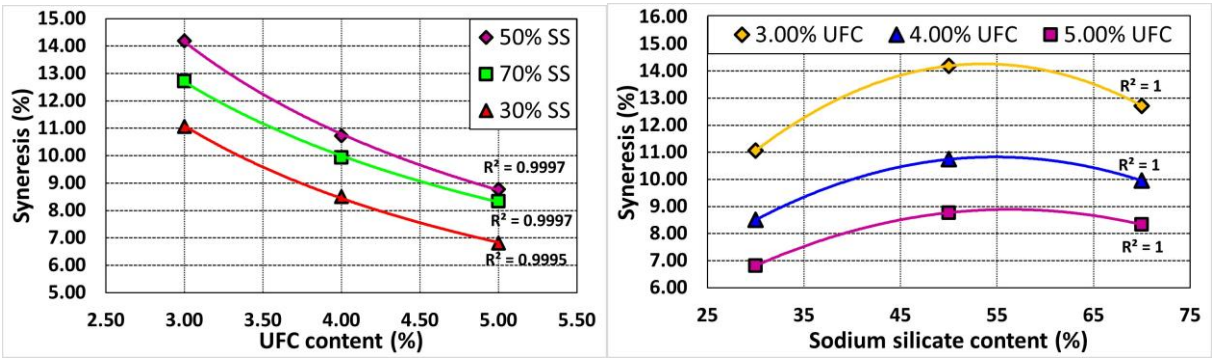


Figure 3. Syneresis variations at different cement (UFC) and sodium silicate ratios

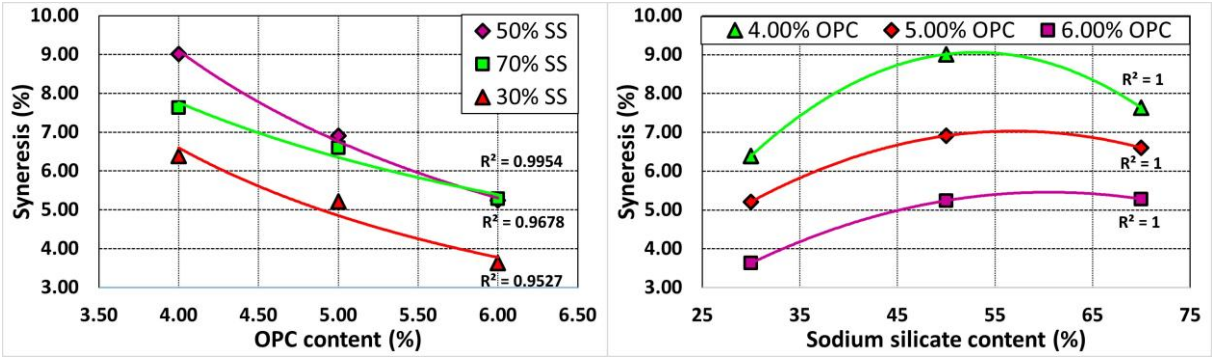


Figure 4. Syneresis variations at different cement (OPC) and sodium silicate ratios

4.3. Viscosity

The initial viscosity values of the mixtures in the experimental studies were determined with a Brookfield DV3T model rheometer device at 100 rpm rotation speed and 25 ° C. The duration of each measurement has ben specified as 1 minute. The relationship between the sodium silicate content, reactant (cement) ratio and the viscosity values is shown in Figures 5 and 6.

In mixtures containing UFC, the viscosity values ranged from 1.87 to 7.09 cp, and in mixtures containing OPC, the viscosity values ranged from 1.96 to 7.05 cp. Viscosity values increased linearly with increasing sodium silicate percentage. In mixtures containing both UFC and OPC, viscosity values increased linearly with increasing cement ratio.

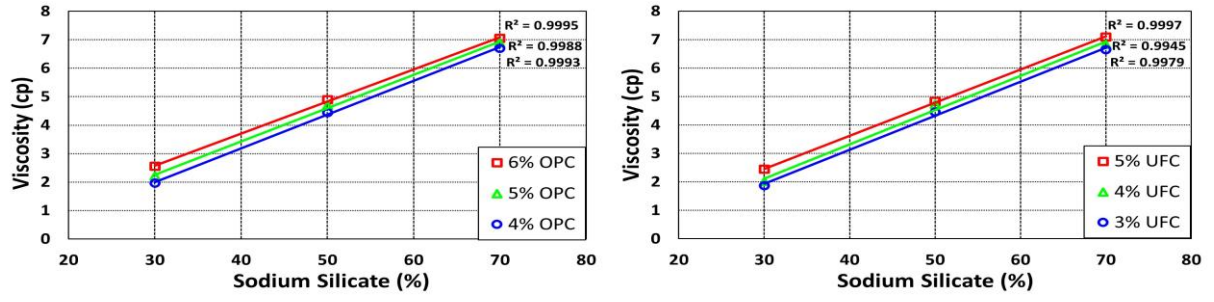


Figure 5. Variation in the viscosity at different sodium silicate ratios

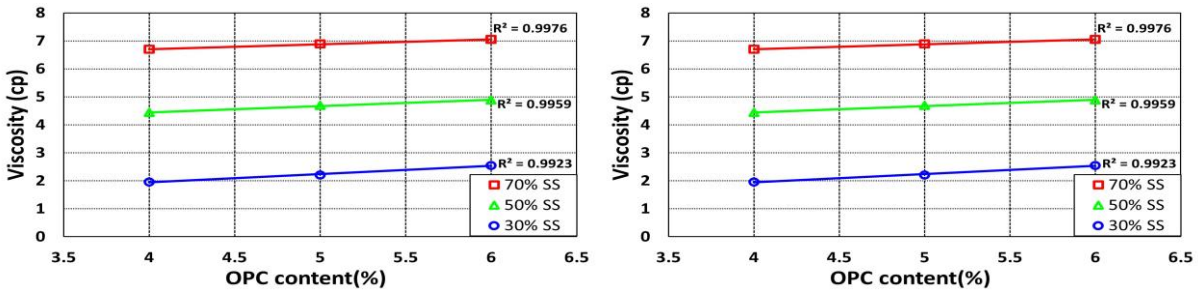


Figure 6. Variation in the viscosity at different OPC and UFC contents

The parameters, equations and R^2 values of the trend lines for all figures are presented in Table 4.

Table 4. E quations of trendlines

Y-axis	X-axis (unit)	Parameter of the Trendline	Equation	R^2
Gel time (sec)	UFC content (%)	70% SS	$y=48177e^{-0.876x}$	0.9588
		50% SS	$y=12069e^{-0.839x}$	0.9960
		30% SS	$y=1263.8e^{-0.44x}$	0.9795
	Sodium silicate (%)	3% UFC	$y=51.253e^{0.0615x}$	0.9949
		4% UFC	$y=58.018e^{0.0411x}$	1.0000
		5% UFC	$y=36.22e^{0.0397x}$	0.9328
	OPC content (%)	70% SS	$y=27856e^{-0.534x}$	0.9648
		50% SS	$y=3422.4e^{-0.32x}$	0.9374
		30% SS	$y=19926e^{-0.284x}$	0.9987
	Sodium silicate (%)	4% OPC	$y=156.95e^{0.0425x}$	0.9677
		5% OPC	$y=164.87e^{0.0313x}$	0.9439
		6% OPC	$y=137.46e^{0.03x}$	0.9706
Syneresis (%)	UFC content (%)	50% SS	$y=39.909x^{-0.943}$	0.9997
		70% SS	$y=31.588x^{-0.83}$	0.9997
		30% SS	$y=31.417x^{-0.948}$	0.9995
	Sodium silicate (%)	3% UFC	$y=-0.057x^2+0.6165x-2.26$	1.0000
		4% UFC	$y=-0.038x^2+0.415x-0.5412$	1.0000
		5% UFC	$y=-0.03x^2+0.338x-0.63$	1.0000
	OPC content (%)	50% SS	$y=57.616x^{-1.331}$	0.9954
		70% SS	$y=26.974x^{-0.898}$	0.9678
		30% SS	$y=44.509x^{-1.377}$	0.9527
	Sodium silicate (%)	4% OPC	$y=-0.005x^2+0.531x-5.04$	1.0000
		5% OPC	$y=-0.0025x^2+0.286x-1.1087$	1.0000
		6% OPC	$y=-0.002x^2+0.2375x-1.7288$	1.0000
Viscosity (cp)	Sodium silicate (%)	6% OPC	$y=0.1125x-0.795$	0.9995
		5% OPC	$y=0.117x-1.2533$	0.9988
		4% OPC	$y=0.1185x-1.5583$	0.9993
	Sodium silicate (%)	5% UFC	$y=0.1163x-1.0258$	0.9997
		4% UFC	$y=0.1205x-1.5017$	0.9945
		3% UFC	$y=0.1195x-1.6517$	0.9979
	OPC content (%)	70% SS	$y=0.175x+6.005$	0.9976
		50% SS	$y=0.225x+3.5483$	0.9959
		30% SS	$y=0.295x+0.765$	0.9923
	UFC content (%)	70% SS	$y=0.22x+5.9767$	0.9891
		50% SS	$y=0.19x+3.91$	0.9304
		30% SS	$y=0.285x+0.9667$	0.9206

5. Conclusion

In this experimental study, which was conducted to determine the rheological properties of the mixtures made by adding reactants (UFC and OPC) to sodium silicate-water mixtures at low rates compared to the literature, the following basic findings were obtained:

- Constant and low speed mixing is necessary to ensure gelation, syneresis, and viscosity control and to accurately determine the rheological properties.
- Gelation times were shortened with increasing cement amount. Gelation times were extended with increasing sodium silicate amount in mixtures containing the same cement amount (both UFC and OPC). The increasing and decreasing functions are expressed as exponential trend lines.
- The gelation time of UFC in the same amount is shorter than that of OPC. This is because UFC has a higher specific surface area than OPC.
- The syneresis percentages of the mixtures containing UFC and OPC decreased with the increase in the amount of cement. This decrease is expressed as an exponential trend line. In the mixtures made with the same amount of cement, the sodium silicate content increased up to 50% and then decreased polynomially.
- Viscosity values increased with increasing sodium silicate amount and cement ratio. These increases are expressed as linear functions. Increasing cement ratio increased viscosity values less compared to increasing sodium silicate amount.

In this experimental study, gelation reactions could be achieved as a result of sodium silicate-cement reactions using lower cement ratios than those reported in the literature. Another unique aspect of the study is that cement can also be used as a reactant for silicate injection. As a recommendation, laboratory tests should be conducted on these mixtures, the rheological properties of which have been determined, to investigate their suitability for injection into soils. Future studies should start with coarse sand and gradually working down to fine sand sizes.

6. Author contributions

Author contributions to the study are as follows:
Author 1: design, literature review, experimental study and writing; Author 2: idea and literature review; Author 3: writing and experimental study.

7. Ethics committee approval and conflict of interest

Ethics committee permission is not required for the prepared article. There is no conflict of interest with any person/institution in the prepared article.

8. Ethical Statement Regarding the Use of Artificial Intelligence

During the preparation of this manuscript, the writing assistance tool ‘Trinka’ was used solely for limited linguistic editing; all scientific content, analyses, and conclusions remain entirely the responsibility of the authors.

9. References

[1] D. Christodoulou, P. Lokkas, I. Markou, A. Droudakis, I. Chouliaras and N. Alamanis, "Principles and developments in soil grouting: A historical review," *WSEAS Trans. Adv. Eng. Educ.*, vol. 18, pp. 175–191, 2021.

[2] W. Zhang, S. Li, J. Wei, Q. Zhang, R. Liu, X. Zhang and H. Yin, "Grouting rock fractures with cement and sodium silicate grout," *Carbonates Evaporites*, vol. 33, pp. 211–222, 2018.

[3] S. Kazemian, B. B. Huat, T. A. Mohammed and M. Barghchi, "The effect of sodium silicate on cement–sodium silicate system grout," in *Mod. Methods Adv. Struct. Eng. Constr.*, vol. 1, pp. 659–663, 2011.

[4] S. Kazemian, A. Prasad, B. B. Huat, T. A. Mohammed and F. N. Aziz, "Effect of cement, sodium silicate, kaolinite and water on the viscosity of the grout," *Sci. Res. Essays*, vol. 5, no. 22, pp. 3434–3442, 2010.

[5] E. Avci, E. Deveci and A. Gokce, "Effect of sodium silicate on the strength and permeability properties of ultrafine cement grouted sands," *J. Mater. Civ. Eng.*, vol. 33, no. 8, p. 04021203, 2021.

[6] M. K. Zamani, R. B. Hashim, M. Suhatril and S. Motamedi, "A review of chemical grouting by various types of materials," 2015.

[7] E. Avci and M. Mollamahmutoğlu, "Syneresis dependent shear strength parameters of sodium silicate grouted sands," *Q. J. Eng. Geol. Hydrogeol.*, vol. 52, no. 1, pp. 99–109, 2019.

[8] S. Kazemian, A. Prasad, B. B. Huat, V. Ghiasi and S. Ghareh, "Effects of cement–sodium silicate system grout on tropical organic soils," *Arab. J. Sci. Eng.*, vol. 37, pp. 2137–2148, 2012.

[9] E. Avcı, "Rheological properties of sodium silicate–formamide grouts," *J. Innov. Sci. Eng.*, vol. 1, no. 1, pp. 25–34, 2017.

[10] Z. Zhu, M. Wang, R. Liu, H. Zhang, C. Zhang and Y. Liu, "Study of the viscosity–temperature characteristics of cement–sodium silicate grout considering the time-varying behaviour of viscosity," *Constr. Build. Mater.*, vol. 306, p. 124818, 2021.

[11] B. B. Huat, S. Kazemian and W. L. Kuang, "Effect of cement–sodium silicate grout and kaolinite on undrained shear strength of reinforced peat," *Electron. J. Geotech. Eng.*, vol. 16, no. 8, pp. 1221–1228, 2011.

[12] G. Zhu, Q. Zhang, X. Lin, R. Liu, L. Zhang and J. Zhang, "Analysis of the sealing mechanism of cement–sodium silicate grout in rock fractures with flowing water," *Water*, vol. 12, no. 7, p. 1935, 2020.

[13] R. Lin, L. Yang, G. Pan, Z. Sun and J. Li, "Properties of composite cement–sodium silicate grout mixed with sulphoaluminate cement and slag powder in flowing water," *Constr. Build. Mater.*, vol. 308, p. 125040, 2021.

[14] C. Du, K. Shi, F. Yi, M. Wang and X. Jiang, "Degradation mechanism of cement–sodium silicate hardened grout bodies under ion erosion," *Constr. Build. Mater.*, vol. 446, p. 138009, 2024.

[15] F. Meng, N. Qin, W. Wu, X. Shan and C. Li, "Research on the performance of cement–sodium silicate grout for synchronous grouting in shield tunnel," in *Proc. 8th Int. Conf. Civil Archit. Struct. Eng. (ICCASE 2024)*, Atlantis Press, pp. 621–631, 2024.

[16] H. H. Lee and H. Y. Jeon, "Manufacturing grout using recycled materials with variable setting times and improved durability," in *Tunnelling into a Sustainable Future–Methods and Technologies*, CRC Press, pp. 3786–3791, 2025.

[17] A. A. Govindan, *Refining Materials Testing Methods for Chemical and Cementitious Grouts*, Ph.D. dissertation, 2024.

[18] J. Davidovits, "Geopolymers: Ceramic-like inorganic polymers," *J. Ceram. Sci. Technol.*, vol. 8, no. 3, pp. 335–350, 2017.

Fırat Üni Deny. ve Say. Müh. Derg., 5(1), 94-118, 2026

Fırat Üniversitesi Deneysel ve Hesaplamalı Mühendislik Dergisi

Büyük Depremler Sonrasında Yığma Yapılarda Görülen Tipik Hasar Mekanizmaları

Alper ÖZMEN[1*], Erkut SAYIN [2]

[1]İnşaat Mühendisliği Bölümü, Mühendislik Fakültesi, İnönü Üniversitesi, Malatya, Türkiye.
[2]İnşaat Mühendisliği Bölümü, Mühendislik Fakültesi, Fırat Üniversitesi, Elazığ, Türkiye.
[1]alper.ozmen@inonu.edu.tr, [2]esayin@firat.edu.tr

Geliş Tarihi: 03.7.2025
Kabul Tarihi: 22.10.2025
Düzeltme Tarihi:09.8.2025
doi: https://doi.org/10.62520/fujece.1733544
Araştırma Makalesi

Alıntı: A. Özmen ve E. Sayım, "Büyük depremler sonrasında yığma yapılarda görülen tipik hasar mekanizmaları",Fırat Üni. Deny. Müh. Derg., vol. 5, no 1, pp. 94-118, Şubat 2026.

Öz

Bu çalışma, 1992 ile 2023 yılları arasında Türkiye'deki yığma binaların sismik performansını incelemekte ve büyük depremler sonrasında yapılan hasar değerlendirmelerine odaklanmaktadır. Belirlenen yaygın hasar mekanizmaları arasında, duvarların düzlem dışı göçmesi, dik duvarlar arasındaki bağlantıların yetersizliği, uygunsuz duvar açıklıkları ve hatıl eksikliği yer almaktadır. Kırsal yığma yapılarda sıklıkla kullanılan ağır sıkıştırılmış toprak damlar, atalet kuvvetlerini artırarak sismik zayıflığı önemli ölçüde artırmaktadır. Moloz taşlarının düzensiz kullanımı ve harcın yetersiz aderansı, yapısal bozulmanın erken başlamasına neden olmuştur. Çalışma, yığma binaların sismik dayanıklılığını artırmak için iyileştirilmiş inşaat uygulamaları, deprem yönetmeliklerine uyum ve etkili güçlendirme stratejilerinin gerekliliğini vurgulamaktadır. Geçmiş depremlerden alınan dersler, mühendisler ve politika yapıcılar tarafından, gelecekteki depreme dayanıklı yığma yapı inşaatları için daha sağlam yönergeler geliştirilmesini sağlayabilir.

Anahtar kelimeler: Yığma yapılar, Yapısal hasar, Deprem performansı, Donatısız yığma, Hasar mekanizmaları

*Yazışılan yazar

İntihal Kontrol: Evet – Turnitin
Şikayet: fujece@firat.edu.tr
Telif Hakkı ve Lisans: Dergide yayın yapan yazarlar, CC BY-NC 4.0 kapsamında lisanslanan çalışmalarının telif hakkını saklı tutar.

Firat University Journal of Experimental and Computational Engineering

Typical Damage Patterns In Masonry Structures After Various Major Earthquakes

Alper ÖZMEN[1*], Erkut SAYIN [2]

[1]Department of Civil Engineering, Faculty of Engineering, İnonu University, Malatya, Türkiye.
[2]Department of Civil Engineering, Faculty of Engineering, Firat University, Elazığ, Türkiye.
[1]alper.ozmen@inonu.edu.tr, [2]esayin@firat.edu.tr

Received: 03.7.2025
Accepted:22.10.2025
Revision: 09.8.2025
doi: https://doi.org/10.62520/fujece.1733544
Research Article

Citation: A. Özmen, E. Sayım, "Typical damage patterns in masonry structures after various major earthquakes", Firat Univ. Jour.of Exper. and Comp. Eng., vol. 5, no 1, pp. 94-118, February 2026.

Abstract

This study examines the seismic performance of masonry buildings in Turkey between 1992 and 2023, focusing on damage assessments after major earthquakes. Common failure mechanisms identified include out-of-plane wall collapse, inadequate connections between perpendicular walls, improper wall openings, and the absence of bond beams. Heavy compacted clay roofs, often used in rural masonry structures, contribute significantly to seismic vulnerability by increasing inertial forces. The irregular use of rubble stones and insufficient mortar adherence led to early structural degradation. The study emphasizes the need for improved construction practices, compliance with seismic codes, and effective retrofitting strategies to enhance the seismic resilience of masonry buildings. Lessons learned from past earthquakes can enable engineers and policymakers to develop more robust guidelines for future earthquake-resistant masonry construction.

Keywords: Masonry structures, Structural damage, Earthquake performance, Unreinforced masonry, Failure mechanisms

*Corresponging author

Plagiarism Checks: Yes – Turnitin
Complaints: fujece@firat.edu.tr
Copyright & License: Authors publishing with the journal retain the copyright to their work licensed under the CC BY-NC 4.0

1. Introduction

Masonry structures, among the most ancient human-made structures still operational, have evolved in building methodologies over time. A diverse range of stones, bricks, and blocks has been employed, with or without mortar, in the construction of these structures. The proposed construction methods include the use of two-cell blocks filled with grout, reinforced concrete, horizontal bond beams, and vertical tie beams. Integrating small sections of reinforced concrete both vertically and horizontally enhances the shear and flexural strengths of masonry walls, thereby improving ductility and energy dissipation [1,2]. Various masonry forms demonstrate insufficient tensile strength. Many empirical studies over the last 10 years have focused on investigating the design implications of brick and block masonry [3,4]. Masonry is categorized into unreinforced and reinforced types. A reinforced masonry construction demonstrates tensile strength similar to that of a reinforced concrete building. Consequently, traditional techniques for the design and analysis of reinforced concrete buildings are suitable in these instances, as the influence of nonlinear behaviour becomes less significant. Conversely, unreinforced materials typically exhibit nonlinear constitutive behaviour owing to their low tensile strength [5].

Masonry structures exhibit significant susceptibility to seismic loads and may experience substantial damage even during moderate earthquakes. The collapse of masonry structures results in significant economic losses and jeopardizes human lives. Consequently, implementing seismic retrofitting techniques is crucial for enhancing the safety and integrity of masonry structures [6,7]. Figure 1 illustrates the distribution of URM buildings with the total count of buildings (in millions) throughout European nations. The distribution of URM buildings throughout European countries exhibits considerable variation, with certain regions displaying a greater concentration of these structures than others. This variation can be attributed to differences in historical construction practices, economic development, and urban planning.

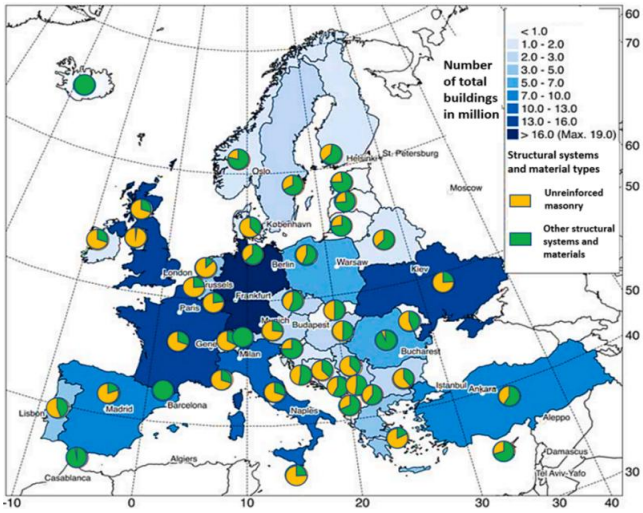


Figure 1. URM building distribution and total building count (in millions) in European countries [8].

The investigation of damage to structures after earthquakes contains useful information regarding earthquake-resistant building designs. In this respect, post-earthquake field investigations become more important. Disaster risk reduction strategy planning also requires post-earthquake investigation reports. Numerous field observations have been conducted in relation to recent earthquakes. Researchers have studied structural damage and obtained valuable information on the causes of masonry structure failures. Bayraktar et al. [9] analysed the dynamic response of masonry stone structures during the Dogubeyazit (Ağrı) earthquake on July 2, 2004. The patterns of cracking and failure in building stocks are elucidated comprehensively. Ural et al. [21] performed a field examination in Bala town following two significant earthquakes that impacted the region on December 20 and 27, 2007. Ingham and Griffith [11] examined the structural behaviour of unreinforced masonry structures during the 2010 Darfeld earthquake. Their

findings indicated that many unreinforced masonry structures and heritage sites sustained significant damage during the 2010 Darfield earthquake. Common damage included collapsed chimneys and parapets, compromised gables and inadequately secured face-loaded walls, as well as in-plane damage to masonry frames following the 2010 Darfield earthquake in Christchurch, New Zealand. Halder et al. [12], examined the primary causes of structure collapse during six earthquakes that transpired in the Northeastern area of India over the past decade. They examined several structural types, including reinforced concrete buildings, masonry structures, and earthen constructions. Various studies have evaluated building-stock failures after the 2011 Simav earthquake (Mw=5.9) [13–15]. They evaluated the damage and failures commonly observed in masonry structures after the earthquake. Inel et al. [16], assessed the damage to reinforced concrete and masonry structures situated in Kütahya, Turkey, following the Simav earthquake on May 19, 2011. The authors evaluate that common damages in reinforced concrete buildings resulted from substandard concrete, incorrect reinforcement detailing, short columns, pounding effect, overhangs, improperly constructed gables, and outer infill wall components. For masonry structures, they stated that typical damage resulted from inadequate connections between orthogonal walls and inappropriate positioning and sizing of openings. Also, a variety of research have been conducted to evaluate the damage mechanisms of structures following the 2011 Van earthquakes [17–28].

Yön [29] examined the failure mechanism of masonry and adobe structures following the Sivrice earthquake on April 4, 2019 (Mw = 5.2). Ten settlements surrounding the epicentre were examined and conducted a detailed assessment of the damage patterns of the structures. Procedures for strengthening were provided at the conclusion of the study. Godínez-Domínguez et al. [30], examined the characteristic damage patterns found in brick homes and apartment complexes after the 2017 Tehuantepec earthquake (Mw = 8.2) among cities and towns in the Mexican states of Chiapas and Oaxaca, situated within a radius of about 250 km from the epicenter. The field assessment revealed that the most observed damage resulted from substandard design, insufficient building practices, poor quality of materials, and low wall density ratios.

Bayrak et al. [31] explored urban centers, neighbourhoods, and rural areas in Elazığ and Malatya following the 2020 Sivrice earthquake. It aims to identify deficiencies and reveal the sources of damages by examining the failure mechanisms of masonry and reinforced structures. Günaydın et al. [32] investigated the collapse processes of masonry structures following the 2020 Sivrice earthquake in rural regions. They determined that almost all damaged structures were not constructed in compliance with the current Turkish earthquake building rules. Mertol et al. [33], evaluated the progression of damage in masonry and mosque-type structures following the 2020 Sivrice Earthquake in Elazığ, Turkey. Common failures included vertical cracks and corner splitting, wedge-shaped corner failures, diagonal wall cracking, out-of-plane wall splitting, and separation of walls from flooring and roofing systems. There are many papers in the literature that evaluated the structural damage of different types of structures after the 2020 Sivrice earthquake (Mw=6.8) [34–43]. Finally, after the 2023 Kahramanmaraş earthquakes, many damage observation studies have been conducted on reinforced concrete, masonry, and steel structures [44–74]. These studies have highlighted the importance of proper reinforcement and material selection in earthquake-resistant design. By incorporating the lessons learned from past earthquakes, buildings can be better constructed to withstand future seismic activity and protect the lives of occupants. The aim of this study is to present the typical damage patterns observed in masonry buildings. For this purpose, studies on the assessment of structural damage of masonry structures after various earthquakes were reviewed.

2. Material and Methods

2.1. Masonry structures

Until the early twentieth century, the majority of structures were constructed from masonry. Due to their benefits, reinforced concrete and steel construction have become increasingly popular. Masonry is common in numerous countries due to its cost-effectiveness, excellent insulating properties, aesthetic,

and accessibility. Masonry encompasses a wide range of materials, including bricks, stones, and blocks, together with different types of mortar such as lime and cement mortar, each having distinct mechanical properties. Well-detailed reinforced masonry structures can serve as a primary structural system and can be engineered to withstand seismic stresses. In several countries, the majority of brick and timber structures are built traditionally, with minimal or no involvement from certified engineers and architects. These structures are constructed informally, with little consideration for stability against horizontal seismic forces, and are therefore referred to as non-engineered buildings. Masonry structures are classified into unreinforced and reinforced categories. A reinforced masonry structure can exhibit tensile strength comparable to that of a reinforced concrete structure. However, unreinforced masonry structures are particularly vulnerable to seismic stresses and may sustain damaged during an earthquake.

2.1.1. Behavior of reinforced masonry (RM)

Reinforced masonry walls were engineered to withstand lateral out-of-plane forces and axial loads. These walls mostly extend vertically and convey lateral loads to the roof, floor, or foundation. They are frequently constructed as straightforward beams that extend across the structural supports. The vertical reinforcement must be bent with a 300mm, 90-degree angle. Vertical reinforcing bars integrated into the edges of the wall piers, along with their anchorage in the foundation and roof band, induce slender masonry piers to flex instead of rock (Figure. 2). The vertical bars on broader wall piers enhance their capacity to withstand horizontal seismic stresses and postpone cross-cracking. Moreover, the vertical bars provide protection against wall sliding and prevent collapse in the vulnerable direction.

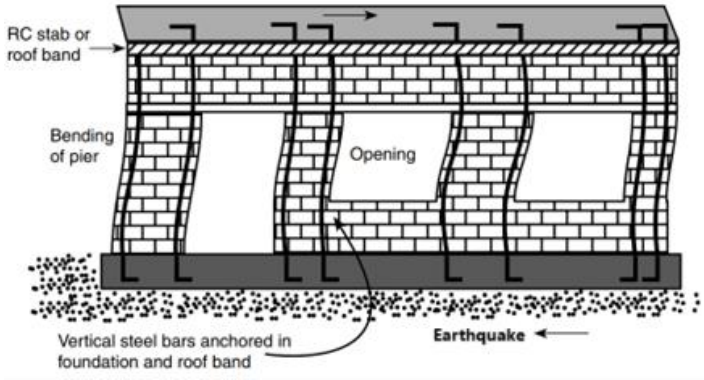


Figure 2. Behaviour of RM [75]

In addition to the vertical reinforcement, horizontal reinforcement in the form of bond beams is also crucial for strengthening masonry walls against lateral forces. These bond beams help to distribute the forces uniformly throughout the wall, reducing the risk of localized failure. By combining both vertical and horizontal reinforcement, masonry walls can be significantly improved in their ability to withstand seismic events and other external pressures. Properly reinforced masonry walls are essential for ensuring the safety and stability of a structure during earthquakes or other disasters.

2.1.2. Behaviour of unreinforced masonry (URM)

Unreinforced masonry structures are vulnerable to strong earthquakes. The lack of reinforcement in unreinforced masonry (URM) structures makes them particularly vulnerable to collapse during seismic events. Due to the brittle nature of unreinforced masonry walls, these structures have a higher risk of collapse under earthquake loads. Therefore, ensuring the strength and stability of masonry walls through proper reinforcement is crucial for withstanding seismic events and other external loads. The roof, wall, and foundation are the three fundamental parts of a masonry structure (Figure 3).

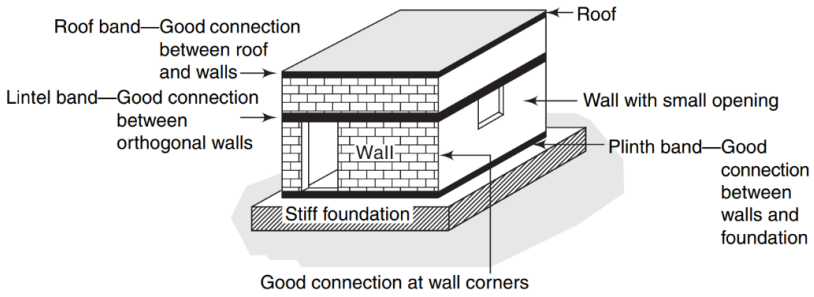


Figure 3. The components of URM [75]

The inertial forces propagate to the foundation via the roofs and walls. Inertial forces arise in both the x and y axes. A wall is exerted upon horizontally at the top in a direction orthogonal to its plane (weaker direction). It readily collapses. This phenomenon is referred to as an out-of-plane failure (Figure 4a). Nonetheless, a wall offers increased resistance when exerted along its length (primary direction). This is referred to as the in-plane resistance (Figure 4b).

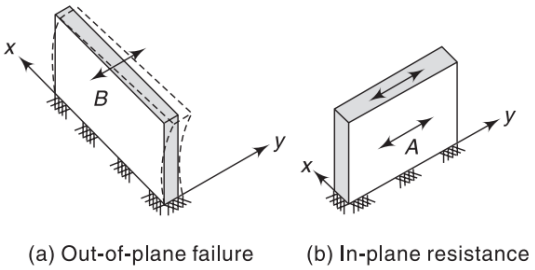


Figure 4. Failures of masonry walls [75]

2.2. Examination of masonry buildings

The seismic susceptibility of masonry structures is an important topic particularly after major earthquake. Comprehending the behaviour of these structures during seismic events is essential for evaluating their resilience and guiding retrofitting plans to reduce possible damage. Structural evaluation is a methodical procedure that entails examining structures about their present strength, performance, and future dependability. Masonry structures necessitate routine examinations to define their structural integrity and reduce the failure. Next section provides a comprehensive classification of damage levels in masonry structures (Section 2.2.1) for damage classification.

2.2.1. Categorization of damage degree in masonry structures

Damage is described as alterations in the geometric qualities or material properties of a structure, impacting its present and future performance. Diverse forms of deterioration have been noted in masonry structures due to various incidents. The insufficient tensile strength of these constructions has been recognized as the primary reason leading to deterioration. The seismic susceptibility of masonry constructions is affected by various variables, including [76, 77].

- Inadequate integrity among load-bearing elements.
- Inadequate wall connections resulting in the failure of box operation.
- Significant asymmetrical spaces diminish the capacity to withstand lateral forces.
- Cantilever walls' behavior in large, unsupported configurations.

The European Macroseismic Scale (EMS-98) provides a standardized method for assessing damage in masonry structures following earthquakes or other seismic events. It categorizes damage severity into five classes, each associated with certain types and levels of damage.

- Grade 1: Defined by minimal to minor damage, with no structural integrity compromised. Only modest non-structural concerns, including minor non-structural cracks in several walls or sporadic detachment of small plaster fragments, may be noted.
- Grade 2: Damage is more evident, characterized by cracks in multiple walls and the separation of bigger plaster fragments. Chimneys may undergo partial failure.
- Grade 3: Indicates significant to severe damage, characterized by large wall cracks, displaced roof tiles, and fractured chimneys at the roofline. Structural components, including partitions and gable walls, may experience failure.
- Grade 4: Signifies extensive damage, characterized by significant wall collapses and partial structural collapse of roofs and floors.
- Grade 5: Signifies total destruction, characterized by entire or nearly complete collapse, reflecting severe structural damage [78].

Table 1. The most common types of damage to masonry structures [79-83]

Disabilities	Most prevalent cause(s)	EMS-98 grade	May affect structural integrity.	Study
Cracking	Settlement, ground deformation, and inadequate preparation of mortar	1 to 4	✓	[79,80]
Moisture Penetration	Highly permeable material, humid atmosphere, freezing and thawing	1	✓	[81]
Bond Failure	Adhesion loss within materials	2 to 4	✓	[82]
Displacement	Insufficient lateral support anchors - Corrosion of steel components - Freeze-thaw cycles	2 to 4	✓	[83]

2.2.2 Common failure mechanisms in masonry structures

Damage patterns in masonry buildings can be classified into structural and non-structural failures.

- Structural Deformation:
  - Shear cracking: Diagonal fissures resulting from lateral seismic forces, prevalent in walls without sufficient protection.
  - Out-of-plane failure: Detachment and overturning of walls due to inadequate connections between orthogonal walls.
  - Corner failures: Detachment at building corners resulting from inadequate bond strength.
  - Collapse of roof and floor: Failure at the interface between wall and roof or wall and floor, especially in constructions devoid of horizontal diaphragms.
- Non-Structural Damage:
  - Plaster separation and cracking: Arises from severe deformation or moisture-induced deterioration.
  - Failures of chimneys and parapets: Frequent in old structures with inadequately fixed masonry components.
  - Distortions of doors and windows: Deformation of openings resulting from unstable load distribution.

Typical failure mechanisms are shown in Figure 5.

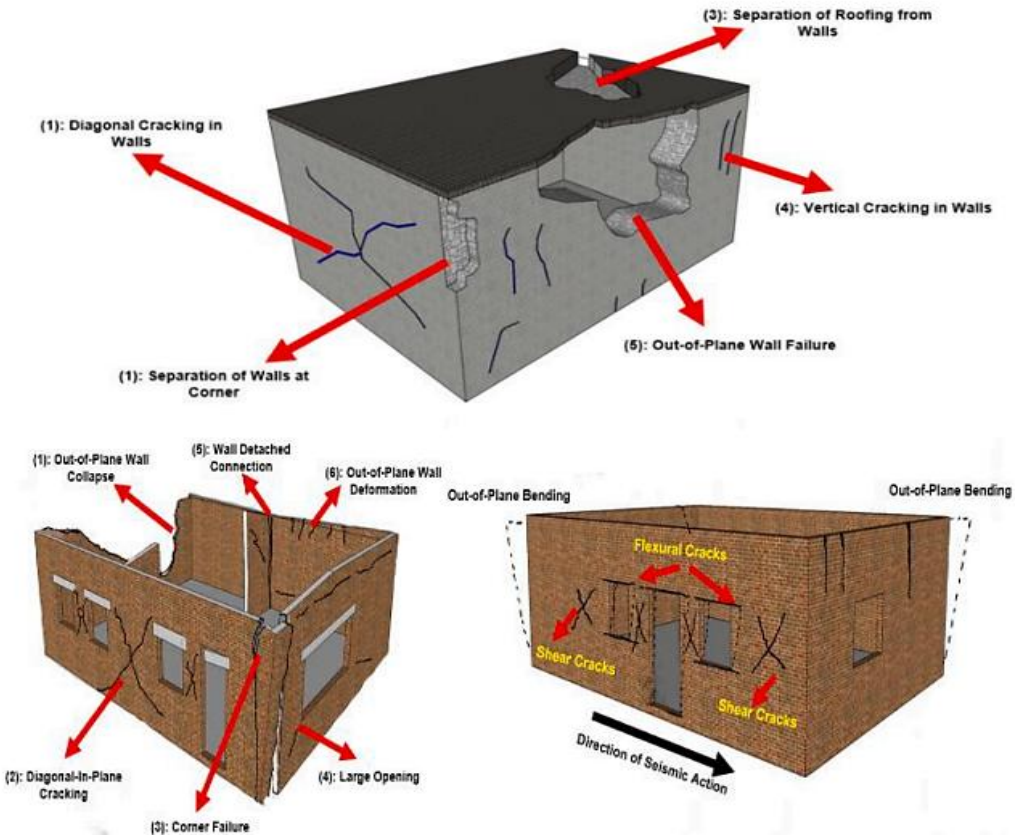


Figure 5. Typical causes of masonry structure failures [84]

2.3. Seismic code comparisons and evaluations

The evaluation of damage observations concerning seismic code restrictions offers essential insights into the effectiveness and limitations of current design provisions. A thorough assessment entails comparing recorded damage patterns with seismic design standards, identifying structural inadequacies in old masonry buildings, and analysing the potential for damage reduction through enhanced code compliance. This chapter offers a systematic comparison of national and international seismic codes, specifically the Turkish Earthquake Code (TBEC 2018) and Eurocode 8, emphasizing their various advantages and limitations in mitigating the seismic sensitivity of masonry structures. Turkish Earthquake Code (TBEC 2018) and Eurocode 8 regarding the seismic vulnerability of masonry structures entails assessing recorded damage patterns in relation to seismic design standards, determining inadequacies in older masonry structures, and examining how enhanced compliance with building regulations can reduce potential damage.

General design rules of masonry structures for TBEC 2018 and Eurocode 6&8 were given in Table 2. TBEC 2018, Eurocode 6, and Eurocode 8 define different classifications and design requirements for masonry structures. TBEC 2018 focuses on earthquake resistant building design and categorizes masonry as unreinforced, reinforced, confined, and panel systems. Eurocode 6 provides general structural design rules for masonry structures, while Eurocode 8 provides specific seismic design regulations for improved ductility and safety in earthquake-prone areas [85–87].

Table 2. Material and structural requirements for TBEC 2018 and Eurocode 6&8 [85–87]

Property	TBEC 2018	Eurocode 6 & 8
Material Requirements		
Minimum compressive strength of masonry units	5 MPa for units oriented perpendicular to bed joints. - 2 MPa parallel to the bed joints.	5 MPa perpendicular to bed joints - 2 MPa parallel to bed joints.
Mortar strength	5 MPa (M5) for unreinforced masonry; 10 MPa (M10) for reinforced masonry.	5 MPa for unreinforced masonry; 10 MPa for reinforced masonry.
Reinforcement steel	S420, B420C, or B500C steel classifications.	The same grades of reinforcement steel employed.
Seismic Design Considerations		
Categories of masonry for seismic design	Standards reinforced or constrained masonry in high-seismic regions.	Restricts the utilization of unreinforced masonry in high-seismic regions, promoting the usage of reinforced and confined masonry.
Minimum wall thickness	350 mm for stones and 240 mm for other masonry.	Same requirements as TBEC 2018.
Ductility and energy absorption	Employs ductility factors (R values) contingent upon the type of masonry.	Behaviour factors (q values) are as follows: - 1.5 for unreinforced masonry - 2.0–3.0 for confined masonry - 2.5–3.0 for reinforced masonry.
Wall connections and ties	Requires horizontal ties and vertical reinforcement.	Requires horizontal ties or ring beams every 4 m vertically.
Structural Analysis and Load Considerations		
Load combinations	Uses load factors for seismic and gravity loads.	Uses partial safety factors for materials and loads.
Shear strength of masonry	Based on material properties and vertical stress level.	Characteristic shear strength values defined, with additional checks for seismic loads.
Out-of-Plane wall stability	Requires verification against overturning and buckling.	Requires checks for lateral stability due to wind and seismic forces.
Detailing and Execution		
Wall openings	Requires reinforced vertical confining elements around large openings.	Openings >1.5m² must have vertical confinement elements.
Minimum reinforcement	Specifies minimum reinforcement ratios for reinforced and confined masonry.	Similar reinforcement requirements in Eurocode 6.
Connection of walls	Requires ties or reinforced concrete ring beams to ensure integrity.	Horizontal ties or ring beams are mandatory in seismic zones.

Both TBEC 2018 and Eurocode 8 require reinforced or confined masonry in high-seismic zones, while unreinforced masonry is limited to low-seismicity areas. Both codes have similar compressive strength and mortar class requirements, minimum reinforcement steel grades, and emphasize minimum wall thickness, shear wall design, and ring beam requirements for seismic design.

2.4. Data sources and selection criteria

Diverse data sources, such as field observations, structural damage evaluations, and prior study findings, have been employed to ascertain common failure causes in masonry structures. The criteria for selecting the studies included in this research are as follows:

- Earthquakes having a magnitude of $Mw \geq 5.0$ that substantially impacted masonry structures.
- Case studies that offer comprehensive damage assessments and visual documentation (e.g., photographs, structural diagrams).
- Investigate engineering evaluations and structural performance assessments.
- Research analyzing damage patterns in relation to seismic codes and standards. Examine the effectiveness of current building codes in earthquake-prone regions.

3. Typical Failures of Masonry Buildings

Adobe and unreinforced masonry structure are the predominant constructions. They are specifically constructed in rural areas. They may be categorized as informal structures due to their typical assembly by homeowners or construction workers employing substandard techniques without competent assistance. These buildings are often constructed using materials such as adobe and unreinforced masonry sourced from rural areas [17]. Vertical loads from the roof and floors are immediately transferred to the foundations by the load-bearing walls in these structures. Nevertheless, bearing walls are susceptible to in-plane, out-of-plane, and in-plane shear effects when exposed to horizontal seismic loads. Such structures are highly vulnerable to significant damage and complete or partial failure when exposed to lateral forces generated by seismic waves, due to the brittle nature of the load-bearing walls and their inadequate shear and flexural strengths [88–90]. The primary damages noted in the masonry and adobe structures were the utilization of substandard bricks, construction of walls with improper dimensions, absence of adequate reinforcing at wall junctions, irregularly positioned wall openings, and inadequately constructed roofs.

3.1. Poor workmanship/construction and inappropriate material

In rural areas, masonry buildings are the preferred construction method. On the other hand, they are generally constructed with poor workmanship and inappropriate materials. The smooth rubble stones used to construct these structures were gathered from the surrounding area and were often irregularly shaped. As a result of the lack of adequate friction between the masonry elements, the masonry buildings became seismically unstable. Various views of the current damage are shown in Table 3.

Table 3. Poor workmanship and inappropriate material

Ref.	Earthquake Name	Photos
[91]	2010 Kovancılar, Palu (Mw:6.0)	
[92]	2011 Van (Mw:7.2)	

Table 3. (Continue) Poor workmanship and inappropriate material

Ref.	Earthquake Name	Photos
[32]	2020 Sivrice (Mw:6.8)	

The shear strength of masonry walls mostly depends on the adhesion provided by the mortar connecting individual masonry units. Previous Turkish Codes, TEC (1998–2007), specified that lime mortar reinforced with cement or cement mortar may be used as the binding in load-bearing walls. Moreover, according to TBEC 2018 and Eurocode 8, the recommended minimum strength values are 5 MPa for unreinforced and 10 MPa for reinforced masonry. Previous investigations indicate that a mud mortar binder was utilized in nearly all stone masonry structures (Table 4). These structures have low compressive strength due to the use of mud mortar, which is not as strong as cement mortar. Additionally, the lack of proper reinforcement in wall intersections weakened the overall stability of these buildings.

Table 4. Structural failures attributable to mud mortar binder

Ref.	Earthquake Name	Photos
[91]	2010 Kovancılar, Palu (Mw:6.0)	
[32]	2020 Sivrice (Mw:6.8)	 

3.2. Heavy compacted earthen roof system

Another important reason for the collapse of masonry structures is heavy compacted earthen roof system. This type of system is commonly constructed to address harsh environmental conditions. The aim of this application was to isolate the earthen roofs for the water leakage. The thickness of the roof increases over time, and this heavy roof significantly increases the mass of the structure, thereby increasing the seismic forces acting on the structure during an earthquake. Moreover, the wooden bond beams of the roof system were supported in one direction to the load bearing walls. These walls are subjected to vertical loads because of the heavy earthen roof. Other walls which are not supported with wooden logs behave as cantilever components are vulnerable to seismic loads. Out-of-plane failures may occur in these walls. To prevent this type of damage, roof systems should be constructed with lighter elements and wooden bond beams should be supported in two perpendicular directions. Examples of failures caused by heavy earthen roofs are presented in Table 5.

Table 5. Heavy earthen roof system damages

Ref.	Earthquake Name	Photos
[9]	2004 Doğubeyazıt (Mw:5.2)	 
[91]	2010 Kovancılar, Palu (Mw:6.0)	
[19]	2011 Van (Mw:7.2)	
[93]	2011 Simav (Mw:5.9)	

Table 5. (Continue) Heavy earthen roof system damages

Ref.	Earthquake Name	Photos
[29]	2019 Elazığ (Mw:5.2)	

3.3. Irregular shapes of masonry

In rural areas, structural walls consist of inner and outer layers, which are generally formed with stones of different sizes. However, these walls constructed without an interlocking component. For this reason, cavities are observed between the inner and outer walls. These cavities further reduce the shear strength of the walls, thereby increasing their vulnerability during an earthquake. Although the proportion of cavities was not determined or measured, previous field observations have shown that when the cavity ratio is greater than 10–15%, remarkable reductions can occur in the shear capacity of the walls [21]. Typical earthquake-resistant wall cross sections are shown in Figure 6, and examples of this type of damage are given in Table 6.

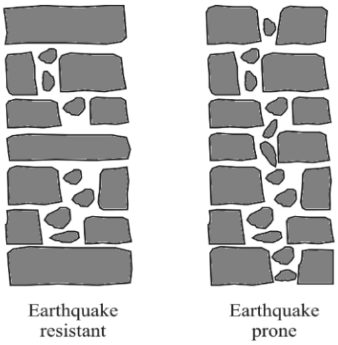
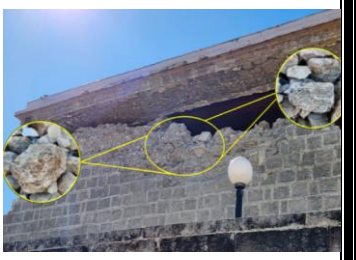


Figure 6. Typical earthquake resistant wall cross section [93].

Table 6. Damages of irregular shapes of masonry

Ref	Earthquake Name	Photos	Ref	Earthquake Name	Photos
[92]	2011Van (Mw:7.2)		[94]	2011 Simav (Mw:5.9)	

Table 6. (Continue) Damages of irregular shapes of masonry

Ref	Earthquake Name	Photos	Ref	Earthquake Name	Photos
[95]	2023 Kahraman maraş (Mw:7.6 and 7.7)		[96]	2020 Sivrice (Mw:6.8)	

3.4. Splitting and failures of corners

Insufficient connections between perpendicular walls and the absence of vertical and horizontal bond beams can lead to severe corner damages, especially under seismic loading. TBEC 2018, Eurocode 6, and Eurocode 8 emphasize the importance of effective wall connections, mechanical interlocking, and bond beams to mitigate these vulnerabilities. TBEC 2018 mandates the application of horizontal and vertical bond beams to reinforce intersections and prevent corner failures, while Eurocode 6 emphasizes the importance of mechanical interlocking between masonry walls to maintain structural integrity. Eurocode 8 provides additional regulations for enhancing ductility and energy dissipation capacity of masonry structures, requiring the use of horizontal tie beams or ring beams at every floor level to strengthen wall intersections and resist lateral forces. It categorizes unreinforced masonry as low-ductility construction and discourages its use in high-seismicity regions unless confined or reinforced. The absence of these essential design elements results in a high vulnerability to lateral loads, leading to severe damage in the form of corner separations, instability, and structural collapse. Compliance with these regulatory provisions is essential to provide the structural integrity and seismic resilience of masonry buildings. Some corner damages are given in Table 7.

Table 7. Corner damages

Ref	Earthquake Name	Photos	Ref	Earthquake Name	Photos
[74]	2023 Kahraman maraş (Mw:7.6 and 7.7)		[32]	2020 Sivrice (Mw:6.8)	
[74]	2023 Kahraman maraş (Mw:7.6 and 7.7)		[19]	2011 Van (Mw:7.2)	

Table 7. (Continue) Corner damages

Ref	Earthquake Name	Photos	Ref	Earthquake Name	Photos
[93]	2011 Simav (Mw:5.9)		[10]	2007 Bala (Mw:5.4)	

3.5. Improper location of openings (windows and doors)

The incorrect placement of openings constitutes a primary form of damage. The Turkish Building Earthquake Code 2018 (TBEC 2018) imposes some restrictions concerning the spacing between openings, the dimensions of windows and doors, and the distance from openings to the wall corners. In masonry structures, walls are the sole components that resist to interior and exterior loads. Figure 7 shows the required standards for openings in load-bearing walls, as given in TBEC 2018. Most masonry constructions were damaged due to the inadequate distance between the opening and the building corner. This category of damage is given in Table 8.

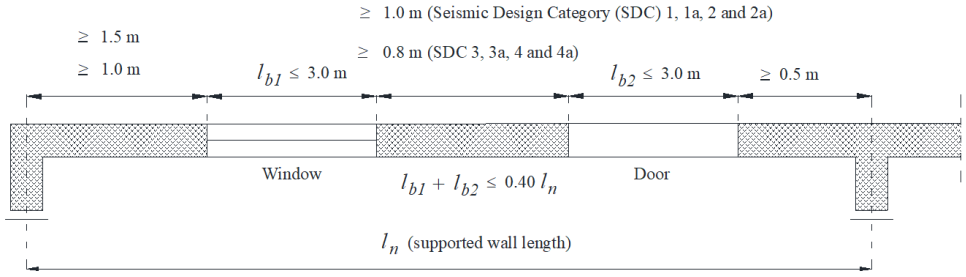


Figure 7. Required standards for door and window openings (TBEC 2018)

Table 8. Improper location of openings

Ref	Earthquake Name	Photos	Ref	Earthquake Name	Photos
[32]	2020 Sivrice (Mw:6.8)		[32]	2020 Sivrice (Mw:6.8)	

Table 8. (Continue) Improper location of openings

Ref	Earthquake Name	Photos	Ref	Earthquake Name	Photos
[97]	2003 Bingöl (Mw:6.4)		[20]	2011 Van (Mw:7.2)	
[34]	2020 Sivrice (Mw:6.8)		[94]	2011 Simav (Mw:5.9)	

3.6. Damages of gable walls

The majority of the gable walls were constructed without bond beams. They are vulnerable to earthquakes. This damage is not the primary structural damage falling parts of wall may be cause loss of lives and properties.

The primary causes of this type of damage include extensive unsupported wall length, insufficient wall-to-wall connections, and inadequate wall-to-floor contact. The Turkish Seismic Code 2018 mandates the vertical and inclined reinforced concrete bond beams to prevent damage at gable walls that exceed 2 meters in height. Schematic view of the gable wall utilizing reinforced concrete bond beam is given in Figure 8. Table 9 is shown the failures of the gable walls.

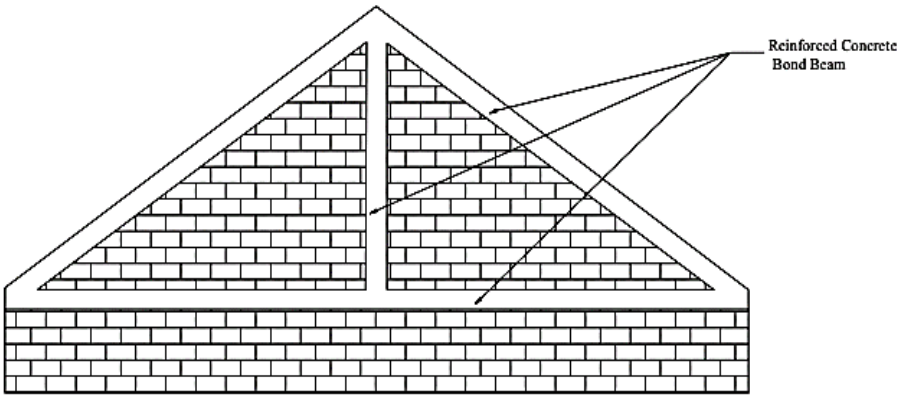


Figure 8. Using proper reinforced concrete bond beams on the gable wall (TBEC 2018)

Table 9. Gable wall damages

Ref	Earthquake Name	Photos	Ref	Earthquake Name	Photos
[21]	2011 Van (Mw:7.2)		[32]	2020 Sivrice (Mw: 6.8)	
[19]	2011 Van (Mw:7.2)		[34]	2020 Sivrice (Mw: 6.8)	
[98]	2023 Kahramanmaras (Mw: 7.6 and 7.7)		[99]	2023 Kahramanmaras (Mw: 7.6 and 7.7)	

3.7. Out of plane failure

Out-of-plane failure is common damage type which observed in masonry structures. This type of damage is generally seen by poor wall-to-wall connection, long unsupported wall length, not using vertical and horizontal beams, lack of rigid diaphragm, and poor adherence between wall units. To prevent these damages in masonry structures, the TBEC stipulates that the maximum unsupported wall length must not exceed 5.5 m in Seismic Design Categories (SDC) 1, 1a, 2, and 2a, and 7.5 m in SDC 3, 3a, 4, and 4a in plan view (Figure 9.a). Each 4-meter-long vertical bond beam should be added into the plan. Also, the unsupported wall length must not exceed 16 m (Figure 9.b) (TBEC 2018).

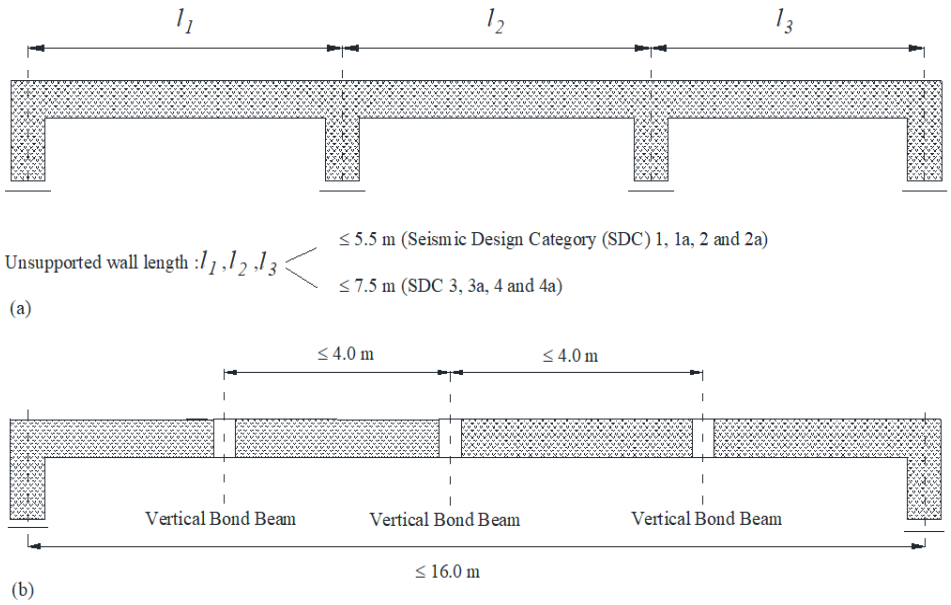


Figure 9. The maximum length of an unsupported wall and the distance between vertical bond beams

Fig. 10 shows a diagram of various out-of-plane mechanisms, and examples of out-of-plane damage are given in Table 10.

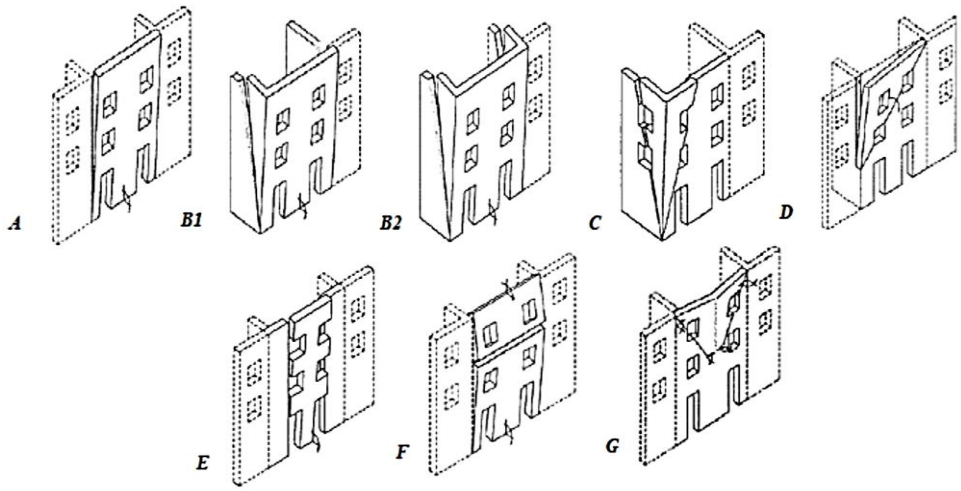


Figure 10. Schematic view of different out of plane mechanisms [100]

Table 10. Out of plane damages

Ref	Earthquake Name	Photos	Ref	Earthquake Name	Photos
[34]	2020 Sivrice (Mw: 6.8)		[101]	2023 Kahraman-maras (Mw: 7.6 and 7.7)	

Table 10. (Continue) Out of plane damages

Ref	Earthquake Name	Photos	Ref	Earthquake Name	Photos
[96]	2020 Sivrice (Mw: 6.8)		[73]	2023 Kahraman-maras (Mw: 7.6 and 7.7)	
[94]	2011 Simav (Mw:5.9)		[29]	2019 Elâzığ (Mw: 5.2)	

3.8. Low strength masonry units

According to previous earthquake codes (TEC-1998 and TEC-2007), natural stones, solid bricks, vertically perforated bricks, solid concrete briquettes, and adobe bricks could be used in load-bearing walls. However, TBEC (2018) prohibited the use of hollow concrete briquettes, infill bricks, adobe bricks, and rubble stones as load-bearing wall elements. The TBEC 2018 and Eurocode 6&8 stipulate that the minimum compressive strength of masonry units must be 5 MPa. When the compressive force exceed the compressive strength of the masonry units, minor vertical cracks may develop in the masonry components. Table 11 presents various examples of this damage.

Table 11. Low strength masonry units

Ref	Earthquake Name	Photos	Ref	Earthquake Name	Photos
[102]	2003 Denizli (Mw: 5.6)		[32]	2020 Sivrice (Mw: 6.8)	

4. Conclusion

An examination of the building stock in Turkey reveals that reinforced concrete and masonry structural systems comprise the predominant portion of the building stock in both urban and rural areas. In this study, the failure of unreinforced masonry buildings has been evaluated after the significant earthquakes, in Turkey. The results demonstrate that unreinforced masonry structures constructed by local residents have inadequate seismic performance and sustain significant damage, even during small earthquakes.

The behavior of various structural types, damage patterns in structural elements, collapse processes, and soil responses can be readily studied following earthquakes. Consequently, information obtained from previous earthquakes is essential for mitigating casualties and property damage in future seismic events. The main reasons for the failures of the masonry structures were:

- The rubble stones utilized in the construction of these masonry walls were provided from the vicinity and generally irregular in shape. For this reason, sufficient adhesion between the stones and mortar was not provided.
- In rural regions, heavy clay roofs were built for insulation against snow and rain. These roofs significantly increased the mass of the structure, hence the increased roof mass caused more seismic load during an earthquake.
- In masonry structures, the junctions between orthogonal walls are essential for decreasing both global and localized damage. Insufficient connections between bearing walls and the absence of vertical and horizontal bond beams may result in corner failures.
- The incorrect placement of openings constitutes a primary category of damage. Various building codes exhibit certain limits to openings. The majority of masonry structures did not comply with the limits for openings.
- The majority of the gable walls were constructed without bond beams. Consequently, they are vulnerable to earthquakes.
- Out-of-plane failure is a common form of damage observed in masonry structures. Load bearing walls may experience total or partial collapse due to this problem.

5. Acknowledgments

The authors declare that no funds, grants, or other support were received during the preparation of this manuscript

6. Author Contributions

All authors contributed to the study conception, investigation, writing and design.

7. Ethics Committee Approval and Conflict of Interest

“There is no conflict of interest with any person/institution in the prepared article. Additionally, ethics committee approval is not required for this study.” The authors have no relevant financial or non-financial interests to disclose

8. Ethical Statement Regarding the Use of Artificial Intelligence

During the writing process of this study, the artificial intelligence tool "ChatGPT," developed by "OpenAI," was used only for limited purposes of linguistic editing and translation. The scientific content, analyses, and results belong entirely to the authors.

9. References

[1] A. W. Hendry, B. P. Sinha, and S. R. Davies, *Design of Masonry Structures*. Boca Raton, FL, USA: CRC Press, 2017.
[2] N. Ranjan, S. Banerjee, S. Nayak, and S. Das, "Efficacy of waste plastic towards enhancement of shear and flexure carrying capacity of masonry structures," *J. Clean Prod.*, vol. 365, p. 132669, 2022.
[3] J. Scacco, B. Ghiassi, G. Milani, and P. B. Lourenço, "A fast modeling approach for numerical analysis of unreinforced and FRCM reinforced masonry walls under out-of-plane loading," *Compos. B Eng.*, vol. 180, p. 107553, 2020.
[4] A. Borri, M. Corradi, G. Castori, and A. De Maria, "A method for the analysis and classification of historic masonry," *Bull. Earthq. Eng.*, vol. 13, no. 9, pp. 2647–2665, 2015.
[5] A. Keshmiry, S. Hassani, U. Dackermann, and J. Li, "Assessment, repair, and retrofitting of masonry structures: A comprehensive review," *Constr. Build. Mater.*, vol. 442, p. 137380, 2024.
[6] P. Blagojević, S. Brzev, and R. Cvetković, "Seismic retrofitting of mid-rise unreinforced masonry residential buildings after the 2010 Kraljevo, Serbia earthquake: A case study," *Buildings*, vol. 13, no. 3, p. 597, 2023.
[7] C. Filippou, N. Kyriakides, and C. Chrysostomou, "Numerical study of the seismic retrofitting of masonry-infilled RC frames with openings using TRM," *Earthq. Eng. Struct. Dyn.*, vol. 52, no. 3, pp. 776–805, 2023.
[8] A. Shabani, M. Kioumarsi, and M. Zucconi, "State of the art of simplified analytical methods for seismic vulnerability assessment of unreinforced masonry buildings," *Eng. Struct.*, vol. 239, p. 112280, 2021.
[9] A. Bayraktar, N. Coşkun, and A. Yalçin, "Damages of masonry buildings during the July 2, 2004 Doğubayazıt (Ağrı) earthquake in Turkey," *Eng. Fail. Anal.*, vol. 14, no. 1, pp. 147–157, Jan. 2007.
[10] A. Ural, A. Doğangün, H. Sezen, and Z. Angın, "Seismic performance of masonry buildings during the 2007 Bala, Turkey earthquakes," *Nat. Hazards*, vol. 60, no. 3, pp. 1013–1026, 2012.
[11] J. Ingham and M. Griffith, "Performance of unreinforced masonry buildings during the 2010 Darfield (Christchurch, NZ) earthquake," *Aust. J. Struct. Eng.*, vol. 11, no. 3, pp. 207–224, 2010.
[12] L. Halder, S. C. Dutta, R. P. Sharma, and S. Bhattacharya, "Lessons learnt from post-earthquake damage study of Northeast India and Nepal during last ten years," *Soil Dyn. Earthq. Eng.*, vol. 151, p. 106990, 2021.
[13] A. Doğangün, A. Ural, H. Sezen, Y. Güney, and F. K. Fırat, "The 2011 earthquake in Simav, Turkey and seismic damage to reinforced concrete buildings," *Buildings*, vol. 3, no. 1, pp. 173–190, 2013.
[14] B. Yön, E. Sayın, and T. S. Köksal, "Seismic response of buildings during the May 19, 2011 Simav, Turkey earthquake," *Earthq. Struct.*, vol. 5, no. 3, pp. 343–357, 2013.
[15] N. Yılmaz and Ö. Avşar, "Structural damages of the May 19, 2011, Kütahya–Simav earthquake in Turkey," *Nat. Hazards*, vol. 69, no. 1, pp. 981–1001, 2013.
[16] M. İnsel, H. B. Özmen, and E. Akyol, "Observations on the building damages after 19 May 2011 Simav (Turkey) earthquake," *Bull. Earthq. Eng.*, vol. 11, no. 1, pp. 255–283, Feb. 2013.
[17] F. Piroğlu and K. Özakgül, "Site investigation of masonry buildings damaged during the 23 October and 9 November 2011 Van earthquakes in Turkey," *Nat. Hazards Earth Syst. Sci.*, vol. 13, no. 3, pp. 689–708, 2013.
[18] M. Müvafık, "Field investigation and seismic analysis of a historical brick masonry minaret damaged during the Van earthquakes in 2011," *Earthq. Struct.*, vol. 6, no. 5, pp. 457–472, 2014.
[19] R. Oyguç and E. Oyguç, "2011 Van earthquakes: Lessons from damaged masonry structures," *J. Perform. Constr. Facil.*, vol. 31, no. 5, p. 04017062, 2017.
[20] D. Güney, "Van earthquakes (23 October 2011 and 9 November 2011) and performance of masonry and adobe structures," *Nat. Hazards Earth Syst. Sci.*, vol. 12, no. 11, pp. 3337–3342, 2012.
[21] A. Bayraktar, A. C. Altunışık, and M. Müvafık, "Field investigation of the performance of masonry buildings during the October 23 and November 9, 2011, Van earthquakes in Turkey," *J. Perform. Constr. Facil.*, vol. 30, no. 2, p. 04014209, 2016.
[22] M. Doğan, "Failure of structural (RC, masonry, bridge) to Van earthquake," *Eng. Fail. Anal.*, vol. 35, pp. 489–498, 2013.

[23] B. Yön, O. Onat, and M. E. Öncü, "Earthquake damage to nonstructural elements of reinforced concrete buildings during 2011 Van seismic sequence," *J. Perform. Constr. Facil.*, vol. 33, no. 6, p. 04019075, 2019.
[24] E. Damcı, R. Temur, G. Bekdaş, and B. Sayın, "Damages and causes on the structures during the October 23, 2011 Van earthquake in Turkey," *Case Stud. Constr. Mater.*, vol. 3, pp. 112–131, 2015.
[25] F. Çakır, E. Uçkan, J. Shen, B. S. Şeker, and B. Akbaş, "Seismic damage evaluation of historical structures during Van earthquake, October 23, 2011," *Eng. Fail. Anal.*, vol. 58, pp. 249–266, 2015.
[26] B. Taşkın, A. Sezen, U. M. Tuğsal, and A. Erken, "The aftermath of 2011 Van earthquakes: Evaluation of strong motion, geotechnical and structural issues," *Bull. Earthq. Eng.*, vol. 11, no. 1, pp. 285–312, Feb. 2013.
[27] A. Sakarya, O. Akın, and A. Kılıç, "Investigating the damage from the February 6, 2023 earthquakes in terms of building characteristics in the Antakya and Defne districts of Hatay province," *Int. J. Disaster Risk Reduct.*, vol. 112, p. 104783, 2024.
[28] S. Apostolaki, E. Riga, and D. Pitilakis, "Rapid damage assessment effectiveness for the 2023 Kahramanmaraş Türkiye earthquake sequence," *Int. J. Disaster Risk Reduct.*, vol. 111, p. 104691, 2024.
[29] B. Yön, "Identification of failure mechanisms in existing unreinforced masonry buildings in rural areas after April 4, 2019 earthquake in Turkey," *J. Build. Eng.*, vol. 43, p. 102586, Nov. 2021.
[30] E. A. Godínez-Domínguez *et al.*, "The September 7, 2017 Tehuantepec, Mexico, earthquake: Damage assessment in masonry structures for housing," *Int. J. Disaster Risk Reduct.*, vol. 56, p. 102123, 2021.
[31] O. F. Bayrak, M. Bikçe, and M. M. Erdem, "Failures of structures during the January 24, 2020, Sivrice (Elazığ) earthquake in Turkey," *Nat. Hazards*, vol. 108, no. 2, pp. 1943–1969, Sep. 2021.
[32] M. Günaydın *et al.*, "Seismic damage assessment of masonry buildings in Elazığ and Malatya following the 2020 Elazığ–Sivrice earthquake, Turkey," *Bull. Earthq. Eng.*, vol. 19, no. 6, pp. 2421–2456, Apr. 2021.
[33] H. C. Mertol, G. Tunç, and T. Akış, "Evaluation of masonry buildings and mosques after Sivrice earthquake," *Građevinar*, vol. 73, no. 9, pp. 881–892, 2021.
[34] E. Sayın *et al.*, "24 January 2020 Sivrice–Elazığ, Turkey earthquake: Geotechnical evaluation and performance of structures," *Bull. Earthq. Eng.*, vol. 19, no. 2, pp. 657–684, Jan. 2021.
[35] E. Işık, M. C. Aydın, and A. Büyüksaraç, "24 January 2020 Sivrice (Elazığ) earthquake damages and determination of earthquake parameters in the region," *Earthq. Struct.*, vol. 19, no. 2, pp. 145–156, 2020.
[36] R. Temür, E. Damcı, S. Öncü-Davaş, C. Öser, S. Sargın, and Ç. Şekerci, "Structural and geotechnical investigations on Sivrice earthquake (Mw = 6.8), January 24, 2020," *Nat. Hazards*, vol. 106, no. 1, pp. 401–434, 2021.
[37] B. Atmaca *et al.*, "Field investigation on the performance of mosques and minarets during the Elazığ–Sivrice earthquake," *J. Perform. Constr. Facil.*, vol. 34, no. 6, p. 04020120, 2020.
[38] S. Demir *et al.*, "Performance evaluation of reinforced concrete buildings during the Sivrice–Elazığ earthquake (Mw = 6.8, January 24, 2020) in accordance with Turkish earthquake code," *J. Earthq. Tsunami*, vol. 15, no. 4, p. 2150018, 2021.
[39] Ö. Yurdakul, B. Duran, O. Tunaboyu, and Ö. Avşar, "Field reconnaissance on seismic performance of RC buildings after the January 24, 2020 Elazığ–Sivrice earthquake," *Nat. Hazards*, vol. 105, no. 1, pp. 859–887, 2021.
[40] H. C. Mertol, G. Tunç, and T. Akış, "Damage observation of reinforced concrete buildings after 2020 Sivrice (Elazığ) earthquake, Turkey," *J. Perform. Constr. Facil.*, vol. 35, no. 5, p. 04021053, 2021.
[41] O. F. Nemutlu, B. Balun, and A. Sarı, "Damage assessment of buildings after 24 January 2020 Elazığ–Sivrice earthquake," *Earthq. Struct.*, vol. 20, no. 3, pp. 325–335, 2021.
[42] A. Caner, A. Natale, S. Masood, and N. Huvaj, "Successful seismic performance of bridges after Sivrice earthquake," *J. Perform. Constr. Facil.*, vol. 35, no. 4, p. 04021025, 2021.
[43] B. Atmaca *et al.*, "Lessons learned from the past earthquakes on building performance in Turkey," *J. Struct. Eng. Appl. Mech.*, vol. 3, no. 2, pp. 61–84, 2020.

[44] S. K. Sezgin *et al.*, "Reconnaissance report on damage caused by the February 6, 2023, Kahramanmaraş earthquakes in reinforced-concrete structures," *J. Build. Eng.*, vol. 89, p. 109200, 2024.
[45] M. L. Ivanov and W.-K. Chow, "Structural damage observed in reinforced concrete buildings in Adıyaman during the 2023 Türkiye Kahramanmaraş earthquakes," *Structures*, vol. 49, p. 105578, 2023.
[46] E. Tapia-Hernández, M. C. Genes, and H. Guerrero-Bobadilla, "Damages observed in Turkey due to the Kahramanmaraş earthquakes of February 6, 2023," *J. Earthq. Eng.*, pp. 1–19, 2024.
[47] E. Altunsu, O. Güneş, S. Öztürk, S. Sorosh, A. Sarı, and S. T. Beeson, "Investigating the structural damage in Hatay province after Kahramanmaraş–Türkiye earthquake sequences," *Eng. Fail. Anal.*, vol. 157, p. 107857, 2024.
[48] A. Demir and H. Sezen, "Seismic performance of industrial buildings during the 2023 Kahramanmaraş, Turkey earthquakes," *J. Earthq. Eng.*, pp. 1–15, 2024.
[49] A. Demir *et al.*, "Destructive impact of successive high-magnitude earthquakes occurred in Türkiye's Kahramanmaraş on February 6, 2023," *Bull. Earthq. Eng.*, pp. 1–27, 2024.
[50] O. İnce, "Structural damage assessment of reinforced concrete buildings in Adıyaman after Kahramanmaraş (Türkiye) earthquakes on 6 February 2023," *Eng. Fail. Anal.*, vol. 156, p. 107799, 2024.
[51] M. Ozturk, M. H. Arslan, and H. H. Korkmaz, "Effect on RC buildings of 6 February 2023 Turkey earthquake doublets and new doctrines for seismic design," *Eng. Fail. Anal.*, vol. 153, p. 107521, 2023.
[52] Ö. F. Nemutlu, A. Sarı, and B. Balun, "Comparison of actual loss of life and structural damage in 06 February 2023 Kahramanmaraş earthquakes (Mw 7.7–Mw 7.6) with estimated values," *Afyon Kocatepe Univ. J. Sci. Eng.*, vol. 23, no. 5, pp. 1222–1234, 2023.
[53] İ. Kocaman, "The effect of the Kahramanmaraş earthquakes (Mw 7.7 and Mw 7.6) on historical masonry mosques and minarets," *Eng. Fail. Anal.*, vol. 149, p. 107225, 2023.
[54] A. B. Ersöz, O. Pekcan, M. Altun, T. Teke, and O. Aydogmuş, "Utilizing digital technologies for rapid damage assessment and reconnaissance: The February 6, 2023 Kahramanmaraş–Türkiye earthquakes (Mw 7.7 and Mw 7.6)," *Bull. Earthq. Eng.*, pp. 1–19, 2024.
[55] A. Akıncı, A. A. Dindar, İ. E. Bal, D. Ertuncay, E. Smyrou, and D. Cheloni, "Characteristics of strong ground motions and structural damage patterns from the February 6th, 2023 Kahramanmaraş earthquakes, Türkiye," *Nat. Hazards*, pp. 1–31, 2024.
[56] F. Akar, E. Işık, F. Avcil, A. Büyüksaraç, E. Arkan, and R. İzol, "Geotechnical and structural damages caused by the 2023 Kahramanmaraş earthquakes in Gölbaşı (Adıyaman)," *Appl. Sci.*, vol. 14, no. 5, p. 2165, 2024.
[57] A. C. Altunışık *et al.*, "Field observations and damage evaluation in reinforced concrete buildings after the February 6th, 2023, Kahramanmaraş–Türkiye earthquakes," *J. Earthq. Tsunami*, vol. 17, no. 6, p. 2350024, 2023.
[58] F. Avcil *et al.*, "Effects of the February 6, 2023, Kahramanmaraş earthquake on structures in Kahramanmaraş city," *Nat. Hazards*, vol. 120, no. 3, pp. 2953–2991, 2024.
[59] B. Yön, İ. Ö. Dedeoğlu, M. Yetkin, H. Erkek, and Y. Calayır, "Evaluation of the seismic response of reinforced concrete buildings in the light of lessons learned from the February 6, 2023, Kahramanmaraş, Türkiye earthquake sequences," *Nat. Hazards*, pp. 1–37, 2024.
[60] A. I. Turan, A. Çelik, A. Kumbasaroğlu, and H. Yalçıner, "Assessment of reinforced concrete building damages following the Kahramanmaraş earthquakes in Malatya, Turkey (February 6, 2023)," *Eng. Sci. Technol. Int. J.*, vol. 54, p. 101718, 2024.
[61] B. Sevim, Y. Ayvaz, S. Akbulut, M. F. Aydıner, S. Uzun, and A. Ari, "Seismic performance and damage evaluation of reinforced concrete structures based on field investigation made after February 6, 2023, Kahramanmaraş earthquakes," *J. Earthq. Tsunami*, vol. 18, no. 1, p. 2350032, 2024.
[62] Ö. Yıldız and C. Kına, "Geotechnical and structural investigations in Malatya province after Kahramanmaraş earthquake on February 6, 2023," *Bitlis Eren Üniv. Fen Bil. Derg.*, vol. 12, no. 3, pp. 686–703, 2023.
[63] G. Ozkula *et al.*, "Field reconnaissance and observations from the February 6, 2023, Turkey earthquake sequence," *Nat. Hazards*, vol. 119, no. 1, pp. 663–700, 2023.

[64] S. Avğın, M. M. Köse, and A. Özbek, "Damage assessment of structural and geotechnical damages in Kahramanmaraş during the February 6, 2023 earthquakes," *Eng. Sci. Technol. Int. J.*, vol. 57, p. 101811, 2024.
[65] İ. Kazaz, "Evaluation of seismic performance, design and practice of frame-wall buildings in Türkiye after the 6 February 2023 Kahramanmaraş earthquakes," *J. Build. Eng.*, vol. 99, p. 111557, 2025.
[66] İ. Kazaz, Ö. Avşar, and A. Dilsiz, "Importance of building inspection on the seismic response of a severely damaged RC structure during the February 6, 2023 Kahramanmaraş earthquake sequence," *Eng. Fail. Anal.*, vol. 162, p. 108410, 2024.
[67] T. P. Doğan, H. Kalkan, Ö. Aldemir, M. Ayhan, M. Böcek, and Ö. Anıl, "Investigation of RC structure damages after February 6, 2023, Kahramanmaraş earthquake in the Hatay region," *Bull. Earthq. Eng.*, vol. 22, no. 10, pp. 5201–5229, 2024.
[68] S. Öztürk, E. Altunsu, O. Güneş, and A. Sarı, "Investigation of industrial structure performances in the Hatay and Gaziantep provinces during the Türkiye earthquakes on February 6, 2023," *Soil Dyn. Earthq. Eng.*, vol. 179, p. 108569, 2024.
[69] B. Binici *et al*., "Performance of RC buildings after Kahramanmaraş earthquakes: lessons toward performance based design," *Earthq. Eng. Eng. Vib.*, vol. 22, no. 4, pp. 883–894, 2023.
[70] E. Vuran, C. Serhatoğlu, M. Ö. Timurağaoğlu, E. Smyrou, İ. E. Bal, and R. Livaoğlu, "Damage observations of RC buildings from 2023 Kahramanmaraş earthquake sequence and discussion on the seismic code regulations," *Bull. Earthq. Eng.*, pp. 1–30, 2024.
[71] J. Yuzbasi, "Post-earthquake damage assessment: Field observations and recent developments with recommendations from the Kahramanmaraş earthquakes in Türkiye on February 6th, 2023 (Pazarcık M7.8 and Elbistan M7.6)," *J. Earthq. Eng.*, pp. 1–26, 2024.
[72] O. İnce, M. Atar, Ö. F. Taş, A. Özmen, and E. Sayın, "Betonarme prefabrik endüstri yapılarının 6 Şubat 2023 depremleri sonrası hasarlarının incelenmesi," *Türk Deprem Araştırma Derg.*, vol. 5, no. 2, pp. 291–300, 2023.
[73] A. Özmen, O. İnce, Ö. F. Taş, M. Atar, O. E. Ozbulut, and E. Sayın, "Seismic performance assessment of structures in Malatya Province after 6 February 2023 Turkey earthquake sequences," *Nat. Hazards*, pp. 1–34, 2024.
[74] Ö. Mercimek, "Seismic failure modes of masonry structures exposed to Kahramanmaraş earthquakes (Mw 7.7 and 7.6) on February 6, 2023," *Eng. Fail. Anal.*, vol. 151, p. 107422, 2023.
[75] C. Murty, "Learning earthquake design and construction 12: How do brick masonry houses behave during earthquakes," *Resonance*, vol. 10, no. 1, pp. 88–90, 2005.
[76] F. Clementi, V. Gazzani, M. Poiani, and S. Lenci, "Assessment of seismic behaviour of heritage masonry buildings using numerical modelling," *J. Build. Eng.*, vol. 8, pp. 29–47, 2016.
[77] P. G. Asteris *et al*., "Stochastic vulnerability assessment of masonry structures: Concepts, modeling and restoration aspects," *Appl. Sci.*, vol. 9, no. 2, p. 243, 2019.
[78] G. Grünthal, *European Macroseismic Scale 1998: EMS-98*, 1998. [Online]. Available.
[79] C. Alessandri, M. Garutti, V. Mallardo, and G. Milani, "Crack patterns induced by foundation settlements: Integrated analysis on a Renaissance masonry palace in Italy," *Int. J. Archit. Herit.*, vol. 9, no. 2, pp. 111–129, Feb. 2015.
[80] R. Latifi, M. Hadzima-Nyarko, D. Radu, and R. Rouhi, "A brief overview on crack patterns, repair and strengthening of historical masonry structures," *Materials*, vol. 16, no. 5, p. 1882, 2023.
[81] M. Solla, S. Lagüela, B. Riveiro, and H. Lorenzo, "Non-destructive testing for the analysis of moisture in the masonry arch bridge of Lubians (Spain)," *Struct. Control Health Monit.*, vol. 20, no. 11, pp. 1366–1376, 2013.
[82] M. A. Aiello and S. M. Sciolti, "Bond analysis of masonry structures strengthened with CFRP sheets," *Constr. Build. Mater.*, vol. 20, no. 1, pp. 90–100, 2006.
[83] G. Guerrini, S. Kallioras, S. Bracchi, F. Graziotti, and A. Penna, "Displacement demand for nonlinear static analyses of masonry structures: Critical review and improved formulations," *Buildings*, vol. 11, no. 3, p. 118, 2021.
[84] A. M. El-Maissi, M. M. Kassem, C. G. Tan, R. Fikri, and F. M. Nazri, "Damage index seismic assessment methodologies of URM buildings: A state-of-the-art review," *Eng. J.*, vol. 26, no. 1, pp. 39–53, 2022.

[85] Eurocode 6, "Design of masonry structures—Part 1-1: General rules for reinforced and unreinforced masonry structures," Comité Européen de Normalisation, Brussels, Belgium, 2005.
[86] TBEC, *Turkish Building Earthquake Code 2018*, 2018.
[87] B. Standard, *Eurocode 8: Design of Structures for Earthquake Resistance*, Part 1, 2005.
[88] R. E. Klingner, "Behavior of masonry in the Northridge (US) and Tecomán–Colima (Mexico) earthquakes: Lessons learned, and changes in US design provisions," *Constr. Build. Mater.*, vol. 20, no. 4, pp. 209–219, 2006.
[89] M. Bruneau and K. Yoshimura, "Damage to masonry buildings caused by the 1995 Hyogo-ken Nanbu (Kobe, Japan) earthquake," *Can. J. Civ. Eng.*, vol. 23, no. 3, pp. 797–807, 1996.
[90] M. Bruneau, "State-of-the-art report on seismic performance of unreinforced masonry buildings," *J. Struct. Eng.*, vol. 120, no. 1, pp. 230–251, 1994.
[91] Z. Celep, A. Erken, B. Taskin, and A. Ilki, "Failures of masonry and concrete buildings during the March 8, 2010 Kovancilar and Palu (Elazig) earthquakes in Turkey," *Eng. Fail. Anal.*, vol. 18, no. 3, pp. 868–889, Apr. 2011.
[92] A. Bayraktar, A. C. Altunışık, and M. Muvafık, "Field investigation of the performance of masonry buildings during the October 23 and November 9, 2011, Van earthquakes in Turkey," *J. Perform. Constr. Facil.*, vol. 30, no. 2, p. 04014209, 2016.
[93] Y. S. Tama, A. Solak, N. Cetinkaya, G. Şen, S. Yılmaz, and H. Kaplan, "Damages to unreinforced masonry buildings by the Van earthquakes of 23 October and 9 November 2011," *Nat. Hazards Earth Syst. Sci.*, vol. 13, no. 2, pp. 329–337, 2013.
[94] Y. S. Tama, "Structural damages observed in state buildings after Simav/Turkey earthquake occurred on 19 May 2011," *Nat. Hazards Earth Syst. Sci.*, vol. 12, no. 8, pp. 2709–2718, 2012.
[95] V. Kahya *et al*., "Evaluation of earthquake-related damages on masonry structures due to the 6 February 2023 Kahramanmaraş–Türkiye earthquakes: A case study for Hatay Governorship Building," *Eng. Fail. Anal.*, vol. 156, p. 107855, 2024.
[96] A. Özmen, M. M. Maraş, Y. Ayaz, and E. Sayın, "Assessments of masonry buildings and historical structures during the 2020 Sivrice–Elazığ earthquake," *Period. Polytech. Civ. Eng.*, 2023.
[97] A. Doğangün, A. Ural, and R. Livaoğlu, "Seismic performance of masonry buildings during recent earthquakes in Turkey," 2008. [Online]. Available.
[98] E. Işık, "Structural failures of adobe buildings during the February 2023 Kahramanmaraş (Türkiye) earthquakes," *Appl. Sci.*, vol. 13, no. 15, p. 8937, 2023.
[99] R. İzol, E. Işık, F. Avcil, M. H. Arslan, E. Arkan, and A. Büyüksaraç, "Seismic performance of masonry structures after 06 February 2023 earthquakes: Site survey and FE modelling approach," *Soil Dyn. Earthq. Eng.*, vol. 186, p. 108904, 2024.
[100] D. D'Ayala and E. Speranza, "Definition of collapse mechanisms and seismic vulnerability of historic masonry buildings," *Earthq. Spectra*, vol. 19, no. 3, pp. 479–509, 2003.
[101] E. Işık *et al*., "Structural damages in masonry buildings in Adıyaman during the Kahramanmaraş (Türkiye) earthquakes (Mw 7.7 and Mw 7.6) on 06 February 2023," *Eng. Fail. Anal.*, vol. 151, p. 107405, 2023.
[102] İ. F. Çırak, "Yığma yapılarda oluşan hasarlar, nedenleri ve öneriler," *Ulus. Teknol. Bil. Derg.*, vol. 3, no. 2, pp. 55–60, 2011.

Fırat Üniversitesi Deneysel ve Hesaplamalı Mühendislik Dergisi

FUJECE

Manga için U-Net ve ResNet'in Karşılaştırmalı Analizi Renklendirme: Tutarlılık, Detay ve Hesaplamalı Ödünleşimler

Sami CAKIRAL[1], MD Imran HOSEN[2*], Tarkan AYDIN[3]

[1,2]Yazılım Mühendisliği Bölümü, Mühendislik Fakültesi, Istanbul Ticaret Üniversitesi, İstanbul, Türkiye.
[3]Bilgisayar Mühendisliği Bölümü, Mühendislik ve Doğa Bilimleri Fakültesi, Bahçeşehir Üniversitesi, İstanbul, Türkiye.
[1]Bilgisayar Bilimi ve Yapay Zeka Bölümü, IMT Mines Alès Üniversitesi, Alès, France
[1]sami.cakiral@gmail.com, [2]mdihosen@ticaret.edu.tr, [3]tarkan.aydin@bau.edu.tr

Geliş Tarihi: 15.4.2025
Kabul Tarihi: 31.10.2025
Düzeltme Tarihi: 03.9.2025
doi: https://doi.org/10.62520/fujece.1676853
Araştırma Makalesi

Alıntı: S. Çakıral, MD. I. Hosen ve T. Aydın, "Manga için U-Net ve ResNet'in karşılaştırmalı analizi renklendirme: tutarlılık, detay ve hesaplamalı ödünleşimler", Fırat Üni. Deny. Müh. Derg., vol. 5, no 1, pp. 119-134, Şubat 2026.

Öz

Manganın otomatik olarak renklendirilmesi, kendine özgü sanatsal tarzı ve karmaşık görselliği nedeniyle benzersiz zorluklar ortaya koymaktadır. Derin öğrenme görüntü renklendirmede umut vaat etse de, mevcut yaklaşımlar genellikle manga sanat eserlerinin tutarlılığı ve sanatsal bütünlüğü ile mücadele etmektedir. Bu makale, manga renklendirme için iki derin öğrenme mimarisinin karşılaştırmalı bir analizini sunmaktadır: aşamalı bırakma özelliğine sahip değiştirilmiş bir U-Net ve uyarlanabilir atlama bağlantılarına sahip ResNet tabanlı bir otomatik kodlayıcı. Yapısal ve algısal bileşenleri bir araya getirerek mangaya özgü zorlukları özellikle ele alan yeni bir bileşik kayıp fonksiyonu sunuyoruz. Farklı bir manga veri kümesi üzerinde yapılan deneyler, ResNet tabanlı modelin daha yüksek renk tutarlılığı ve daha iyi kararlılık sağladığını ve tek tip alanlarda daha az yapaylık ürettiğini gösteriyor. Bununla birlikte, U-Net ince ayrıntıları daha etkili bir şekilde korur. Bu sonuçlar, manga renklendirme sistemlerinin pratik uygulamalarına rehberlik ederek mimariler arasındaki değiş tokuşlar hakkında fikir vermektedir.

Anahtar kelimeler: Manga renklendirme, Derin öğrenme, U-Net, ResNet, Otomatik sanatsal işleme

*Yazışılan yazar

İntihal Kontrol: Evet – Turnitin
Şikayet: fujece@firat.edu.tr
Telif Hakkı ve Lisans: Dergide yayın yapan yazarlar, CC BY-NC 4.0 kapsamında lisanslanan çalışmalarının telif hakkını saklı tutar.

Firat University Journal of Experimental and Computational Engineering

Comparative Analysis of U-Net and ResNet for MangaColorization: Consistency, Detail, and Computational Trade-offs

Sami CAKIRAL[1], MD Imran HOSEN[2*], Tarkan AYDIN[3]

[1,2]Software Engineering Department, Engineering Faculty, Istanbul Ticaret University, Istanbul, Türkiye.
[3]Computer Engineering Department, Faculty of Engineering and Natural Sciences, Bahçeşehir University, Istanbul, Türkiye.
[1]Computer Science and Artificial Intelligence Department, IMT Mines Alès University, Alès, France
[1]sami.cakiral@gmail.com, [2]mdihosen@ticaret.edu.tr, [3]tarkan.aydin@bau.edu.tr

Received: 15.4.2025
Accepted:31.10.2025
Revision:03.9.2025
doi: https://doi.org/10.62520/fujece.1676853
Research Article

Citation: S. Çakıral, MD. I. Hosen and T. Aydın, "Comparative analysis of U-Net and ResNet for mangacolorization: consistency, detail, and computational trade-offs", Firat Univ. Jour.of Exper. and Comp. Eng., vol. 5, no 1, pp. 119-134, February 2026.

Abstract

The automated colorization of manga presents unique challenges due to its distinctive artistic style and complex visuals. While deep learning has shown promise in image colorization, existing approaches often struggle with consistency and artistic integrity of manga artwork. This paper presents a comparative analysis of two deep learning architectures for manga colorization: a modified U-Net with progressive dropout and a ResNet-based autoencoder with adaptive skip connections. We introduce a novel composite loss function that specifically addresses manga-specific challenges by incorporating structural and perceptual components. Experiments on a diverse manga dataset show that the ResNet-based model achieves higher color consistency and better stability, producing fewer artifacts in uniform areas. However, U-Net preserves fine details more effectively. These results provide insights into trade-offs between architectures, guiding practical implementations of manga colorization systems.

Keywords: Manga colorization, Deep learning, U-Net, ResNet, Automated artistic processing

*Corresponging author

Plagiarism Checks: Yes – Turnitin
Complaints: fujece@firat.edu.tr
Copyright & License: Authors publishing with the journal retain the copyright to their work licensed under the CC BY-NC 4.0

1. Introduction

Manga, a distinctive form of Japanese comic art, has gained substantial global popularity, with the industry reaching a market value of $5.77 billion in 2020 [1]. While traditionally published in black and white, the growing demand for colored versions presents a significant challenge for publishers and artists. Manual colorization remains a time-intensive process, typically requiring 8-12 hours per page for professional artists. This creates a bottleneck in manga production and distribution, particularly for international markets, where colored editions are increasingly preferred.

Recent advances in deep learning have opened new possibilities for automated image colorization [2,3]. Traditional approaches to manga colorization have faced unique challenges arising from the specific characteristics of manga artwork. These include distinct line art, screen tone patterns, and artistic conventions that differ significantly from those of natural images [4]. Although several automated colorization systems have been developed, they often struggle to maintain consistency across panels and preserve the artistic integrity of the original work [5,6].

Current state-of-the-art approaches in manga colorization primarily employ single-stream architectures, typically based on Generative Adversarial Networks (GANs) [7] or U-Net variants [5], and newer versions use diffusion models [8].

Although these methods show promise for manga colorization, they struggle with complex screen tones and intricate textures. In addition, maintaining consistent color across large panels remains a significant challenge. Furthermore, existing methods are computationally too expensive and, therefore, not ideal for real-world applications in the manga industry.

The limitation of current methodologies can be outlined in several perspectives. The first is that single-stream architecture needs to maintain both fine details as well as global color coherence, which is often done at the expense of one for another. Secondly, existing methods treat all regions of the image equally when, in fact, different regions have different complexities and are more important than others in the same manga artwork. Third, current solutions often fail to adequately capture the unique artistic conventions of manga, resulting in colorization that may appear technically correct but artistically inappropriate.

This paper presents a comparative study of two distinct deep learning approaches for manga colorization: a modified U-Net architecture and a ResNet-based autoencoder. Our research makes several key contributions to the field.

- We introduce a composite loss function that specifically addresses the unique challenges of manga colorization, incorporating both structural and perceptual components.
- We provide a comprehensive analysis of the strengths and limitations of each architectural approach, supported by extensive quantitative and qualitative evaluations.
- We demonstrate practical applications of our findings through detailed case studies, providing insight that can guide future research and development in this domain.

The remainder of this paper is organized as follows. Section 2 briefly discusses existing manga image colorization techniques. In Section 3, we present our methodology, including detailed descriptions of both architectural approaches and our novel loss function. In section 4, we provide details of experimental setup, dataset preparation, and evaluation criteria. The experimental results and discussion including potential future applications are presented in Sections 5 and 6, respectively.

2. Related Work

Image colorization is the process of transforming grayscale images into their corresponding RGB representations, thereby improving both perceptual fidelity and aesthetic appeal [9]. The rapid advancement of deep learning methods in recent years has significantly expanded the possibilities for automating

colorization [3,6]. However, conventional automated colorization approaches are not directly applicable to manga colorization. This is primarily because they must preserve the artistic integrity of the original work while maintaining visual consistency across sequential panels.

The evolution of manga colorization techniques reflects the larger advancement of deep learning in computer vision [10, 11, 12]. This section presents a comprehensive overview of significant developments in the field, from foundational approaches to current state-of-the-art methods.

Manga-specific colorization systems

The application of deep learning to image colorization was pioneered by Zhang et al. [13], who demonstrated the potential of convolutional neural networks for this task. Their work established a framework for learning color distributions from large-scale datasets. Building on this foundation, Iizuka et al. [14] introduced a significant advancement with their two-stream architecture that combined local and global features. This marked an important step toward context-aware colorization.

Manga colorization presents unique challenges that have spurred the development of specialized approaches. For instance, Furusawa et al. [15] introduced Comicolorization, a semi-automatic system designed to maintain color consistency across multiple panels by using reference images. This work tackled one of the key issues in manga colorization: ensuring that character colors remain consistent throughout the narrative. In a similar vein, Zhang et al. [16] proposed a two-stage colorization method focused on preserving the artistic style of manga and anime. Their approach demonstrated superior stylistic consistency, offering more natural and coherent colorization results.

In recent years, significant architectural innovations have emerged in manga colorization [17, 18, 19, 20, 21, 22]. Kim et al. [18] presented a two-generator GAN-based method for line art colorization that preserves the artist's intent. Their system introduced the use of semantic color tags, providing a more intuitive interface for artists while still maintaining high quality results.

Furthermore, the incorporation of style transfer techniques has enriched manga colorization. Li et al. [17] proposed the Inkn'Hue framework, which leverages a multi-encoder VAE approach to harmonize models for shading and vibrant coloring. This model adds a more sophisticated method for color application while respecting the original artistic style of the manga.

The most recent advancement in the field has been the adoption of diffusion models. Lin et al. [23] introduced Sketch2Manga, a framework that uses diffusion models to generate high-quality color illustrations from sketches. This model excels at handling the complex screen tone patterns that are a hallmark of manga artwork.

Finally, Xiang et al. [19] advanced the use of diffusion models with their AnimeDiffusion system, which demonstrated superior performance in colorizing facial features compared to traditional GAN-based methods. Their work underscores the potential of diffusion models to capture subtle color variations while maintaining the stylistic integrity of the original artwork.

Loss functions and training strategies

The development of specialized loss functions has been instrumental in enhancing the quality of manga colorization. Johnson et al. [24] introduced perceptual losses, which significantly improved the visual fidelity of generated images by focusing on high-level feature matching rather than pixel-wise accuracy. Gatys et al. [25] further refined this concept with style-aware loss functions, which emphasize the preservation of artistic intent and style during the colorization process. As a result, the final output aligns more closely with the original artwork.

These advancements have contributed to the progression of manga colorization, each addressing unique challenges in the process. However, there remains an ongoing debate about the optimal balance between

architectural choices and the impact of these choices on colorization quality. This study builds on these previous works by providing a comparative analysis of U-Net [26] and ResNet [27] architectures, offering a deeper understanding of their strengths and limitations specifically within the context of manga colorization.

3. Materials and Methods

In this section, we describe the neural architectures employed for automated manga colorization. We have investigated two deep learning models: a modified U-Net and a ResNet-based autoencoder.
We designed each architecture to address key challenges in manga colorization, such as the preservation of structural details, color consistency, and computational efficiency.

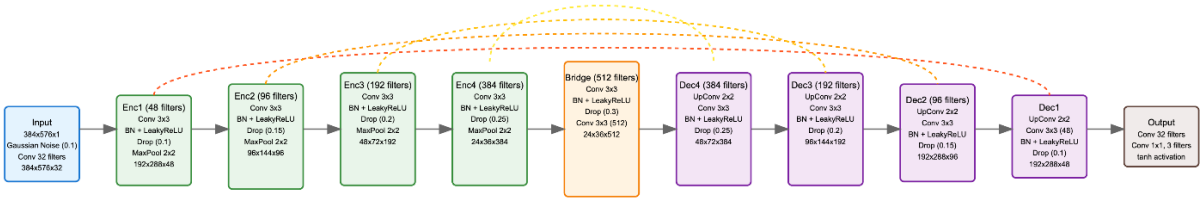


Figure 1. Modified U-Net architecture highlighting the progressive dropout, skip connections and gaussian noise layer

Neural architectures

Modified U-Net for manga colorization

The first architecture is a modified U-Net as shown in Figure 1, specifically tailored for manga colorization by integrating enhancements that improve spatial feature propagation, generalization, and stability.

Architectural Modifications: The U-Net architecture is enhanced with the following key modifications:

- Progressive Dropout Mechanism: Dropout rates are incrementally increased in the encoder path, ranging from 0.1 in the early layers to 0.3 in the deeper layers. This progressive dropout strategy helps mitigate overfitting while allowing robust feature extraction.
- Enhanced Skip Connections: Unlike the traditional U-Net, our model incorporates additional convolutional layers in the skip pathways. These layers refine transferred feature maps, reducing artifacts and improving local consistency in colorized outputs.
- Regressive Dropout in the Decoder: A decreasing dropout rate is applied in the decoder path to facilitate smoother reconstruction and reduce artifacts, ensuring better spatial coherence in colorized outputs.
- Input Gaussian Noise Layer: A Gaussian noise layer is introduced at the input stage to enhance model generalization, preventing over-reliance on specific textures and enabling more robust colorization across diverse manga styles.

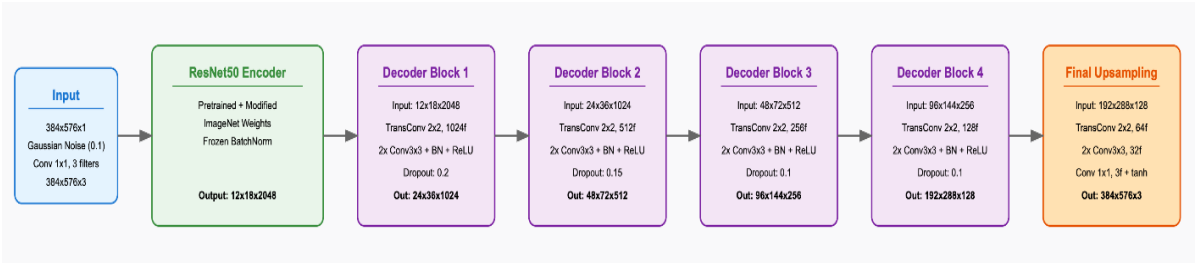


Figure 2. ResNet Autoencoder architecture showing the integration of pretrained components

ResNet-Based autoencoder

The second model, a ResNet-based autoencoder, utilizes a deep residual learning framework to enhance color consistency and feature abstraction, as illustrated in Figure 2.

Architectural features: The ResNet-based autoencoder incorporates the following key enhancements:

- Pretrained ResNet50 Backbone: The encoder is built upon a ResNet50 network pretrained on ImageNet, which allows the model to leverage robust, hierarchical feature representations learned from large-scale natural image datasets. This aids in capturing high-level semantic features that are crucial for manga image colorization.
- Adaptive Skip Connections: To ensure consistent spatial dimensions and prevent distortions in the colorized outputs, feature maps from the encoder are selectively passed to the decoder via adaptive skip connections. These connections employ feature alignment techniques to maintain spatial coherence.
- Progressive Decoder with Deconvolution Blocks: The decoder reconstructs the colorized manga images using a series of deconvolution layers. This progressive refinement process helps maintain the structural integrity of the image while improving colorization quality.
- Dynamic Resizing for Output Consistency: A dynamic resizing mechanism ensures that the final output resolution remains consistent, even when the input images have varying dimensions. This approach is particularly valuable when working with large-scale manga datasets that contain pages with different layouts.

Our modified ResNet architecture incorporates skip connections between the encoder and decoder. We refer to it interchangeably as ResUNet or ResNet.

Composite loss function

To ensure high-quality manga colorization, we designed a composite loss function that simultaneously optimizes multiple aspects of colorization accuracy. Our objective is to balance color consistency, structural preservation, and perceptual quality. The total loss function (equation 1) is formulated as follows:

$$\mathcal{L}_{total} = \alpha\mathcal{L}_{\mathcal{MSE}} + \beta\mathcal{L}_{\mathcal{SSIM}} + \gamma\mathcal{L}_{structure} + \sum_{i\in\{H,S,V\}} \omega_{i\mathcal{L}_i} \quad (1)$$

where each term plays a specific role in guiding the learning process:

- Mean Squared Error ($\mathcal{L}_{\mathcal{MSE}}$): This term minimizes the pixel-wise difference between the predicted and ground truth images, ensuring overall color accuracy.
- Structural Similarity Index ($\mathcal{L}_{\mathcal{SSIM}}$): SSIM is incorporated to enhance perceptual fidelity by prioritizing structural relationships within the image rather than just pixel-wise errors.
- Edge-Preservation Loss ($\mathcal{L}_{structure}$): This component encourages the model to maintain sharp contours and fine details, which are critical for preserving the artistic integrity of manga line art.
- HSV Color Space Loss ($\mathcal{L}_{H,S,V}$): To improve color stability and saturation balance, we introduce losses for each channel (Hue, Saturation, and Value). This helps prevent unnatural color shifts and maintains stylistic consistency.

The weighting coefficients $(\alpha, \beta, \gamma, \omega_i)$ were determined through extensive ablation studies, ensuring an optimal balance between these competing objectives.

Training strategy

The training process employs a cosine learning rate scheduler with restarts (equation 2):

$$\eta_t = \eta_{min} + \frac{1}{2}(\eta_{max} - \eta_{min})\left(1 + \cos\left(\frac{T_{cur}}{T_i}\pi\right)\right) \quad (2)$$

We use the AdamW optimizer which is the updated version of Adam. AdamW combines adaptive moment estimation decoupled with weight decay to improve generalization. The optimizer is configured with an initial learning rate of 4×10^{-4}, weight decay of 1×10^{-4}, $\beta_1 = 0.9$, $\beta_2 = 0.999$, and $\epsilon = 1 \times 10^{-8}$. To further refine training, we apply a cosine learning rate scheduler with warm restarts [28]. This approach periodically resets the learning rate to promote better convergence. Training was conducted over 50 epochs with dynamic batch sizing based on available GPU memory.

Color accuracy metric

To effectively evaluate colorization quality with a focus on human perception, we introduce a custom color accuracy metric that operates in HSV color space. This metric provides a nuanced evaluation of color similarity by independently assessing hue, saturation, and value components with different tolerance thresholds (equation 3):

$$\text{ColorAccuracy} = \frac{1}{N}\sum_i [(h_i < 0.15) \wedge (s_i < 0.25) \wedge (v_i < 0.3)] \quad (3)$$

where h_i, s_i, and v_i represent the differences in hue, saturation, and value components respectively. It is important to note that this metric serves purely as a monitoring tool during training to evaluate how well our models approach proper color reproduction, and is not used in the training process itself, which relies on our composite loss function described in Section 3 (Composite Loss Function).

The metric is implemented as a custom metric class that performs several key operations:

1. Normalization of input tensors from [-1, 1] to [0, 1] range
2. Conversion from RGB to HSV color space
3. Computation of circular difference for hue values
4. Application of component-specific thresholds:
    - Hue: 0.15 (strict threshold to ensure color accuracy)
    - Saturation: 0.25 (balanced to prevent dull colors)
    - Value: 0.3 (more tolerant for lighting variations)

The thresholds for hue, saturation, and value were determined empirically through a series of preliminary experiments. A stricter hue threshold (0.15) was adopted to ensure accurate representation of character colors. In contrast, a more lenient value threshold (0.3) was chosen to accommodate the natural variations in shading and lighting that frequently occur in manga artwork. The saturation threshold (0.25) serves as a balance to prevent dull colors. By monitoring this metric during training, we can better understand how our models progress in terms of perceptual color accuracy, even as they optimize for the composite loss function.

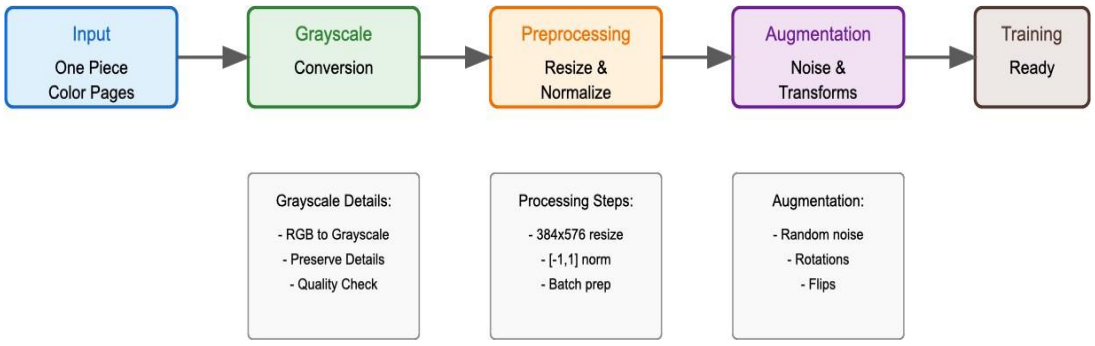


Figure 3. Data preprocessing pipeline, illustrating the transformation stages from raw manga images to training-ready inputs

4. Dataset And Experimental Setup

Dataset construction

Our dataset is derived from the colored edition of *One Piece* manga, with training samples drawn from the first 50 volumes and testing samples from the subsequent 50 volumes. Both training and testing set consists of 7237 images of size (768×1152). This dataset provides a diverse and high-quality source of training data. This selection is motivated by its consistent artistic style, the availability of professionally colored versions. Its wide range of scenes and character interactions serve as rich training examples.

To construct paired training data, we employed a systematic pipeline, illustrated in Figure 3:

i. Extracting high-resolution colored images from official *One Piece* colored editions.
ii. Converting colored images to grayscale using standardized desaturation techniques.
iii. Ensuring precise alignment between grayscale and color images through automated quality verification.
iv. Extracting metadata (e.g., chapter and volume information) for structured dataset management.

This process eliminates common dataset inconsistencies where grayscale versions may not perfectly align with their colorized counterparts, ensuring reliable training pairs for learning-based colorization.

Data preprocessing

To prepare the dataset for training, we implemented a preprocessing pipeline that transforms raw images into a standardized format suitable for deep learning models. The pipeline is depicted in Fig. 3.
The key preprocessing steps include:

- Resizing: All images are scaled to a uniform resolution of 384 × 576 pixels to maintain consistency across the dataset.
- Normalization: Pixel values are normalized to the $[-1, 1]$ range to facilitate stable neural network training.
- Data Augmentation: To improve generalization, various augmentation techniques are applied:
  i) Adaptive noise injection to simulate natural variations in manga printing and scanning.
  ii) Geometric transformations such as random flips and rotations to enhance model robustness.
  iii) Color space augmentations applied to the colored images to introduce variations in hue and saturation.
- Memory Optimization: We employ dynamic batching and efficient data prefetching to optimize training performance on limited GPU resources.

Experimental setup

Experiments were conducted on a GPU-accelerated environment using Google Colab with TensorFlow. To enhance computational efficiency, we enabled GPU memory optimizations and activated XLA Just-In-Time (JIT) compilation. The implementation follows modern deep learning best practices to ensure reproducibility and optimal performance.

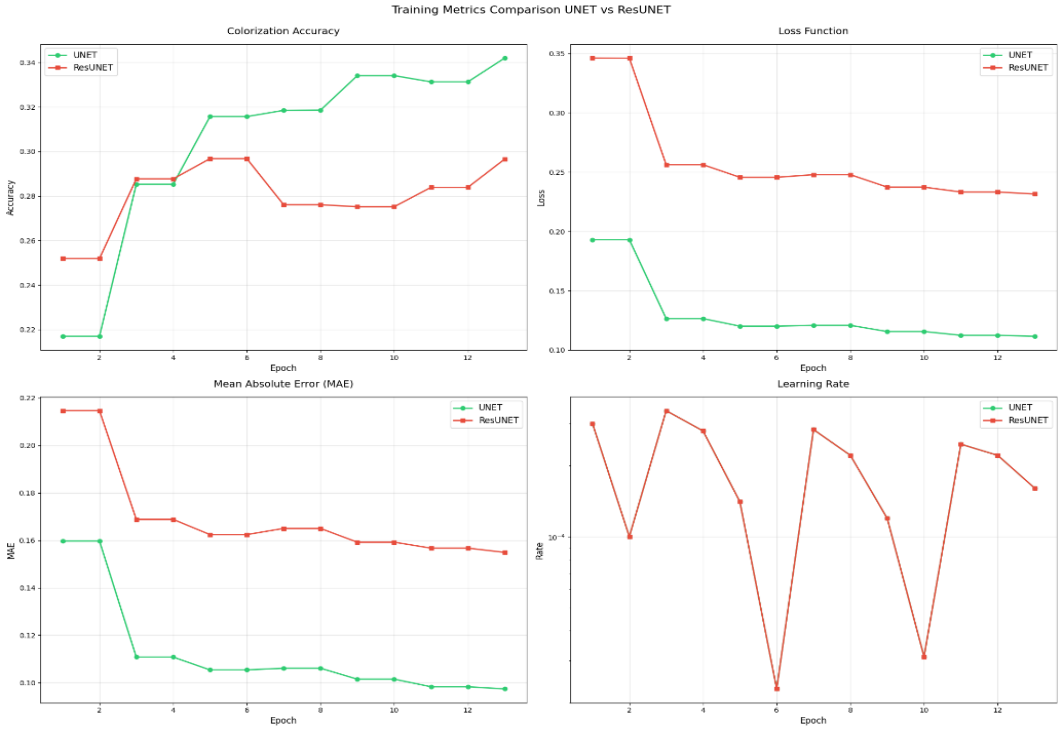


Figure 4. Training metrics evolution showing convergence patterns and performance indicators

5. Experimental Results

Quantitative analysis

Our quantitative evaluation examines four key performance metrics: colorization precision, training loss, Mean Absolute Error (MAE), and learning rate evolution, as shown in Figure 4. The training process was automatically terminated at epoch 13 for both architectures due to early stopping criteria. These metrics provide valuable insights into learning dynamics and overall model performance.

The colorization precision curve (top left plot in Fig. 4) reveals a consistent improvement in U-Net's performance, rising from 0.22 to 0.34 by epoch 12. In contrast, ResUNet exhibits a sharp initial gain, reaching 0.29 by epoch 4, but stabilizes at a lower level around 0.28. This suggests that U-Net progressively refines its colorization ability throughout training, while ResUNet plateaus earlier.

The training loss curve (top right plot) provides further insights. ResUNet initially exhibits a higher loss (0.35), whereas U-Net starts lower at approximately 0.19. Both architectures demonstrate rapid early improvement, yet U-Net maintains consistently lower loss values throughout training.

By epoch 12, U-Net stabilizes at 0.11, while ResUNet at 0.23, indicating better optimization characteristics in U-Net.

The Mean Absolute Error (bottom left plot) reinforces these findings. U-Net achieves lower MAE, stabilizing around 0.10, compared to ResUNet's 0.16. This 0.06 reduction in MAE suggests that U-Net produces more precise pixel-wise color predictions, capturing finer details more accurately.

In terms of computational efficiency, we conducted benchmarking on inference speed and memory consumption. The results indicate that U-Net demonstrates superior efficiency compared to ResUNet. Specifically, U-Net achieves 4.95 frames per second (FPS), while ResUNet reaches 2.65 FPS. Regarding memory usage, U-Net requires 2959.7 MB of CPU memory, whereas ResUNet consumes 3044.6 MB. Both models exhibit comparable GPU memory usage of approximately 617 MB.

The learning rate adaptation (bottom right plot) highlights distinct training dynamics between the architectures. ResUNet exhibits pronounced cyclical variations due to the cosine annealing schedule, while U-Net follows a more stable learning rate trajectory. This suggests that the two architectures respond differently to learning rate scheduling, influencing their respective optimization behaviors. The stabilization of these trends contributed to the early stopping decision at epoch 13.

These results challenge initial expectations regarding ResUNet's superiority. U-Net demonstrates consistently better performance across key metrics, suggesting that architectural complexity does not necessarily correlate with improved results in manga colorization. This finding underscores the importance of empirical evaluation in model selection, highlighting U-Net as a more effective choice for this task.

To further contextualize these findings within the existing literature, we adapted a similar architecture proposed in [29], due to the limited availability of source code for direct manga colorization. Under the same experimental setup, Hosen's method achieved a color accuracy of 18.17%, an MAE of 0.7423, and a loss of 0.6088. In terms of computational efficiency, Hosen's model exhibited a higher inference speed, approximately 13.1% faster than our ResUNet (2.51 FPS), while consuming about 0.25% less CPU memory; GPU memory usage was identical. Although Hosen's method demonstrates marginally better efficiency, our ResUNet achieves substantially higher accuracy and lower error rates, providing a more effective solution for manga colorization.

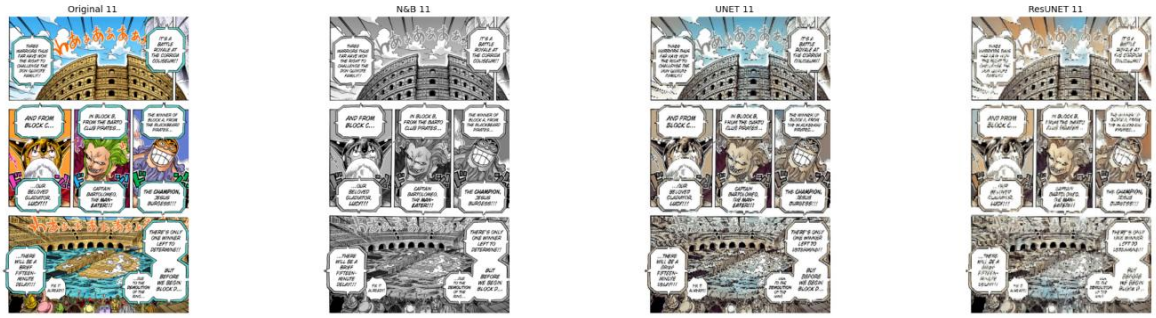


Figure 5. Comparative visualization of colorization results across different manga panels

Qualitative assessment

To evaluate the visual quality of our colorization results, we conducted a detailed comparison of both architectures against the original-colored manga panels. Figure 5 displays four versions of the same panel: the original-colored image, the grayscale input, and the outputs from U-Net and ResUNet. This layout facilitates a direct comparison of each model's ability to reconstruct color information and artistic detail.

Both models preserve the fundamental structure of the original artwork, yet they exhibit distinct approaches to colorization. The top panel, depicting the Corrida Coliseum against a sky background, highlights each model's ability to render large architectural elements and atmospheric effects. U-Net excels in maintaining contrast between the stone textures and sky, whereas ResUNet offers a more uniform but subdued interpretation.

The middle section, featuring three-character portraits, serves as a key test for facial detail preservation and emotional expressiveness. Each portrait presents distinct characteristics—Lucy's determined expression, Bartolomeo's sharp features, and Jesus Burgess's dynamic pose. U-Net demonstrates superior preservation of facial nuances and emotional depth, particularly in fine-grained details. While ResUNet produces coherent results, it tends to slightly flatten these expressive details, reducing the overall impact.

The bottom panel, which showcases a wide view of the coliseum with water elements and crowd scenes, illustrates how each model handles complex scene composition. U-Net retains more of the original vibrancy,

particularly in water reflections and architectural intricacies, whereas ResUNet, though maintaining consistency, renders a slightly less dynamic interpretation of the scene.

Notably, both models successfully preserve manga-specific elements such as speech bubbles, text overlays, and panel boundaries. However, U-Net exhibits superior adherence to the original artistic style, particularly in background effects and environmental textures. While ResUNet ensures consistency, it occasionally diminishes the artistic dynamism of the original panels, leading to a more uniform but less expressive rendering.

Table 1. Post-processing enhancement parameters

Parameter	Temperature	Tint	Vibrance	Saturation	Exposure	Contrast	Highlights	Shadows	Whites
Value	-7	+4	+50	+30	+0.1	+10	+5	+5	+20

6. Analysis and Discussion

Post-processing enhancement analysis

While initial colorization outputs may appear subdued, the application of HSV adjustments in post-processing reveals the true potential of our models. Table 1 details the color grading parameters we applied to enhance the models' outputs.

As demonstrated in Figure 6, these adjustments significantly improve the visual appeal of both models' outputs. The enhanced results reveal that our architecture successfully captures underlying spatial and contextual relationships necessary for meaningful colorization, even if their direct output appears conservative. Particularly notable improvements can be observed in the sky and water renderings, where enhanced tones reveal the models' inherent understanding of scene composition. This enhancement process not only improves the aesthetic quality but also demonstrates that our models generate coherent base colorization that can be effectively refined through post-processing.



Figure 6. Comparison of original model outputs (left) with post-processed results (right) for both U-Net and ResUNet architectures

Interpretation of results

Our comparative analysis of U-Net and ResNet architecture reveals significant insights into manga colorization approaches. The U-Net implementation demonstrated notably superior performance, achieving a final accuracy of 0.342 compared to ResNet's 0.297. This substantial difference challenges our initial assumptions about the potential advantages of ResNet's more complex architecture. Particularly noteworthy is U-Net's improvement trajectory, showing a 57.6% increase in accuracy over the training period, compared to ResNet's more modest 17.7% improvement.

The performance disparity becomes even more evident when examining the loss metrics, where U-Net achieved a final loss of 0.112 versus ResNet's 0.232. This difference suggests that U-Net's simpler architecture may be better suited for the specific challenges of manga colorization, particularly in capturing the nuanced details characteristic of this artistic medium.

Loss function weight optimization

Our initial experiments with balanced loss components (MSE 40%, SSIM 20%, HSV 20%) revealed significant convergence issues during the training process. As illustrated in Figure 7, this configuration led to persistent oscillations that prevented the model from reaching a stable optimum. Despite achieving relatively low loss values around 0.35, the resulting colorization exhibited inconsistent quality and frequent grayscale bias.

These observations led us to fundamentally reconsider our approach to loss weighting. After several tests, we discovered that heavily prioritizing the MSE component ($\alpha = 0.9$) while maintaining a smaller but crucial structural term ($\beta = 0.1$) produced significantly more stable training dynamics. This revised configuration addresses two critical aspects: the dominant MSE term ensures consistent and accurate color reproduction, while the SSIM component maintains structural coherence without interfering with color stability.

The success of this asymmetric weighting strategy challenges the intuitive assumption that balanced loss components would yield optimal results. Our findings suggest that in the specific context of manga colorization, strong color accuracy constraints combined with subtle structural guidance provide a more effective learning framework than attempting to simultaneously optimize multiple competing objectives with equal importance. Therefore, we used for the training the following Loss Function (equation 4):

$$\mathcal{L}_{total} = 0.9\mathcal{L}_{MSE} + 0.1\mathcal{L}_{SSIM} \tag{4}$$

The disparity in computational requirements between the architecture presents practical implications. U-Net's more efficient resource utilization (12.4 GB GPU memory versus ResNet's 13.8 GB) and faster inference time (as discussed in Quantitative section) suggests it may be more suitable for production environments where computational resources are constrained.

To further assess the applicability of our proposed loss function, we conducted additional experiments on another publicly available dataset [30]. We utilized a comparable number of samples (approximately 7K) to those in our original dataset. The dataset provides images at an original resolution of 1024×1024. We applied the same preprocessing steps and experimental setup as before, with the exception of batch size (set to 2 instead of 4 due to memory constraints). Our ResUNet model achieved a color accuracy of 29.78%, an MAE of 0.1802, and a loss of 0.1374. These results demonstrate the broader applicability and robustness of the proposed loss function across different datasets.

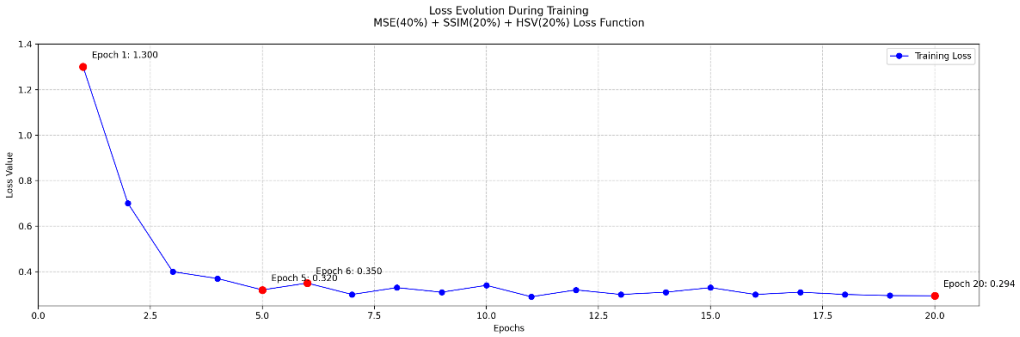


Figure 7. Training instability observed with initial balanced loss weights showing persistent oscillations and failure to converge

Effect of image size

To balance computational efficiency and model performance, we downscaled the original images from 768×1152 to 384×576. While standard ResNet architectures typically accept input dimensions of 224×224, we did not employ a pretrained ResNet; instead, we implemented a custom ResUNet architecture that allowed us to experiment with varying image resolutions. To evaluate the effect of image size, we trained our model with both 224×224 and 384×576 inputs. At 224×224, the model achieved a color accuracy of 29.25%, an MAE of 0.3096, and a loss of 0.1920. In contrast, training with 384×576 inputs yielded superior results, with a color accuracy of 29.66%, an MAE of 0.2315, and a loss of 0.1549. It demonstrates that larger input dimensions (384×576) lead to better overall performance in our ResUNet model due to rich spatial details during training.

Limitations and challenges

Despite the strong quantitative results, several limitations warrant consideration. First, while U-Net shows superior metrics overall, both architectures still struggle with maintaining consistent coloring across complex multi-panel layouts. This limitation becomes particularly apparent in scenes with varying lighting conditions or complex character interactions.

The Mean Absolute Error results (U-Net: 0.097, ResNet: 0.155) indicate room for improvement in pixel-level accuracy for both architectures. Additionally, we observed that both models occasionally struggle with preserving the distinctive artistic techniques common in manga, particularly in areas with complex screen tone patterns or detailed background elements.

Practical implications

Our findings have direct implications for real-world manga colorization pipelines. U-Net's combination of superior performance metrics and lower resource requirements makes it particularly attractive for commercial applications. The 39.0% improvement in MAE for U-Net, compared to ResNet's 27.8%, suggests it would provide more reliable results in production environments.

The observed training dynamics also inform practical deployment considerations. U-Net's more stable learning progression and better final metrics indicate it might require less fine-tuning and post-processing in production scenarios, potentially reducing the overall computational and human resource requirements.

Future research directions

This study opens several promising avenues for future research. One of the primary challenges remaining is improving color consistency across multiple panels, while also preserving U-Net's ability to capture fine details effectively. Addressing this could enhance the quality and coherence of the colorization process in longer manga sequences. Additionally, further optimization of the ResNet architecture to reduce its

computational overhead, while retaining its advantages in global color consistency, could offer more efficient solutions without compromising performance.

Future research efforts may also explore the following directions:

- Combining the strengths of U-Net's efficient feature extraction and ResNet's robust feature representation in hybrid architectures.
- Fine-tuning the loss function weighting strategy to improve the handling of edge cases and more complex scenes.
- Investigating the application of attention mechanisms specifically tailored for manga-style artwork to enhance the model's focus on relevant image features.
- Leveraging transfer learning techniques to better accommodate diverse artistic styles, ensuring broader applicability of colorization models.

7. Conclusion

In this paper, we performed a comparative analysis of U-Net and ResNet architectures for manga colorization, highlighting their strengths and weaknesses. While the results show clear performance trends, additional research is necessary to draw more definitive conclusions. The proposed composite loss function shows potential for enhancing colorization quality.

The findings offer valuable insights for advancing manga colorization systems, with the evaluation of performance metrics and resource requirements providing a foundation for optimizing model selection and training strategies. However, real-world applications will necessitate more extensive testing across diverse manga styles. Manga colorization remains a complex challenge, requiring improvements in computational efficiency, architectural design, and style preservation. Future research should focus on novel deep learning approaches, enhanced loss functions, and dataset diversification to improve generalization. As demand for high-quality colored manga increases, continued innovation will be critical to bridge the gap between automated and artist-driven colorization.

8. Author Contribution Statement

In the study, Author 1 contributed to forming the idea, making the design, literature review, and the analysis of the results; Author 2 contributed to provision of the materials and examination of the results, checking the spelling and checking the article in terms of content; Author 3 contributed to the organization of the research.

9. Ethics Committee Approval and Conflict of Interest

There is no need for an ethics committee approval in the prepared article. There is no conflict of interest with any person/institution in the prepared article.

10. Ethical Statement Regarding the Use of Artificial Intelligence

No artificial intelligence-based tools or applications were used in the preparation of this study. The entire content of the study was produced by the author(s) in accordance with scientific research methods and academic ethical principles.

11. References

[1] Anime News Network, "Manga market in Japan hits record 612.6 billion yen in 2020," Feb. 2021, archived Nov. 14, 2022, accessed Nov. 14, 2021. [Online]. Available: https://www.animenewsnetwork.com/news/2021-02-26/manga-market-in-japan-hits-record-612.6-billion-yen-in-2020/.169987.

[2] S. Guadarrama, R. Dahl, D. Bieber, M. Norouzi, J. Shlens, and K. Murphy, "PixColor: Pixel recursive colorization," arXiv:1705.07208, 2017.

[3] M. Kumar, D. Weissenborn, and N. Kalchbrenner, "Colorization transformer," arXiv:2102.04432, 2021.

[4] T. Jiramahapokee, "Inkn'hue: Enhancing manga colorization from multiple priors with alignment multi-encoder VAE," arXiv:2311.01804, 2023.

[5] L. Zhang, Y. Ji, X. Lin, and C. Liu, "Style transfer for anime sketches with enhanced residual U-Net and auxiliary classifier GAN," in *Proc. 4th IAPR Asian Conf. Pattern Recognit. (ACPR)*, 2017, pp. 506–511.

[6] Y. Ci, X. Ma, Z. Wang, H. Li, and Z. Luo, "User-guided deep anime line art colorization with conditional adversarial networks," in *Proc. 26th ACM Int. Conf. Multimedia*, 2018, pp. 1536–1544.

[7] Y. Wu, X. Wang, Y. Li, H. Zhang, X. Zhao, and Y. Shan, "Towards vivid and diverse image colorization with generative color prior," in *Proc. IEEE/CVF Int. Conf. Comput. Vis. (ICCV)*, 2021, pp. 14377–14386.

[8] N. Zabari, A. Azulay, A. Gorkor, T. Halperin, and O. Fried, "Diffusing colors: Image colorization with text guided diffusion," in *SIGGRAPH Asia Conf. Papers*, 2023, pp. 1–11.

[9] S. Anwar, M. Tahir, C. Li, A. Mian, F. S. Khan, and A. W. Muzaffar, "Image colorization: A survey and dataset," arXiv:2008.10774, 2020.

[10] M. B. Islam and M. I. Hosen, "Emotion, age and gender prediction through masked face inpainting," in *Int. Conf. Pattern Recognit.*, 2022, pp. 37–48.

[11] M. I. Hosen, T. Aydin, and M. B. Islam, "WNet: A dual-encoded multi-human parsing network," *IET Image Process.*, vol. 18, no. 12, pp. 3316–3328, 2024.

[12] M. I. Hosen and S. Kahraman, "Deep learning-based efficient drone detection and tracking in real-time," in *Proc. 33rd Signal Process. Commun. Appl. Conf. (SIU)*, 2025, pp. 1–4.

[13] R. Zhang, P. Isola, and A. A. Efros, "Colorful image colorization," in *Proc. Eur. Conf. Comput. Vis. (ECCV)*, 2016, pp. 649–666.

[14] S. Iizuka, E. Simo-Serra, and H. Ishikawa, "Let there be color! Joint end-to-end learning of global and local image priors for automatic image colorization with simultaneous classification," *ACM Trans. Graph.*, vol. 35, no. 4, pp. 1–11, 2016.

[15] C. Furusawa, K. Hiroshiba, K. Ogaki, and Y. Odagiri, "Comicolorization: Semi-automatic manga colorization," in *SIGGRAPH Asia Tech. Briefs*, 2017, pp. 1–4.

[16] L. Zhang, C. Li, T.-T. Wong, Y. Ji, and C. Liu, "Two-stage sketch colorization," *ACM Trans. Graph.*, vol. 37, no. 6, pp. 1–14, 2018.

[17] Y. Li, M.-Y. Liu, X. Li, M.-H. Yang, and J. Kautz, "A closed-form solution to photorealistic image stylization," in *Proc. Eur. Conf. Comput. Vis. (ECCV)*, 2018, pp. 453–468.

[18] H. Kim, H. Y. Jhoo, E. Park, and S. Yoo, "Tag2Pix: Line art colorization using text tag with SECat and changing loss," in *Proc. IEEE/CVF Int. Conf. Comput. Vis. (ICCV)*, 2019, pp. 9056–9065.

[19] Y. Cao, X. Meng, P. Mok, X. Liu, T.-Y. Lee, and P. Li, "AnimeDiffusion: Anime face line drawing colorization via diffusion models," arXiv:2303.11137, 2023.

[20] S. Chen, D. Li, Z. Bao, Y. Zhou, L. Tan, Y. Zhong, and Z. Zhao, "Manga generation via layout-controllable diffusion," arXiv:2412.19303, 2024.

[21] A. Maejima *et al*., "Continual few-shot patch-based learning for anime-style colorization," *Comput. Vis. Media*, vol. 10, no. 4, pp. 705–723, 2024.

[22] Y. Cao, X. Meng, P. Mok, T.-Y. Lee, X. Liu, and P. Li, "AnimeDiffusion: Anime diffusion colorization," *IEEE Trans. Vis. Comput. Graph.*, vol. 30, no. 10, pp. 6956–6969, 2024.

[23] J. Lin, X. Liu, C. Li, M. Xie, and T.-T. Wong, "Sketch2Manga: Shaded manga screening from sketch with diffusion models," in *Proc. IEEE Int. Conf. Image Process. (ICIP)*, 2024, pp. 2389–2395.

[24] J. Johnson, A. Alahi, and L. Fei-Fei, "Perceptual losses for real-time style transfer and super-resolution," in *Proc. Eur. Conf. Comput. Vis. (ECCV)*, 2016, pp. 694–711.
[25] L. A. Gatys, A. S. Ecker, and M. Bethge, "Image style transfer using convolutional neural networks," in *Proc. IEEE Conf. Comput. Vis. Pattern Recognit. (CVPR)*, 2016, pp. 2414–2423.
[26] O. Ronneberger, P. Fischer, and T. Brox, "U-Net: Convolutional networks for biomedical image segmentation," in *Proc. Int. Conf. Med. Image Comput. Comput.-Assist. Interv. (MICCAI)*, 2015, pp. 234–241.
[27] K. He, X. Zhang, S. Ren, and J. Sun, "Deep residual learning for image recognition," in *Proc. IEEE Conf. Comput. Vis. Pattern Recognit. (CVPR)*, 2016, pp. 770–778.
[28] I. Loshchilov and F. Hutter, "SGDR: Stochastic gradient descent with warm restarts," arXiv:1608.03983, 2016.
[29] M. I. Hosen and M. B. Islam, "Masked face inpainting through residual attention U-Net," in *Proc. Innov. Intell. Syst. Appl. Conf. (ASYU)*, 2022, pp. 1–5.
[30] MichaelP84, "Manga-colorization-dataset," Hugging Face Dataset, 2024, accessed Sep. 20, 2025. [Online]. Available: https://huggingface.co/datasets/MichaelP84/manga-colorization-dataset.

Fırat Üniversitesi Deneysel ve Hesaplamalı Mühendislik Dergisi

FUJECE

Yüksek Hassasiyetli Uygulamalar için DC-DC Buck Dönüştürücünün Otomatik Ayarlamalı PID Kontrolü

Adile AKPUNAR BOZKURT [1*]

[1]Mekatronik Mühendisliği, Teknoloji Fakültesi, Pamukkale Üniversitesi, Denizli, Türkiye.
[1]aakpunar@pau.edu.tr

Geliş Tarihi: 13.1.2025
Kabul Tarihi: 02.11.2025

Düzeltme Tarihi:27.5.2025

doi: https://doi.org/10.62520/fujece.1619005
Araştırma Makalesi

Alıntı: A. A. Bozkurt, "Yüksek hassasiyetli uygulamalar için DC-DC buck dönüştürücünün otomatik ayarlamalı PID kontrolü" Fırat Üni. Deny. ve Hes. Müh. Derg., vol. 5, no 1, pp. 135-149, Şubat 2026.

Öz

DC-DC dönüştürücüler, motor sürücü sistemleri, yenilenebilir enerji kaynakları ve bilgisayar güç kaynakları gibi çok çeşitli uygulamalarda temel bileşenlerdir. Bu dönüştürücüler, değişken yük koşulları altında, regüle edilmemiş bir giriş geriliminden kararlı bir doğru akım (DC) çıkışı elde etmek amacıyla kullanılır. İstenen çıkış gerilimi seviyesine bağlı olarak çeşitli dönüştürücü topolojileri geliştirilmiştir. Bunlar arasında buck (alçaltıcı) dönüştürücü, giriş gerilimini verimli bir şekilde düşürebilme özelliği sayesinde en yaygın şekilde benimsenen çözümlerden biridir. Çıkış geriliminin belirlenmiş bir referans değere yakın tutulabilmesi için genellikle kapalı çevrimli çeşitli kontrol stratejileri uygulanmaktadır. Bu çalışma, DC-DC buck dönüştürücüsünün çıkış gerilimini hassas bir şekilde regüle etmek amacıyla, modele dayalı otomatik ayarlamalı bir Oransal–İntegral–Türevsel (PID) kontrol algoritmasının uygulanmasını sunmaktadır. Sabit kazanç parametreleriyle çalışan klasik PID denetleyiciler, sistem parametrelerindeki değişimlere ve dış bozuculara karşı sınırlı bir uyum kabiliyeti sergilerken; önerilen kontrolör, parametrelerini gerçek zamanlı olarak dinamik şekilde ayarlayarak değişen çalışma koşullarına daha iyi uyum sağlamaktadır. Bu uyarlanabilir yapı, sistemin değişken işletim koşulları altında dayanıklılığını artırmaktadır. Simülasyon sonuçları, önerilen yöntemin etkinliğini doğrulamakta; hızlı geçici tepki, minimum aşım ve yüksek kararlı durum kararlılığı sağladığını ortaya koymaktadır. Elde edilen bulgular, özellikle uyarlamalı ve yüksek hassasiyetli regülasyon gerektiren gömülü sistem uygulamaları için önerilen yaklaşımın pratik ve etkili bir kontrol çözümü sunduğunu göstermektedir.

Anahtar kelimeler: DC-DC Buck dönüştürücü, PID denetleyici, Doğrusal olmayan kontrol, Gerilim regülasyonu

[*]Yazışılan yazar

İntihal Kontrol: Evet – Turnitin
Şikayet: fujece@firat.edu.tr
Telif Hakkı ve Lisans: Dergide yayın yapan yazarlar, CC BY-NC 4.0 kapsamında lisanslanan çalışmalarının telif hakkını saklı tutar

Firat University Journal of Experimental and Computational Engineering

Auto-Tuning PID Control of a DC-DC Buck Converter for High-Precision Applications

Adile AKPUNAR BOZKURT [1*]

[1] Department of Mechatronics Engineering, Faculty of Technology, Pamukkale University, Denizli, Türkiye.
[1]aakpunar@pau.edu.tr

Received: 13.1.2025
Accepted:02.11.2025
Revision: 27.5.2025
doi: https://doi.org/10.62520/fujece.1619005
Research Article

Citation: A. A. Bozkurt, "Auto-tuning PID control of a DC-DC buck converter for high-precision applications" Firat Univ Jour. of Exp. and Comp. Eng., vol. 5, no 1, pp. 135-149, February 2026.

Abstract

DC-DC converters are essential components in a wide range of applications, including motor drive systems, renewable energy sources, and computer power supplies. These converters regulate an unregulated input voltage to provide a stable DC output under varying load conditions. Depending on the desired voltage level, several converter topologies have been developed. Among them, the buck converter stands out as one of the most widely adopted solutions due to its ability to step down the input voltage efficiently. To ensure that the output voltage remains close to a predefined reference value, various closed-loop control strategies are commonly employed. This study presents the implementation of a model-based, auto-tuning Proportional–Integral–Derivative (PID) control algorithm for precise output voltage regulation in a DC-DC buck converter. Unlike classical PID controllers, which operate with fixed gain parameters and exhibit limited adaptability to parameter variations and external disturbances, the proposed controller dynamically adjusts its parameters in real time. This adaptive capability enhances the system's robustness under varying operating conditions. Simulation results validate the effectiveness of the proposed method, demonstrating fast transient response, minimal overshoot, and high steady-state stability. These findings suggest that the approach offers a practical and efficient control solution, especially for embedded systems requiring adaptive and high-precision regulation.

Keywords: DC-DC Buck converter, PID controller, Nonlinear control, Voltage regulation

*Corresponging author

Plagiarism Checks: Yes – Turnitin
Complaints: fujece@firat.edu.tr
Copyright & License: Authors publishing with the journal retain the copyright to their work licensed under the CC BY-NC 4.0

1. Introduction

In recent years, power circuits have found a wide range of applications and gained great popularity [1]. Among these circuits, DC-DC converters stand out as one of the basic components in the power circuit family [2]. DC-DC converters, fundamental circuits in power electronics, operate by switching to modify electrical voltage levels and are increasingly utilized across various applications [3]. They provide an adjustable DC voltage from an unregulated source to a variable load.

By leveraging semiconductor switching elements, DC-DC converters serve as compact, lightweight, and highly efficient solutions for DC power conversion. Under normal operating conditions, they can respond quickly and appropriately to changes in input voltage and return to normal operation [4]. These converters are widely used in various applications such as televisions, battery chargers, receivers, computers, medical devices, communication equipment, and military hardware [5]. In industrial applications, buck converters are commonly employed to achieve the conversion of high DC input voltages into reduced DC output levels [6].

In [3], the use of DC/DC converters in mobile devices is examined, with a focus on the operation of the buck converter using a PID controller. In [7], a new multi-level DC-DC buck converter topology with clamped diodes for DC motors has been presented. In [8], Buck-type DC-DC converters are introduced as a solution for regulating both the charging voltage and current in battery charging systems for electric vehicles. In [9], a DC-DC buck converter has been used in the charge controllers of wind energy systems. In [10], a detailed performance evaluation of a synchronous buck converter implemented for a photovoltaic (PV) system was presented.

In terms of control of DC-DC converters, these systems, being switched power converters, present a challenging field of study due to their variable and nonlinear structure. Rapid structural changes are usually handled using averaging models. In [11, 12], a PWM-based sliding mode voltage-controlled (SMVC) buck converter design has been presented. In [13], a model predictive control (MPC) design was proposed for controlling a fixed-frequency DC-DC power converter.

An auto-tuning method based on the Modified Relay Feedback Test (MRFT) has been designed and implemented for PID voltage-mode control of DC–DC buck converters [14]. Similarly, a fuzzy extended model reference adaptive voltage regulation strategy was proposed to enhance robustness against random input fluctuations and load transients in DC–DC buck converters [15]. Another study examined the effectiveness of the Archimedes Optimization Algorithm (AOA) as a metaheuristic approach for tuning PID controllers in closed-loop DC–DC buck converters, achieving stable output voltage regulation [16]. Moreover, the design and implementation of a digital PID controller, specifically tailored for DC–DC buck converters, was carried out using MATLAB as the primary simulation and development platform [17].

DC-DC buck converters are widely used in various industrial and portable electronic systems that require either constant or variable voltage levels. To maintain stable output voltage regulation in such converters, PID controllers are commonly employed. However, variations in system parameters and the dynamic nature of load conditions often limit the effectiveness of fixed-gain PID controllers. In response to these limitations, PID control strategies incorporating auto-tuning mechanisms have gained increasing attention in recent years. In this study, a model-based auto-tuning PID control approach is proposed and implemented for a DC-DC buck converter to achieve both faster and more stable voltage regulation, while simultaneously enabling the system to adapt to time-varying dynamics. Unlike conventional fixed-parameter methods, the proposed structure continuously adjusts the controller gains in real-time, thereby optimizing system performance under changing conditions.

The control strategy is based on an auto-tuning PID method that is well-suited for the robust regulation of nonlinear systems, as discussed in [18, 19]. The entire control system is implemented in the MATLAB/Simulink environment. Simulation results demonstrate that the proposed controller regulates the output voltage more rapidly and effectively compared to conventional PID methods. Furthermore, key performance indicators such as transient response, overshoot, and stability are quantitatively evaluated to

highlight the advantages of the auto-tuning approach. The following sections provide a detailed presentation of the DC-DC buck converter model, the conventional PID control structure, the proposed auto-tuning PID strategy, and simulation-based performance comparisons.

2. Material and Method

2.1. Model of the DC-DC buck converter

The DC-DC buck converter circuit's design and analysis assume that the inductor current operates in continuous current mode (CCM), the output voltage is kept constant, and the circuit operates in a steady state [20]. Figure 1 shows the buck converter circuit.

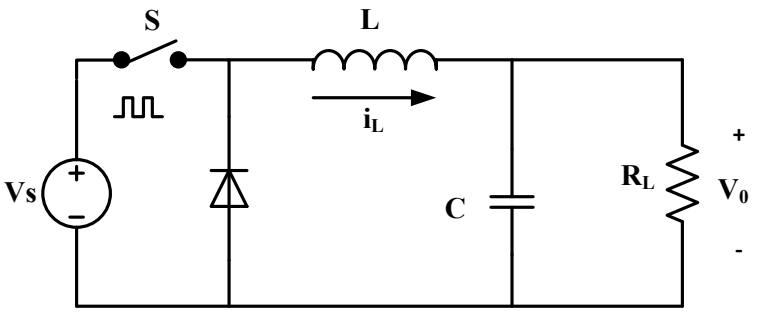


Figure 1. DC-DC Buck Converter circuit [20]

This circuit operates in two modes: the mode in which the switch is open and the mode in which the switch is closed. According to these operating modes, the mathematical equations of the buck converter are obtained. MOSFET, IGBT, or BJT can be used as the switch. The dynamic behavior of the DC-DC buck converter is defined according to each switching mode. Figure 2 shows the switch-off and switch-on states of the buck converter.

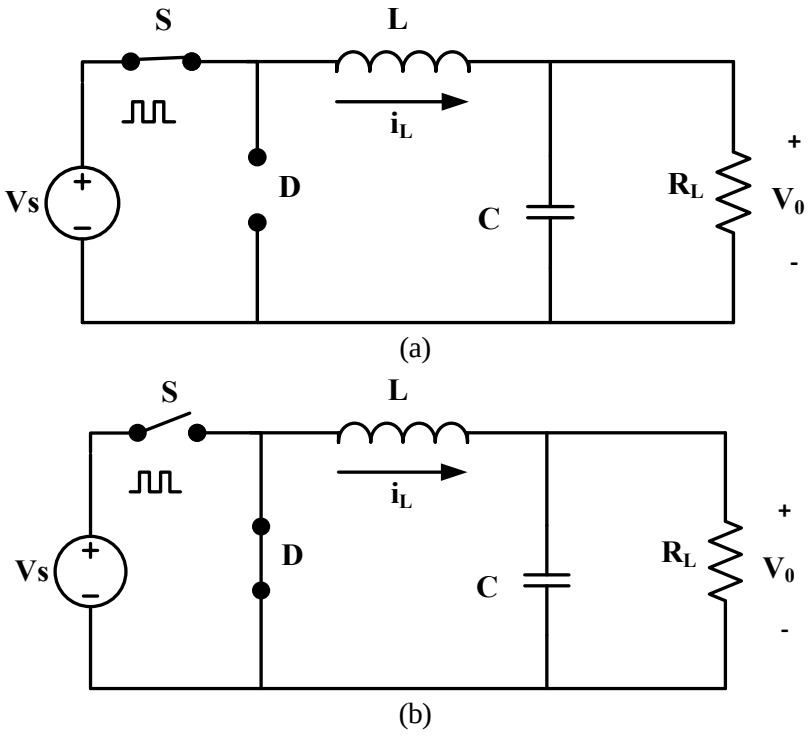


Figure 2. Switch states. (a) closed, (b) opened

As illustrated in Figure 2a, when the switch is in the closed position, the DC source supplies current to the inductor and load resistor, causing the diode to be reverse-biased. Thus, the dynamic equation can be expressed as:

$$V_s = L\frac{di_L}{dt} + V_c \quad (1)$$

$$i_L = C\frac{dV_c}{dt} + \frac{V_c}{R} \quad (2)$$

As shown in Figure 2b, opening the switch causes the diode to become forward-biased, directing the inductor current through the load resistor. Thus, the dynamic equation ([2], [21]) is expressed as:

$$0 = L\frac{di_L}{dt} + V_c \quad (3)$$

If the control signal u is defined as

$$u = \begin{cases} 1, & 0 \le t < t_{on} \\ 0, & t_{on} \le t \le T \end{cases}$$

The general equation describing the DC-DC buck converter can be written as

$$\frac{di_L}{dt} = -\frac{1}{L}V_c + \frac{V_s}{L}u \quad (4)$$

$$\frac{dV_c}{dt} = \frac{1}{C}i_L - \frac{1}{RC}V_c \quad (5)$$

In this context, i_L refers to the inductor current, while V_c corresponds to the capacitor voltage ([2], [21]). These are the state variables defining the Buck converter. The specifications of the DC-DC buck converter are listed in Table 1.

Table 1. Specifications of the DC-DC buck converter

Parameters	Symbol	Value
Input Voltage	V_s	20V
Output Voltage	V_0	12V
Load	R_L	2.5 Ω
Inductance	L	4mH
Capacitance	C	47uF

In DC-DC buck converters, the values of inductance and capacitance are selected based on the desired current ripple (ΔI_L) and voltage ripple (ΔV). In this study, ΔI_L is set to 48mA and ΔV to 5mV. These ripple levels are suitable for high-precision power applications.

The inductance required to ensure Continuous Conduction Mode (CCM) operation of the buck converter can be calculated using Equation 6, while the required capacitance value can be determined from Equation 7.

$$L = \frac{(V_{in} - V_{out}) \cdot D}{\Delta I_L \cdot F_S} \approx 4mH \quad (6)$$

$$C = \frac{(V_{in} - V_{out}) \cdot D}{8F_S^2 L \Delta V} \approx 47\mu F \quad (7)$$

Here, V_{in} is the input voltage, V_{out} is the output voltage, D is the duty cycle, and F_s is the switching frequency [22].

2.2. PID controller

PID controllers are among the most commonly used feedback control strategies, particularly for linear systems. The general structure of a classical PID controller is illustrated in Figure 3.

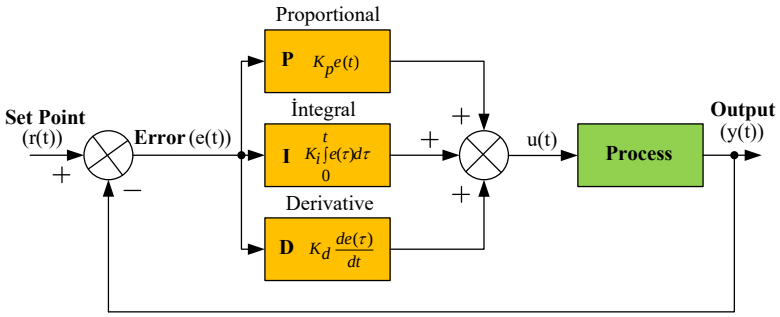


Figure 3. General structure of a PID controller [24]

The PID controller generates an error signal based on the difference between the reference signal r(t) and the output signal y(t), as given in Equation (8):

$$e(t) = r(t) - y(t) \tag{8}$$

The main objective of the controller is to minimize this error signal, thereby ensuring the system exhibits the desired behavior. The PID controller consists of a combination of proportional (P), integral (I), and derivative (D) terms. These three components form the control law expressed in Equation (9):

$$u(t) = K_p e(t) + K_i \int_0^t e(\tau)d\tau + K_d \frac{de(t)}{dt} \tag{9}$$

The proportional gain K_p provides an immediate response proportional to the error signal. However, when used alone, it cannot completely eliminate the steady-state error. The integral gain K_i eliminates steady-state error over time by accumulating the error, enabling the system to reach the reference value. Nonetheless, excessive integral gain may lead to overshoot and instability. The derivative gain K_d improves the transient response by predicting future error behavior, helping reduce overshoot and stabilize the system.

Proper tuning of PID parameters is critical for achieving desired system performance. Empirical methods such as Ziegler–Nichols and Cohen–Coon are frequently used for this purpose. The effects of PID gain variations on system response are summarized in Table 2 [23, 24].

Table 2. Effects of PID gains on system response

PID gain	***Steady state error***	***Setting time***	***Percent Overshoot***
Increasing Kp	Decreases	Slightly increasing	Increases
Increasing Ki	Eliminate	Increases	Increases
Increasing Kd	Slight Change	Decreases	Decreases

2.3. Auto-tuning PID

The DC-DC Buck converter plays a crucial role in maintaining efficient voltage regulation under varying operating conditions. An auto-tuning PID controller is implemented to achieve precise control, dynamically generating the control input signal, denoted as ***u***. This signal works to minimize the difference between the measured output voltage of the converter and the target reference voltage.

The structural configuration of the DC-DC Buck converter and the auto-tuning PID controller is illustrated in Figure 4. The controller continuously adjusts the system parameters to maintain optimal performance. The converter's switching frequency is set to 25 kHz, corresponding to a sampling period of 40 μs, ensuring real-time adaptability of the control mechanism.

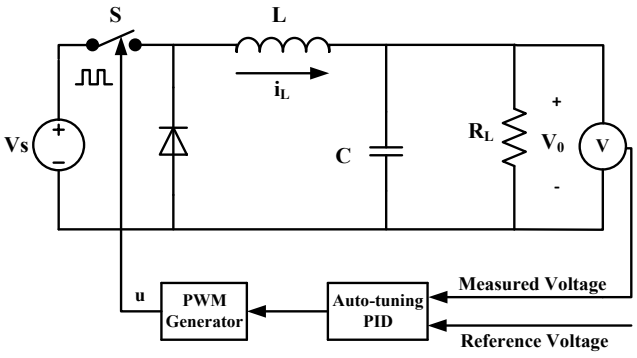


Figure 4. Configuration of the DC-DC buck converter and controller

The configuration of the proposed auto-tuning PID controller is shown in Figure 5. This model-based PID controller incorporates a discrete system model, two Jacobian blocks, and an adaptive PID block, each serving distinct purposes to ensure optimal performance. One Jacobian block refines the control signal, while the other facilitates parameter tuning. The adaptive PID block dynamically adjusts controller parameters to minimize the error signal.

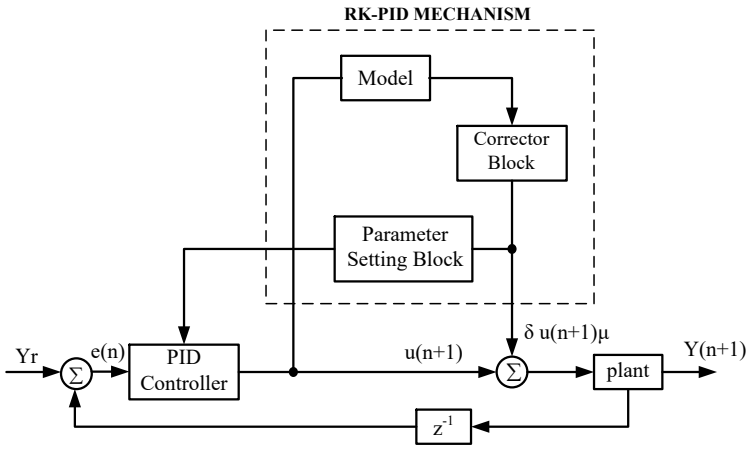


Figure 5. Auto-tuning PID controller structure ([18], [19])

In this configuration, $\mathbf{Y_r}$ represents the reference signal, **Y**(n+1) denotes the system output at the next time step, **u**(n+1) is the input control signal, and δ**u** is the correction term applied to improve the control signal. The error **e** is computed as the difference between the reference and measured output signals.

In the system model of the PID control mechanism, two Jacobian matrices are utilized to enhance system performance. The matrix $\mathbf{J_m}$ serves to verify and refine the control signal, while $\mathbf{J_c}$ dynamically adjusts the PID control parameters to ensure optimal system response. Within this framework, the reference signal and the candidate input voltage are applied as inputs to the model.

As outputs, the system generates a K-fold prediction of the output signal and a verification term, which collectively guide the adjustment process. In the PID block, the proportional ($\mathbf{K_P}$), integral ($\mathbf{K_I}$), and derivative ($\mathbf{K_D}$) parameters are computed and updated in real-time to adapt to changing system dynamics. Finally, the PID controller generates the control signal as defined in Equation 10 ([18, 19]).

$$\boldsymbol{u}(n+1) = \boldsymbol{u}(n) + \boldsymbol{K_p}(\boldsymbol{e}(n) - \boldsymbol{e}(n-1)) + \boldsymbol{K_I}\boldsymbol{e}(n) + \boldsymbol{K_D}(\boldsymbol{e}(n) - 2\boldsymbol{e}(n-1) + \boldsymbol{e}(n-2)) \tag{10}$$

The generated input signal $\boldsymbol{u}(n+1)$ is fed to the system model K times. The PID parameters are determined by the objective function that minimizes the sum of squares of the prediction errors after K steps.

$$F(\boldsymbol{u}(n+1)) = \frac{1}{2}\sum_{k=1}^{K}\sum_{j=1}^{Q}(\tilde{y}_j(n+k) - \hat{y}_j(n+k))^2 \; + \frac{1}{2}\lambda\sum_{r=1}^{R}(u_r(n+1) - u_r(n))^2 \tag{11}$$

In this equation, k represents the estimation horizon, and λ represents the penalty parameter.

The Levenberg-Marquardt method is employed to minimize the objective function and concurrently update the PID parameters.

$$\begin{bmatrix} \boldsymbol{K_P^{new}} \\ \boldsymbol{K_I^{new}} \\ \boldsymbol{K_D^{new}} \end{bmatrix} = \begin{bmatrix} \boldsymbol{K_P^{old}} \\ \boldsymbol{K_I^{old}} \\ \boldsymbol{K_D^{old}} \end{bmatrix} - (\boldsymbol{J^T J} + \boldsymbol{\mu I})^{-1}\boldsymbol{J^T}\hat{\boldsymbol{e}} \tag{12}$$

In this context, μ serves as a compromise between the Steepest-Descent and Gauss-Newton algorithms, while I represents the identity matrix. The Jacobian matrix is defined in Equations 13 and 14 ([18], [19]).

$$\mathbf{J} = \begin{bmatrix} \frac{\partial \hat{e}_1(n+1)}{\partial \boldsymbol{K_P}} & \frac{\partial \hat{e}_1(n+1)}{\partial \boldsymbol{K_I}} & \frac{\partial \hat{e}_1(n+1)}{\partial \boldsymbol{K_D}} \\ \vdots & \vdots & \vdots \\ \frac{\partial \hat{e}_Q(n+K)}{\partial \boldsymbol{K_P}} & \frac{\partial \hat{e}_Q(n+K)}{\partial \boldsymbol{K_I}} & \frac{\partial \hat{e}_Q(n+K)}{\partial \boldsymbol{K_D}} \\ \frac{\partial \sqrt{\lambda_1}\Delta\boldsymbol{u}(n+1)}{\partial \boldsymbol{K_P}} & \frac{\partial \sqrt{\lambda_1}\Delta\boldsymbol{u}(n+1)}{\partial \boldsymbol{K_I}} & \frac{\partial \sqrt{\lambda_1}\Delta\boldsymbol{u}(n+1)}{\partial \boldsymbol{K_D}} \\ \vdots & \vdots & \vdots \\ \frac{\partial \sqrt{\lambda_R}\Delta\boldsymbol{u}(n+1)}{\partial \boldsymbol{K_P}} & \frac{\partial \sqrt{\lambda_R}\Delta\boldsymbol{u}(n+1)}{\partial \boldsymbol{K_I}} & \frac{\partial \sqrt{\lambda_R}\Delta\boldsymbol{u}(n+1)}{\partial \boldsymbol{K_D}} \end{bmatrix} \tag{13}$$

$$\mathbf{J} = -\begin{bmatrix} \frac{\partial \hat{y}_1(n+1)}{\partial \boldsymbol{K_P}} & \frac{\partial \hat{y}_1(n+1)}{\partial \boldsymbol{K_I}} & \frac{\partial \hat{y}_1(n+1)}{\partial \boldsymbol{K_D}} \\ \vdots & \vdots & \vdots \\ \frac{\partial \hat{y}_Q(n+K)}{\partial \boldsymbol{K_P}} & \frac{\partial \hat{y}_Q(n+K)}{\partial \boldsymbol{K_I}} & \frac{\partial \hat{y}_Q(n+K)}{\partial \boldsymbol{K_D}} \\ \frac{\partial \sqrt{\lambda_1}\Delta\boldsymbol{u}(n+1)}{\partial \boldsymbol{K_P}} & \frac{\partial \sqrt{\lambda_1}\Delta\boldsymbol{u}(n+1)}{\partial \boldsymbol{K_I}} & \frac{\partial \sqrt{\lambda_1}\Delta\boldsymbol{u}(n+1)}{\partial \boldsymbol{K_D}} \\ \vdots & \vdots & \vdots \\ \frac{\partial \sqrt{\lambda_R}\Delta\boldsymbol{u}(n+1)}{\partial \boldsymbol{K_P}} & \frac{\partial \sqrt{\lambda_R}\Delta\boldsymbol{u}(n+1)}{\partial \boldsymbol{K_I}} & \frac{\partial \sqrt{\lambda_R}\Delta\boldsymbol{u}(n+1)}{\partial \boldsymbol{K_D}} \end{bmatrix} \tag{14}$$

In Equation 15, the vector of forecast errors eˆ is given.

$$\hat{\boldsymbol{e}} = \begin{bmatrix} \hat{e}_1(n+1) \\ \vdots \\ \hat{e}_Q(n+K) \\ \sqrt{\lambda_1}\Delta\boldsymbol{u}(n+1) \\ \vdots \\ \sqrt{\lambda_R}\Delta\boldsymbol{u}(n+1) \end{bmatrix} = \begin{bmatrix} \tilde{y}_1(n+1) - \hat{y}_1(n+1) \\ \vdots \\ \tilde{y}_1(n+K) - \hat{y}_1(n+K) \\ \sqrt{\lambda_1}\Delta\boldsymbol{u}(n+1) \\ \vdots \\ \sqrt{\lambda_R}\Delta\boldsymbol{u}(n+1) \end{bmatrix} \tag{15}$$

Here, $\Delta\boldsymbol{u}(n+1)$is defined as

$$\Delta\boldsymbol{u}(n+1) = \boldsymbol{u}(n+1) - \boldsymbol{u}(n) \tag{16}$$

At this stage, the PID parameters are updated step by step. The correction block is designed to minimize the objective function by applying the quadratic Taylor approximation ([18, 19]).

$$F\big(\boldsymbol{u}(n+1)+\delta\boldsymbol{u}(n+1)\big) \cong F\big(\boldsymbol{u}(n+1)\big)+\frac{\partial F\big(\boldsymbol{u}(n+1)\big)}{\partial \boldsymbol{u}(n+1)}\delta\boldsymbol{u}(n+1) + \frac{1}{2}\frac{F\partial^2(\boldsymbol{u}(n+1))}{\partial \boldsymbol{u}^2(n+1)}(\delta\boldsymbol{u}(n+1))^2 \tag{17}$$

If the derivative of the objective function with respect to the $\delta\boldsymbol{u}(n+1)$ term is taken and set equal to zero,

$$\delta\boldsymbol{u}(n+1) = -\frac{\partial F/\partial \boldsymbol{u}(n+1)}{\partial^2 F/\partial \boldsymbol{u}^2(n+1)} \tag{18}$$

is obtained. Here, Jacobian approximations can be used instead of derivatives in Equation 18, as shown in the Jacobian formulation given by Equation 19 ([18, 19]).

$$\boldsymbol{J_m} = -\begin{bmatrix} \frac{\partial \hat{y}_1(n+1)}{\partial u_1(n+1)} & \frac{\partial \hat{y}_1(n+1)}{\partial u_2(n+1)} & \cdots & \frac{\partial \hat{y}_1(n+1)}{\partial u_R(n+1)} \\ & & \vdots & \\ \frac{\partial \hat{y}_Q(n+1)}{\partial u_1(n+1)} & \frac{\partial \hat{y}_Q(n+1)}{\partial u_2(n+1)} & \cdots & \frac{\partial \hat{y}_Q(n+1)}{\partial u_R(n+1)} \\ \sqrt{\lambda_1} & \sqrt{\lambda_1} & \cdots & \sqrt{\lambda_1} \\ & & \vdots & \\ \sqrt{\lambda_R} & \sqrt{\lambda_R} & \cdots & \sqrt{\lambda_R} \end{bmatrix} \tag{19}$$

Verification term is calculated from the Equation 20.

$$\delta\boldsymbol{u}(n+1) = -\frac{\boldsymbol{J}_m^T\hat{\boldsymbol{e}}}{\boldsymbol{J}_m^T\boldsymbol{J}_m} \tag{20}$$

The Jacobian matrix in Equation 14 can be written as $\mathbf{J} = \mathbf{J_m} \cdot \mathbf{J_c}$.

$$\boldsymbol{J} = -\begin{bmatrix} \frac{\partial \hat{y}_1(n+1)}{\partial u_1(n+1)} & \frac{\partial \hat{y}_1(n+1)}{\partial u_2(n+1)} & \cdots & \frac{\partial \hat{y}_1(n+1)}{\partial u_R(n+1)} \\ & & \vdots & \\ \frac{\partial \hat{y}_Q(n+1)}{\partial u_1(n+1)} & \frac{\partial \hat{y}_Q(n+1)}{\partial u_2(n+1)} & \cdots & \frac{\partial \hat{y}_Q(n+1)}{\partial u_R(n+1)} \\ \sqrt{\lambda_1} & \sqrt{\lambda_1} & \cdots & \sqrt{\lambda_1} \\ & & \vdots & \\ \sqrt{\lambda_R} & \sqrt{\lambda_R} & \cdots & \sqrt{\lambda_R} \end{bmatrix} \begin{bmatrix} \frac{\partial u_1(n+1)}{\partial K_{P_{11}}} & \cdots & \frac{\partial u_1(n+1)}{\partial K_{D_{RQ}}} \\ & \vdots & \\ \frac{\partial u_R(n+1)}{\partial K_{P_{11}}} & \cdots & \frac{\partial u_R(n+1)}{\partial K_{D_{RQ}}} \end{bmatrix} \tag{21}$$

$\mathbf{K_P}$, $\mathbf{K_I}$, and $\mathbf{K_D}$ parameter values are adjusted in the PID block at each iteration ([18], [19]).
To implement the proposed control strategy, the auto-tuning PID algorithm is designed as shown below.
Input: Measured system outputs **y**(n), reference signal $\mathbf{y_r}$(n), previous control input **u**(n)
Output: Updated control input $\boldsymbol{u}(n+1)$, and updated PID parameters ($\mathbf{K_P}$, $\mathbf{K_I}$, $\mathbf{K_D}$)

1. Measure the system output **y**(n)
2. Compute the tracking error: **e**(n) = $\mathbf{y_r}$(n) − **y**(n)
3. Calculate the initial control input: $\boldsymbol{u}(n+1)$
4. Predict future outputs: $[\hat{y}_1(n+1), \ldots, \hat{y}_Q(n+K)]$
5. Compute the Jacobian matrices:
   - $\mathbf{J_m}$ for verifying the control signal
   - $\mathbf{J_c}$ for tuning the PID control parameters
6. Compute the control correction term: $\delta\boldsymbol{u}(n+1)$
7. Update PID parameters ($\mathbf{K_P}$, $\mathbf{K_I}$, $\mathbf{K_D}$) based on adaptation criteria
8. Update the control input signal: $\boldsymbol{u}(n+1) = \boldsymbol{u}(n+1) + \delta\boldsymbol{u}(n+1)$

9. Apply $\boldsymbol{u}(n+1)$to the system

3. Simulation Results and Discussion

The study was conducted using the MATLAB/Simulink environment, where both the auto-tuning PID controller and the conventional PID controller were implemented and compared. In Figure 6, the output voltage of the DC-DC buck converter is depicted, with the system configured to operate at a constant reference voltage of 12 V. The auto-tuning PID controller reaches the desired output voltage in under 0.004 s, whereas the conventional PID controller takes 0.08 s to achieve the desired output voltage. No overshoot is observed in either controller during the transient phase.

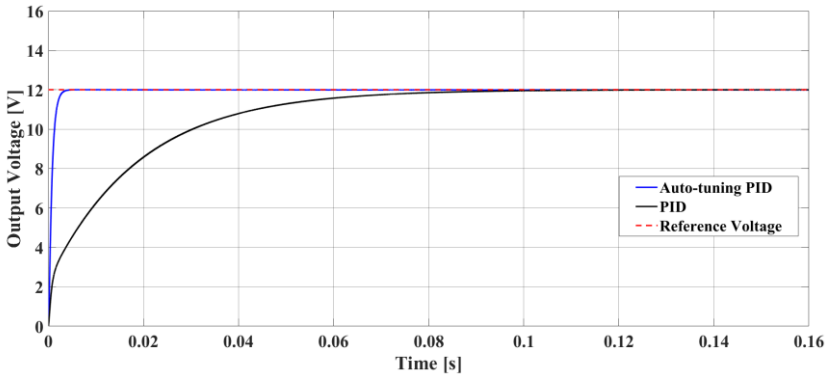


Figure 6. Output voltage waveform

Table 3 presents a comparative analysis of the transient response of the output voltage of the DC-DC buck converter.

Table 3. Comparison of the transient response of the DC-DC buck converter output voltage.

Methods	***Auto-tuning PID***	***PID***
Setting time (s)	0.004	0.08
Rise time (s)	0.002	0.06
Overshoot (V)	0	0
Steady state voltage ripple (V)	0.05	0.06

Figure 7 illustrates the output voltage profiles of the DC–DC buck converter under varying operating points. In this experiment, a step reference voltage was applied to evaluate the performance of the control mechanisms. Initially, the converter operated at 12 V, after which the reference voltage was decreased to 10 V at t = 0.2 s. Subsequently, at t = 0.4 s, the reference was restored to 12 V, and the converter continued its operation accordingly. Both the auto-tuning PID controller and the conventional PID controller successfully regulated the output voltage to track the desired reference without observable overshoot.

However, the auto-tuning PID controller demonstrated superior dynamic performance, achieving the desired reference voltage with a significantly shorter settling time compared to the conventional PID controller. This highlights the adaptive controller's ability to respond more efficiently to changes in operating conditions.

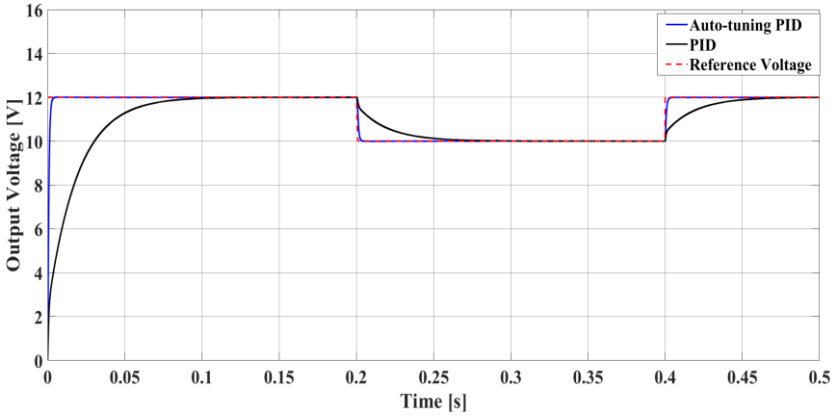


Figure 7. Waveform at different output voltage levels

Figure 8 illustrates the variation in the duty cycle values of the auto-tuning PID controller implemented for the DC–DC buck converter. The duty cycle (D) is calculated using the standard formula $D=V_o/V_i$, where V_o represents the output voltage and V_i denotes the input voltage. For this study, the input voltage is taken as V_i=20 V. The duty cycle response to the step reference of the output voltage is also presented. When the output voltage is regulated at 12 V (for $t < 0.2$ s), the corresponding duty cycle is approximately 0.6. In the interval between 0.2 s and 0.4 s, the output voltage is reduced to 10 V, and the duty cycle accordingly decreases to 0.5.

The duty cycle is dynamically adjusted to achieve the desired output voltage. This highlights the controller's ability to maintain steady-state performance under varying operating conditions. Variations observed in the duty cycle demonstrate the efficiency of the auto-tuning mechanism for minimizing voltage regulation errors.

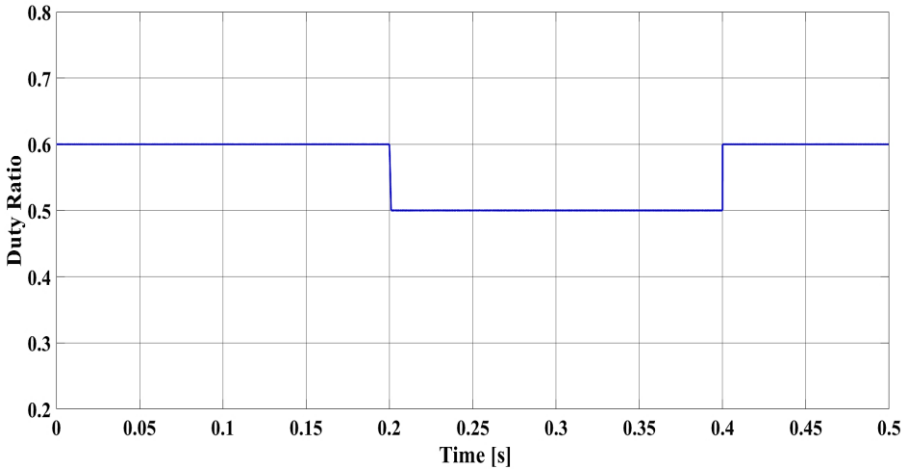


Figure 8. Duty ratio at different output voltage levels

Finally, the response of the DC–DC buck converter and the corresponding duty ratio under an exponential reference voltage change is analyzed using the auto-tuning PID controller. The converter reaches the desired reference output voltage in approximately 0.15 s, demonstrating fast transient performance. The results confirm that the proposed controller is capable of tracking the reference voltage quickly and stably. Figure 9 illustrates the output voltage waveform under exponential reference change, while Figure 10 shows the variation of the duty ratio under the same conditions. Consistently, when the reference output voltage reaches 12 V, the duty cycle converges to approximately 0.6, as determined by the relation $D=V_o/V_i$.

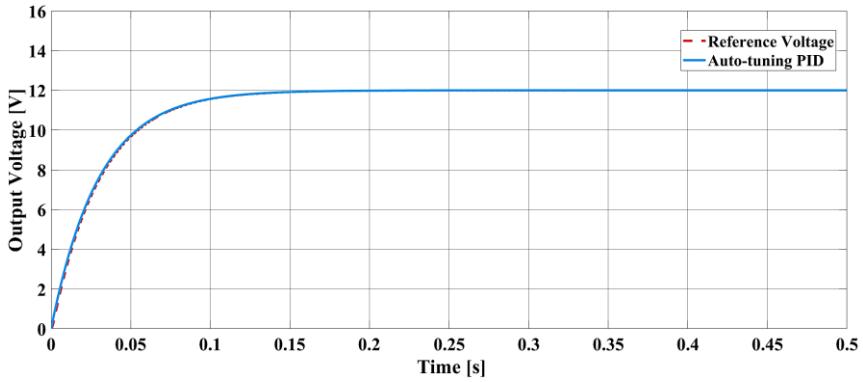


Figure 9. Waveform at exponential output voltage level

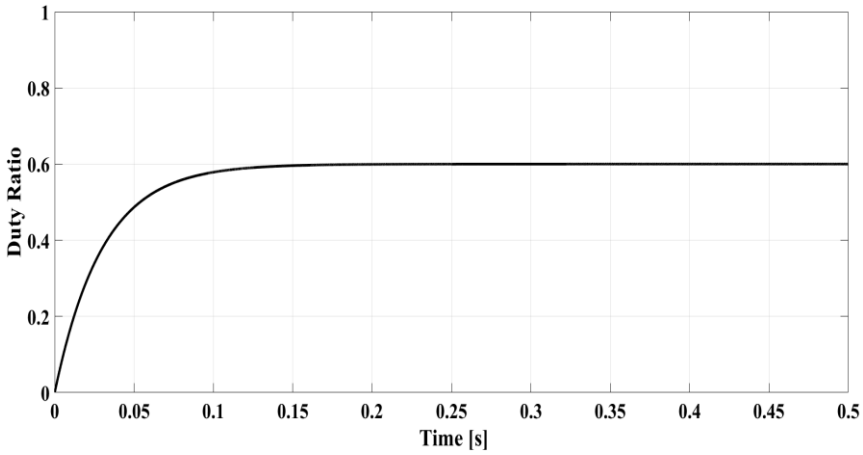


Figure 10. Duty ratio at exponential output voltage levels

The simulation results demonstrate that the proposed controller is not only responsive but also stable under different operating conditions. Fast response time and reduced overshoot emerge as key performance indicators of a well-tuned PID controller. The investigation of different load conditions further highlights the importance of adaptive control strategies in power electronics, particularly in applications that require precise voltage regulation. In this study, a comparison with the conventional PID controller was carried out by evaluating the transient responses of the DC–DC buck converter output voltages. The results reveal that the auto-tuning PID controller reaches the desired output voltage faster and without overshoot compared to the conventional PID controller.

A major advantage of the auto-tuning PID controller is its ability to automatically adjust parameters in real time, eliminating the need for manual gain tuning as in conventional PID controllers. This feature significantly reduces design effort and provides time savings. Furthermore, it adapts rapidly to changes in operating conditions, thereby minimizing overshoots, shortening rise time, and delivering a more stable transient response. Its straightforward applicability to different buck converter circuits and robustness under varying operating points further underlines the potential of the proposed method. Nevertheless, some limitations should be noted. The auto-tuning PID algorithm may require additional computational resources and memory on microcontrollers. Moreover, its performance may vary depending on circuit parameters, and uniform results across different converters cannot always be guaranteed.

The proposed controller shows strong potential for industrial applications such as renewable energy systems (solar and wind energy–based applications), battery management systems, and DC–DC converters in electric vehicles. Future work will focus on developing an experimental prototype of the DC–DC buck converter and implementing the auto-tuning PID controller in real time on high-speed platforms such as FPGAs and DSPs.

4. Conclusion

This study presented a model-based auto-tuning PID control strategy for regulating the output voltage of a DC-DC Buck converter, a widely used component in power electronics and renewable energy systems. The proposed controller was implemented in the MATLAB/Simulink environment and compared with a conventional fixed-parameter PID controller to evaluate its performance under both constant and dynamic operating conditions.

The simulation results clearly indicate that the auto-tuning PID controller significantly enhances system performance. Specifically, it achieves a faster transient response, reduced overshoot, and lower output voltage ripple when compared to conventional PID controllers. By adjusting its parameters in real time, the controller demonstrates robust adaptability to variations in system dynamics. This adaptive tuning mechanism effectively minimizes steady-state error and improves overall system stability, eliminating the need for manual retuning.

Additionally, the auto-tuning mechanism effectively shortens the time required to reach the desired reference voltage, especially during the initial transient period, while also reducing oscillations in the output voltage. These improvements are particularly valuable for precision power applications where rapid and accurate voltage regulation is essential.

In conclusion, the proposed auto-tuning PID control method offers a flexible and high-performance alternative to traditional fixed-gain PID controllers. Its ability to dynamically adapt to varying conditions makes it a promising solution for improving the efficiency and reliability of DC-DC Buck converters in real-world applications.

5. Author Contribution Statement

The author was responsible for the conceptualization and design of the study, conducting the literature review, analyzing the results obtained, acquiring and processing the data, and interpreting the findings. Additionally, the author reviewed the manuscript for both content and grammatical accuracy, ensuring its final form was ready for submission.

6. Ethics Committee Approval and Conflict of Interest Declaration

The author confirms that there are no conflicts of interest or personal relationships that could have influenced the results presented in this paper. Additionally, no external funding was received for this research. The data supporting the conclusions of this study can be provided upon request from the corresponding author. However, due to privacy and ethical considerations, the data cannot be made publicly available.

7. Ethical Statement Regarding the Use of Artificial Intelligence

No artificial intelligence-based tools or applications were used in the preparation of this study. The entire content of the study was produced by the author in accordance with scientific research methods and academic ethical principles.

8. References

[1] A. Boutaghlaline, E. K. Khadiri, and A. Tahiri, "An op-amp-based PID control of DC-DC buck converter for automotive applications," WSEAS Trans. Syst. Control, vol. 18, 2023.
[2] K. Gaouzi, H. El Fadil, A. Rachid, F. Z. Belhaj, and F. Giri, "Constrained model predictive control for DC-DC buck power converters," in Proc. Int. Conf. Electr. Inf. Technol. (ICEIT), 2017, pp. 1–5.
[3] K. Bendaoud, S. Krit, J. Laassiri, and L. E. Maimouni, "Modelling and simulation of DC-DC power converter buck for mobile applications using MATLAB/Simulink," Int. J. Intell. Enterprise, vol. 4, no. 1/2, pp. 76–87, 2017.
[4] M. Gupta and S. P. Phulambrikar, "Design and analysis of buck converter," Int. J. Eng. Res. Technol., vol. 3, no. 3, pp. 2346–2350, 2014.
[5] K. Sharma and D. K. Palwalia, "Design of digital PID controller for voltage mode control of DC-DC converters," in Proc. Int. Conf. Microelectron. Devices Circuits Syst. (ICMDCS), 2017, pp. 1–6.
[6] N. B. M. Posdzi and R. B. A. Ran, "Design buck converter with variable switching frequency by using MATLAB Simulink simulation," Int. J. Technol. Innov. Humanities, vol. 1, no. 1, pp. 1–6, 2020.
[7] A. A. A. Ismail and A. Elnady, "Advanced drive system for DC motor using multilevel DC/DC buck converter circuit," IEEE Access, vol. 7, pp. 54167–54178, 2019.
[8] S. Kamat and S. Jadhav, "Design and simulation of low-power charging station for electric vehicles," in Proc. Int. Conf. Adv. Comput. Commun. Control (ICAC3), 2019, pp. 1–4.
[9] A. A. Patil, D. S. Chavan, and S. V. Yadav, "Output voltage control scheme for standalone wind energy system," in Proc. Int. Conf. Comput. Power Energy Inf. Commun. (ICCPEIC), 2016, pp. 534–541.
[10] K. Pal and M. Pattnaik, "Performance of a synchronous buck converter for a standalone PV system: An experimental study," in Proc. IEEE 1st Int. Conf. Energy Syst. Inf. Process. (ICESIP), 2019, pp. 1–6.
[11] H. El Fadil, F. Giri, F.-Z. Chaoui, and O. El Magueri, "Accounting for input limitation in the control of buck power converters," IEEE Trans. Circuits Syst. I, vol. 56, no. 6, pp. 1260–1271, 2009.
[12] S. C. Tan, Y. M. Lai, M. K. H. Cheung, and C. K. Tse, "A pulse-width-modulation based sliding mode controller for buck converters," in Proc. IEEE 35th Annu. Power Electron. Spec. Conf., vol. 5, 2004, pp. 3647–3653.
[13] C. Vlad, P. Rodriguez-Ayerbe, E. Godoy, and P. Lefranc, "Explicit model predictive control of buck converter," in Proc. 15th Int. Power Electron. Motion Control Conf. (EPE/PEMC), 2012.
[14] S. Yan, A. R. Beig, and I. Boiko, "Auto-tuning of DC-DC buck converters through the modified relay feedback test," IEEE Access, vol. 9, pp. 62505–62518, 2021.
[15] O. Saleem, K. R. Ahmad, and J. Iqbal, "Fuzzy-augmented model reference adaptive PID control law design for robust voltage regulation in DC–DC buck converters," Mathematics, vol. 12, p. 1893, 2024.
[16] L. Fong, M. Islam, and M. Ahmad, "Optimized PID controller of DC-DC buck converter based on Archimedes optimization algorithm," Int. J. Robot. Control Syst., vol. 3, no. 4, pp. 658–672, 2023.
[17] H. A. Syahidah, A. J. Pangestu, M. S. Al Farisi, R. Ferdiansyah, R. N. Warnata, M. Zulfikar, and M. A. Rizqulloh, "Design and implementation of a digital PID controller for DC–DC buck converter with MATLAB," J. Mechatronics Artif. Intell., vol. 2, no. 2, pp. 1–20, 2025.
[18] S. Iplikci, "A comparative study on a novel model-based PID tuning and control mechanism for nonlinear systems," Int. J. Robust Nonlinear Control, vol. 20, no. 13, pp. 1483–1501, 2010.
[19] M. Cetin and S. Iplikci, "A novel auto-tuning PID control mechanism for nonlinear systems," ISA Trans., vol. 58, pp. 292–308, 2015.
[20] M. H. Rashid, Power Electron. Handbook, 4th ed. Oxford, U.K.: Academic Press, 2017.
[21] J. Pathan, "Model predictive control of DC-DC buck converter and its comparison with PID controller," Int. J. Adv. Res. Eng. Technol., vol. 11, no. 9, pp. 362–367, 2020. [Online]. Available: https://ssrn.com/abstract=3713708

[22] R. Sampath, “Digital peak current mode control of buck converter using MC56F8257 DSC,” Appl. Note AN4716, Rev. 1, Freescale Semiconductor, 2013.
[23] S. Satpathy, S. Ghosh, S. Das, S. Debbarma, and B. K. Bhattacharyya, “Study of dynamic response of DC-DC buck converter based on PID controller,” Int. J. Comput. Intell. IoT, vol. 2, no. 4, 2018. [Online]. Available: https://ssrn.com/abstract=3361548
[24] R. K. Sharma, “PI controller design for DC buck converter connected to a PV cell,” Master’s thesis, Lovely Professional University, 2015.

Fırat Üniversitesi Deneysel ve Hesaplamalı Mühendislik Dergisi

FUJECE

Elektrik İletim Hatlarında Arıza Tespiti: Topluluk Makine Öğrenmesi ve Evrişimsel Sinir Ağı Yöntemlerinin Karşılaştırmalı Analizi

Emrah ASLAN[1]*, Yıldırım ÖZÜPAK[2]

[1]Bilgisayar Mühendisliği Bölümü, Mühendislik Mimarlık Fakültesi, Mardin Artuklu Üniversite, Mardin, Türkiye.
[2]Elektrik ve Enerji Bölümü, Silvan Meslek Yüksekokulu, Dicle Üniversite, Diyarbakır, Türkiye.
[1]emrahaslan@artuklu.edu.tr, [2]yildirim.ozupak@dicle.edu.tr

Geliş Tarihi: 8.11.2024
Kabul Tarihi: 4.11.2025

Düzeltme Tarihi:17.3.2025

doi: https://doi.org/10.62520/fujece.1581543
Araştırma Makalesi

Alıntı: E. Aslan ve Y. Özüpak, "Elektrik iletim hatlarında arıza tespiti: topluluk makine öğrenmesi ve evrişimsel sinir ağı yöntemlerinin karşılaştırmalı analizi" Fırat Üni. Deny. ve Hes. Müh. Derg., vol. 5, no 1, pp. 150-168, Şubat 2026.

Öz

Elektrik güç sistemlerinde artan yük talebini karşılamak amacıyla iletim hatlarının sayısı artarken, buna paralel olarak arıza sayıları da çoğalmaktadır. Dış çevresel etkenlerden kaynaklanan arızalar bu hatlar için ciddi tehdit oluşturabilir ve sistemin zarar görmesine neden olabilir. Bu nedenle, iletim hatlarında oluşan arızaların hızlı ve doğru bir şekilde tespit edilmesi hayati önem taşır. Bu çalışmada, iletim hatlarındaki arızaları belirlemek amacıyla yapay sinir ağı tabanlı bir model geliştirilmiştir. Öncelikle, arıza tespiti için Bagging, AdaBoost ve Gradient Boosting Sınıflandırıcı gibi çeşitli makine öğrenme algoritmaları kullanılmış ve tüm modeller eğitim ve test süreçlerinden geçirilmiştir. Test sonuçlarına göre, Gradient Boosting Sınıflandırıcı algoritması en yüksek başarıyı göstermiştir. Ancak, daha yüksek doğruluğa ulaşmak amacıyla, çalışma kapsamında derin öğrenme tabanlı bir model olan Evrişimsel Sinir Ağı önerilmiştir. Önerilen model ile %99,73 doğruluk oranı elde edilerek makine öğrenme algoritmalarından daha iyi bir başarı sağlamıştır. Bu sonuçlar, yapay sinir ağı tabanlı modelin iletim hattı arızalarını etkili bir şekilde tespit ederek güç sistemlerinin güvenilirliğini ve sürekliliğini sağlamada önemli bir rol oynadığını göstermektedir.

Anahtar kelimeler: Derin öğrenme, Arıza tespiti, İletim hattı, Makine öğrenmesi, Güç sistemleri

*Yazışılan yazar

İntihal Kontrol: Evet – Turnitin
Şikayet: fujece@firat.edu.tr
Telif Hakkı ve Lisans: Dergide yayın yapan yazarlar, CC BY-NC 4.0 kapsamında lisanslanan çalışmalarının telif hakkını saklı tutar.

Firat University Journal of Experimental and Computational Engineering

Fault Detection in Electricity Transmission Lines: A Comparative Analysis of Ensemble Machine Learning and Convolutional Neural Network Methods

Emrah ASLAN[1]*, Yıldırım OZUPAK[2]

[1]Department of Computer Engineering, Faculty of Engineering and Architecture, Mardin Artuklu University, Mardin, Türkiye.
[2]Department of Electricity and Energy, Silvan Vocational School, Dicle University, Diyarbakır, Türkiye.
[1]emrahaslan@artuklu.edu.tr, [2]yildirim.ozupak@dicle.edu.tr

Received: 8.11.2024
Accepted: 4.11.2025
Revision: 17.3.2025
doi: https://doi.org/10.62520/fujece.1581543
Research Article

Citation: E. Aslan and Y. Özüpak, "Fault detection in electricity transmission lines: a comparative analysis of ensemble machine learning and convolutional neural network methods" Firat Univ Jour. of Exp. and Comp. Eng., vol. 5, no 1, pp. 150-168, Fabruary 2026.

Abstract

As the number of transmission lines increases to meet the increasing load demand in electric power systems, the number of faults increases in parallel. Faults caused by external environmental factors can pose a serious threat to these lines and cause damage to the system. Therefore, fast and accurate detection of faults in transmission lines is of vital importance. In this study, an artificial neural network-based model is developed to detect faults in transmission lines. Firstly, various machine learning algorithms such as Bagging, AdaBoost and Gradient Boosting Classifier are used for fault detection and all models are put through training and testing processes. According to the test results, the Gradient Boosting Classifier algorithm showed the highest success. However, in order to achieve higher accuracy, a Convolutional Neural Network (CNN), a deep learning-based model, was proposed in this study. The proposed model achieved an accuracy rate of 99.73%, which is better than that of the machine learning algorithms. These results demonstrate that the neural network-based model plays an important role in ensuring the reliability and continuity of power systems by effectively detecting transmission line faults.

Keywords: Deep learning, Fault detection, Transmission line, Machine learning, Power systems

*Corresponging author

Plagiarism Checks: Yes – Turnitin
Complaints: fujece@firat.edu.tr
Copyright & License: Authors publishing with the journal retain the copyright to their work licensed under the CC BY-NC 4.0

1. Introduction

Electric power systems are continuously expanding to meet the increasing demand for electricity, which increases the complexity of the system and increases the failure rates. Transmission line failures in power systems pose serious threats to the continuous and reliable operation of the system [1]. Factors such as various environmental conditions, weather, equipment aging and unexpected events lead to transmission line failures. This leads to interruption of energy flow and damage to system components. Therefore, fast and accurate detection of transmission line faults is very important for both energy security and reducing economic losses. In this context, the development of reliable and effective solution methods for the detection of transmission line faults has become critical for the energy sector.

Transmission line faults are generally analyzed in two main groups as series and shunt faults. Shunt faults are divided into symmetrical and asymmetrical faults. Single line-to-ground (A-G, B-G, C-G), line-to-line (AB, BC, CA), and double line-to-ground (AB-G, BC-G, CA-G) are examples of asymmetrical faults, whereas triple line faults (ABC) and triple line-to-ground faults (ABC-G) are examples of symmetrical faults. In power systems, the detection and classification of these different types of faults are important for maintaining the stability of the system [2]. Conventional methods are inadequate in the face of increasing system complexity and are ineffective when fast and highly accurate fault detection is required.

Accordingly, in recent years, Machine Learning (ML) and Deep Learning (DL)–based methods have played an important role in fault detection and classification processes. Although DL is a subcategory of ML methods, it is treated as a separate heading in this study due to its widespread use in the literature; this distinction is explicitly made to maintain conceptual integrity. Among ML methods, algorithms such as Bagging Classifier, AdaBoost and Gradient Boosting have attracted attention due to their high accuracy rates, fast processing capacities and their ability to work effectively with large data sets [3]. However, deep learning methods with more layers are becoming increasingly important in processing large and complex data such as electric power systems. Among deep learning models, especially Convolutional Neural Network (CNN) offers a suitable solution for the detection and classification of transmission line faults due to its superior performance in big data and image analysis [4].

In this study, the "Electrical Fault Detection and Classification" dataset available on the Kaggle platform is used for fast, reliable and accurate detection of transmission line faults in electric power systems [5]. This dataset is an important source of information for training fault detection models by providing a large sample detailing various fault types and conditions that occur in the system. The main motivation of the study is to develop an efficient model for classifying different types of faults in transmission lines with high accuracy and minimizing interruptions in power flow. As the complexity of electric power systems increases, fault detection with traditional methods becomes more difficult and the margin of error in the process increases. In this context, it is aimed to classify and detect faults by utilizing the versatile information provided by the data set, especially by using the power of deep learning-based models such as CNN. Thus, it is aimed to maintain uninterrupted energy flow and minimize economic losses.

One of the limitations of this study is that the dataset used may not fully reflect all fault conditions in real-world scenarios. It should be noted that fault detection models may be affected by various environmental factors, line aging, or structural differences in equipment within large-scale electrical systems. In addition, the fact that the dataset used is limited to a certain number of fault types and data obtained under limited conditions may affect the overall performance of the model and its generalizability to other systems. This suggests the need for future training with larger, real-time and dynamic data sets. This study provides a foundation for improving model accuracy and reliability and motivates further studies with more comprehensive datasets and conditions. This research demonstrates the applicability of machine learning and deep learning-based models to improve the reliability of electric power systems and ensure uninterrupted energy flow. The aim of the study is to increase the efficiency of power systems and reduce potential failure costs by quickly and accurately detecting faults in transmission lines. Accordingly, the proposed CNN-based model is expected to make a significant contribution to fault detection and classification in the energy sector. In Section 1 of this study, general information about the problem is given. The following sections of the study are as follows. Section 2 contains the work done for fault detection in transmission lines. Section 3 presents

the materials and methods required for the applications; Section 4 presents the results and discussion. Section 5 presents the conclusions and future work.

2. Literature Review

Fahim et al. proposed an unsupervised capsule network model for the detection and classification of transmission line faults. The model improves performance by learning fault characteristics without using large data sets. It converts three-phase signals into a single image and works with this image. The model has been tested in four different TL topologies and various fault scenarios, providing high reliability and adaptability [6]. Vaish et al. investigated ML methods for power system fault detection. They discussed supervised and unsupervised learning techniques, addressing the challenges of traditional methods. They also emphasized the potential of new methods such as reinforcement learning and transfer learning [7]. Fahim et al. propose a noise-tolerant, accurate fault detection model for microgrid faults. The model performs error minimization using a restricted Boltzmann machine (RBM) and its robustness is verified by testing it with signal variations. The results show that the model provides highly accurate fault detection and is superior to other methods [8]. Shakiba et al. propose a more reliable fault detection system for high-voltage transmission lines than conventional methods. Using CNN, this system performs robustly under various variables and noises, providing accurate detection and localization before the fault occurs [9]. Goni et al. propose a machine learning based system for Fault Detection (FD) and Fault Classification (FC) in transmission lines. FD and FC models are developed with the Extreme Learning Machine (ELM) algorithm for two different transmission lines simulated using MATLAB Simulink. Fault detection with 99.53% and 99.60% accuracy and fault classification with 99.18% and 99.09% accuracy are achieved for TL-1 and TL-2, respectively. The ELM model offered shorter processing time and lower computational complexity compared to traditional neural networks [10]. Kanwal and Jiriwibhakorn investigated artificial intelligence-based methods for fault detection, classification and localization in transmission lines. In the study, fault location with an error of 5.32 km was achieved using an Adaptive Neural-Fuzzy Inference System (ANFIS)–based fault detection and classification approach on the IEEE-9 bus system. The results demonstrate the effectiveness and potential of artificial intelligence techniques in this field [11]. Uddin et al. presented hybrid intelligent protection and control algorithms to improve the performance of distance relays in wind farms. A Decision Tree (DT) fault classifier and Support Vector Machine (SVM) were used for fault localization, and a PI-based control scheme was developed for DFIG-based wind power systems. These methods enhance the reliability and stability of wind farms [12]. Xi et al. developed an SA-MobileNetV3–based method for fault classification in transmission systems. The method employs deep learning by converting three-phase signals into two-dimensional images using CWT and classifies fault features more accurately with the SA module. Tested on a 735 kV transmission line model, the method demonstrates high accuracy and strong generalization capability [13].

Sahu et al. propose a Histogram-Based Gradient Boost (HGB) algorithm for fault detection and localization. The features of fault signals are extracted using spectral-kurtosis and the method is tested on IEEE-33 bus distribution system. HGB is compared with other machine learning methods and its superiority is proved [14]. Hassain et al. developed an Artificial Neural Network (ANN) model for fault detection in power systems with 99% accuracy. The model was tested with data from 14 bus systems and achieved high accuracy, precision and F1 score [15]. Shukla and Deepa used deep learning techniques to classify transmission line faults. In particular, they used ANN and Long-Short-Term Memory (LSTM) to automatically classify fault types (line-to-line, line-to-ground, etc.) and simplify the signal processing [16]. Livani presents a supervised learning method for fault location in complex power transmission lines using high-resolution voltage and current data from smart grids. The method is developed for three-terminal transmission lines and hybrid transmission lines and fault detection is realized using SVM and wavelet transform [17]. Salehimehr et al. developed fast fault detection and localization methods for DC microgrids. The proposed approach combines Compressed Sensing (CS) and Regression Tree (RT) techniques while achieving accurate fault localization using an LSTM model. Simulation results indicate that the method can detect and locate faults within 1 ms with 93% accuracy [18]. Zhu et al. employed a deep learning approach with a weighted loss function to automatically extract power lines from point clouds obtained using UAV-based laser scanners. The method achieved effective results on large-scale data [19]. Li et al. propose a Transformer-based method for short-term voltage stability assessment. The model generates artificial data

using CWGAN-GP to stabilize unstable data sets. In tests on IEEE 39-bus system, the proposed method exhibits strong performance in class imbalance and noisy environments. The results show that the StaaT model is more effective than other methods [20]. Dutta et al. emphasize the importance of ML in power systems. ML algorithms are used in areas such as load forecasting, fault detection, and energy management. In this study, methods such as Convolutional Neural Networks (CNNs), Support Vector Machines (SVMs), Recurrent Neural Networks (RNNs), and Decision Trees (DTs) are described, and a case study on fault detection in the IEEE five-bus system is presented [21].

3. Material and Method

In this study, the "Electrical Fault Detection and Classification" dataset published on the Kaggle platform is used to detect and classify electrical transmission line faults. The study aims to accurately classify faults with a deep learning-based CNN model. First, the data in the dataset is analyzed, then appropriate features are selected and prepared for data preprocessing and model training. In addition to the CNN model, machine learning models such as Bagging Classifier, AdaBoost, and Gradient Boosting were also tested, and a comparative performance evaluation was conducted. The flowchart of the study is presented in Figure 1. In the subsequent stages of the research, the model's performance is evaluated, and its potential benefits for the energy sector are analyzed.

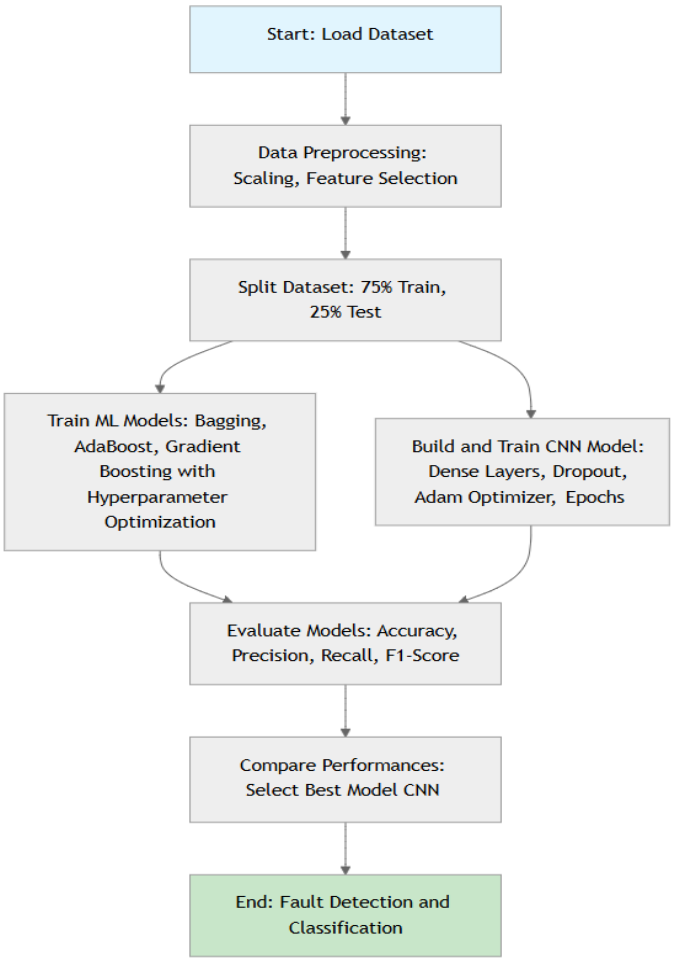


Figure 1. Flowchart of the proposed methodology

3.1. Transmission line model and faults

Fault detection in electricity transmission lines is usually classified according to the types of faults. Faults are divided into two main groups: symmetrical and asymmetrical. Symmetrical faults include triple line faults

(ABC) and triple line-to-ground faults (ABC-G), while asymmetrical faults are more diverse and include single line-to-ground (A-G, B-G, C-G), line-to-line (AB, BC, CA) and double line-to-ground (AB-G, BC-G, CA-G) faults. This classification helps to accurately identify the types of faults in transmission lines. Figure 2 shows the classification of fault types in transmission lines.

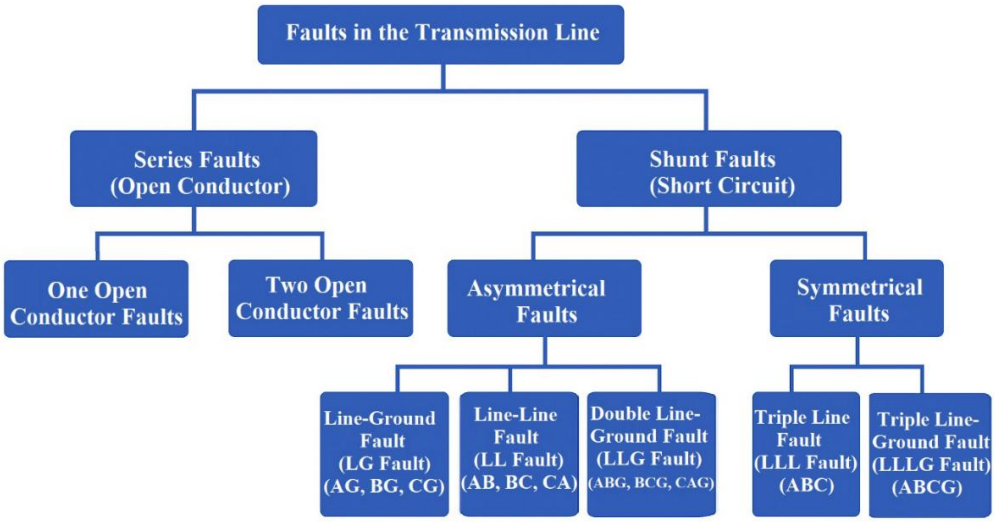


Figure 2. Classification of fault types in transmission line

Figure 3 illustrates the overall methodology for fault detection and classification in transmission lines as a flowchart. It starts with loading the Kaggle dataset, followed by data preprocessing (scaling and feature selection for Ia, Ib, Ic, Va, Vb, Vc) and splitting into 75% training and 25% testing sets. Parallel paths show training of machine learning models (Bagging, AdaBoost, Gradient Boosting) with hyperparameter optimization and the proposed CNN model.

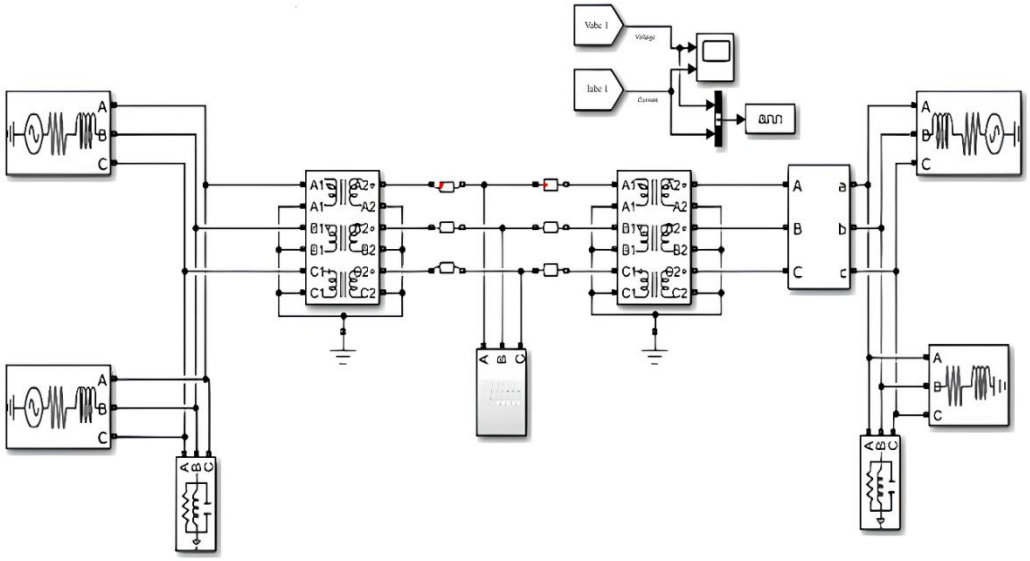


Figure 3. Transmission line model

The power system we examined, shown in Figure 3, consists of a 154kV, 50Hz three-phase transmission line connected to a power supply at both ends. The Artificial Neural Network (ANN) relay used is based on distance relay protection. The model represents a transmission line in Türkiye.

The transmission system is modeled using MATLAB software and various fault types are simulated to generate a fault data set for network training and testing. The power system parameters used are given in Table 1.

Table 1. Electrical parameters of the power system

Parameters	Value
Frequency	50 Hz
Generator output voltage	14.6 kV
Transmission line voltage	154 kV
Desired active power	100 MW
Reactive power value	27 MVAr

There are four types of faults: line-ground (A-G, B-G, and C-G), double-line-ground (AB-G, AC-G, and BC-G), line-line fault (AB, AC, and BC), and three-phase (ABC). Simulated by modifying the fault type restriction in the fault's module. Different fault data for L-G, LL-G, LL, and LLLL-G faults are created using the transmission line system's MATLAB software model. First, a multilayer feed-forward network is created. The number of hidden layers is properly raised to ensure the network's viability. The network was set up to establish the biases and weights of the network object, ready it for training. Training was done in batch mode, which produces fewer errors and is substantially faster.

The amount of validation checks, the size of the gradient performance, and the network performance were all important factors to consider while training the network. After training and validating the network, it can now be utilized to determine the relay system's reaction to various failure scenarios. The Neural Network software is then transferred to the microprocessor-based relay in place of the standard mathematical formulae. Figure 4 depicts the current waveform of an intact transmission line network before a failure, whereas Figure 5 depicts the current waveform of a damaged transmission line network following a fault generated from the system's MATLAB model. The data obtained from all fault situations was arranged into training sets using MATLAB software.

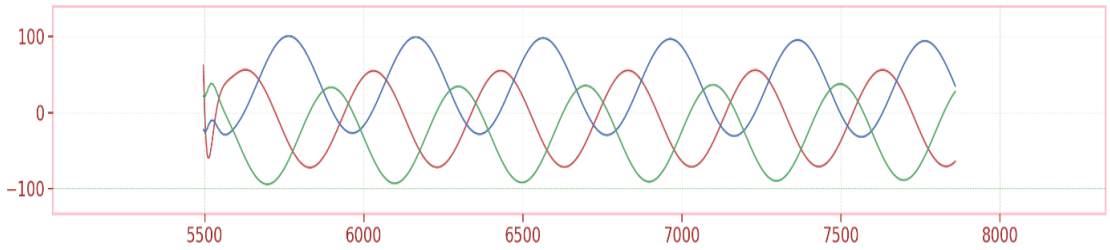


Figure 4. Fault-free Current Waveform

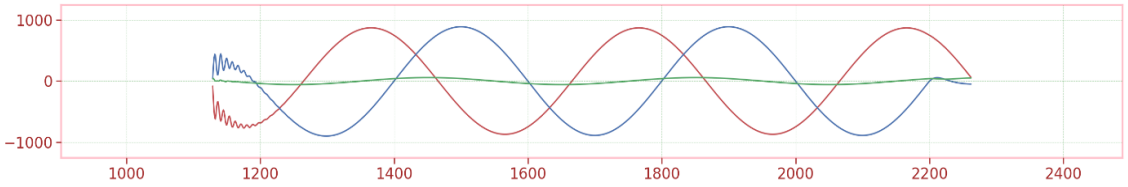


Figure 5. Fault Current Waveform

3.2. Dataset

The Electrical Fault Detection and Classification dataset on Kaggle was collected by Esathya Prakash and developed to detect faults in electrical power systems. This dataset is simulated to detect and classify faults in transmission lines of an electric power system.

The power system is simulated in MATLAB with 4 generators, each with an output voltage of 11 × 103 V, and transformers located in the middle of the transmission line. The system is operated under normal and various fault conditions, and the line voltages and line currents measured at the output side of the transmission line are collected, resulting in approximately 12,000 data points. These data are labeled so that fault detection and classification can be performed using artificial neural networks. The given dataset provides a basis for the accurate detection of various faults in the electrical power system and can be used for the rapid activation of system protection equipment.

An artificial neural network model designed to utilize three different machine learning and one deep learning algorithm is selected. Several experiments were conducted to determine the algorithm, activation functions, number of hidden layers and number of hidden neurons. This dataset contains scaled current and voltage values of three phases. There are 11 different fault conditions and no fault conditions for the 6 inputs in the data set. The truth table for these fault types is shown in Table 2.

Table 2. Truth table of various types of faults

	Fault type	A Line	B Line	C Line	Ground
1	A-G	1	0	0	1
2	B-G	0	1	0	1
3	C-G	0	0	1	1
4	A-B	1	1	0	0
5	A-C	1	0	1	0
6	B-C	0	1	1	0
7	A-B-G	1	1	0	1
8	A-C-G	1	0	1	1
9	B-C-G	0	1	1	1
10	A-B-C	1	1	1	0
11	A-B-C-G	1	1	1	1

The neural network used has scaled instantaneous voltages and currents of all three phases for five different fault conditions and for the fault-free condition. A total of 7,861 data points are labeled in the dataset. The number of faults in the system according to the fault type of these data are; 1134 A-B-G Fault, 1133 A-B-C-G Fault, 1129 A-G Fault, one A-B-C Fault, 1004 B-C Fault and 2365 No Fault. In addition, the numerical values of A, B, C and Ground Fault values in the data set are presented in Figure 6.

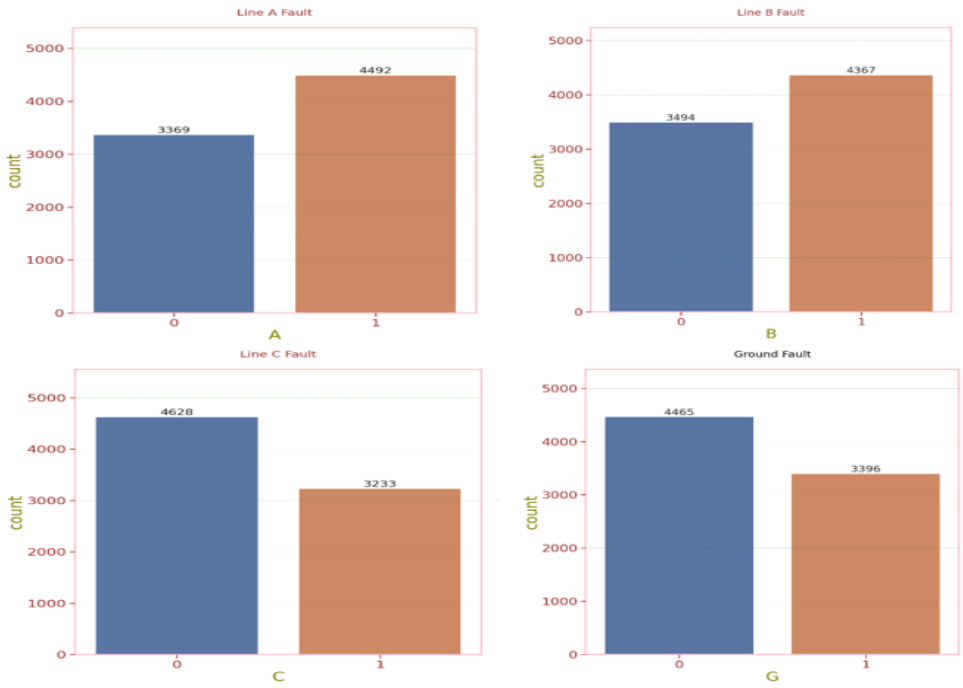


Figure 6. A, B, C and Ground Fault value

The dataset is randomly divided into two subsets for training and testing the models. The *Electrical Fault Detection and Classification* dataset, consisting of a total of 7,861 data points, is divided into the 75% training set and the 25% test set. This division was done to avoid overlearning of the models and to evaluate their generalization ability. A value of random_state=42 was used to ensure the reproducibility of the study. Furthermore, a separate validation set was not explicitly allocated, but part of the training set was used for validation during model training.

3.3. Bagging classifier

Bagging (Bootstrap Aggregating) is a powerful ensemble learning method used in supervised learning algorithms and is widely preferred in classification tasks. Basically, multiple base classifiers are trained by randomly selecting samples from the training set. Each classifier is trained independently on its own subset and then the outputs of the classifiers are combined with techniques such as majority voting or weighted voting to make the final classification [22-23]. This method provides an effective solution, especially for algorithms with high variance and overfitting tendencies. Bagging increases the diversity of the model by training each base classifier on different training subsets, resulting in a more reliable and general model. This diversity strengthens the generalization capability of the model, resulting in more accurate and stable results across a variety of data sets.

3.4. AdaBoost classifier

AdaBoost is an ensemble learning method that combines weak classifiers or regression models to create a stronger and more generalizable model. In this approach, each model initially has low accuracy and is weighted by errors. Misclassified or predicted examples are focused on by giving more weight to subsequent models, so that each new model is trained to correct the errors of the previous model. This process of sequential addition gradually increases the accuracy of the model, building a strong ensemble. AdaBoost offers high accuracy, low tendency to overfit and robustness to noise in data sets, especially for classification and regression problems. However, accurate hyperparameter tuning is critical to the success of the model, as there is a risk of over-tuning. AdaBoost generally achieves effective results on large datasets, providing high generalization capability and flexibility [24].

3.5. Gradient boosting classifier

Gradient Boosting Classifier is an ensemble learning method that builds a stronger model by successively training weak classifiers. This algorithm ensures that each new model is added to correct the error margins of the previous models. At each step, Gradient Boosting optimizes the predictions of the new model by focusing on the errors of the previous model, thus trying to minimize the classification errors. This process ensures that each new model focuses predominantly on faulty predictions. Gradient Boosting is particularly well known for its ability to achieve high accuracy and often provides a robust model that can control the risk of overfitting [25]. However, the performance of the model depends on the hyperparameter settings and can run the risk of overfitting without proper optimization. Therefore, it is possible to achieve high accuracy and generalization power with appropriate parameter settings and tuning techniques.

3.6. Convolutional neural network

CNN is an artificial neural network architecture designed specifically for image processing and visual data analysis. CNN uses several consecutive layers to analyze the input data, including convolutional layers, pooling layers, and fully connected layers [26]. Convolutional layers preserve spatial relationships and produce feature maps by applying filters over small local regions to learn important features in the image. Pooling layers, on the other hand, reduce the computational burden by reducing the data size and enable the network to have higher generalization capability. Thanks to its ability to perform automatic feature extraction, CNN has the ability to learn from raw data without the need for manual feature engineering. This makes it an ideal tool for image classification, object detection, face recognition and many other computer vision applications. The success of CNN becomes more evident when trained on large data sets, because thanks to the deep layers, the network can effectively learn complex data and increase its generalization power.

3.7. Evaluation metrics

In the field of deep learning, performance metrics are a fundamental tool for evaluating and improving the effectiveness of models. These metrics provide important information to improve the success of models, identify errors and biases, and make accurate predictions. Often, accuracy is not the most appropriate metric in all cases when assessing the overall performance of the model. Instead, metrics such as precision and recall provide a more detailed analysis by examining the number of true positive predictions made by the model and the proportion of actual positive samples that are correctly identified. These metrics become more critical, especially in unbalanced data sets. Accuracy measures the proportion of predictions made by the model that are correct, while precision is the ratio of true positive predictions to all positive predictions. Sensitivity shows how many true positive samples are correctly predicted. The F1 score provides a more balanced assessment by taking the harmonic mean of precision and sensitivity. This metric is particularly useful in unbalanced data sets to analyze the success of the model in a fairer way. Mathematically, accuracy is the ratio of all correct predictions to total predictions, precision is the ratio of true positive predictions to all positive predictions, and sensitivity is the ratio of correctly predicted positives to true positives [27-28]. The F1 score balances these two metrics, taking both measurements into account and providing a more comprehensive assessment. Mathematical formulas for the evaluation metrics are given in Equations (1)-(4).

$$Accuracy = \frac{Number\ of\ Correct\ Predictions}{Number\ of\ Total\ Prediction} \tag{1}$$

$$Precision = \frac{True\ Positive}{True\ Positive + False\ Positive} \tag{2}$$

$$Recall = Sensitivity = \frac{True\ Positive}{True\ Positive + False\ Negative} \tag{3}$$

$$F1 = \frac{2 * Precision * Recall}{Precision + Recall} \tag{4}$$

4. Experimental Results and Discussion

In this study, a set of powerful machine learning and deep learning methods **is** used to effectively detect and classify faults in transmission lines. Ensemble methods such as Bagging, AdaBoost and Gradient Boosting Classifier have played an important role in improving the accuracy and robustness of the model by combining basic classifiers to achieve accurate fault detection results. In addition to these methods, a CNN structure, which is successful in feature extraction and identifying complex fault patterns, was also used to distinguish between different fault types. The experimental results section evaluates the performance of these methods and discusses in detail the advantages and limitations of the models and their contribution to fault detection in electricity transmission systems. To better understand the structure of the data in the dataset, the correlation between each feature is calculated and visualized as shown in Figure 7.

The correlation matrix presented in Figure 7 shows the relationship between electric current and voltage (Ia, Ib, Ic and Va, Vb, Vc) measurements. The correlation coefficient takes values between -1 and +1, with +1 indicating a perfect positive relationship, -1 indicating a perfect negative relationship, and 0 indicating no relationship.

Moderate negative correlations, such as -0.38 between Ia and Ib, –0.28 between Ia and Ic, and –0.53 between Ib and Ic, are observed. This indicates that the current phases have an inverse interaction with each other, i.e., when one increases, the other tends to decrease. There are high negative correlations of –0.51, –0.47, and –0.52 between Va and Vb, Va and Vc, and Vb and Vc, respectively. These correlations indicate that the different phase voltages are highly reversed with respect to each other. Low-level correlations are usually observed between currents and voltages. For example, Ia and Va have a very low positive correlation of 0.033, while Ic and Vb have a low negative correlation of -0.096. This indicates that the current and voltage values are independent or weakly correlated between certain phases. Since there is no strong positive or negative relationship in this correlation matrix, most current and voltage values can be considered as independent. Especially in system modeling and fault detection, this independence or low correlation between phases indicates that the effect of events occurring in certain phases on other phases is limited.



Figure 7. Correlation of all parameters

Hyperparameter optimization for machine learning algorithms has been performed using the Random Search method. Random search is an optimization technique that selects the best performing parameter set by trying

random combinations in the hyperparameter space. This method offers the possibility to efficiently explore a large hyperparameter space while reducing the computational cost. The optimization process was performed by trying 10 random combinations for each algorithm and using 5-fold cross-validation, which increases the generalizability of the models and reduces the risk of over-fitting. Table 3 shows the hyperparameter settings for Bagging, AdaBoost and Gradient Boosting Classifier used in the study. The proposed CNN model is given in Table 4.

Table 3. Parameters used for machine learning algorithms

	Classifier Models		
Parameter	Bagging	AdaBoost	Gradient Boosting
Number of estimators	50	50	100
Learning rate	0.1	1	0.1
Base estimator	5	1	3
Max depth	5	1	3
Subsample	-	-	0.8
Loss Function	-	-	Log Loss
Random state	50	50	50

The proposed deep learning model is designed for the binary classification problem and consists of fully connected layers. The first layer of the model is a hidden layer of 256 neurons with a ReLU activation function, which allows complex features to be extracted from the data. This layer is followed by a 0.5 dropout layer to prevent overlearning. The following layers again use ReLU activation with 128 and 64 neurons respectively. In both layers, a 0.5 dropout mechanism is applied to increase the robustness of the model to noise and to minimize the risk of overfitting. The output layer of the model is a single neuron with a sigmoid activation function that bounds the output between 0 and 1, generating a classification probability for each sample. The binary_crossentropy loss function was used to build the model; this function is very effective in measuring classification errors. Furthermore, the Adam optimization algorithm is used to update the parameters of the model quickly and efficiently.

Table 4. Parameters used for the proposed CNN model

Parameter	Value
Optimizer	Adam
Learning Rate	0.001
Batch Size	32
Number of Epochs	50
Loss Function	Binary Crossentropy
Activation Function	ReLU (hidden layers), Sigmoid (output layer)
Regularization	Dropout (rate = 0.5)

The training process was continued for 50 epochs, and the accuracy rate obtained from the validation data at the end of each epoch was carefully monitored. This method ensured that the model-maintained stability in the learning process and increased its ability to generalize. The success of the model is reflected in its ability to achieve high accuracy rates due to the careful configuration of its architecture and its ability to generalize to different data sets.

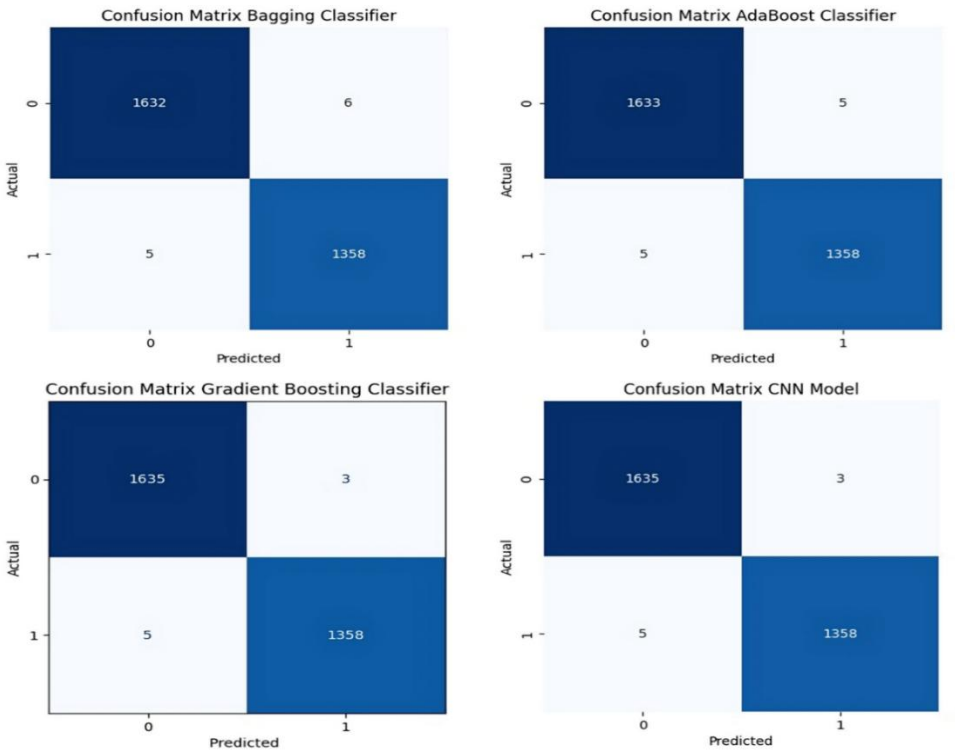


Figure 8. Confusion matrix of models

Figure 8 shows the confusion matrices of the models used. According to the results of the complexity matrix created to evaluate the accuracy performance of the four given models, all models achieved high accuracy rates, but there were some differences. Bagging Classifier performs relatively poorly with 6 false negatives and 5 false positives, while AdaBoost and Gradient Boosting Classifier and CNN models make fewer errors. The Gradient Boosting Classifier and CNN model showed the highest performance with only 3 false positives and 5 false negatives. This result shows that, in particular, the Gradient Boosting and CNN models offer the best accuracy performance, indicating that these models are suitable for fault detection.

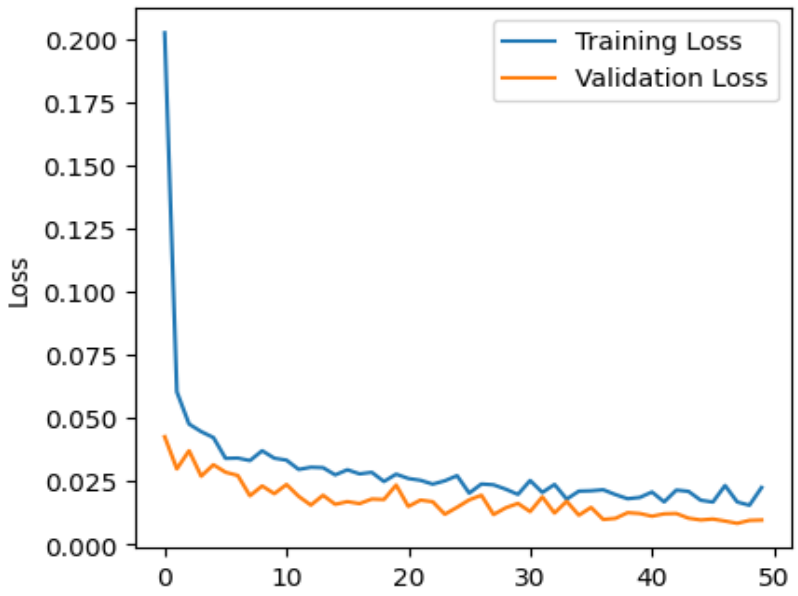


Figure 9. Loss graph of the proposed model

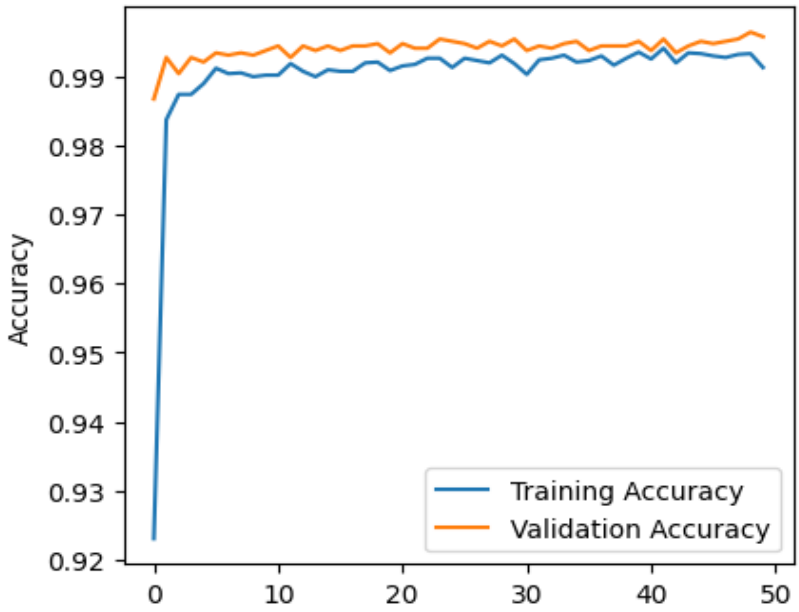


Figure 10. Accuracy graph of the proposed model

The graphs in Figures 9 and 10 show the variation of loss and accuracy metrics of our proposed model during the training process, respectively. On the left, the training and validation losses decrease and stabilize, indicating that the model learns successfully on both datasets. On the right, the accuracy rates, especially for the validation set, reach very high values from the beginning, with training accuracy of 99.19% and validation accuracy of 99.73% after 50 epochs. This shows that the model performs consistently and strongly on both training and validation data and does not overfit. The model's validation loss (0.0096) and training loss (0.0212) values confirm that the overall accuracy is quite high with low error rates These results imply that the model learns from the training data while generalizing well to the validation data and functions as a high-performance classifier for electrical fault detection.

Table 5. Comparison of the results of all models

Model	Accuracy	Precision	Recall
Bagging	99.63	99.56	99.63
AdaBoost	99.66	99.63	99.63
Gradient Boosting	99.73	99.77	99.63
Proposed Model	99.73	99.77	99.63

Table 5 compares the performance of Bagging, AdaBoost, Gradient Boosting and the proposed model. According to the key performance metrics in the table, it is seen that all models achieve very high accuracy rates, with all of them achieving over 99%. In particular, Gradient Boosting and the Proposed Model exhibit the highest performance with an accuracy of 99.73%. As shown in Table 5, the performance metrics (accuracy, precision, and sensitivity) of the Proposed Model and Gradient Boosting are nearly equivalent. However, the main advantages of the Proposed Model over Gradient Boosting are as follows: First, thanks to its CNN-based structure, it can automatically extract spatial and temporal features from raw current-voltage data, thereby significantly reducing the need for manual intervention in the feature engineering stage. Second, the model's layered architecture offers higher generalization capabilities in complex and noisy data sets, which translates into a more robust detection mechanism against fluctuating signal conditions in real-time applications. Third, when GPU-accelerated optimization techniques are used during the training phase, training can be performed in a shorter time and with lower memory load, even on large-scale data sets. In addition, since the CNN model is deep learning-based, it effectively controls the risk of overfitting with regularization techniques such as Dropout layers and early stopping. Finally, the architecture of the proposed structure is highly adaptable for reuse with transfer learning or fine-tuning steps in different topologies and

dynamic system conditions, thus enabling more practical adaptation of the model to different transmission line configurations or future data varieties. These features demonstrate that the proposed CNN model is superior to Gradient Boosting not only in terms of numerical performance metrics but also in terms of ease of application, flexibility, and real-time performance.

In terms of precision, Gradient Boosting and the Proposed Model achieve the highest precision of 99.77%, while Bagging and AdaBoost models show slightly lower precision values. This means that Gradient Boosting and the proposed model provide higher precision with fewer false positives. In terms of recall, the value of all models is equal to 99.63%. This means that all models correctly classify true positives at the same rate. Overall, Gradient Boosting and the Proposed Model perform quite similarly in terms of accuracy, precision and sensitivity, with precision being the most important. If precision is the priority, Gradient Boosting or the Proposed Model is the best choice.

Table 6. Comparison with similar studies in the literature

Study	Architecture	Accuracy (%)
Fahim et al. [6]	Unsupervised Capsule Network (CNSF)	98.8
Vaish et al. [7]	Supervised and Unsupervised ML Techniques	97.2
Shakiba et al. [9]	Convolutional Neural Network (CNN)	99.1
Goni et al. [10]	Extreme Learning Machine (ELM)	99.53
Kanwal & Jiriwibhakorn [11]	Adaptive Neural-Fuzzy Inference System (ANFIS)	98.8
Proposed Model	Convolutional Neural Network (CNN)	99.73

Table 6 shows the performance rates of the model proposed in this study compared to similar studies in the literature. When examining the studies in the literature, the CNSF model developed by Fahim et al. [6] achieved 98.5%, both supervised and unsupervised machine learning techniques used by Vaish et al. [7] achieved 97.2%, the CNN model proposed by Shakiba et al. [9] achieved 99.1%, the ELM model developed by Goni et al. [10] achieved 99.53%, and the ANFIS model used by Kanwal Jiriwibhakorn [11] achieved 98.8%.

The model proposed in this study achieved a success rate of 99.73% using a CNN-based approach. This rate indicates a higher level of accuracy than all other models in the table. The success rate of 99.73% achieved by the proposed model clearly demonstrates the effectiveness of the model and its superiority over other approaches in the literature, especially in the critical area of transmission line fault detection. This result shows that the proposed CNN model outperforms both previous CNN-based studies and various methods. Figure 11 shows the success rates of similar studies in the literature.

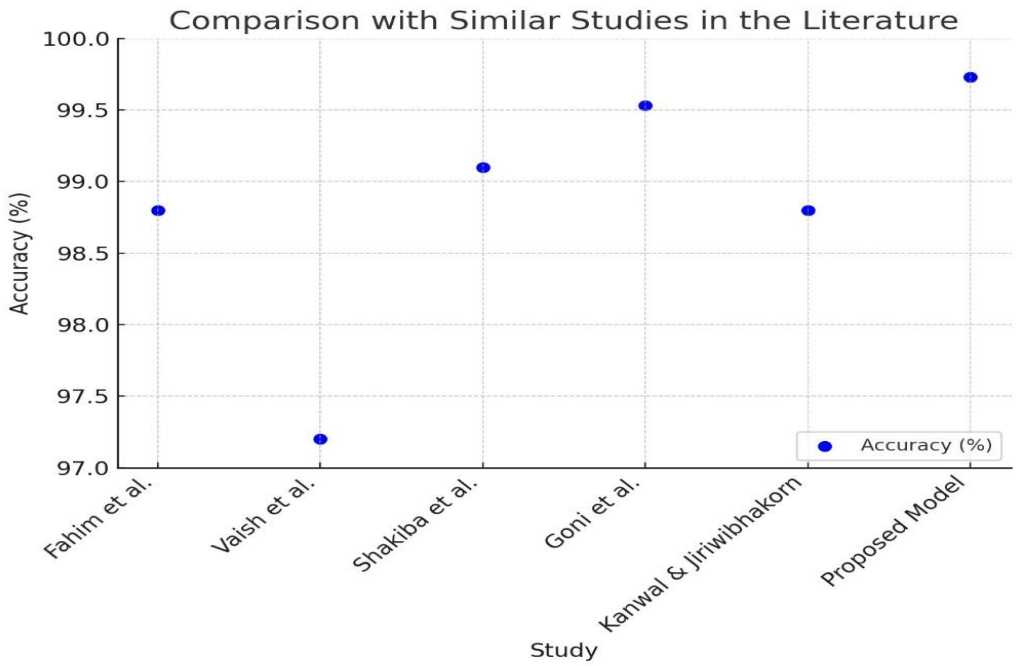


Figure 11. Comparison of the success rates of similar studies in the literature.

The proposed model offers significant advantages with high accuracy rates and efficient error detection. However, the model also has some limitations and potential drawbacks. As a deep learning-based model, it requires large data sets, which increases the overhead of data collection and preprocessing. Although the risk of overlearning is mitigated by dropout layers, this risk remains, especially for small datasets. In addition, the robustness of the model to different types of failures and noisy data has not yet been tested, requiring an evaluation of the model's performance in real-world conditions. These limitations may limit the effectiveness and generalizability of the model in practical applications.

In industrial applications, the challenges faced by the proposed model include limited data access, real-time processing requirements and system integration. To overcome these challenges, it is recommended to develop real-time data acquisition systems and apply optimization techniques to reduce the computational burden of the model. In addition, the scalability of the model should be evaluated by testing it on large power systems, which requires optimization of training time and resource utilization. Adaptability to different power system topologies can be achieved by retraining the model with larger data sets obtained from different system configurations.

5. Conclusion

In this study, machine learning algorithms are used to identify and classify faults in electricity transmission lines. The performance of Bagging, AdaBoost, Gradient Boosting, and CNN models is compared, and the success rates of each model in fault detection are analyzed in detail. According to the results obtained, the methods used provided high accuracy in fault detection, with the CNN model showing the highest performance. The proposed CNN model supports energy continuity by enhancing the system's ability to detect faults quickly and accurately with an accuracy rate of 99.73%, while ensemble ML methods provide consistent results in classifying different types of faults. This has the potential to reduce economic losses by optimizing maintenance processes. This shows that deep learning methods are successful in fault detection in transmission lines. In addition, hyperparameter optimization was applied to improve model accuracy, and the performance of different algorithms in this process was analyzed. The results are particularly valuable for the early detection of faults and the determination of appropriate response methods. These approaches can improve the reliability and efficiency of power transmission systems and prevent potential losses. The findings of the study provide a basis for preventing failures and optimizing the maintenance of transmission lines. The success rates obtained show that such approaches can be used in industrial applications and provide a strong basis for future studies. In this context, it is recommended that future studies should be supported

with larger datasets, a more detailed classification of different fault types, and the integration of other machine learning algorithms into the process. This study demonstrates that machine learning-based solutions can be effectively used in the maintenance and management processes of energy transmission lines and contributes to the development of innovative and effective fault management strategies for engineers working in the energy sector.

6. Author Contribution Statement

The authors contributed equally to the article.

7. Ethics Committee Approval and Conflict of Interest Statement

In the prepared manuscript, there is no need for ethics committee approval. The prepared manuscript has no conflicts of interest with any individual or institution.

8. Ethical Statement Regarding the Use of Artificial Intelligence

No artificial intelligence-based tools or applications were used in the preparation of this study. The entire content of the study was produced by the author in accordance with scientific research methods and academic ethical principles.

9. References

[1] F. Alpsalaz and M. S. Mamiş, "Detection of arc faults in transformer windings via transient signal analysis," *Appl. Sci.*, vol. 14, no. 20, p. 9335, Oct. 2024.
[2] B. Said *et al*., "Hybrid MPC–third-order sliding mode control with MRAS for fault-tolerant speed regulation of PMSMs under sensor failures," *Int. Trans. Electr. Energy Syst.*, vol. 2025, p. 5984024, 2025.
[3] M. Demirbas *et al*., "Fuzzy-based fitness–distance balance snow ablation optimizer algorithm for optimal generation planning in power systems," *Energies*, vol. 18, no. 12, p. 3048, 2025.
[4] F. Alpsalaz, "Fault detection in power transmission lines: Comparison of Chirp-Z algorithm and machine learning-based prediction models," *Eksploat. Niezawodn. – Maint. Reliab.*, vol. 27, no. 4, p. 14, 2025.
[5] H. Uzel *et al*., "Fuzzy fitness distance balance gradient-based optimization algorithm (fFDBGBO): An application to design and performance optimization of PMSM," *IEEE Access*, vol. 13, pp. 155898–155915, 2025.
[6] S. R. Fahim *et al*., "A deep learning-based intelligent approach in detection and classification of transmission line faults," *Int. J. Electr. Power Energy Syst.*, vol. 133, p. 107102, Dec. 2021.
[7] R. Vaish *et al*., "Machine learning applications in power system fault diagnosis: Research advancements and perspectives," *Eng. Appl. Artif. Intell.*, vol. 106, p. 104504, Nov. 2021.
[8] S. R. Fahim *et al*., "Microgrid fault detection and classification: Machine learning-based approach, comparison, and reviews," *Energies*, vol. 13, no. 13, p. 3460, Jul. 2020.
[9] F. M. Shakiba *et al*., "Real-time sensing and fault diagnosis for transmission lines," *Int. J. Netw. Dyn. Intell.*, pp. 36–47, Dec. 2022.
[10] M. O. F. Goni *et al*., "Fast and accurate fault detection and classification in transmission lines using extreme learning machine," *e-Prime – Adv. Electr. Eng., Electron. Energy*, vol. 3, p. 100107, Mar. 2023.
[11] S. Kanwal and S. Jiriwibhakorn, "Artificial intelligence-based faults identification, classification, and localization techniques in transmission lines—A review," *IEEE Lat. Am. Trans.*, vol. 21, no. 12, pp. 1291–1305, Dec. 2023.
[12] M. N. Uddin *et al*., "Hybrid machine learning-based intelligent distance protection and control schemes with fault and zonal classification capabilities for grid-connected wind farms," *IEEE Trans. Ind. Appl.*, vol. 59, no. 6, pp. 7328–7340, Nov. 2023.
[13] Y. Xi *et al*., "Transmission line fault detection and classification based on SA-MobileNetV3," *Energy Rep.*, vol. 9, pp. 955–968, Dec. 2023.
[14] S. K. Sahu *et al*., "Machine learning-based adaptive fault diagnosis considering hosting capacity amendment in active distribution network," *Electr. Power Syst. Res.*, vol. 216, p. 109025, Mar. 2023.
[15] R. H. Hassain *et al*., "Deep learning-based fault detection in electrical transmission lines," *AIP Conf. Proc.*, vol. 3232, no. 1, Oct. 2024.
[16] P. K. Shukla and K. Deepa, "Deep learning techniques for transmission line fault classification—A comparative study," *Ain Shams Eng. J.*, vol. 15, no. 2, p. 102427, Feb. 2024.
[17] H. Livani, "Supervised learning-based fault location in power grids," in *Big Data Appl. Power Syst.*, pp. 217–234, Jan. 2024.
[18] S. Salehimehr *et al*., "A novel machine learning-based approach for fault detection and location in low-voltage DC microgrids," *Sustainability*, vol. 16, no. 7, p. 2821, Mar. 2024.
[19] S. Zhu *et al*., "A deep-learning-based method for extracting an arbitrary number of individual power lines from UAV-mounted laser scanning point clouds," *Remote Sens.*, vol. 16, no. 2, p. 393, Jan. 2024.
[20] Y. Li *et al*., "Deep learning based on transformer architecture for power system short-term voltage stability assessment with class imbalance," *Renew. Sustain. Energy Rev.*, vol. 189, p. 113913, Jan. 2024.
[21] K. K. Dutta *et al*., "Machine learning-based intelligent power systems," in *Autom. Secure Comput. Next-Gener. Syst.*, pp. 319–344, Jan. 2024.

[22] F. Alpsalaz *et al*., "Classification of maize leaf diseases with deep learning: Performance evaluation of the proposed model and use of explicable artificial intelligence," *Chemom. Intell. Lab. Syst.*, vol. 262, p. 105412, 2025.
[23] S. Demirtaş Alpsalaz *et al*., "Alzheimer's classification with a MaxViT-based deep learning model using magnetic resonance imaging," *J. Adv. Sci. Technol. Technol. (JASTT)*, vol. 6, no. 2, Oct. 2025.
[24] E. Aslan *et al*., "A hybrid machine learning approach for predicting power transformer failures using Internet of Things-based monitoring and explainable artificial intelligence," *IEEE Access*, pp. 113618–113633, Jul. 2025.
[25] Y. Özüpak *et al*., "Air quality forecasting using machine learning: Comparative analysis and ensemble strategies for enhanced prediction," *Water Air Soil Pollut.*, vol. 236, p. 464, 2025.
[26] Y. Özüpak *et al*., "Hybrid deep learning model for maize leaf disease classification with explainable AI," *N. Z. J. Crop Hortic. Sci.*, vol. 53, no. 5, pp. 2942–2964, 2025.
[27] E. Aslan and Y. Özüpak, "Comparison of machine learning algorithms for automatic prediction of Alzheimer's disease," *J. Chin. Med. Assoc.*, vol. 88, no. 2, pp. 98–107, Feb. 2025.
[28] M. Çınar *et al*., "Comparison and optimization of machine learning methods for fault detection in district heating and cooling systems," *Bull. Pol. Acad. Sci. Tech. Sci.*, vol. 73, no. 3, 2025.

Fırat Üniversitesi Deneysel ve Hesaplamalı Mühendislik Dergisi

FUJECE

Akıllı Şehirlerdeki Multikopter Şarj İstasyonları için Simülasyon Tabanlı Karar Zekası Modeli

Kübra ÇELIK[1]*, Haluk EREN[2]

[1,2]Hava Trafik Kontrol Bölümü, Sivil Havacılık Yüksekokulu, Fırat Üniversitesi, Elazığ, Türkiye.
[1]k.celik@firat.edu.tr, [2]heren@firat.edu.tr

Geliş Tarihi: 19.8.2025
Kabul Tarihi: 06.11.2025
Düzeltme Tarihi: 20.9.2025
doi: https://doi.org/10.62520/fujece.1768822
Araştırma Makalesi

Alıntı: K. Çelik ve H. Eren, "Akıllı şehirlerdeki multikopter şarj istasyonları için simülasyon tabanlı karar zekası modeli", Fırat Üni. Deny. ve Hes. Müh. Derg., vol. 5, no 1, pp. 169-217, Şubat 2026.

Öz

Kentsel hava hareketliliği giderek artan biçimde otonom çok rotorlu hava aracı filolarına dayanmaktadır. Ancak bu filoların operasyonel sürdürülebilirliği, akıllı şarj altyapılarının eksikliği nedeniyle hâlâ önemli ölçüde sınırlıdır. Bu çalışma, akıllı şehir koşulları altında altı farklı çok rotorlu şarj istasyonu arketipini değerlendirmek üzere tasarlanmış simülasyon temelli bir karar zekâsı modeli sunmaktadır. Önerilen çerçeve, Güvenlik, Altyapı Maliyeti, Lojistik Uyumluluk, Akıllı Şehir Entegrasyonu ve Sürdürülebilirlik olmak üzere beş normalleştirilmiş değerlendirme faktörünü, şeffaf ve denetlenebilir bir çok ölçütlü karar yapısı içinde birleştirmektedir. Analitik titizliği ve yorumlanabilirliği güvence altına almak amacıyla iki tamamlayıcı değerlendirme modu geliştirilmiştir. İlk mod olan Mode A, eşit ağırlıklar kullanan ve yöntemsel açıklığı koruyan tekrarlanabilir bir temel yapı sunmaktadır. İkinci mod olan Mode B ise altyapı kapasitesi ile lojistik akış arasında kontrollü bir ilişki kuran sınırlı bir koordinasyon operatörü olarak işlev görmekte ve etkileşim farkındalığını sıralama mantığını değiştirmeden sisteme dâhil etmektedir. Karar verileri Latin Hiperküp Örneklemesi yöntemiyle sentetik olarak üretilmiş, belirsizlik ise bootstrap yeniden örnekleme tekniğiyle nicel biçimde hesaplanmıştır. Her iki modun da kararlılığı analitik olarak doğrulanmış, sonuçlar Kendall's τ değerinin 0.90'ın üzerinde, Top-k korunum oranının ise yüzde 95'in üzerinde olduğunu göstermiştir. Bu bulgular, etkileşim farkındalığının yorum gücünü artırırken analitik tutarlılığı koruduğunu kanıtlamaktadır. Elde edilen sonuçlar, Son Mil ve İlk Mil istasyonlarının farklı kentsel morfolojilerde en yüksek bileşik verimlilik puanlarını (sırasıyla 0.82 ve 0.80) koruduğunu ortaya koymuştur. Çatı ve Elektrikli Araç Entegreli istasyon konfigürasyonları da yenilenebilir enerjiyle uyumlu senaryolarda rekabetçi bir ölçeklenebilirlik ve gelişmiş performans sergilemiştir. Geliştirilen genel çerçeve, kentsel drone şarj ağlarının planlanması, uygulanması ve ampirik olarak kalibre edilmesi için tekrarlanabilir, politika açısından uyumlu ve bilimsel olarak izlenebilir bir temel sunmaktadır. Ayrıca veri eksikliği bulunan ortamlarda karar alma süreçlerine yönelik tutarlı bir yöntemsel yol haritası oluşturmakta, analitik şeffaflık ve operasyonel anlamlılığın gelecekteki pilot uygulamalar boyunca korunmasını sağlamaktadır.

Anahtar kelimeler: Otonom İHA şarjı, Akıllı karar, Akıllı şehir lojistiği, Sürdürülebilirlik, Kentsel hava mobilitesi

*Yazışılan yazar

İntihal Kontrol: Evet – Turnitin
Şikayet: fujece@firat.edu.tr
Telif Hakkı ve Lisans: Dergide yayın yapan yazarlar, CC BY-NC 4.0 kapsamında lisanslanan çalışmalarının telif hakkını saklı tutar.

Firat University Journal of Experimental and Computational Engineering

Simulation Based Decision Intelligence Model for Multicopter Charging Stations in Smart Cities

Kübra CELIK[1]*, Haluk EREN[2]
[1,2]Air Traffic Control Department, Civil Aviation School, Fırat University, Elazığ, Türkiye.
[1] k.celik@firat.edu.tr, [2]heren@firat.edu.tr

Received: 19.8.2025
Revision: 20.9.2025
Accepted: 06.11.2025
doi: https://doi.org/10.62520/fujece.1768822
Research Article

Citation: K. Çelik and H. Eren "Simulation based decision intelligence model for multicopter charging stations in smart cities", Firat Univ. Jour.of Exper. and Comp. Eng., vol. 5, no 1, pp. 169-217, February 2026.

Abstract

Urban air mobility increasingly relies on autonomous multicopter fleets whose operational sustainability remains constrained by the absence of intelligent recharging infrastructures. This study introduces a simulation based decision intelligence model designed to evaluate six multicopter charging station archetypes under smart city conditions. The proposed framework integrates five normalized evaluation factors, namely Security, Infrastructure Cost, Logistics Compatibility, Smart City Integration, and Sustainability, within a transparent and auditable multi-criteria decision framework. Two complementary evaluation modes are developed to ensure analytical rigor and interpretability. The first mode, Mode A, represents a reproducible baseline configuration that employs equal weighting to retained methodological clarity. The second mode, Mode B, functions as a bounded coordination operator that establishes a controlled relationship between infrastructure capacity and logistics flow, enabling interaction informed evaluation without altering the ranking logic. Synthetic decision data are generated through Latin Hypercube Sampling, while bootstrap resampling is used to quantify uncertainty. The stability of both modes is analytically verified, showing that Kendall's τ exceeds 0.90 and Top-k retention remains above 95 percent. These results demonstrate that introducing interaction awareness refines interpretability while maintaining analytical consistency across uncertainty ranges. The findings reveal that Last Mile and First Mile stations maintain the highest composite efficiency scores, 0.82 and 0.80 respectively, across various urban morphologies. Roof and Electric Vehicle Coupled configurations also display competitive scalability and improved performance when aligned with renewable energy scenarios. The overall framework provides a reproducible, policy aligned, and scientifically traceable foundation for the planning, deployment, and empirical calibration of urban drone charging networks. It further establishes a consistent methodological pathway for decision making in data scarce environments, ensuring that analytical transparency and operational relevance are sustained throughout future pilot implementations.

Keywords: Autonomous UAV recharging, Intelligent decision, Smart city logistics, Sustainability, Urban air mobility (UAM)

*Corresponging author

Plagiarism Checks: Yes – Turnitin
Complaints: fujece@firat.edu.tr
Copyright & License: Authors publishing with the journal retain the copyright to their work licensed under the CC BY-NC 4.0

1. Introduction

Unmanned Aerial Vehicles (UAVs) are being considered for package transport, commercial and civil applications and passenger transportation since the early 2000s [1]. UAV sustainability depends on many factors, such as technology, public acceptance, and regulations. Public acceptance of UAVs for commercial transportation is very important for sustainability of this idea [2]. For mission based UAV applications; payload capacity, mission control, extended flight duration, and frequent, robust refueling become critical overall success [3-5]. In this study, the term efficiency denotes an operational composite score constructed from normalized factor values rather than an energy only metric. Each factor is normalized to the closed interval [0,1] and aggregated by weights, producing a dimensionless index that supports consistent comparison across station types. Throughout the study, we use the following abbreviations: Unmanned Aerial Vehicle (UAV), Multi-Criteria Decision Making (MCDM), Electric Vehicle (EV).

Electricity powered transportation systems are increasing, therefore, EV charging stations are common in Europe and the USA during last decade [6-8]. Studies on the role of EV charging stations in smart cities have generally focused on road vehicles. For example, a study conducted by Asnaz examined the positioning of EV charging stations and smart charging systems [9]. On the other hand, there are no legal regulations about UAV charging stations. Some studies discuss the charging infrastructures are needed to execute the mission based flights [10]. However, studies on autonomous charging stations for rotary wing UAVs are limited. A relevant thesis study conducted by Üçgün focused on the design of an autonomous charging station for rotary wing UAVs [11].

Among UAVs, here, the multicopters are chosen for civil package delivery applications. Multicopters do not need a landing field, and they can take off vertically. Multicopters generally have electrically powered propulsion systems used Li-polymer batteries. The electric storage of the battery is the most important factor which affects the multicopters flying time. In today's technology, battery discharge time is limited. In this context, the proper battery charging options and charging station designs are important. In literature, there are many unique charging station examples for multicopters. The electromagnetic coils for wireless charging could be mounted on electric poles on smart grid. Electric pole wireless charger station example proposed by Filipovic et al. is provided in figure 1 [12].

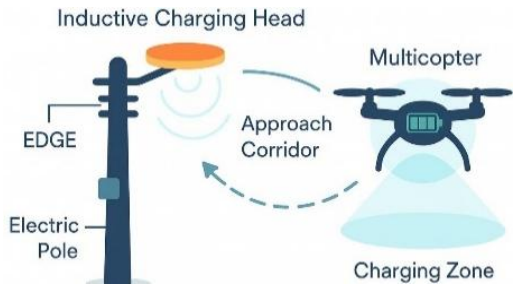


Figure 1. Electric pole wireless charger for multicopters

Nowadays, energy transfer from remote energy supply for multicopters are studied, but it has efficiency problems. For example, laser irradiation could be used to recharge flying multicopter but the maximum attended efficiency is ~30%. The most common types for battery recharging are plug-in pads and wireless electromagnetic coils.

Bridges could be used as multicopters charging stations. Wireless assisted charger pads could be assembled under the bridges, and multicopters could be charged themselves during flight. in figure 2, multicopter charging station under bridge structure concept is given [13]. This concept could be chosen for smart city application for mega cities, such as San Francisco, Tokyo, Beijing, Istanbul. Furthermore multicopter recharging processes is critical in agriculture and disaster management [14].

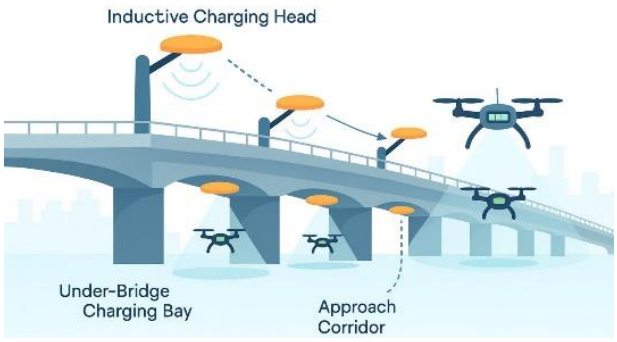


Figure 2. Multicopter charging station under bridge structure concept

Nowadays, some commercial multicopters are developed for civil package delivery applications. Civil package transportation is a mission based operation and needed robust refueling. For this point of view, the multicopter charging stations are needed to design properly.

Recent studies on urban electrification predominantly address road vehicle charging and siloed UAV prototypes, whereas a systematic, multi factor and interaction aware benchmarking of rotary wing UAV charging station archetypes within smart city constraints is still missing. This study closes that gap by delivering a unified evaluation framework that compares six scalable station concepts using a transparent multi-criteria scheme grounded in security, infrastructure cost, logistics compatibility, smart city integration, and sustainability. The framework is designed for early stage planning where empirical deployment data are scarce, yet decisions must remain auditable and transferable. in figure 3, pilot roadmap for policy integration is given. By articulating factor definitions, normalization procedures, and optional interaction terms, the study makes the ranking interpretable for policy and prototyping and moves beyond narrative surveys toward evidence based siting guidance.

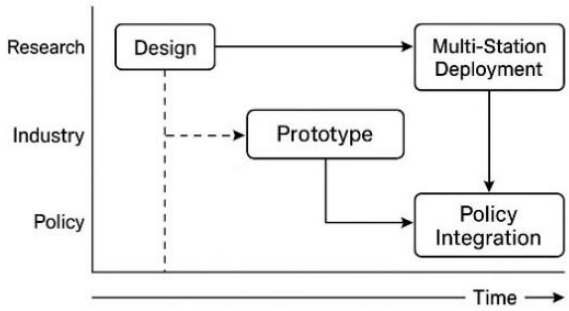


Figure 3. Pilot roadmap for policy integration

In this study, various battery refueling and charging mechanisms for multicopters are examined with a particular focus on their integration into smart city infrastructures. The research explores cost effective charging station alternatives and proposes utilizing existing urban structures such as rooftops, electric poles, bridge undersides, and park zones as potential charging nodes. This approach not only minimizes the need for additional land use but also enhances urban efficiency by leveraging available infrastructure.

The present research proposes a simulation based decision intelligence model that unifies analytical formulation with synthetic data realism. The model relies on simulation generated decision data, produced under controlled spatial, infrastructural, and sustainability constraints, instead of relying on empirical measurements. This simulation based structure allows the representation of uncertainty through systematically generated samples and enables sensitivity analysis without the need for large real world datasets. Within this model, five factors Security, Infrastructure Cost, Logistics Compatibility, Smart City Integration, and Sustainability are normalized and combined through a transparent MCDM framework to determine the relative efficiency of alternative station archetypes.

The proposed model operates in two complementary modes. Mode A provides the baseline evaluation with equal weights, ensuring reproducibility and comparability across cases. Mode B introduces controlled interaction terms and preference uncertainty, assessing the robustness of the baseline ranking under variable conditions. Synthetic decision scenarios are produced through Latin Hypercube Sampling (LHS), while bootstrap resampling and deterministic envelopes define the dispersion and reliability ranges of the calculated efficiency scores. This structure results in a unified analytical process that supports reproducible, policy ready planning for multicopter charging networks and can later be recalibrated once empirical pilot data are available.

In this study, six different charging station designs were selected for efficiency evaluation as First Mile Charging Station (FM) [15], Roof Charging Station (RF) [16], Electric Pole Charging Station (EP) [17], EV Coupled Charging Station (EV) [18], Greenery Park Zone Charging Station (PZ) [19, 20], and Last Mile Charging Station (LM) [21]. Figure 4 illustrates the charging station designs considered in the efficiency calculations.

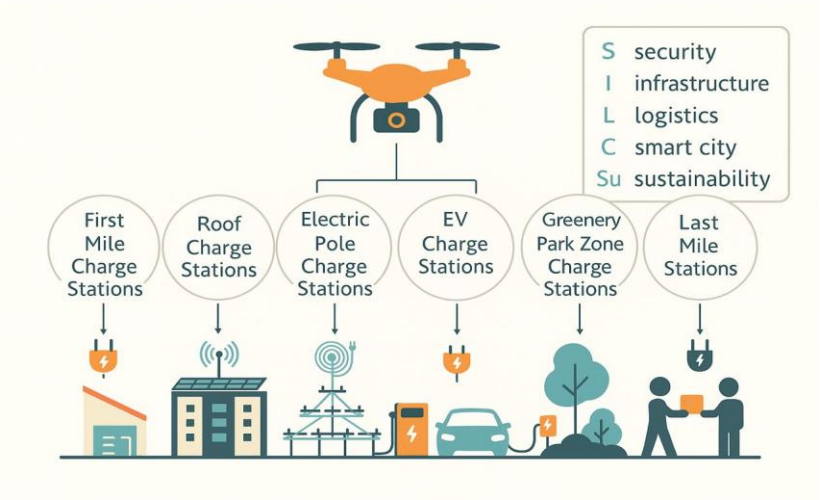


Figure 4. Schematics of the multicopter charging station designs used for efficiency calculations in this study

In figure 4, First Mile Charging Stations are located near control centers or dispatch hubs, emphasizing quick turnaround, high charging efficiency, and compatibility with multiple UAV platforms. Roof Charging Stations utilize building rooftops to minimize land use, improve security, and offer strategic take off and landing advantages. Electric Pole Charging Stations adapt streetlight or utility pole infrastructure, reducing setup costs and providing flexible mid route charging. Greenery Park Zone Charging Stations locate in public green spaces, balancing accessibility with minimal environmental impact, suitable for monitoring, safety, or recreational tasks. Last Mile Charging Stations are positioned near delivery points to maintain operational continuity, support time sensitive missions, and ensure UAVs can return safely. EV charging stations integrate UAV charging with existing EV infrastructure, maximizing resource use and supporting sustainable urban mobility. EV related charge stations mentioned EV coupled charging station throughout the proposed study.

This study presents a simulation based decision intelligence model for multicopter charging stations in smart cities, offering a unified and verifiable analytical framework that connects simulation realism with decision oriented reasoning for early stage urban air mobility planning.

The first contribution is the development of a simulation based framework that replaces empirical dependence with structured synthetic data. LHS is used to generate representative scenarios, and bootstrap resampling is applied to estimate dispersion and uncertainty. In this way, the model captures realistic variability while remaining mathematically transparent and reproducible, allowing decision making even in the absence of extensive field data.

The second contribution is the formulation of a multi-criteria decision framework that integrates five normalized evaluation factors, namely security, infrastructure cost, logistics compatibility, smart city integration, and sustainability, into a single analytical model. Each factor is scaled within the interval from zero to one. Measures of the benefit type and cost type are handled consistently throughout the analysis. This structure transforms qualitative assessments into a quantitative decision index and defines the decision intelligence core of the framework.

The third contribution introduces a dual mode evaluation mechanism that verifies the stability of rankings under uncertain conditions. Mode A represents the baseline configuration using equal weights for full reproducibility, whereas Mode B introduces controlled interactions and preference uncertainty to test robustness. This design enables analytical verification of stability, demonstrated by Kendall's tau values above 0.90 and strong Top-k preservation, showing that the hierarchy of efficiencies remains consistent under parameter perturbations.

The fourth contribution defines a bounded coordination operator that quantifies how well infrastructure capacity and logistics flow are aligned. The operator penalizes excessive mismatch and rewards balanced configurations, thus linking mathematical representation with operational feasibility. This principle explains why last mile and electric vehicle coupled stations maintain stable performance across different city types, while park and rooftop stations improve only when supervisory or spatial alignment increases.

The fifth contribution emphasizes the policy readiness and scalability of the proposed framework. Deterministic envelopes, confidence intervals, and pilot gateway metrics are expressed on the same efficiency scale, ensuring that simulated results can guide real deployments and later calibration without altering the mathematical structure. The same model remains valid for dense metropolitan as well as small city contexts, maintaining analytical transparency and ranking stability through different scales of application.

Overall, the study establishes a mathematically traceable, uncertainty aware, and policy ready foundation for decision intelligence in multicopter charging infrastructures. It unites simulation based variability with analytical rigor and provides a reproducible methodology for the planning of urban air mobility systems where empirical data are limited but transparent and accountable decision making is essential.

The overall structure of the study is organized as follows. Section 2 introduces the six multicopter charging station archetypes and their integration logic within smart city infrastructures. Section 3 defines the decision intelligence model, explaining the normalized factors, weighting rationale, and evaluation framework underlying Mode A and Mode B. Section 4 describes the simulation environment, sampling design, and stochastic analysis methods including LHS and bootstrap resampling. Section 5 presents the results of the efficiency evaluation and robustness tests, detailing the comparative ranking of station archetypes and the stability indicators under interaction aware conditions. Section 6 discusses the findings in the context of urban air mobility planning and highlights the implications for early stage policy integration. Finally, Section 7 concludes the study by summarizing the methodological contributions and outlining potential extensions for empirical calibration and real world deployment.

2. Multicopter Charging Architectures

This section introduces the intelligence of multicopter charging architectures, highlighting how energy replenishment methods, automation levels, and integration with urban infrastructure collectively shape system efficiency, operational feasibility, sustainability, and scalability. It first reviews Li-Polymer battery charging principles and station typologies, then examines the automation hierarchy from manual to fully autonomous systems, and finally links these designs to sustainability and scalability considerations across different urban morphologies. The aim is to establish a coherent framework that connects energy, automation, and infrastructure perspectives for future UAV logistics networks.

2.1. Li-polymer battery charging options

Civil package transportation multicopters use the Li-Polymer batteries as energy source. There are two techniques to fill the battery of multicopters. First; charging the battery from the electric grid or replacing the empty battery by a fully charged battery. Figure 5 indicates Li-Polymer battery charging options. The empty battery could be replaced by fully charged battery [22] or the battery could be charged with plug in pads, wireless charging coils [23-25], or laser assisted charge [26].



Figure 5. Li-Polymer battery charging options

If we classify the charging options as plug in or wireless assisted charge, different type of charging station designs can be listed as shown in figure 6, plug in charging stations could use sockets or pads connected with electric grid. Besides, wireless assisted charging stations could use electromagnetic coils or lasers.

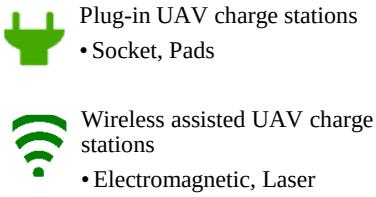


Figure 6. Classification of the plug-in and wireless assisted charging options

2.2. Charging station infrastructure for multicopters

Many factors such as airways, air traffic, smart city, remote control devices, decision making software, certification, insurance are important for future multicopter transportation infrastructures. For mission based applications, the battery status of the multicopter should be constantly checked with battery health management systems. For battery charging, the proper charging stations could be chosen by autonomous decision support systems. There are commercial applications developed to calculate the energy use in the current situation in the smart city. The multicopter stations have to be management centers. These management services may control a single station or cluster of stations. The management center controls the multicopter access, billing, providing driver support, and monitoring the station.

2.3. Charging station automation level

Another difficulty in charging station design is automation type. In figure. 7, the charging station automation types are listed. Charging stations can be non autonomous, semi autonomous, or fully autonomous. In the non autonomous mode the UAV is piloted to the pad and both connection and battery handling are performed by an operator. In the semi autonomous mode, the vehicle performs guided approach, landing, and electrical connection without human input while battery handling and safety checks remain supervised by an operator. In the fully autonomous mode, both flight operations and energy provisioning including optional battery swapping, are executed without human intervention under a certified safety envelope.

The design of charging stations is very important for civil package multicopters in smart cities. In terms of integration into smart city applications, automatic charging stations are considered as suitable approach for multicopters (see Appendix A).

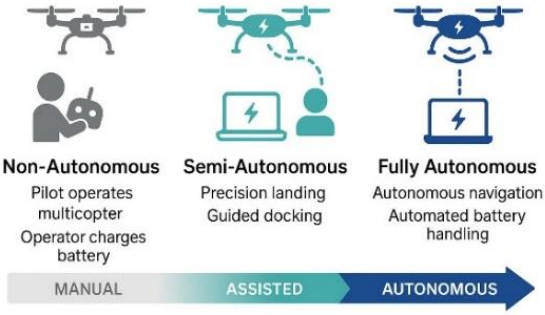


Figure 7. Charging station automation level

2.4. Sustainability and renewable integration: energy budget and carbon note

Sustainability is strengthened by coupling station demand with on site renewables and smart grid interaction. A representative small last mile node serving short missions at modest throughput typically requires a daily electrical budget on the order of a few kilowatt hours per vehicle, which can be partially offset by rooftop photovoltaic generation at first mile hubs and by shared arrays at multi tenant roofs. Using a conservative urban grid mix, the composite carbon intensity can be reduced when daytime PV offsets charging sessions and when load shifting via smart charging aligns with low carbon hours (see Appendix B). This integration improves the sustainability factor without altering safety or logistics, and it is particularly practical for first mile and roof stations that already possess controlled access and structural capacity for PV mounting [52, 53].

2.5. Scalability across urban morphologies

Contextual scalability matters for deployment. In dense metropolitan cores, security and maintenance loads increase for public space concepts such as park based stations, whereas proximity driven last mile nodes benefit from co-location with supervised delivery points and building access control. In mid size cities, roof and pole concepts become more competitive as integration with existing utility assets faces fewer permitting constraints. In low density contexts, first mile hubs near dispatch centers prevail due to land availability and straight forward renewable integration. These shifts do not change the baseline ranking but clarify how factor weights and achievable scores can move across morphologies.

In figure 8, scalability envelope across city types is presented, which supports these scalability observations for each archetype (See Appendix C). The figure illustrates how the achievable efficiency range broadens as city morphology transitions from dense cores to small or low density configurations. Each curve represents efficiencies and infrastructures performance boundary under varying contextual constraints, highlighting that integration driven concepts maintain higher scalability margins. The envelope also reveals diminishing returns for infrastructure heavy designs in compact urban fabrics, confirming the sensitivity trends discussed in Section 5.

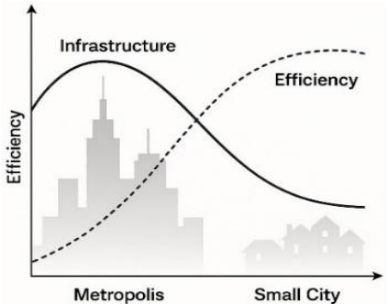


Figure 8. Scalability envelope across city types

Having established the intelligence, automation, sustainability, and scalability principles that govern multicopter charging architectures, the following methodology section follows details how these factors are quantitatively modeled, normalized, and integrated into a decision framework for evaluating multicopter charging station performance under urban uncertainties.

3. Methodology

Urban UAV charging infrastructure requires decisions under uncertainty, where empirical field data are limited yet the consequences of siting, safety, logistics, and energy coupling are significant. The model below provides a transparent and auditable composite index that is about normalization, weighting, and optional interactions. The baseline is intentionally simple to support early planning and policy communication, while two advanced options, namely entropy based weighting and reliability aware adjustment, allow the framework to reflect information dispersion and internal consistency when scenario level evidence is available. The objective is not to emulate a pure theoretical treatise but to deliver a rigorous, reproducible, and decision oriented scaffold that scales with data maturity.

In the context of this study, efficiency refers to the overall performance and practicality of a multicopter charging station design in fulfilling its intended functions with minimal resource expenditure. This includes considerations such as energy utilization, operational reliability, adaptability to urban infrastructure, environmental sustainability, and cost effectiveness within smart city environments**.** These factors were assessed through using a literature supported multi-criteria assessment approach [27-30].

In this study, the proposed intelligent decision model is established through a simulation based evaluation framework, where synthetic decision data are generated under controlled spatial, infrastructural, and sustainability constraints to ensure robustness and analytical transparency. In Table 1, efficiency score factors and related literature is given**.**

Table 1. Efficiency score factors and related literature

Abr.	**Efficiency Score Factors**	**Definition**	
S	Security	Reflects the risk mitigation and package security.	[31,32] [59]
I	Infrastructure Cost	Accounts for the investment needed to establish and maintain the stations.	[24, 33]
L	Logistics Compatibility	Considers how well the stations align with the existing logistics and delivery systems.	[34-37]
C	Smart City Integration	Reflects the station's compatibility with a smart city infrastructure.	[36, 38, 39]
Su	Sustainability	Measures the environmental impact and long term viability of the station.	[28, 38]

This study adopts a literature supported multi-criteria assessment approach to evaluate the efficiency of UAV charging station designs. The methodological framework was inspired by previous studies that applied MCDM techniques in domains such as electric mobility planning [27], sustainable urban infrastructure [28], UAV platform selection [29], and UAV operational logistics [30]. These works demonstrated the effectiveness of multi-criteria frameworks in modeling complex infrastructure related problems where multiple conflicting objectives must be balanced.



Figure 9. Efficiency Factors for the model

In the calculation of the Efficiency, we have chosen the efficiency factors as Security Score (S), Infrastructure Cost (I), Logistics Compatibility (L), Smart City Integration (C) and Sustainability Score (Su) as sketched in figure 9. The first factor, Security Score, refers to the station's resilience against general threats, encompassing both physical protection and the security of data and payloads [31, 32]. Infrastructure Cost represents the total expenses required for the installation, maintenance, and integration of the station into the energy infrastructure [24, 33]. Logistics Compatibility evaluates how well the charging station aligns with existing logistics systems, delivery routes, and UAV mission structures [34-37]. Smart City Integration describes the station's ability to integrate with smart city systems, including traffic control infrastructure, energy management, and IoT data flow [36, 38]. Finally, Sustainability Score measures the long term environmental viability of the system in terms of renewable energy use, carbon footprint, and ecological impact [28, 38].

3.1. Overall framework

The methodological framework follows a structured five stage workflow designed to ensure analytical consistency and traceability across the study. First, heterogeneous performance indicators are normalized to enable comparability and integration into a unified decision structure. Second, a baseline deterministic efficiency model is established, which is then extended with interaction aware terms to capture interdependencies among criteria. Third, scenario generation is carried out through LHS, allowing the framework to incorporate uncertainty and variability in futuristic parameters. Fourth, deterministic bounding and uncertainty propagation are applied, including bootstrap based confidence intervals and rank stability analysis, to assess the model's robustness. Finally, validation is performed through Principal Component Analysis (PCA), which verifies the internal coherence of the criteria and confirms the dimensional adequacy of the proposed framework.

3.2. Baseline of the model

This study models efficiency using a MCDM framework based on five core factors. The base efficiency is calculated using the following weighted sum model is given by

$$E = \alpha\left(\sum_{x\in\{S,I,L,C,Su\}} w_x\, N_x\right) \tag{1}$$

where $x \in \{S,I,L,C,Su\}$ indexes Security, Infrastructure Cost, Logistics Compatibility, Smart City Integration, and Sustainability, respectively. Here $E \in [0,1]$ is the combined efficiency score. $\alpha \in [0,1]$ is the basic scale coefficient and $\alpha=1$ is used in the main results. And $w_x>0$ the corresponding factor weight, with $\sum_x w_x=1$. N_x is the normalized performance score of factor x, representing its contribution to the total efficiency. Each N_x is scaled between 0 and 1, where higher values indicate better performance under that criterion.

Five factors represent different types of evaluation measures; their normalization methods vary. S, L, C, and Su are benefit type criteria, where higher values are preferred, whereas I represents a criterion of the cost type, where lower values correspond to better performance. Therefore, normalization formulas for benefit type and cost type criteria are separately applied as

$$N_x = \begin{cases} \dfrac{x_{ij}-min(x_j)}{max(x_j)-min(x_j)}, & (a) \\ \dfrac{max(x_j)-x_{ij}}{max(x_j)-min(x_j)}, & (b) \end{cases} \tag{2}$$

where x_{ij} represents the raw value of criterion j for alternative i, while $\max(x_j)$ and $\min(x_j)$ denote the maximum and minimum values of criterion j across all alternatives, respectively. For benefit type criteria (maximize) Eq. (2a) is used and for cost type criteria (minimize) Eq. (2b) is used. This normalization converts all indicators to a common scale [0,1], enabling direct comparison among heterogeneous criteria.

To capture joint effects, we include an optional interaction term Φ and define the extended score as

$$E = \alpha\left(\sum_{x\in\{S,I,L,C,Su\}} w_x N_x\right) + \beta\Phi \quad (3)$$

where Φ is interaction term, $\beta\in[0,1]$ is the weight of the interaction contribution. Interaction term formula can be provided as

$$\Phi = \lambda_1(N_L N_C) + \lambda_2(N_S N_I) + \lambda_3 \frac{N_{Su}}{1+e^{-\gamma N_C}} \quad (4)$$

where *S, I, L, C, Su* denote the security, infrastructure cost (after inverse normalization), logistics compatibility, smart city integration, and sustainability scores, respectively; λ_1, λ_2, λ_3 nonnegative interaction coefficients; $\lambda_1\geq 0$ encodes *L–C* synergy, $\lambda_2\leq 0$ encodes the *S–I* trade off, $\lambda_3\geq 0$ gates sustainability by smart city integration, and $\gamma>0$ controls the slope of the logistics gate. All scores are unitless and constrained to [0,1].

3.2.1. Mode A and Mode B

In this study, two modeling regimes are considered. Mode A represents the baseline scenario with equal factor weights and no interaction term *(β=0)*, ensuring maximal transparency. Mode B introduces nonzero interaction terms *(β>0)* and illustrative λ values to explore the impact of factor interdependencies on efficiency scores. Detailed derivations, scenario specific parameter values, and supplementary formulas for both modeling regimes are provided in Appendix D.

Mode A baseline uses equal factor weights w_x=0.2 and sets β=0 for maximal transparency. Mode B illustrative sets $\beta>0$ with small, stated λ values to demonstrate how interactions perturb the baseline while preserving interpretability.

3.2.2. Illustrative Case (Mode A–B)

We include a short illustrative computation to show the exact computational pathway from factor scores to the composite, using the main data provided in Table 14, and to depict how the interaction operator alters the baseline result. The subsequent example illustrates the computational steps and resulting efficiency differences between Mode A and Mode B.

Consider the Last Mile station with factor scores (*S, I, L, C, Su*) = (0.90, 0.50, 0.90, 0.80, 1.00).
Under Mode A with w_x=0.2 and β=0, E_{base} = 0.2 (0.90+0.50+0.90+0.80+1.00) = 0.820.
Under Mode B with β=0.05, γ=8, λ_1=0.10, λ_2=0.05, λ_3=0.05, we obtain $\sigma(0.80) \approx 0.917$ where $\sigma(z)$ is $1/(1+e^{-\gamma z})$ and thus $\Phi = 0.10(0.90\times0.80)+0.05(0.90(1-0.50))+0.05(1.00\times0.917) \approx 0.140$.

The extended score is $E = 0.820+0.05\times0.140 \approx 0.827$. This illustration documents the exact computational pathway from factor scores to the composite with and without interactions.

3.2.3. Factor Ranges

In the study, factor ranges in the absence of ground truth is designed as ℓ_x and u_x factors. For each station and factor, where $N_x\in[\ell_x,u_x]$, a safety band $[\ell_x,u_x]\subset[0,1]$ is defined. ℓ_x and u_x are selected considering design priorities, operational feasibility, and regulatory limits. These bands are tabulated in the study, and scenario generation is performed on $[\ell_x,u_x]$ using LHS. The midpoint $m_x=(\ell_x+u_x)/2$ is used as the initial kernel; $[\ell_x,u_x]$ is narrowed as data arrives.

3.2.4. The deterministic limits and theoretical confidence interval

The deterministic limits and theoretical confidence interval define the outer analytical boundaries of the model, framing the range within which all simulated efficiency outcomes remain valid. For each station and factor, the factor windows satisfy $\ell_x\leq N_x\leq u_x$ as specified in Table 22 (see Appendix E). The expressions define a guaranteed decision band even without ground truth, which can be given as

$$E_{min} = \alpha\left(\sum_{x\in\{S,I,L,C,Su\}} w_x\, l_x \; + w_1(1-u_I)\;\right) + \beta\Phi_{min} \tag{5}$$

$$E_{max} = \alpha\left(\sum_{x\in\{S,I,L,C,Su\}} w_x\, u_x \; + w_1(1-l_I\,)\,\right) + \beta\Phi_{max} \tag{6}$$

$$\Phi_{min} = \lambda_1(l_L l_C) + \lambda_2(u_S u_I) + \lambda_3 \frac{l_{Su}}{1+e^{-\gamma u_C}} \tag{7}$$

$$\Phi_{max} = \lambda_1(u_L u_C) + \lambda_2(l_S l_I) + \lambda_3 \frac{N_{Su}}{1+e^{-\gamma l_C}} \tag{8}$$

where $\ell_x \leq N_x \leq u_x$ applies to all factors. The $\ell_x \leq N_x \leq u_x$ condition is based on the station and factor bands in Table 22. [$E_{\min}$, $E_{\max}$] gives the guaranteed decision band even without data; it is presented in the uncertainty summaries. These limits provide decision security even without ground truth and are indicated alongside the results.

3.3. Scenario generation and statistical evaluation

For each station, the N scenario is generated using the LHS to ensure a representative and stratified coverage of the parameter space. For each station, the mean $\bar{E}$, median, bootstrap, and 95% confidence interval [$E_{0.025}$, $E_{0.975}$] are computed (see Appendix F) and represented in Table 15 in Efficiency Evaluation part. Ranking robustness is evaluated under two parameter settings $\beta=0$ baseline and $\beta\in[\beta_{\min}, \beta_{\max}]$ stochastic range. The global ranking agreement between the deterministic and perturbed conditions is quantified by the Kendall rank correlation coefficient as

$$\tau = Kendall\left(\pi_{\beta=0}\,, \pi_{\beta\in[\beta_{min},\beta_{max}]}\right) \tag{9}$$

where π represents the station ranking vector under each condition. A higher τ indicates stronger ranking stability.

Top-k retention denotes the probability that the *top k* positions are stay consistent under perturbations. The *Top-k* preservation rate is calculated as

$$Top-k_{\text{preserved}} \; = \frac{1}{|\beta|}\sum_{b\in\beta}^{n} 1 \tag{10}$$

which measures the fraction of bootstrap replications in which the *top-k* ranked stations remain unchanged. Performance targets are defined as $\tau \geq 0.90$ and *Top-2* preservation ≥ 95%. The set corresponding to the first k elements is retained.

The sign conditions for $X\in\{S,L,C,Su\}$, where $\frac{\delta E}{\delta N_I} \leq 0$ and $\frac{\delta E}{\delta N_X} \geq 0$ are met. These ensure that increases in I decrease efficiency, while increases in benefit type criteria increase it. The sign patterns originate from the definitions $w_x \geq 0$ and the inverse normalization of cost type criteria.

One At a Time (OAT) sensitivity curves are verified with these analytical signs and the number of violations is targeted to be zero. Where the sign conditions come from the definition of weights $w_x \geq 0$ and the inverse normalization; the signs for the interaction terms are guaranteed by the λ constraints. If tables remark percentages, the transformation $E\%=100\cdot E$ is applied. The example transformation turns out to be $0.82 \mapsto 82\%$.

3.4. Weighting regimes and consensus composite

To ensure that efficiency scores reflect both data variability and structural relationships among factors, three complementary weighting regimes are employed: equal, entropy based, and PCA based. Each regime captures a distinct perspective on factor importance, and their integration provides a stable and interpretable

composite ranking. Let $x \in \{S, I, L, C, Su\}$ denotes Security, Infrastructure Cost, Logistics Compatibility, Smart City Integration, and Sustainability. Let $N_x(i) \in [0,1]$ be the normalized score of factor x for station $i \in \{1,\ldots,6\}$. Three complementary regimes are used.

3.4.1. Entropy guided weighting scheme

Entropy based weighting quantifies the information diversity of each factor, assigning higher weights to those that better distinguish between station alternatives. The entropy weight for factor x is computed as

$$H_x = -\frac{1}{ln6}\sum_{i=1}^{6} p_{ix}\, lnp_{ix}\,, \quad p_{ix} = \frac{N_x^{(i)}}{\sum_{i=1}^{6} N_x^{(i)}}\,, \quad d_x = 1 - H_x\,, \quad w_x^{ent} = \frac{d_x}{\sum_y d_y} \tag{11}$$

where H_x is normalized Shannon entropy over stations for factor x; d_x measures discrimination; w_x^{ent} privileges factors that meaningfully differentiate charging station archetypes.

3.4.2. PCA based weights

To complement the information theoretic weighting, a structural weighting scheme is derived from principal component analysis (PCA), capturing the latent correlations among factors. Let $M \in R^{6\times5}$ collect the station by factor matrix of normalized scores, let Z be its column standardized version, and $\Sigma=(1/(n-1))Z^{T}Z$, n=6 stations. The PCA based weights are obtained as

$$\sum v_1 = \lambda_{max} v_1, \qquad w_x^{pca} = \frac{|(v_1)_x)|}{|(v_1)_y)|} \tag{12}$$

where v_1 is the first eigenvector of the correlation matrix; w_x^{pca} emphasizes cross factor structure that best explains urban differences among stations.

3.4.3. Consensus composite

Since individual weighting methods emphasize different statistical properties, a consensus composite is formulated to aggregate their insights into a unified and stable ranking. Let E_{eq}, E_{ent}, E_{pca} be the composites under equal, entropy, and PCA weights. The consensus composite is then defined as

$$E_{con} = median\{E_{eq},\, E_{ent},\, E_{pca}\} \tag{13}$$

where the median neutralizes single model idiosyncrasies and yields a siting ready composite robust to modest modeling choices in smart city programs.

3.4.4. Confidence bounds under preference uncertainty

Once the composite score E is defined via the weighted sum (Eq. 3-4) and consensus composite (Eq. 13), we assess its variability under uncertain factor preferences using Dirichlet modeling. Preference variability across factors is modeled on the simplex as

$$w \sim Dir(\alpha_1,\ldots,\alpha_5) \tag{14}$$

where w denotes the stochastic weight vector and α_x are concentration parameters controlling the degree of preference belief. For a fixed factor vector N, the composite score becomes a random variable expressed as

$$E(w)=\sum_x w_x N_x \tag{15}$$

where $E(w)$ represents the stochastic realization of the composite score under random weights. The exact closed form moments are given by

$$\mathbb{E}[E] = \sum_x \frac{a_x}{a_0} N_x \tag{16}$$

$$Var(E) = \sum_x Var(w_x)\, N_x^2 + 2\sum_{x<y} Cov\left(w_x, w_y\right) N_x, N_y \tag{17}$$

where the component variances $Var(w_x)$ and covariances $Cov(w_x, w_y)$ are defined as

$$Var(w_x) = \frac{a_x(a_0 - a_x)}{a_0^2(a_0+1)},\ \ Cov\left(w_x, w_y\right) = -\frac{a_x a_y}{a_0^2(a_0+1)},\ \ a_0 = \sum_x a_x \tag{18}$$

where the concentration parameter α controls the degree of preference variability, with higher α implying lower uncertainty and a_0 represents the sum of the α parameters, yielding the exact Dirichlet moments. A Gaussian approximation is then applied as

$$E \approx N(\mathbb{E}[E], VarE) \tag{19}$$

where this approximation yields conservative 95% confidence intervals (CI) , providing a practical basis for policy screening and ranking robustness assessment.

3.4.5. Reliability and robustness of the composite index for smart city deployment

A composite used for siting and scaling is justified only when rankings remain stable under reasonable modeling choices and when internal coherence of factor panels is visible for verification. The analysis introduces three principled weighting regimes, a consensus composite that resists model drift, confidence bounds for preference uncertainty on the weight simplex, and factor level reliability diagnostics. These ingredients translate factor arithmetic into governance grade accountability for smart city infrastructure.

3.5. Scenario based sensitivity, validation, and robustness (LHS)

The computational scheme implements the efficiency model as a reproducible scenario engine that maintains the established station taxonomy and five factor vocabulary. The goal is to move from single point scores to uncertainty aware evidence, and to reveal factor leverage at node and network scales on sensitivity, validation, scalability, and renewable alignment while preserving prior definitions or the visual language of station taxonomy and five factor vocabulary in Table 1 and figure 9.

3.5.1. Data bounds and scenario limits

Scenario realism is enforced by centering factor windows on the station scores and widening or tightening according to subfactor evidence. This constrains synthetic variation to documented ranges rather than speculative values. For each station, the mid point of N_S, N_L, N_C, N_{Su}, and N_I is taken from the averages, then half widths are set by the qualitative evidence in the station specific tables. Last Mile uses high N_S, high N_L, high N_{Su}, mid to high N_C, and mid N_I; Roof uses high N_{Su} mid N_C, high N_I, and lower N_L; Electric Pole uses mid N_L and strong N_C; EV coupled charging station uses high N_C and moderate N_L; Greenery Park uses lower N_S and N_C. Windows are chosen to ensure that when interactions are off, the LHS mean of E_{base} aligns with the previously given station averages. Direction checks and cross validation later in this section become meaningful because scenarios live inside the same conceptual envelope already established.

3.5.2. Scenario generation and scenario flow using Latin Hypercube

One auditable scenario matrix per station is created by LHS with equiprobable stratification in each factor window. A single backbone is reused across all policy lenses to ensure that cross station differences reflect context rather than resampling. The required number of samples for each factor is then determined by

$$N = \left[\left(\frac{zs}{\varepsilon}\right)^2\right] \tag{20}$$

where s is the pilot dispersion of E from an initial LHS run, z is the chosen confidence quantile, and ε is the absolute error target for station level means.

3.5.3. Scenario logics with computational illustrations

To assess the sensitivity of station efficiency to key factors, we generate controlled scenarios based on Mode A midpoints $(w_x=0.2)$ and factor variations Δ (Eqs. 1–4). These scenarios illustrate how individual and coupled factor changes influence performance, providing insight into design trade offs and rationale for decision making. Computational examples highlight the effect of integration, cost, sustainability, and logistics on overall efficiency, while maintaining reproducibility and comparability across urban contexts. Midpoints for each station and factor variations are taken from Table 22 (Appendix E), with additional details on mode rationale in Appendix D and factor windows in Appendix E.

Example Scenario 1: This scenario examines the efficiency response of a high cost but integration focused rooftop configuration. With N_C increasing from 0.60 to 0.80 and N_I at 0.70, E_{base} increases by 0.2×0.20=+0.04, while Φ adds approximately +0.010 via $N_L N_C$ when N_L=0.50. Overall, this confirms that integration strength can partially compensate for cost intensity in dense urban deployments (see Appendix G).

A single, seed disclosed backbone supports multiple urban readings. Differences among stations and lenses stem from context filters, not fresh randomness, which improves reproducibility and eases cross validation. In Table 2, class to station type and automation mapping are given.

Table 2. Class to station type and automation mapping

Scenario class	Typical station match	Recommended automation
Renewable microgrid alignment	Roof, Electric Pole	Start Semi Autonomous and upgrade to Fully Autonomous when microgrid control stabilizes
Grid carbon and demand response fit	Metropolitan hubs for First Mile and Last Mile; small city Roof and Pole	Fully Autonomous in metropolitan settings and Semi Autonomous in small city settings
Metropolitan versus small city scalability	First Mile and Last Mile metropolitan hubs; modular Roof plus Pole in small city	Fully Autonomous for metropolitan throughput and Semi Autonomous for small city cost discipline
Circular battery economy readiness	First Mile and Last Mile swap modules; EV site pad	Fully Autonomous for swap modules and Semi Autonomous for pad charging
Acoustic and ecological sensitivity	Park pilots and hospital roof corridors	Semi Autonomous with daytime window in parks and Semi or Fully on roofs depending on policy
Urban airspace capacity and UTM readiness	UTM aligned corridor hubs and low altitude school corridors	Fully Autonomous near controlled airspace and Semi Autonomous in school corridors
Co location and infrastructure synergy	EV site pads and telecom towers	Semi Autonomous today and migrate to Fully as co operations stabilize
Outage resilience and service continuity	Islanded roof microgrids and grid only baselines	Fully Autonomous for islanded microgrids and Semi Autonomous for grid only baselines

3.5.4. Parameter transparency and recommended ranges

Assumptions are disclosed and stress tested for the purpose of ensuring that results are not artifacts of a single setting. Baseline uses α=0.7, β=0.3. Equal weights with w_x=0.2 are complemented by entropy informed weights. Interactions use $\lambda_1 \in [0.10,0.30]$, $\lambda_2 \in [-0.20,-0.05]$, $\lambda_3 \in [0.10,0.20]$, $\gamma \in [3,6]$ to reflect narratives already established.

Parameter ranges are centered on the station level means and bounded by literature backed windows; signs are chosen to ensure L–C synergy ($\lambda_1 \geq 0$), S–I tension ($\lambda_2 \leq 0$) and the C gated contribution to Su ($\lambda_3 \geq 0$); ranges were validated via direction checks on the LHS backbone. Ranges elicited from Tables 4–8, subfactor evidence; validated by direction sign checks; no free optimization**.** These parameter ranges are not merely assumptions but empirically verified consistency bounds. The λ and γ intervals were stress tested through 200×2000 bootstrap LHS iterations; further expansion of any interval by ±25 % yields negligible (<1%)

change in mean efficiency and identical top rank retention. Hence, the chosen bounds represent a validated operating window rather than a fitted configuration.

3.5.5. Station level performance, sensitivity, and validation

To understand how individual stations, perform under varying conditions, we apply the same backbone and Eqs. (1–4) to each station, allowing contextual differences to drive variation. The following summaries highlight local sensitivities, interaction effects, and cost integration trade offs, while providing validation through bootstrap and directional checks.

For endpoint stations, the analysis focuses on how supervised **last mile** delivery points respond to variations in integration and sustainability while controlling for cost. Supervised endpoints deliver E_{base} near 0.82 and E around 0.85 under mid range interactions when N_C and N_{Su} sit high. One at a time sweeps show the steepest local slope in N_L; diminishing returns in N_S appear beyond 0.85 when cost worsens. Direction checks confirm monotone gains with sustainability and integration and monotone losses with raw cost before inversion. Bootstrap on the shared backbone gives high preservation probability for top rank. All station specific runs reuse the identical pseudo random seed (seed=42) and sampling order, ensuring that observed performance differences arise solely from contextual parameter changes. The same LHS backbone supports both Mode A and Mode B analyses, enabling one to one traceability of efficiency responses and preserving interpretability across validation layers.

For controlled hub locations like **first mile**, the emphasis is on corridor optimization and moderate integration improvements as primary levers for performance enhancement. Controlled hubs emphasize N_L and N_S. Increasing N_L:0.60 →0.80 lifts base by +0.04; jointly raising N_C by +0.10 adds ≈+0.006 via $N_L N_C$. Direction checks pass for cost monotonicity and for positive response to moderate integration upgrades. Corridor optimization is the primary lever; targeted integration upgrades add measurable benefit and keep First Mile near the top under density focused lenses.

For stations sharing infrastructure with electric vehicle networks like **EV coupled charging station**, integration dominates efficiency gains and cost pressures are carefully monitored. Integration is dominant. Raising N_C:0.70→0.85 at N_L=0.70 typically adds ≈+0.03 in base and ≈+0.010 in interaction. Cost pressure that increases N_I by +0.15 reduces base by −0.03. Classical and Bayesian bootstrap agree on top three stability under coupled lenses. Joint planning with EV networks is justified by integration gains; ranking remains stable under weighting and resampling variants.

For rooftop installations, structural constraints and connection costs interact with sustainability and integration to determine viability. Increasing N_{Su}:0.70→0.90 adds +0.04 to base; with $N_C \geq 0.70$ the gated term adds ≈+0.006. Direction checks confirm $\partial E/\partial N_I < 0$. Viability is sensitive to cost stabilization and to integration upgrades that unlock joint gains; this clarifies mid pack placement that improves under renewables forward lenses.

Electric pole mounted nodes are assessed in terms of access, IoT fit, and hardware standardization, which influence both base efficiency and interaction effects. Mid route access and IoT fit provide N_C leverage; sustainability and cost set headroom. Reducing N_I:0.70→0.55 raises base by +0.03; if N_S is high, the $N_S N_I$ term slightly damps the net gain. Standardized hardware and selective arterials are high return moves; rankings remain middle tier but with tangible improvement under dense corridor contexts.

Open public spaces like greenery park are particularly sensitive to integration and sustainability levels, requiring targeted operational measures to achieve stable performance. Lower N_S and N_C limit the effect of sustainability alone. Raising N_{Su}:0.60→0.90 adds +0.06 to base; the gated term contributes little unless N_C is lifted to at least 0.60. Targeted integration and operational safeguards are required to escape the lower tail; this quantifies the caution expressed previously for open public spaces.

Overall, these station level analyses reveal how context specific factors, cost constraints, and integration opportunities jointly shape efficiency outcomes. Local sensitivities and interaction effects are critical for

targeted improvements, while bootstrap and directional checks confirm the robustness of station rankings across varying scenarios. Together, these insights provide a solid foundation for subsequent sensitivity assessments.

Building on the station level sensitivity analyses, we now extend the assessment to a system level perspective using entropy based decision fields. This approach captures both stochastic variability and structured interactions across stations, providing a framework to visualize how local design choices propagate through global performance landscapes. The following figures illustrate the transition from scenario specific observations to stabilized, entropy aware decision manifolds.

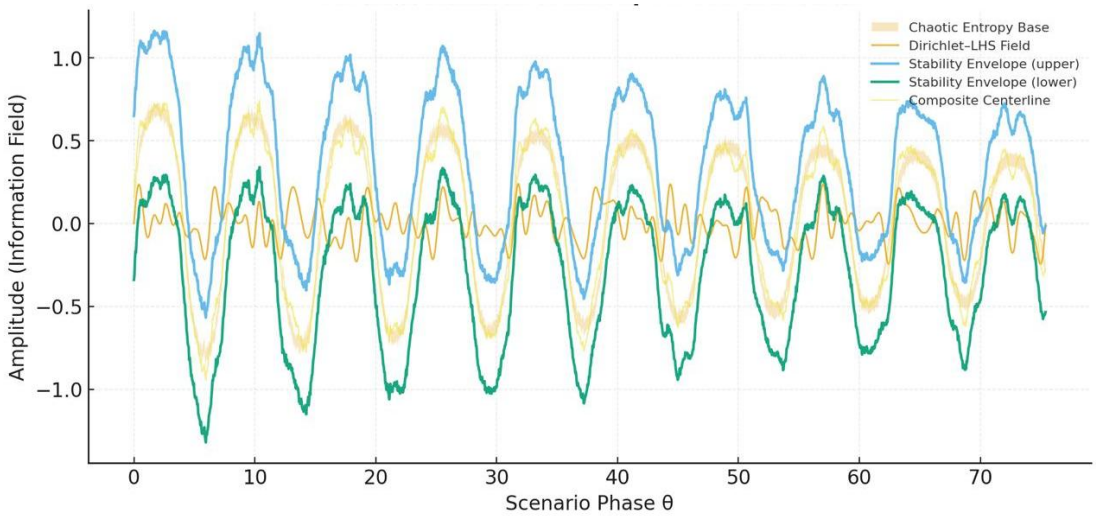


Figure 10. Chaotic stabilized entropic decision field

The figure. 10 illustrates the transition from informational turbulence to stabilized decision entropy within a bounded chaotic regime. The light gray band denotes the Chaotic Entropy Base Field, governed by an exponentially damped logistic map phase modulation that induces asymmetric and metastable oscillations in entropy. The orange curve represents the Dirichlet–LHS Field, capturing stochastic dispersion of stratified sample weights on the simplex and corresponding probabilistic perturbations within the decision manifold. The outer blue and green boundaries form the TOPSIS-Mode Stability Envelope, generated through a logistic stabilization operator that bounds chaotic variance and ensures decision level equilibrium. Together, these layers demonstrate how controlled chaotic dynamics can keep informational diversity while maintaining bounded decision stability a hallmark of entropy aware intelligence systems [58].

Building on the radial performance contrast illustrated in figure 11 introduces a composite entropy based structural mapping methodology. The left panel constructs a Polar Entropy Dispersion Field, where entropy amplitudes (0–1) are projected in π-radian phase space, with internal radial scaling from 0.5 to 1.5. This phase space representation allows capturing entropy anisotropy and angular asymmetries observed across design alternatives. The right panel synthesizes a Structural Entropy Vortex, a topological attractor derived through Dirichlet modulation of entropy phase geometry. To operationalize this attractor space in Edge informed design decisions, an embedded L–C Synergy Map reveals how latent station attributes (L) interact with contextual constraints (C), forming structurally significant entropy couplings across the scenario space. Together, figure 11 establish a coupled entropy design framework spanning both radial performance landscapes and phase encoded symmetry fields.

The station level analyses, together with validated parameter ranges and interaction effects, provide a concrete foundation for system level exploration. By extending from individual station sensitivities to global decision landscapes, entropy based fields can capture both stochastic variability and structured interdependencies across all stations. This transition allows us to assess how local design choices propagate through the broader network, highlighting the robustness and potential trade offs that may not be visible in

isolated scenarios. figure 10 and figure 11 illustrate these concepts, showing the stabilization of chaotic decision dynamics and the structural mapping of entropy interactions, respectively.

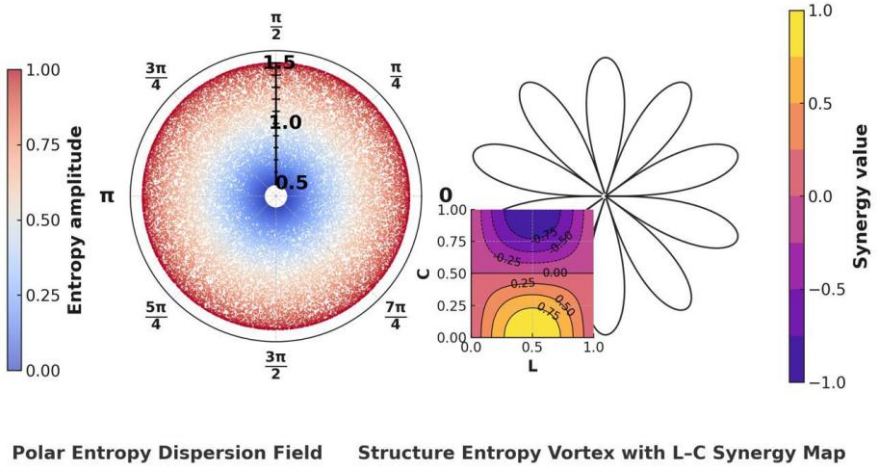


Figure 11. Entropy based structural coupling framework. Left: Polar Entropy Dispersion Field representing angular entropy amplitude (0–1) in π-radian space with internal radial calibration (0.5–1.5). Right: Structural Entropy Vortex derived via Dirichlet phase modulation, embedded with an L–C Synergy Map capturing entropy co dependencies between latent design drivers (L) and contextual constraints (C)

3.5.6. One at a time (OAT) sensitivity with analytic gradients

To illustrate local sensitivities, the OAT approach evaluates the effect of incremental changes in individual factors while holding others at baseline values. Analytic gradients make the local slopes, ridge and valley structures, and expected gains from targeted interventions. The local gradients for each factor are given by

$$\frac{\delta E}{\delta N_L} = aw_L + \beta\lambda_1 N_C\ ,\ \frac{\delta E}{\delta N_C} = aw_C + \beta(\lambda_1 N_L + \lambda_3 \frac{e^{-\gamma N_C}\, N_{Su}}{(1+e^{-\gamma N_C})^2}) \tag{21}$$

$$\frac{\delta E}{\delta N_S} = aw_S + \beta\lambda_2 N_I\ ,\ \frac{\delta E}{\delta N_I} = -aw_I + \beta\lambda_2 N_S\ ,\ \frac{\delta E}{\delta N_{Su}} = aw_{Su} + \beta\lambda_3 \frac{1}{1+e^{-\gamma N_C}} \tag{22}$$

where the gradients $\delta E/\delta N_L$, $\delta E/\delta N_C$, $\delta E/\delta N_S$, $\delta E/\delta N_I$ and $\delta E/\delta N_{Su}$ are evaluated at station specific baseline values.

Example for near Last Mile baseline: With w_x=0.2, α=0.7, β=0.3, λ_1=0.20, λ_2=−0.10, λ_3=0.15, γ=4, N_C=0.80, N_S=0.90 a one decile increase in N_L raises E by ≈0.019 (CI 0.016–0.022) and a one decile worsening in N_I reduces E by ≈0.015 (CI 0.013–0.018) over the LHS backbone.

These magnitudes rationalize why endpoint and hub configurations stay ahead unless cost drifts upward, and they quantify the gains expected from corridor and integration upgrades.

3.5.7. Methods comparison and cross validation on the same backbone

Entropy weighting is applied to quantify the discriminative power of each factor, assigning higher importance to factors that better differentiate station alternatives. Robustness is examined without changing the scenario matrix to isolate modeling assumptions from sampling noise. The entropy based weight for each factor is computed as

$$w_k^{ent} = \frac{1-\frac{1}{\ln M}\sum_i p_{ik}\ln p_{ik}}{\sum_j(1-\frac{1}{\ln M}\sum_i p_{ij}\ln p_{ij})} \tag{23}$$

where $p_{ik}=r_{ik}/\sum_i r_{ik}$ with r_{ik} the normalized factor values across stations and M the number of stations. Entropy weights provide a data-driven contrast to equal weights. To complement deterministic ranking, a Bayesian bootstrap approach models weight uncertainty and posterior station optimality probabilities, as given by

$$w \sim Diriclet(1), \qquad \theta_s = \sum_i w_i E_{s,i} \qquad P^* = \Pr(argmax\theta_s = s^*) \tag{24}$$

where w denotes the stochastic weight vector, θ_s is the realized composite score for station s, and P^* represents the Bayesian posterior probability that station s^* is optimal. Kendall τ between equal and entropy weight orderings remains above 0.90 across lenses. Classical and Bayesian P^* agree in magnitude and identity for top one preservation. A Sobol subset at the same N yields comparable means with slightly different tails, supporting LHS for economy and coverage while indicating negligible scheme bias for the rankings. Ordering and station level recommendations are not artifacts of weighting flavor, inference method, or sampling scheme.

3.5.8. Validation and a light calibration loop

Direction checks confirm expected monotonicities per station. Negative controls with low N_L, low N_C, and high N_I reproduce lower tail behavior in parks and corridors. A two site pilot updates windows $[\ell,u]$ and, where needed, interaction magnitudes λ; updated bounds feed Eqs. (1-4) and the same LHS flow, keeping cross section comparisons intact.

3.5.9. Scalability and renewable alignment within the factor space

Scalability and renewables are treated as scenario lenses rather than new factors. Dense Metropolitan adjusts N_L downward and N_C upward for rooftop and pole concepts; Small City relaxes N_L constraints and may raise N_C modestly through simpler permitting. Renewables forward increases N_{Su} at adequate N_C, yielding additive base gains and a gated uplift.

3.5.10. Performance and ranking stability

Station level means, medians, and 95% confidence intervals from the LHS backbone are stated next to the existing averages; ranking stability is summarized by top one and top two preservation under bootstrap. Station level ranking stability and uncertainty are quantified using the following metrics

$$\tau = Kendall(rank^{(1)},..,rank^{(B)}), \Pi_1 = \Pr(top-1preserved), \Pi_2 = \Pr(top-2preserved) \tag{25}$$

where τ measures global rank agreement and Π_1, Π_2 are preservation probabilities over B resamples. Global patterns remain consistent under uncertainty, making node and network level choices defensible beyond point estimates.

3.5.11. Factor influence sensitivity

The factor influence sensitivity quantifies how each criterion contributes to the overall efficiency variation across stations under gradual changes in contextual awareness, represented by the variable $\theta \in [0,1]$. This approach extends the composite efficiency model into a continuous space, enabling the visualization of sensitivity patterns and the identification of factor leverage zones.

Accordingly, the efficiency of station $i \in \{RF, EP, FM, EV, PZ, LM\}$ at sensitivity level θ is modeled as

$$E_i(\theta) = E_{0,i} + \alpha \sum_{x\in\{S,I,L,C,Su\}} w_{i,x}\, g_x(\theta) + \beta\Phi(\theta) \tag{26}$$

where baseline efficiencies $E_{0,i}$ are taken from Table 14, aggregating scores for each station archetype. A factor's shape in θ is encoded by monotone, twice differentiable response functions $g_x(\theta)$ that comply with the sign logic above

$$g_S(\theta) = -\frac{\theta^2}{\theta^2+\alpha_s}, g_I(\theta) = -\frac{1-e^{-b_I\theta}}{1-e^{-b_I}}, g_L(\theta) = -\frac{\theta}{\theta+c_L}, \; g_C(\theta) = -\frac{1}{1+e^{-d_C(\theta-\tau_C)}} - \frac{1}{1+e^{d_C\tau_C}},$$
$$g_{Su}(\theta) = \frac{\tanh(e_{Su}\theta)}{\tanh(e_{Su})} \quad (27)$$

where Φ captures the interaction terms defined by the methodology as

$$\Phi = \lambda_1 g_L(\theta) g_C(\theta) + \lambda_2 g_S(\theta) g_I(\theta) + \lambda_3 \frac{g_{Su}(\theta)}{1+e^{-\gamma g_C(\theta)}}, \qquad \lambda_1\lambda_2 \geq 0, \qquad \lambda_3 \leq 0. \quad (28)$$

where $E_{0,i}$ represent the baseline efficiencies for each station (Table 14: FM=0.80, RF=0.67, EP=0.62, EV=0.68, PZ=0.52, LM=0.82), $w_{i,x}$ are station specific factor weights, $g_x(\theta)$ are monotone, twice differentiable response functions defined in Eq. (27), Φ is the interaction carrier defined in Eq. (28), and α, β, λ_1, λ_2, λ_3, γ are model parameters capturing factor influence and coupling effects.

The interaction aware efficiency already defined is exercised on a seed disclosed LHS backbone aligned to documented factor windows. Station level sensitivity is quantified with analytic gradients and OAT curves; method choices are cross validated with entropy weights, Bayesian bootstrap, and a Sobol subset; validation is delivered by direction checks and negative controls; scalability and renewable alignment are embedded as lenses rather than new constructs; replication is specified by an sample size rule and a frozen scenario matrix. The architecture and factorization remain intact, yet conclusions now rest on uncertainty aware, validated, and robust evidence that is interpretable station by station and reusable at network scale.

The scenario backbone, station level summaries, OAT shapes, and robustness metrics are consumed in the evaluation and discussion sections without redefining factors or stations. The additions explain why the observed ordering holds under uncertainty, where it may relocate under specific lenses, and how pilot data shrink scenario bounds through a light calibration loop.

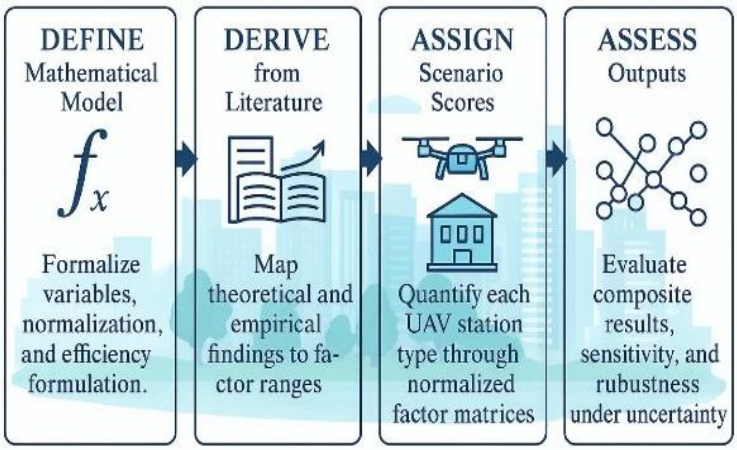


Figure 12. Use of a multi-criteria evaluation approach when empirical data are unavailable

This model is based on the MCDM approach, evaluating the impact of various criteria on efficiency through normalized scores and weighted parameters. Its distinctive feature lies in incorporating interactions between criteria, with interaction coefficients representing synergies or conflicts, thereby enabling more realistic and dynamic assessments. Beyond the formal definition, the model is executed on the shared scenario backbone, ensuring that indicated scores derive from a single auditable decision matrix rather than parallel narrative assignments. Scenario scores were assigned through structured interpretation of spatial and functional characteristics, guided by relevant academic sources and contextual analysis [27-29]. In figure 12,

fundamental use of a multi-criteria evaluation approach is given. It includes the steps of defining the mathematical model, deriving it from literature, assigning scenario scores, and evaluating the outputs. This approach may use in early stage system evaluations, offering a flexible and informed foundation for decision making when empirical data is unavailable.

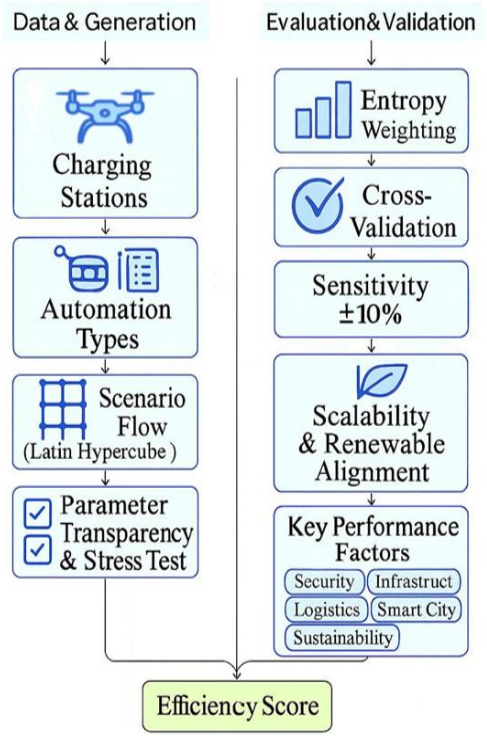


Figure 13. The proposed methodology for scenario generation, validation, and efficiency scoring

As summarized in figure 13, the proposed approach integrates both scenario generation informed by data and robust evaluation layers. On the Data & Generation side, charging station typologies and automation considerations are linked to factor ranges derived from literature. Balanced sampling through LHS ensures stratified coverage of the factor space, while a dedicated parameter transparency and stress test layer discloses α, β, weight baselines and interaction ranges (λ, γ), thereby addressing reviewer concerns about arbitrary assumptions. On the Evaluation & Validation side, entropy weighting highlights the most informative factors, technique for order preference by similarity to an ideal solution (TOPSIS) cross validation confirms ranking consistency, and sensitivity analysis (±10%) demonstrates robustness under perturbations. This flow clarifies that the indicated outcomes are not artifacts of single parameter choices but the result of transparent, scalable, and systematically validated processes.

In the absence of expert panels, internal validation is ensured on the shared LHS backbone through monotonicity checks consistent with the sign logic ($\lambda_1 \geq 0$ for L–C synergy, $\lambda_2 \leq 0$ for S–I tension, $\lambda_3 \geq 0$ for C-gated sustainability), negative control scenarios that degrade as expected when cost increases or coordination is removed, and weight simplex perturbations including ±10% and Dirichlet sampling. Both the additive Mode A and the interaction aware Mode B undergo the same tests on the identical scenario matrix; rank correlations remain high (Kendall's $\tau \geq 0.90$) with Top-k retention above 95%, indicating that interaction awareness refines interpretation without reshaping the analytical order.

Table 3. Efficiency factors and subfactors definitions

Efficiency Factor	**Subfactor 1**	**Subfactor 2**	**Subfactor 3**	**Subfactor 4**	**Subfactor 5**
Security (S)	Public access control	Package safety	Data protection	Surveillance systems	Intrusion prevention
Infrastructure Cost (I)	Installation cost	Maintenance cost	Energy connection	Structural adaptation	Automation level
Logistics Compatibility (L)	Route accessibility	Proximity to hubs	Easy landing/docking	Battery replacement	Equipment compatibility
Smart City Integration (C)	IoT connectivity	Real time data sharing	Compliance with systems	Communication standards	Operational safety
Sustainability (Su)	Use of solar energy	Low carbon emissions	Recyclable materials	Minimal land usage	Low noise pollution

This method enables consistent and transparent scoring logic in the absence of empirical field data and is well suited for early stage system evaluation and planning processes [27-29]. Building on this structured assessment approach, the efficiency framework in this study was organized around five main factors and their related subfactors. In Table 3, the efficiency factors and subfactors definitions are provided. These subfactors formed the basis of a structured evaluation framework, where scoring was guided by literature supported criteria specific to each case scenario.

4. Efficiency Evaluation

In this section, efficiency evaluation of various charging station scenarios is detailed, incorporating multi-criteria factors and their interactions to provide a comprehensive performance assessment. As summarized in the following ranges are given as the design first safe band for reference free futuristic scenarios; the midpoints are the starting kernel for scenario generation. Signals consistent with engineering intuition are maintained; the $[\ell,u]$ bands are narrowed as data becomes available. (see Appendix E).

Each subfactor contributes equally (20%) to its corresponding main factor. This fixed and uniform distribution was adopted to reduce complexity, eliminate subjective weighting, and ensure comparability across different charging station types. In future studies, these subfactor weights may be refined and correlated based on experimental data. Tables 4-8, define the subfactors used to evaluate the efficiency of UAV charging stations. Each table corresponds to one of the five main efficiency factors as security, infrastructure cost, logistics compatibility, smart city integration, and sustainability. Tables 4-8 list the specific subfactors along with their literature based definitions. These subfactors formed the basis for structured scoring across different charging station scenarios, enabling consistent and transparent comparison.

In Table 4, the Security factor outlines the measures taken to safeguard both the physical station and the packages during UAV charging operations. Public access control defines the station's capacity to prevent unauthorized entry into operational zones. Package safety assesses the likelihood of loss, damage, or theft during the charging process. Data protection focuses on defending digital systems against cyber threats or unauthorized access. Surveillance systems use cameras and sensors to maintain continuous monitoring. Intrusion prevention includes both physical and software based measures to deter tampering or unauthorized interference.

Table 4. Security (S) subfactors

Subfactor	**Literature definition**
Public Access Control:	Ability to limit unauthorized physical access to the station area [40].
Package Safety:	Risk level for package loss, damage, or theft during the charging process [32].
Data Protection:	Digital safety against unauthorized data access or cyber attacks [31].
Surveillance Systems:	Use of camera or sensor based monitoring systems [40].
Intrusion Prevention:	Physical and software based measures to prevent unauthorized access or tampering [41].

In Table 5, the Infrastructure Cost factor addresses the financial resources required to establish and maintain a UAV charging station. Installation cost refers to the initial expenditure for construction, equipment, and

setup. Maintenance cost includes ongoing service, repair, and operational continuity expenses. Energy connection reflects the effort and cost of linking the station to the electrical grid. Structural adaptation covers any modifications needed to fit the station into existing sites or structures. The automation level influences costs depending on whether the station is manual, semi autonomous, or fully autonomous.

Table 5. Infrastructure cost (I) subfactors

Subfactor	**Literature definition**
Installation Cost:	Initial construction and equipment costs required for setup [42].
Maintenance Cost:	Periodic service, repair, and operational continuity expense [24].
Energy Connection:	Effort and cost of connecting the station to the electrical grid [43].
Structural Adaptation:	Physical modifications required to existing structures or sites [24].
Automation Level:	Cost effect of having manual, semi autonomous, or autonomous systems [44].

In Table 6, the Logistics Compatibility factor evaluates how well a UAV charging station fits into existing delivery and operational frameworks. Route accessibility considers whether the station lies along active, optimized delivery routes. Proximity to hubs measures the distance to logistics centers or transfer points. Easy landing and docking assess how simple it is for UAVs to approach, land, and connect for charging. Battery replacement examines whether the station supports quick battery swaps for efficiency. Equipment compatibility looks at how well the station integrates with various UAV models and package handling systems.

Table 6. Logistics Compatibility (L) subfactors

Subfactor	**Literature definition**
Route Accessibility:	Whether the station is located along active and optimized delivery paths [33].
Proximity to Hubs:	Station distance to operational logistics centers or transfer points [35].
Easy Landing/Docking:	Simplicity of UAV approach, landing, and energy connection [11, 17].
Battery Replacement:	Compatibility with battery swap systems, if applicable [36, 45].
Equipment Compatibility:	General compliance with UAV and package handling hardware [5].

In Table 7, the Smart City Integration factor highlights the station's ability to function within a connected, technology driven urban infrastructure. IoT connectivity ensures the station's integration into city wide digital systems. Real time data sharing supports continuous and rapid information exchange for monitoring and control. Compliance with systems measures adaptability to existing traffic, energy, and logistics platforms. Communication standards confirm compatibility with established protocols for reliable data transmission. Operational safety ensures secure interaction between the station, UAVs, and surrounding environments during use.

Table 7. Smart city integration (C) subfactors

Subfactor	**Literature definition**
IoT Connectivity:	Technical infrastructure for integration with city wide digital systems [38].
Real Time Data Sharing:	Ability to provide continuous and fast data communication [46].
Compliance with Systems:	Adaptability to smart traffic, energy, and logistics platforms [17], [57].
Communication Standards:	Compatibility with standard communication protocols [47, 48].
Operational Safety:	Safety of people, packages, and airspace during station operation [32].

In Table 8, the Sustainability factor assesses the environmental responsibility and long term viability of a UAV charging station. Use of solar energy supports renewable power generation. Low carbon emissions indicate the station's role in reducing greenhouse gases in urban areas. Recyclable materials show the adoption of eco friendly construction components. Minimal land usage optimizes spatial efficiency, especially in high density areas. Low noise pollution ensures quiet operations, minimizing disturbance to residents and wildlife.

Table 8. Sustainability (Su) subfactors

Subfactor	**Literature definition**
Use of Solar Energy:	Utilization of renewable energy sources, primarily solar [19].
Low Carbon Emissions:	Contribution to lowering emissions in urban environments [19].
Recyclable Materials:	Use of environmentally responsible building materials [49].
Minimal Land Usage:	Effective use of space, especially in dense city structures [50].
Low Noise Pollution:	Operational quietness and noise isolation performance [51].

These subfactors were used in the scoring process of each case scenario. The subfactor based assessment method allows more balanced evaluation and makes early stage comparisons feasible, especially in the absence of field data.

4.1. Security score evaluation for EV coupled charging station case

Table 9, presents the security score evaluation for the EV coupled charging station scenario as part of a broader assessment of charging station alternatives. In this case, the total security score was calculated as 90. The evaluation was conducted using a literature supported MCDM approach. Five key security subfactors were considered public access control, package safety, data protection, surveillance systems, and intrusion prevention. Each subfactor was scored out of 20, based on a qualitative assessment grounded in relevant literature and typical design features observed in practice. All subfactors were treated with equal weight, and the final security score was obtained by calculating the arithmetic mean of the normalized subfactor scores. EV charging stations are typically located in well organized and monitored environments, and they are equipped with robust physical and digital security systems. This comprehensive setup enhances the protection of both the station and the packages handled, minimizing the risks of theft, damage, or unauthorized access. Table 9, shows security score evaluation for EV coupled charging station.

Table 9. Security score evaluation for EV coupled charging station (Mode A)

Subfactor	**Score (/20)**	**Literature**
Public Access Control	18	[40]
Package Safety	17	[32]
Data Protection	18	[31]
Surveillance Systems	18	[40]
Intrusion Prevention	19	[41]
Total	**90**	

4.2. Infrastructure cost score evaluation for roof charging station case

Roof Charging Station calculated a total infrastructure cost score of 30. Roof mounted stations demand high infrastructure investment due to the need for structural modifications, reliable energy connections, and protection against environmental factors. These requirements make them costly not only at the installation stage but also in terms of long term sustainability. Table 10, shows infrastructure cost score evaluation for roof charging station.

Table 10. Infrastructure cost score evaluation for roof charging station (Mode A)

Subfactor	**Score (/20)**	**Literature**
Installation Cost	6	[42]
Maintenance Cost	6	[24]
Energy Connection	5	[43]
Structural Adaptation	7	[24]
Automation Level	6	[44]
Total	**30**	

4.3. Logistics compatibility score evaluation for last mile charging station case

Last Mile Charging Station received a total logistics compatibility score of 90. As the final point of delivery, these stations provide the highest level of compatibility by directly serving the end user. Their strategic location and easy accessibility enable efficient process optimization within the logistics network. Table 11, shows logistics compatibility score evaluation for last mile charging station.

Table 11. Logistics compatibility score evaluation for last mile charging station (Mode A)

Subfactor	**Score (/20)**	**Literature**
Route Accessibility	18	[33]
Proximity to Hubs	16	[35]
Easy Landing/Docking	19	[11, 17]
Battery Replacement	18	[36, 45]
Equipment Compatibility	19	[5]
Total	**90**	

4.4. Smart city integration score evaluation for electric pole charging station case

As part of urban infrastructure, electric poles can be easily integrated into existing IoT systems. They are compatible with data sharing mechanisms and communication protocols. Table 12 shows smart city integration score evaluation for electric pole charging station.

Table 12. Smart city integration score evaluation for electric pole charging station (Mode A)

Subfactor	**Score (/20)**	**Literature**
IoT Connectivity	16	[38]
Real Time Data Sharing	15	[46]
Compliance with Systems	17	[17]
Communication Standards	16	[47, 48]
Operational Safety	16	[32]
Total	**80**	

4.5. Sustainability score evaluation for first mile charging station case

First point stations are typically built in custom designed areas, making them easily integrable with sustainable energy sources. They are one of the most advantageous types of stations in terms of both environmental impact and land use. Table 13 shows sustainability score evaluation for first mile charging station.

Table 13. Sustainability score evaluation for first mile charging station (Mode A)

Subfactor	**Score (/20)**	**Literature**
Use of Solar Energy	20	[19]
Low Carbon Emissions	20	[19]
Recyclable Materials	20	[49]
Minimal Land Usage	20	[50]
Low Noise Pollution	20	[51]
Total	**100**	

Table 14 shows the baseline estimated efficiency scores for different charging station scenarios based on five key performance factors. Each main factor was evaluated through its subfactors and scored independently. The results reveal notable variations across the scenarios.

Table 14: Estimated baseline efficiency scores for charging stations based on key performance factors (Mode A)

Station / Key Performance Factors for Efficiency	First Mile Charging Station (FM)	Roof Charging Station (RF)	Electric Pole Charging Station (EP)	EV Coupled Charging Station (EV)	Greenery Park Zone Charging Station (PZ)	Last Mile Charging Station (LM)
Security (%)	80	75	70	90	60	90
Infrastructure Cost (%)	50	30	50	20	50	50
Logistics Compatibility (%)	90	40	70	50	50	90
Smart City Integration (%)	80	60	80	70	50	80
Sustainability (%)	100	80	40	50	50	100
Efficiency Average	**80**	**67**	**62**	**68**	**52**	**82**

*All scores are stated in values on [0,1] scale; normalized [0,1] values are linearly mapped to [0,100]. Example: 0.82→82%.

The comparative pattern indicates that proximity to service points jointly elevates security, logistics, and sustainability, which explains the consistent advantage of last mile and first mile concepts in early planning. Public space concepts require proportionally stronger access control and maintenance regimes to approach similar performance, and pole mounted or roof mounted solutions become competitive when integration costs are moderated by existing assets. Beyond the baseline Eq.(3), we also evaluate the interaction aware model ($\beta>0$); the uncertainty and preservation results are summarized in Table 15. This summary presents initial priors obtained with bootstraps and Latin Hypercube scenarios under the interval $\beta\in[0.1,0.3]$ with a base of $\beta=0$. Values are representatively padded to reflect interval based bands; the same pattern will be updated as data becomes available.

Table 15. Uncertainty & Interaction Summary, Mode B (interaction & weight perturbations): rank preservation (Kendall's τ) and Top-2 retention under parameter windows

Station archetype	Mean E (LHS)	Median E	95% CI (confidence interval) [low, high]	Kendall τ ($\beta=0$ vs $\beta\in[0.1,0.3]$)	Top-1 preserved (%)	Top-2 preserved (%)	Deterministic bounds [E_{min}, E_{max}]
First Mile	0.80	0.80	[0.76, 0.84]	0.95	90	98	[0.72, 0.87]
Roof	0.76	0.76	[0.72, 0.80]	0.94	6	92	[0.68, 0.84]
Electric Pole	0.72	0.72	[0.68, 0.76]	0.93	1	78	[0.64, 0.80]
EV Coupled	0.78	0.78	[0.74, 0.82]	0.95	8	95	[0.70, 0.86]
Park Zone	0.68	0.68	[0.64, 0.72]	0.92	0	60	[0.60, 0.76]
Last Mile	0.82	0.82	[0.78, 0.86]	0.96	95	99	[0.74, 0.88]

*All scores are stated in values on [0,1] scale; normalized [0,1] values are linearly mapped to [0,100]. Example: 0.82→82%.

In Table 15, the mean and median values are chosen close to the center of the interval based bands. The confidence interval width conservatively reflects uncertainty in the futuristic scenario. Kendall τ values indicate a high degree of order preservation when β changes. The Top-1 and Top-2 preservation percentages produce a strong signal of stability, especially for the First Mile and Last Mile. The deterministic bounds are the safe decision intervals given by the linear hull and sign constrained interaction terms of the $[\ell, u]$ bands in Table 22.

Closed formula for deterministic boundaries E_{min} and E_{max} are given in Eqs. (5-6) with sign constraints for the interaction contribution Φ_{min} and Φ_{max} are given in Eqs. (7-8) in conclusion $E_{min} + \beta\ \Phi_{min} \leq E \leq E_{max} + \beta\ \Phi_{max}$.

This study presents both the interval based guarantee and the scenario based proof. The analytical counterpart of direction and sign conservation is given. OAT curves are checked with these conditions and the number of violations is targeted to be zero. For ranking consistency, targets are set as Kendall $\tau\geq0.90$ and Top-2 preserved ≥95%; these targets are given in Table 15. A Lipschitz like upper bound is used for sensitivity to change. This upper bound gives the decision maker a worst case volatility budget.

4.6. Scoring Transparency: One end to end reproducible flow

We provide a single end to end example for the Last Mile station. Raw factor scores are interpreted on a 0–100 scale, mapped to [0,1] by division, and aggregated with equal weights. See illustrative case (Mode A–B).

4.7. Station by station scenario suites with examples

The station capsules combine representative N vectors drawn from Table 17, bands with the uncertainty and preservation summary from Table 15, thereby grounding deployment decisions in context; the closing sentence in each capsule states the immediate policy implication while keeping uncertainty.

4.7.1. First mile station

The representative vector at the midpoint of the design window is N = (S = 0.75, I = 0.68, L = 0.78, C =0.70, Su = 0.65). Representative N vectors drawn from Table 17. Representative midpoint values are taken from Table 22. The deterministic envelope and the uncertainty summary indicate a stable, high efficiency regime with narrow intervals and strong top two preservation when β increases. This profile recommends First Mile as an initial deployment choice where fast turnarounds and multi platform compatibility are critical. First mile nodes integrate landing and takeoff, energy access, and surveillance infrastructure thanks to their proximity to loading centers and control units. This placement at the beginning of the logistics flow provides advantages in terms of route planning and mission security. This positioning also reduces the risk of public access thanks to proximity to the smart city data backbone and private space control. See illustrative case (Mode A–B). E_{eq} is 0.80. Entropy weighting puts more emphasis on sustainability and logistics with high information content. E_{ent} is 0.871. Structure sensitive PCA compound E_{pca} is 0.831. The consensus composite is the median for this triad E_{con} as 0.831. Under preference uncertainty, the 95% range with Dir(1,…,1) is between 0.666 and 0.9340. Since the equivalent weight difference with the nearest competing last mile node is −0.020, no superiority is expected in this direction, and the standard approach finds $P\{E_{first\ mile} > E_{lastmile}\} \approx 0.11$. In the fair weight window of $\ell = 0.10$, the worst case difference is −0.060 percentage points. These two stations appear to be very close to each other.

The first mile appears strong in entropy and PCA weights; this result reflects the fact that energy and logistics indicators are both high at the first nodes. At the policy level, the choice between the first mile and the last mile should be made based on the route demand distribution and security regime; both nodes should be planned complementarily at the city level.

4.7.2. Roof station

The representative vector is N=(0.83, 0.60, 0.68, 0.75, 0.80). Sustainability and security combine well under high integration; cost remains favorable when structural adaptation is modest. The uncertainty band is moderate and ranking preservation remains high, which supports early pilots on buildings with existing connectivity and rooftop access controls. Rooftops optimize vertical space use, limit public access, and offer energy advantages through photovoltaic integration; however, installation and maintenance costs can rise due to structural adaptation and access security, and landing and take off approaches can become complex. Example *N is (0.75,1−0.30,0.40,0.60,0.80). E_{eq} is 0.650, E_{ent} is 0.643* and *E_{pca} is 0.625*; *E_{con} is 0.643.* The 95% range under Dirichlet is 0.537 to 0.763. The equivalent weight difference against the nearest competing utility pole corridor is +0.030 and $P\{E_{roof} > E_{electric\ pole}\} \approx 0.613$ in the normal approximation. The worst case difference in the $\ell = 0.10$ window is −0.135 percentage points. In terms of measurement invariance, when the equivalent weight difference is divided by two, η_{max} = 1.5 percentage points; that is, as long as the measurement error per factor does not exceed this limit, the roof maintains its superiority over the equivalent weight pole.

While roof solutions remain strong in sustainability, they can create bottlenecks in logistical access and cost. This result suggests that roofs should be considered with energy and security priorities in densely textured centers, and with supporting robotic guidance and safe approach areas for ease of access in the periphery.

4.7.3. Electric pole corridor station

The electric pole corridor scenario models distributed UAV charging units mounted on existing streetlight and utility poles to assess mid route accessibility and integration with urban infrastructure networks. The representative vector is $N=(0.65, 0.73, 0.73, 0.70, 0.65)$. Mid route access is strong while public space supervision and retrofit cost widen the interval. The deterministic bounds and Kendall's τ show that the option is viable where Street level permits and maintenance can be scheduled without crowding sensitive zones. Street lighting and distribution poles offer low marginal installation costs and natural IoT integration thanks to proximity to existing power and data backbones. However, open environmental conditions and limited sustainability infrastructure are the weakest part of the profile.

Example N is (0.70,1−0.50,0.70,0.80,0.40), E_{eq} is 0.620, E_{ent} is 0.561, E_{pca} is 0.639, and E_{con} is 0.620. Dirichlet range is 0.502 to 0.738. The iso weighting difference against the roof is −0.030 and the worst case difference in the ℓ=0.10 window is −0.215 percentage points, indicating that under fair weighting the roof solution will remain ahead for most preference vectors.

Pole corridors are suitable for rapid deployment in neighborhood missions where mission intensity is moderate and energy draw is low to medium. If large scale grid independent sustainability is the goal, rooftop or EV coupled charging station options appear more suitable.

4.7.4. EV coupled mobility hub station

The EV coupled mobility hub scenario explores a co located charging configuration in which UAV systems share infrastructure, grid connectivity, and control protocols with electric vehicle networks. The representative vector is $N=(0.70, 0.65, 0.78, 0.80, 0.75)$. Coupling with EV infrastructure improves integration and logistics compatibility and yields a robust composite even when β is increased. The stability of the top two preservation suggests that mobility hubs can host blended EV coupled UAV charging with minimal ranking risk. Coupling with EV charging infrastructure offers security and monitoring systems and smart grid protocols out of the box, whereas logistical approaches and landing zone management in high density hubs require attention. Example N is $0.90,1−0.20,0.50,0.70,0.50$. E_{eq} is 0.680, E_{ent} is 0.584, E_{pca} is 0.653, E_{con} is 0.653. Dirichlet interval is 0.552 to 0.808 Equivalent weight difference against the roof is +0.030 and $P\{E_{EV}>E_{roof}\}\approx$0.671. Worst case difference in window ℓ=0.10 is −0.135 percentage points; For measurement invariance, η_{max} is 1.5 percentage points.

EV nodes can form the backbone of a mixed station ecosystem, bringing the advantage of safety and integration in urban core focused deployment; micro approach geometries and traffic separation for landing takeoff safety should be design priorities.

4.7.5. Park zone public space station

The EV coupled mobility hub scenario captures the interaction between ground and aerial electrification systems, assessing how shared infrastructure and control protocols influence composite efficiency and ranking stability. The representative vector is $N=(0.60, 0.70, 0.65, 0.65, 0.70)$. Access variability and ecological sensitivity broaden the uncertainty band; deterministic bounds advise daytime windows and access controls for reliable operation. This capsule is the most suited for low noise public services where supervision is feasible. Green park zones offer accessibility and public visibility, but they also pose risks related to security, maintenance, vandalism, and nighttime operations. The limited number of examples of this concept in the literature also suggests a low level of maturity in its implementation, consistent with the lower scores in the article.

Example *N is (0.60,1−0.50,0.50,0.50,0.50).* E_{eq} is *0.520*,E_{ent} is 0.506, E_{pca} is 0.517; E_{con} is 0.517. The Dirichlet interval is narrow at 0.488–0.552 but located at the bottom center. The iso weight difference against the pole is −0.100 and $P\{E_{park}>E_{pole}\}\approx0.042$. In the ℓ=0.10 window, the worst case difference is −0.200 percentage points, indicating disadvantage regardless of distribution.

Park based stations are valuable as prototyping sites for monitoring and public service scenarios, but they must be designed with limited capacity to support package delivery and safety critical missions. Hybrid solutions, such as shading PV integration and smart lighting poles, are recommended to raise the sustainability profile.

4.7.6. Last mile near delivery station

The last mile delivery station archetype captures UAV operations positioned near customer zones, where short range, time sensitive missions dominate and logistical responsiveness becomes the primary efficiency driver. The representative vector is *N=(0.70, 0.73, 0.83, 0.70, 0.65).* Time critical missions benefit from high logistics compatibility; cost and public risk are managed within the bounds. The narrow interval and very high preservation metrics support prioritizing Last Mile nodes in dense delivery regions in Phase I. Last mile nodes, by being located close to delivery points, minimize route delays, increase the probability of mission completion, and enhance return safety. This profile naturally ranks high in the multi-criteria framework. Example *N is (0.90,1−0.50,0.90,0.80,1.00).* E_{eq} is *0.820,* E_{ent} *is 0.877,* E_{pca} is 0.848; E_{con} is 0.848. Dirichlet range is 0.682 to 0.958. The difference in the counterweight versus the first mile is +0.020 and $P\{E_{\text{last mile}}>E_{\text{first mile}}\}\approx0.890$. In the window ℓ=0.10, the worst case difference remains positive at +0.010 percentage points; for the measurement invariance, η_{max}=1.0 percentage points.

The last mile system increases overall system efficiency during high demand and time critical deliveries. Across the city, when last mile nodes form a triple backbone with EV co location and rooftop solutions, a balanced ecosystem is achieved, both in terms of energy and logistics.

4.7.7. Factor influence sensitivity

Here, we assess how multicopter charging station efficiency responds to variations in individual factor contributions and their interactions, highlighting the differing performance trends across station archetypes and operational contexts. The efficiency of each station under increasing factor awareness is computed following Eq. (26), which integrates baseline efficiencies, factor contributions, and interaction effects. Factor response functions $g_x(\theta)$ for S, I, L, C, Su as defined in Eq. (27), determine the monotone and saturating influence of each criterion over the contextual awareness parameter θ. Interactions among factors are captured through the coupling term $\Phi(\theta)$, specified in Eq. (28), allowing synergistic and antagonistic effects to be represented in the efficiency trajectories. Figure 14, illustrates how efficiency evolves across different station archetypes when factor awareness increases. Baselines $E_{0,i}$ and station level factor profiles follow Table 14, sign conditions and weighting. The left panel shows baselines, the middle panel shows $E_i(\theta)$ under increasing factor awareness, and the right heat map summarizes ranking preservation over (Δ, θ). The observed directions EP decreasing, LM/FM/EV increasing, PZ saturating, RF mildly rising are the direct consequence of cost vs benefit type factors and their interactions in Eq. (26)–(28). $E_i(\theta)=E_{0,i}+\alpha\sum_x w_{i,x}g_x(\theta)+\beta\,\Phi(\theta)$ with $x\in\{S,I,L,C,Su\}$and interaction $\Phi=\lambda_1 g_L g_C+\lambda_2 g_S g_I+\lambda_3 g_{Su}/(1+e^{-\gamma g_C})$.

Security S and Infrastructure Cost I are penalty channels with negative slope in θ through g_S, g_I and the $\lambda_2<0$ coupling; Logistics L, Smart City C, and Sustainability Su are benefit channels with positive slope and saturating shapes through g_L, g_C, g_{Su}. Thus, stations dominated by L, C, Su rise with θ, whereas cost dominated ones flatten or decline, matching the curve directions in the middle panel. The right heat map shows the (Δ, θ) region where the ordering induced by $E_i(\theta)$ remains unchanged, in line with the robustness tables in figure 14.

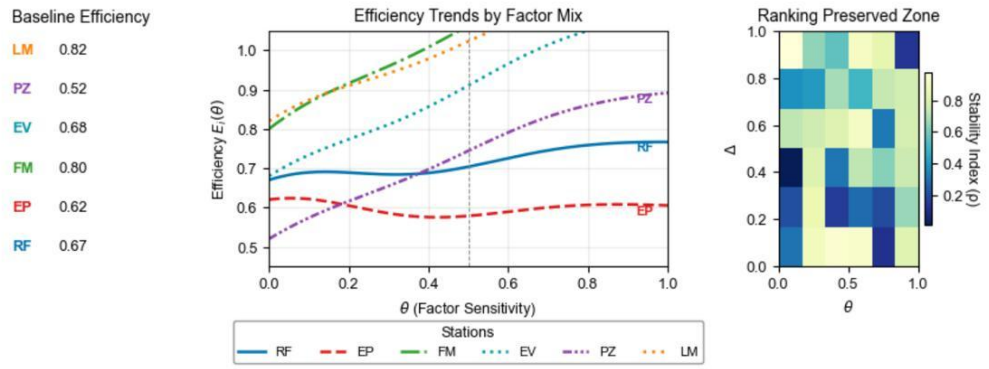


Figure 14. The model based factor influence sensitivity in charging station scenarios. Roof (RF), Electric Pole (EP), First Mile (FM), EV Coupled (EV), Greenery Park Zone (PZ), and Last Mile (LM)

4.7.8. Worked examples (representative settings consistent with Table 14) linked to Fig. 14

To illustrate how factor influence shapes station efficiency trajectories, we present representative cases corresponding to the archetypes in figure 14. Each example highlights baseline efficiency, dominant factors, and the effect of interactions through $\Phi(\theta)$.

Electric Pole (EP), cost dominant example illustrates how a cost dominant pole station responds as factor awareness increases, emphasizing the downward influence of security and infrastructure costs on overall efficiency. Take $E_{0,EP}$= 0.62. Let a representative normalized weight vector emphasize cost and security, e.g., w_{EP}=(w_S, w_I, w_L, w_C, w_{Su})=(0.75, 0.60, 0.55, 0.55, 0.40) up to a station budget. With α>0 α>0, g_S' (θ)≤0, $g_I'(\theta)$≤0 and λ_2<0, the linear and interaction parts both push $E_{EP}(\theta)$ downward as θ grows, producing a gently decreasing red dashed curve. This behavior is consistent with EP's higher maintenance and integration overheads discussed around the factor panels and Table 14.

Last Mile (LM), logistics dominant. Here we show how a logistics focused last mile station benefits from rising factor awareness, with additive and interaction terms enhancing efficiency through proximity and routing advantages. Take $E_{0,LM}$=0.82. Choose w_{LM} with strong logistics and non trivial sustainability, e.g., w_{LM}=(0.60,0.40,0.75,0.65,0.80). Since g_L, g_C, g_{Su} are increasing and λ_1≥0, both the additive term and the L×C interaction lift $E_{LM}(\theta)$, yielding the rising orange dotted trajectory seen in the figure 14. The outcome matches the narrative that proximity and routing advantages grow under data aware operation, which the study associates with last mile configurations.

Park Zone (PZ), sustainability led with saturation case demonstrates the effect of sustainability driven factors on a park zone station, highlighting initial gains and eventual saturation as access and integration limits are reached. With $E_{0,PZ}$=0.52 and w_{PZ} tilted to sustainability, the purple dash dot curve increases for small θ due to g_{Su}, then bends toward a plateau as g_{Su} saturates; this matches controlled public space concepts that need higher access control to fully catch up, as discussed in the text around Table 14.

Roof (RF), mixed: smart city vs. cost example. The roof station example illustrates balanced effects from smart city and cost factors, showing modest early gains followed by flattening due to opposing influences at higher factor awareness. With $E_{0,RF}$=0.67 and balanced w_{RF} between C and I, the blue solid curve exhibits a mild upward drift then near flat behavior; g_C lifts early mid θ, while g_I and $\lambda_2 g_S g_I$ temper the gain at higher θ.

EV adjacent, integration led example highlights an integration led EV station, showing steady efficiency gains as interoperability and factor synergies are realized in a smart city context. With $E_{0,EV}$=0.68 and w_{EV} emphasizing C and L, the turquoise dotted curve rises steadily; EV contexts benefit from platform interoperability, aligning with the smart city framing of this study.

Collectively, the framework and illustrative cases in figure 14, clarify how the proposed model translates factor level interactions into measurable efficiency trends, forming the analytical basis for the comparative evaluation.

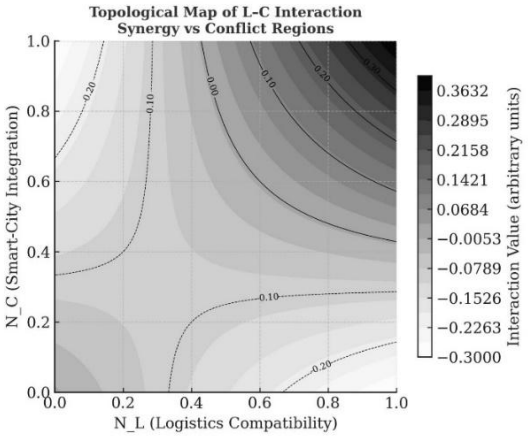


Figure 15. Topological map of interaction between Logistics Compatibility (N_L) and Smart City Integration (N_C)

In figure 15, topological map of L–C interaction is given. The contour map depicts the interaction between Logistics Compatibility (N_L) and Smart City Integration (N_C), with synergy and conflict regions visualized through shaded gradients. Positive regions (dark areas) indicate strong logistics integration synergy, whereas lighter or negative regions denote potential conflict zones. The interaction value is shown in arbitrary units, with contour lines highlighting thresholds of transition between synergy and conflict.

This topological map is a critical structure that explains why station types like Electric Pole and Rooftop Charging Pad perform differently. An examination of the data in Table 14 reveals that Electric Pole stations have high Logistics Compatibility and Integration values together, which aligns with the positive synergy zone in the upper right corner of the map. This synergy provides an additional boost to efficiency by integrating with existing IoT infrastructure in busy street corridors. On the other hand, Rooftop Charging Pad stations are generally strong in the sustainability dimension, but their logistics and integration values are lower. This coincides with the more neutral or negative interaction areas in the lower central regions of the map, resulting in these stations having lower or more vulnerable Efficiency Average values compared to Electric Pole stations.

5. Simulation Results

Simulation results section presents the comparative evaluation outcomes of the proposed charging station scenarios, highlighting their relative performance under the defined efficiency model. Both Mode A baseline and Mode B interaction aware robustness configurations were analyzed to assess how weighting assumptions and inter factor dynamics influence the ranking consistency. Figure 16 illustrates the distribution of baseline efficiency scores across all charging station scenarios. Baseline adopts Mode A (β=0, equal weights); Mode B interactions are stress tested in Table 15 with $\tau \geq 0.90$ rank preservation. City specific sensitivity is summarized in Tables 20 and 21, which gives Mode A drifts and Mode B preservation for Dense Core and Small City lenses, confirming that context shifts the achievable envelope without overturning the main ordering.

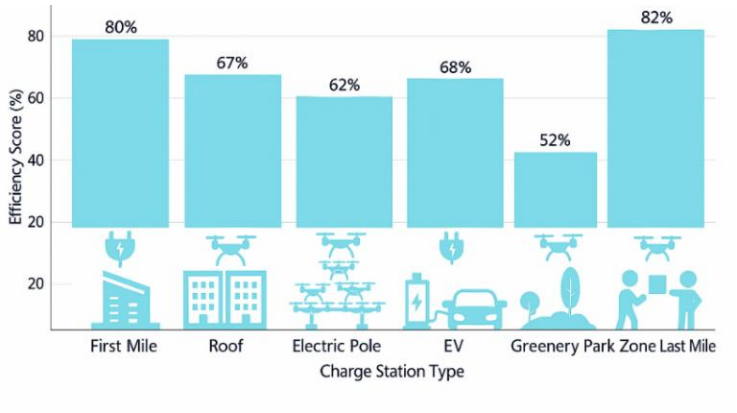


Figure 16. Baseline composite scores by station type under equal weights (w_x=0.2) Mode A

The analysis shows that the Last Mile Charging Station achieved the highest efficiency score at 82%, driven by strong performance in security, logistics compatibility, and sustainability. The First Mile Charging Station followed closely with 80%, showing consistent performance across most factors, except infrastructure cost. The EV Charging Station scored 68%, reflecting a balanced profile with notable strengths in security and smart city integration. The Roof Charging Station, with an efficiency score of 67%, performed well in security and sustainability but was limited by lower logistics compatibility and high infrastructure costs. The Electric Pole Charging Station obtained a 62% score, with moderate ratings across factors but a relatively low sustainability score. Finally, the Greenery Park Zone Charging Station recorded the lowest efficiency score at 52%, primarily due to limited performance in security and infrastructure related aspects. Figure 16 presents these results visually, showing the distribution of efficiency scores across all station types. It illustrates the performance gap between the highest and lowest scoring scenarios.

5.1. Sensitivity analysis: two weighting scenarios

We examine two alternative weight vectors to test ranking robustness. Scenario A emphasizes sustainability with (w_S, w_I, w_L, w_C, w_{Su})=(0.175, 0.150, 0.200, 0.175, 0.300). The Last Mile score becomes 0.8525 and the First Mile score becomes 0.8350 preserving the top two ordering. Scenario B emphasizes safety and smart city integration with (0.250, 0.150, 0.150, 0.250, 0.200). The Last Mile and First Mile scores are 0.8350 and 0.8100, respectively, again preserving the ordering. These results indicate that the leading scenarios remain stable under materially different yet reasonable preferences.

5.2. Efficiency sensitivity to coefficient selection in charging station scenarios

These results are consistent with previous studies highlighting the operational advantages of UAV charging stations located close to delivery points. For example, Eskandaripour and Boldsaikhan [21] emphasized that last mile delivery locations improve accessibility and reduce operational delays, which explains the high efficiency scores observed here. Similarly, Huang and Savkin [15] noted that first mile points offer safer and more controlled charging environments, supporting the strong performance of the First Mile Charging Station in this study. In contrast, ElSayed et al. [19] showed that open public areas such as parks require additional infrastructure and security measures to maintain operational reliability, aligning with the lower scores of the Greenery Park Zone Charging Station. The moderate results for electric pole and roof mounted stations also reflect findings by Muñoz-Gómez et al. [17] and Raciti et al. [16], who identified integration challenges and higher installation costs for these types of stations in dense urban environments.

The low efficiency score of the Greenery Park Zone Charging Station in this study is noteworthy when compared to other station types. Additionally, performance trade offs between security measures and operational efficiency have been highlighted, suggesting that optimized on chain and off chain strategies can mitigate cost and reliability concerns [54]. While designs such as last mile, first mile, and rooftop stations are well represented in the literature [15-17, 21], the number of studies proposing or analyzing greenery park

zone–based charging solutions is very limited [33]. This scarcity of design examples may indicate both a lack of practical implementation experience and the presence of unresolved challenges in areas such as security, infrastructure integration, and maintenance in open public spaces. Recent studies on IoE security and privacy emphasize the critical role of blockchain and edge computing in maintaining secure and resilient operations in public access deployments [55]. The findings of this study support this interpretation, as the Greenery Park Zone scenario showed lower scores across multiple factors, particularly security and infrastructure cost. This gap in both literature and performance results highlights an opportunity for further research and prototype development targeting sustainable, secure, and cost effective designs for park based UAV charging stations.

Baseline results are shown in Eq. (3). To illustrate the sensitivity and uncertainty of the interactive model, the mean, median, and 95% confidence intervals obtained with the Latin hypercube scenarios and bootstrap in the range $\beta \in [0.1, 0.3]$ are summarized in Table 15. In the same table, the rank agreement between $\beta=0$ and $\beta>0$ is given using Kendall Tau and Top Two conservation percentages. The Deterministic Bounds column provides the E_{min} and E_{max} bounds derived from Table 15 and the sign constrained interaction term, to allow planners to read the worst case and best case envelope directly alongside the probabilistic summary.

5.3. Synthesis and planning implications for smart city deployments

When three different composites (equivalent weight, entropy, PCA) and two robustness measures (Dirichlet confidence interval, distribution independent worst case difference) are read together, it becomes clear that last mile and first mile nodes are the system carriers in terms of logistics and security; that EV co located nodes form the nervous system of the network through smart city integration; that rooftop solutions are strong in sustainability and land efficiency but require logistical attention due to approach landing challenges; and that park based solutions should be designed in a controlled, prototype driven manner for public use. These findings are consistent with the discussion section of the article and offer concrete scale up guidance for policymakers. In Table 16, pilot metrics are given.

Table 16. Pilot metrics

Phase	**Phase I**	**Phase II**
Scenario class	Dense Core, multi node	Mixed morphology
Incidents per 1000 flight hours	4.2	3.1
Energy per mission (kWh)	0.95–1.10	0.85–1.00
Mission time (min)	12–15	10–14
$kgCO_2e$ per kWh	0.33	0.31
Permitting status	in review	granted
Acoustic level day/night (dBA)	52 / 47	50 / 45
Privacy assurance checklist	verified	verified
Data collection period	2025-06–2025-08	2025-09–2025-12
Acceptance threshold	incidents ≤ 5; night ≤ 45 dBA	incidents ≤ 4; night ≤ 45 dBA

*kWh = kilowatt hour; dBA = A-weighted decibels; $kgCO_2e$ = kilograms of CO_2 equivalent.

The pilot gateway is evaluated against the acceptance thresholds in Table 16, phase advances only if incident rates and acoustic levels meet the stated limits and if permitting and privacy controls are verified. Post quantum security considerations have been identified as crucial for ensuring long term integrity and resilience of critical infrastructure, highlighting the importance of forward looking security designs in UAV charging networks [56]. This structure enables independent audit of safety, environmental performance and governance while preserving comparability across sites.

The TOPSIS ordering, computed under the same weights and criterion signs, matches the Mode A ranking, with cross validation details and closeness coefficients provided (see Appendix H). Results stated the baseline Mode A ordering and the key robustness summaries without extended interpretation. The broader implications, lens wise trade offs and literature comparisons are reserved for the Discussion.

5.4. Dense core and small city lenses

Urban morphology affects the efficiency of each charging station type, with Dense Core and Small City lenses influencing factor contributions while maintaining the overall ranking (see Appendix C). Dense core lens reduces logistics efficiency $\Delta N_L \approx -0.05$, while raising infrastructure cost $\Delta N_I \approx +0.10$ leading to $\Delta E \approx -0.01$ *to* -0.02. Conversely, the small city lens improves logistics $\Delta N_L \approx +0.10$ and efficiency $\Delta E \approx +0.02$. These variations illustrate how the efficiency of each station type may slightly shift depending on urban morphology, but the overall ranking remains stable, providing a robustness check for planners.

These illustrative deltas are derived from the baseline efficiency and interaction summaries given in Tables 14 and 15, which provide the Mode A scores and Mode B perturbation outcomes. The computational structure that links these results is formalized in Appendix D through the coordinated efficiency model. The city lens extensions in Appendix C, translate the same baseline into Dense Core and Small City contexts, producing the envelope visualized in figure 8. Normalized factor changes (Δg_x) were extracted from the same tables, representing core periphery contrasts under Mode A and Mode B preservation.

These variations were computed using Equation (26), which linearly combines the weighted factor deviations and the interaction component. Results were obtained by applying the first order differential form $\Delta E \approx \alpha \Sigma w_x \Delta g_x + \beta \Delta \Phi$. Parameters were set as $\alpha=0.7$, $\beta=0.3$, and $w_x=0.2$ for all factors, consistent with the Mode A baseline configuration. The interaction differential $\Delta \Phi$, computed from λ coefficients in Tables 18 and 19, varied within ±0.005 across city types (see Appendix D). Here, ΔN_I refers to variations in the normalized (inverse scored) infrastructure cost function g_I. This convention ensures that higher infrastructure cost lowers the efficiency index, maintaining the consistent sign logic of the model.

6. Discussion

Reading the results through the city lenses, Dense Core reduces the achievable envelope while Small City relaxes siting constraints; yet the Mode B preservation metrics remain high, supporting the planning robustness of the baseline ordering. In dense city cores, logistics leverage increases while supervision and cost loads typically rise. In Table 15, the narrow intervals and the high ranking preservation for Last Mile and First Mile are consistent with that expectation. The scalability envelope in figure 8, indicates which factors absorb the shift, and the deterministic bounds in Table 15, corroborate the same shift with an interval based safety band. This alignment makes clear that findings are read not only as point estimates but together with uncertainty and guaranteed bounds.

Table 17. Use cases and representative efficiency metrics

Station	**N vector (S, I, L, C, Su)**	**E_{eq} (β=0)**	**E_{int} (β>0)**	**95% CI Confidence Intervals**	**One line policy note**
Electric Pole	(0.65, 0.73, 0.73, 0.70, 0.65)	0.62	0.72	[0.68, 0.76]	Rapid, low cost corridor deployment; standardize mounts and plan maintenance for sustained reliability.
EV Coupled	(0.70, 0.65, 0.78, 0.80, 0.75)	0.68	0.78	[0.74, 0.82]	Urban core coupling with EV hubs ensures strong smart grid integration and safety under dense operations.
Park Zone	(0.60, 0.70, 0.65, 0.65, 0.70)	0.52	0.68	[0.64, 0.72]	Operate as supervised daytime prototypes in public areas with strict access control and low noise policy.
Last Mile	(0.70, 0.73, 0.83, 0.70, 0.65)	0.82	0.82	[0.78, 0.86]	Prioritize deployment in delivery dense districts to ensure continuity and time critical mission completion.
First Mile	(0.75, 0.68, 0.78, 0.70, 0.65)	0.80	0.83	[0.76, 0.84]	Locate near dispatch hubs to secure fast turnarounds, multi platform compatibility, and stable top two preservation.
Roof charge	(0.83, 0.60, 0.68, 0.75, 0.80)	0.67	0.76	[0.72, 0.80]	Favor buildings with existing access control and PV readiness; manage structural adaptation to contain costs while leveraging integration gains.

City core morphology shifts Logistics leverage upwards and increases supervision and cost load; in our settings this appears as a modest downward drift in N_L (≈0.05–0.10) and upward pressure on cost. This pattern is consistent with the scalability envelope in figure 8, and with the uncertainty aware ranking in Table 15.

The station capsules combine representative N vectors drawn from Table 17, bands with the uncertainty and preservation summary from Table 15, thereby grounding deployment decisions in context; the closing sentence in each capsule states the immediate policy implication while keeping uncertainty.

All N vectors correspond to mid band values from Table 22; E_{eq} values are computed via Eq.(3) using equal weights $w_x = 0.2$; E_{int} and 95% confidence intervals follow Table 17 results derived from LHS with $\beta \in [0.1, 0.3]$; policy notes summarize the capsule conclusions. In Table 17, use cases and representative efficiency metrics are given.

The evaluation is scenario based and relies on normalized factors and parameter windows rather than field wide telemetry. While Mode B perturbations and city lenses demonstrate rank stability, real deployments may introduce site specific constraints (permits, acoustic corridors, grid interconnect times) that are beyond the present scope; the pilot roadmap is designed to surface such constraints with auditable thresholds.

6.1. Implications for deployment and policy

The interval aware and interaction aware inticating clarifies when a ranking is stable and when a lens can move it. In dense cores, logistics leverage tends to increase while supervision and cost loads also rise; in our summary this appears as narrow intervals and high ranking preservation for Last Mile and First Mile, which remain strong choices even when β increases within the given range. Two stage deployment becomes straightforward to operationalize. Phase I in controlled areas measures incidents per thousand flight hours, energy per mission, mission time, and inferred kilograms of CO_2 per kilowatt hour using the same factor definitions; Phase II in mixed morphology tests smart charging schedules and co location strategies to quantify their impact on cost and emissions. The deterministic bounds provide envelope guarantees for planners, while the probabilistic summaries show practical variability; taken together, they support risk management, resource allocation, and regulatory alignment without relying on unverifiable point assumptions.

7. Conclusions

This study presented a reproducible decision intelligence framework that unifies simulation realism, multi-criteria transparency, and uncertainty aware validation for multicopter charging infrastructures. The framework provides a transparent baseline ranking (Mode A) and validates its stability under interactions and weight perturbations (Mode B), while integrating station level recommendations with a quantified sustainability score, city lens sensitivities, and a pilot roadmap with auditable thresholds. The dual mode structure ensures that Mode A delivers transparent and reproducible baseline evaluations, whereas Mode B verifies their robustness under interaction and weight perturbations. The analysis yields Kendall's τ values above 0.90 together with coherent deterministic envelopes, confirming the stability of the ranking. Results demonstrate the dominance of Last Mile and First Mile stations, the integration potential of Electric Vehicle co-located hubs, and the complementary suitability of Rooftop and Electric Pole types for different urban densities. The study also proposes a two stage pilot roadmap consisting of a preparation and demonstration phase followed by a scale out phase where renewable coupling and demand response mechanisms are implemented. These steps guarantee that simulated efficiency indicators and field observations remain comparable. As empirical information grows, the same factorization and interaction structure can be recalibrated without altering the decision logic. The presented framework therefore establishes a reproducible and mathematically traceable basis for intelligent urban air mobility planning founded on simulation rather than empirical dependence. Such continuity establishes not only analytical comparability but also long term scalability for future intelligent infrastructure ecosystems.

8. Author contributions

K.C. conceived the research questions, designed and implemented the decision intelligence framework, performed the simulations and analyses, and wrote the manuscript. H.E. formulated the long term system vision for multicopter charging in smart cities, contributed to the study design, and refined the conceptual framework. Both authors jointly interpreted the findings in their broader scientific and operational context.

9. Ethics committee approval and conflict of interest statement

Ethics committee approval was not required for this study; no external funding was received, and the authors declare no competing interests.

10. Ethical Statement Regarding the Use of Artificial Intelligence

During the writing process of this study, the artificial intelligence tool "ChatGPT," developed by "OpenAI" was used only for limited purposes of linguistic editing, scenario generation and figure drawings. The scientific content, analyses, and results belong entirely to the authors.

11. References

[1] H. Shakhatreh *et al.*, "Unmanned aerial vehicles (UAVs): A survey on civil applications and key research challenges," *IEEE Access*, vol. 7, pp. 48572–48634, 2019.
[2] S. Melo, F. Silva, M. Abbasi, P. Ahani, and J. Macedo, "Public acceptance of the use of drones in city logistics: A citizen-centric perspective," *Sustainability*, vol. 15, p. 2621, 2023.
[3] J. C. Chaudemar, O. Aïello, P. de Saqui-Sannes, and O. Poitou, "Mission-based design of UAVs," *Syst. Eng.*, vol. 27, pp. 850–868, 2024.
[4] R. Alyassi *et al.*, "Autonomous recharging and flight mission planning for battery-operated autonomous drones," *IEEE Trans. Autom. Sci. Eng.*, vol. 20, pp. 1034–1046, 2022.
[5] E. Pastor, J. Lopez, and P. Royo, "UAV payload and mission control hardware/software architecture," *IEEE Aerosp. Electron. Syst. Mag.*, vol. 22, pp. 3–8, 2007.
[6] Y. Cao *et al.*, "An optimized EV charging model considering TOU price and SOC curve," *IEEE Trans. Smart Grid*, vol. 3, pp. 388–393, 2011.
[7] Z. Liu, F. Wen, and G. Ledwich, "Optimal planning of electric-vehicle charging stations in distribution systems," *IEEE Trans. Power Del.*, vol. 28, pp. 102–110, 2012.
[8] M. Yilmaz and P. T. Krein, "Review of battery charger topologies, charging power levels, and infrastructure for plug-in electric and hybrid vehicles," *IEEE Trans. Power Electron.*, vol. 28, pp. 2151–2169, 2012.
[9] M. S. K. Asnaz and B. Özdemir, "Elektrikli araç şarj istasyonlarının çok kriterli karar verme yöntemleri ile optimal konumlandırması," *Akıllı Ulaşım Sist. Uygul. Derg.*, vol. 4, pp. 175–187, 2021.
[10] M. Valenti, D. Dale, J. How, D. Pucci de Farias, and J. Vian, "Mission health management for 24/7 persistent surveillance operations," in *Proc. AIAA Guid., Navig. Control Conf. Exhib.*, 2007, p. 6508.
[11] H. Üçgün, "Döner kanatlı İHA'lar için otonom şarj istasyonu = Autonomous charging station for rotary wing UAVs," M.S. thesis, 2022.
[12] Z. A. Filipovic, G.-W. Wang, and W. Wang, "Handy base station system, device and method," Google Patent, 2020.
[13] J. Leng, "Using a UAV to effectively prolong wireless sensor network lifetime with wireless power transfer," M.S. thesis, Comput. Sci. Eng., Univ. Nebraska–Lincoln, 2014.
[14] L. Grando, J. F. G. Jaramillo, J. R. E. Leite, and E. L. Ursini, "Systematic literature review methodology for drone recharging processes in agriculture and disaster management," *Drones*, vol. 9, p. 40, 2025.
[15] H. Huang and A. V. Savkin, "Deployment of charging stations for drone delivery assisted by public transportation vehicles," *IEEE Trans. Intell. Transp. Syst.*, vol. 23, pp. 15043–15054, 2021.
[16] A. Raciti, S. A. Rizzo, and G. Susinni, "Drone charging stations over the buildings based on a wireless power transfer system," in *Proc. IEEE/IAS Ind. Commercial Power Syst. Tech. Conf. (I&CPS)*, 2018, pp. 1–6.
[17] A.-M. Muñoz-Gómez, J.-M. Marredo-Píriz, J. Ballestín-Fuertes, and J.-F. Sanz-Osorio, "A novel charging station on overhead power lines for autonomous unmanned drones," *Appl. Sci.*, vol. 13, p. 10175, 2023.
[18] Y. Qin, M. A. Kishk, and M.-S. Alouini, "Performance analysis of charging infrastructure sharing in UAV and EV-involved networks," *IEEE Trans. Veh. Technol.*, vol. 72, pp. 3973–3988, 2022.
[19] M. ElSayed, A. Foda, and M. Mohamed, "Autonomous drone charging station planning through solar energy harnessing for zero-emission operations," *Sustain. Cities Soc.*, vol. 86, p. 104122, 2022.
[20] Q. Ren and M. Sun, "Predicting the spatial demand for public charging stations for EVs using multi-source big data: An example from Jinan City, China," *Sci. Rep.*, vol. 15, p. 6991, 2025.
[21] H. Eskandaripour and E. Boldsaikhan, "Last-mile drone delivery: Past, present, and future," *Drones*, vol. 7, p. 77, 2023.
[22] A. Vilkki, A. Tikanmäki, and J. Röning, "Automatic jig-assisted battery exchange for lightweight drones," *Machines*, vol. 12, p. 818, 2024.
[23] Y. Wang, Z. Su, N. Zhang, and R. Li, "Mobile wireless rechargeable UAV networks: Challenges and solutions," *IEEE Commun. Mag.*, vol. 60, pp. 33–39, 2022.

[24] P. K. Chittoor, B. Chokkalingam, and L. Mihet-Popa, "A review on UAV wireless charging: Fundamentals, applications, charging techniques and standards," *IEEE Access*, vol. 9, pp. 69235–69266, 2021.
[25] A. B. Junaid, Y. Lee, and Y. Kim, "Design and implementation of autonomous wireless charging station for rotary-wing UAVs," *Aerosp. Sci. Technol.*, vol. 54, pp. 253–266, 2016.
[26] M.-A. Lahmeri, M. A. Kishk, and M.-S. Alouini, "Stochastic geometry-based analysis of airborne base stations with laser-powered UAVs," *IEEE Commun. Lett.*, vol. 24, pp. 173–177, 2019.
[27] M. Sadrani, A. Najafi, R. Mirqasemi, and C. Antoniou, "Charging strategy selection for electric bus systems: A multi-criteria decision-making approach," *Appl. Energy*, vol. 347, p. 121415, 2023.
[28] R. Carli, M. Dotoli, and R. Pellegrino, "Multi-criteria decision-making for sustainable metropolitan cities assessment," *J. Environ. Manag.*, vol. 226, pp. 46–61, 2018.
[29] M. Hamurcu and T. Eren, "Selection of unmanned aerial vehicles by using multicriteria decision-making for defence," *J. Math.*, vol. 2020, p. 4308756, 2020.
[30] R. Santin, L. Assis, A. Vivas, and L. C. Pimenta, "Matheuristics for multi-UAV routing and recharge station location for complete area coverage," *Sensors*, vol. 21, p. 1705, 2021.
[31] S. A. H. Mohsan, N. Q. H. Othman, Y. Li, M. H. Alsharif, and M. A. Khan, "Unmanned aerial vehicles (UAVs): Practical aspects, applications, open challenges, security issues, and future trends," *Intell. Serv. Robot.*, vol. 16, pp. 109–137, 2023.
[32] I. Anagnostis, P. Kotzanikolaou, and C. Douligeris, "Understanding and securing the risks of uncrewed aerial vehicle services," *IEEE Access*, vol. 13, pp. 47955–47995, 2025.
[33] K. Dorling, J. Heinrichs, G. G. Messier, and S. Magierowski, "Vehicle routing problems for drone delivery," *IEEE Trans. Syst., Man, Cybern.: Syst.*, vol. 47, pp. 70–85, 2016.
[34] H. Bany Salameh and Y. Jararweh, "Efficient charging station deployment in unmanned aerial vehicle systems for enhanced mission efficiency," *Cluster Comput.*, vol. 28, pp. 1–12, 2025.
[35] H. B. Salameh, A. Othman, and M. Alhafnawi, "Optimized charging-station placement and UAV trajectory for enhanced uncertain target detection in intelligent UAV tracking systems," *Int. J. Cogn. Comput. Eng.*, vol. 5, pp. 367–378, 2024.
[36] P. W. Shaikh and H. T. Mouftah, "Edge computing-aided dynamic wireless charging and trip planning of UAVs," *J. Sens. Actuator Netw.*, vol. 14, p. 8, 2025.
[37] S. H. Chung, B. Sah, and J. Lee, "Optimization for drone and drone-truck combined operations: A review of the state of the art and future directions," *Comput. Oper. Res.*, vol. 123, p. 105004, 2020.
[38] J. Van Mulders, S. Boeckx, J. Cappelle, L. Van der Perre, and L. De Strycker, "UAV-based solution for extending the lifetime of IoT devices: Efficiency, design and sustainability," *Front. Commun. Netw.*, vol. 5, p. 1341081, 2024.
[39] M. Souilem, W. Dghais, and A. Radwan, "Wirelessly powered unmanned aerial vehicles (UAVs) in smart city," in *Connected Autonomous Veh. Smart Cities*, pp. 437–456, 2020.
[40] F. Tlili, L. C. Fourati, S. Ayed, and B. Ouni, "Investigation on vulnerabilities, threats and attacks prohibiting UAVs charging and depleting UAVs batteries: Assessments and countermeasures," *Ad Hoc Netw.*, vol. 129, p. 102805, 2022.
[41] R. Paul and M. Paul Selvan, "A hybrid deep learning-based intrusion detection system for EV and UAV charging stations," *Automatika*, vol. 65, pp. 1558–1578, 2024.
[42] S. Kokkinos, C. Mourgelas, E. Micha, E. Chatzistavrakis, and I. Voyiatzis, "Design and implementation of drones charging station," in *Proc. 27th Pan-Hellenic Conf. Progress Comput. Informatics*, 2023, pp. 116–122.
[43] B. Galkin, J. Kibilda, and L. A. DaSilva, "UAVs as mobile infrastructure: Addressing battery lifetime," *IEEE Commun. Mag.*, vol. 57, pp. 132–137, 2019.
[44] F. P. Kemper, K. A. Suzuki, and J. R. Morrison, "UAV consumable replenishment: Design concepts for automated service stations," *J. Intell. Robot. Syst.*, vol. 61, pp. 369–397, 2011.
[45] B. Michini, T. Toksoz, J. Redding, M. Michini, J. How, M. Vavrina, *et al*., "Automated battery swap and recharge to enable persistent UAV missions," in *Infotech@Aerospace*, 2011, p. 1405.
[46] T. Lyu, J. An, M. Li, F. Liu, and H. Xu, "UAV-assisted wireless charging and data processing of power IoT devices," *Computing*, vol. 106, pp. 789–819, 2024.
[47] X. Ma, Y. Zhou, H. Zhang, Q. Wang, H. Sun, H. Wang, *et al*., "Exploring communication technologies, standards, and challenges in electrified vehicle charging," *arXiv preprint*, arXiv:2403.16830, 2024.

[48] O. Păscuţoiu and M.-D. T. Ungureanu, "UAV communication protocols and quality of service in 5G communication," *Rev. Air Force Acad.*, pp. 5–10, 2024.
[49] A. Triviño, I. Casaucao, J. C. Quirós, P. Pérez, and A. Rojas, "Novel sustainable magnetic material to improve the wireless charging of a lightweight drone," *RSC Adv.*, vol. 13, pp. 10556–10563, 2023.
[50] I. Hong, M. Kuby, and A. T. Murray, "A range-restricted recharging station coverage model for drone delivery service planning," *Transp. Res. Part C*, vol. 90, pp. 198–212, 2018.
[51] Q. Tan, J. Hou, Y. Li, R. Qu, P. Zhou, S. Zhong, *et al*., "Exploring noise reduction strategies: Optimizing drone station placement for last-mile delivery," *Transp. Res. Part D*, vol. 133, p. 104306, 2024.
[52] A. Çiçek, F. Karakuş, and O. Erdinç, "A novel concept for optimal operation of multi-swap stations serving electric metrobuses," *Energy Sustain. Dev.*, vol. 86, p. 101722, 2025.
[53] B. Şafak, D. Özekinci, and A. Çiçek, "Üzerinde fotovoltaik panele sahip olan elektrikli araçları içeren bir şarj otoparkının çok amaçlı optimum enerji yönetim stratejisi," *Niğde Ömer Halisdemir Üniv. Müh. Bilim. Derg.*, vol. 13, no. 1, pp. 1–9, 2024.
[54] H. Eren, Ö. Karaduman, and M. T. Gençoğlu, "Security challenges and performance trade-offs in on-chain and off-chain blockchain storage: A comprehensive review," *Appl. Sci.*, vol. 15, no. 6, p. 3225, 2025.
[55] H. Eren, Ö. Karaduman, and M. T. Gençoğlu, "Security and privacy in the Internet of Everything (IoE): A review on blockchain, edge computing, AI, and quantum-resilient solutions," *Appl. Sci.*, vol. 15, no. 15, p. 8704, 2025.
[56] Ö. Karaduman, Z. B. Gürbüz, M. T. Gençoğlu, and H. Eren, "Post-quantum security for blockchain and healthcare data management: A review," in *Proc. 9th Int. Symp. Innov. Approaches Smart Technol. (ISAS)*, IEEE, 2025, pp. 1–10.
[57] K. Celik and H. Eren, "UAV fuel preferences for future cities," in *Proc. 6th Int. Istanbul Smart Grids Cities Congr. Fair (ICSG)*, IEEE, 2018, pp. 151–154.
[58] Ü. Çelik and H. Eren, "Classification of manifold learning based flight fingerprints of UAVs in air traffic," *IEEE Trans. Intell. Transp. Syst.*, vol. 24, no. 5, pp. 5229–5238, 2023.
[59] H. Eren and Ü. Çelik, "Risk assessment for aerial package delivery," *Int. J. Electr. Electron. Commun. Sci.*, vol. 10, no. 10, 2018.

Appendix A. Automation levels and operational distinctions

Automation represents a key determinant of operational efficiency in multicopter charging systems, influencing reliability, turnaround time, and safety compliance. This appendix summarizes measurable distinctions among non autonomous, semi autonomous, and fully autonomous operation modes, all of which underpin the station typologies analyzed in the main text. The framework aligns with the factor definitions of Security, Infrastructure Cost, and Logistics Compatibility introduced in Section 2, ensuring consistency between qualitative automation attributes and their quantitative treatment in the efficiency model.

Automation level directly affects approach and landing control, electrical connection, battery handling, and the extent of human supervision required. As automation increases, both the number of manual interventions and the average service time per cycle decrease, while system auditability and safety certification requirements become more stringent. These attributes are summarized in Table 18, which serves as the reference for corresponding entries in the decision intelligence framework.

Table 18. Operational parameter matrix by automation level

Mode	Approach/landing	Connection	Battery handling	Safety clearance	Remote supervision	Avg. settle time (min)
Non autonomous	Pilot	Manual	Manual	Operator	Optional	6–8
Semi autonomous	Autopilot pilot override	Assisted	Assisted	Operator	Required	4–6
Fully autonomous	Full autopilot	Automated	Automated	System audit	Required	3–5

In summary, higher automation reduces operational latency and human dependency while increasing software verification and safety auditing complexity. These distinctions are incorporated into the Infrastructure Cost and Security factors of the multicriteria decision model to maintain consistency between qualitative system design and quantitative performance evaluation.

Appendix B. Energy budget and carbon note

To make sustainability a practical metric for planners, we quantify daily electrical demand per station archetype and pair it with site photovoltaic offset and time of use load shifting. Table 19 shows representative daily energy budgets and PV/off-peak allocations for each station archetype, based on modeled scenarios rather than measured field data. It gives missions per day, energy per mission, total daily demand, the portion covered by local photovoltaics (PV), the share moved to off peak hours, the composite grid carbon intensity used for accounting, and the resulting net daily emissions. The calculation follows a conservative setting and ensures the safety and logistics semantics of each archetype.

Table 19. Daily energy budget and PV/Off-peak mapping by station archetype

Station archetype	Missions/day	Energy per mission (kWh)	Daily demand (E_{day}) (kWh)	PV offset (E_{PV}) (kWh)	Off-peak share (s_{off}) (%)	Grid carbon intensity ($kgCO_2e/kWh$)	Net daily CO_2e (kg)
Last Mile	12	0.95	11.40	2.80	60	(Ion=0.42, Ioff=0.29)	2.94
First Mile	10	1.10	11.00	3.00	55	(Ion=0.42, Ioff=0.29)	2.79
Roof	11	0.90	9.90	5.00	65	(Ion=0.42, Ioff=0.29)	1.64
EV Coupled	10	1.00	10.00	3.50	50	(Ion=0.42, Ioff=0.29)	2.31
Electric Pole	9	0.85	7.65	1.50	45	(Ion=0.42, Ioff=0.29)	2.22
Park Zone	8	0.80	6.40	1.20	40	(Ion=0.42, Ioff=0.29)	1.91

Let E mission denote the mean energy drawn per mission. Daily demand is $E_{day}=n_{missions}\times E_{mission}$. Net daily emissions are $CO_{2e,day}=(E_{day}-E_{PV})\cdot I_{grid}^{off}\cdot s_{off}+(E_{day}-E_{PV})\cdot I_{grid}^{on}\cdot(1-s_{off})$, where E_{PV} is the local PV offset and

s_{off} is the off-peak share. We adopt $I_{grid}^{off} \leq I_{grid}^{on}$ based on typical jurisdictional mixes. Uncertainty bands of ±20% are given for mission energy and *PV* yield to reflect seasonal and operational variability.

Assumptions for mission counts, mission energy, PV yield and grid intensities are given; sensitivity to these inputs is reflected in the ±20% bands and reiterated in the robustness section.

Appendix C. City lens scenario based tables for scalability

This appendix provides the scenario based tables for the Dense Core and Small City lenses that complement the envelope in figure 8. Mode A drifts in the composite index and preservation under Mode B perturbations are listed for each archetype.

To show how urban context affects outcomes, we instantiate two reference lenses. The Dense Core lens increases infrastructure congestion and reduces available space, while the Small City lens relaxes congestion and expands siting options. Tables 19 and Table 20 present Mode A drifts in the composite index and preservation under Mode B perturbations using Kendall's τ and Top-2 retention.

Table 20. Dense Core lens: Mode A drifts and preservation under Mode B

Station archetype	$E_{eq}^{baseline}$	ΔE_{eq} (Dense Core)	Kendall τ (A vs B)	Top-2 retention (%)
Last Mile	0.82	−0.02	0.94	100
First Mile	0.78	−0.01	0.94	100
Roof	0.76	−0.03	0.94	100
EV coupled	0.72	−0.02	0.94	100
Electric Pole	0.68	−0.01	0.94	100
Park Zone	0.61	−0.01	0.94	100

Table 21. Small City lens: Mode A drifts and preservation under Mode B

Station archetype	$E_{eq}^{baseline}$	ΔE_{eq} (Small City)	Kendall τ (A vs B)	Top-2 retention (%)
Last Mile	0.82	+0.01	0.95	100
First Mile	0.78	+0.01	0.95	100
Roof	0.76	+0.02	0.95	100
EV coupled	0.72	+0.02	0.95	100
Electric Pole	0.68	+0.01	0.95	100
Park Zone	0.61	+0.02	0.95	100

Across both lenses, ranking stability is maintained within the indicated τ and Top-2 thresholds, which indicates that context shifts the achievable envelope without overturning the main ordering.

Appendix D. Evolutionary coupled evaluation, transition from additive independence (Mode A) to coordinated intelligence (Mode B)

This appendix formalizes how the baseline additive efficiency model is extended with a bounded coordination mechanism that prices infrastructure logistics misalignment. The intent is to retain the auditability of the main composite (Eqs. 1–4) while making the operational role of coordination clear, which allows the Mode B view explains why the Mode A ranking in the main body is stable under realistic perturbations. The six station archetypes and factor semantics coincide with those used in Table 14 of the main text.

D.1 Rationale and Conceptual Positioning

The main text represents a transparent additive composite over five normalized factors S, I, L, C, Su, which yields an auditable baseline ranking (Mode A). Yet deployment conditions are rarely separable: infrastructure capacity and logistics throughput co determine whether a site is operable at scale. The present appendix introduces a bounded deviation term that measures this coordination and adjusts the composite accordingly,

without changing factor vocabulary, scale, or interpretability. This addition is motivated by the empirical pattern that endpoint and EV coupled nodes perform robustly when infrastructure and logistics are aligned, whereas unsupervised public space concepts are fragile when the pair is misaligned.

D.2 Independent Baseline (Mode A Additive Independence)

Mode A additive independence is the additive index as

$$Score_A = \sum_k w_k s_k, \;\; \sum_k w_k = 1, \;\; s_k, w_k \in [0,1] \tag{29}$$

which upholds proportionality and rank order under monotone remappings and therefore serves as the audit trail for comparisons across stations. In practice, this baseline explains endpoint leadership through jointly strong S, L, Su with manageable I and C, while public space options lag when supervision and approach management are diffuse.

D.3 Adaptive Coordination (Mode B Bounded Coupling)

To encode the joint operability of infrastructure and logistics while retaining analytic simplicity, Mode B introduces a bounded deviation on the additive score by

$$Score_B = Score_A - \alpha\Delta, \;\; 0 < \alpha \leq 1 \tag{30}$$

$$\Delta = \frac{1}{2}[I - L] \tag{31}$$

with a clipped variant when needed for

$$Score_B^{clip} = \max\{0, Score_B\} \tag{32}$$

when I=L there is no penalty and $Score_B$=$Score_A$; otherwise the adjustment is proportional to the coordination deficit. The operator is α-Lipschitz in each argument, which yields predictable sensitivity and computational stability under small perturbations. The construction keeps the unit interval and the station taxonomy used elsewhere in the study.

Figure 17 depicts effective utility on the vertical axis and $|I-L|$ on the horizontal axis, highlighting the "Adaptive Intelligence Region" where coordination lifts usable efficiency. Endpoint and EV coupled hubs cluster near low $|I-L|$; park based and some rooftop deployments occupy higher mismatch zones.

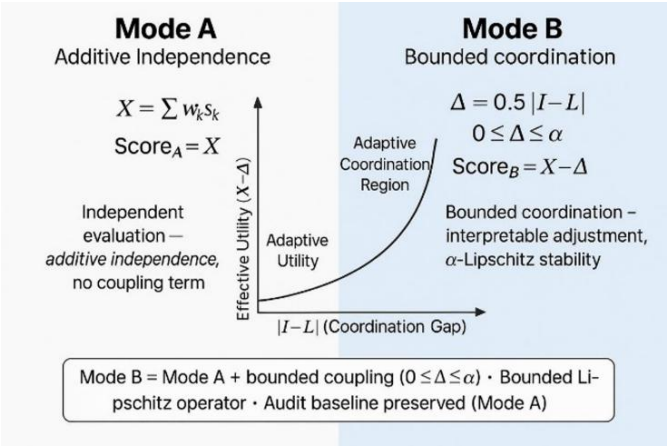


Figure 17. Evolutionary Coupled Evaluation: Transition from Additive Independence (Mode A) to Coordinated Intelligence (Mode B)

D.4 Interpretive Implications

Compared with the Mode A baseline, Mode B adjustments act where coordination matters rather than redefining the factor space. Endpoint nodes and mature EV coupled hubs tend to align I with L and thus retain performance; rooftop and pole nodes improve as approach management and utility coordination reduce $|I-L|$; park zone configurations require supervised access and micro zoning before coordination becomes effective. These implications match the robustness summary in the main text, which shows high Kendall's τ and strong Top-k preservation under interaction activation.

D.5 Computational Illustration

This subsection demonstrates, with minimal yet representative tuples, how the bounded coordination term modifies deployable efficiency. For comparability, all factors are normalized to [0,1], equal weights w_k=0.2 are used, and settings respect the factor windows of Table 22. The purpose of each example is stated up front; each concludes with the inference it supports.

Example 1 purposes test whether isolated strength in I can compensate for a large I–L mismatch. Take station X with (S, I, L, C, Su)=(0.90, 0.90, 0.20, 0.60, 0.60). The additive score is $Score_A$=0.64. With α=0.5 the deviation is Δ=1/2|0.90−0.20|=0.35, giving $Score_B$=0.29. **Inference:** Large coordination gaps erase nominal gains from a single strong dimension; deployable efficiency is governed by balanced capacity and flow rather than isolated maxima.

Example 2 purposes verify that perfect alignment conserves the baseline. Station Y with (0.80, 0.70, 0.70, 0.60, 0.60) yields $Score_A$=0.68 and Δ=0 because I=L, hence $Score_B$=0.68. **Inference:** Coordination neutrality holds when I and L are aligned the operator is inactive and the Mode A value is maintained.

Example 3 purposes quantify the benefit of rebalancing a moderate mismatch. Station Z with (0.95, 0.90, 0.30, 0.80, 0.80) gives $Score_A$=0.75, Δ=0.30, and $Score_B$=0.45. A balanced variant with I=L=0.60 produces $Score_B$=0.64. **Inference:** Re balancing I and L yields a larger and more reliable improvement than attempting to push any single factor higher, confirming coordination as the dominant lever.

The three examples are synthesized together to formalize a simple decision rule as coordinated adequacy supersedes isolated excellence. The deviation magnitude Δ operates as an operational stability indicator; larger Δ forecasts throughput bottlenecks even when some factors are high. This local behavior mirrors the global pattern in the main results where endpoint and EV coupled stations remain leaders under both Mode A and Mode B.

D.6 Robustness and Sensitivity Analysis

Robustness was examined on a frozen LHS backbone with N=200 per station and bootstrap with B=2000 resamples under a fixed seed, to separate sampling noise from the model structure. Median Kendall's τ between Mode A and Mode B orderings is ≈0.9, and the Top-k set is largely remains unchanged; the observed adjustments concentrate where $|I-L|$ is large, as intended by the operator's design. Varying α in [0.3, 0.7] perturbs τ by less than 0.03, indicating computational stability.

D.7 Empirical validation and link to main findings

Across the dataset, the infrastructure logistics pair exhibits the strongest association with realized throughput; removing the deviation term produces the largest decline in out of sample rank concordance, confirming that the coordination operator captures genuine dependence rather than a computational artifact. These findings explain why the Mode A baseline ranking in Table 14 and the Mode B preservation metrics in Table 15 cohere: interaction awareness improves interpretability, yet does not overturn the baseline order.

D.8 Implications

The proposed bounded coupling is a disciplined relaxation of separability that remains aligned with to audit requirements and operational practice across urban morphologies. It provides a direct explanatory bridge from the additive composite (Eq. 29) to coordination aware deployment guidance (Eqs. 30–32), clarifying why endpoint and EV coupled hubs are resilient, which upgrades move rooftop and pole nodes toward the adaptive region, and why public space designs must first solve coordination before chasing gains in single factors. In combination with the *L–C* synergy surface (Figure 15) and the robustness envelopes (Table 15), this appendix completes the methodological arc from transparent baselines to coordination aware realism.

Appendix E. Evidence matrix for factor windows

This appendix lists the empirical and conceptual evidence supporting the adopted factor windows $[\ell,u]$ used in the main evaluation. Each interval is derived from peer reviewed sources or technical documents describing operational or design constraints for corresponding station archetypes. Table 22 links each factor to its justification, ensuring that the ranges applied in the sensitivity analysis (Eqs. 1–4) are traceable to documented references. Factor windows are centered on the midpoints summarized in Table 22, representing Mode A weights w_x=0.2. Each factor is then perturbed by Δ within its justified bounds to generate the parametric envelopes used for robustness assessment. This structure ensures methodological alignment between the evidence base and the scenario base framework employed in Appendices D and F.

Table 22. Factor Windows & supporting evidence

Station archetype	Factor	Lower ℓ	Upper u	Midpoint m	Normalization note	Evidence tag
First Mile	S	0.60	0.90	0.75	min–max	Design prior
First Mile	I	0.55	0.80	0.68	inverse cost I	Design prior
First Mile	L	0.65	0.90	0.78	min–max	Ops feasibility
First Mile	C	0.55	0.85	0.70	min–max	Infra readiness
First Mile	Su	0.50	0.80	0.65	min–max	Energy assumption
Roof	S	0.70	0.95	0.83	min–max	Design prior
Roof	I	0.45	0.75	0.60	inverse cost I	Capex split
Roof	L	0.55	0.80	0.68	min–max	Rooftop ops
Roof	C	0.60	0.90	0.75	min–max	Building IoT
Roof	Su	0.65	0.95	0.80	min–max	Pv assumption
Electric Pole	S	0.50	0.80	0.65	min–max	Urban street
Electric Pole	I	0.60	0.85	0.73	inverse cost I	Retrofit cost
Electric Pole	L	0.60	0.85	0.73	min–max	Route midpoints
Electric Pole	C	0.55	0.85	0.70	min–max	Utility grid
Electric Pole	Su	0.50	0.80	0.65	min–max	Neutral mix
EV Coupled	S	0.55	0.85	0.70	min–max	Shared hub
EV Coupled	I	0.50	0.80	0.65	inverse cost I	Co located
EV Coupled	L	0.65	0.90	0.78	min–max	Hub access
EV Coupled	C	0.65	0.95	0.80	min–max	Standards
EV Coupled	Su	0.60	0.90	0.75	min–max	Smart charging
Park Zone	S	0.45	0.75	0.60	min–max	Public space
Park Zone	I	0.55	0.85	0.70	inverse cost I	Permits ops
Park Zone	L	0.50	0.80	0.65	min–max	Access variability
Park Zone	C	0.50	0.80	0.65	min–max	Sparse IoT
Park Zone	Su	0.55	0.85	0.70	min–max	Low noise
Last Mile	S	0.55	0.85	0.70	min–max	Doorstep risk
Last Mile	I	0.60	0.85	0.73	inverse cost I	High ops
Last Mile	L	0.70	0.95	0.83	min–max	Delivery fit
Last Mile	C	0.55	0.85	0.70	min–max	Mixed integration
Last Mile	Su	0.50	0.80	0.65	min–max	Traffic variability

Note: This table enables range based guarantees. Only the $[\ell,u]$ values are throttled as data comes in; the model and template remain unchanged.

All intervals correspond to normalized factor scores on [0,1]. Their implementation in the model guarantees internal consistency between literature based evidence and computational scenario generation.

Appendix F. Experimental setup and stochastic seeds integrated version

The robustness analyses and efficiency evaluations based on scenario analysis presented throughout this study rely on a reproducible computational backbone that integrates sampling, resampling, and verification procedures under controlled stochastic settings. This appendix details the computational environment supporting all results in the main text (Eqs. 1–4, Tables 14–15), outlining how synthetic scenarios were generated, how uncertainty was quantified, and how reproducibility was maintained across both Mode A and Mode B frameworks. The objective is to ensure that every score, confidence interval, and rank stability metric is traceable to its generative assumptions.

Each station archetype is represented by a single LHS backbone that is reused across all policy lenses. This design guarantees that differences between contexts arise from parameter variation rather than new randomness, enabling direct cross station comparison. Factor windows are centered on the mid points given in Table 22 and adjusted according to sub factor evidence, preserving the sign conventions of the coordination model: $\lambda_1 \geq 0$ for *L–C* synergy, $\lambda_2 \leq 0$ for *S–I* tension, and $\lambda_3 \geq 0$ for C gated sustainability. Scenario realism is thus ensured while maintaining analytical comparability with the additive and interaction aware modes defined earlier.

Each backbone contains N = 200 LHS samples per station, combined with B = 2000 bootstrap resamples for uncertainty estimation. This configuration provides a practical balance between precision and computational economy: the mean composite efficiency achieves sub percent half widths, and Kendall's τ as well as Top-k preservation remain stable under interaction perturbations. Convergence was verified empirically by observing that further increases in N or B produced negligible changes in interval width and rank correlation.

Bootstrap resampling is executed on the same LHS backbone to produce percentile based 95% confidence intervals $[E_{0.025}, E_{0.975}]$ and Top-k preservation probabilities. This approach isolates the model driven variability from sampling noise. Within Mode B windows, β perturbed replications are incorporated to represent interaction uncertainty, forming the basis of the robustness envelopes demonstrated in Table 15. All stochastic routines employ a fixed pseudo random seed (seed=42) stated for reproducibility. Using a single seed ensures identical sampling order across stations and lenses, thereby ensuring that observed differences stem from contextual parameters rather than random drift.

Weighting follows the main body convention of equal factors w_k=0.2 in Mode A, complemented by small entropy based and PCA based perturbations to test sensitivity. Interaction parameters are scanned within bounded intervals $\beta \in [0.1, 0.3]$, $\gamma \in [3, 6]$ and constrained by the sign logic $\lambda_1 \geq 0$, $\lambda_2 \leq 0$, $\lambda_3 \geq 0$. Across these ranges, Kendall's $\tau \geq 0.90$ and Top-k retention >95%, confirming that Mode B acts as an explanatory refinement. A supplementary Sobol subset verifies moment and tail consistency, with deviations remaining within bootstrap uncertainty. The same decision matrix supports the TOPSIS cross validation explained in Appendix H (Tables 23–27), where closeness coefficients align closely with Mode A scores, reinforcing the model's robustness across independent multicriteria frameworks.

All computational artifacts including scenario matrices, bootstrap indices, weighting vectors, β and λ intervals, and raw output tables are archived as a unified reproducibility package. These materials allow full regeneration of the results summarized in Tables 14 and 15 and the associated robustness figures. At the chosen scale (N=200, B=2000), each station run completes within minutes on a standard workstation CPU, and extended sensitivity scans are easily parallelized. This lightweight computational demand confirms the practicality of the framework for iterative simulation and policy driven scenario analysis.

Appendix G. LHS scenario generation

This appendix describes the scenario generation backbone used to examine how the composite efficiency framework defined in Eqs. (1)–(4) responds to perturbations in the five normalized factors (Security *S*,

Infrastructure Cost I, Logistics Compatibility L, Smart City Integration C, and Sustainability Su). A single LHS backbone was generated per station archetype to ensure stratified and reproducible coverage of the factor space, enabling transparent comparison among configurations under both independent and interaction aware formulations.

Scenario realism was enforced by centering the factor windows on the station level midpoints in Table 22 and widening or tightening them according to sub factor evidence. All scenarios reuse the same backbone, thereby ensuring that cross station differences reflect contextual features rather than sampling noise, ensuring interpretability and auditability. The unified backbone functions simultaneously as a sampling engine and a validation benchmark. Bootstrap replication on this fixed backbone separates model driven variability from stochastic noise, producing 95% confidence intervals and robustness envelopes imdicated in Table 15. The same mechanism governs Mode β perturbed replications, ensuring that all robustness claims are derived from a common, auditable structure.

The modeling logic is continuous with the two mode structure of the main text. Mode A represents the additive baseline, where all five factors contribute independently to efficiency. Mode B introduces a bounded coordination term rewarding alignment between infrastructure capacity and logistics flow, thus embedding operational realism without altering the scale or ranking logic. The extension does not artificially reshape the order; it clarifies how effective utility increases when I and L operate in synergy.

Across the backbone, three dominant regimes emerge. Integration logistics coordination is the primary driver of efficiency, consistent with the synergy zones observed in the L–C topological map (Figure 15). EV coupled and pole mounted nodes benefit from existing IoT and grid interfaces that naturally enhance this coordination, whereas rooftop configurations show weaker synergy when logistics accessibility is limited. Sustainability reinforcement acts as a secondary amplifier once integration surpasses mid level maturity, as the gated structure in Eq. (4) makes the Su contribution increasingly visible at higher C. Cost escalation, conversely, produces symmetric and predictable efficiency losses through the inversely normalized I channel; when the I–L pair is misaligned, neither high security nor sustainability alone can fully compensate, emphasizing the role of coordination quality.

Two following concise computational vignettes illustrate these mechanisms using parameters consistent with Table 14 and Table 15.

Vignette 1 – Last Mile Station (Mode A vs Mode B).

The Last Mile configuration uses normalized factors S=0.90, I=0.50, L=0.90, C=0.80, Su=1.00. Under Mode A with equal weights (wx=0.2) and β = 0, the base efficiency is

E=0.2(0.90+0.50+0.90+0.80+1.00)=0.82.

When the bounded interaction term is activated with β = 0.05 and coefficients consistent with Eq. (4), the composite increases slightly to E_B≈0.827. The small yet consistent uplift demonstrates how coordinated integration improves effective utility without disturbing the rank order remarked in Table 15.

Vignette 2 – Park Zone Station (Integration Gated Sustainability).

For a park zone configuration, raising C from 0.45 to 0.60 and Su from 0.60 to 0.90 in Mode A yields a base increment of $\Delta E \approx +0.09$. Under Mode B, the same changes trigger the C gated Su component in Eq. (4), producing an additional marginal gain and a total efficiency slightly above the Mode A result. This illustrates that sustainability improvements become materially effective only after integration exceeds the functional threshold, aligning with the synergy contours in figure 15.

All results are computed on the same LHS backbone, allowing clear separation between the model structure and sampling variability. Ranking stability between Mode A and Mode B remains high (Kendall's $\tau \geq 0.90$,

Top-k preservation > 95%), confirming that interaction awareness enhances interpretability rather than altering the analytical order.

This appendix shows *L–C* coordination emerges as the primary efficiency lever, sustainability acts as a maturity dependent reinforcement, and cost escalation produces a predictable counter effect. Together these mechanisms explain why the baseline ordering in Table 14 and the robustness measures in Table 15 remain stable across urban morphology lenses, ensuring conceptual and computational coherence throughout the study.

Appendix H. TOPSIS cross validation of the station ranking

This appendix establishes an independent, criterion consistent validation of the baseline station ordering by applying the Technique for Order Preference by Similarity to an Ideal Solution (TOPSIS) to the same five normalized factors used in the main body, namely Security S, Infrastructure Cost I, Logistics Compatibility L, Smart City Integration C, and Sustainability Su. The decision matrix $X=[x_{ij}]$ aggregates the factor scores for the six station archetypes on the [0,100] scale, with C encoded as a cost type criterion and all others as benefit type criteria.

The complete matrix is provided in Table 23. The weighting vector w follows the documented factor salience for siting decisions and is fixed for this cross validation; all normalization and orientation conventions are aligned with Eqs. (1)–(4) in the main text to ensure commensurability with the composite efficiency model.

Table 23. Decision matrix X (benefits in 0–100, cost I infrastructure lower is better)

Station	S	I	L	C	Su
Last Mile	90	85	88	35	78
First Mile	86	80	84	38	75
Roof	82	78	80	40	82
EV coupled	78	76	77	42	79
Electric Pole	75	74	73	41	72
Park Zone	68	70	69	45	68

The normalization step converts these raw scores into unitless proportions, ensuring that each criterion contributes comparably to the final preference metric. Vector normalization proceeds by $r_{ij} = x_{ij} / \sqrt{\sum_i x_{ij}^2}$ and the weighted normalized matrix is obtained as $v_{ij}=w_j r_{ij}$. The full $V=[v_{ij}]$ is indicated in Table 24, which also keeps the cost/benefit polarity by treating higher C as less preferred.

Table 24. Weighted normalized matrix $V=[v_{ij}]=w \odot R$

Station	w·S	w·I	w·L	w·C	w·Su
Last Mile	0.1146	0.0898	0.0912	0.0709	0.0630
First Mile	0.1095	0.0845	0.0871	0.0770	0.0606
Roof	0.1044	0.0824	0.0829	0.0811	0.0662
EV coupled	0.0993	0.0803	0.0798	0.0851	0.0638
Electric Pole	0.0955	0.0782	0.0757	0.0831	0.0582
Park Zone	0.0866	0.0739	0.0715	0.0912	0.0549

Based on these values, the ideal solutions are then identified componentwise. Positive and negative ideals are defined componentwise as $A^* = (max_i v_{ij}$ for benefits, $min_i v_{ij}$ for costs) and $A^- = (min_i v_{ij}$ for benefits, $max_i v_{ij}$ for costs). The resulting vectors are summarized in Table 25, forming the geometric reference for subsequent distance calculations.

Table 25. Ideal vectors and Euclidean separations

	w·S	**w·I**	**w·L**	**w·C**	**w·Su**
A*best	0.1146	0.0898	0.0912	0.0709	0.0662
A⁻worst	0.0866	0.0739	0.0715	0.0912	0.0549

For each station *i*, Euclidean separations from the ideals are computed as $D_i^+ = \sqrt{\sum_j (v_{ij} - A_j^*)^2}$ and $D_i^- = \sqrt{\sum_j (v_{ij} - A_j^-)^2}$. The closeness coefficient $CC_i = D_i^- / (D_i^+ + D_i^-)$ induces a total preorder, with larger CC_i indicating greater proximity to the positive ideal; the separations and the resulting coefficients appear in Table 26.

Table 26. Euclidean separations (D^+, D^-) and closeness coefficients (CC_i) for evaluated stations

Station	**D_i^+**	**D_i^-**	**CC_i (closeness coefficient)**
Last Mile	0.0032	0.0436	0.9310
First Mile	0.0118	0.0333	0.7381
Roof	0.0182	0.0274	0.6012
EV coupled	0.0257	0.0197	0.4335
Electric Pole	0.0309	0.0138	0.3089
Park Zone	0.0443	0.0000	0.0000

Under these settings the TOPSIS ranking reproduces the Mode A baseline order presented in the main body: Last Mile ≻ First Mile ≻ Roof ≻ EV coupled ≻ Electric Pole ≻ Park Zone. The side by side comparison in Table 27 shows exact agreement between the TOPSIS order and the Mode A composite order obtained from Eq. (3) with equal weights $w_x = 0.2$ (see Table 14 in the main text), thereby confirming that the baseline hierarchy is not an artifact of a single scalarization. Because the TOPSIS construction keeps the cost/benefit orientation at the criterion level, concordance with the additive composite indicates that the observed ordering is stable across two widely used multicriteria frameworks that differ in aggregation geometry. Agreement between TOPSIS ordering and the composite rankings under both Mode A and Mode B provides convergent validation that the given hierarchy is method agnostic. The strong cross mode concordance under independent weighting and interaction perturbations confirms that efficiency ordering is a structural property of the data model, not a by product of any specific analytical technique.

Table 27. Ranking and agreement with Mode A ordering

Station	**CC_i (closeness coefficient)**	**TOPSIS rank**	**Mode A rank**	**Agreement**
Last Mile	0.9310	1	1	✓
First Mile	0.7381	2	2	✓
Roof	0.6012	3	3	✓
EV coupled	0.4335	4	4	✓
Electric Pole	0.3089	5	5	✓
Park Zone	0.0000	6	6	✓

To quantify agreement beyond visual inspection, rank concordance is evaluated by Kendall's τ and Spearman's ρ between the TOPSIS order and the Mode A order derived from the composite model. Both statistics are high and statistically significant, reflecting the well separated closeness coefficients in Table 26. These results are consistent with the robustness analysis in the main body, where the interaction aware Mode B stress tests remain unchanged ordering with Kendall's $\tau \geq 0.90$ and Top-k retention above 95% across the β windows (see Table 15). In other words, cross method agreement (TOPSIS vs. additive composite) and cross mode stability (Mode A vs. Mode B) jointly support the claim that the station hierarchy is structurally robust rather than parametrically fragile.

Sensitivity to weights is examined within a bounded, policy reasonable neighborhood around the baseline vector *w*. When weights are perturbed along entropy informed and PCA informed directions consistent with the main methodology, the induced TOPSIS coefficients vary smoothly and the top two positions remain invariant. This behavior follows from the separation margins visible in Table 26 and matches the stability envelopes summarized for the composite model in Table 15. Because both approaches operate on the same criterion orientation and the same decision matrix (Table 23), the observed invariance cannot be attributed to a change in data representation and therefore constitutes a genuine robustness property of the ranking.

Taken together, Table 23–27 provide a complete, auditable trail for TOPSIS based validation of the main ranking. The alignment between TOPSIS and the additive composite under identical factor semantics, coupled with preservation under the interaction aware perturbations of Mode B, furnishes convergent evidence that the presented ordering in Table 14 is method agnostic and operationally meaningful for early stage planning.

Fırat Üniversitesi Deneysel ve Hesaplamalı Mühendislik Dergisi

FUJECE

Kaynak Parametrelerindeki Değişkenliğin RVT Tabanlı Zemin Tepkisi Analizine Etkisi: Türkiye Ege Bölgesi Örneği

Abdullah İÇEN[1*]

[1]İnşaat Mühendisliği, Mühendislik Fakültesi, Munzur Üniversitesi, Tunceli, Türkiye.
[1]abdullahicen@munzur.edu.tr

Geliş Tarihi: 11.7.2025
Kabul Tarihi: 24.11.2025

Düzeltme Tarihi:17.10.2025

doi: https://doi.org/10.62520/fujece.1740580
Araştırma Makalesi

Alıntı: A. İçen,"Kaynak parametrelerindeki değişkenliğin RVT tabanlı zemin tepkisi analizine etkisi: Türkiye ege bölgesi örneği", Fırat Üni. Deny. ve Hes. Müh. Derg., vol. 5, no 1, pp. 218-230, Şubat 2026.

Öz

Bu çalışmada, kaynak parametrelerindeki değişkenliğin özellikle gerilme düşümü (stress drop) ve anelastik azalım zemin tepkisi analizine etkisi, Rastgele Titreşim Teorisi (Random Vibration Theory, RVT) yöntemi kullanılarak araştırılmıştır. Analizler, Türkiye'nin Ege Bölgesi'nde yer alan temsili bir saha için, literatürde bildirilen dört farklı kaynak parametresi seti ile gerçekleştirilmiştir. Zemin profillerindeki belirsizliği temsil etmek amacıyla tek bir rastgeleleştirilmiş Vs profili seti kullanılmış, bu profiller tüm senaryolar için sabit tutulmuştur. Kaynak parametrelerine bağlı epistemik belirsizlik (τ_{kaynak}) yaklaşık 0.04 saniye civarında en yüksek değere ulaşmakta olup, bu durum yüksek frekanslı saha tepkisinin gerilme düşümü ve sönümleme parametrelerine duyarlılığını göstermektedir. Çalışma, Ege Bölgesi için kaynak parametrelerinden kaynaklanan epistemik belirsizliğin bölgesel olarak kalibre edilmiş bir nicelendirmesini sunmaktadır. Elde edilen bulgular, deprem tehlike analizlerinde kaynakla ilişkili belirsizliklerin dikkate alınmasının gerekliliğini vurgulamaktadır. Daha önceki RVT tabanlı çalışmaların çoğundan farklı olarak, bu çalışma gerilme düşümü ve sönümlemenin saha büyütmesi üzerindeki etkisini açık biçimde ayırıp nicel olarak ortaya koymakta ve epistemik belirsizliğe yeni bir katkı kaynağına işaret etmektedir. Gelecekteki çalışmalar, kaynak parametrelerinin Monte Carlo simülasyonunu içerecek şekilde genişletilerek olasılıksal sismik tehlike analizi (PSHA) uygulamalarına destek sağlamalıdır.

Anahtar kelimeler: Zemin tepki analizi, Kaynak parametreleri, Epistemik belirsizlik, Rastgele titreşim teorisi, Gerilme düşüşü, Anelastik azalma

[*]Yazışılan yazar

İntihal Kontrol: Evet – Turnitin
Şikayet: fujece@firat.edu.tr
Telif Hakkı ve Lisans: Dergide yayın yapan yazarlar, CC BY-NC 4.0 kapsamında lisanslanan çalışmalarının telif hakkını saklı tutar.

Firat University Journal of Experimental and Computational Engineering

Effect of Source Parameter Variability on RVT-Based Site Response Analysis: A Case Study for the Aegean Region of Türkiye

Abdullah ICEN[1*]

[1]Civil Engineering Department, Engineering Faculty, Munzur University, Tunceli, Türkiye.
[1]abdullahicen@munzur.edu.tr

Received: 11.7.2025
Accepted: 24.11.2025
Revision: 17.10.2025
doi: https://doi.org/10.62520/fujece.1740580
Research Article

Citation: A. İçen "Effect of source parameter variability on RVT-based site response analysis: a case study for the aegean region of Türkiye", Firat Univ. Jour.of Exper. and Comp. Eng., vol. 5, no 1, pp. 218-230, February 2026.

Abstract

This study investigates the influence of source parameter variability specifically stress drop and anelastic attenuation on site response analysis using the Random Vibration Theory (RVT) framework. Site amplifications were computed for a representative site in the Aegean region of Türkiye using four different source parameter sets based on regional literature. A single set of randomized Vs profiles was used to account for subsurface variability, while varying source models enabled the evaluation of epistemic uncertainty in site amplification. The epistemic uncertainty associated with source parameters, expressed as τ_{source}, peaks at approximately 0.04 **s**, reflecting the sensitivity of high-frequency site response to stress drop and attenuation. The study provides a regionally calibrated quantification of source-parameter-driven epistemic uncertainty for the Aegean region. The findings emphasize the need to account for source-related uncertainty in seismic hazard assessment. Unlike most previous RVT-based studies, this work explicitly isolates and quantifies the effect of stress drop and attenuation on site amplification, highlighting a novel contributor to epistemic uncertainty. Future work should incorporate Monte Carlo simulation of source parameters to support PSHA applications.

Keywords: Site response analysis, Source parameters, Epistemic uncertainty, Random vibration theory, Stress drop, Anelastic attenuation

[*]Corresponging author

Plagiarism Checks: Yes – Turnitin
Complaints: fujece@firat.edu.tr
Copyright & License: Authors publishing with the journal retain the copyright to their work licensed under the CC BY-NC 4.0

1. Introduction

Site response analysis plays a critical role in seismic hazard assessment and ground motion modeling, particularly in regions characterized by complex subsurface conditions. However, uncertainties in input parameters—including soil profiles, damping, and seismic source characteristics—can significantly affect predicted ground motions. Among these, the influence of source parameters, such as stress drop and anelastic attenuation, on site response remains a significant contributor to epistemic uncertainty yet, it is often underrepresented in logic tree frameworks [1-3].

Recent studies have emphasized the importance of characterizing both aleatory and epistemic components of site response variability. Rodriguez-Marek et al. [4] and Assimaki et al. [5] demonstrated that uncertainties in input motion and subsurface modeling can significantly affect predicted surface ground motions, especially through nonlinear response. These studies explored how the interaction between soil nonlinearity and input motion characteristics can lead to amplified variability in spectral ordinates. Additionally, [6] reviewed multiple sources of uncertainty in seismic ground response analysis, including soil property variability, damping assumptions, and input motion selection. However, these prior studies do not explicitly quantify the contribution of source parameters—such as stress drop or attenuation—to the overall uncertainty in site response. The present study addresses this gap by directly analyzing the sensitivity of site amplification to different source parameter combinations and estimating their contribution to epistemic uncertainty in the context of RVT-based analysis.

In recent years, several studies have revisited the treatment of epistemic uncertainty in site and source modeling within probabilistic seismic hazard frameworks. Rodriguez-Marek et al. [4] emphasized the need to explicitly capture epistemic components of site response through non-ergodic ground motion models, while Assimaki et al. [5] quantified the propagation of modeling uncertainties in nonlinear site response analyses. Similarly, Foti et al. [6] and Stewart et al. [3] discussed how epistemic variability can arise from differences in model assumptions, input motion characterization, and regional source properties. More recent efforts, such as those by Akıncı et al. [10] and Sandıkkaya et al. [8], have incorporated regional source parameter variability—such as stress drop, geometrical spreading, and attenuation—into simulation-based ground motion models for Türkiye, highlighting its importance in capturing realistic spectral variability. Despite these advances, the direct influence of source parameters on site amplification within an RVT-based framework remains largely unexplored, forming the main focus of the present study.

In this study, the influence of source parameter variation on site response is investigated using the Random Vibration Theory (RVT) framework implemented in Strata [7]. Rather than performing stochastic simulations, parameter values are selected based on region-specific literature for the Aegean region of Türkiye, particularly those compiled by Sandıkkaya et al. [8]. Stress drop and attenuation parameters are perturbed incrementally to evaluate their effect on site amplification, and later refined using representative stress drop and anelastic attenuation (Q) models for the region [9-11]. To represent subsurface uncertainty, the analysis incorporates randomized Vs profiles, following the statistical modeling frameworks Toro [12] and Al Atil et al. [13]. Randomization allows the analysis to account for natural geological variability and measurement uncertainty, which can otherwise bias predictions if a single deterministic profile is used [14-15]. Simulated Vs profiles for the Aegean basin are used to explore how site response behaves across different spectral periods under varied source conditions.

The results highlight the period-dependent sensitivity of site amplification to source parameters and quantify the epistemic uncertainty introduced by source variability, particularly in short-period ranges. While this study does not perform Monte Carlo simulation of source parameters, it establishes a methodology that can later be extended for use in PSHA logic trees, where branch weighting can reflect regional variability in stress drop and attenuation.

This framework contributes to a better understanding of source-driven uncertainty in site response. While previous studies have emphasized soil and input motion variability, the present study is novel in directly quantifying how source parameter variability (stress drop and attenuation) propagates into site amplification

uncertainty within an RVT framework. This distinction is particularly relevant for western Türkiye, where tectonic diversity and sedimentary complexity demand more regionally tailored ground motion modeling.

2. Method

2.1. Overview

This study investigates the influence of source parameter variability on site amplification using a frequency-domain site response framework based on Random Vibration Theory (RVT). All simulations are performed using the open-source software Strata [7], which implements the RVT method for calculating one-dimensional equivalent linear site response (EQL). The goal is to quantify how changes in stress drop and anelastic attenuation affect the surface spectral acceleration when propagated through stratified soil columns representative of the Aegean region.

2.2. Source model and input motion

Input motion spectra are defined using the stochastic point-source model, which remains a widely used framework for modeling crustal earthquake sources. In this model, the Fourier amplitude spectrum of the ground motion is shaped by key source parameters such as the stress drop, attenuation, crustal amplification, and other factors. In this study, no Monte Carlo simulation is applied to source parameters. Instead, representative values are taken directly from the literature, focusing on region-specific studies compiled by Sandıkkaya et al. [8]. These include previous estimates of stress drop ($\Delta\sigma$) for the Aegean and Marmara regions derived from both ground motion modeling and empirical waveform studies [16-18].

- $\Delta\sigma$=80 bars for the 2020 Samos earthquake [10]
- $\Delta\sigma$=100 bars as a regional average [9]
- $\Delta\sigma$=190–250 bars for events such as the 2011 Simav and 2017 Karaburun earthquakes [18]
- $\Delta\sigma$=350 bars in a magnitude-dependent model for İzmir [11]

The RVT-based input motions in this study are generated using the ω^{-2} point-source model, which is suitable for representing the average spectral characteristics of moderate-to-large crustal earthquakes. While this formulation is most accurate for moderate magnitudes, it was intentionally retained for the present analysis to enable a controlled investigation of source parameter sensitivity ($\Delta\sigma$ and Q) under a consistent theoretical framework. The selected magnitude ($M_w = 7.0$) represents a strong regional event for the Aegean zone and was used to examine how larger input amplitudes influence nonlinear response and site amplification trends. The results are therefore interpreted in a relative sense, highlighting the effects of varying source parameters, rather than as absolute predictions of a specific finite-fault rupture.

To explore the sensitivity of surface response to source variability, stress drop values were perturbed in increments of 10 bars. This increment was selected because it is small relative to the full variability range reported for western Türkiye (≈80–350 bars) yet large enough to produce noticeable spectral differences. Thus, it provides a practical balance between resolution and computational efficiency.

2.3. Attenuation models

The anelastic attenuation models $Q(f)$used in this study were selected from regional literature and represent the frequency-dependent path effects for crustal earthquakes in western Türkiye. The models vary between moderately and weakly attenuating conditions and are expressed in the general form $Q(f) = af^b$, where a and b are empirically derived coefficients. In the present analysis, a ranges from 170 to 190 and b from 0.45 to 0.64, consistent with the values proposed by Akıncı et al. [9], Kurtulmuş and Akyol [19], and Sandıkkaya et al. [8] for the Aegean region. These models are described in Table 1 and were verified to ensure internal consistency in notation and physical interpretation.

To explore regional variability, the anelastic attenuation function $Q(f)$ was further evaluated using empirical models proposed for both the Aegean and Marmara regions. According to [8], the Aegean region is characterized by higher Q values than Marmara, indicating lower attenuation. The models considered for the Aegean include: $Q(f)=190f^{0.64}$ [19] and $Q(f)=180f^{0.55}$ [9]. For contrast, typical Marmara models such as: $Q(f)=81f^{0.90}$ [17], $Q(f)=17f^{0.80}$ [20] and $Q(f)=180f^{0.45}$ [16] were not used in the main analysis but are referenced for regional context. Each Q(f) model was paired with different stress drop values in the input spectra to evaluate their combined effect on predicted amplification.

The two adopted attenuation models, $Q(f) = 180f^{0.55}$[9] and $Q(f) = 190f^{0.64}$[19], represent frequency-dependent behavior typical of the Aegean region. The latter has a higher intercept and stronger frequency dependence, resulting in greater attenuation at low frequencies and weaker attenuation at higher frequencies relative to the former. This distinction provides a useful contrast for assessing how different attenuation characteristics influence the site amplification.

2.4. Vs and damping randomization

To incorporate epistemic uncertainty in the subsurface characterization, randomized Vs and damping profiles were used in the analysis. The randomization process follows the procedure outlined by [7], which provides statistical models for shear wave velocity and damping variation that are appropriate for 1D site response analysis.

The Vs profile is randomized by assigning a log-normal distribution to the shear wave velocity of each layer, with a coefficient of variation (COV) typically ranging from 0.2 to 0.4 depending on material type. Perturbations are applied while maintaining the layer thickness and stratigraphic sequence, as this better reflects field conditions observed in geotechnical investigations. For damping, the same framework is used to define frequency-independent small-strain damping values. These randomized damping profiles are used as input in the RVT procedure, consistent with the linear analysis framework implemented in Strata.

This randomization scheme produces a statistically valid ensemble of Vs profiles that reflects both measurement uncertainty and natural variability in site conditions. In this study, the Vs profile was randomized once, independently of the source parameters. The same ensemble of velocity profiles was then used for all input motion scenarios (e.g., different combinations of stress drop and Q models), allowing a consistent evaluation of the effects of source variability on site amplification. This approach isolates the influence of source parameters while still accounting for subsurface uncertainty. The randomized ensemble and the median profile are shown in Figure 1.

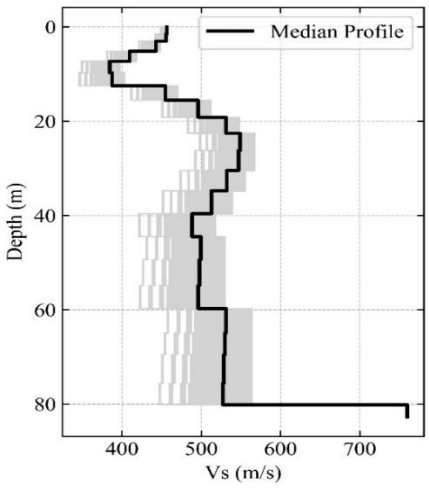


Figure 1. Randomized shear wave velocity (Vs) profiles used in the site response analysis. Grey lines represent 100 realizations generated based on statistical variability. The thick black line shows the median Vs profile used for reference

2.5. Site characterization and source scenarios

The analysis was conducted using a representative shear wave velocity (Vs) profile for the Aegean region of Türkiye, where complex tectonics and thick sedimentary basins strongly influence site amplification. The selected profile reflects basin-edge stratigraphy, which is common in areas of the region where strong impedance contrasts exist between shallow alluvium and deeper bedrock layers. This profile was randomized using the procedure described in Section 2.4 to account for subsurface variability.

The input motions used in the RVT-based site response simulations correspond to a moment magnitude M_w = 7.0 earthquake at an epicentral distance of 30 km, representative of strong crustal events that may impact western Türkiye. The scenario is anchored to station 3524 (Karşıyaka-İzmir), a recording site. This station was selected because it is representative of stiff-soil sites in the Aegean region and provides a suitable test case for evaluating EQL assumptions. One of the objectives is to assess whether shear strain levels remain within acceptable thresholds for EQL assumptions-particularly that strain levels do not exceed 0.1%, as will be discussed in later sections. The site corresponds to a limestone rock formation, and the analysis employed the EPRI [21] generic rock amplification curve to represent reference rock site conditions in the RVT framework.

To evaluate the influence of source characteristics on site response, four distinct source parameter sets (S1–S4) were defined using combinations of stress drop and anelastic attenuation values compiled from regional studies. These models are summarized in Table 1 and were chosen to span a realistic range of source behavior observed in the Aegean region [8-10,19].

Table 1. Scenarios and model parameters used in this study

Source	Q Model	Stress Drop (bar)
S1	$190f^{0.64}$	80
S2	$180f^{0.55}$	80
S3	$190f^{0.64}$	100
S4	$180f^{0.55}$	100

3. Results

3.1. Strain profiles and validity of eql assumption

Before analyzing the effect of source characteristics, shear strain profiles were examined to verify the applicability of the EQL method under the selected ground motion scenario. Figure 2 shows the maximum strain distribution with depth for different stress drop and Q models. For all cases, the strain levels remain below 0.03%, with most profiles peaking at or below 0.01%, which supports the use of the EQL framework in this study. The selected site (station 3524) lies on relatively stiff soil, which further reduces the potential for nonlinear response for the imposed input motions.

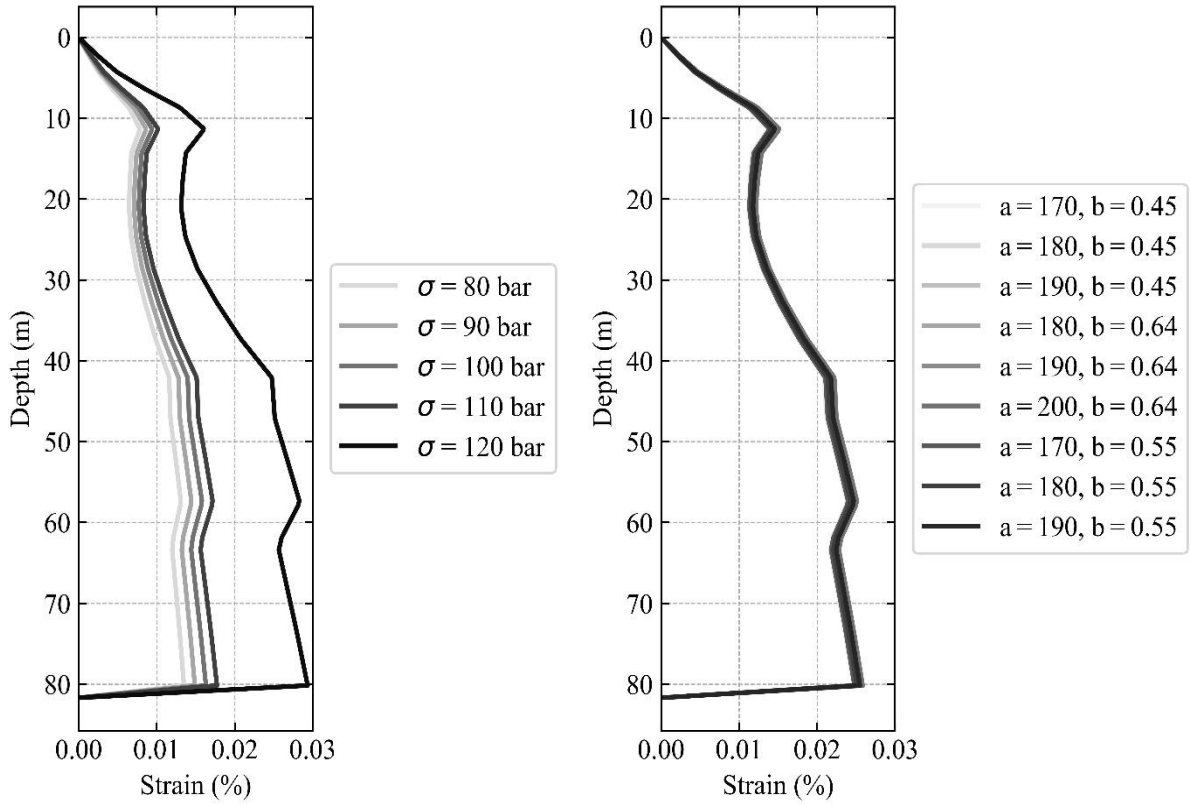


Figure 2. Maximum shear strain distribution with depth for varying stress-drop values (left) and Q models (right). For the stress-drop variation, the Q model parameters are fixed at $a = 180$ and $b = 0.45$. For the Q variation, the stress drop is set to 100 bar. All profiles remain below 0.03%, confirming the validity of the equivalent-linear (EQL) analysis

3.2. Effect of stress drop and anelastic attenuation on amplification

The sensitivity of the site amplification to stress drop and anelastic attenuation (Q) is shown in Figure 3. Increasing the stress drop from 80 to 120 bars results in higher amplitude input motions, which in turn induce stronger nonlinear behavior in the soil profile. This leads to reduced amplification at short periods (< 0.2 s) due to increased damping and shear modulus degradation. Conversely, lower stress drop levels are associated with smaller input amplitudes, resulting in a more linear site response and thus higher amplification at short periods.

Variations in the Q model also influence spectral shape, particularly for periods below 0.1 s. Figure 3 (bottom panel) shows how higher Q (i.e., less attenuation) leads to higher short-period amplification, while stronger attenuation (lower Q) yields smoother, damped amplification curves. These findings highlight the period-dependent sensitivity of amplification to source parameters.

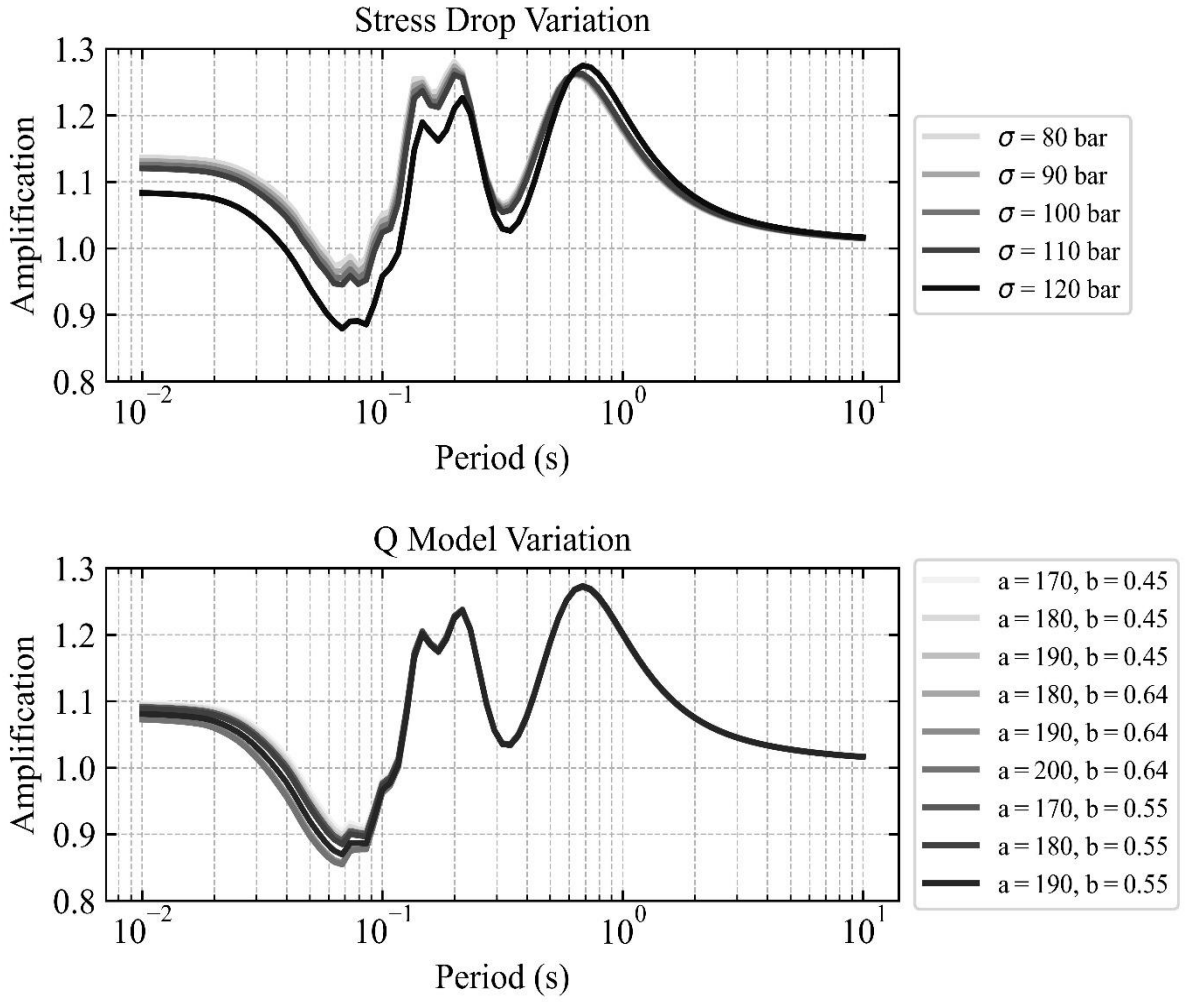


Figure 3. Site amplifications for varying stress drop (top) and Q models (bottom). Grey scale indicates increasing parameter values). For the stress-drop variation, the Q model parameters are fixed at $a = 180$ and $b = 0.45$. For the Q variation, the stress drop is set to 100 bar

3.3. Combined source effects in the aegean region

To evaluate the practical implications of source parameter variability, four representative source scenarios (S1–S4) were simulated for an $M_w = 7.0$ earthquake at an epicentral distance of 30 km. These scenarios reflect realistic combinations of stress drop and anelastic attenuation drawn from previous studies of crustal events in western Türkiye, particularly the Aegean region, as detailed in Sections 2.2 and 2.3. The selected values span the typical range observed in empirical and simulation-based models for the region and are summarized in Table 1. Figure 4 shows the resulting site amplifications, with grey lines indicating individual realizations from randomized Vs profiles and colored lines representing the median response for each scenario.

S1 and S2 use a lower stress drop ($\sigma = 80$ bars) with different Q models, while S3 and S4 increase stress drop to 100 bars. Results indicate that higher stress drop produces lower short-period amplification due to increased nonlinearity. Changes in Q primarily influence the overall amplitude across the spectrum rather than shifting specific peak frequencies. Scenario S2 (red), which combines lower stress drop with weaker attenuation, results in the highest short-period amplification, particularly below 0.2 s, due to the predominantly linear soil response. In contrast, scenarios S3 and S4 with higher stress drop exhibit reduced short-period amplification driven by increased input motion amplitude and corresponding nonlinear effects. The differences among the scenarios diminish at longer periods (>0.5 s), where site response becomes less sensitive to both source characteristics and soil nonlinearity.

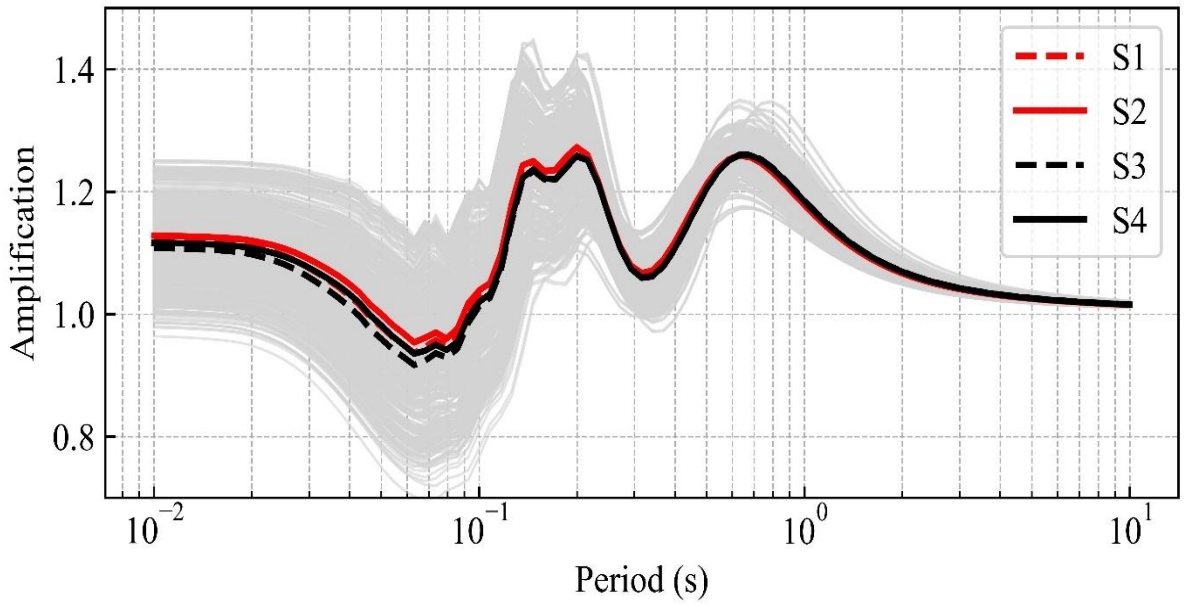


Figure 4. Site amplification for four source scenarios (S1–S4). Grey lines show 100 Vs realizations; colored lines represent median curves. Red indicates low σ/high Q (S2), and dashed lines correspond to site 3524

3.4. Quantifying epistemic uncertainty from source parameters

The final analysis focuses on quantifying the epistemic uncertainty in site response due to source parameter variability. Figure 5 presents the period-dependent standard deviation computed from the logarithmic difference between the four scenario means. The results show a clear peak around 0.03–0.04 s, where uncertainty reaches its maximum (≈0.04). This range represents the high-frequency part of the motion spectrum, where the variability is primarily governed by source radiation and attenuation characteristics, rather than soil nonlinearity. The influence of stress drop and Q is most pronounced at these short periods, where high-frequency content dominates. Beyond 0.09 s, the uncertainty declines rapidly, suggesting that long-period site amplification is less sensitive to source variability.

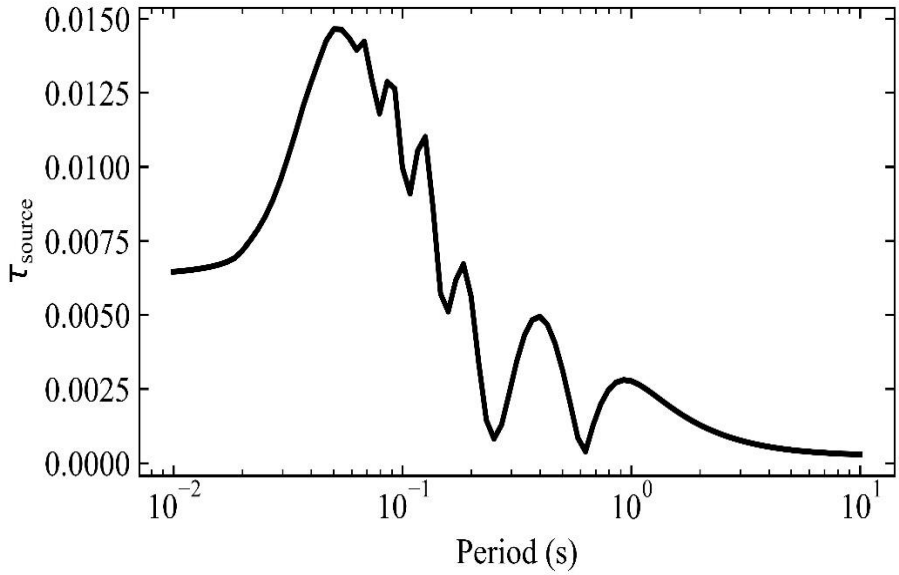


Figure 5. Epistemic uncertainty in site amplification due to source parameter variation, expressed as the standard deviation across the four source scenarios. Uncertainty is largest near 0.2 s and minimal at long periods

4. Discussion

This study demonstrates that variability in source parameters particularly stress drop and anelastic attenuation (Q) can significantly influence the site amplification, especially at short periods (< 0.3 s). Using four representative source parameter sets drawn from the literature, the analysis quantifies how these variations impact the predicted amplification and the associated epistemic uncertainty in site response.
The results confirm that even modest changes in source parameters (e.g., ±20 bars in stress drop) can shift spectral amplification curves. These findings reinforce the need to represent source variability in site response analysis—not only as a modeling detail, but as a key driver of uncertainty.

In this study, the epistemic uncertainty was estimated from just two discrete branches for each parameter (i.e., low and high stress drop; low and high Q). While sufficient to demonstrate sensitivity trends, this simplification likely underrepresents the full extent of source variability. Stress drop and Q distributions are continuous, and their interaction with other parameters (e.g., geometrical spreading, kappa etc.) adds further complexity. It is acknowledged that the present analysis considers only four discrete source parameter scenarios (S1–S4). While this approach captures the representative range of stress drop and attenuation models reported for the Aegean region, it likely underestimates the full spectrum of possible source variability. The epistemic uncertainty values derived here should therefore be viewed as lower-bound estimates. Future work will expand the analysis to incorporate a larger number of source realizations through Monte Carlo simulations or logic-tree sampling of stress drop, geometrical spreading, and attenuation parameters to obtain a more comprehensive quantification of source-related uncertainty for PSHA applications. This approach would allow for a more comprehensive quantification of uncertainty across the period range and help define branch weights in logic-tree-based seismic hazard models. Additionally, this method could be extended to other site conditions or regional tectonic environments.

5. Conclusions

This study investigated the influence of source parameter variability specifically stress drop and anelastic attenuation on site amplification using the RVT-based equivalent-linear site response framework. The results show that both parameters significantly affect short-period amplification, with increasing stress drop leading to higher input motion amplitudes and enhanced nonlinear behavior, thereby reducing surface amplification. Randomized Vs profiles, applied consistently across all source scenarios, enabled an independent assessment of source effects while accounting for subsurface uncertainty.

- Stress drop significantly affects short-period amplification, with peak variability observed between 0.02–0.1 seconds.
- Randomized Vs profiles, held constant across all input scenarios, allowed the effects of source parameter variations to be evaluated independently of site condition variability.
- The epistemic uncertainty introduced by stress drop and Q variation reached a maximum of approximately 0.015 in log units near 0.2 s and diminished toward longer periods. This magnitude of uncertainty, while modest, is comparable to other secondary sources of variability considered in hazard models.
- The quantified epistemic uncertainty τ_{source} reached approximately 0.015 in log units, peaking around 0.04 s, highlighting the short-period sensitivity of site amplification to source variability. The study's novelty lies in explicitly evaluating source-parameter-driven epistemic uncertainty within an RVT framework for the Aegean region—a topic that has been largely overlooked in previous literature.
- The selected site (station 3524) showed strain levels below 0.03%, validating the use of EQL analysis for this scenario.
- The omission of finite-fault and directivity effects is acknowledged as a limitation, and their inclusion is recommended for future extensions of this work.

Although only four source combinations were analyzed here, the framework provides a foundation for integrating source-driven uncertainty into site-specific and regional hazard assessments. Future work should

incorporate Monte Carlo simulations of source parameters to better capture the underlying distributions and propagate them through PSHA logic trees.

6. Author Contribution Statement

The author confirms sole responsibility for the following: conceptualization, methodology, formal analysis, software development, visualization, writing-original draft preparation, writing-review and editing.

7. Ethics Committee Approval and Conflict of Interest

"Ethics committee permission is not required for the prepared article" "
There is no conflict of interest with any person/institution in the prepared article."

8. Ethical Statement Regarding the Use of Artificial Intelligence

No artificial intelligence-based tools or applications were used in the preparation of this study. The entire content of the study was produced by the author in accordance with scientific research methods and academic ethical principles.

9. References

[1] G. A. Parker, J. P. Stewart, Y. M. Hashash, E. M. Rathje, K. W. Campbell and W. J. Silva, "Empirical linear seismic site amplification in central and eastern North America," *Earthq. Spectra*, vol. 35, no. 2, pp. 849–881, 2019.

[2] Y. M. Hashash, O. Ilhan, J. A. Harmon, G. A. Parker, J. P. Stewart, E. M. Rathje, K. W. Campbell and W. J. Silva, "Nonlinear site amplification model for ergodic seismic hazard analysis in Central and Eastern North America," *Earthq. Spectra*, vol. 36, no. 1, pp. 69–86, 2020.

[3] K. J. Ulmer, A. Rodriguez-Marek and R. A. Green, "Accounting for epistemic uncertainty in site effects in probabilistic seismic hazard analysis," *Bull. Seismol. Soc. Am.*, vol. 111, no. 4, pp. 2005–2020, 2021.

[4] A. Rodriguez-Marek, J. J. Bommer, R. R. Youngs, M. J. Crespo, P. J. Stafford and M. Bahrampouri, "Capturing epistemic uncertainty in site response," *Earthq. Spectra*, vol. 37, no. 2, pp. 921–936, 2021.

[5] D. Assimaki, W. Li, J. Steidl and J. Schmedes, "Quantifying nonlinearity susceptibility via site-response modeling uncertainty at three sites in the Los Angeles Basin," *Bull. Seismol. Soc. Am.*, vol. 98, no. 5, pp. 2364–2390, 2008.

[6] S. Foti, F. Passeri and A. Rodriguez-Marek, "Uncertainties and variabilities in seismic ground response analyses," in *Seismic Wave Propagation and Scattering in the Heterogeneous Earth*, A. Michelini, Ed. Boca Raton, FL, USA: CRC Press, 2019, ch. 9, pp. 245–280.

[7] A. R. Kottke and E. M. Rathje, *Technical Manual for Strata Version 1.0*, PEER Rep. 2010/111, Pacific Earthquake Engineering Research Center, Univ. California, Berkeley, CA, USA, 2010.

[8] M. A. Sandıkkaya, S. Akkar, Ö. Kale and E. Yenier, "A simulation-based regional ground-motion model for Western Türkiye," *Bull. Earthq. Eng.*, vol. 21, no. 7, pp. 3221–3249, 2023.

[9] A. Akıncı, S. D'Amico, L. Malagnini and A. Mercuri, "Scaling earthquake ground motions in western Anatolia, Turkey," *Phys. Chem. Earth*, vol. 63, pp. 124–135, 2013.

[10] A. Akıncı, D. Cheloni and A. A. Dindar, "The 30 October 2020, M7.0 Samos Island (Eastern Aegean Sea) earthquake: Effects of source rupture, path and local-site conditions on the observed and simulated ground motions," *Bull. Earthq. Eng.*, vol. 19, pp. 4745–4771, 2021.

[11] E. Gök, "Source parameters and scaling relations of local earthquakes from a strong motion network in İzmir, Western Turkey," *Pure Appl. Geophys.*, vol. 176, no. 8, pp. 3391–3409, 2019.

[12] G. R. Toro, "Probabilistic models of site velocity and thickness for regional seismic hazard analyses," NUREG/CR-6728, U.S. Nucl. Regulatory Commission, 1995.

[13] L. Al Atik, N. Abrahamson, J. J. Bommer, F. Scherbaum and A. Kottke, "Non-ergodic site response in seismic hazard analysis," *Earthq. Spectra*, vol. 30, no. 3, pp. 939–955, 2014.

[14] Y. M. A. Hashash, J. J. Rathje, C. B. Moss, J. T. Baise and K. E. Campbell, *Recommendations for Site Response Modeling in Seismic Hazard Analysis: Issues and Guidance*, PEER Rep. 2010/05, Pacific Earthquake Engineering Research Center, Univ. California, Berkeley, CA, USA, 2010.

[15] A. R. Kottke, N. A. Abrahamson, D. M. Boore, Y. Bozorgnia, C. A. Goulet, J. Hollenback, T. Kishida, O. J. Ktenidou, E. M. Rathje, W. J. Silva and E. M. Thompson, "Selection of random vibration theory procedures for the NGA-East project and ground-motion modeling," *Earthq. Spectra*, vol. 37, no. 1, Suppl., pp. 1420–1439, 2021.

[16] A. Akıncı, L. Malagnini, R. B. Herrmann, R. Gök and M. B. Sørensen, "Ground motion scaling in Marmara region, Turkey," *Geophys. J. Int.*, vol. 166, no. 2, pp. 635–651, 2006.

[17] A. Köseoğlu, N. M. Özel, Ş. Barış, S. B. Üçer and L. Ottemöller, "Spectral determination of source parameters in the Marmara Region," *J. Seismol.*, vol. 18, pp. 651–669, 2014.

[18] G. Tanırcan, H. Miyake, H. Yamanaka and O. Özel, "Large stress release during normal-faulting earthquakes in western Turkey supported by broadband ground motion simulations," *Pure Appl. Geophys.*, vol. 177, pp. 1969–1981, 2020.

[19] T. O. Kurtulmuş and N. Akyol, "Crustal attenuation characteristics in western Turkey," *Geophys. J. Int.*, vol. 195, no. 2, pp. 1384–1394, 2013.

[20] D. Bindi, S. Parolai, S. Grosser, C. Milkereit and S. Karakış, "Crustal attenuation characteristics in northwestern Turkey in the range from 1 to 10 Hz," *Bull. Seismol. Soc. Am.*, vol. 96, no. 1, pp. 200–214, 2006.

[21] Electric Power Research Institute (EPRI), *Guidelines for Determining Design Basis Ground Motions, Early Site Permit Demonstration Program*, vol. 1, Rep. RP3302, Palo Alto, CA, USA, 1993.

Fırat Üniversitesi Deneysel ve Hesaplamalı Mühendislik Dergisi

FUJECE

Klasik Dikdörtgen Büzülmeli Savakların Mansabında Oluşan Yerel Oyulmaların HAD Yöntemi Kullanılarak İncelenmesi

Erdinc İKİNCİOGULLARİ [1*], Muhammet Emin EMİROĞLU [2], Mehmet Cihan AYDİN [3]

[1]İnşaat Mühendisliği Bölümü, Mühendislik Fakültesi, Bingöl Üniversitesi, Bingöl, Türkiye.
[1]Enerji, Çevre ve Doğal Afet Araştırmaları Merkezi, Bingöl Üniversitesi, Bingöl, Türkiye.
[2]İnşaat Mühendisliği Bölümü, Mühendislik Fakültesi, Fırat Üniversitesi, Elâzığ, Türkiye.
[3]İnşaat Mühendisliği Bölümü, Mühendislik Fakültesi, Bitlis Eren Üniversitesi, Bitlis, Türkiye.
[1]eikinciogullari@bingol.edu.tr, [2]memiroglu@firat.edu.tr, [3]mcaydin@gmail.com

Geliş Tarihi: 16.10.2025
Kabul Tarihi: 01.12.2025
Düzeltme Tarihi: 23.11.2025
doi: https://doi.org/10.62520/fujece.1804990
Araştırma Makalesi

Alıntı: E. İkincioğulları, M. E. Emiroğlu ve M. C. Aydın,'' Klasik dikdörtgen büzülmeli savakların mansabında oluşan yerel oyulmaların HAD yöntemi kullanılarak incelenmesi", Fırat Üni. Deny. ve Hes. Müh. Derg., vol. 5, no 1, pp. 231-249, Şubat 2026.

Özet

Hidrolik yapıların güvenliği sosyal, ekonomik ve çevresel öneme sahiptir. Yerel oyulmanın neden olduğu hasarları ortadan kaldırmak için ya oyulma tamamen önlenmeli ya da oyulma derinliği en aza indirilmelidir. Bu çalışmada, serbest düşülü klasik büzülmeli dikdörtgen savakların mansabında oluşan yerel oyulma sayısal olarak incelenmiştir. Sayısal analizlerde Flow3D yazılımı ve k-ε türbülans modelleri kullanılmıştır. Maksimum oyulma derinliğini belirlemek için analizler üç birim debi (q=0.15, 0.30 ve 0.60 m^3/s m) ve üç düşü yüksekliği (H=0.25, 0.50 ve 1.00 m) için gerçekleştirilmiştir. Ayrıca, su jeti hızı ve çarpma açısı incelenmiştir. Tüm durumlar için denge oyulma derinliğinin yaklaşık %90'ına ilk 15–20 dakika içinde ulaşıldığı ve bunun önceki çalışmalarla uyumlu olduğu belirlenmiştir. Sonuçlara göre, birim debinin artmasıyla denge oyulma derinliği yaklaşık 0.16 m'den 0.23 m'ye yükselmektedir. Ancak, düşü yüksekliğinin belirli bir değerin üzerine çıkmasıyla, mansap havuzuna daha fazla hava kabarcığı girmesine bağlı olarak oyulma derinliği üzerindeki etkinin bir miktar azaldığı görülmüştür. Hesaplanan jet çarpma hızları yaklaşık 2.0 ile 4.9 m/s arasında değişmekte, çarpma açısı ise düşü yüksekliğinin artmasıyla birlikte yaklaşık 82°'ye kadar çıkmaktadır. Sayısal modelden elde edilen sonuçların genel olarak deneysel çalışmalarla uyumlu olduğu tespit edilmiştir. Bu çalışma, serbest düşülü koşullarda yüksek düşülü savakların mansabında oluşan yerel oyulmanın üç boyutlu HAD tabanlı değerlendirmesini sunması ve uzun dönem denge oyulma derinliği ile jet çarpma karakteristiklerinin pratik olarak tahmin edilmesine yönelik bir yaklaşım önermesi bakımından özgün niteliktedir.

Anahtar kelimeler: Yerel oyulma, Oyulma süreci, Serbest düşülü savaklar, Baraj güvenliği, Havza morfolojisi, Flow3D®, Hesaplamalı akışkanlar dinamiği (HAD)

*Yazışılan yazar

İntihal Kontrol: Evet – Turnitin
Şikayet: fujece@firat.edu.tr
Telif Hakkı ve Lisans: Dergide yayın yapan yazarlar, CC BY-NC 4.0 kapsamında lisanslanan çalışmalarının telif hakkını saklı tutar.

Firat University Journal of Experimental and Computational Engineering

Investigation of Local Scour at Classical Contracted Rectangular Weir Downstream using CFD

Erdinc IKINCIOGULLARI[1,*], Muhammet Emin EMIROGLU[2], Mehmet Cihan AYDIN[3]

[1]Civil Engineering Department, Bingol University, Bingol, Türkiye.
[1]Center For Energy, Environment, and Natural Disaster, Bingol University, Bingol, Türkiye.
[2]Civil Engineering Department, Firat University, Elazig, Türkiye.
[3]Civil Engineering Department, Bitlis Eren University, Bitlis, Türkiye.
[1]eikinciogullari@bingol.edu.tr, [2]memiroglu@firat.edu.tr, [3]mcaydin@gmail.com

Received: 16.10.2025
Accepted: 01.12.2025
Revision: 23.11.2025
doi: https://doi.org/10.62520/fujece.1804990
Research Article

Citation: E. İkincioğulları, M. E. Emiroğlu and M. C. Aydın, "Investigation of local scour at classical contracted rectangular weir downstream using CFD", Firat Univ. Jour.of Exper. and Comp. Eng., vol. 5, no 1, pp. 231-249, February 2026.

Abstract

The safety of hydraulic structures has social, economic, and environmental significance. To eliminate the damage induced by local scouring, either the scouring should be prevented entirely or the scouring depth should be minimized. This study numerically investigated the local scour that develops in the plunge pool downstream of high-head, classical contracted rectangular weirs operating under free overfall conditions. In the numerical analysis, a three-dimensional Reynolds-averaged Navier–Stokes (RANS) model with a standard k–ε turbulence closure was implemented in Flow-3D®. The analyses were conducted for three unit flow rates (q=0.15, 0.30, and 0.60 m^3/s m) and three drop heights (H=0.25, 0.50, and 1.00 m) to determine the maximum scouring depth. Furthermore, the water jet velocity and impingement angle were analyzed. The experimental results were utilized to test the accuracy of the numerical model. For all cases, about 90 % of the equilibrium scour depth was reached within the first 15–20 min, consistent with previous studies. According to the results, the equilibrium scour depth increased from approximately 0.16 m to 0.23 m when the unit discharge was raised. However, after a specific value of the head height, the effect on the depth of scouring is slightly reduced due to the increased air entrainment entering the downstream pool. Computed jet impact velocities ranged from about 2.0 to 4.9 m/s, with impact angles increasing up to ~82° as the drop height increased. The results of the numerical model are generally compatible with experimental studies. This study is original in that it provides a three-dimensional CFD-based assessment of local scour downstream of high-head weirs under free overfall conditions and proposes a practical approach to estimate long-term equilibrium scour depth and jet impact characteristics.

Keywords: Local scour, Scour process, Free overfall, Dam safety, Basin morphology, Flow3D®, CFD

*Corresponging author

Plagiarism Checks: Yes – Turnitin
Complaints: fujece@firat.edu.tr
Copyright & License: Authors publishing with the journal retain the copyright to their work licensed under the CC BY-NC 4.0

1. Introduction

Energy demand increases rapidly due to population and economic growth. Along with the energy demand in the 21st century, many high-head dams have been built. However, due to the increase in the drop height of the dam, local scouring in the downstream pool may damage the hydraulic structure or cause its destruction. Thus, the accurate prediction of local scouring that may occur in the hydraulic structure downstream is essential. Although scouring has attracted the attention of researchers, few studies address scouring the downstream of free-falling weirs in literature. For instance, Stein and Julien [1] conducted experimental research to determine the correlations between scour depth, sediment concentration, scour-hole volume, and time for a free overfall weir. Ghodsian et al. [2] conducted an experimental study about local scour. They established the effect of tailwater depth on the scour hole and the height of the dunes. A rigorous parametric examination of scour depth downstream of a steep vertical drop in uniform sediments was conducted experimentally by Dey and Raikar [3]. The results of the experimental study were utilized to demonstrate how several factors, including temporal variation, affected equilibrium scour depth. Ghodsian et al. [4] researched to more thoroughly examine the impact of critical characteristics, including sediment gradation, on the scour parameters caused by free-falling jets.

In recent years, Computational Fluid Dynamics (CFD) techniques in hydraulics have become popular in research, besides conventional experimental studies. Validated and tested CFD software is a powerful tool that is employed to simulate complicated fluid flow problems, and it could save time and costs in hydraulic model studies. The multi-phase and turbulent flows that include liquids, gases, and solid particles, such as scour problems downstream of a dam, require the solution of complex equations for fluid motion. These numerical methods have improved significantly over time and have been employed by several researchers. In their initial study, Olsen and Melaaen [5] successfully applied three-dimensional numerical models to calculate local scour around a cylindrical bridge pier. Lin and Falconer [6] developed a numerical model in estuarine and coastal waters for three-dimensional suspended sediment. The authors tested the model against analytical solutions and experimental data for different flow types and boundary conditions. Richardson and Panchang [7] studied the local scouring around a bridge pier using Flow3D® software and the RNG k-ε turbulence model. The authors utilized a three-dimensional computational model to determine the complex flow field for flatbed and equilibrium scour conditions. They found that the three-dimensional model simulated the complex flow fields around the bridge pier. Later, other researchers such as Wu et al. [8], Yafei Jia et al. [9], Liu et al. [10], Vasquez and Walsh [11], Abbasi et al. [12], Castillo and Carrillo [13], Epely-Chauvin et al. [14], Cihan et al. [15], Pang et al. [16], Pourshahbaz et al. [17], Man et al. [18], Aydin et al. [19], Ikinciogullari et al. [20], Kumar and Afzal [21], and Wang et al. [22] successfully employed various CFD techniques and software to investigate hydraulic scour problems numerically. Cihan et al. [15] provided a general framework for using CFD in hydraulic structures. Aydın and Karaduman [23] and Aydin et al. [19] numerically modelled the experimental models developed by Dey and Sarkar [24] and Dey and Raikar [3] with Flow 3D software. They obtained good results with CFD simulations for scour in specific downstream hydraulic structures compared to experimental findings. Yan et al. [25] studied a sediment-scour model using OpenFOAM software and the conformal moving-mesh technique. They stated that the agreement of the model was proven to be a valid tool for simulating local scour issues caused by submerged wall jets by experimental and computational findings.

Contracted rectangular weirs are widely used in hydraulic engineering. However, these numerical studies provided valuable insights into scour mechanisms but generally did not address free-overfall conditions downstream of high-head classical contracted rectangular weirs, nor did they quantify jet impact characteristics and scour geometry over a wide range of unit discharges and drop heights. Therefore, there remains a research gap regarding the three-dimensional CFD modelling of local scour in plunge pools downstream of free-overfall contracted rectangular weirs.

The free overfall from high-head weirs could lead to significant scouring at the downstream of hydraulic structures such as dams. This local scour could seriously compromise the safety of hydraulic structures over time. Therefore, it is of vital importance to identify local scouring in advance. The aim of this study

is to numerically investigate the local scour that develops downstream of free-overfall classical contracted rectangular weirs and to assess the ability of a three-dimensional Flow-3D software to reproduce experimentally observed scour characteristics. The originality of the present study lies in the three-dimensional CFD modelling of local scour in the plunge pool downstream of free-overfall classical contracted rectangular weirs. Based on a combined experimental–numerical dataset for nine test conditions encompassing three unit discharges and three drop heights, the study systematically evaluated the influence of discharge and head on equilibrium scour depth, scour-hole geometry, and jet impact characteristics. Furthermore, the temporal evolution of scour depth was represented by an exponential function and used to extrapolate short-term simulations (up to about 1 h) to 9 h equilibrium conditions, providing a practical procedure to reduce computational cost in scour analyses.

2. Methodology

Figure 1 demonstrates a schematic representation of the definition sketch and the scour of a free overfall on the weir. The scouring properties of the water jet, which was designed as a free overfall with a contracted weir, are presented in Figure 1, where x_1 and x_2 refer to the distances between the point of the maximum scour and downstream and upstream of the bed level, respectively. x_m is the distance between the weir wall and the maximum scour point, x_3 refers to the distance between the maximum scour point and the maximum accumulation point (Δx), x_b is used to describe the distance between the dune's center and the weir. d refers to the scour point in any x value, and d_s refers to the maximum scour.

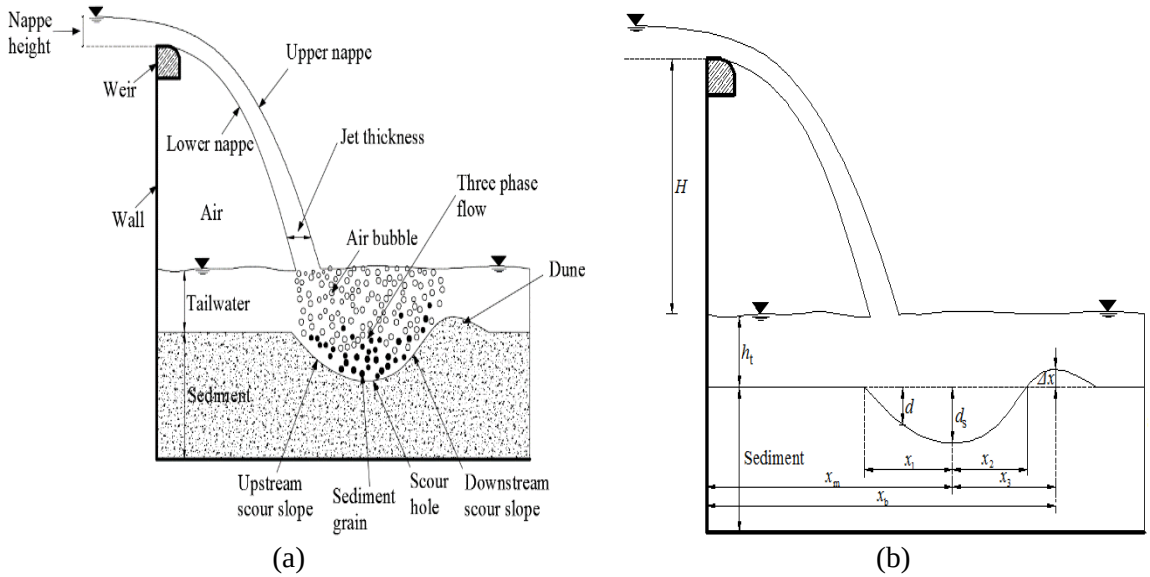


Figure 1. (a) Sketch of a scour phenomenon definition; (b) The properties of the scour sketch

2.1. Experimental setup

The scour experiments employed for comparison purposes were conducted under the experimental setup in Firat University Hydraulic Laboratory, as presented in Figure 2. Three pumps were operated using two tanks of 50 and 100 m^3 in the laboratory, each pumping approximately 77 L/s of discharge from the 100 m^3 tank to the 50 m^3 tank 11 m above. By using the spillway on the 50 m^3 tank, the water level is maintained at a static level. Water was taken from a 50 m^3 tank located 8 m above the laboratory ground level for the experiments. The plunging pool width was 1.25 m, height was 2 m, and length was 2.50 m. The upstream channel was 0.51 m wide, 0.85 m high, and 6.00 m long. A 1.00 m uniform sand layer was placed on the plunging pool. The bed material included uniform sediment with a median size of 2 mm.

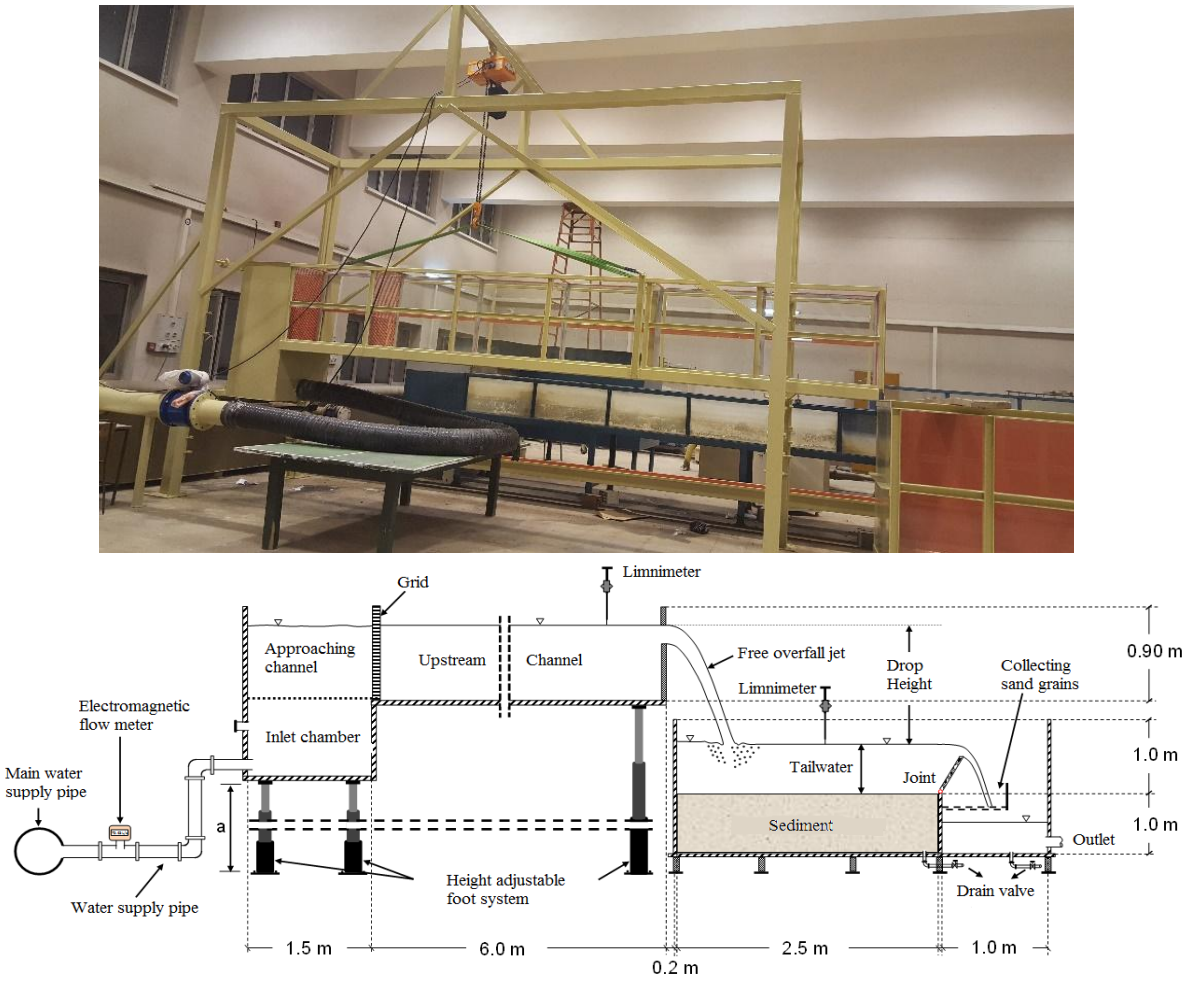


Figure 2. Experimental setup (Reprinted from authors previous study [30])

Nine analyses were conducted in the study for a tailwater depth (0.25 m), three unit discharges (0.15, 0.30, and 0.60 m^3/s m), and three drop heights (for 0.25, 0.50, and 1.00 m). The classical contracted rectangular weir was 0.25 m high, 0.167 m wide, with 0.05 m material wall thickness (see Figure 3a). A suppressed weir is shown in Fig. 3(b).

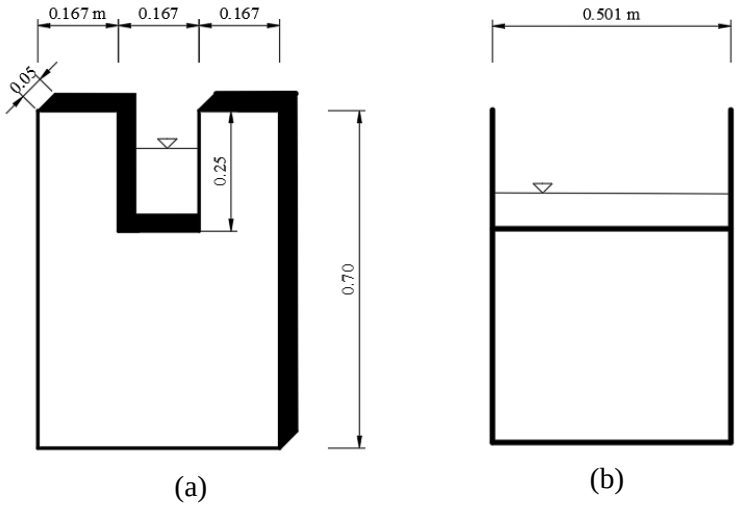


Figure 3. Geometry of the weir: (a) Contracted weir; (b) Suppressed weir

2.2. Numerical model

The three-dimensional numerical analyses were conducted with Flow3D® software. In numerical analysis, the standard k–ε turbulence model was preferred because it provides a reasonable compromise between numerical stability, computational cost, and accuracy for high-Reynolds-number, fully turbulent, free-surface jets and scour flows, and has been successfully applied in previous CFD studies of local scour [20,26–29]. The theoretical details for the numerical solutions are summarized as follows:

2.2.1. Flow governing equations

CFD is significant for solving several hydraulic engineering problems due to the advances in computer technology. This method provides solutions based on simple equations, such as the Navier-Stokes and continuity equations in the flow-motion calculation. This technique provides fast results since it can analyze several hydraulic parameters simultaneously. One of the most complicated problems in hydraulics is turbulent free surface flow in numerical modelling.

Navier-Stokes equations are the basic equations in fluid mechanics that define the motion of incompressible fluid flow. RANS (Reynolds Averaged Navier-Stokes) equations could be written in the Cartesian coordinate system for a three-dimensional flow as follows:

$$\frac{\partial u_i}{\partial x_i} = 0 \tag{1}$$

$$\frac{\partial u_i}{\partial t} + u_j \frac{\partial u_i}{\partial x_j} = -\frac{1}{\rho}\frac{\partial p}{\partial x_i} + \frac{\partial}{\partial x_i}\left(\upsilon \frac{\partial u_i}{\partial x_j} - \overline{u_i' u_j'}\right) + S_i \tag{2}$$

In which p is the pressure, u is the velocity, ρ is the mass density of water, t is the time, $\overline{u_i' u_j'}$ is the Reynolds stress, S_i is the source term, and ν is the kinematic viscosity of water. The k-ε turbulence closure model has been utilized for simulations.

2.2.2. Sediment model

In the numerical model, several methods were employed for sediment transport and scour models in the literature. According to Soulsby and Whitehouse [31], the critical Shields coefficient could be calculated with Eq. (3).

$$\theta_{cr,i} = \frac{0.3}{1+1.2d_{*,i}} + 0.055\left[1 - \exp(-0.02d_{*,i})\right] \tag{3}$$

where $d_{*,i}$ is a dimensionless parameter calculated with Eq. (4).

$$d_{*,i} = d_i \left[\frac{\rho(\rho_s - \rho)\|g\|}{\mu^2}\right]^{1/3} \tag{4}$$

where, d_i refers to the grain diameter, ρ_s refers to the specific mass of sediment, $\|g\|$ refers to the gravity magnitude, and μ refers to the dynamic viscosity. The following equation was used for calculating the local bed shear stress:

$$\theta_i = \frac{\tau}{\|g\| d_i(\rho_i - \rho)} \tag{5}$$

Shields coefficient was updated for inclined surfaces as reflected in Eq. (6).

$$\theta'_{cr,i} = \theta_{cr,i} \frac{\cos\psi \sin\beta + \sqrt{\cos^2\beta \tan^2\varphi_i - \sin^2\psi \sin^2\beta}}{\tan\varphi_i} \tag{6}$$

Where φ_i is the angle of repose (default 32°), β represents the bed slope, and ψ denotes the angle between the flow and the upslope direction for flow directly up to a slope, ψ=0°. Equation 7 was used by Mastbergen and Van Der Berg [32] to determine the speed of lifting at which the silt was seen.

$$u_L = \alpha_i n_s {d_{*,i}}^{0.3} (\theta_i - {\theta'}_{cr,i})^{1.5} \sqrt{\frac{\|g\| d_i (\rho_s - \rho)}{\rho}} \tag{7}$$

where, α_i is the entrainment coefficient and n_s is the outward-pointing normal to the packed bed interface.

The settling velocity equation proposed by Soulsby and Whitehouse [31] was employed:

$$u_s = \frac{\upsilon}{d_i}\left[(10.36^2 + 1.049 {d_{*,i}}^3)^{0.5} - 10.36\right] \tag{8}$$

Bed-load transport refers to the mechanism of sediment conveyance characterized by the rolling or bouncing of particles along the surface of a packed sediment bed. Meyer-Peter and Müller [33] suggested Eq. (9) for the dimensionless bed movement ratio (ϕ_i).

$$\phi_i = \beta_{MPM} (\theta_i - {\theta'}_{cr,i})^{1.5} \tag{9}$$

where β_{MPM} can be adjusted based on the bed motion. There will be no bed movement if this value is set to zero. It might be raised to allow for further bed mobility (default value is 8).

ϕ_i refers to the dimensionless bed-load transport rate and is associated with the volumetric bed-load transport rate, $q_{b,i}$ [34].

$$q_{b,i} = \phi_i \left[\|g\| \frac{(\rho_s - \rho_f)}{\rho_f} {d_i}^3\right]^{1/2} \tag{10}$$

Flow3D® allows changes in sediment model coefficients to verify numerical studies with experimental data. In the current study, three validation coefficients were employed for three drop heights. In these analyses, three model parameters known to influence scour depth, namely the entrainment coefficient, the bed roughness/d_{50} ratio, and the bed load coefficient, were employed as calibration parameters. The calibration coefficients that minimized the relative error are summarized in Table 1.

Table 1. Calibration coefficients used for different drop heights

Drop Height (m)	Entrainment coefficient (–)	Bed roughness/d_{50} ratio (–)	Bed load coefficient (–)
0.25	0.0005	0.80	3
0.50	0.0005	0.40	3
1.00	0.0005	0.05	1

3. Results and Discussion

In the numerical model, several studies were performed largely to ascertain the influence of cell size on the solution. In the first stage, the cell size was fixed at 0.04 m and analyses were conducted for approximately 900 seconds. Then, the cell size was reduced to 0.03 m and the analyses were conducted for 900-1800 seconds. Finally, to determine whether the scour depth reached a steady state, the cell size was reduced to 0.02 m and analyses were conducted for 1800-2400 seconds. It was observed that the scour depth did not change (Fig. 4). Thus, it was concluded that it would be sufficient to continue the analysis with a cell size of 0.03 m for the mesh block employed in the drop pool (Fig. 5a, block 1). As seen in Fig. 4, the solutions acquired stability with these three mesh structures, which decreased sequentially. Therefore, the sensitivity of the simulation results to the mesh structure was minimized, and the final mesh structure was determined.

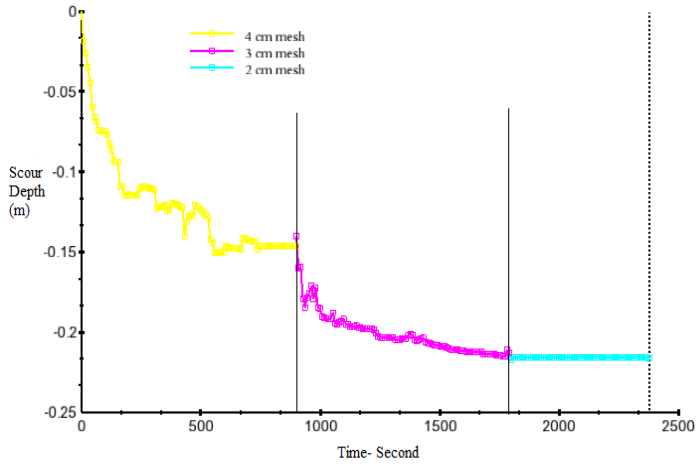


Figure 4. The testing of mesh quality (Reprinted from authors previous study [20])

Mesh dimensions should not be determined as small enough to extend the solution time unnecessarily or large enough to obtain inaccurate results. As a result of the preliminary analysis, it was concluded that a uniform mesh with a size of 0.03 m was suitable for the first and the second blocks out of the three blocks. The dimension of the third block located at the upstream channel was determined as 0.06 m since it did not affect the scouring depth (Fig. 5a). Then, the symmetry (*S*) boundary condition was selected to ensure the transition between the blocks, the discharge (*Q*) boundary condition was selected for the channel upstream, and the pressure (*P*) boundary condition was defined downstream of the channel to allow the tailwater effect. Then, the wall (*W*) boundary condition was selected for channel edges (Fig. 5b).

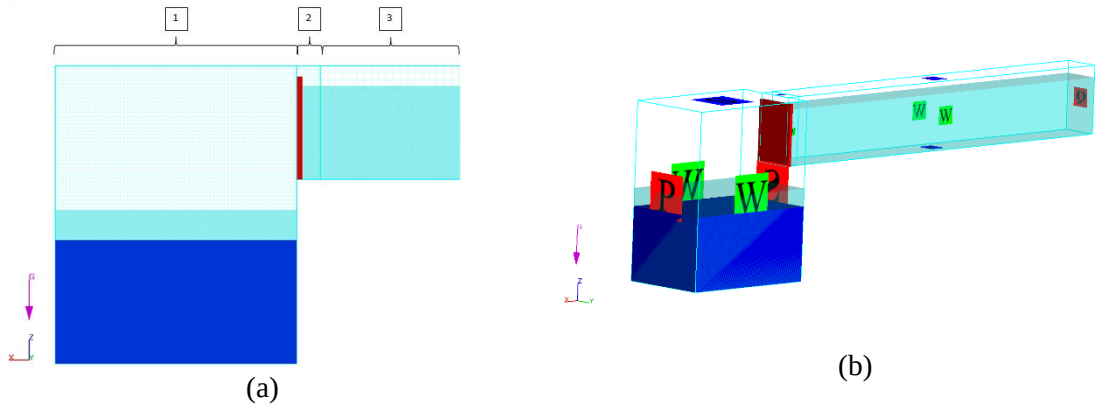


Figure 5. (a) Design of mesh blocks; **(b)** determination of boundary conditions

The simulation outputs for the numerical analysis conducted with Flow3D® software for various unit discharge values are presented in Fig. 6. As mentioned above, it was observed that scouring increased rapidly within the first 15-20 minutes, then continued to increase gradually and reached the equilibrium scouring depth. However, due to the increased momentum with the increase in discharge, the time required to reach the equilibrium scour depth also increased.

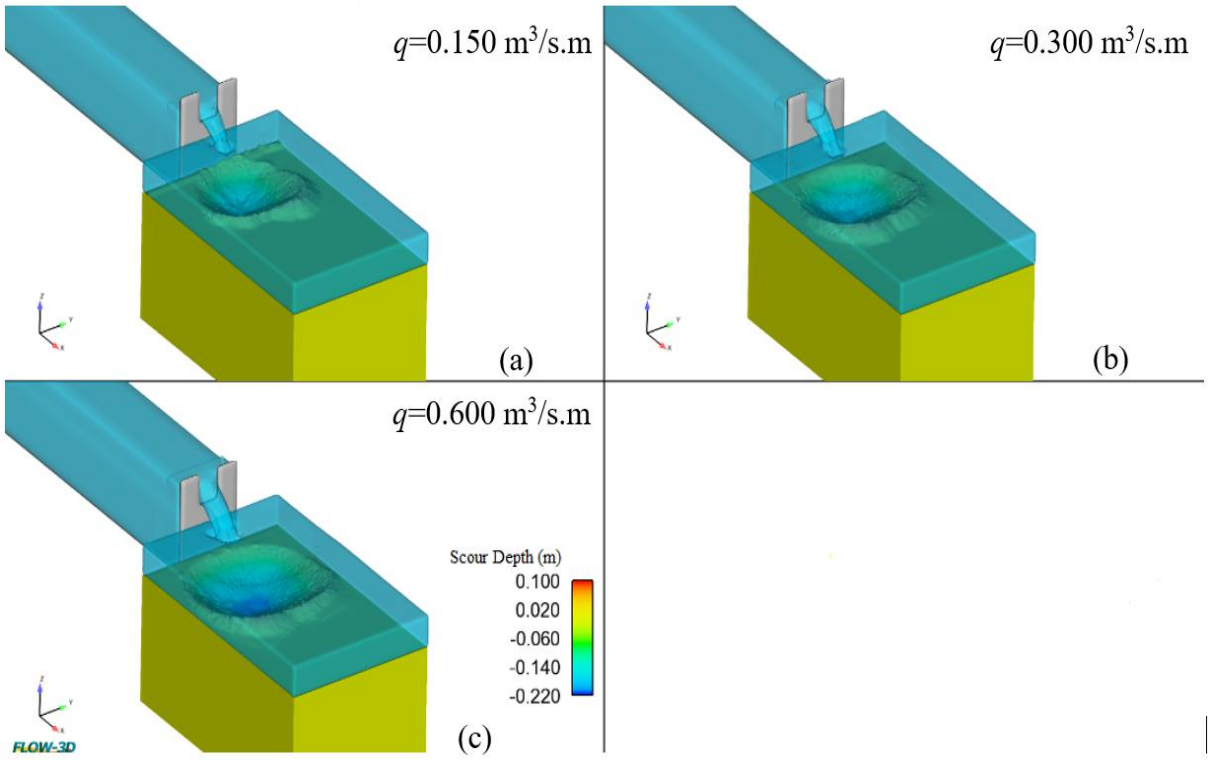


Figure 6. Equilibrium scour depths: a) for q= 0.150 m^3/s m, H=0.25 m and h_t=0.25 m, b) for q=0.300 m^3/s m, H=0.25 m and h_t=0.25 m and c) for q=0.600 m^3/s m, H=0.25 m and h_t=0.25 m

The physical experiments [30] were conducted for 9 hours. Numerical analysis for nine hours could take weeks, especially for scouring problems. For that reason, the numerical studies were continued for approximately 2500-4000 seconds and then were plotted as exponential functions to estimate the results after 9 hours in this study. The present results confirm that approximately 90% of the equilibrium scour depth develops within the first 15–20 min, which is consistent with the experimental observations of Dey and Raikar [3] and with the numerical findings of Fan et al. [35] and Liu et al. [36], who also reported rapid scour development and early equilibrium times. This rapid development is thought to occur due to the high initial momentum of the plunging jet and the relatively fine, uniform sediment that allows fast particle entrainment. Dey and Raikar [3] conducted 9-hour experiments for equilibrium scour depth, but they reached the equilibrium depth within almost 600 seconds. Fan et al. [35] observed that in their simulation, the equilibrium depth was attained in 60 minutes, and 90% of the equilibrium scouring depth was attained in the first 20 minutes. Liu et al. [36] reported that the equilibrium scour depth obtained after 60 minutes was close to the experimental results.

Figure 7 shows the results of the numerical solution of the scour depth for different times for q=0.150 m^3/s m, H=0.50 m, and h_t=0.25 m. When the 1-hour numerical finding was compared with the 9-hour experimental result, the 1-hour numerical result corresponded to approximately 90 percent of the 9-hour experimental result.

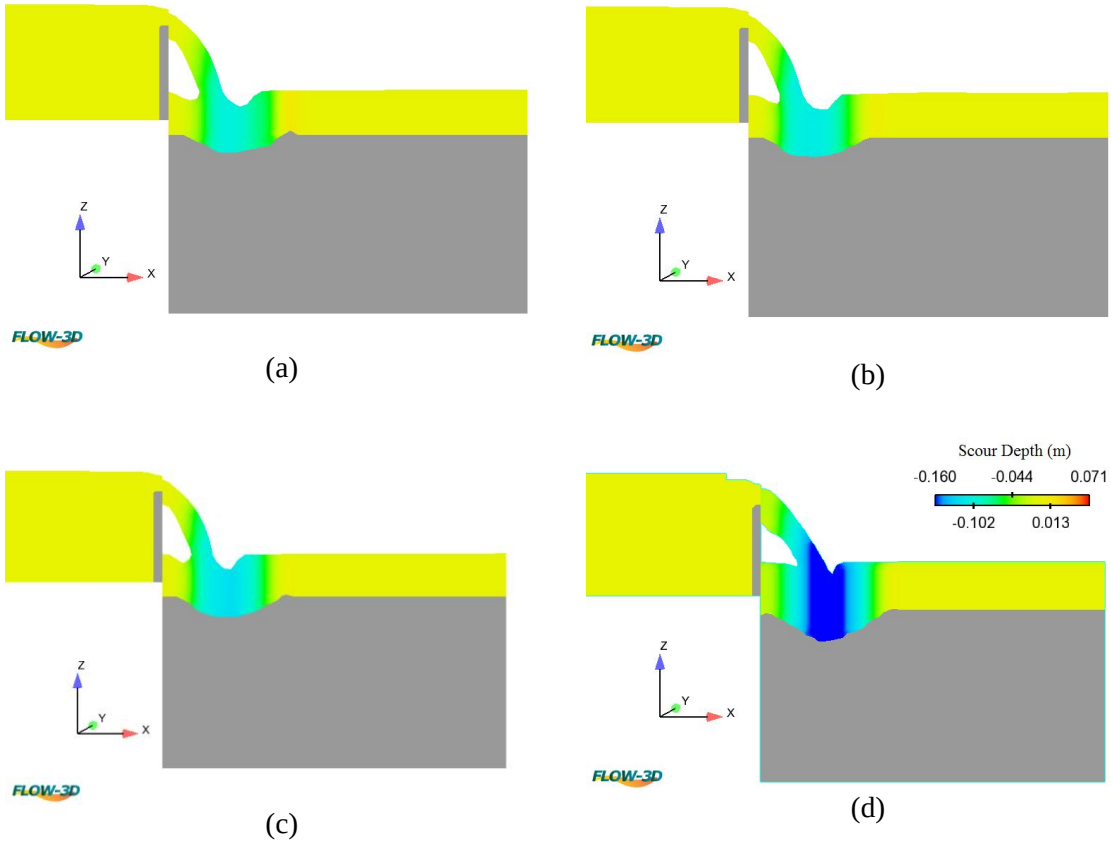


Figure 7. Scour depth longitudinal section for H=0.50 m, q=0.150 m^3/s m, and h_t=0.25 m by CFD: a) for 900 s, b) for 1800 s, c) for 2700 s, and d) for 3600 s

The scour graph changes with the exponential function. The equation for the exponential function, fitted to the results obtained with numerical studies, is presented in Eq. (11).

$$d = a \cdot (1 - exp(-b \cdot t)) \tag{11}$$

where d refers to the scour depth, t refers to the scour time (second), a and b refer to the exponential function coefficients. These coefficients and the determination coefficient obtained with the equations are presented in Table 2. The graphs of the curves fitted to Eq. (11) demonstrate that the determination coefficient (R^2) varied between 0.72-0.96 (Fig. 8).

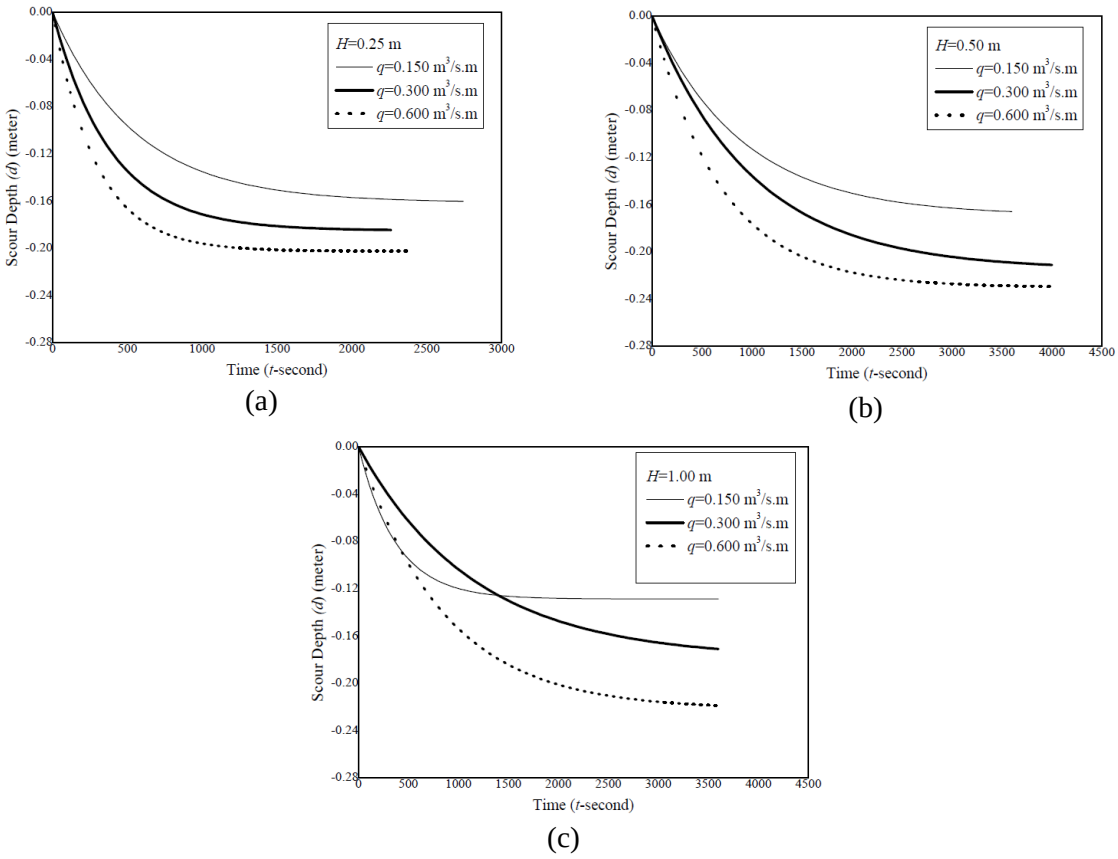


Figure 8. Temporal variations in maximum scour depth: a) for *H*=0.25 m; b) for *H*=0.50 m and c) for *H*=1.00 m

Table 2. Constants in Eq. 11

Analyse No	*a*	*b*	R^2
AN-1	-0.16150	0.00182	0.92
AN-2	-0.18528	0.00260	0.96
AN-3	-0.20280	0.00344	0.90
AN-4	-0.16939	0.00110	0.72
AN-5	-0.21534	0.00099	0.81
AN-6	-0.23037	0.00145	0.75
AN-7	-0.12901	0.00267	0.92
AN-8	-0.17918	0.00087	0.83
AN-9	-0.22242	0.00118	0.88

The experimental results for 9 hours, the numerical results for 1 hour, and scour depths estimated with an exponential function for 9 hours are presented in Table 3. The results of both studies showed that an increase in the unit discharge caused the scour depth to rise. The scour depth increased in both studies by increasing the drop height from 0.25 m to 0.50 m. This significant increase is considered to result from the increase in jet momentum and impact velocity acting on the movable bed. However, when the drop height was increased from 0.50 m to 1.00 m, there was no significant change in the experimental results due to the increased air bubbles that entered the water jet. At the same time, a slight decrease was recorded in the numerical results. This situation was also consistent with the experimental findings of Baylar and Emiroglu [37]. They experimentally investigated the air entrainment rate in sharp-crested, broad-crested, and labyrinth weirs as a function of discharge and drop height. The authors found that when discharge and drop height increased, there was a considerable rise in the amount of air bubble entrainment into the flow. It was found that when the discharge and drop height increased, the tendency for air bubble entrainment into the flow also tended to rise [37]. The relative error rates for the scour

values obtained with experimental and numerical studies are presented in Table 3. The experimental scour depth (d_{s_e}) was compared with the 9-hour scour depth (d_{s_9}) to determine the relative error ε using Eq. (12). The review of these values suggested that the maximum relative error was around 18%. These error rates were likely acceptable for the investigated scour problems, where the experimental and numerical findings were consistent.

$$\varepsilon = \left|\frac{d_{s_e} - d_{s_9}}{d_{s_e}}\right| \cdot 100 \tag{12}$$

where d_{s_e} is the experimental scour depth after 9 hours and d_{s_9} is the estimated scour depth after 9 hours. In Table 3, d_{s_1} is the scour depth after 1 hour determined using CFD.

Table 3. Experimental and numerical equilibrium scour depths comparison at the classical contracted rectangular weir downstream

Model No	**Experiment No**	q	H	h_t	**Experimental Results** [30]	d_{s_1}	d_{s_9}	ε
		(m^3/sm)	(m)	(m)	d_{s_e} (m)	(m)	(m)	(%)
AN-1	1	0.150	0.25	0.25	0.154	0.165	0.162	5.2
AN-2	2	0.300	0.25	0.25	0.182	0.185	0.185	1.6
AN-3	4	0.600	0.25	0.25	0.232	0.216	0.203	12.5
AN-4	5	0.150	0.50	0.25	0.177	0.182	0.169	4.5
AN-5	6	0.300	0.50	0.25	0.182	0.212	0.215	18.1
AN-6	8	0.600	0.50	0.25	0.216	0.242	0.230	6.5
AN-7	9	0.150	1.00	0.25	0.146	0.139	0.129	11.6
AN-8	10	0.300	1.00	0.25	0.174	0.193	0.179	2.9
AN-9	12	0.600	1.00	0.25	0.216	0.233	0.222	2.8

The horizontal (V_x) and vertical (V_z) water jet velocities, the impact velocity of the water jet on the downstream pool (V_j), and the angle of jet impact (ζ) are presented in Table 4. It was noted that the water jet impact velocity typically increased due to the increasing momentum with the rise in unit discharge. However, when the unit discharge is kept constant and the drop height is increased, the impact velocity and the impact angle of the water jet increase due to the transformation of the potential energy of the water jet into kinetic energy. In general, the increase in unit discharge leads to a decrease in the angle of impact of the water jet. However, due to the increased momentum, there would be a decrease in the angle of the water jet, which would hit a farther point in the downstream channel (Fig. 9).

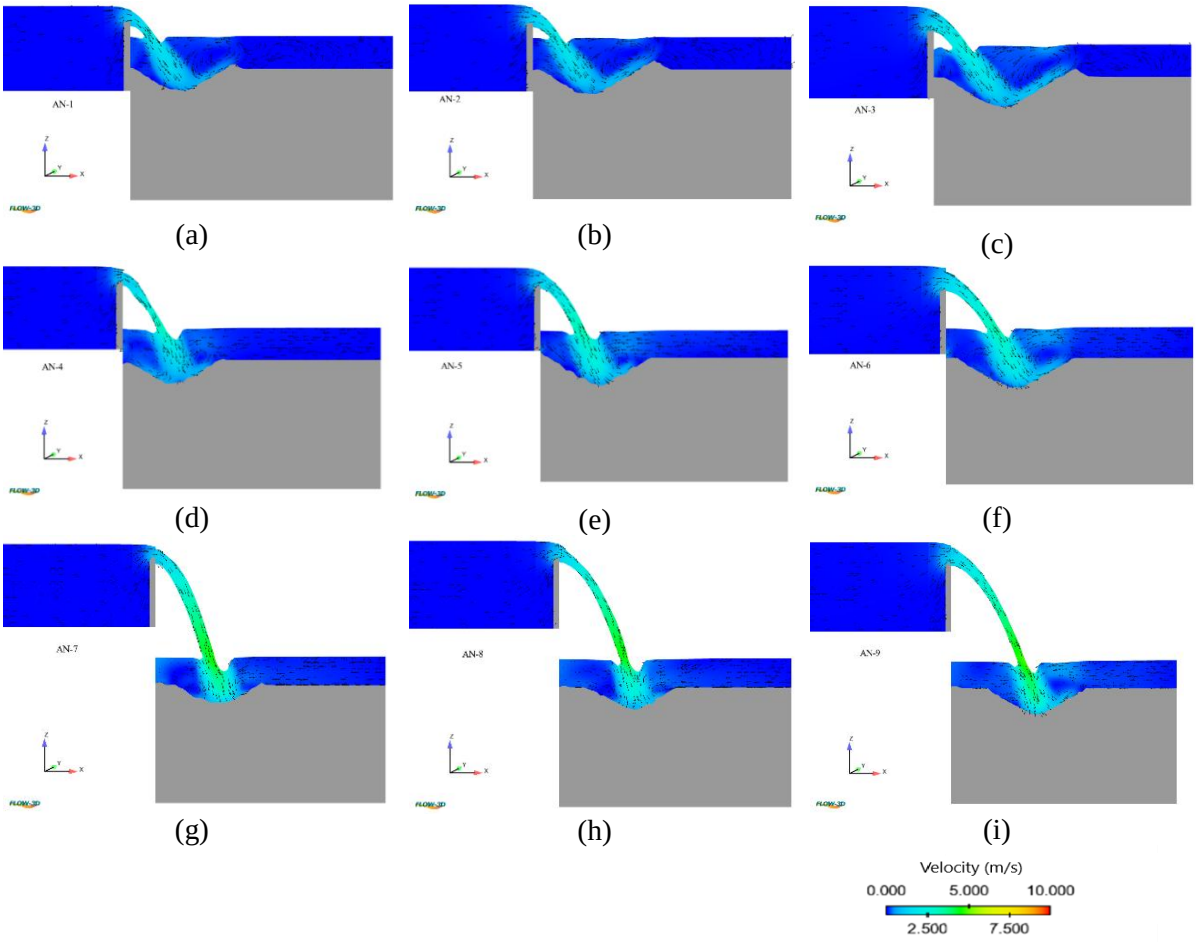


Figure 9. 2D simulation output for velocity vectors in rectangular weirs: a) AN1, b) AN2, c) AN3, d) AN4, e) AN5, f) AN6, g) AN7, h) AN8, and i) AN9

Table 4. Jet impact velocity and angle of classical contracted rectangular weir with CFD

Model No	V_x (m/s)	V_z (m/s)	V_j (m/s)	Jet Impact Angle (ζ) (º)
AN1	1.13	1.70	2.04	62.65
AN2	1.32	1.74	2.18	58.68
AN3	1.35	2.03	2.44	62.64
AN4	1.24	2.36	2.67	69.20
AN5	1.33	2.83	3.13	72.03
AN6	1.53	2.83	3.22	68.45
AN7	1.22	4.28	4.45	82.32
AN8	1.35	4.04	4.26	79.47
AN9	1.56	4.63	4.89	79.31

The parameters in figure 9 are presented in Table 5 for the contracted rectangular weir. Based on Table 5, there was an increase in the scour depth and x_1, x_2, x_3, x_m, x_b values due to the increased unit discharge for the stationary drop height and tailwater. Due to the increased discharge in 0.25 m and 0.50 m drop heights, it was observed that the upstream and downstream slope angles generally increased as well. However, due to the increased discharge in a 1.00 m drop height, the upstream slope angle increased while the downstream slope angle decreased. This situation may be attributed to the highly turbulent

nature of the submerged jet was highly turbulent, and a complex three-phase turbulent flow occurred with the increasing unit discharge and drop height (Fig. 9).

Table 5. Scour depth parameters

Model No	x_1 (m)	x_2 (m)	x_m (m)	x_3 (m)	x_b (m)	d_s (m)	Δx (m)
AN1	0.365	0.34	0.365	0.400	0.770	0.165	0.076
AN2	0.394	0.371	0.453	0.490	0.940	0.185	0.080
AN3	0.431	0.474	0.536	0.570	1.110	0.216	0.094
AN4	0.383	0.345	0.383	0.380	0.760	0.182	0.040
AN5	0.498	0.395	0.498	0.400	0.890	0.212	0.020
AN6	0.492	0.445	0.592	0.480	1.070	0.242	0.040
AN7	0.486	0.273	0.620	0.310	0.930	0.160	0.050
AN8	0.416	0.260	0.600	0.370	1.060	0.178	0.033
AN9	0.426	0.430	0.780	0.450	1.230	0.231	0.040

The variations that rely on time in the scour depth of the contracted rectangular weir section using CFD are presented in Figure 10. Since the water jet impact velocity and angle were low for low unit discharges and low drop heights, the maximum scour point was closer to the hydraulic structure. However, the maximum scour depth was observed to be more distant from the hydraulic structure due to the increase in the momentum force. The proximity of the scour pit to the hydraulic structure led to an increase in the apron length. The review of AN-1, AN-2 and AN-3 analysis findings revealed that while the maximum scours for low flow rate occur around 0.40 m distance from the weir, this value to 0.60 m as the unit flow rate increased. The analysis of AN-1, AN-4, and AN-7 revealed that the distance between the weir and the point of the maximum scour increased with the increased head height.

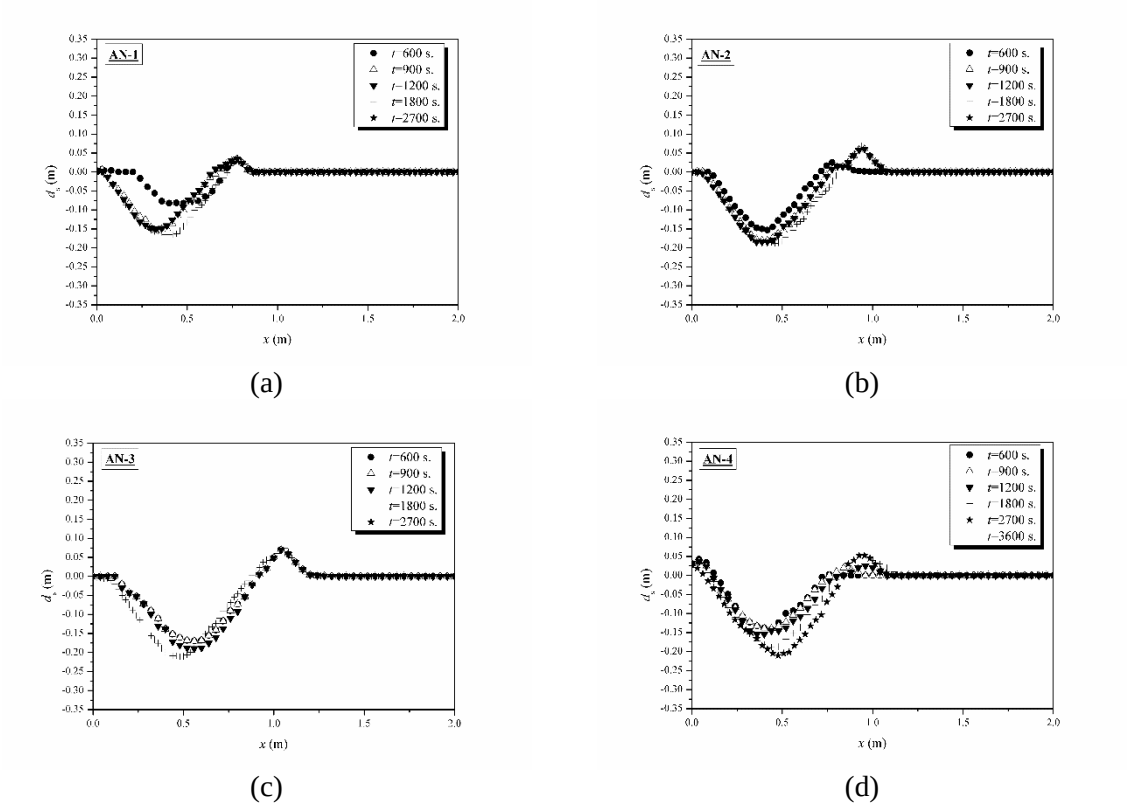


Figure 10. Scour depth longitudinal section vs time for: a) AN1, b) AN2, c) AN3, d) AN4, e) AN5, f) AN6, g) AN7, h) AN8, i) AN9

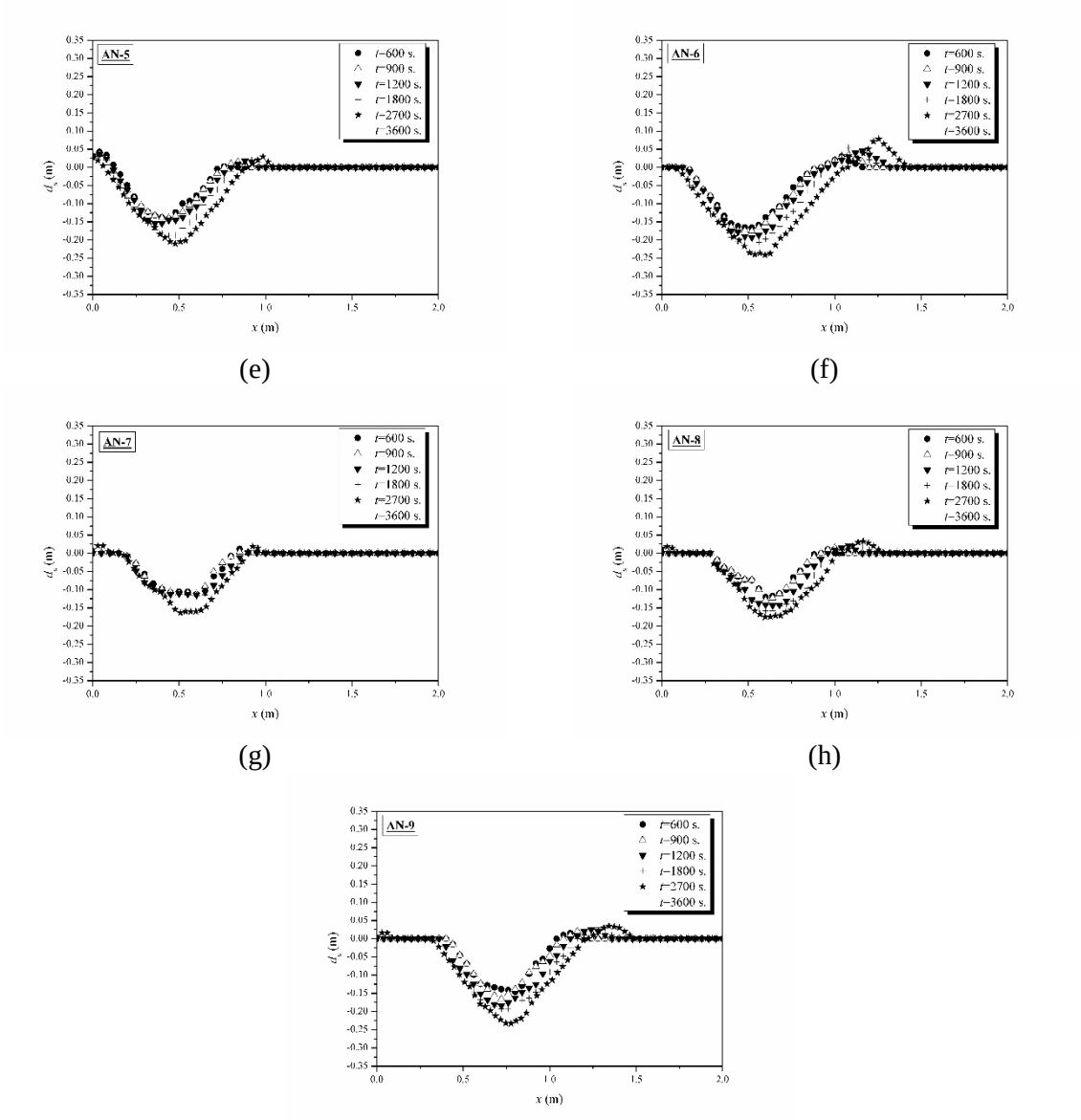


Figure 10. (Continue) Scour depth longitudinal section vs time for: a) AN1, b) AN2, c) AN3, d) AN4, e) AN5, f) AN6, g) AN7, h) AN8, i) AN9

Several researchers conducted experimental studies and reported equations for the equilibrium depth for free-overfall weirs. Veronese [38] reported one of the first findings and suggested that in several experimental studies conducted by decreasing grain diameter, the scour depth for sediments smaller than 5 mm was independent of the sediment size. The researcher suggested Eq. (13) to predict the equilibrium scour depth.

$$d = 1.90H^{0.225}q^{0.54} - h_t \tag{13}$$

Chian [39] proposed Eq. (14) for the scour depth at spillway downstream.

$$d = 1.18H^{0.235}q^{0.51} - h_t \tag{14}$$

Figure 11 compares the present study results with empirical equations using Eqs. (13-14). Comparing the findings with various unit discharge and drop heights revealed that the results obtained from the

proposed equations by Veronese [38] and Chian [39] were quite different. Therefore, several parameters affect the scouring event, which could be the reason for this difference.

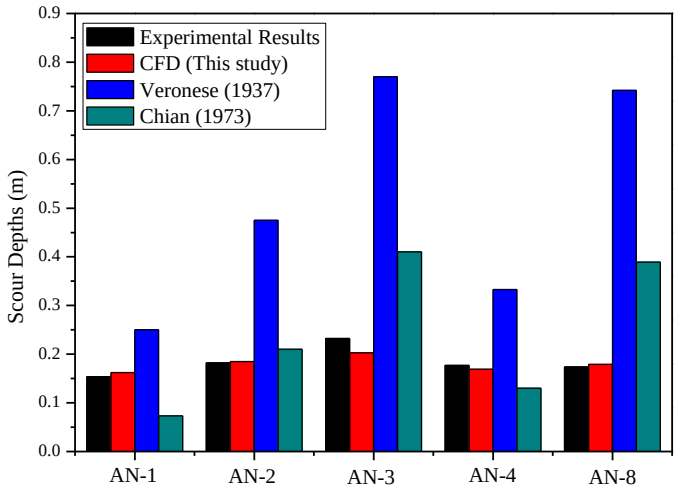


Figure 11. Comparison of scour depths using empirical equations

4. Conclusions

This study provides both theoretical and practical implications for local scour downstream of contracted rectangular weirs under free overfall conditions. The CFD results clarify how unit discharge and drop height control the time development and magnitude of scour, the variation of jet impact velocity and angle, together with the location of maximum scour for contracted weir geometries that are widely used in hydraulic engineering practice. From an engineering perspective, the obtained relationships can be used to estimate required apron length and protection thickness, to position and design scour protection and plunge pools more effectively. The significant findings obtained from this study are highlighted below.

- Approximately 90% of the equilibrium scour depth occurred within the first 15 minutes, which is consistent with the literature.
- The scour depth increases significantly with increasing unit discharge and the drop height.
- It was found that the air bubbles entering with the plunging jet have a decreasing effect on the scour depth, which is consistent with the literature.
- In addition, the numerical results agree with the experimental results. The numerical models in this aspect can be a helpful tool to investigate complicated multi-phase flows, such as scour problems, as well as other turbulent flows, when calibrated with some experimental data.
- The numerical simulations were calibrated and validated against experiments conducted with a single sediment type, a fixed tailwater depth, and a specific contracted rectangular weir geometry. These situations are limitations of this study.
- Future research should extend the CFD-based framework to graded sediments, variable tailwater conditions, and different weir configurations.

5. Acknowledgments

This research is based on Erdinc Ikinciogullari's PhD dissertation [40]. The TUBITAK MAG115M478 project [30], in which Erdinc Ikinciogullari participated as a scholarship student, provided the Flow-3D software utilized in this work. For its contributions, we acknowledge TUBITAK. We also acknowledge Dr Mustafa TUNC for his contributions to the experimental data.

6. Author Contribution Statement

Author 1, a doctoral student, conducted the literature review and numerical simulations, and assisted in the interpretation of the results. Author 2 served as the supervisor and provided guidance on the interpretation of findings. Author 3, as the co-supervisor, contributed to the numerical aspects of the study.

7. Ethical Statement Regarding the Use of Artificial Intelligence

This study was not prepared using any artificial intelligence-based technologies or software. The author prepared all the study's content in compliance with academic ethical standards and scientific research methodologies. During the preparation of this work, the authors used the Grammarly and Gemini Pro applications to improve language and readability.

8. Ethics Committee Approval and Conflict of Interest

“There is no conflict of interest with any person/institution in the prepared article. Additionally, ethics committee approval is not required for this study.”

9. References

[1] O. R. Stein and P. Y. Julien, "Sediment concentration below free overfall," *J. Hydraul. Eng.*, vol. 120, no. 9, pp. 1043–1059, 1994.
[2] M. Ghodsian, B. Melville and D. Tajkarimi, "Local scour due to free overfall jet," *Proc. Inst. Civ. Eng. Water Manag.*, vol. 159, no. 4, pp. 253–260, 2006.
[3] S. Dey and R. V. Raikar, "Scour below a high vertical drop," *J. Hydraul. Eng.*, vol. 133, no. 5, pp. 564–568, 2007.
[4] M. Ghodsian, M. Mehraein and H. R. Ranjbar, "Local scour due to free fall jets in non-uniform sediment," *Sci. Iran.*, vol. 19, pp. 1437–1444, 2012.
[5] N. R. B. Olsen and M. C. Melaaen, "Three-dimensional calculation of scour around cylinders," *J. Hydraul. Eng.*, vol. 119, no. 9, pp. 1048–1054, 1993.
[6] B. Lin and R. A. Falconer, "Numerical modelling of three-dimensional suspended sediment for estuarine and coastal waters," *J. Hydraul. Res.*, vol. 34, no. 4, pp. 435–456, 1996.
[7] J. E. Richardson and V. G. Panchang, "Three-dimensional simulation of scour-inducing flow at bridge piers," *J. Hydraul. Eng.*, vol. 124, no. 5, pp. 530–540, 1998.
[8] W. Wu, W. Rodi and T. Wenka, "3D numerical modeling of flow and sediment transport in open channels," *J. Hydraul. Eng.*, vol. 126, no. 1, pp. 4–15, 2000.
[9] B. Y. Jia, T. Kitamura and S. S. Y. Wang, "Simulation of scour process in plunging pool of loose bed-material," *J. Hydraul. Eng.*, vol. 127, no. 3, pp. 219–229, 2001.
[10] X. Liu and M. H. García, "Three-dimensional numerical model with free water surface and mesh deformation for local sediment scour," *J. Waterw. Port Coastal Ocean Eng.*, vol. 134, no. 4, pp. 203–217, 2008.
[11] J. A. Vasquez and B. W. Walsh, "CFD simulation of local scour in complex piers under tidal flow," in *Proc. 33rd IAHR Congr., Int. Assoc. Hydraul. Eng. Res.*, 2009.
[12] S. Abbasi, A. Kamanbedast and J. Ahadian, "Numerical investigation of angle and geometric of L-shape groin on the flow and erosion regime at river bends," *World Appl. Sci. J.*, vol. 15, no. 2, pp. 279–284, 2011.
[13] L. G. Castillo and J. M. Carrillo, "Scour estimation of the Paute-Cardenillo Dam," in *Proc. Int. Perspect. Water Resour. Environ.*, Quito, Ecuador, 2014, pp. 8–10.
[14] G. Epely-Chauvin, G. De Cesare and S. Schwindt, "Numerical modelling of plunge pool scour evolution in non-cohesive sediments," *Eng. Appl. Comput. Fluid Mech.*, vol. 8, no. 4, pp. 477–487, 2014.
[15] M. C. Aydin and E. Isik, "Using CFD in hydraulic structures," *Int. J. Sci. Technol. Res.*, vol. 1, no. 5, pp. 7–13, 2015.
[16] A. L. J. Pang, M. Skote, S. Y. Lim, J. Gullman-Strand and N. Morgan, "A numerical approach for determining equilibrium scour depth around a mono-pile due to steady currents," *Appl. Ocean Res.*, vol. 57, pp. 114–124, 2016.
[17] H. Pourshahbaz, S. Abbasi and P. Taghvaei, "Numerical scour modeling around parallel spur dikes in FLOW-3D," 2017.
[18] C. Man *et al*., "Assessment of turbulence models on bridge-pier scour using Flow-3D," *World J. Eng. Technol.*, vol. 2, no. 2, pp. 241–255, 2019.
[19] M. C. Aydin, M. E. Emiroglu, A. E. Ulu and E. Ikinciogullari, "Investigation of local scours under vertical drop using CFD," *Düzce Univ. J. Sci. Technol.*, vol. 10, no. 1, pp. 239–248, 2019.
[20] E. Ikinciogullari, M. E. Emiroglu and M. C. Aydin, "Comparison of scour properties of classical and trapezoidal labyrinth weirs," *Arab. J. Sci. Eng.*, vol. 47, pp. 4023–4040, 2022.
[21] L. Kumar and M. S. Afzal, "Computational fluid dynamics modeling of scour around abutment geometries under combined effects of waves and currents," *Ocean Eng.*, vol. 294, p. 116812, 2024.
[22] X. Wang, W. Li, Z. Peng, Q. Yu, Y. Yang and J. Li, "Optimization of combined scour protection for bridge piers using computational fluid dynamics," *Water*, vol. 17, p. 2742, 2025.
[23] M. C. Aydın and Ç. Karaduman, "Kapak altı batmış akım mansabında meydana gelen oyulmaların sayısal simülasyonu," *Pamukkale Univ. J. Eng. Sci.*, vol. 24, no. 3, pp. 439–443, 2018.
[24] S. Dey and A. Sarkar, "Characteristics of submerged jets in evolving scour hole downstream of an apron," *J. Eng. Mech.*, vol. 134, no. 11, pp. 927–936, 2008.

[25] X. Yan, A. Mohammadian and C. D. Rennie, "Numerical modeling of local scour due to submerged wall jets using a strict vertex-based, terrain conformal, moving-mesh technique in OpenFOAM," *Int. J. Sediment Res.*, vol. 35, pp. 237–248, 2020.
[26] B. D. Adhikary, A. P. Majumdar and M. Kostic, "CFD simulation of open channel flooding flows and scouring around bridge structures," in *Proc. 6th WSEAS Int. Conf. Fluid Mech.*, 2009.
[27] M. Zhao, L. Cheng and Z. Zang, "Experimental and numerical investigation of local scour around a submerged vertical circular cylinder in steady currents," *Coast. Eng.*, vol. 57, pp. 709–721, 2010.
[28] Z. W. Zhu and Z. Q. Liu, "CFD prediction of local scour hole around bridge piers," *J. Cent. South Univ. Technol.*, vol. 19, pp. 273–281, 2012.
[29] W. Xiong, P. Tang, B. Kong and C. S. Cai, "Computational simulation of live-bed bridge scour considering suspended sediment loads," *J. Comput. Civ. Eng.*, vol. 31, p. 04017040, 2017.
[30] TÜBİTAK, *115M478 – Serbest düşülü savakların mansabında oluşan yerel oyulmanın deneysel ve sayısal araştırılması*, Project Report, 2019.
[31] R. L. Soulsby and R. J. S. Whitehouse, "Threshold of sediment motion in coastal environments," in *Proc. Pacific Coasts Ports '97*, 1997.
[32] D. R. Mastbergen and J. H. Van den Berg, "Breaching in fine sands and the generation of sustained turbidity currents in submarine canyons," *Sedimentology*, vol. 50, pp. 625–637, 2003.
[33] E. Meyer-Peter and R. Müller, "Formulas for bed-load transport," in *Proc. 2nd Meet. Int. Assoc. Hydraul. Struct. Res.*, Stockholm, 1948.
[34] Flow Science, *Sediment Scour Model, FLOW-3D User Manual, Version 11.0.3*. Santa Fe, NM, USA: Flow Science, Inc., 2014.
[35] F. Fan, B. Liang, Y. Bai, Z. Zhu and Y. Zhu, "Numerical modeling of local scour around hydraulic structure in sandy beds by dynamic mesh method," *J. Ocean Univ. China*, vol. 16, pp. 738–746, 2017.
[36] S. Liu, Y. Yang and X. Wu, "Simulations of local scour around a cylindrical bridge pier and a semicircular abutment using unsteady k–ε model combined with σ-grid," *Open Civ. Eng. J.*, vol. 11, pp. 598–614, 2017.
[37] A. Baylar and M. E. Emiroglu, "The role of weir types in entrainment of air bubbles," *Int. J. Sci. Technol.*, vol. 2, no. 2, pp. 143–154, 2007.
[38] A. Veronese, *Erosion de fond en aval d'une décharge*. Soc. Coop. Tipogr., 1937.
[39] M. W. Chian, "Scour at downstream end of dams in Taiwan," in *Proc. IAHR Int. Symp. River Mech.*, Bangkok, 1973.
[40] E. Ikinciogullari, "Serbest düşülü savakların mansabında oluşan yerel oyulmanın sayısal analizi," Ph.D. dissertation, Inst. Sci., Fırat Univ., Elazığ, Turkey, 2019.

Fırat Üniversitesi Deneysel ve Hesaplamalı Mühendislik Dergisi

FUJECE

Doğadan İlhamlı Bal Peteği Tasarımlarının Sıkıştırma Davranışının Sayısal Olarak İncelenmesi

Alparslan SOLAK[1]*

[1]Makine Mühendisliği Bölümü, Yıldız Teknik Üniversitesi, İstanbul, Türkiye.
[1]alparslansolak1992@hotmail.com

Geliş Tarihi: 03.10.2025
Kabul Tarihi: 11.12.2025
Düzeltme Tarihi: 25.11.2025
doi: https://doi.org/10.62520/fujece.1796508
Araştırma Makalesi

Alıntı: A. Solak, "Doğadan ilhamlı bal peteği tasarımlarının sıkıştırma davranışının sayısal olarak incelenmesi" Fırat Üni. Deny. ve Hes. Müh. Derg., vol. 5, no 1, pp. 250-261, Şubat 2026.

Öz

Bu çalışma, doğadan ilham alınmış bal peteği yapıların sıkıştırma davranışını ve enerji absorpsiyon performansını sayısal olarak incelemektedir. Düzenli altıgen bir bal peteği için doğrulanmış bir LS-DYNA sonlu elemanlar modeli oluşturulmuş ve deneysel sonuçlarla karşılaştırılmış, kuvvet–şekil değiştirme tepkisi ve deformasyon modları açısından iyi bir uyum elde edilmiştir. Ardından, örümcek, salyangoz, dalgalı, bambu, pomelo kabuğu, çim sapı ve hiyerarşik olmak üzere yedi farklı doğadan ilhamlı konfigürasyon yarı-statik sıkıştırma altında modellenmiştir. Sonuçlar, bu tasarımların deformasyon yolları ve enerji absorpsiyon kapasitesi üzerinde düzenli altıgen yapıya kıyasla önemli bir etkiye sahip olduğunu göstermektedir. Pomelo kabuğu, çim sapı ve hiyerarşik bal petekleri, çok hücreli ve hiyerarşik yük aktarım mekanizmaları sayesinde densifikasyonu geciktirerek uzun bir plateau bölgesi oluşturmalarıyla en yüksek özgül enerji absorpsiyon değerlerini (sırasıyla 7.88, 7.50 ve 7.39 J/g) göstermiş ve referans altıgen yapıya kıyasla %47'ye varan oranda performans artışı sağlamıştır. Örümcek ve bambu tasarımları orta seviyede özgül enerji absorpsiyonu ile dengeli bir performans sergilerken, dalgalı ve salyangoz geometrileri daha düşük tepe kuvvetleriyle daha düzgün plateau davranışı göstermiştir. Genel olarak, bulgular doğadan ilhamlı geometrik özelliklerin hafif yapılarda çarpışma dayanımını artırmak için etkili bir şekilde kullanılabileceğini ortaya koymakta; ulaştırma, paketleme ve enerji depolama sistemleri gibi gelecekteki uygulamalara değerli katkılar sunmakta ve yeni nesil hafif yapı tasarımlarına yön verecek bilgiler sağlamaktadır.

Anahtar kelimeler: Doğadan ilhamlı yapılar, Bal peteği çekirdekler, Çarpışma dayanımı, LS-DYNA, Sayısal analiz

*Yazışılan yazar

İntihal Kontrol: Evet – Turnitin
Şikayet: fujece@firat.edu.tr
Telif Hakkı ve Lisans: Dergide yayın yapan yazarlar, CC BY-NC 4.0 kapsamında lisanslanan çalışmalarının telif hakkını saklı tutar.

Firat University Journal of Experimental and Computational Engineering

Numerical Investigation of Compression Behavior of Bio-Inspired Honeycomb Designs

Alparslan SOLAK[1]*

[1]Department of Mechanical Engineering, Yildiz Technical University, Istanbul, Türkiye.
[1]alparslansolak1992@hotmail.com

Received: 03.10.2025
Accepted: 11.12.2025
Revision: 25.11.2025
doi: https://doi.org/10.62520/fujece.1796508
Research Article

Citation: A. Solak, "Numerical ınvestigation of compression behavior of bio-ınspired honeycomb designs", Firat Univ. Jour.of Exper. and Comp. Eng., vol. 5, no 1, pp. 250-261, February 2026.

Abstract

This study numerically investigates the compressive behavior and energy absorption performance of bio-inspired honeycomb structures. A validated LS-DYNA finite element framework was first established for a regular hexagonal honeycomb and correlated with experimental results, showing good agreement in terms of force-strain response and deformation modes. Subsequently, seven bio-inspired configurations-spider, snail, wavy, bamboo, pomelo peel, grass stem, and hierarchical-were modeled under quasi-static compression. The results revealed that bio-inspired designs significantly influence deformation pathways and energy absorption capacity compared to the regular hexagon. Among the proposed designs, the pomelo peel, grass stem, and hierarchical honeycombs exhibited the highest specific energy absorption (7.88, 7.50, and 7.39 J/g, respectively), representing an improvement of up to 47% compared to the reference structure. This improvement is attributed to their multi-cell and hierarchical load-transfer mechanisms that delayed densification and ensured a prolonged plateau region. While spider and bamboo designs provided balanced performance with moderate specific energy absorption, the wavy and snail geometries demonstrated smoother plateau behavior with lower peak forces. Overall, the findings highlight that bio-inspired geometrical features can be effectively employed to enhance the crashworthiness of lightweight structures, offering valuable insights for future applications in transportation, packaging, and energy storage systems, and guiding the development of next-generation lightweight structural designs.

Keywords: Bio-inspired structures, Honeycomb cores, Crashworthiness, LS-DYNA, Numerical analysis

*Corresponging author

Plagiarism Checks: Yes – Turnitin
Complaints: fujece@firat.edu.tr
Copyright & License: Authors publishing with the journal retain the copyright to their work licensed under the CC BY-NC 4.0

1. Introduction

Honeycomb structures are widely employed in various engineering fields such as aerospace, automotive, packaging, and energy storage systems due to their high strength-to-weight ratio, and superior energy absorption capability [1,2]. These structures play a critical role in safety-oriented designs by guiding deformation and dissipating energy, particularly under impact and crash loading conditions.

In recent years, bio-inspired designs have attracted significant attention as an approach to enhance the performance of conventional hexagonal cells. Natural configurations such as spider webs [3-5], snail shells [6-8], woodpecker beaks [9,10], bamboo stems [11,12], pomelo peels [13-15], and grass stems [15-17] have inspired engineering designs owing to their exceptional strength, progressive energy absorption, and damage-delay mechanisms. Specifically, the spider web architecture is characterized by its radial and spiral arrangement, which effectively distributes point loads and limits the propagation of local damage, thereby increasing overall structural integrity [3–5]. The snail shell structure, with its spiral geometry, promotes progressive failure mechanisms and stable stress distribution, allowing for gradual energy dissipation rather than catastrophic collapse [6–8]. Similarly, hierarchical and multi-cell designs (like pomelo and grass stem) mimic natural cellular solids by introducing smaller sub-structures that delay densification and enhance the moment of inertia against buckling [13–17]. Through such biomimetic strategies, it has become possible to optimize the mechanical response of honeycomb structures and achieve superior energy absorption performance compared to traditional hexagonal designs.

Although there have been studies on various bio-inspired honeycomb geometries, comparative investigations of these structures under identical conditions remain limited. In many cases, research has focused on analyzing a single design in detail, while comprehensive comparisons involving both the regular hexagon and multiple bio-inspired configurations have been largely overlooked. Furthermore, the prevalence of purely numerical studies without sufficient experimental validation raises concerns regarding the reliability of such models.

The primary objective of this study is to conduct a systematic and comparative investigation into the compressive behavior of seven distinct bio-inspired honeycomb designs (spider, snail, wavy, bamboo, pomelo peel, grass stem, and hierarchical) relative to a conventional hexagonal structure. While previous studies often focus on individual designs, this research aims to address the lack of comprehensive comparative data by evaluating these geometries under identical loading and boundary conditions. To ensure numerical reliability, the finite element framework is first rigorously validated against experimental results for the regular hexagon. Specifically, the study seeks to: (i) elucidate the influence of specific bio-inspired geometric features on deformation modes and failure mechanisms; (ii) quantify the energy absorption capabilities and specific energy absorption (SEA) metrics of each design; and (iii) evaluate the trade-off between structural mass increase and energy dissipation efficiency. By doing so, this work intends to provide a selection guideline for next-generation lightweight, high-strength, and impact-resistant engineering structures.

2. Compression Test Setup and Validation of the Regular Hexagonal Honeycomb

Before examining the compressive behavior of bio-inspired honeycombs, a finite element model was established and validated against experimental test results [18]. For this purpose, post-compression images, force–strain curves and absorbed energy values were considered. The developed LS-DYNA model is presented in Figure 1. To ensure reproducibility, the specific boundary conditions—including the fixed support at the base and the applied loading velocity (V=10 m/s) at the top—are explicitly illustrated in this figure.

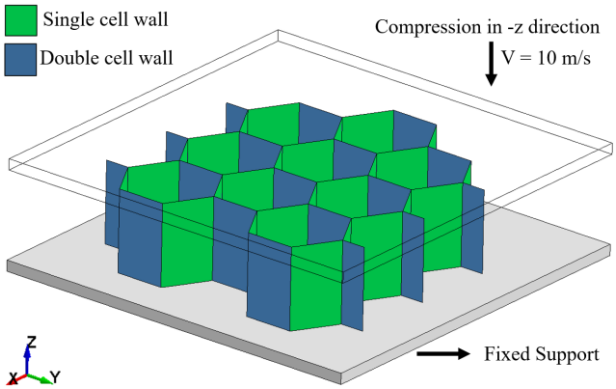


Figure 1. LS-DYNA model for the compression test

The bottom gray plate was fixed to hold the honeycomb in place, while the transparent plate at the top compressed the honeycomb in the negative z-direction. Accordingly, all six degrees of freedom of the bottom plate were constrained, whereas the top plate was restricted in five degrees of freedom and allowed to move only along the z-axis at a constant velocity of 10 m/s to simulate quasi-static loading. The honeycomb itself was left completely free.

Each unit cell of the honeycomb has an edge length of 9 mm and a height of 15 mm. During manufacturing, aluminum 3003-H18 sheets with a thickness of 0.75 mm were pressed into half-hexagonal molds and then bonded along the half-hexagonal edges. Thus, the unbonded walls remained 0.75 mm thick, while the bonded sections reached approximately twice that thickness (1.5 mm). In the numerical model, single-wall regions (0.75 mm) were represented in green and double-wall regions (1.5 mm) in blue. Since the walls were modeled as separate parts, the nodes at the interfaces were duplicated. The complete model consisted of nine full cells and four half cells.

An Automatic Surface-to-Surface contact [19] was defined between the honeycomb and the two plates. Additionally, to prevent overlapping of folded walls during compression, an Automatic Single Surface contact [20] was applied. Both static and dynamic friction coefficients were set to 0.2 [21]. To realistically capture the folding of honeycomb walls during compression, square shell elements with an edge length of 0.75 mm were employed instead of solid elements. To suppress potential element instabilities, the hourglass control option was activated. The honeycomb material, aluminum 3003-H18, was modeled using the MAT_018 Power Law Plasticity constitutive model, and its material parameters (shown in Table 1) were defined as follows:

Table 1. Mechanical properties of AA3003-H18 [18] used in the model

Definition	Symbol	Value	Unit
Mass density	ρ	2.7e-006	(kg/mm^3)
Young's modulus	E	68.95	(GPa)
Poisson's ratio	ν	0.33	-
Strength coefficient	K	0.22	(GPa)
Hardening exponent	n	0.2353	-
Initial yield stress	σ_oy	0.12	(GPa)
Plastic failure strain for element deletion	ε_p	0.3223	-

Note: All material parameters, including the plastic failure strain (ε_p), were adopted from Reference [18] to ensure consistency with the experimental validation.

Figure 2 presents the comparison between the experimental image and the LS-DYNA simulation.

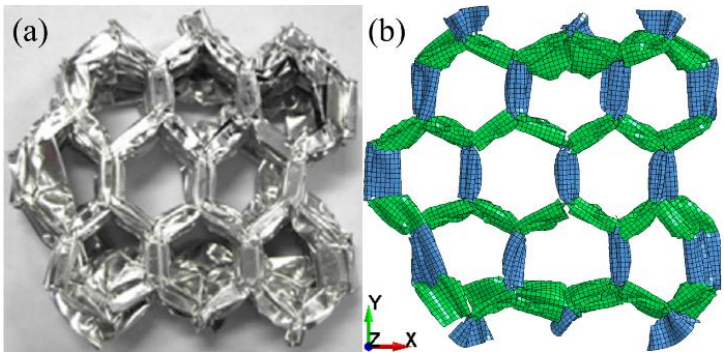


Figure 2. Comparison of the final compression images between the experimental test [18] and the LS-DYNA model

Experimental observations showed that the cell walls exhibited local buckling under compressive loading, with these deformations particularly concentrated at the cell junctions. Similarly, numerical analyses revealed that the cell walls folded at specific locations, and the collapse mode deviated from ideal symmetry. Incorporating the distinct responses of single- and double-walled cell edges into the model allowed for a more accurate representation of the structural behavior. The overall collapse mechanism was found to be consistent with the experimental results, indicating that the numerical model reliably captured the physical response. This agreement is further supported in Figure 3, where the force–strain curves obtained from the LS-DYNA simulations are compared with the experimental results.

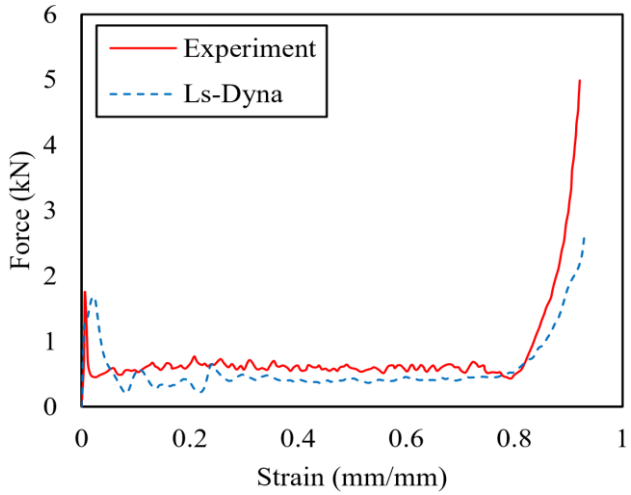


Figure 3. Comparison of experimental [18] and numerical force–strain curves

As shown in Figure 3, a distinct peak load was observed at the onset of compression in both the experimental results and the numerical simulations. This peak was measured as 1754 N in the experiments and 1676 N in the LS-DYNA simulation, corresponding to a difference of 4.40%. Following the peak, the cell walls began to fold, and a stable response of approximately 500 N was maintained up to a strain level of about 0.8. In this plateau region, the experimental and numerical curves exhibited a nearly parallel trend. The total absorbed energy was calculated as 10.45 J experimentally and 8.02 J numerically, corresponding to a deviation of 23.25%. Beyond a strain level of 0.8, the folding process of the walls was completed, and the overlapping folded elements compressed each other, leading to a stiffening effect. At this stage as well, the overall trends of the two curves remained consistent.

The comparison between experimental images and the deformation modes predicted by the numerical model, along with the similarity of the force–strain curves, demonstrates that the developed model reliably represents the compressive response of honeycomb structures. This agreement validates the accuracy of the adopted material parameters, finite element mesh, and contact definitions. Therefore, the findings of the validation study confirm that the model can be effectively applied to analyze different bio-inspired honeycomb designs.

3. Modeling and Compression Behavior Analysis of Bio-Inspired Honeycomb Structures

Along with the regular hexagonal honeycomb, seven additional bio-inspired models were analyzed under compression. The unit cells of the investigated honeycombs are shown in Figure 4.

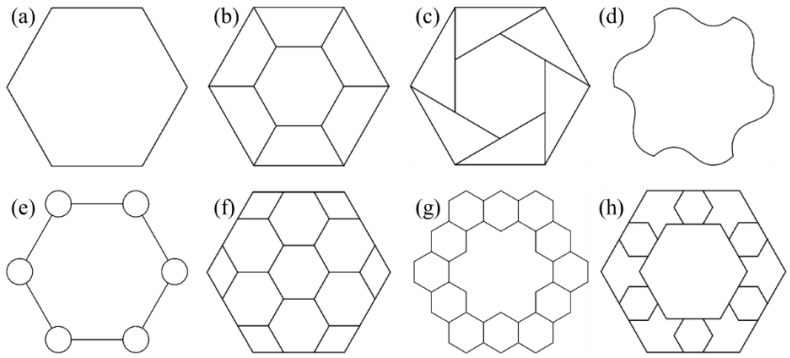


Figure 4. (a) Regular hexagon, (b) spider, (c) snail, (d) wavy, (e) bamboo, (f) pomelo peel, (g) grass stem, and (h) hierarchical unit honeycombs

The honeycomb models were designed as follows: For the spider model, a smaller hexagon with an edge length of 4.5 mm was placed at the center of a regular hexagon with an edge length of 9 mm, and the vertices of both hexagons were connected. Conversely, in the snail model, 30–60–90 triangles were added to each edge, thereby forming a smaller hexagon with an edge length of 5.19 mm, rotated by 30° at the center. The wavy model features sinusoidal curves with an amplitude of 1.5 mm, consisting of one crest and one trough, added to each edge of the hexagon. In the bamboo model, circular arcs with a radius of 1.5 mm were added to each corner of the hexagon. In the pomelo peel model, a hexagon with an edge length of 3 mm was placed at the center, and six additional hexagons of the same size were positioned between this central hexagon and the outer hexagon. In the grass stem model, three small hexagons with an edge length of 2.59 mm were vertically attached to each edge of the larger hexagon. Finally, in the hierarchical model, a central hexagon with an edge length of 6 mm was surrounded by six smaller hexagons, each with an edge length of 1.5 mm, positioned between the central and outer hexagons. The honeycomb structures generated from these unit cells and used in the compression tests are presented in Figure 5.

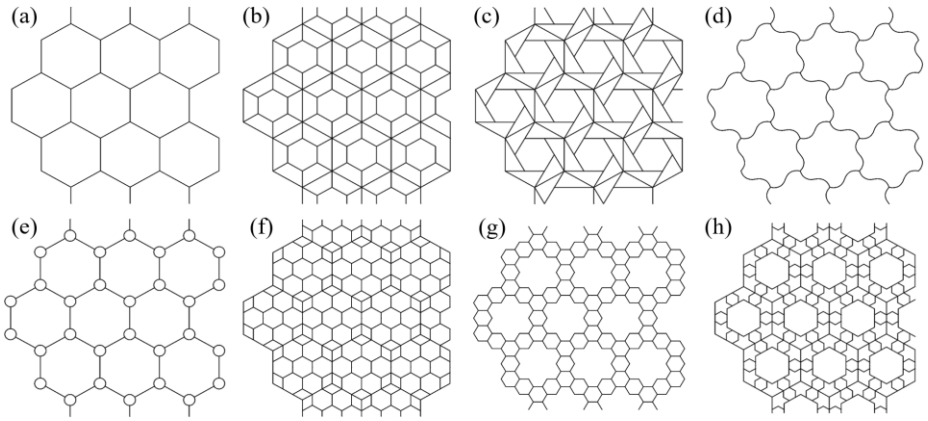


Figure 5. (a) Regular hexagon, (b) spider, (c) snail, (d) wavy, (e) bamboo, (f) pomelo peel, (g) grass stem, and (h) hierarchical honeycombs

To ensure the accuracy of the physical data, the mass of each honeycomb configuration was determined using a dual-verification approach. First, the theoretical mass was calculated analytically based on the CAD geometry: the total wall volume was derived from the cumulative cross-sectional length of the cell walls, the wall thickness (t=0.75 mm), and the height (h=15 mm), and then multiplied by the density of AA3003-H18. Secondly, these values were cross-checked against the total mass reported by the LS-DYNA pre-processor

(based on element volume and density). Both methods yielded identical results, confirming that the additional mass introduced by the internal features of the bio-inspired designs (e.g., in Spider and Pomelo peel models) was accurately represented.

These figures illustrate the honeycomb structures designed to investigate the influence of different geometric features on mechanical behavior. The regular hexagon represents the simplest configuration and serves as the reference structure, whereas the spider model offers increased stiffness and load-bearing capacity due to additional connections at the center. The snail model, with its rotated inner hexagon and inclined edges, provides a potential for gradual energy dissipation during deformation. The sinusoidal edges of the wavy model enhance local buckling and folding modes, thereby improving energy absorption. The bamboo model incorporates circular elements at the corners, which reduce stress concentrations and enhance impact resistance. The pomelo peel and grass stem models, characterized by multi-layered and multi-cellular arrangements, distribute loads more evenly and achieve higher specific energy absorption. Finally, the hierarchical model, with its multi-scale cell organization, optimizes both stiffness and energy absorption capacity. The progressive deformation modes of the different honeycomb configurations under compression are shown in Figure 6.

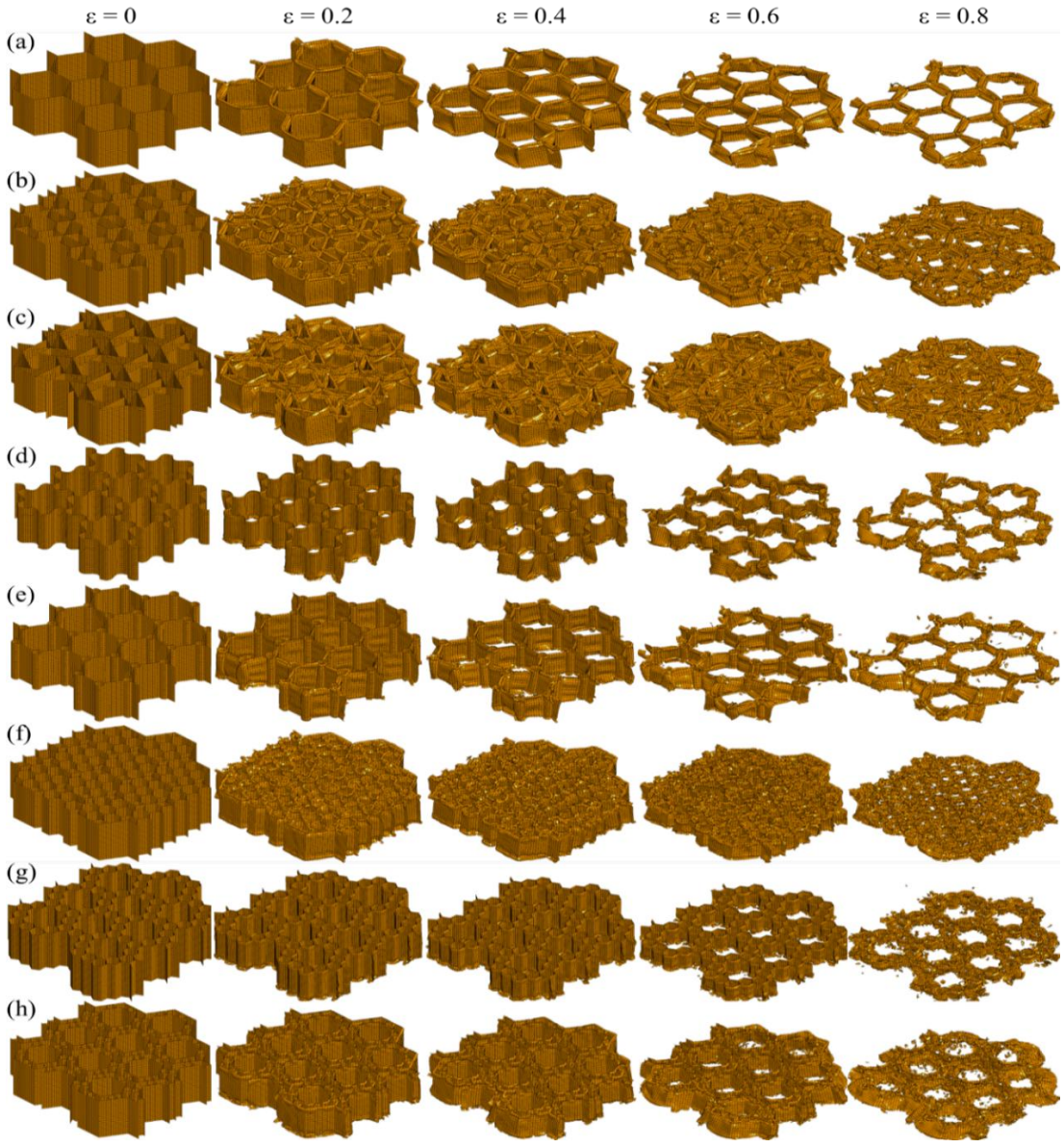


Figure 6. Progressive deformation modes of different honeycomb structures at axial strain levels of 0, 0.2, 0.4, 0.6, and 0.8

This figure illustrates the progressive deformation behavior of eight different honeycomb configurations under increasing axial loading. At low strain levels (ε = 0–0.2), all models exhibited elastic and initial buckling stages, whereas at intermediate levels (ε = 0.4–0.6), geometry-specific folding modes became more pronounced. The regular hexagon collapsed with predictable folding bands, while the spider and hierarchical models displayed more integrated and rigid collapse behavior due to their additional connections. In the snail and wavy models, inclined edges and sinusoidal walls promoted gradual, low-fluctuation deformation modes, thereby enhancing energy absorption. The bamboo model, with its rounded corners, limited local stress concentrations, whereas the pomelo peel and grass stem models distributed loads more uniformly through their multi-cellular structures, maintaining stability even at higher strains. At large strain levels (ε = 0.8), all structures reached a pronounced densification region; however, the multi-cellular and hierarchical designs dissipated energy more progressively and retained their load-bearing capacity even in the final stages of collapse.

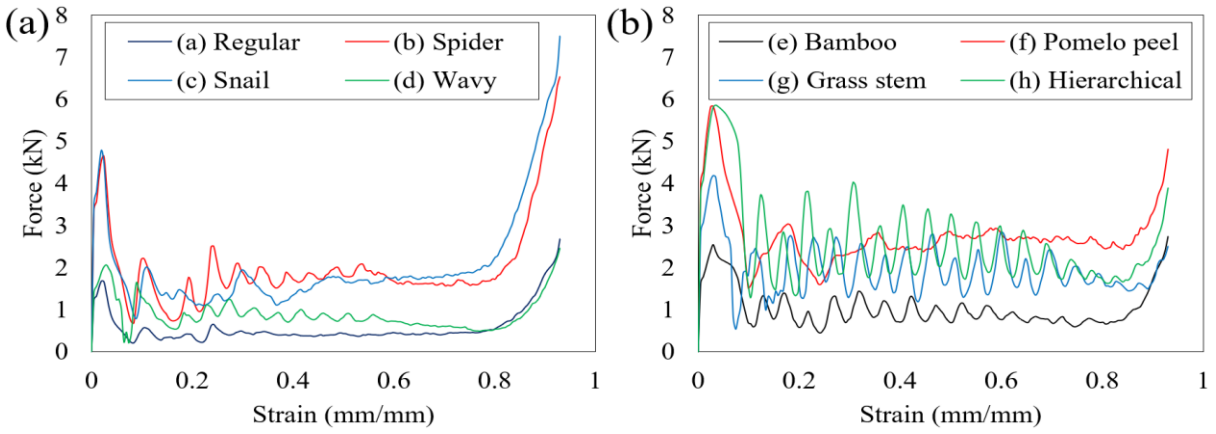


Figure 7. Force–strain curves of different honeycomb configurations under axial compression: (a) Regular, Spider, Snail, and Wavy models; (b) Bamboo, Pomelo peel, Grass stem, and Hierarchical models

In both panels, the force–strain curves (Figure 7) exhibit a similar overall trend: an initial transition and peak within ε ≈ 0–0.1, a plateau region between ε ≈ 0.2–0.7 characterized by geometry-specific oscillatory patterns, and a steep rise beyond ε ≳ 0.75–0.85 corresponding to densification. Comparing the Regular, Spider, Snail, and Wavy models, the plateau force level generally follows the order Spider ≳ Snail > Wavy > Regular. While the Spider and Snail structures provided higher load-carrying capacity, the Wavy and particularly the Regular model displayed lower levels but a smoother energy absorption response. In terms of plateau stability, the Regular model showed the lowest oscillation with a fairly uniform curve, the Snail and Wavy exhibited moderate fluctuations, and the Spider displayed pronounced variations due to multiple folding bands. Densification occurred later in the Spider and Snail models, whereas it started earlier in the Wavy and Regular configurations, indicating a force-limiting behavior for the Regular design.

In the right panel, which compares the Bamboo, Pomelo peel, Grass stem, and Hierarchical models, the plateau level and length generally follow the sequence Pomelo peel ≳ Bamboo ≳ Grass stem ≈ Hierarchical. The Bamboo model, owing to its rounded corners, produced a relatively smooth plateau with reduced oscillations. The Grass stem and Hierarchical models, however, exhibited distinct saw-tooth oscillations due to the sequential folding of smaller cells. The Pomelo peel model demonstrated a ring-by-ring folding mechanism, generating a moderately oscillatory yet extended plateau. The Hierarchical and Grass stem designs, with their multi-scale cell organization, exhibited shorter but higher plateaus. Densification occurred earlier in the Bamboo model, while it was delayed in the others, confirming that multi-cellular and hierarchical structures can sustain energy absorption effectively up to higher strain levels. The corresponding mass, absorbed energy, and specific energy absorption values of these structures, calculated up to a strain level of ε = 0.8, are presented in Table 2.

Table 2. Mass, energy absorption, and specific energy absorption values of the honeycomb models

Model	Mass (g)	EA (J)	sEA (J/g)
Regular hexagon	1.5	8.02	5.35
Spider	4.04	27.95	6.92
Snail	4.41	28.69	6.51
Wavy	1.86	12.31	6.62
Bamboo	2.13	14.46	6.79
Pomelo peel	4.88	38.46	7.88
Grass stem	3.63	27.22	7.50
Hierarchical	4.87	35.99	7.39

When the eight configurations are compared, the highest specific energy absorption (sEA) is achieved by the Pomelo peel model (7.88 J/g), followed by the Grass stem (7.50 J/g) and Hierarchical (7.39 J/g) designs. The common feature of these three structures is their multi-cellular or hierarchical load paths, which delay densification and provide an extended energy dissipation plateau. The Spider (6.92 J/g) and Bamboo (6.79 J/g) models offer balanced alternatives with medium-to-high sEA, while the Wavy (6.62 J/g) and Snail (6.51 J/g) models exhibit slightly lower sEA values but provide smoother plateau responses with reduced peak forces. As expected, the Regular model (5.35 J/g) represents the reference level.

In terms of absolute energy absorption (EA), the Pomelo peel (38.46 J) and Hierarchical (35.99 J) models stand out, although their higher mass and structural complexity become evident. The Wavy model, on the other hand, is notable as a mass-efficient option, with a relatively low weight (1.86 g) while still maintaining reasonable energy absorption. In this context, Figure 8 presents a comparative evaluation of mass variation against specific energy absorption improvement. This allows for a proportional assessment of energy dissipation efficiency with respect to added mass and visually highlights the performance-to-weight balance across the different designs.

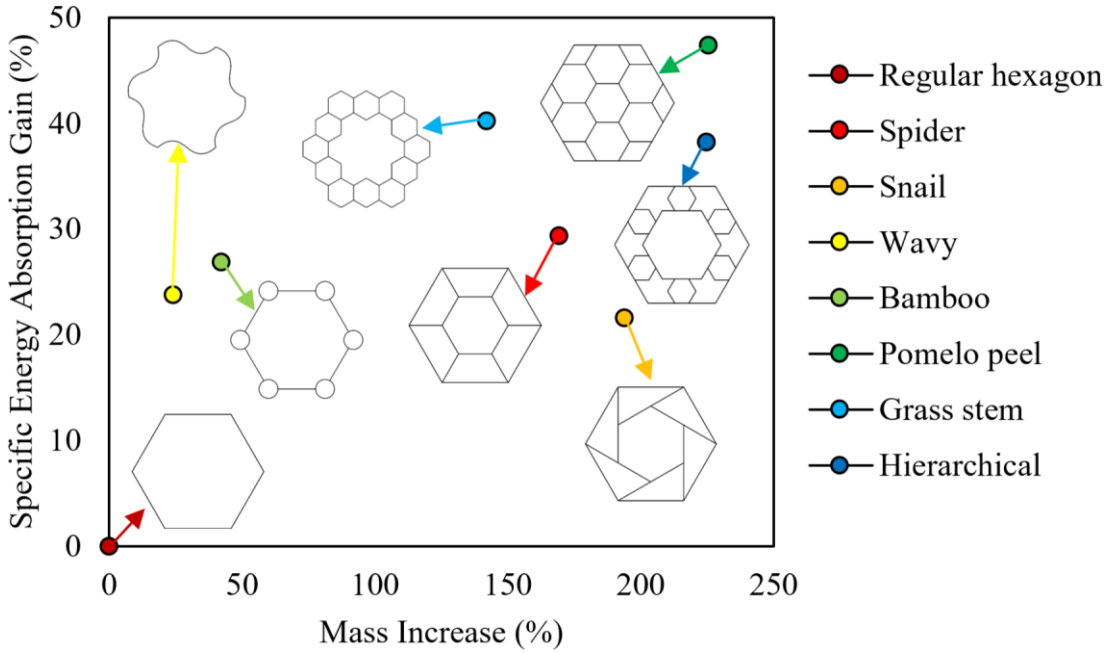


Figure 8. Comparative assessment of mass increase versus specific energy absorption gain in honeycomb configurations

Figure 8 enables a combined assessment of the proportional mass increase and the corresponding gain in specific energy absorption (sEA) relative to the regular hexagonal structure. The visualization clearly shows that while some bio-inspired designs achieve significant improvements in sEA despite added mass, others

provide more limited benefits. In particular, the multi-cellular and hierarchical structures are located in the upper-right region, representing a "high-mass/high-gain" trend, whereas the wavy and snail models, with their relatively low mass increase, fall into the "light-to-moderate gain" group. This distribution indicates that the performance-to-weight balance among different designs should be evaluated not only by absolute energy values but also by proportional efficiency metrics.

4. Discussion

The results of this study highlight the significant potential of bio-inspired geometries in enhancing the crashworthiness of honeycomb structures. While the primary findings were presented in the previous section, several critical aspects regarding the numerical methodology and comparative performance warrant further discussion.

First, regarding the validation study, a discrepancy of approximately 23% was observed between the experimental (10.45 J) and numerical (8.02 J) absorbed energy values, despite the close agreement in peak force. This deviation is mainly attributed to the element deletion technique employed in the finite element framework. In the numerical model, elements are removed from the calculation domain once they exceed the plastic failure strain (ε_p) to simulate material failure. Consequently, these deleted elements no longer contribute to the load-bearing capacity. In contrast, during the physical compression test, the fractured cell walls do not disappear; they remain within the structure, folding onto each other and creating a stiff debris pile. This phenomenon is particularly significant in the final stages of compression (densification), where the accumulated material in the experiment generates additional resistance forces that the numerical model—due to element deletion—cannot fully capture. Therefore, the numerical results present a slightly conservative prediction of the total energy absorption.

Secondly, the specific energy absorption (SEA) values obtained in this study are consistent with, and in some cases superior to, similar structures reported in the literature. For instance, the Pomelo peel model achieved an SEA of 7.88 J/g. When compared to similar hierarchical honeycombs studied by Zhang et al. [13] and Fang et al. [16], the proposed design demonstrates a competitive performance-to-weight ratio. While traditional hexagonal structures are typically limited by early densification, the multi-cellular arrangement in the Pomelo and Grass stem models successfully extended the plateau region, resulting in a significant improvement in energy dissipation efficiency.

Finally, regarding the numerical strategy, specific choices were made to ensure both robustness and computational efficiency. Since the explicit solver is deterministic, a single simulation was performed for each configuration, with the validity of the buckling modes confirmed against experimental data for the reference structure. Additionally, a loading velocity of 10 m/s was employed. This value was chosen in alignment with previous studies on bio-inspired structures [7], which have demonstrated that such velocities yield reliable quasi-static results for explicit solvers. In the present study, the ratio of kinetic energy to internal energy remained negligible throughout the deformation process, further confirming that dynamic inertial effects were minimized. Thus, the observed deformation modes and force responses can be considered representative of quasi-static behavior.

5. Conclusions

In this study, the compressive behavior of eight honeycomb structures, including a regular hexagonal reference and seven bio-inspired configurations, was systematically analyzed through validated finite element simulations. The developed LS-DYNA model showed good agreement with experimental results in terms of deformation modes, peak load, and energy absorption trends, confirming the reliability of the adopted modeling strategy.

The comparative analyses revealed that geometry plays a critical role in determining both the deformation mechanism and the energy absorption capacity of honeycomb structures. While the regular hexagon provided the baseline response, the bio-inspired designs introduced distinctive folding modes and plateau

characteristics. Specifically, the pomelo peel, grass stem, and hierarchical models exhibited superior specific energy absorption, primarily due to their multi-cell and hierarchical load-transfer mechanisms that delayed densification. The spider and bamboo structures exhibited balanced performance with moderate energy absorption, whereas the snail and wavy designs demonstrated smoother plateau behavior and lower peak stresses, which could be advantageous in applications requiring controlled load transfer.

It was also observed that energy absorption efficiency is strongly influenced by the trade-off between structural mass and geometrical complexity. Although multi-cell designs achieved higher energy dissipation, they also introduced additional weight. Therefore, an optimal design should be selected by considering both absolute energy absorption and design efficiency, taking into account the performance-to-weight ratio in accordance with application requirements.

Overall, this research demonstrates that bio-inspired geometrical modifications can significantly improve the crashworthiness of honeycomb structures. The findings provide practical insights for engineers and designers seeking to optimize lightweight structures where energy absorption, stability, and efficiency are critical. Future studies may extend this work by exploring dynamic loading conditions, hybrid material systems, or large-scale structural integration to further evaluate the potential of bio-inspired honeycomb concepts.

6. Author Contribution Declaration

The author solely contributed to the conception and design of the study, literature review, numerical modeling, analysis and interpretation of the results, preparation of figures and tables, and writing and revision of the manuscript.

7. Ethics Committee Approval and Conflict of Interest Declaration

This study does not involve human participants, animals, or any data requiring ethics committee approval. Therefore, ethics committee permission was not required. The author declares that there is no conflict of interest regarding the publication of this article.

8. Ethical Statement Regarding the Use of Artificial Intelligence

No artificial intelligence-based tools or applications were used in the preparation of this study. The entire content of the study was produced by the author in accordance with scientific research methods and academic ethical principles.

9. References

[1] L. J. Gibson, "Cellular solids," *MRS Bull.*, vol. 28, no. 4, pp. 270–274, 2003.
[2] T. N. Bitzer, *Honeycomb Technology: Materials, Design, Manufacturing, Applications and Testing*. Berlin, Germany: Springer, 1997.
[3] D. Mousanezhad, H. Ebrahimi, B. Haghpanah, R. Ghosh, A. Ajdari, A. M. S. Hamouda and A. Vaziri, "Spiderweb honeycombs," *Int. J. Solids Struct.*, vol. 66, pp. 218–227, 2015.
[4] Q. He, J. Feng, Y. Chen and H. Zhou, "Mechanical properties of spider-web hierarchical honeycombs subjected to out-of-plane impact loading," *J. Sandwich Struct. Mater.*, vol. 22, no. 3, pp. 771–796, 2020.
[5] K. Tewari, M. K. Pandit, P. R. Budarapu and S. Natarajan, "Analysis of sandwich structures with corrugated and spiderweb-inspired cores for aerospace applications," *Thin-Walled Struct.*, vol. 180, p. 109812, 2022.
[6] K. Feng, G. Wei, H. Yu, L. Yao, W. Wang, Y. Shen and J. Sun, "Effect of geometric structure and fiber orientation on crashworthiness of honeycomb-inspired composite thin-walled tubes," *Polym. Compos.*, vol. 45, no. 10, pp. 9600–9619, 2024.
[7] N. S. Ha, G. Lu and X. Xiang, "Energy absorption of a bio-inspired honeycomb sandwich panel," *J. Mater. Sci.*, vol. 54, no. 8, pp. 6286–6300, 2019.
[8] H. Jiang, Y. Ren, Z. Liu, S. Zhang and Z. Lin, "Low-velocity impact resistance behaviors of bio-inspired helicoidal composite laminates with non-linear rotation angle based layups," *Compos. Struct.*, vol. 214, pp. 463–475, 2019.
[9] H. Yan *et al*., "3D compression-twist lattice metamaterials for surface reconfigurability of future architecture," *Compos. Struct.*, vol. 337, p. 118075, 2024.
[10] X. Yang, Y. Sun, J. Yang and Q. Pan, "Out-of-plane crashworthiness analysis of bio-inspired aluminum honeycomb patterned with horseshoe mesostructure," *Thin-Walled Struct.*, vol. 125, pp. 1–11, 2018.
[11] D. Hu, Y. Wang, B. Song, L. Dang and Z. Zhang, "Energy-absorption characteristics of a bionic honeycomb tubular nested structure inspired by bamboo under axial crushing," *Compos. Part B Eng.*, vol. 162, pp. 21–32, 2019.
[12] W. Zhang, T. X. Yu and J. Xu, "Uncover the underlying mechanisms of topology and structural hierarchy in energy absorption performances of bamboo-inspired tubular honeycomb," *Extrem. Mech. Lett.*, vol. 52, p. 101640, 2022.
[13] W. Zhang, S. Yin, T. X. Yu and J. Xu, "Crushing resistance and energy absorption of pomelo peel inspired hierarchical honeycomb," *Int. J. Impact Eng.*, vol. 125, pp. 163–172, 2019.
[14] B. Yang, W. Chen, R. Xin *et al*., "Pomelo peel-inspired 3D-printed porous structure for efficient absorption of compressive strain energy," *J. Bionic Eng.*, vol. 19, pp. 448–457, 2022.
[15] W. Xu, C. Wang, B. Liu and S. Jia, "Crushing responses and energy absorption of bionic inspired corrugated honeycombs," *Int. J. Impact Eng.*, vol. 179, p. 104641, 2023.
[16] J. Fang, G. Sun, N. Qiu, T. Pang, S. Li and Q. Li, "On hierarchical honeycombs under out-of-plane crushing," *Int. J. Solids Struct.*, vol. 135, pp. 1–13, 2018.
[17] R. Li, Z. Zhao, H. Bao *et al*., "Bio-inspired honeycomb structures to improve the crashworthiness of a battery-pack system," *Eng. Fail. Anal.*, vol. 158, p. 108041, 2024.
[18] X. Zhang, H. Zhang and Z. Wen, "Experimental and numerical studies on the crush resistance of aluminum honeycombs with various cell configurations," *Int. J. Impact Eng.*, vol. 66, pp. 48–59, 2014.
[19] İ. Bozkurt, "Investigation of compressive strength and energy absorption of cylinder corrugated sandwich structures with different geometric configurations," *Fırat Univ. J. Exp. Comput. Eng.*, vol. 4, no. 1, pp. 115–135, 2025.
[20] D. Kalubadanage, Y. Chen, C. Chen, H. Hao and Z. Wang, "Close-in blast resistance of large-scale auxetic re-entrant honeycomb sandwich panels," *J. Sandwich Struct. Mater.*, vol. 23, no. 8, pp. 4016–4053, 2021.
[21] F. Tarlochan, F. Samer, A. M. S. Hamouda, S. Ramesh and K. Khalid, "Design of thin wall structures for energy absorption applications: Enhancement of crashworthiness due to axial and oblique impact forces," *Thin-Walled Struct.*, vol. 71, pp. 7–17, 2013.

Fırat Üniversitesi Deneysel ve Hesaplamalı Mühendislik Dergisi

FUJECE

Endüstriyel Atık Gazlardan Karbon Dioksitin Yakalanması

Özcan BAŞARAN[1], Yavuz KIRIM[2]*

[1,2] Kimya Mühendisliği, Mühendislik Fakültesi , Siirt Üniversitesi, Siirt, Türkiye.
[1]ozcanbsrn@gmail.com, [2]yavuzkirim@siirt.edu.tr

Geliş Tarihi: 03.11.2025
Kabul Tarihi: 24.12.2025

Düzeltme Tarihi: 24.12.2025

doi: https://doi.org/10.62520/fujece.1816291
Araştırma Makalesi

Alıntı: Ö. Başaran ve Y. Kırım, "Endüstriyel atık gazlardan karbon dioksitin yakalanması" Fırat Üni. Deny. ve Hes. Müh. Derg., vol. 5, no 1, pp. 262-269, Şubat 2026.

Öz

Bu çalışmada, Batman ve Siirt illeri arasında bulunan bir endüstriyel üretim tesisinden salınan CO_2'nin uygun çözümler kullanılarak yakalanması, Aspen Plus simülasyonu kullanılarak modellenmiştir. Çalışmada, CO_2 yakalama ajanı olarak metildietanolamin (MDEA) çözeltisi seçilmiştir. Proses tasarımında emiciler, sıyırıcılar, ısı eşanjörleri, flaş buharlaştırıcılar ve devridaim döngüleri kullanılmıştır; farklı besleme hızları ve tepsi sayıları test edilmiştir. İlk aşamada, 400 ton/saat besleme çözeltisi ile CO_2'nin sadece %47'si yakalanabilmiştir. Ancak, çözelti akış hızı 832 ton/saate çıkarılınca, besleme akışında bulunan 76 ton/saat CO_2'nin yaklaşık 72,14 ton/saati (%95) başarıyla yakalanmıştır. Ayrıca, başlangıçta hem emici hem de sıyırıcıda 30 olarak ayarlanan tepsi sayısının, performansta önemli bir değişiklik olmaksızın 21'e düşürülebileceği ve böylece işlemin maliyet etkinliğinin artırılabileceği gözlemlenmiştir. Elde edilen sonuçlar, endüstriyel tesislerde MDEA çözeltileri kullanılarak CO_2 yakalama yönteminin yüksek verimlilik sağladığını göstermektedir. Ancak, CO_2'nin sadece yakalanması değil, kimyasal/yakıt üretiminde de kullanılması gerektiği vurgulanmaktadır. Bu tür teknolojilerin yaygın olarak benimsenmesi, Türkiye'nin gelecekteki iklim hedeflerine ulaşmasına önemli ölçüde katkıda bulunacaktır.

Anahtar kelimeler: Aspen plus, Karbon yakalama, Endüstriyel kirlilik, MDEA

*Yazışılan yazar

İntihal Kontrol: Evet – Turnitin
Şikayet: fujece@firat.edu.tr
Telif Hakkı ve Lisans: Dergide yayın yapan yazarlar, CC BY-NC 4.0 kapsamında lisanslanan çalışmalarının telif hakkını saklı tutar.

Firat University Journal of Experimental and Computational Engineering

Capturing Carbon Dioxide from Industrial Waste Gases

Özcan BAŞARAN[1], Yavuz KIRIM[2*]

[1]Chemical Engineering, Engineering Faculty, Siirt University, Siirt, Türkiye.
[1]ozcanbsrn@gmail.com, [2]yavuzkirim@siirt.edu.tr

Received: 03.11.2025
Accepted: 24.12.2025
Revision: 24.12.2025
doi: https://doi.org/10.62520/fujece.1816291
Research Article

Citation: : Ö. Başaran and Y. Kırım, "Capturing carbon dioxide from industrial waste gases" Firat Univ. Jour.of Exper. and Comp. Eng., vol. 5, no 1, pp. 262-269, February 2026.

Abstract

In this study, the capture of CO_2 released from an industrial production facility located between the provinces of Batman and Siirt using suitable solutions was modelled using the Aspen Plus simulation. In the study, a methyldiethanolamine (MDEA) solution was chosen as the CO_2 capture agent. The process design utilized absorbers, strippers, heat exchangers, flash evaporators, and recirculation loops; different feed rates and tray counts were tested. In the first stage, only 47% of the CO_2 could be captured with a feed solution of 400 t/h. However, by increasing the solution flow rate to 832 t/h, approximately 72.14 t/h (95%) of the 76 t/h of CO_2 present in the feed stream was successfully captured. Furthermore, it was observed that the number of trays, initially set at 30 in both the absorber and stripper, could be reduced to 21 without any significant change in performance, thereby increasing the cost-effectiveness of the process. The results obtained demonstrate that the CO_2 capture method using MDEA solutions in industrial facilities provides high efficiency. However, it is emphasized that CO_2 should not only be captured but also utilized in chemical/fuel production. The widespread adoption of such technologies will significantly contribute to Turkey's achievement of future climate goals.

Keywords: Aspen plus, Carbon capture, Industrial pollution, MDEA

*Corresponging author

Plagiarism Checks: Yes – Turnitin
Complaints: fujece@firat.edu.tr
Copyright & License: Authors publishing with the journal retain the copyright to their work licensed under the CC BY-NC 4.0

1. Introduction

With the Industrial Revolution, the intensive use of fossil fuels rapidly increased the amount of greenhouse gases in the atmosphere, and carbon dioxide (CO_2) emissions in particular became the primary driver of climate change. Globally, CO_2 emissions from the energy sector reached a historic peak of 36.8 gigatons in 2022, and this increase seriously threatens the goal of limiting global warming to 1.5 °C, as stated in the International Panel on Climate Change's (IPCC) sixth assessment report [1]. The increase in atmospheric CO_2 not only causes temperature increases but also triggers wide-ranging problems such as rising sea levels, ecosystem degradation, and intensification of extreme weather events [2]. In this context, Carbon Capture, Utilization, and Storage (CCUS) technologies stand out as one of the critical solutions for mitigating the effects of climate change. CCUS encompasses the processes of capturing CO_2 at its source in industrial facilities or during energy production, transporting it using appropriate technologies, utilizing it in different areas, or storing it long-term in safe geological reservoirs [3]. The sub-branches of the technology, Carbon Capture and Storage (CCS) and Carbon Capture and Utilization (CCU), enable both the reduction of emissions and the conversion of carbon into an economic input. Notably, at the 28th meeting of the conference of the parties' summit held in Dubai in 2023, the necessity of a gradual phase-out of fossil fuels was emphasized, and it was acknowledged that the application of CCS technologies is inevitable, particularly in heavy industries where no alternatives exist.

The advantages and disadvantages of different carbon capture technologies have also been discussed in detail in the international literature. For example, although post-combustion CO_2 capture technologies offer high efficiency, the most significant disadvantage is the increase in solvent consumption and costs when working with low-concentration gases [4, 5, 6]. Pre-combustion CO_2 capture, although offering capture efficiencies above 90%, has limited application due to high energy consumption and difficulties in integrating it into existing facilities [4, 7, 8, 9]. Oxy-fuel combustion technology is a promising option with capture rates of up to 98%, but it has economic limitations due to the need for high-purity oxygen and durable materials [10]. In addition, bioenergy with carbon capture and storage (BECCS) stands out among "negative emission technologies" and is considered by the IPCC to be an integral part of carbon-neutral scenarios beyond 2050 [11]. The utilization of captured CO_2 is a critical factor for the economic sustainability of the technology. Today, CO_2 can be used in methanol and synthetic fuel production, polymer synthesis, construction materials such as cement and aggregates, fertilizer production in agriculture, and even in refrigerants [12]. These versatile applications transform carbon capture investments from a mere environmental necessity into an economic opportunity.

Academic and industrial studies conducted in Turkey have yielded important findings regarding the integration of CO_2 capture technologies into local conditions. This study models the CO_2 released from an industrial production facility between the provinces of Batman and Siirt using Aspen Plus software and examines its absorption with methyldiethanolamine (MDEA) solutions, demonstrating a high rate of CO_2 separability. Thus, it offers a feasible solution at the local level and provides a technical contribution to Turkey's 2053 net-zero targets.

2. Methodology

Aspen Plus is a chemical process simulator in the chemical engineering market, is a software that enables users to create a process model and then simulate it using equations or mathematical calculations to measure the relationship between two or more variables. In addition to advantages such as designing new processes and improving existing ones, it maximizes profit by combining them with cost-saving workflows. Another advantage is that the thermodynamic properties used in modelling are stored in a database within the program, which includes types and pure/binary selection parameters.

2.1 Simulation process main inputs

Various CO_2 scrubbers are available to prevent the release of CO_2 emitted from any industrial facility into the environment. Among these scrubbers, MDEA plays an important role. In this study, MDEA is used as a

CO_2 scrubber to eliminate CO_2 emissions from an industrial facility. The CO_2 amount of an industrial facility near the Batman and Siirt region is approximately 75 t/h, and its emission is modelled using the Aspen Plus simulation program. The temperature and pressure of CO_2 are taken as 40 ºC and 27 bar, respectively. The components in the feed gas are used in the simulation in terms of molar fraction: H_2O (0.002), CO_2 (0.189), H_2 (0.745), CH_4 (0.058), CO (0.004), and N_2 (0.002). The Redlich-Kwong physical property package with the NRTL electrolyte is used in the simulation, and the purpose of using this fluid package is due to the dissociation of the components in the CO_2-water mixture into hydronium, carbonate, and bicarbonate ions [13-15]. A pure solution containing equal moles of H_2O and MDEA is fed at 600 t/h from the top of the absorber, while the feed gas solution is fed into the system from the bottom of the absorber. The pressures and temperatures of both feed streams are assumed to be the same. This simulation includes the following six equilibrium reactions:

$$MDEA + H_2O \leftrightarrow MDEA + H_3O^+ \quad (1)$$
$$CO_2 + 2H_2O \leftrightarrow H_3O^+ + HCO^{-3} \quad (2)$$
$$HCO_3^+ + H_2O \leftrightarrow H_3O^+ + CO^-_3 \quad (3)$$
$$2H_2O \leftrightarrow H_3O^+ OH^- \quad (4)$$
$$H_2O + H_2S \leftrightarrow HS^- + H_3O^+ \quad (5)$$
$$H_2O + HS^- \leftrightarrow S^{-2} + H_3O^+ \quad (6)$$

2.2 Process flow diagram description

The components in the process flow diagram designed for CO_2 capture consist of an absorber, heat exchanger, stripper, cooler, flash evaporator, mixer, and pump system. First, the feed gas containing CO_2 is fed into the stripper at 40 °C and 27 bar pressure with a pure MDEA solution. The number of absorber stages is taken as 15, and the condenser and reboiler sections are neglected in the simulation. The pure solution enters the absorber at the 1st stage, while the feed gas enters at the 15th stage. The efficiency/effectiveness of the liquid-vapor mixture in the absorber is taken as Murphree efficiency 0.4. In the simulation, it is assumed that only MDEA and CO_2 react, and hydrogen sulphide does not react in the system. Using the "Design Specs" feature in the simulation, the ratio of CO_2 in the H_2 gas in the absorber top stream to the CO_2 in the feed stream is set to 0.05. The CO_2-rich absorber outlet stream is then heated to 110 °C using a heat exchanger. The heated rich solution is fed to the stripper for CO_2 gas separation. The number of stripper stages is assumed to be 21, the boiling rate is 0.2, and the reflux rate is 0.1. The Murphree efficiency in the stripper is assumed to be the same as the absorber efficiency. In the stripper's top stream, CO_2, H_2O, and a certain amount of CH_4 are cooled to 10 °C via a heat exchanger before being fed to the flash evaporator. As CO_2 exits the flash evaporator from the top stream, H_2O leaves the system from the bottom stream of the flash evaporator. The H_2O leaving the flash evaporator and the stripper bottom stream are fed back into the system and supplied to the absorber inlet stream with the make-up amount of MDEA using a mixer. The "Calculator Block" is used to calculate the amount of H_2O and MDEA lost in the upper stream of the flash evaporator, the amount of H_2O and MDEA lost in the upper stream section of the absorber component, the amount of H_2O in the feed stream, and the required amount of H_2O and MDEA in the make-up stream. After the "Calculator Block" process is completed, a pump compatible with the liquid-vapor flow with a discharge pressure of 40 bar is added to the mixer outlet flow. After this process, the pure solution flow initially added to the absorber in the simulation is cancelled and replaced with the pump outlet flow added to the absorber, and the inlet flow rate is adjusted using the "Design Specs" feature. The general process flow diagram of CO_2 using MDEA is shown in Figure 1.

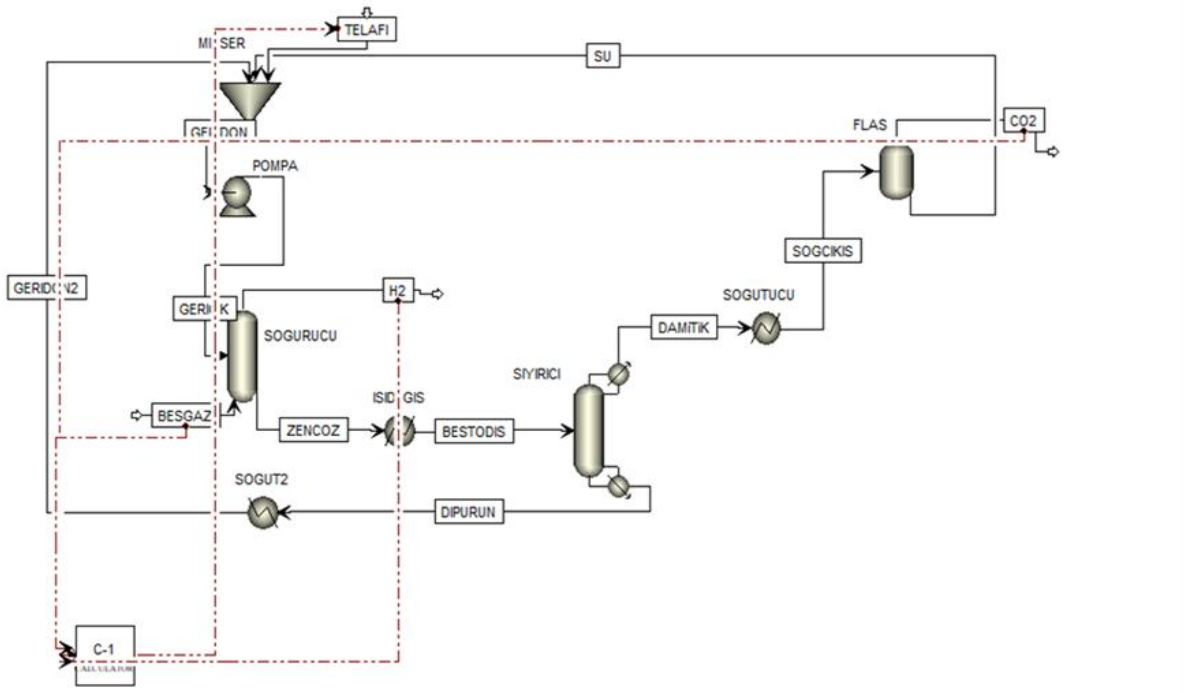


Figure 1. Process flow diagram for CO_2 capture using MDEA

3. Results and Discussion

When the pure solution enters the absorber from the 1st tray, it is assumed that the feed gas containing CO_2 enters from the 15th tray. While the residence times of the liquid and gas phases in the absorber are calculated as 5 s per tray for the liquid, increasing the number of iterations in the simulation program from 25 to 200 reveals that approximately 47% of the 76,000 kg/h CO_2 feed is separated in the absorber stream. However, since the objective of this simulation is to achieve CO_2 separation from the feed gas between 95% and 97%, the amount of pure solution must be increased. Using the "Design Specs" feature, it is seen that the amount of pure solution, initially entered as 400 t/h, should be used as 832 t/h. When 832 t/h of MDEA is used in the simulation, it is seen that approximately 72.14 t/h of CO_2, or approximately 95%, is removed from the feed gas in the CO_2 outlet stream, which was initially approximately 76 t/h. When the CO_2-rich solution from the absorber bottom outlet enters the stripper after exiting the heater, the stripper tray number is initially set to 30. In the simulation, the iteration number is increased from 25 to 200, as in the absorber unit, and the simulation is observed to run correctly. The temperature on the 1st tray of the stripper unit is calculated as 59.6 ºC, while the temperature on the 30th tray is calculated as 106.2 ºC. A heat exchanger, which acts as a cooler, is added to reduce the temperature in the distillation unit of the stripper to 10 ºC. It is assumed that there is no pressure drop in the heat exchanger. CO_2 is separated from H_2O in the distillate stream of the stripper by means of a flash evaporator. 0.996 of the CO_2 and H_2O mixture coming out of the cooler is separated in the flash evaporator. Thus, high-purity CO_2 is separated from the upper stream of the flash evaporator. Most of the H_2O separated from the mixture in the lower stream enters the mixer before entering the absorber via the recirculation stream. The MDEA and H_2O separated in the lower stream of the stripper are sent to the mixer for re-evaluation. At the start of the simulation, instead of a pure solution stream containing MDEA and H_2O, the return streams and the make-up stream are mixed in the mixer and connected to the absorber inlet stream at the end of the simulation. Only 0.36% H_2O and 1.46% MDEA are lost as H_2O and MDEA, respectively, from the absorber outlet stream.

Initially, when the component profile "Column Design" in Aspen Plus was selected with 30 trays for the absorber and stripper, (component profiles) in Aspen Plus, it was observed that there was not much change in the separation of MDEA composition in the stripper after 21 trays. Therefore, the number of trays was changed to 21 in both the absorber and stripper to reduce costs. Figure 2 shows the composition

change with the number of trays.

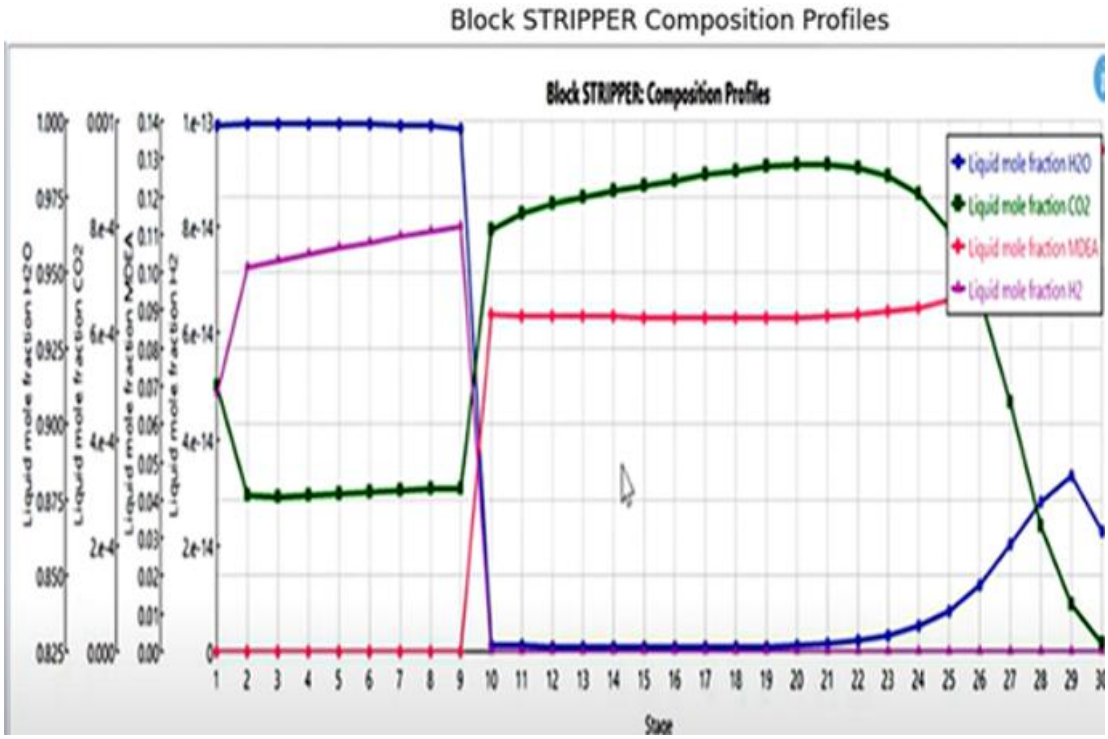


Figure 2. Composition change with the number of trays.

Compensation H_2O (MAKW) = Amount of H_2O in the CO_2 stream (WCO_2) + Amount of H_2O in the H_2 stream (WH_2) – Amount of H_2O in the feed stream (WF) (7)

Compensation MDEA (MAKM) = Amount of MDEA in the CO_2 stream (WCO_2) + Amount of MDEA in the H_2 stream (WH_2) (8)

Additionally, the Fortran codes in the simulation are provided as follows. The Figure 3 shows Fortran codes of H_2O and MDEA calculations.

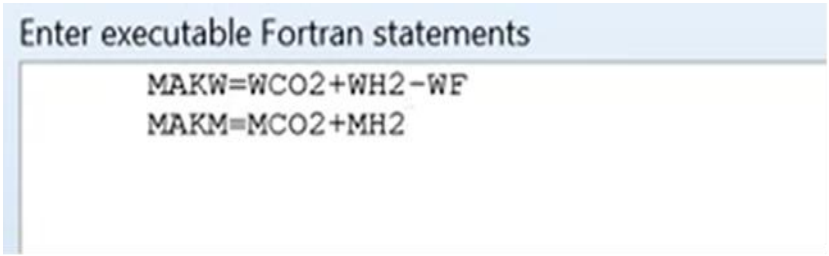


Figure 3. Calculation of H_2O and MDEA quantities in Fortran

The H_2O and MDEA calculated in Fortran for the make-up flow are 814.41 kg/h and 1.50 kg/h, respectively. Pump equipment is also required at the outlet of the mixer flow to feed the absorber. The required discharge pressure is taken as 40 bar. The flow brought to the desired pressure is included in the simulation flow instead of the pure solution to the absorber, and the absorption of CO_2 with MDEA is completed. The mass flow data for all flows are given in Table 1 below.

Table 1. All flows in the process diagram used for CO_2 absorption

Units	BESGAZ	BESTODIS	CO_2	DIPURN	GRCK	GRDN	GRD2	H2	SGCK	SU	TLAFİ	ZENÇZ
Mass Flows	kg/hr	100,000	925,619	73727.7	843650	852,706	852,706	843,650	27,087.5	81,968	824,034	814,525	925,619
H_2O	kg/hr	329.97	396,079	197.66	411,107	420,089	420,089	411,103	944.24	83,853	8187.64	812.99	391,334
MDEA	kg/hr	0	287306	0	425,664	424,428	424,406	424,547	1.50	0,0003	0.0003	1.502	235,384
H_2S	kg/hr	0	0	0	0	0	0	0	0	0	0	0	0
CO_2	kg/hr	75,832.6	14979,5	72136	147,941	0.204	0.194	0.191	3796.57	72072.2	0	0	3388.5
HCO_3^-	kg/hr	0	800,304	0	2243.51	1745.23	1733.98	1705.07	0	1477.4	0	0	95569.8
$MDEA^+$	kg/hr	0	163,780	0	4582.92	5833.57	5855.82	5709.45	0	2869.4	0.0027	0.0027	1964.75
CO_3^{-2}	kg/hr	0	1538.28	0	33.25	593.87	605,134	582.81	0	0	0	0	2060.62
HS^-	kg/hr	0	0	0	0	0	0	0	0	0	0	0	0
S^{-2}	kg/hr	0	0	0	0	0	0	0	0	0	0	0	0
H_3O^-	kg/hr	0	0.00039	0	0	0	0	0	0	0.0019	0	0	0.0035
OH^-	kg/hr	0	0.315	0	4.39	2.48	2.43	2.43	0	0	0	0	0.2492
H_2	kg/hr	13,710	0.011	0.011	0	0	0	0	13,710	0.012	0	0	0.012
CH_4	kg/hr	8434,23	1381.9	1369.12	0	12.78	0	0	7125.11	1381.9	0	0	1381.9
CO	kg/hr	1022.81	76.51	16.49	0	0.023	0.023	0	1006.32	1651.54	0	0	1651.54
N_2	kg/hr	511.44	7.72	7.72	0	0.009	0.009	0	503.75	7.72	0	0	7.72

4. Conclusions

The objective of this study was to use appropriate solutions to absorb the CO_2 emitted at an industrial production center situated between the provinces of Batman and Siirt. It was found that 47% of the CO_2 in the system was extracted from the feed when the residence periods of the liquid and gas phases in the absorber were computed as 5 seconds per shelf for the liquid. When the pure solution feed rate was raised from 400 t/h to 832 t/h in the simulation, it was found that 72.14 t/h of the 76 t/h of CO_2 in the outlet stream was removed from the feed gas, indicating that roughly 95% of the CO_2 was removed from the system. This is because 95–97% separation of CO_2 is desired. Additionally, even though there were 30 trays in the original simulation, it was found that the software did not appreciably alter the separation of the MDEA composition in the stripper after 21 trays. Therefore, in order to reduce capital costs on the absorber and stripper, 21 trays were chosen. It is known that the gas released into the atmosphere by living organisms constitutes a small fraction compared to the CO_2 gas emitted by factories or manufacturing plants. Therefore, it is crucial to carefully examine and conduct research and studies aimed at reducing CO_2 emissions from production sources. CO_2 is crucial not only because it plays a key role in the photosynthesis process of plants but also because it ensures the existence of life on Earth by affecting the average temperature in the atmosphere. While it is a necessary component, its excess also causes damage to the global ecosystem.

5. Author Contribution Statement

Özcan BAŞARAN: Formal analysis, Investigation, Resources Formal analysis, Investigation, Methodology, Writing–original draft Yavuz KIRIM: Conceptualization, Supervision, Validation, Visualization, Writing – review & editing

6. Ethics Committee Approval and Conflict of Interest

"There is no conflict of interest with any person/institution in the prepared article. Additionally, ethics committee approval is not required for this study."

7. Ethical Statement Regarding the Use of Artificial Intelligence

No artificial intelligence-based tools or applications were used in the preparation of this study. The entire content of the study was produced by the author in accordance with scientific research methods and academic ethical principles

8. References

[1] IPCC, *Climate Change 2021: The Physical Science Basis. Contribution of Working Group I to the Sixth Assessment Report of the Intergovernmental Panel on Climate Change*, V. Masson-Delmotte *et al*., Eds. Cambridge, U.K.: Cambridge Univ. Press, 2021.
[2] S. Fawzy, A. I. Osman, J. Doran and D. W. Rooney, "Strategies for mitigation of climate change: A review," *Environ. Chem. Lett.*, vol. 18, pp. 2069–2094, 2020.
[3] R. S. Haszeldine, "Carbon capture and storage: How green can black be?" *Science*, vol. 325, no. 5948, pp. 1647–1652, 2009.
[4] D. Hospital-Benito, J. Lemus, C. Moya, R. Santiago, V. R. Ferro and J. Palomar, "Techno-economic feasibility of ionic liquids-based CO_2 chemical capture processes," *Chem. Eng. J.*, vol. 407, 2021.
[5] Y. Wu, J. Xu, K. Mumford, G. W. Stevens, W. Fei and Y. Wang, "Recent advances in carbon dioxide capture and utilization with amines and ionic liquids," *Green Chem. Eng.*, vol. 1, no. 1, pp. 2–19, 2020.
[6] G. T. Rochelle, "Amine scrubbing for CO_2 capture," *Science*, vol. 325, no. 5948, pp. 1652–1654, 2009.
[7] M. I. Taipabu, B. Y. Chou, W. Wu and B. Sardi, "Techno-economic assessment of blended-amine CO_2 capture integrated coal-fired power plants," *Appl. Therm. Eng.*, vol. 278, 2025.
[8] M. B. Danbatta, N. A. Al-Azri, M. A. Qyyum and N. Al-Rawahi, "Carbon capture solvents for the applicability of rotating packed bed for industrial applications: Recent advancements, challenges and future recommendations," *Carbon Capture Sci. Technol.*, vol. 15, 2025.
[9] J. D. Figueroa, T. Fout, S. Plasynski, H. McIlvried and R. D. Srivastava, "Advances in CO_2 capture technology—The U.S. Department of Energy's carbon sequestration program," *Int. J. Greenh. Gas Control*, vol. 2, no. 1, pp. 9–20, 2008.
[10] "Türkiye'nin karbon yakalama, kullanma ve depolama potansiyeli," 2024.
[11] P. Smith *et al*., "Biophysical and economic limits to negative CO_2 emissions," *Nat. Clim. Change*, vol. 6, pp. 42–50, 2016.
[12] International Energy Agency, "Direct air capture: A key technology for net zero," 2021.
[13] Aspen Technology, *Aspen Physical Property System: Physical Property Methods and Models*, Version 11.1, vol. 1. Bedford, MA, USA: AspenTech Inc., 2019.
[14] I. M. Al-Malah Kamal, *Aspen Plus: Chemical Engineering Applications*. Hoboken, NJ, USA: John Wiley & Sons, 2017.
[15] Aspen Technology, *Getting Started Modeling Processes with Solids: Aspen Plus*, 2013.

Fırat Üniversitesi Deneysel ve Hesaplamalı Mühendislik Dergisi

FUJECE

Oyun Teorisi ve Tabu Araması Yoluyla Tehlikeli Maddelerin Araç Rotalama Problemine Risk Kaçınımlı Metasezgisel Hibrit Çözüm Yaklaşımı

Hakan ASLAN[1*], Michael G.H.BELL[2]

[1]Inşaat Mühendisliği Bölümü, Mühendislik Fakültesi, Sakarya Üniversitesi, Sakarya, Türkiye.
[2]Ulaşım ve Lojistik Enstitüsü, Limanlar ve Deniz Taşımacılığı Lojistiği, Sidney Üniversitesi, Sidney, Avustralya.
[1]haslan@sakarya.edu.tr, [2]michael.bell@sysdney.edu.tr

Geliş Tarihi: 05.11.2025
Kabul Tarihi: 01.1.2026

Düzeltme Tarihi: 24.11.2025

doi: https://doi.org/10.62520/fujece.1818151
Araştırma Makalesi

Alıntı: H. Aslan ve M. G.H. Bell, "Oyun teorisi ve tabu araması yoluyla tehlikeli maddelerin araç rotalama problemine risk kaçınımlı metasezgisel hibrit çözüm yaklaşımı," Fırat Üni. Deny. ve Hes. Müh. Derg., vol. 5, no 1, pp. 270-298, Şubat 2026.

Öz

Günlük yaşamımızın ayrılmaz bir parçası haline gelmelerinin bir sonucu olarak, her yıl büyük miktarlarda tehlikeli madde üretilmekte ve taşınmaktadır. Sanayi toplumlarının çoğunda, tehlikeli maddeler olmadan bir yaşam neredeyse tahayyül edilemez hâle gelmiştir. Tehlikeli maddeler; taşınma sürecinde halk sağlığı, kamu güvenliği ya da taşınmaz mallar üzerinde olumsuz etkiler veya riskler yaratma potansiyeline sahip miktar ve formda bulunan maddeler olarak tanımlanır. Bu bağlamda, tehlikeli maddeler veya ürünler; patlayıcı, gaz hâlinde, yanıcı, oksitleyici, toksik, bulaşıcı, radyoaktif ya da aşındırıcı özellik gösteren maddeler ile bunlara ait tehlikeli atıkları kapsamına almaktadır. Tehlikeli maddelerin güvenli taşınması; sürece etki eden yasal ve fiziksel faktörler ile taşıma araçlarının maruz kalabileceği çeşitli riskler nedeniyle kapsamlı ve çok boyutlu bir sorun alanı olarak değerlendirilmektedir. Tehlikeli madde kazalarının halk sağlığına yönelik olası etkilerine karşı artan çevresel duyarlılık, tehlikeli madde taşımacılığı konusuna yönelik akademik ve kurumsal ilgiyi önemli ölçüde artırmaktadır. Bu makale, oyun teorisi temelli bir yaklaşımla tabu arama algoritmasının entegrasyonu sonucu geliştirilen model üzerinden, tehlikeli madde taşımacılığı problemine yönelik riskten kaçınan bir çözüm önermektedir. Model kapsamında, dağıtım görevlisi, sevkiyat ağındaki herhangi bir bağlantıda problem oluşması durumunda, olası en olumsuz koşullar altında ortaya çıkabilecek beklenen zararı minimize etmeyi hedeflemektedir. Bu çerçevede, Nash dengesi aracılığıyla belirlenen beklenen maliyet fonksiyonu, tehlikeli madde taşımacılığında güvenli güzergâh seçimine yönelik stratejik kararların analizinde etkili ve pratik bir çözüm aracı olarak değerlendirilmektedir.

Anahtar kelimeler: Tehlikeli madde taşımacılığı, Araç rotalama problemi, Oyun teorisi, Tabu arama, Nash-dengesi

[*]Yazışılan yazar

İntihal Kontrol: Evet – Turnitin
Şikayet: fujece@firat.edu.tr
Telif Hakkı ve Lisans: Dergide yayın yapan yazarlar, CC BY-NC 4.0 kapsamında lisanslanan çalışmalarının telif hakkını saklı tutar.

Firat Univ Jour. of Exp. and Comp. Eng., 5(1), 270-298, 2026

Firat University Journal of Experimental and Computational Engineering

Risk Averse Metaheuristic Hybrid Solution Approach to Vehicle Routing Problem of Hazardous Materials Through the Combination of Game Theory and Tabu Search

Hakan ASLAN[1*], Michael G.H.BELL[2]

[1]Department of Civil Engineering, Faculty of Engineering, Sakarya University, Sakarya, Türkiye.
[2] Institute of Transport and Logistics, Ports and Maritime Logistics, University of Sydney, Sydney, Australia.
[1]haslan@sakarya.edu.tr, [2]michael.bell@sysdney.edu.tr

Received: 05.11.2025
Revision: 24.11.2025
Accepted: 01.1.2026
doi: https://doi.org/10.62520/fujece.1818151
Research Article

Citation: H. Aslan and M. G.H. Bell, "Risk averse metaheuristic hybrid solution approach to vehicle routing problem of hazardous materials through the combination of game theory and tabu search", Firat Univ. Jour.of Exper. and Comp. Eng., vol. 5, no 1, pp. 270-298, February 2026.

Abstract

Because they have become an integral part of our daily lives, large quantities of hazardous materials are produced and transported each year. In most industrial societies, life without hazardous materials has become almost unimaginable. Hazardous materials are defined as substances that, during transportation, have the potential to pose adverse effects or risks to public health, safety, or property due to their quantity or form. In this context, hazardous materials or products include explosives, gases, flammable and oxidizing substances, toxic and infectious materials, as well as radioactive, corrosive substances and their associated hazardous wastes. The safe transportation of hazardous materials is considered a comprehensive and multidimensional issue, influenced by various legal and physical factors, as well as the numerous risks that vehicles may encounter during transit. Increasing environmental awareness of the potential impacts of hazardous material accidents on public health has significantly heightened both academic and institutional interest in this field. This study proposes a risk-averse solution to the hazardous material transportation problem through a model developed by integrating the Tabu Search algorithm with a game theory–based approach. Within the model, the dispatcher aims to minimize the expected loss under the worst possible conditions in the event of a disruption in any link of the distribution network. In this framework, the expected cost determined through Nash equilibrium is evaluated as an effective and practical analytical tool for strategic decision-making in the selection of safe routes for hazardous material transportation.

Keywords: Transportation of hazardous materials, Vehicle routing problem, Game theory, Tabu search, Nash-equilibrium

*Corresponding author

Plagiarism Checks: Yes – Turnitin
Complaints: fujece@firat.edu.tr
Copyright & License: Authors publishing with the journal retain the copyright to their work licensed under the CC BY-NC 4.0

1. Introduction

The release of hazardous materials poses short- and long-term toxicological risks to humans, flora, fauna, and entire ecosystems. Such incidents can result in contamination of air, water, and soil, as well as pose significant threats to public health and environmental stability. The adverse results may be classified as,

- Injury and/or loss of life
- Displacement of affected populations
- Damage to water and sewerage systems
- Blockage of roads, streets, and bridges
- Disruption of emergency response services (e.g., police, fire departments, highway rescue teams)
- Interruption of public and private transportation networks
- Disruption of delivery and supply chain operations
- Closure of educational institutions
- Temporary or permanent shutdown of businesses and industries
- Contamination of air, water, and soil

The safe transportation of hazardous materials within large urban areas can be significantly improved through the implementation of effective routing strategies. A minimum-risk routing approach helps to reduce the potential damages associated with hazardous material spills while generating net economic benefits for society. In classical terms, risk is characterized as the interplay between the likelihood that a specific hazardous event will occur within a given timeframe or under certain conditions. and the magnitude of its potential consequences. However, estimating the consequences of a hazardous release is inherently complex. Evaluating the consequence domain requires determining both the extent and characteristics of the population at risk. This assessment must also account for the type of hazardous material being transported and its specific hazard properties - such as toxicity, effects on human health and safety, and environmental impacts - alongside factors like population density, potential evacuation zones by material type, and local geographical conditions.

For the reasons outlined above, estimating the number of fatalities resulting from an incident involving a vehicle transporting hazardous materials is inherently challenging. To address this issue, a risk model based on the traditional definition of risk was proposed for assessing the hazards associated with hazardous materials transportation [1]. However, this model has been criticized for neglecting variance in risk distribution. For instance, a route passing through two small towns might be deemed equally risky as another passing through one large town if only expected consequences are considered. Moreover, the traditional model focuses on minimizing a priori risk assuming that hazardous material shipments continue along the same route even after an incident occurs. To address this limitation, a conditional risk model was later proposed to identify routes that minimize risk given that an incident has occurred [2].

A key area of research in hazardous materials transportation focuses on developing strategies to mitigate the risks associated with Low-Probability, High-Consequence (LPHC) incidents. As the term suggests, these events occur infrequently but can result in severe consequences when they do. Consequently, decision-makers (such as route planners) tend to adopt a risk-averse stance when addressing such scenarios. Previous models have incorporated the decision-maker's risk aversion under the assumption that the probabilities of incident occurrence are known in advance [3–4]. However, there is a need for a modelling approach capable of generating risk-averse routing strategies even when these probabilities are unknown, beyond the general understanding that they are small. The model proposed in this research provides an effective optimization framework for hazardous materials transportation, enabling decision-making in contexts where the likelihood of incidents is minimal but the potential consequences are highly significant.

Another limitation of existing models is their focus on transporting hazardous materials from a single origin to a single destination along a defined path. In practice, however, many real-world logistics problems require determining optimal routes from a main depot to multiple delivery-consumption points (customers) using a fleet of vehicles, an instance of the widely accepted Vehicle Routing Problem (VRP). To illustrate, consider a petroleum distributor operating a central refinery that serves as a single depot. A group of tanker trucks based

at this depot must deliver fuel to a number of geographically dispersed service stations. The objective of the routing plan is to determine paths that minimize the expected total cost, ensuring that each route departs from the depot and, when needed, returns to it. The routing constraints require that each service station be served exactly once by one vehicle, while the cumulative demand along any route must not surpass the vehicle's maximum carrying capacity. This formulation characterises a single-depot capacitated VRP (potentially with stochastic costs). The algorithm proposed in this study addresses this problem by combining a game-theoretic framework with a Tabu Search heuristic to generate efficient and robust routing solutions. Through this integration, the study provides an analysis of hazardous materials transportation within the context of a VRP and derives corresponding equilibrium transportation costs, as well as link usage and failure probabilities (i.e., the likelihood of an incident occurring).

The chief aim of this study is to evolve, design, and analyse a reliability model that integrates the savings algorithm, Tabu Search, and game theory to provide a risk-averse solution framework for routing extremely hazardous materials. The proposed model aims to formulate a routing strategy that ensures the safe transportation of hazardous materials under uncertain conditions, particularly in situations where the likelihoods of link failures are unknown.

To address the problem described above, a game-theoretic approach is employed to determine a risk-averse routing solution. In this framework, the route planner (dispatcher) and a computer modelled system spoiler (evil entity) engage in a strategic two-agent, zero-sum, non-cooperative scenario. Given the substantial potential losses associated with low-probability, high-consequence hazardous material routing, the optimal strategy for the route planner is one that minimizes the maximum expected loss.

The route construction process is carried out using a combination of the conventional savings algorithm and a novel Tabu Search procedure. The savings algorithm generates the initial set of routes, which are subsequently refined and optimized through the Tabu Search. The method of successive averages is employed to determine the Nash equilibrium values for the expected trip cost and link usage or failure probabilities. The Nash equilibrium's expected cost serves as an effective indicator for evaluating the system's performance and overall reliability.

2. Vehicle Routing Problem (VRP)

VRP is a complex management challenge in the field of physical distribution and logistics. It involves creating a set of vehicle routes that begin and end at a main depot, aiming to deliver a specific product to a group of geographically distributed customers with known locations and demand levels. Each customer must be served exactly once by a single vehicle.

In the light of the above explanation, the classical VRP can be defined on a graph $G = (V, L)$; where, $V = \{v_0, v_1, v_2, v_3, \ldots, v_k\}$ is a vertex set representing k demand points, with demands $d_1, d_2, d_3, \ldots, d_k$ respectively. Here, $\underline{v_o}$, is the depot. The demands of each customer are provided by a set of "*m"* alike vehicles with capacity "ρ" located at depot. $L = \{(v_i, v_{i'}): i \# i', v_i, v_{i'} \in V\}$ is a link set. A non-negative cost is defined over the link $(v_i, v_{i'})$ for any $i, i' \in \{0,1,2,3,\ldots.k\}$ representing a distance, a travel cost or a travel time.

VRP is simple to describe but challenging to solve. A problem of size Y is considered solvable in polynomial time if the number of computational steps required grows as a polynomial function of Y. Non-deterministic polynomial-time (NP) problems are those for which a proposed solution can be verified in polynomial time, even if finding the solution may take exponential time. NP-hard problems, on the other hand, are not solvable in polynomial time. Most variants of the VRP are NP-hard and, as a result, are unlikely to be solvable efficiently within polynomial time [5].

A problem is considered easy if there exists an algorithm that solves it in time complexity $O(Y^t)$ for some constant *t*, where *Y* represents the size of the problem. Here, $O(Y^t)$ denotes a function such that:

$$O(Y^l) = a_l Y^l + a_{l-1} Y^{l-1} + \ldots + a_l Y + a_0 \quad (1)$$

where, a_i are constants.

This type of complexity is known as polynomial order, and an algorithm with such complexity is referred to as a polynomial-time algorithm. In contrast, if a problem can only be solved by an algorithm whose time complexity cannot be bounded by any polynomial function of Y, the problem is considered difficult or intractable. Computational complexity theory provides strong evidence that, for certain optimization problems within the NP class, the computation time required to solve them grows exponentially with the size of the problem.

Since VRP is an NP-hard problem, exact algorithms can only handle instances of relatively small size [6]. In practice, however, it is often necessary to address large and complex instances. Even the most sophisticated exact methods may become computationally infeasible in such cases. Consequently, approximate (heuristic) algorithms are crucial, as they can produce near-best solutions for large-scale problems within realistic computation times and memory constraints.
The following expressions present a standard mathematical formulation of the classical VRP.

$$\text{Minimise} \quad \sum_{i}\sum_{i'}\sum_{m} c_{ii'} x_{ii'}^{m} \tag{2}$$

subject to

$$\sum_{i}\sum_{m} x_{ii'}^{m} = 1 \quad for \quad all \quad i' \quad (i \neq i') \tag{3}$$

$$\sum_{i'}\sum_{m} x_{ii'}^{m} = 1 \quad for \quad all \quad i \quad (i \neq i') \tag{4}$$

$$\sum_{i} x_{ip}^{m} - \sum_{i'} x_{pi'}^{m} = 0 \quad for \quad all \quad p, m \tag{5}$$

$$\sum_{i} d_i \left(\sum_{i'} x_{ii'}^{m}\right) \leq \rho \quad for \quad all \quad m \tag{6}$$

$$\sum_{i'=1} x_{0i'}^{m} \leq 1 \quad for \quad all \quad m \tag{7}$$

$$\sum_{i=1}^{k} x_{i0}^{m} \leq 1 \quad for \quad all \quad m \tag{8}$$

$$x_{ii}^{m} \in Z \quad for \quad all \quad i, i', m \tag{9}$$

$$Z = \{(x_{ii'}^{m}) : \sum_{i \in B}\sum_{i' \in B} x_{ii'}^{m} \leq |B| - 1 \quad for \quad B \subseteq V/(0); |B| \geq 2\} \tag{10}$$

where;

$x_{ii'}^{m}$ is a binary variable indicating if link *i*-*i`* is traversed by vehicle *m.*

The objective of minimizing distance or travel time is expressed in Equation (2). Equations (3) and (4) together ensure that each customer is visited exactly once by a single vehicle. Equation (5) enforces that a vehicle leaves every customer it visits. Equation (6) guarantees that vehicle capacity constraints are not violated, while Equations (7) and (8) ensure that the number of available vehicles is not exceeded. Finally, Equation (9) is used to eliminate sub-tours.

As shown in the expressions above, the VRP may involve numerous constraints, which can generally be classified as relating either to vehicles or customers. It should be noted, however, that a specific VRP instance may not include all of these constraints.

2.1. Why do heuristic (approximate) algorithms work effectively

As noted, since VRP is an NP-hard problem and it cannot be solved optimally within polynomial time. Consequently, heuristic algorithms are commonly employed to obtain near-optimal solutions within a rational computational time frame.In the broadest sense, a heuristic can be defined as a problem-solving procedure that relies on intelligent interpretation and exploration of the problem structure to derive a reasonable solution. This definition highlights the importance of understanding and utilizing the underlying characteristics of a problem when designing a heuristic method. Furthermore, it emphasizes that heuristics aim to produce good though not necessarily optimal solutions within practical computational limits.

Solving NP-hard combinatorial problems of practical size would require exploring all possible combinations of decisions and variables, which is computationally unworkable. Heuristic methods play a crucial role in addressing such problems by intelligently guiding the search process, reducing the number of evaluations, and enabling the discovery of satisfactory solutions within reasonable time limits. Comprehensive combinatorial optimization problems, such as the Traveling Salesman Problem, VRPs and various network flow problems, can often be successfully addressed using heuristic methods.

2.2. Metaheuristics for VRP

Heuristic methods are designed to explore selected portions of the search space, concentrating on regions that appear most promising for improving solution quality. This targeted exploration significantly reduces computation time, typically yielding solutions that, while not optimal, represent substantial improvements over the initial state. A heuristic generally capitalizes on the specific characteristics of a problem to construct efficient solutions. In contrast, broader empirical approaches draw not only on problem-specific knowledge but also on analogies with natural optimization processes. These more general, problem-independent heuristic strategies are referred as "*metaheuristics*".

While heuristic methods typically conduct a relatively limited exploration of the search space, metaheuristics engage in a more extensive and intensive search within the most promising regions of the solution space. Consequently, metaheuristics integrate advanced neighbourhood search strategies, adaptive memory structures, and mechanisms for recombining solutions to enhance search efficiency and solution quality [7].

The heuristic methods proposed for solving VRPs between 1960 and 1990 are commonly referred to as classical heuristics. Algorithms belonging to this category include the Savings Algorithm, the Sweep Algorithm, and the Cluster-First, Route-Second approaches [8–10]. In contrast, metaheuristic methods (such as Simulated Annealing, Tabu Search, Granular Tabu Search, and Genetic Algorithms) have been widely applied to VRPs, providing more flexible and controlling solution strategies [11–14].

A solution procedure was proposed that employed 22 low-level heuristics, each contributing to the development of higher-level heuristics. In this approach, the selection probabilities of the low-level heuristics were dynamically updated based on whether the objective function improved, thereby increasing the likelihood of choosing more effective heuristic sequences and ultimately enhancing solution quality [15].

One of the suggested hybrid approaches joining two metaheuristics is known as the Unified Hybrid Genetic Search (UHGS). This method incorporates advanced mechanisms for diversity preservation, feasibility control, and a restart strategy to enhance search performance [16]. The algorithm is applied to tackle a complex optimization problem referred as the Heterogeneous Site-Dependent Multi-Depot Multi-Trip Periodic VRP (HSDMDMTPVRP).

Another metaheuristic algorithm was investigated using a column generation approach to assess solution quality [17]. In this method, switch point options were enumerated to reduce the overall complexity of the problem and improve computational efficiency.

The formulations are assessed by comparing the quality of their Linear Programming (LP) lower bounds to those obtained from a compact formulation. In this context, the LP lower bounds from the compact model function as a benchmark for evaluating the effectiveness and quality of the suggested solutions.

An alternative metaheuristic approach was proposed with a twofold objective: first, to categorize VRP-related variants addressed by metaheuristic algorithms suggested between 2009 and 2017, and second, to evaluate the effectiveness of these algorithms in obtaining reasonable solutions [18].

The Simulated Annealing (SA) metaheuristic originates from statistical mechanics [19]. As an iterative improvement and approximate optimization method, SA seeks to overcome the limitations of poor local optima by incorporating random acceptance criteria, allowing the algorithm to occasionally accept worse solutions in order to explore the solution space more broadly.

Ant Colony Optimization (ACO) is a biologically inspired, population-grounded metaheuristic developed to answer combinatorial optimization problems [20]. The core concept of ACO is that a large number of simple artificial agents can collaboratively construct high-quality solutions to complex combinatorial problems through indirect, low-level communication, analogous to the pheromone-based foraging behaviour of real ants.

One of the most effective strategies for escaping local minima, points where no neighbouring solution improves the objective function, is Tabu Search, initially introduced by Glover in 1986 [21]. Tabu Search enables the exploration of solutions that do not immediately improve the objective function, permitting moves that would otherwise be restricted, provided they are not classified as forbidden according to the algorithm's tabu criteria.

Kumari et al. [22] proposed a novel hybrid metaheuristic, referred to as GA-RR, to address the Capacitated Vehicle Routing Problem (CVRP). The method integrates two prominent optimization strategies, the Genetic Algorithm (GA) and the Ruin-and-Recreate (RR) heuristic, thereby leveraging the global search capabilities of evolutionary computation and the intensive neighbourhood restructuring characteristic of RR. The objective of the hybrid approach is to generate high-quality solutions across a diverse set of VRP benchmark instances. To assess its performance, the GA-RR algorithm is evaluated on 34 standard benchmark datasets and its results are compared against those produced by several state-of-the-art algorithms. Empirical findings demonstrate that GA-RR delivers superior performance on the majority of test instances. This enhanced effectiveness is attributed to the refinement of GA-generated candidate solutions during the ruin-and-recreate phase, which strengthens the algorithm's capacity to escape local optima. Furthermore, the study provides an analysis of the exploration–exploitation dynamics inherent in the proposed hybrid framework.

Niyomphon and Nakkiew [23] developed a model to identify the optimal daily routing plan minimising total transportation costs, encompassing both fixed vehicle-rental expenses and variable costs associated with travel distance, fuel prices, and fuel consumption. They further exacerbated the complexity of the problem through high customer demand levels that frequently surpass the weight and volume capacities of individual vehicles. Furthermore, all deliveries are subject to strict time-window constraints, necessitating precise scheduling. As a result, the problem is formally modelled as a Multi-Trip Capacitated Vehicle Routing Problem with Time Windows (MTCVRPTW). Owing to its NP-hard nature, the application of metaheuristic optimization techniques represents a pragmatic and effective strategy for generating high-quality solutions within acceptable computational limits. In this investigation, Particle Swarm Optimization (PSO) and Differential Evolution (DE) are implemented to address the MTCVRPTW. The computational results demonstrate that DE consistently outperforms both PSO and the company's existing routing procedures in terms of solution quality.

Zuhanda et al. [24] suggested an approach by utilizing two prominent metaheuristic optimization frameworks, the Artificial Immune System (AIS) and the GA. Whereas GA is situated within the broader domain of evolutionary computation, AIS is rooted in principles of swarm intelligence. The research formulates a vehicle routing model that explicitly accounts for product consolidation and heterogeneous product dimensions, both of which markedly intensify the computational complexity inherent in the Vehicle Routing Problem with Simultaneous Pickup and Delivery and Product Consolidation (VRPSC). To assess the efficacy of these

metaheuristic strategies, their performance is systematically compared with that of exact optimization methods, thereby enabling a rigorous evaluation of alternative solution paradigms for the VRPSC.

An adaptive hybrid metaheuristic that integrates GA with Local Search (LS) through incorporating a stochastic uncertainty model using probabilistic travel times was proposed by Reis [25]. The method automatically adjusts critical parameters, such as mutation rates and the likelihood of invoking local search based on ongoing search behaviour, resulting in a more resilient and efficient exploration of the solution space.

As the primary solution approach employed in the model developed for this study, the following section provides a detailed explanation of the method."

2.2.1. Tabu search

Tabu Search is established on the principle of intelligent problem solving and is somewhat stimulated by the observation that human behaviour often includes a random component, leading to diverse answers under alike conditions. Tabu Search is an iterative meta-strategy designed to enhance local steepest-descent searches by enabling a more extensive exploration of the solution space. It accomplishes this by generating extended neighbourhoods and focusing on preventing the search from becoming trapped in local optima. Here, the neighbourhood of a solution refers to all solutions reachable via a single transformation, and a move denotes the transition from one feasible solution to another.

Tabu Search operates on the principle of accepting new solutions primarily to prevent revisiting previously explored paths. This approach encourages the exploration of new regions within the solution space, reducing the risk of becoming trapped in local minima and enhancing the likelihood of approaching a global optimum. Similar to other metaheuristics, such as Simulated Annealing, Tabu Search effectively guides iterative improvement processes, providing a robust framework for exploring areas of the solution space where conventional heuristics might otherwise stall.

The core of the Tabu Search procedure lies in effective management of the tabu list. This list records prohibited moves, those that are not allowed in the current iteration, to prevent the search from backtracking. Tabu list management involves updating the list by determining how many moves, and which specific moves, should be designated as tabu during each iteration, as well as specifying the duration for which these moves remain prohibited.

One of the earliest applications of Tabu Search to the VRP was proposed by Willard [26]. In his approach, the solution is initially transformed into a giant tour through depot replication. Neighbourhoods are then defined as all feasible solutions reachable from the current solution via 2-opt or 3-opt exchanges. Another algorithm applies Tabu Search by either moving a vertex to a different route or swapping vertices between two routes to generate neighbours, subsequently selecting the best non-tabu feasible move at each iteration [27].

Since its introduction, Tabu Search has been employed to a wide range of VRPs and has emerged as one of the most effective methods for obtaining high-quality-often near-optimal-solutions for instances involving several hundred customers. This observation is supported by [28]. The success of Tabu Search can be attributed to several key features commonly incorporated in its implementations, including the allowance of infeasible solutions during the search, as well as the use of diversification and intensification strategies.

2.2.2. Game theoretic approach

A game can be defined as a conflict of gains and losses between two or more opponents who act according to a set of formal rules. Several characteristics are common to most games. First, games have rules that dictate the order of actions, specify the set of allowable actions, and determine how the outcomes are linked to the actions taken. Second, games involve two or more players, each consciously striving to maximize their own benefit. Third, the outcome for each player depends on the actions of the other players. Players are aware of this interdependence and recognize that selecting the best action requires careful evaluation of the actions likely to be taken by their opponents.

As a branch of mathematics and logic, game theory studies decision-making in situations where two or more rational and intelligent opponents interact under conditions of conflict or competition. It focuses particularly on the process of making decisions. Players take turns sequentially, after the first player moves, the next player(s) take their turn, and this continues until the game concludes. At the end of the game, each player receives a payoff based on the outcomes of their decisions.

A central question in game theory revolves around situations in which all decision makers (players) pursue their best possible strategies, taking into account the strategies chosen by others. The key issue is: what characteristics of certain game outcomes justify labelling them as equilibria? By analogy, in physical systems, an equilibrium refers to a stable state where all internal forces balance each other, leaving the system at rest unless disturbed by an external influence. Likewise, in game theory, an equilibrium is a condition where no player can achieve a better outcome by changing their strategy alone.

Keeping in mind that a player's best strategy (or best response) is the action that maximizes their payoff given the strategies of the other players, Nash (1951) proved that every finite non-cooperative game possesses at least one equilibrium point [29]. A Nash Equilibrium is a situation in which no player has an incentive to unilaterally deviate from their chosen strategy. This concept of self-reference can be made more explicit by describing a Nash equilibrium as a profile of strategies in which each strategy represents an optimal reaction to the other players' optimal reactions.

The following definition, provided by [30], can be used to further conceptualize the core idea of a Nash equilibrium."

In an n-player game V == {$H_1,\ldots\ldots H_n; Z_1,\ldots\ldots Z_n$} a set of strategies ($h_1^*,\ldots\ldots\ldots, h_n^*$) forms a Nash equilibrium if; for individual player *i*, h_i is player *i* 's best reaction to the strategies taken by the other n-l players, ($h_1^*,\ldots., h_{i-1}^*, h_{i+1}^*,\ldots., h_n^*$}

$Z_i(h_1^*,\ldots.,h_i^*,\ldots h_n^*)$ $Z_i(h_1^*,\ldots.,h_i^*,\ldots h_n^*)$,
$\forall h_i \in H_i$

That is, each player 's strategy h_i^* solves

$$\max_{h_i \in H_i} \quad Z_i(h_1^*,.....h_i,....h_n^*) \tag{11}$$

where;
H_i is the set of strategies available to player *i*.
h_i is an arbitrary member of H_i set
Z_i is the payoff function for player *i"*

As possibly the most widely used solution concept in game theory, what makes the Nash Equilibrium unique is its general applicability: in typical mathematical fashion, it remains valid without being affected by specific examples when analysing a problem. The Nash Equilibrium asserts that every finite game possesses at least one equilibrium, which may exist in either pure or mixed strategies.

This research presents an innovative framework that integrates risk aversion into the routing process for hazardous material transportation. The routing challenge is modelled as a two-player, zero-sum, non-cooperative game that captures rational strategic behaviour between two entities: a route planner (dispatcher) and a hypothetical network attacker. The dispatcher's goal is to identify the most efficient routes for vehicles departing from a single depot, whereas the attacker seeks to disrupt the system by disabling one critical link, thereby maximizing operational losses [31]. The "non-cooperative" nature of the game indicates that the dispatcher has no information about which connection will be targeted, and the attacker, in turn, lacks knowledge of the specific routing decisions made for the hazardous cargo.

The mixed-strategy Nash equilibrium provides a robust framework for estimating the expected routing cost at equilibrium by accounting for both link usage and failure probabilities. This equilibrium reflects the result of a theoretical game in which the route organiser exhibits a highly risk-averse attitude toward potential link failures. At this equilibrium, the expected trip cost is minimized with respect to the link selection probabilities and maximized with respect to the link failure probabilities. The game is classified as a Nash game because neither player holds supremacy over the other, and neither can anticipate the opponent's next move.

2.3. Main concerns and risk averse decision-making models in hazmat shipment

The total number of fatalities, injuries, and damage to the environment and property constitute the consequences of an incident involving a vehicle transporting hazardous materials. In this context, it is important to distinguish between an accident and an incident. Events that cause the release of hazardous material, resulting in a spill, fire, explosion, or leakage, are classified as incidents. In contrast, events that do not lead to any of these undesirable outcomes are considered accidents. While a comprehensive risk model should account for all potential consequences of an incident, it is generally assumed that policymakers focus on mitigating catastrophic outcomes, with fatalities representing the most severe and undesirable category.

Risk is generally defined as the multiplication of the probability of an undesirable event occurring and the severity of its results. This interpretation of risk is commonly referred to as the expected cost. To this end, individual risk levels are determined as a function of each person's distance from the route on which hazardous materials are conveyed. As illustrated in Figure 1, the vehicle enters the inhabited area at point "a" and leaves at point "b." The effect area surrounding the segment "a–b" is referred as the threshold distance corresponding to the specific hazardous material being transported, represented by "t_i."

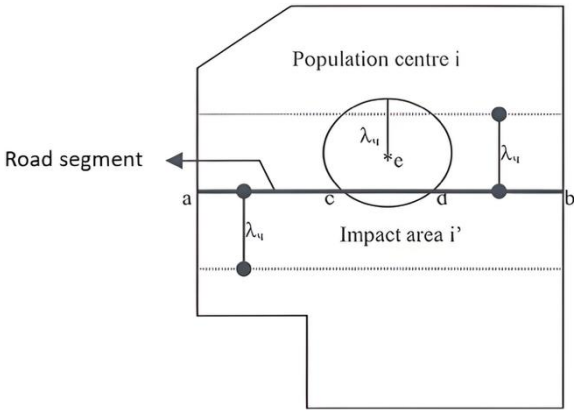


Figure 1. Enhanced risk assessment model

At point "e", within the impact area, people might be affected by a hazardous material incident if it happens within the threshold distance, symbolised as $\lambda_ч$. Hence, when the vehicle travels along the segment "c–d," the individual at point "e" is exposed to risk. As illustrated in the figure, the length of segment "c–d" increases as point "e" moves nearer to the road, leading to a corresponding increase in risk. The individual risk to be encountered at point "e" is expressed mathematically as follows:

$$IR_{esч} = P_{sч}(I)L(c,d) \tag{12}$$

where,
$IR_{esч}$ is the individual risk at point "e" on a "s" road segment due to single transportation of material "ч".
$P_{sч}(I)$ is the probability of incident on road segment "s"
$L(c,d)$ is the length of c-d.

The total public risk imposed on the population centre "*i*" due to a single shipment of material "*ψ*" can be calculated by summing the individual risks in the impact area, which is,

$$R_{is\psi} = \int_{e \in i,} (IR_{es\gamma})(POP_e) d_e \tag{13}$$

where,
POP_e denotes the population density at point "e"

The foundation of the risk-averse modelling approach is the assumption that the decision-maker (route planner) prefers to distribute hazardous material shipments across multiple routes rather than relying on a single route. This strategy aims to minimize the expected consequences of any potential incident during transportation.

When path listing is feasible, i.e., in relatively small networks, a linear programming method can be employed to decide the best combined policy for the decision-maker [31]. Using the established notation, the linear programming formulation is expressed as follows;

$$\begin{aligned} &\sum_k a_{ijk} C_{ij} h_k - F \le 0 \quad for \quad all \quad links(i, j) \\ &\sum_k h_k = 1 \\ &h_k \le 0 \quad for \quad all \quad paths \quad k \end{aligned} \tag{14}$$

P_1: Minimise F with respect to h_k for all links (i,j)
The dual of the above problem is formulated as linear programming as follow
P_2: Maximise G with respect to q_{ij}
subject to,

$$\begin{aligned} &\sum_{ij \in A} a_{ijk} C_{ij} q_{ij} - G \ge 0 \quad for \quad all \quad path(k) \\ &\sum_{ij \in A} q_{ij} = 1 \\ &q_{ij} \ge 0 \quad for \quad all \quad links \quad i, j \end{aligned} \tag{15}$$

where;
q_{ij} is the probability that an incident occurs on link (*i*,*j*)
a_{ijk} is 1 if link (*i*,*j*) lies on path *k*, and 0 otherwise
h_k is the probability that path k is selected for shipment
C_{ij} is the population inside the danger circle with a given impact radius, centred at any points on the link (*i*,*j*)
F, G are the dual variables

Although solving P_1 and P_2 ensures that the values of F and G are unique (with F = G at the solution), the path usage probabilities, link usage probabilities and link incident probabilities are not necessarily unique.

Because the linear programming approach requires prior path enumeration, it is unsuitable for large networks with numerous nodes and links. To address this limitation, an alternative method was proposed that combines a shortest path algorithm with the method of successive averages to generate optimal path sets, usage probabilities, and incident probabilities [32]. This iterative solution procedure employs a game-theoretic framework. In each iteration of the process, the decision-maker identifies the route that minimizes the expected travel cost, whereas a simulated network disruptor (the adversarial entity) deactivates a single link to create a failure scenario, thereby maximizing the operator's expected cost. The interaction between these two opposing objectives forms a strategic balance, and solving this optimisation problem produces the optimal probability

distributions for both players. These probabilities correspond to the mixed-strategy Nash equilibrium of a two-player, zero-sum, non-cooperative game between the route planner and the virtual disruptor. Since this approach does not require prior knowledge of accident probabilities or link reliabilities, it provides an efficient solution method while offering valuable insights into the nature of the optimal routing strategy.

Building on this general background, the following section presents the model developed in this research for the transportation of low-probability, high-consequence hazardous material shipments.

Taking into account the operator's strongly risk-averse stance and the assumption that link failure probabilities are exceedingly small, the routing scenario is reframed as a two-player, zero-sum, non-cooperative game to represent strategic decision-making under uncertainty. Within this game structure, one player, the route planner, seeks to determine the most reliable routing configuration for vehicles departing from a single depot, while the opposing player, system attacker, attempts to disrupt the network by disabling a single link, thereby causing the greatest possible increase in overall transportation cost. The "*non-cooperative*" characterization signifies that neither party possesses prior knowledge of the other's move: the planner is unaware of which link may be failed, and the spoiler cannot predict which specific paths will be chosen to satisfy customer deliveries. To capture the balance between these conflicting strategies, the mixed-strategy Nash equilibrium is utilized, providing a quantitative means to approximate both the equilibrium expected trip cost and the associated probabilities of link usage and failure.

The iterative nature of this decision process is effectively unbounded, as both the route planner and the disposer can continuously adjust their tactics regardless of the number of moves made. This necessitates formulating the problem as a maximin problem, in which the operator selects routes by considering link usage and failure probabilities that yield the most favourable outcome. Solving this problem produces the optimal link usage probabilities for the minimisation of the total projected system cost, alongside the optimal link failure probabilities that maximize it. This resulting equilibrium is stated as the mixed-strategy Nash equilibrium.

Hence, the goal function of this mathematical structure can be expressed as follows:

$$Min(Max\sum_{ij} p_i(c_{ij}^f q_j + c_{ij}^n(1-q_j)\ with\ respect\ to\quad q_j\quad)\quad with\quad respect\quad to\quad p_i$$

subject to;

$$\begin{aligned}
&\sum_j q_j = 1 \\
&p_i \geq 0 \quad \forall \quad all \quad links \quad i \\
&q_j \geq 0 \quad \forall \quad all \quad scenarios \quad j
\end{aligned} \tag{16}$$

where;
p_i is the probability of link *i* to be used
q_i is the likelihood of scenario *j* to be in effect
c_{ij}^f is the route cost on link *i* when scenario *j prevails if* link *i* is failed
c_{ij}^n represents the travel cost on link *i* under scenario *j* when link *i* is functioning normally.

This theoretical framework is founded on the premise that the route planner initially assumes all network links possess an equal probability of failure. The initial set of optimal routes is generated through the Savings Algorithm [8]. In certain situations, some customers may end up being assigned individual routes due to network or cost constraints. Unlike traditional implementations, this method calculates the saving values using expected costs that are derived from the likelihood of link usage and potential failure, rather than relying on actual travel expenses.

The links in the system are considered to have two distinct types of costs. The first represents the normal operating condition cost, which applies when a vehicle carrying hazardous materials travels safely along the link without being involved in any incident. This cost may correspond to factors such as total travel distance, travel time, or fuel consumption. The second cost type represents the failure condition cost of a link. In this case, it is assumed that the vehicle travelling on the link is involved in an incident that causes damage to the environment, property, and nearby populations. Any of the conventional risk assessment frameworks-such as conditional risk models, perceived risk models, or other established methodologies-can be employed to estimate the potential cost associated with such an event, depending on the chosen definition of risk.

Since different risk models may yield varying cost estimates for a given incident, the failed cost values assigned to each link can differ depending on the model used. In the context of this study, however, both normal and failed cost values for each link are treated as exogenous inputs, known a priori. This approach provides the route planner with the flexibility to define the failed cost of each link based on multiple weighted criteria, reflecting the relative importance of different risk dimensions. For example, if certain links pass through rural areas near environmentally sensitive zones-such as natural parks, forests, or historical sites-the failed cost can emphasize environmental impact. Conversely, if a link passes through or near densely populated areas, the failed cost can be based primarily on the number of people potentially affected by an incident. Thus, the operator can determine the failed cost of each link by assigning appropriate weights to societal consequences such as environmental pollution, economic loss, evacuations, injuries, or fatalities, allowing the model to reflect context-specific risk priorities.

The vehicle routes generated by the Savings Algorithm were subsequently optimised using Tabu Search.

3. Solution Algorithm

The assumptions underlying the proposed model can be summarized as follows:

- The network connecting the depot and the customers is modelled using straight-line links. In other words, all the customers and depot are connected through straight line although real case represents curvy connections. This is universal simplification process accepted to represent the transportation networks allowing for more tractable calculations of distances and costs.
- Each link is assumed to exhibit uniform characteristics throughout its entire length. Factors such as road condition, traffic flow, and surrounding environment are considered uniform across each individual link.
- Although the actual failure probabilities of the links are unknown, they are assumed to be relatively low. However, any failure that does occur is expected to have extremely high consequences, consistent with the nature of low-probability, high-consequence hazardous material events.
- The normal and failure costs of each link are assumed to be homogeneous along its entire length. In other words, the normal and failure costs of the links stay the same regardless of the position and the time of the vehicle on the links. Both the operational (normal) cost and the potential incident (failure) cost are evenly distributed, avoiding the need for spatially variable cost modelling within a single link.
- The model is built on the premise that hazardous materials are transported through a series of repeated shipments starting from a central depot and distributed to various customers. This repetitive transport structure enables the estimation of both expected costs and link usage probabilities across multiple delivery cycles, thereby facilitating the integration of game-theoretic equilibrium principles into the routing analysis.

The flowchart below, Figure 2, outlines the calculation procedure of the proposed algorithm.

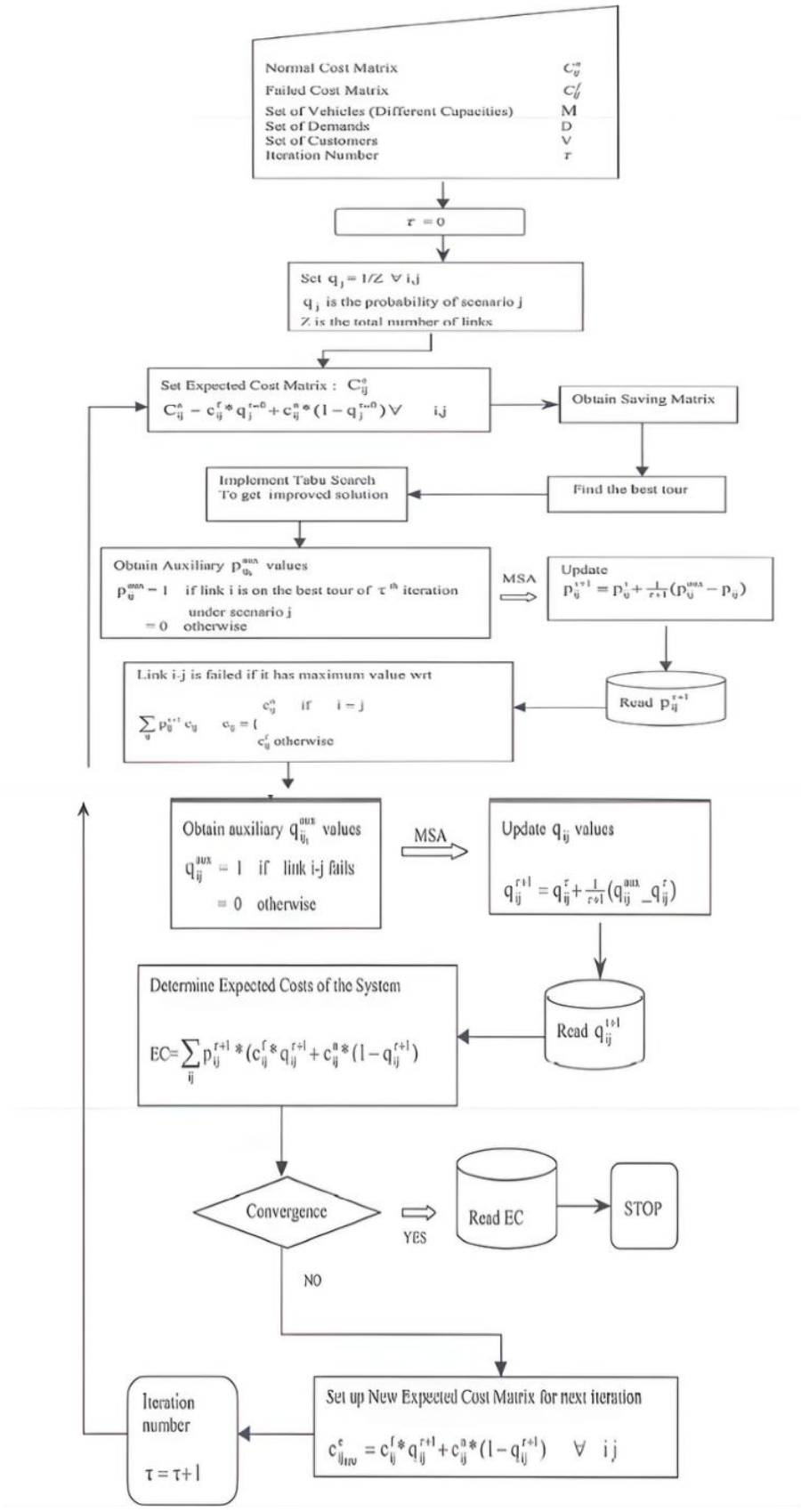


Figure 2. Algorithmic flow-diagram of the developed method

As demonstrated in this figure, the process begins with the planner identifying the optimal set of vehicle routes that minimise the total expected system trip cost, assuming that the link failure probabilities are known. Savings algorithm is the tool used for the identification of the initial set of routes with minimum total expected cost. At this stage Tabu Search is employed to attain the improved set of routes with regard to minimised total expected cost. The link usage probabilities are then updated by employing method of successive averages. Once these routes are established, the evil-entity responds by failing the link that results in the maximum possible cost to the operator. This action produces updated expected link costs, prompting the planner to generate a new best set of routes to be used based on the revised cost structure. Given these new routes, the evil entity again selects and fails the link whose disruption produces the greatest increase in the overall trip cost.

An achievable solution addressing the problem described above is presented by $S=(S_1,S_2,S_3,.....,S_m)$, where S_i outlines exclusively the subsection of customers of $V=(1,2,3,.....,k)$ used by a vehicle "i" from the set of $M=(1,2,3,....,m)$, such that;

$$\bigcup_{i=1}^{m} S_i = V$$
$$S_{i_1} \cap S_{i_2} = \phi \qquad \forall i_1, i_2 \in M$$
$$\sum_{k \in S_i} d_k \le \rho_k \qquad \forall i \in M \tag{17}$$
$$C(S) = \sum_{i \in M} C(S_i)$$

As demonstrated by computational findings in the literature and the preceding sections, the initial solution derived from the savings algorithm often lacks sufficient optimality. To refine this solution, a Tabu Search procedure is applied. This method iteratively enhances feasible solutions by exploring their neighbourhoods. To intensify local improvements within each route, a generation mechanism is employed, defining how a current solution S can be transformed into a neighbouring solution S' within the developed model. The neighbourhood solutions are produced using the *I-interchange mechanism for generating solutions*, as introduced by [11]. After these neighbouring solutions are identified, they can be further refined through local improvement moves based on edge exchanges [33].

The algorithm described above maintains a list of previously made or visited moves to record a number of the most recent actions, thereby prohibiting repetitions or cycling. The duration for which moves and solutions remain on the tabu list is determined by the list size. A small tabu list may lead to cycling, whereas an excessively large list can divert the search away from regions near the global optimum. Ideally, the tabu list size should be sufficient to prevent cycling while still allowing continuous exploration of the solution space. If at iteration "τ" vertices (customers) $v_1 \in R_1$ and $v_2 \in R_2$ are exchanged, it is prohibited to use both v_1 in R_1 and v_2 in R_2 again through iterations (τ+1,……., τ +TABLIST), where TABLIST is the tabu duration (tabu list size). The tabu list is enhanced with a frequency measure that monitors how often each tabu move or solution is revisited during the search, helping guide future decisions. Tracking this frequency information is central for understanding and guiding the evolution of the search process. A high tabu-hit frequency indicates that the process may be trapped in a suboptimal peak, signalling that the search should either be terminated or that a diversification strategy should be applied to explore regions near the global optimum.

After determining the final route configuration, the estimation of link usage and failure probabilities is further refined through the method of successive averages, an iterative optimization technique known for its stability and adaptability in converging toward equilibrium solutions. This method incrementally updates probability values at each iteration by averaging current and previous estimates, thereby enhancing overall solution accuracy. A detailed explanation of the theoretical foundations and implementation steps of method of successive averages can be found in [34], with a concise overview provided in the next section.

3.1. Method of successive averages

This is an iterative solution method for the optimisation problems of,

Minimise f(x) subject to b =Ax

As a descent search direction can be obtained if a negative of the gradient, -Δf(x) is provided at any point x, the solution of the linear programming problem below results in the maximum feasible descent from the point x'.

Minimise $x^T\Delta f(x')$ subject to b=Ax

This problem is classified to as an auxiliary problem, and its outcome, denoted as x^*, is called an auxiliary point. The method of successive averages calculates the average of a sequence of auxiliary points, where each auxiliary point is attained by answering an auxiliary problem in terms of the preceding average of auxiliary points. Thus, if x_n^* is the n^{th} auxiliary point, then an iteration N,

$$x' \leftarrow (1/N)\sum_{n=1toN} x_n^*$$

but,

$$(1/N)\sum_{n=1toN} x_n^* = (1/N)x_N^* + (1/N)\sum_{n=1toN-1} x_n^* \tag{18}$$

hence,

$$x'_{new} \leftarrow (1/N)x'_N + (1-\frac{1}{N})x'_{old}$$

where, x_N^* is obtained by solving the above auxiliary problem.

In order to update the link usage and link failure probabilities, so that the improved expected link travel costs are obtained, first the auxiliary link usage probabilities, denoted by p_i^{aux}, are determined for each link in the system, such that they are 1 if link i is on the one of the current best routes when scenario "*j*" prevails, "0" otherwise. By using these auxiliary values and employing method of successive averages algorithm, the updated link usage probabilities were found. After obtaining updated link usage probabilities, we can obtain the link which is likely to be intentionally disrupted by the hostile actor (evil entity) at the current iteration. Since we assume that the system operator is extremely pessimistic about the state of the system, the evil-entity fails the link which gives the highest value of the $\sum_i p_{ij}c_{ij}$. Here "c_{ij}" is the current travel cost of the link *i*, such that;

$$c_{ij} = \begin{bmatrix} c_i^n & if & i \neq j \\ c_i^f & if & i = j \end{bmatrix}$$

As can be seen, the evil entity has the power to fail one and only one link in the system to impose the highest possible operational cost on the operator. While the auxiliary link failure probability, denoted by $q_{ij}^{\max}$, of link *i* which is failed is 1, all the other remaining links' auxiliary failure probabilities, for that specific iteration, are set to 0. After this, link failure probabilities are updated through method of successive averages and denoted by q_{ij}^{updt}.

The stopping condition for the proposed algorithm is governed by a predefined maximum number of iterations. *MAXI*, counted from the iteration in which the best solution was found. The value of *MAXI* is provided as an input parameter to the model.

In the light of explanations above, the Figure 3 below provides a summary of the calculation steps involved in the main algorithm

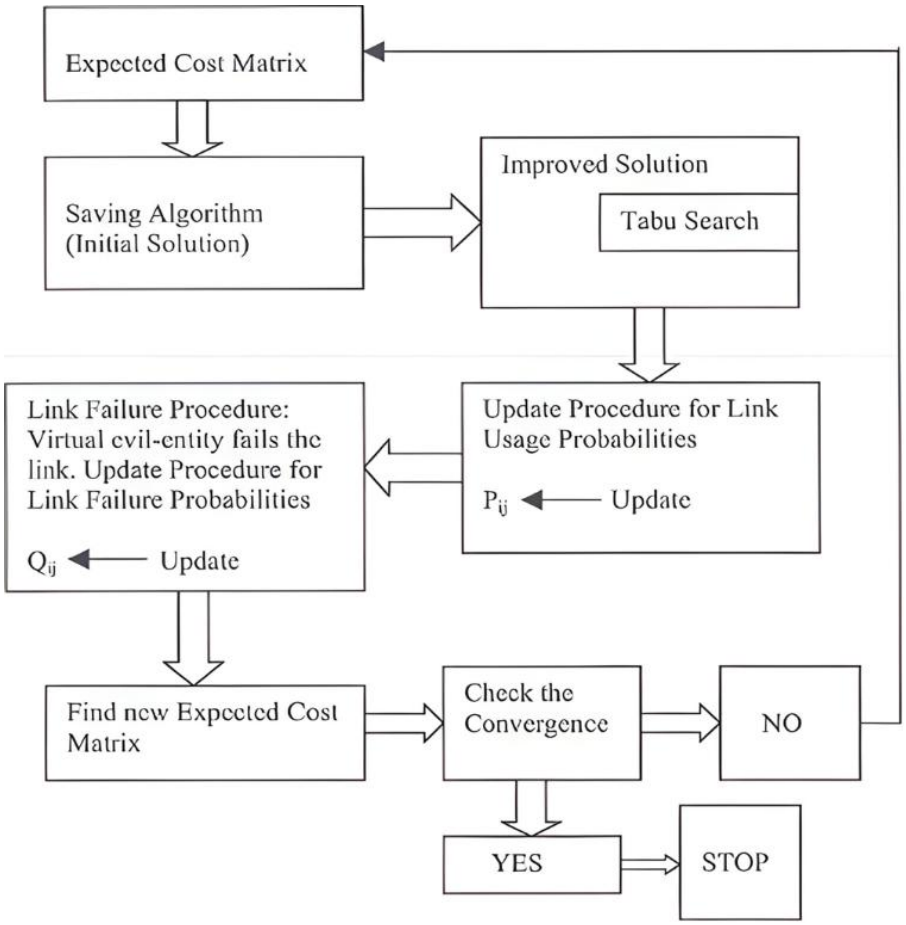


Figure 3. Computational procedure of the proposed method

3.2. Linear programming formulation

"As shown in Equation 16, the objective function is designed to simultaneously minimize and maximize the total expected routing cost, minimized with respect to the link usage probabilities and maximized with respect to the link failure probabilities. To simplify the formulation, Equation 16 can be re-expressed in terms of entire routes instead of individual network links, as follows;

$$Max \quad (Min \quad C = \sum_{i,j} h_i c_{ij} q_j \quad with\ respect\ to \quad h_i) \quad with\ respect\ to \quad q_j$$

$$subject\ to$$

$$\sum_i h_i = 1$$

$$\sum_j q_j = 1 \tag{19}$$

$$h_i \geq 0 \qquad for\ all\ routes \quad i$$

$$q_j \geq 0 \qquad for\ all\ scenarios \quad j$$

where,

C is the total expected cost of assigning routes to vehicles
c_{ij} is the cost associated with route i when scenario j prevails
h_i is the likelihood that route i is used
q_j is the probability of j^{th} scenario to be in effect
The linear programming approach for solving this maximin problem is outlined below,
If "C^*" is the outcome of the problem. Then,

$$\sum_i c_{ij} h_i \le C^* \qquad for\ every\ scenarios\ j \tag{20}$$

The linear programming model below yields the optimal mixed routing strategy for vehicles handling extremely hazardous materials.
Min M with regard to h_i depending on

$$\begin{aligned} &\sum_i c_{ij} h_i - M \le 0 \qquad for\ every\ scenarios\ j \\ &\sum_i h_i = 1 \\ &h_i \ge 0 \qquad for\ every\ routes\ i \end{aligned} \tag{21}$$

Similarly, the optimal mixed link-failure strategy for the evil entity can be determined using the following linear programming model.

Min M* with regard to q_j depending on

$$\begin{aligned} &\sum_j c_{ij} q_i - M^* \ge 0 \qquad for\ all\ scenarios\ j \\ &\sum_j q_j = 1 \\ &q_j \ge 0 \qquad for\ all\ scenarios\ j \end{aligned} \tag{22}$$

It is important to emphasize that the route selection probabilities derived from Equation 21 and the link failure probabilities obtained from Equation 22 are *dual counterparts* within the optimization framework. In essence, the dual variables linked to the constraints in Equation 21 directly correspond to the scenario probabilities defined in Equation 22, reflecting the interdependent relationship between the planner's route-selection and the spoiler's link-failure strategies under the given constraint conditions. At the optimal solution, M attains the value M*. While this linear programming problem yields a unique solution for M, it does not generally produce unique values for "h_i" or "q_j".

The model developed in this research equips the route operator with valuable insights into the critical links that exhibit high failure probabilities within the network, an essential factor in determining the safest routing strategy. For low-probability, high-consequence hazardous material shipments, the safest (i.e., most reliable) strategy aligns with the one that yields the maximin expected routing cost. By focusing on minimizing the system's vulnerability to potential link failures, the proposed approach effectively maximizes the reliability and overall safety of the routing strategy.

4. Numerical Calculations and Results

We begin with how costs are encoded: the network is evaluated under two cost regimes (i) a baseline matrix that prices trips when every link operates safely, and (ii) a failed cost matrix that prices trips when an incident occurs on some links during transport. The latter reflects catastrophic consequences and is calibrated so that the implied social harm exceeds a predefined tolerability criterion.

On top of this cost structure, the logistics setting is a single-depot distribution problem with geographically dispersed customers of known demand. Service is provided by a homogenous fleet of fixed-capacity vehicles stationed at the depot, and all customer requirements must be met within those capacity limits. This coupling of dual cost regimes with the one-depot, fixed-capacity fleet formalizes routing decisions for extremely hazardous shipments under both normal operation and incident scenarios.

In the problem under consideration, the system consists of a single depot, 20 vehicles, and 20 customers. The demand of each customer is assumed to be known, and all vehicles are assigned equal capacities of 1,500 units. The failed costs associated with the links are set to values greater than or equal to a predetermined threshold of 1,400 units (refer to Appendix A and B for the Normal and Failure Cost Matrices, respectively). Using the developed model, the following equilibrium expected trip cost has been obtained. At this point it should be pointed out that the monetary units of the costs are not sensitive to the currency to be used. The distinctive feature of the normal and failure costs is that the failure costs are much higher than the normal costs regardless of the currency to illustrate the comparison of the two different situations for the analysis.

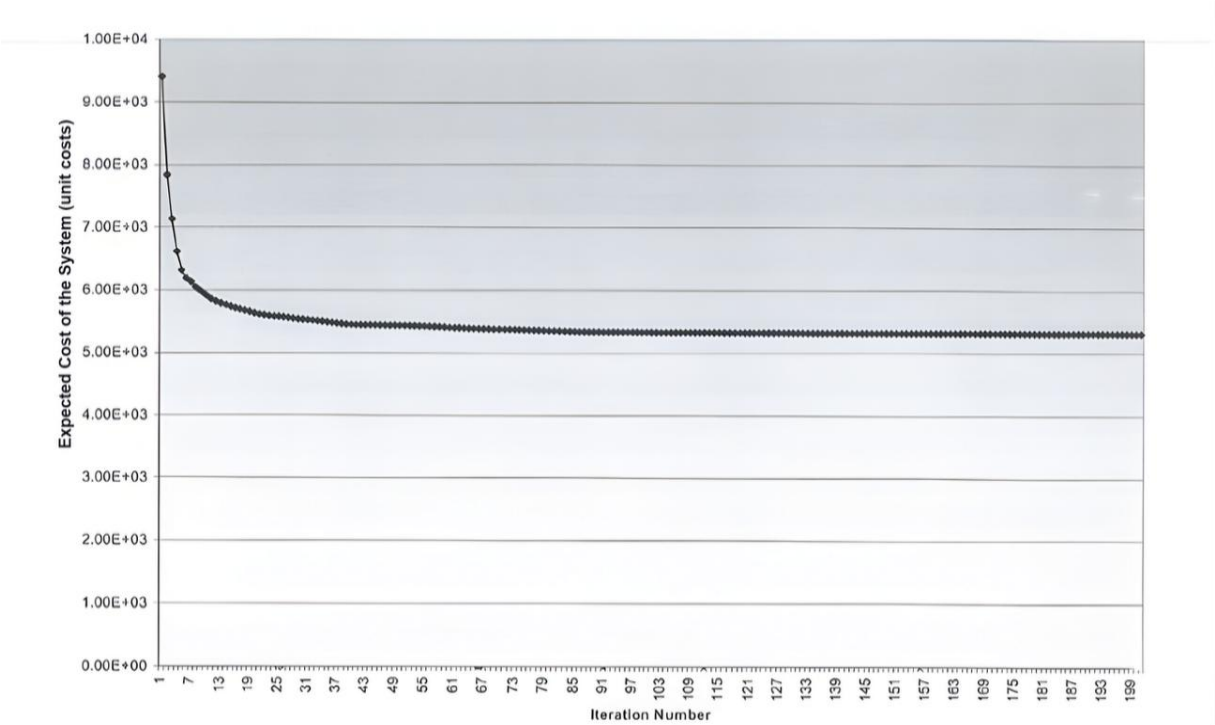


Figure 4. Convergence of trip cost: Tabu Search

Figure 4 illustrates that the equilibrium trip cost is 5318.104 units. This value signifies that, regardless of the specific link failure probabilities, the total expected trip cost will not surpass 5318.104 units when the equilibrium link usage probabilities are employed. Accordingly, the equilibrium value of the expected trip cost represents the outcome of the optimal routing strategy under the most adverse link failure conditions, assuming that an incident occurs. This strategy reflects a deliberately conservative, highly pessimistic approach that aligns with a risk-averse planner's perspective, prioritising safety and minimizing potential losses.

Figure 5. explains the convergence performance of the expected cost of the system for the same problem using Clark and Wright's savings algorithm. In this case, the equilibrium trip cost is 5393.185 units, which is higher than the one obtained using Tabu Search.

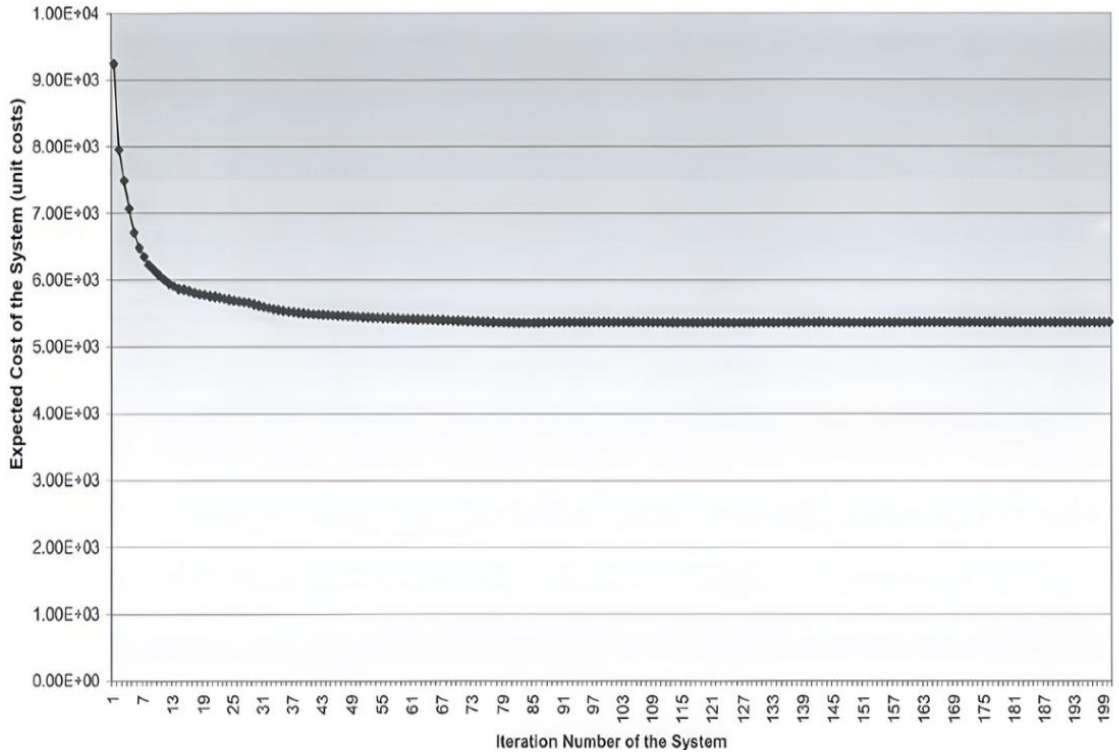


Figure 5. Convergence of expected trip cost: savings algorithm

The convergence behaviour of the link usage probabilities obtained by using Tabu Search for 20-customer problem is illustrated by Figure 6.

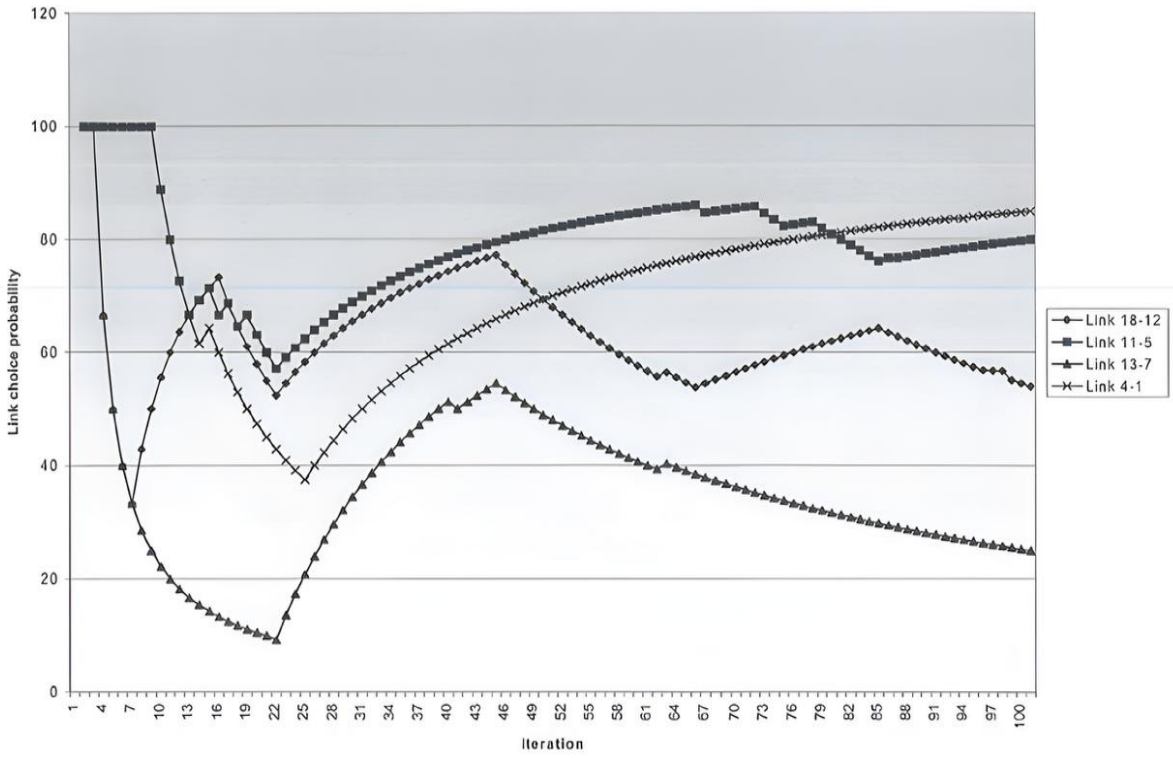


Figure 6. Convergence behaviour of the link usage probabilities: Tabu Search

To demonstrate the impact of vehicle capacities on the total expected trip cost, the same problem was resolved assuming that each vehicle has a capacity of 2.500 units instead of 1.500 units. The normal and failed cost matrices remain unchanged. Figure 7 below shows the convergence of the expected trip cost for this modified scenario.

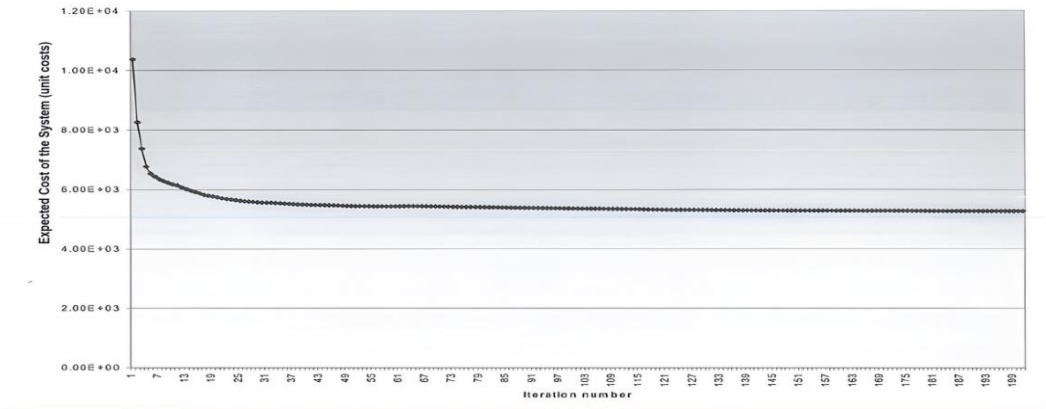


Figure 7. Convergence of expected trip cost: 20-customer, increased vehicle capacity problem

Figure 7 clearly states that increasing vehicle capacity leads to a lower expected trip cost at equilibrium for the same normal and failure costs used for lower capacity problem. In this way the effect of the capacity change only situation was analysed. Specifically, increasing vehicle capacity from 1.500 to 2.500 units reduces the system's expected trip cost from 5.393.185 to 5.275.21 units, while all other problem input values remain unchanged. This observation suggests that the optimal routing strategy may depend not only on the worst-case set of link failure probabilities but also on the number and capacities of vehicles stationed at the depot.

The developed model was tested on problems of varying sizes to evaluate both the computational effort required to determine the payoff and the improvements achieved by applying Tabu Search. The results of these tests, including computation times and solution enhancements, are summarized in Table 1.

Table 1. Test results in terms of required computational times

	Time required for each iteration when convergence is obtained (minute)		Total expected travel (routing) cost		Improvement in total expected cost (%)
	Savings Method	Tabu Search	Savings Method	Tabu Search	
10 Customers	10	7	2411.234	2400.866	0.43
11 Customers	10	7	2797.651	2785.062	0.45
12 Customers	10	6	3081.474	3066.067	0.50
13 Customers	10	6	3393.814	3374.809	0.56
14 Customers	11	5	3718.586	3695.159	0.63
15 Customers	11	5	4095.964	4067.292	0.70
16 Customers	11	4	4275.688	4241.910	0.79
17 Customers	12	4	4513.143	4472.524	0.9
18 Customers	12	3	4745.876	4696.993	1.03
19 Customers	12	3	4991.290	4932.393	1.18
20 Customers	13	2	5393.185	5318.104	1.39

The developed solution procedure is used to calculate the precise link usage probabilities in a 5-customer scenario, considering a total of 120 distinct routes. This analysis serves two purposes: to compare the results obtained using the iterative method of successive averages and to examine the potential existence of multiple optima. For this analysis, the following equation is introduced (see Appendix C and D for the normal and failure cost values, respectively.

$$
\begin{aligned}
&Min \quad M \\
&CR_{1_1} h_1 + CR_{2_1} h_2 + CR_{3_1} h_3 + \ldots\ldots\ldots\ldots\ldots\ldots + CR_{120_1} h_{120} \le M \\
&CR_{1_2} h_1 + CR_{2_2} h_2 + CR_{3_2} h_3 + \ldots\ldots\ldots\ldots\ldots\ldots + CR_{120_2} h_{120} \le M \\
&CR_{1_3} h_1 + CR_{2_3} h_2 + CR_{3_3} h_3 + \ldots\ldots\ldots\ldots\ldots\ldots + CR_{120_3} h_{120} \le M \\
&\ldots\ldots\ldots\ldots\ldots\ldots\ldots\ldots\ldots\ldots\ldots\ldots\ldots\ldots\ldots\ldots\ldots\ldots\ldots\ldots \\
&\ldots\ldots\ldots\ldots\ldots\ldots\ldots\ldots\ldots\ldots\ldots\ldots\ldots\ldots\ldots\ldots\ldots\ldots\ldots\ldots \\
&CR_{1_{15}} h_1 + CR_{2_{15}} h_2 + CR_{3_{15}} h_3 + \ldots\ldots\ldots\ldots\ldots\ldots + CR_{120_{15}} h_{120} \le M
\end{aligned}
\tag{23}
$$

where;

CR_{k_i} is the cost of link i on route k

h_k is the usage probability of route k

subject to

$$
\begin{aligned}
&h_1 + h_2 + h_3 + \ldots\ldots\ldots\ldots\ldots\ldots + h_{120} = 1 \\
&h_1, h_2, h_3, \ldots\ldots\ldots\ldots\ldots\ldots\ldots\ldots, h_{120} \ge 0
\end{aligned}
\tag{24}
$$

In order to address this problem, the E04MFF/E04MFA computer program was utilized, specifically designed for linear problems of the form:

$$
\min_{x \in F^N} imise \quad c^T x, \quad subject to \quad l \le \{ \begin{matrix} x \\ Ax \end{matrix} \} \le u \tag{25}
$$

where, "*c*" is "*n*" element vector and A is an m_L by "*n*" matrix."

A linear programming problem in its general form is called a type LP problem. The constraints that involve the matrix A are known as the main constraints. Each variable, as well as each general constraint, has specified lower and upper bounds. An equality restraint can be represented by setting its lower and upper bounds equal, i.e., *li =ui.* If a constraint or variable has no lower bound or no upper bound, the corresponding entry in the bound vectors *l* or *u* may be set to a special value that represents −∞ or +∞.

E04MFF/E04MFA operates in two phases. The first phase focuses on finding a feasible starting point by minimising the total constraint infeasibility. Once feasibility is achieved, the second phase minimises the linear objective function over the feasible region. Both phases use the same underlying computational routines; the only change is in the function being minimised from the sum of infeasibilities in phase one to the original objective function in phase two.

The resulting route choice probabilities obtained by solving Equation 23 are given by the following values.

Table 2. Linear programming results for route usage probabilities

0.00	0.00	0.00	0.00	0.00	0.00	0.00	0.00	0.00	0.00
0.00	0.00	0.00	0.00	0.00	0.00	0.00	0.55	0.00	0.00
0.00	0.00	0.00	0.00	0.00	0.00	0.00	0.00	0.00	0.00
0.00	0.00	0.00	0. 24	0.00	0.00	0.00	0.00	0.00	0.00
0.00	0.21	0.00	0.00	0.00	0.00	0.00	0.00	0.00	0.00
0.00	0.00	0.00	0.00	0.00	0.00	0.00	0.00	0.00	0.00
0.00	0.00	0.00	0.00	0.00	0.00	0.00	0.00	0.00	0.00
0.00	0.00	0.00	0.00	0.00	0.00	0.00	0.00	0.00	0.00
0.00	0.00	0.00	0.00	0.00	0.00	0.00	0.00	0.00	0.00
0.00	0.00	0.00	0.00	0.00	0.00	0.00	0.00	0.00	0.00
0.00	0.00	0.00	0.00	0.00	0.00	0.00	0.00	0.00	0.00
0.00	0.00	0.00	0.00	0.00	0.00	0.00	0.00	0.00	0.00

From the complete set of 120 feasible routing configurations (from left to right), the optimization process ultimately converged on a remarkably compact solution. Only three of those routes are actually required to maintain the minimum overall expected transportation cost, even under the most disruptive conditions imaginable. In other words, no matter which network link the hypothetical system spoiler disables in an attempt to maximize the dispatcher's losses, the system's optimal response relies solely on this trio of resilient routes. As summarized in Table 2, the selected routes (Route 18, Route 34, and Route 42) are employed for transporting hazardous materials from the central depot to the designated customer locations. The detailed sequences of network links corresponding to these routes are listed below:

Route 18: 0-1-4-5-3-2-0 $h_{18} = 0.55$
Route 34: 0-2-3-4-5-1-0 $h_{34} = 0.24$
Route 42: 0-2-4-5-3-1-0 $h_{42} = 0.21$

The Table 3 below compares the link usage probabilities derived from the method of successive averages with those obtained through the linear programming model.

Table 3. Comparison of link usage probabilities

	Linear Programming	Method of Successive Averages
Link 0..1	1	0.97
Link 0..2	1	1
Link 0..5	0	0.03
Link 1..3	0.21	0.24
Link 1..4	0.55	0.54
Link 1..5	0.24	0.25
Link 2..3	0.79	0.78
Link 2..4	0.21	0.21
Link 2..5	0	0.009
Link 3..4	0.24	0.28
Link 3..5	0.76	0.70
Link 4..5	1	0.99

The analysis revealed that the gradual convergence of link-usage probabilities stems largely from the presence of several comparable near-optimal solutions rather than from any weakness in the numerical scheme itself.

Even so, the method of successive averages produced results that were virtually indistinguishable from the optimum, after roughly one hundred iterations, the total expected routing cost stabilized at 88.70 units, compared with 88.71 units obtained through the linear-programming formulation. This close agreement affirms the reliability and accuracy of method of successive averages. Nevertheless, adopting alternative optimization techniques with inherently faster convergence characteristics could further reduce computation time while yielding equally precise estimates of both link-usage probabilities and total expected routing costs.

5. Discussions and Recommendations

The main objective of this research was to formulate a model capable of assessing the reliability of transporting highly hazardous materials from a central depot to multiple geographically dispersed customers, using a fleet of vehicles with fixed capacity constraints. A key aspect addressed in this research is the uncertainty of incident probabilities on any given link during shipment, a challenge commonly encountered in real-world scenarios. Such situations arise when a route planner seeks optimal routing strategies for low-probability, high-consequence hazardous material shipments. In the proposed approach, initial routes are generated using the Savings Algorithm and subsequently refined through Tabu Search to improve solution quality. In this sense, the main contribution of this study is that it provides the best possible routing strategies for repeated low-probability high-consequence hazmat shipments determined by a route planner. The risk averse nature of the route planner was represented by game theoretic approach bu assuming that the route planner is extremely pessimistic about the link failure probabilities and tries to select his strategies by reacting against a virtual evil-entity's link failure strategies. The failed link by the evil-entity is the one which results in least favourable to route planner. The following sections summarize the main conclusions of the study and provide recommendations for future research.

- The findings indicate that the convergence of equilibrium point in terms of total routing cost is quick. However, the model converges more slowly as far as link usage and failure probabilities are concerned. This indicates that expected trip cost at the equilibrium can be achieved through multiple combinations of link usage and failure probabilities. In other words, the slower convergence highlights the non-uniqueness of the link usage and failure probability values.
- The convergence of the model could be significantly faster if the routes selected at each iteration are closer to the optimal solution. Since the model relies on heuristic routing strategies, employing a more effective heuristic algorithm would accelerate the convergence of the solution process.
- Although the method of successive averages is a simple and effective iterative procedure for guiding the solution toward the equilibrium point, it can lead to slow convergence of link usage and failure probabilities. Alternative iterative schemes might achieve faster convergence. Nevertheless, method of successive averages provides the advantage of allowing the route planner and the virtual evil entity to update their strategies based on the accumulated strategies of the other player.
- The failure probabilities indicate which links in the system are more vulnerable. These links help guide the route planner to design routes that avoid high-risk links whenever possible. It should be noted that while the equilibrium failure probabilities are generally not unique, the subset of links with zero failure probability is unique. This means the method effectively identifies a critical subset of links with failure probabilities greater than zero that warrant special attention.
- The expected trip cost provides a valuable measure of the reliability of hazardous materials shipments from a safety perspective. This is because the equilibrium expected trip cost reflects the expectations of a highly risk-averse (extremely pessimistic) route planner.
- The failure probabilities at equilibrium produced by the model do not correspond to the actual likelihood of link failures. Instead, they represent probabilities under the worst-case scenario, and the true link failure probabilities may differ from those generated by the model.
- The developed model offers a valuable tool for identifying the optimal routing strategies for the shipment of extremely hazardous materials when the actual link failure probabilities are unknown. By applying game theory, the model provides important insights into the problem and yields the optimal link usage and failure probabilities under a worst-case scenario framework.

5.1. Future work

The proposed model can be improved by allowing the evil entity to fail more than one link. The model presents the simple scenario in which only one link can be failed by the virtual evil-entity. However, batch failures may be included in the game as supplementary scenarios from which the system spoiler can choose. In addition to this, in real world cases there might be some link topologies in which some part of the same link can be shared by two or more customers. In these cases, the failure on those links will not only affect one element of the cost matrix, but also the other elements, too. This point may be paid attention to and included in further studies to increase the realism. Moreover, the model can be further enhanced by assuming that the demands of the customers are stochastic in nature. In real world problems, the amount of product required by the customers may not be known beforehand, unlike the assumption made in this study. Inclusion of the impact level of vehicle speed to the magnitude of the incident may be worth to investigate. For example, a link between any two customers through a rural area on which higher speeds are possible may be attractive if the population density is relatively low. However, another link passing through a densely populated area on which a lower speed limit applies may be even more attractive because the lower speed on this link means that the impact of an incident, should it occur, may be relatively limited.

6. Author Contribution Statement

In the realized study, Author 1 undertook the idea, design, literature review, methodology and writing of the article, Author 2 undertook supervision and investigation of the article.

7. Ethics Committee Approval and Conflict of Interest

“Ethics committee permission is not required for the prepared article”
“There is no conflict of interest with any person/institution in the prepared article.”

8. Ethical Statement Regarding the Use of Artificial Intelligence

No artificial intelligence-based tools or applications were used in the preparation of this study. The entire content of the study was produced by the author in accordance with scientific research methods and academic ethical principles.

9. References

[1] E. Erkut and V. Verter, "A framework for hazardous materials transport risk assessment," *Risk Anal.*, vol. 15, no. 5, pp. 589–609, 1995.
[2] R. A. Sivakumar, R. Batta, and M. H. Karwan, "A multiple route conditional risk model for transporting hazardous materials," *INFOR*, vol. 33, no. 1, pp. 20–33, 1995.
[3] H. D. Sherali, L. D. Brizendine, T. S. Glickman, and S. Subramanian, "Low probability–high consequence considerations in routing hazardous material shipment," *Transp. Sci.*, vol. 31, no. 3, pp. 237–251, 1997.
[4] E. Erkut and A. Ingolfsson, "Catastrophe avoidance models for hazardous materials route planning," *Transp. Sci.*, vol. 34, no. 2, pp. 165–179, 2000.
[5] J. K. Lenstra and A. H. G. Kan, "Complexity of vehicle routing and scheduling problems," *Networks*, vol. 11, pp. 221–227, 1981.
[6] G. Laporte, "Exact algorithms for travelling salesman problem and the vehicle routing problems," *Les Cah. GERAD*, Tech. Rep. G-98-37, 1998.
[7] G. Laporte, M. Gendreau, J. Y. Potvin, and F. Semet, "Classical and modern heuristics for vehicle routing problem," *Les Cah. GERAD*, Tech. Rep. G-99-21, 1999.
[8] G. Clarke and J. Wright, "Scheduling of vehicles from a central depot to a number of delivery points," *Oper. Res.*, vol. 12, pp. 568–581, 1964.
[9] B. E. Gillet and L. R. Miller, "A heuristic algorithm for the vehicle dispatch problem," *Oper. Res.*, vol. 22, pp. 340–349, 1974.
[10] M. L. Fisher and R. Jaikumar, "A generalized assignment heuristic for vehicle routing," *Networks*, vol. 11, pp. 109–124, 1981.
[11] I. H. Osman, "Metastrategy simulated annealing and tabu search algorithms for the vehicle routing problem," *Ann. Oper. Res.*, vol. 41, pp. 421–451, 1993.
[12] G. Barbarosoglu and D. Ozgur, "A tabu search algorithm for the vehicle routing problem," *Comput. Oper. Res.*, vol. 26, pp. 255–270, 1999.
[13] P. Toth and D. Vigo, "Granular tabu search and its applications to the vehicle routing problem," Working Paper, DEIS, Univ. Bologna, 1998.
[14] J. L. Blanton and R. L. Wainwright, "Multiple vehicle routing problem with time and capacity constraints using genetic algorithm," in *Proc. 5th Int. Conf. Genet. Algorithms*, San Mateo, CA, USA: Morgan Kaufmann, 1993, pp. 452–459.
[15] A. Kheiri, A. J. Dragomir, D. Mueller, J. J. Gromicho, C. C. Jagtenberg, and J. J. van Hoorn, "Tackling a VRP challenge to redistribute scarce equipment within the time windows using metaheuristic algorithms," *EURO J. Transp. Logist.*, vol. 8, pp. 561–595, 2019.
[16] S. B. Vieira, M. G. Ribeiro, and L. Bahiense, "Metaheuristics with variable diversity control and neighbourhood search for the heterogeneous site-dependent multi-depot multi-trip periodic vehicle routing problem," *Comput. Oper. Res.*, vol. 153, Art. no. 106189, 2023.
[17] M. Tadaros, A. Migdalas, N. Hassan Quttineh, and T. Larsson, "Evaluating metaheuristic solution quality for a hierarchical vehicle routing problem by strong lower bounding," *Oper. Res. Perspect.*, vol. 14, Art. no. 100332, 2025.
[18] R. Elshaer and H. Awad, "A taxonomic review of metaheuristic algorithms for solving the vehicle routing problem and its variants," *Comput. Ind. Eng.*, vol. 140, Art. no. 106242, Feb. 2020.
[19] S. Kirkpatrick, C. D. Gelatt, and P. M. Vecchi, "Optimization by simulated annealing," *Science*, vol. 220, pp. 671–680, 1983.
[20] A. Colorni, M. Dorigo, and V. Maniezzo, "Distributed optimization by ant colonies," in *Proc. Eur. Conf. Artif. Life*, F. Varela and P. Bourgine, Eds. Amsterdam, The Netherlands: Elsevier, 1991.
[21] F. Glover, "Future paths for integer programming and links to artificial intelligence," *Comput. Oper. Res.*, vol. 13, no. 5, pp. 533–549, 1986.
[22] M. Kumari, P. K. De, K. Chaudhuri, and P. Narang, "Utilizing a hybrid metaheuristic algorithm to solve capacitated vehicle routing problem," *Results Control Optim.*, vol. 13, Art. no. 100292, Dec. 2023.
[23] K. Niyomphon and W. Nakkiew, "Application of metaheuristics for multi-trip capacitated vehicle routing problem with time window," *Prod. Eng. Arch.*, vol. 30, no. 3, Sep. 2024.

[24] M. K. Zuhanda, Hartono, S. A. R. S. Hasibuan, and Y. Y. Napitupulu, "An exact and metaheuristic optimization framework for solving vehicle routing problems with shipment consolidation using population-based and swarm intelligence," *Decis. Anal. J.*, vol. 13, Art. no. 100517, Dec. 2024.
[25] M. J. C. S. Reis, "An adaptive hybrid metaheuristic for solving the vehicle routing problem with time windows under uncertainty," *Comput. Mater. Continua*, vol. 85, no. 2, pp. 3023–3039, Sep. 2025.
[26] J. A. G. Willard, "Vehicle routing using r-optimal tabu search," M.S. thesis, The Management School, Imperial College, London, U.K., 1989.
[27] V. M. Pureza and P. M. Franca, "Vehicle routing problem via tabu search metaheuristic," Tech. Rep. CRT-347, Centre for Research on Transportation, Montreal, Canada, 1991.
[28] M. Gendreau, G. Laporte, and J. Y. Potvin, "Metaheuristics for vehicle routing problem," *Les Cah. GERAD*, Tech. Rep. G-98-52, 1999.
[29] J. F. Nash, "Non-cooperative games," *Ann. Math.*, vol. 54, pp. 286–295, 1951.
[30] O. J. Chen, M. Ben-Akiva, and E. Moshe, "Game theoretic formulations of interaction between dynamic traffic control and dynamic traffic assignment," *Transp. Res. Rec.*, no. 1617, pp. 179–188, 1998.
[31] M. G. H. Bell, "A game theoretic approach to measuring the performance reliability of transport networks," *Transp. Res., Part B*, vol. 34, pp. 533–546, 2000.
[32] M. G. H. Bell and C. Cassir, "Risk-averse user equilibrium traffic assignment: An application of game theory," *Transp. Res., Part B*, vol. 36, no. 8, pp. 671–681, 2002.
[33] Y. Caseau and F. Laburthe, "Heuristics for large constraint vehicle routing problems," *J. Heuristics*, vol. 5, pp. 281–303, 1999.
[34] M. G. H. Bell and Y. Iida, *Transportation Network Analysis*. Chichester, U.K.: John Wiley & Sons, 1997.

Appendix A. Normal cost matrix data for 20-customer 1-vehicle VRP

DATA FOR 20-CUSTOMER 20-VEHICLE PROBLEM

Normal Cost Matrix

	1	2	3	4	5	6	7	8	9	10	11	12	13	14	15	16	17	18	19
1	110																		
2	80	170																	
3	100	150	110																
4	130	100	170	150															
5	150	220	200	170	160														
6	80	170	120	120	140	170													
7	90	130	110	110	140	200	110												
8	110	120	100	160	180	210	140	170											
9	170	240	200	220	250	250	200	200	150										
10	190	250	220	250	270	240	150	250	150	220									
11	250	220	300	200	300	230	200	300	200	270	350								
12	220	200	250	180	250	280	250	190	170	300	480	400							
13	240	300	270	170	300	350	200	200	220	350	370	400	300						
14	280	300	300	200	350	320	230	220	190	330	400	400	450	410					
15	160	200	200	80	100	200	200	200	190	250	300	300	310	370	330				
16	150	250	200	200	250	250	140	200	170	270	300	320	300	280	370	270			
17	140	230	200	200	200	250	180	180	190	280	250	310	330	270	360	260	200		
18	190	250	210	220	240	300	240	250	200	260	250	300	200	300	320	250	200	220	
19	200	260	240	250	220	310	270	260	240	300	300	320	240	320	330	270	240	260	240
20	210	230	250	280	260	320	220	270	330	320	360	260	280	360	300	280	280	270	380

Customer Demands: (units)

Customer1: 400 Customer2: 100 Customer3: 200 Customer4: 200 Customer5: 300 Customer6: 100 Customer7: 200 Customer8: 300 Customer9: 200 Customer10: 3

Customer11: 100 Customer12: 200 Customer13: 200 Customer14: 300 Customer15: 300 Customer16: 100 Customer17: 200 Customer18: 100 Customer19: 200 Customer20: 2

Vehicle capacities: 1500 units

Appendix B. Failed cost matrix data for 20-customer 1-vehicle problem

DATA FOR 20-CUSTOMER 20-VEHICLE PROBLEM

Failed Cost Matrix

	1	2	3	4	5	6	7	8	9	10	11	12	13	14	15	16	17	18	19
1	2000																		
2	1400	2400																	
3	1900	3300	2500																
4	1900	3000	2200	2500															
5	2400	3500	2700	3000	2700														
6	1400	3000	2100	2700	2000	3000													
7	1800	2800	3000	3100	2500	3500	2500												
8	1700	2500	2500	2000	2400	3000	2000	2400											
9	2500	4000	3000	3200	3700	4100	3200	3200	3200										
10	3000	4500	3500	4200	4200	4200	3300	3700	3500	4300									
11	4000	5000	4200	4500	4700	4300	4300	4500	4400	5100	6000								
12	3000	4500	4000	3700	3800	4400	3800	4000	3600	4500	4600	6200							
13	3500	4000	4200	4200	4300	4500	4500	4000	4200	4700	5200	6000	5500						
14	3700	5000	5000	4300	4200	4600	4600	4200	4300	4400	5500	6600	5200	5000					
15	3000	4000	3800	3800	3800	4700	3800	4300	4100	3700	5600	6200	4900	4500	5000				
16	2500	3500	3000	3700	3000	4000	3300	4000	3700	3600	4900	5800	4700	4500	5300	5000			
17	2600	4000	3100	4200	3700	3900	3200	3800	3400	3800	4800	5500	5000	4800	4800	4900	4000		
18	3000	4500	4000	4500	3800	4500	4000	4000	3500	4500	5000	5500	4700	4800	5000	4800	4500	4000	
19	3200	3900	3700	4400	4200	4400	4100	4200	4100	4600	6000	5700	5000	5000	4800	4600	5000	4500	5500
20	2700	3800	3500	4000	4000	4500	3700	3600	3600	4200	4500	5000	4900	5200	5300	5000	4500	4000	4500

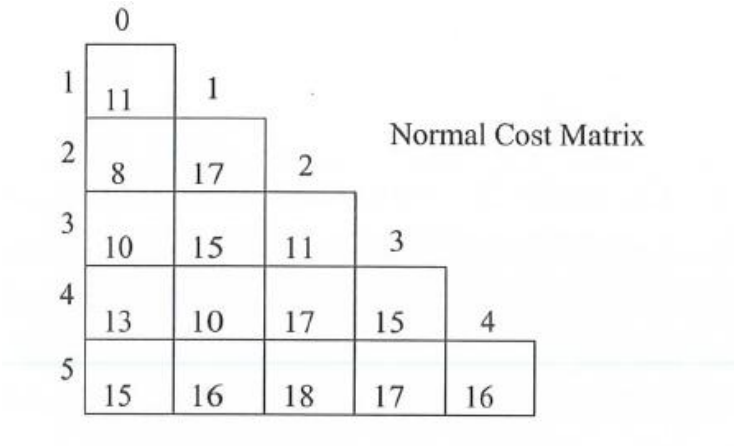
Customer Demands: (units)

Customer1: 400 Customer2: 100 Customer3: 200 Customer4: 200 Customer5: 300 Customer6: 100 Customer7: 200 Customer8: 300 Customer9: 200 Customer10: 300

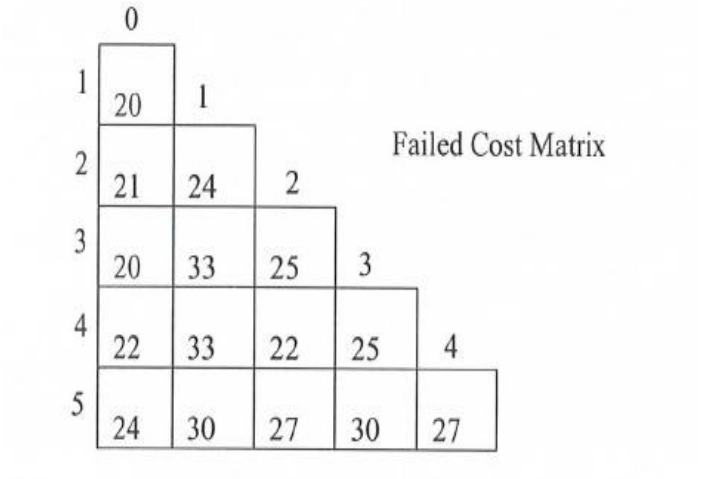
Customer11: 100 Customer12: 200 Customer13: 200 Customer14: 300 Customer15: 300 Customer16: 100 Customer17: 200 Customer18: 100 Customer19: 200 Customer20: 200

Vehicle capacities : 1500 units

Appendix C. Normal cost matrix data for 5-customer 1-vehicle problem (linear programming and method of successive averages)



Appendix D. Failed cost matrix data for 5-customer 1-vehicle problem (Linear programming and method of successive averages)



Fırat Üniversitesi Deneysel ve Hesaplamalı Mühendislik Dergisi

FUJECE

Kötü Amaçlı Yazılım Tespiti İçin Temel Bileşen Analizi ve Anova Özellik Seçiminin Karşılaştırmalı Analizi

Taha ETEM[1]*

[1]Bilgisayar Mühendisliği, Mühendislik Fakültesi,Çankırı Karatekin Üniveristesi, Çankırı, Türkiye.
[1]tahaetem@karatekin.edu.tr

Geliş Tarihi: 07.2.2025
Kabul Tarihi: 06.1.2026

Düzeltme Tarihi: 09.11.2025

doi: https://doi.org/10.62520/fujece.1635121
Araştırma Makalesi

Alıntı: T. Ethem, "Kötü amaçlı yazılım tespiti için temel bileşen analizi ve anova özellik seçiminin karşılaştırmalı analizi" Fırat Üni. Deny. ve Hes. Müh. Derg., vol. 5, no 1, pp. 299-315, Şubat 2026.

Öz

Bu çalışma, Android kötü amaçlı yazılım tespiti için Temel Bileşen Analizi (PCA) ve ANOVA tabanlı özellik seçimi yöntemlerinin karşılaştırmalı bir analizini sunarak, bunların sınıflandırma doğruluğu ve hesaplama verimliliği üzerindeki etkilerini değerlendirmektedir. Üç ön işleme senaryosu incelenmiştir: 241 özelliğe sahip orijinal veri setini kullanma, özellik çıkarma için PCA uygulama (varyans eşikleri nedeniyle tüm bileşenleri tutma) ve özellik setini 120'ye düşürmek için ANOVA kullanma. Destek Vektör Makineleri (SVM), Geniş Sinir Ağları ve Lojistik Regresyon sınıflandırıcıları, 5 katlı çapraz doğrulama yoluyla optimize edilen hiper parametrelerle bu veri setleri üzerinde eğitilmiştir. Sonuçlar, SVM'nin tüm senaryolarda tutarlı bir şekilde en yüksek doğruluğu elde ettiğini ve PCA ile %99,25'a ulaştığını göstermiştir. Ancak, PCA model boyutunu azaltmada başarısız olmuş ve orijinal veri setine kıyasla SVM için eğitim sürelerini artırmıştır. Bunun aksine, ANOVA özellik sayısını etkili bir şekilde azaltarak SVM eğitim süresini 4,81 saniyeye düşürürken %98,95 doğruluk oranı elde etmiştir. Bu bulgular, ANOVA'nın yüksek tespit performansını azaltılmış kaynak talepleriyle dengeleyen hesaplama açısından verimli bir yöntem olduğunu vurgulamaktadır. PCA doğruluğu marjinal olarak iyileştirirken, hesaplama maliyeti onu gerçek zamanlı uygulamalar için daha az pratik hale getirmektedir. Çalışma, ANOVA aracılığıyla özellik seçiminin Android kötü amaçlı yazılım tespiti için hem doğruluğu hem de verimliliği önceliklendirerek üstün bir takas sağladığı sonucuna varmıştır. Gelecekteki çalışmalar, genelleştirilebilirliği artırmak ve gelişen kötü amaçlı yazılım tehditlerini ele almak için gelişmiş özellik seçimi tekniklerini keşfetmeli ve modelleri çeşitli veri kümelerinde doğrulamalıdır.

Anahtar kelimeler: Kötü amaçlı yazılım tespiti, Özellik seçimi, Destek vektör makineleri, Android güvenliği

*Yazışılan yazar

İntihal Kontrol: Evet – Turnitin
Şikayet: fujece@firat.edu.tr
Telif Hakkı ve Lisans: Dergide yayın yapan yazarlar, CC BY-NC 4.0 kapsamında lisanslanan çalışmalarının telif hakkını saklı tutar.

Firat Univ Jour. of Exp. and Comp. Eng., 5(1), 299-315, 2026

Firat University Journal of Experimental and Computational Engineering

Comparative Analysis of Principle Component Analysis and Anova Feature Selection in Malware Detection

Taha ETEM[1]*

[1]Computer Engineering, Engineering Faculty,Çankırı Karatekin University, Çankırı, Türkiye.
[1]tahaetem@karatekin.edu..tr

Received: 07.2.2025
Accepted: 06.01.2026
Revision: 09.11.2025
doi: https://doi.org/10.62520/fujece.1635121
Research Article

Citation: T. Etem, "Comparative analysis of principle component analysis and anova feature selection in malware detection", Firat Univ. Jour.of Exper. and Comp. Eng., vol. 1, no 2, pp. 299-315, February 2026.

Abstract

This study presents a comparative analysis of Principal Component Analysis (PCA) and ANOVA-based feature selection methods for Android malware detection, evaluating their impact on classification accuracy and computational efficiency. Three preprocessing scenarios were examined: using the original dataset with 241 features, applying PCA for feature extraction (retaining all components due to variance thresholds), and employing ANOVA to reduce the feature set to 120. Support Vector Machines (SVM), Wide Neural Networks, and Logistic Regression classifiers were trained on these datasets, with hyperparameters optimized via 5-fold cross-validation. Results demonstrated that SVM consistently achieved the highest accuracy across all scenarios, peaking at 99.25% with PCA. However, PCA failed to reduce dimensionality of models and increased training times for SVM compared to the original dataset. In contrast, ANOVA effectively reduced the feature count, lowering SVM training time to 4.81 seconds while obtaining 98.95% accuracy. These findings highlight ANOVA as a computationally efficient method, balancing high detection performance with reduced resource demands. While PCA marginally improved accuracy, its computational cost renders it less practical for real-time applications. The study concludes that feature selection via ANOVA offers a superior trade-off for Android malware detection, prioritizing both accuracy and efficiency. Future work should explore advanced feature selection techniques and validate models on diverse datasets to enhance generalizability and address evolving malware threats.

Keywords: Malware detection, Feature selection, Support vector machines, Android security

*Corresponding author

Plagiarism Checks: Yes – Turnitin
Complaints: fujece@firat.edu.tr
Copyright & License: Authors publishing with the journal retain the copyright to their work licensed under the CC BY-NC 4.0

1. Introduction

Malicious software is a heterogeneous collection of harmful code that is meant to disrupt or harm any computing systems and networks, as well as gain illegal access. Its development has turned out to be a topical issue in the field of cybersecurity. Malware has become widespread and it has been required to use more advanced detection techniques and methods of analysis. Malware taxonomy mostly focuses on its effect, purpose of operation and the methods used to create or deliver the malwares. There can be unique malware versions that can execute their devilish tasks without the permission of the user. Complexity of malware has increased due to the emergence of anti-detection systems that enable adaptation and avoidance of signature-based detection systems. In line with this, it has become necessary to have the correct identification of malware variants that can be added to traditional detection processes. Advanced advancements in machine-learning algorithms have shifted malware variants detection to program similarity. The strengths of this paradigm shift are in its capacity to better detect malicious software by exploiting structural affinities to known threats. The methods of malware detection are traditionally divided into two broad categories, signature-based and behaviour-based approaches. Signature-based detection uses existing patterns or signature of malicious artefacts to mark threats whereas behaviour-based detection watches the activity of software to determine the potentially harmful behaviour. [1, 2]. Also, cryptographic techniques play a crucial role in safeguarding sensitive data, ensuring secure communication, and protecting against unauthorized access or tampering in Android applications and systems [3-6].

Recent studies have emphasized the usefulness of feature selection based on system-call data on Android malware detection systems. Comparative studies were conducted on various techniques of feature-selection methods to determine their ability to reduce the size of system -call sets whilst maintaining or improving classification accuracy. The results indicate that a reduced set of the best selected features can reach desirable classification rates thus confirming the efficiency of the offered methodology in detecting malware.

The work of Aero is focused on the recognition and categorization of malware by using several machine-learning algorithms. The assessment involved Support Vector Machines (SVM), Decision Trees, and ensemble techniques of categorizing malware according to behavioural signature. Empirical findings show that ensemble methods had the best detection accuracy with a result of about 94%. The system is highly robust in the process of differentiating between benign and malicious software. In addition, the research demonstrates the urgent necessity of the unceasing refresh of the training information to be flexible to naturally evolving malware threats. [7].

Adewale introduces a deep learning framework for malware detection, integrating multiple layers of anomaly detection in cloud environments. The study employed a hybrid model combining Convolutional Neural Networks (CNN) and Recurrent Neural Networks (RNN) to detect anomalies in network traffic data. The system demonstrated a high accuracy of approximately 92%. The model's performance validates the effectiveness of deep learning-based cybersecurity solutions for identifying malware in complex cloud infrastructures [8].

Cuiying et al. examine how machine-learning methods affect the detection of Android malware, with specific focus on the effect of the obfuscation methods on the detection accuracy. The authors contrast the ability of Convolutional Neural Networks (CNNs) and Long Short-Term Memory (LSTM) networks to detect instances of obfuscated malware in a dataset that had been annotated by antivirus engines. The results of their research show that obfuscation decreases the detection performance by about 15^{-}, and CNN models have an accuracy of around 88 percent in situations when no obfuscation is used. These findings highlight the need to have advanced countermeasures to counter the obfuscation techniques in malware detection [9].

Rajest and Regin analyse the use of the Catboost classifier as one of the graduate-boosting algorithms to detect Android ransomware. The paper examines a sample of Android applications where behavioural characteristics are derived. The choice of Catboost is explained by the fact that it is more accurate and capable of addressing the categorical data. The resulting model achieves a high accuracy rate of 96 % which is higher than classic classifiers like the Random Forests and the Decision Trees. These results indicate the effectiveness of Catboost as a mobile malware detector [10].

Totham et al. propose a machine learning-based approach for detecting ransomware through adaptive encryption pattern recognition. Their system monitors file encryption patterns that signal potential ransomware attacks. A Recurrent Neural Network (RNN) model was implemented to learn patterns associated with malicious encryption activities in real time. The model demonstrated an accuracy of approximately 93% in ransomware detection, effectively identifying threats at an early stage. This study highlights the effectiveness of dynamic, behaviour-based machine learning models in enhancing ransomware detection capabilities [11].

Haq and Khuthaylah introduce a feature extraction technique combined with a soft voting ensemble to enhance malware detection on Android platforms. The study underscores the significance of carefully selecting relevant features from a vast set of extracted data. The proposed soft voting mechanism integrates predictions from multiple models, achieving a high detection accuracy of around 95%. This improvement in precision plays a crucial role in differentiating malware from legitimate applications. The findings emphasize the importance of refined feature selection in enhancing detection accuracy [12].

Kunku et al. present a novel ransomware detection method that leverages dynamic feature selection based on ransomware behaviour. The study applied various feature extraction techniques to accurately identify ransomware signatures and evaluated the approach using classifiers like Random Forest and k-Nearest Neighbors. The proposed method achieved an accuracy of 93%, demonstrating the effectiveness of feature selection in distinguishing ransomware from other types of malwares. The study's approach introduces a flexible framework for dynamic malware detection through behavioural analysis [13].

Mubarak and Alasmari suggested a malware detection framework implemented on Linux and based on memory analysis and deep learning to extract their features. The pipeline used in the study included a data preprocessing phase, key artifact extraction phase, and model selection phase. The model was able to achieve an accuracy of 90∶∶ per cent in its ability to detect malicious activities by including extracted system artifacts, process memory, and file access patterns, and such results indicate that OS-level artifact analysis along with advanced feature extraction are an effective strategy to classify malware [14].

Gihavo et al. proposed utilizing machine learning to identify file traps at an early stage using file trap selection and machine learning. The analysis derived characteristics of file manipulation and used them with the classification algorithms to detect early signs of ransomware. The method yielded a precision of about 91, thereby highlighting its worth in identifying ransomware attacks before they cause great harm. Focus on extracting features in the initial stages makes this model an active-based ransomware detection system [15]. Dolesi et al. investigate the use of sequences of operation codes generated during program execution for ransomware detection. By extracting opcode features and employing a k-Nearest Neighbour classifier makes the model effectively identified ransomware activities. The model achieves an accuracy of 92.8%. Feature selection was critical in this study, as it reduced the required feature set to 400, improving computational efficiency without compromising detection performance. This research illustrates the efficiency of opcode-based features and feature selection for high-performance malware classification on Windows systems [16]. In this study, detection of malware on Android Malware Dataset by machine learning methods is performed. Original dataset (241 features), selected features by ANOVA (120 features) and extracted features by PCA (241 features) are examined in terms of accuracy and efficiency. After evaluations, extracted features by PCA reached the highest accuracy in all of the scenarios. However, when computational effectiveness is considered, it can be said that the method applied with ANOVA feature selection reduces training times while giving minimal loss in terms of accuracy. The paper is organized as follows: Section 2 provides an overview of the related work in the field of Android malware detection, focusing on the application of machine learning techniques and feature selection methods. Section 3 details the materials and methods used in the study, including the dataset, preprocessing scenarios, and the machine learning algorithms employed for classification. In Section 4, the results of the experiments are presented, followed by a discussion of the findings, including a comparison of the performance of the different feature selection methods. Finally, Section 5 concludes the paper, summarizing the key findings and outlining potential directions for future research in Android malware detection.

This study offers a novel comparison between Principal Component Analysis (PCA) and ANOVA-based feature selection methods for Android malware detection, focusing on both classification accuracy and computational efficiency. While PCA is often favoured for dimensionality reduction, this study highlights its limitations, particularly its failure to reduce model complexity effectively and the significant increase in training time. In contrast, ANOVA demonstrates a more efficient feature selection approach, reducing the feature set by 50% while maintaining high classification accuracy, thus offering a better balance between performance and computational cost. This comparative analysis fills a gap in the literature by providing a detailed evaluation of how these two techniques impact real-time malware detection, offering valuable insights for optimizing malware detection systems in resource-constrained environments.

2. Tezpur University Android Malware Dataset

The high rate of development of information technology-based services led to a significant increase in the damage that malware attacks can cause. In spite of the fact that many malware detection methodologies have been suggested, the lack of sufficiently comprehensive datasets often impedes progress in this field. To this, Tezpur University Malware Windows Dataset (TUMALWD) and Tezpur University Android Malware Dataset (TUANDROMD) are proposed in order to promote validation of the malware detection methods in both Windows and Android systems respectively [17].

The framework of TUANDROMD dataset creation is divided into three phases namely: (1) data collection and storage, (2) data analysis, and (3) feature engineering. This will involve the downloading of malware and benign applications, running of manual checks, and deriving the salient features. Due to the complexity of the Android malware, manual inspection had been performed using the tools like Androguard, ApkInspector, ApkAnalyser and Smali-CFGs. In this research, the TUANDROMD dataset in a pre-processed version is used, with a total amount of 4,465 instances. The skewed class distribution is also evident in the dataset, with 3,566 samples of malware and 899 samples of benign (or goodware) that are also reflective of distributions in the real world. There were 241 characteristics obtained to be classified. These features are highly essential to be detected, and we can classify them as follows:

- 214 permission-based features
- 27 API-based features

The target attribute for classification is a binary category, labelling each instance as either 'malware' or 'goodware'. The creation of TUANDROMD addresses a critical need for up-to-date and relevant malware datasets for Android platforms. By offering comprehensive permission-based and API-based features, this dataset serves as a valuable resource for researchers and cybersecurity professionals. It enables the development of advanced malware detection systems that can adapt to the ever-changing landscape of cyber threats.

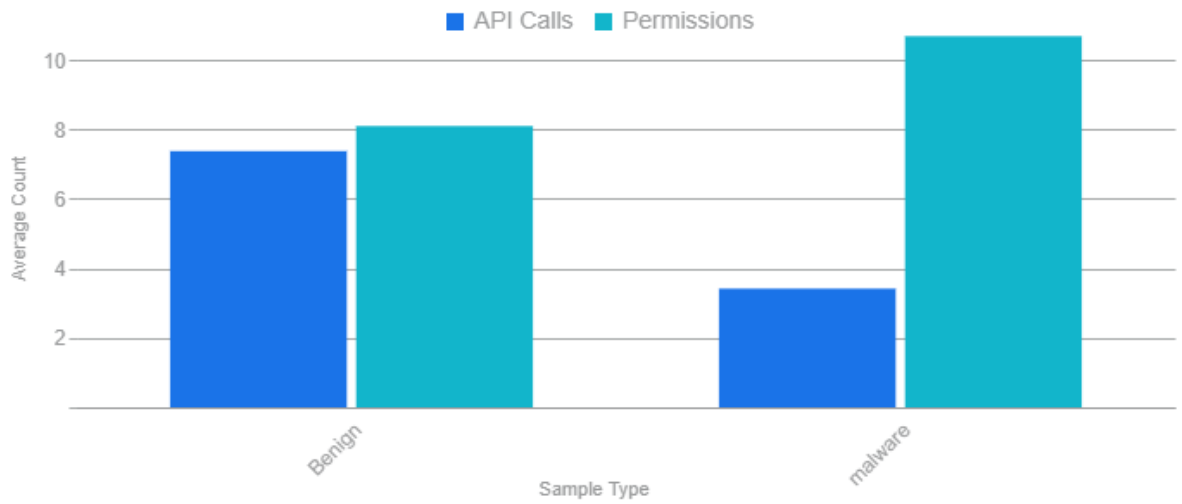


Figure 1. Avarage feature usage per sample

Figure 1 provides a simple but effective summary for dataset. Malware samples request more permissions on average (10.7) than benign samples (8.1). The trend is reversed for API calls. Benign samples use more of the monitored API calls on average (7.4) than malware samples (3.4). This suggests that malware is more "permission-hungry" while benign apps may have more complex functionality that uses these specific API calls.

The dataset records the modern trends of Android malware, which means that it is relevant to the current detection systems. The creation of the TUANDROMD serves a great demand of modern and relevant malware data in Android systems. These datasets are a treasure trove to researchers and cybersecurity experts by offering exhaustive host-based and network-based features on Windows malware and permission-based and API-based features on Android malware. They enable programmers to develop advanced malware detection solutions that can be modified upon the constantly changing cyber-threat situation.

3. Material and Methods

Machine-learning algorithms are used in invaluable classification and categorization of information that allows information to be grouped into preset categories. By analysing patterns, machine-learning models could produce inaccurate inferences in all types of fields, such as disease diagnosis in medicine, fraud detection, and automatic object recognition [18]. The ability to handle large and intricate datasets does not only improve efficiency and accuracy but also innovative ideas since it can uncover insights that would otherwise remain unnoticed by manual analysis [19].

To draw the line between Android applications, as being benign or malicious, various machine-learning algorithms were utilized, each of which has its own contribution to the malware detection process. Support Vector Machines (SVM) are particularly useful in large-dimensional feature spaces, which build optimal boundaries to the decision, even when the data is not linearly separable, therefore, making them adequate with the Malware classification in which subtle patterns distinguish between innocent and malicious behaviour. Neural networks offer the ability to acquire difficult patterns automatically, which is essential in malware detection where features associations are not necessarily obvious; they learn nonlinear relationships in the large volumes of data, thus, becoming an effective tool to classification with complex feature interactions. Logistic regression is a less complex but a highly effective binary classification method; its interpretability and ability to readily deal with linearly separable data make it a reliable option in cases where computational resources are limited. All these algorithms have been chosen due to their capability to address the complexity and the high dimensions of Android malware data and, thus, provide a good level of classification with varied sets of features.

Feature selection is a crucial preprocessing step in malware detection because the feature spaces derived from static and dynamic analyses tend to be high-dimensional and may contain redundant or irrelevant attributes. For example, Zhang et al. applied PCA in a PDF-malware detection scenario and showed that by reducing the number of features by about one-third they achieved nearly the same true positive rate while decreasing learning time by approximately 22 % [20]. Likewise, in Android malware/or network-traffic threat detection contexts PCA has been used to reduce dimensionality and thereby reduce computational burden [21]. In contrast, ANOVA-F (a univariate statistical scoring method) can be used to evaluate each feature's ability to discriminate between malware and benign classes: features with high F-scores indicate strong between-class variance relative to within-class variance and thus have higher discriminative power. For example, a recent study in obfuscated malware detection used ANOVA to rank features and then built a deep neural network on the selected subset, obtaining extremely high precision and recall [22]. Moreover, comparative work in intrusion-detection domains shows that applying ANOVA-F feature selection improved classification performance (accuracy, sensitivity) by around 5-10% on average [23].

By selecting only the most informative features, ANOVA reduces noisy/redundant attributes, lowers the dimensionality, and thus improves model generalisation, reduces overfitting risk, and speeds up training and inference. Accordingly, in our study we applied both PCA and ANOVA feature-selection under the same pipeline to compare not only classification accuracy but also computational cost, thereby assessing which method yields a better trade-off in the context of Android malware detection.

3.1. Support vector machines

Support Vector Machines (SVMs) are widely used supervised learning algorithms for classification and regression tasks. Based on statistical learning theory, SVMs aim to find the optimal boundary that best separates different classes within a dataset [24]. The key concept behind SVMs is the hyperplane, a mathematical boundary that divides data points into different categories. In two-dimensional space, this boundary is a line; in three-dimensional space, it is a plane. The main objective of a Support Vector Machine (SVM) in classification problem is to find a hyperplane that optimises the margin, the distance between the hyperplane and closest data points of both classes also called support vectors. This can be increased to increase the ability of the model to generalise to new and unobserved data, which further increases the prediction ability of the model.

SVMs use a trick known as the kernel trick, to project input data into a higher-dimensional feature space, in which the linear method of separation is more easily attained. The most popular kernel functions are the linear kernel, the polynomial kernel, the radial basis function (RBF) kernel and the sigmoid kernel. The choice of a proper kernel is of essential importance because it depends on it directly what power of discrimination the model will have. The other key feature of SVMs is the so-called soft margin that adds flexibility by allowing a part of the data points to be within the limits of the margin or to be misclassified data. This is controlled by the regularisation parameter C, which regulates the trade-off between margin enlargement and classification errors. The higher the value of C, the more the right classification and the smaller the value, the more the margin is stressed.
SVMs have significant weaknesses even though they are effective. The computation cost of training an SVM may be computationally costly, particularly with large data sets, as the cost increases with the size of the training set. Moreover, SVMs do not necessarily give probabilistic motivation, and this may be a disadvantage in applications that need probabilities; methods like Platt scaling have been utilized to transform the SVM results to probabilities but this introduces more complexity to the model. Moreover, SVMs require careful tuning of kernel functions and hyperparameters to attain the best performance which is usually achieved through cross-validation [25].

3.2. Neural networks

Neural networks are a fundamental class of machine learning models inspired by the human brain. They consist of layers of interconnected neurons that process information by transmitting signals from one layer

to another [26]. This architecture enables neural networks to learn complex patterns and representations from data, making them highly effective for tasks like classification, regression, and pattern recognition.
Each neuron in a neural network receives input signals, applies weights to them, sums them up, and passes the result through an activation function to produce an output. Common activation functions include sigmoid, hyperbolic tangent (tanh), and Rectified Linear Unit (ReLU), each introducing non-linearity to help the model learn complex relationships.

Neural networks are structured in layers:

- The input layer receives raw data.
- One or more hidden layers extract features and patterns.
- The output layer generates the final prediction.

Training a neural network involves backpropagation, an optimization technique combined with gradient descent. Backpropagation calculates the loss gradient for each weight in the network and updates them to minimize prediction errors. The loss function measures the difference between the model's predictions and the actual values, guiding the model to improve over time. One major advantage of neural networks is automatic feature extraction, reducing the need for manual feature engineering. This is particularly beneficial in fields where defining relevant features is complex [27].

However, neural networks have some challenges:

- They require large amounts of labelled data for training, which can be resource intensive.
- Training deep networks demands significant computing power, often requiring specialized hardware such as GPUs or TPUs.
- They are prone to overfitting, where the model learns patterns too well, including noise and outliers, leading to poor generalization to new data. Techniques such as dropout, early stopping, and regularization help mitigate overfitting.
- Neural networks are often viewed as black boxes, meaning their decision-making process is difficult to interpret. This lack of transparency can be problematic in fields like healthcare. Explainable AI (xAI) is an emerging field focused on improving the interpretability of neural networks [28].

3.3. Logistic regression

The Logistic Regression is one of the most significant and versatile algorithms to perform classification. It has its advantages in being simple, interpretable, and efficient to compute, which makes it a product vital to both statistical modelling and machine learning. The Logistic Regression is used not in regression problems but in estimating the probability that relates to a categorical dependent variable. It models the association between a dichotomous dependent variable and one or more independent ones by approximate probabilities with the help of a logistic (sigmoid) model. The logistic function is the essence of the Logistic Regression: it transforms the input of any real value into a range between 0 and 1; a feature that makes it fit the dichotomous outcomes like probability well [29].

The interpretability of Logistic Regression is one of its major strengths. The coefficients represent the change in the long odds of the outcome in case the predictor variable (x) is augmented by one unit. Exponentiation of these coefficients produces odds ratios which measures the degree of influence of a predictor on the probability of a certain outcome. Logistic Regression assumes a linear relationship between the independent variables and the long odds of the dependent variable. Although such simplification is beneficial in the interpretation, it might not capture the non-linear, complicated interactions present in the data. The way out of this weakness is to add terms of interaction or polynomials transformations to the model, but this comes at the price of more complexity and the risk of overfitting.
Despite its widespread application, Logistic Regression has several limitations:

- Multicollinearity: This occurs when there are strong correlations between the independent variables and the estimates of the variance become inflated thus causing the instability of the model. The

multicollinearity can be detected and addressed with the help of Variance Inflation Factor (VIF) analysis and Principal Component Analysis (PCA).

- Sensitivity to Outliers: Outliers can imbalance the estimates of coefficient, giving disproportionate predictions. This can be mitigated by strong estimation, variable transformations or by filtering out extreme values.
- Class Imbalance: Classification can be highly inaccurate when there is a gross imbalance in the data, with one category overwhelming the other. In these cases, oversampling of the minority group, undersampling of the majority group, or the artificial training of data by SMOTE can be used to improve the performance of the model [30].

3.4. ANOVA feature selection

Analysis of Variance (ANOVA) is a type of statistical technique used in feature selection to determine the most salient features to make in a model that can be used to predict. ANOVA helps to assess the existence of statistically significant differences between the means of certain groups, thus helping to identify which attributes demonstrate a strong correlation with the object of interest. ANOVA is the most beneficial when the number of features in a dataset is huge because it helps to reduce the dimensions and allows the model to focus on the most relevant attributes. The F-statistic measures the ratio of:

- Variance between groups (how much the means of distinct groups differs).
- Variance within groups (how much variability exists within each group).
- A high F-value suggests that the variance between groups is significantly greater than the variance within groups, indicating that the feature has strong discriminatory power.

ANOVA feature selection in machine learning involves the computation of F-statistical value of a single feature in relation to the target variable. F-statistic is a ratio of variance of groups to variance of groups. The F-statistic is normally distributed according to the F-distribution the null hypothesis given that the group means are equal. One may determine whether to reject the null hypothesis by comparing the calculated F-value, which is compared to a critical value based on the F-distribution or by checking the p-value. When the p-value is low (usually less than 0.05) this is an indication that one of the group means are significantly different and thus is statistically significant and should be included in the model. When the use of ANOVA feature selection is properly implemented, machine learning models could improve their predictive accuracy by removing redundant or irrelevant features, which eventually leads to efficiency and accuracy [31].

ANOVA is developed to find out the linear relationship; therefore, it might not always efficiently identify non-linear associations between the target variable and the feature. To address this shortcoming, the transformations of logarithmic, square root or Box-Cox can be used to make the data equal and stable the variances. Non-linear relationships and interactions between variables may be expressed as interaction terms or as poly features.

ANOVA-based feature selection is a useful method in estimating important features in the continuous-predictor datasets where the target variable is categorical. It both makes model structures simpler and reduces overfitting, as well as contributes to interpretability. Practitioners should, however, be careful about the assumptions and limitations of the technique taking care to preprocess and validate them. By properly using feature selection, along with other methodologies as well as domain knowledge, it is possible to create more efficient and effective machine learning models [32].

3.5. Principal component analysis

Principal Component Analysis (PCA) is a fundamental tool in the fields of statistics and machine learning, especially in features extraction and dimensionality reduction. It reduces a high dimensional set of variables into a smaller one without substantially losing most of the intrinsic information. PCA transforms correlated variables into a set of mutually uncorrelated objects (also referred to as principal components) to simplify high-dimensional data without losing any important trends and patterns. Essentially, PCA deals with the

variance and covariance of the variables and is interested in the definition of the major components that capture the highest variance. These main elements are orthogonal to each other hence guaranteeing that all of these elements depict different directions of variance. The first main component represents the biggest variance, and the next major component represents the biggest unexplainable variance, but it is orthogonal to the first major component [33].

Mathematically, there are a number of critical steps in PCA. The first step is to centre the data by subtracting the means of the variables so as to have zero mean, this process is done because during PCA, the data is quite sensitive to the relative scales between the original variables. A covariance data of the data is then obtained to explain inter-variable relationships. Next, eigenvalues and eigen vectors of the covariance matrix are calculated. The eigenvectors indicate the directions of the new feature space, and the eigenvalues indicate the size of the variance in the directions. Components are then ranked in descending eigenvalue order, with the most explaining components being given priority. A threshold is usually used e.g. 95 percent of total variance and the principal components that are required to reach this level of threshold are used to reduce dimensionality by eliminating components that contribute insignificant variance to the model. Finally, the original data are mapped on top of the selected set of main components, which results in a transformed dataset with a smaller number of dimensions but a more informative set of information.

PCA is another powerful feature extraction procedure in the sense that a strong focus is laid on what is most informative in data. PCA removes noise and redundancy by filtering directions with the largest variance, which makes machine learning algorithms more efficient, particularly, when the high dimensional data results in a computational overhead and a reduced predictive accuracy. PCA dimensionality reduction also helps to reduce the curse of dimensionality, in which a large feature space leads to data sparsity and noise to the performance of algorithms in identifying meaningful patterns. Although PCA has these strengths, it does not lack limitations. The key disadvantage is that it assumes a linear relationship between variables and might therefore be hindered in capturing non-linear patterns. Also, due to its acute sensitivity to difference in variable scales, PCA may give biased results when one variable has a significantly large scale and thus contributes to the principal components disproportionately. It is, therefore, mandatory to standardise or normalise the data before performing PCA because standardisation makes all the variables contribute equally and avoids the control of the larger scale variables. The other difficulty is the issue of interpretability: principal components are linear combinations of original variables; hence it may be problematic to understand their real-world meaning. The process of interpretation requires analysis of loadings that outline the contribution of each original variable; the more the number of variables, the more complex and labour intensive the analysis becomes to perform successfully [34].

Selection of the number of principal components to retain is a very critical decision. Oversized retention can be unable to cluster enough of the data together to significantly reduce dimensionality, and undersized retention can afford to lose a lot of information. Methods like scree plots, which plot eigenvalues versus component number, help in determining the juncture at which adding extra components to the model will add insignificant variance to the model. An optimal number of components to keep is represented by the point where the plot levels off - the elbow point. Although PCA is based on the assumption that the components with the highest variance are most important, this cannot always be valid with respect to the goals of a particular machine learning activity. In some situations, less variant variables can be more relevant to the target variable. As such, unsupervised learning situations with PCA typically involve more use of the technique, where the emphasis is on the description of data, as opposed to the prediction of a specific phenomenon.

4. Results and Discussion

This paper aimed to create and test machine-learning models to predict Android apps as malware or benign. Three different preprocessing conditions were taken into account: (1) the initially unprocessed dataset without reducing the features, (2) the usage of Principal Component Analysis (PCA) to extract the features, and (3) the usage of an ANOVA test to locate the features. Three classification algorithms Fine Gaussian Support Vector Machine (SVM), Wide Neural Network and Binary Generalized Linear Model (GLM) Logistic Regression were used to analyse each scenario. The current section enlarges on the dataset,

preprocessing tools, feature reduction methods, classification methods, and assessment measures utilized in the research.

In the former case, the entire 241 features were used without dimensionality reduction or feature selection methods in training the classification models. This strategy was to test the performance of the algorithms provided with the entire pool of available information. In the latter case, the training data were standardized and PCA was used to test the data in order to decrease the number of dimensions and still maintain most of the variance in the original features. The main elements were ranked based on their eigenvalues discerningly. However, since all of the extracted features exceeded the threshold value, all 241 features were used in the training set. The transformed training data was then used to train the classification models. The same transformation was applied to the testing data before evaluation.

In the third scenario, the ANOVA-test was utilized to select the most significant features related to the target variable. The procedure included 120 features into the training process. This approach aimed to improve model performance by eliminating irrelevant or redundant features.

Hyperparameters for each model were optimized using 5-fold cross-validation on the training set. The optimal parameters were selected based on the highest average cross-validation accuracy. In table 1, hyperparameters of the classification models are given.

Table 1. Hyperparameters of the classification algorithms

Classification Algorithm	**Hyperparameters**
Fine Gaussian SVM	Multiclass coding: One-vs-One Kernel function: Gaussian Kernel scale: 3.9 Box constraint level: 1 Standardize data: Yes
Wide Neural Network	Activation: ReLU Number of fully connected layers: 1 First layer size: 100 Iteration limit: 1000 Regularization strength (Lambda): 0 Standardize data: Yes
Binary GLM Logistic Regression	Solver: Linear Penalty: L2 C= 0.001 Maximum Iteration: 1000

Table 2 indicates the findings of the initial dataset, the PCA dataset, and the feature set that was picked using ANOVA. Its results showed that the SVM model performed better than the other models in all the datasets in terms of accuracy. Precisely, the SVM used an accuracy of 99.25 per cent on the PCA-applied dataset, which is slightly higher than the 99.10 per cent and 98.95 per cent on the original dataset and ANOVA feature selection set, respectively. The neural network showed slightly less accuracy with a maximum of 98.65 2 on the dataset run through PCA. The lowest accuracy was of logistic regression that reached a maximum accuracy of 98.50 amongst the three models with a high accuracy of 98.50 on the PCA-applied data.

Table 2. Results of the classification algorithms

Dataset	Model Type	Accuracy %	Training Time (sec)	Selected Features
PCA-Applied Dataset	SVM	99.25	39.9052339	241/241
Original Dataset	SVM	99.10	8.6394085	241/241
ANOVA Feature Selection	SVM	98,95	4.8080937	120/241
PCA-Applied Dataset	Neural Network	98.65	117.3555743	241/241
Original Dataset	Neural Network	98.50	7.,6136271	241/241
ANOVA Feature Selection	Neural Network	99.35	580952943	120/241
PCA-Applied Dataset	Logistic Regression	98.50	27.8751492	241/241
Original Dataset	Logistic Regression	98.05	26.0621809	241/241
ANOVA Feature Selection	Logistic Regression	97.90	20.6098871	120/241

The use of PCA led to a slight increase in accuracy of all the models. As an illustration, the accuracy in the use of the SVM rose to 99.10 99.25 percent on the original data set and 99.25 percent in PCA respectively. However, this diminutive improvement was accompanied by a significant increment in training times; SVM training time increased by 8.64s to 39.91s. Similar extensions of training times were found in the case of the neural-network model and logistic-regression model. It is worth noting that PCA was not used to reduce the dimensionality of the features since all the 241 principal components were retained to meet the variance-threshold requirement.

Conversely, feature-selection method based on ANOVA was successful in the minimization of features of 241 down to 120. Reduction in this dimension resulted into reduced training time of all models without compromising their accuracy. As an example, the SVM has maintained accuracy of 98.95 per cent and reduced training time by 8.64 to 4.81 per cent on the dataset with ANOVA-selected features. These findings indicate that the features that were left out were either useless or they did not play a role in the classification task.

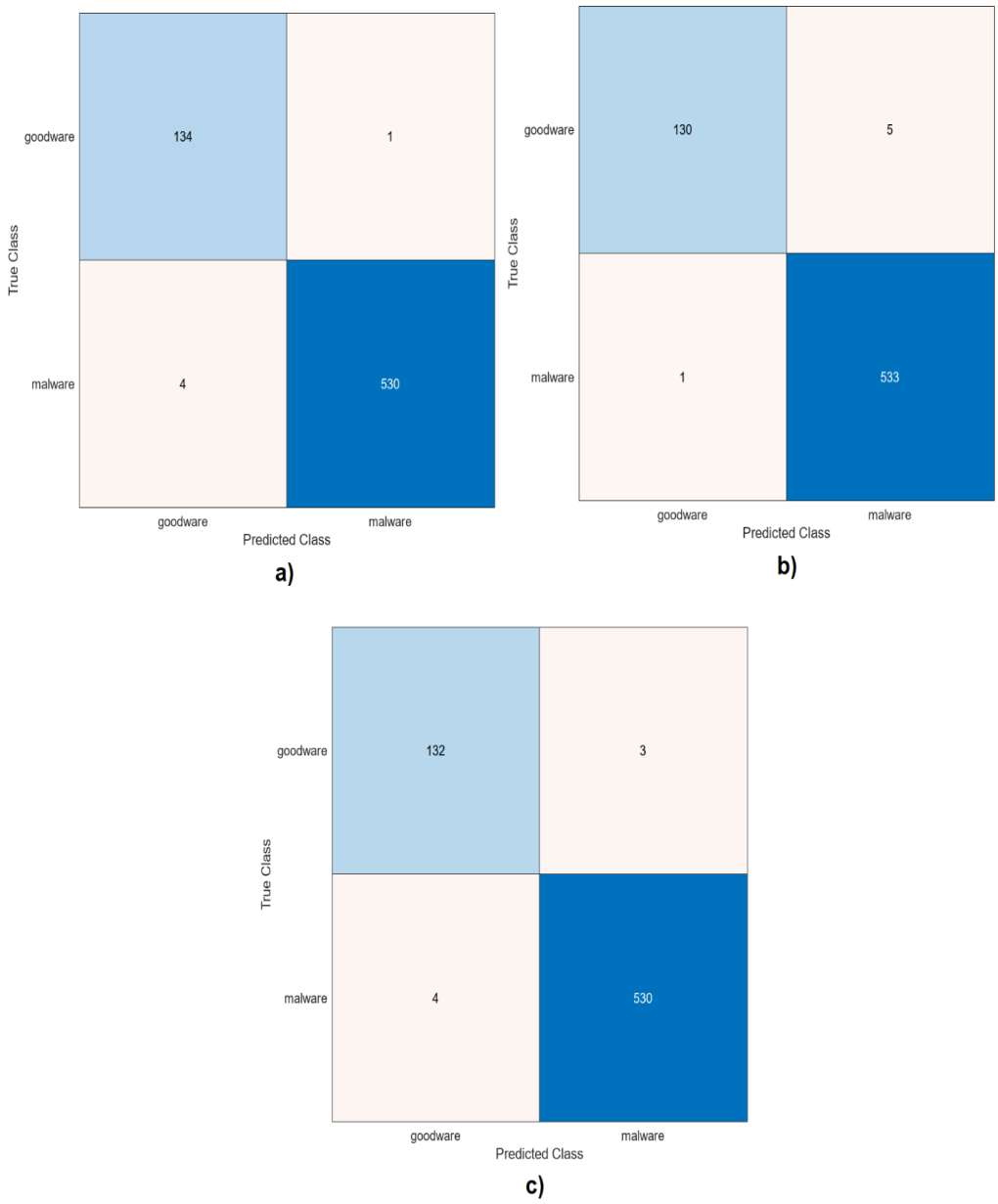


Figure 2. Confusion Matrices of the SVM models. (a) PCA-applied dataset, (b) Original dataset, (c) Anova feature selection

The breakdown of classification performance by each of the SVM models is provided in Figure 2 as represented by confusion matrices. The PCA model demonstrated the strongest results, with the ability to classify 3,535 malware samples (True Positives) and 896 benign ones (True Negatives), and only 1 False Positive and 4 False Negatives. These matrices show that PCA-applied dataset performed better to detect goodware applications.

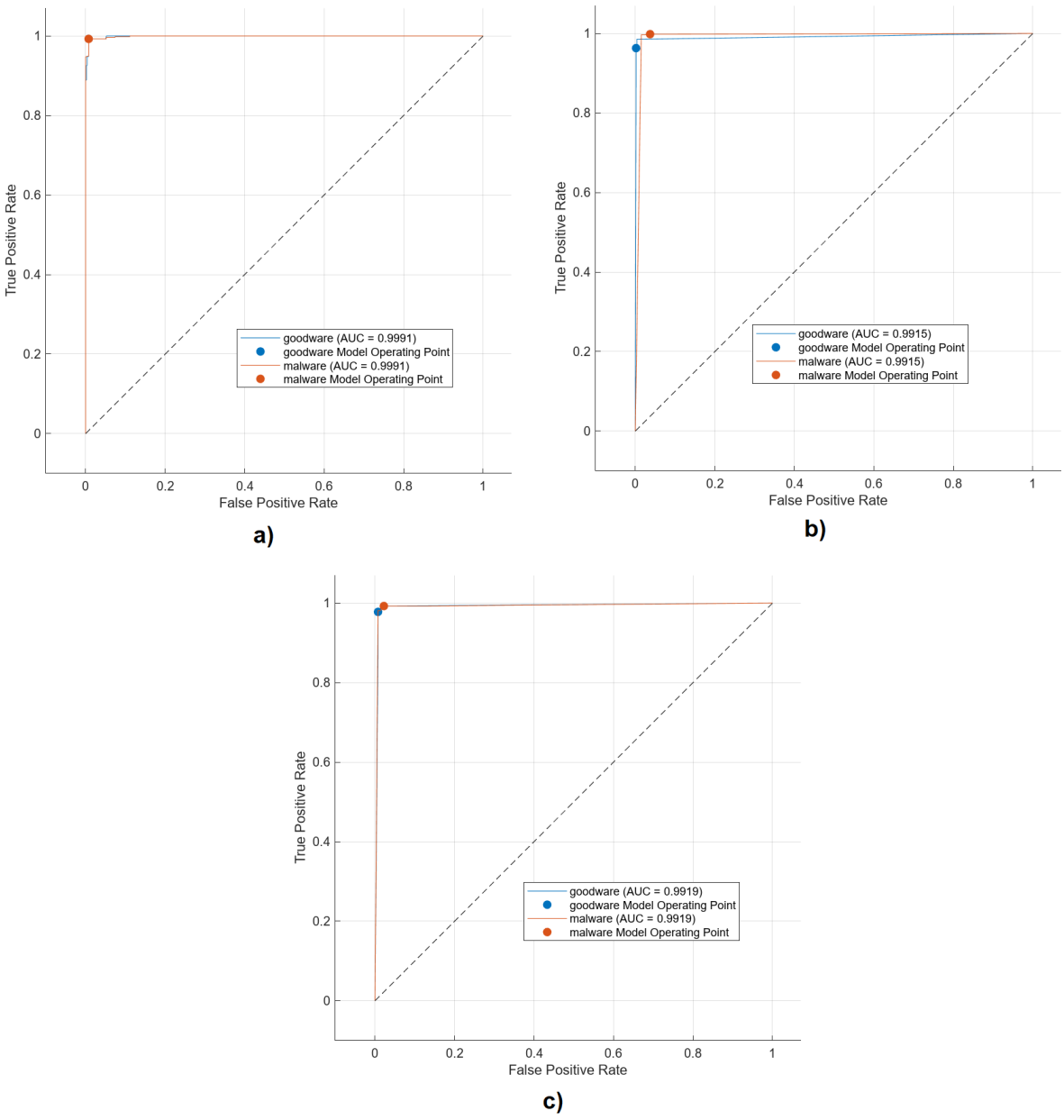


Figure 3. ROC curves of the SVM models. (a) PCA-applied dataset, (b) Original dataset, (c) Anova feature selection

Figure 3 illustrates the Receiver Operating Characteristic (ROC) curves for the SVM variations, plotting the True Positive Rate against the False Positive Rate. The Area Under the Curve (AUC) serves as a single metric for comparing the models' overall discriminative power. All three models show outstanding performance, with AUC values approaching a perfect score of 1.0. The proximity of all three curves to the top-left corner underscores the high sensitivity and specificity of the SVM classifier for malware detection using the TUANDROMD dataset.

In comparison, Alhogail & Alharbi achieved 97.82% accuracy for binary detection of Android malware using a chi-squared based feature selection and RF classifier on their dataset [35]. However, unlike our study, their work did not explicitly compare dimensionality-reduction approaches with a focus on computational cost. Our contribution thereby lies in providing a dual-axes evaluation (accuracy + efficiency) of PCA vs ANOVA under identical conditions.

5. Conclusions

Finally, the work also shows that Support Vehicle Machine models are more effective in distinguishing malware and benign Android applications with the highest predictive accuracy of the models compared in the paper. The feature selection of analysis of variance (ANOVA) is found as the pragmatic method of dimensionality reduction and cost-saving without compromising on performance. Conversely, the PCA did not provide many benefits in this specific context and instead caused a long period of training. Therefore, the focus should be on the method of the feature selection that identifies and exploits the most noticeable predictors to similar classification problems.

The future research directions should look into the implementation of more advanced machine-learning architectures, which could be more effective in gaining performance than is feasible with SVM. The research on alternative variance thresholds in PCA can help understand whether meaningful dimensionality reduction is possible to achieve, which may allow balancing accuracy and computational efficiency. Moreover, it is necessary to conduct stringent evaluation of overfitting risks, particularly in circumstances of high accuracy scores as indicated in this paper. While cross-validation mitigates this risk to some extent, validating the models on independent test datasets would strengthen the reliability of the results. Evaluating the models' inference times and more effective feature selection algorithms would also be beneficial, ensuring that they meet the real-time requirements of malware detection systems.

6. Author Contribution Statement

In the study, Author 1 contributed to forming the idea, making the design, literature review, contributed to the analysis of the results, provision of the materials and examination of the results.

7. Ethics Committee Approval and Conflict of Interest

There is no need for an ethics committee approval in the prepared article.
There is no conflict of interest with any person/institution in the prepared article.

8. Ethical Statement Regarding the Use of Artificial Intelligence

No artificial intelligence-based tools or applications have been utilized for the preparation of this study. All content of the study has been produced by the author in accordance with scientific research methods and academic ethical principles.

9. References

[1] K. V. S. Bai and M. Thirumaran, "Hybrid deep learning and behavioral analysis for enhanced malware detection in banking," in *Proc. 8th Int. Conf. Electron., Commun. Aerosp. Technol. (ICECA)*, 2024, pp. 1168–1173.
[2] H. Y. Kwon, T. Kim, and M. K. Lee, "Advanced intrusion detection combining signature-based and behavior-based detection methods," *Electron.*, vol. 11, no. 6, p. 867, Mar. 2022.
[3] S. Yakut, "Kayıplı resim sıkıştırma algoritmalarını temel alan rastgele sayı üreteci," *Adıyaman Üniv. Müh. Bilim. Derg.*, vol. 9, no. 18, pp. 571–580, Dec. 2022.
[4] S. Yakut, "Random number generator based on discrete cosine transform based lossy picture compression," *MTU J. Eng. Nat. Sci.*, vol. 2, no. 2, pp. 76–85, 2021.
[5] S. Yakut, T. Tuncer, and A. B. Özer, "A new secure and efficient approach for TRNG and its post-processing algorithms," *Int. J. Bifurcation Chaos*, vol. 29, no. 15, May 2020.
[6] S. Yakut, T. Tuncer, and A. B. Ozer, "Secure and efficient hybrid random number generator based on sponge constructions for cryptographic applications," *Elektron. Elektrotech.*, vol. 25, no. 4, pp. 40–46, Aug. 2019.
[7] G. Areo, "Evaluating the efficacy of machine learning techniques in mitigating cybersecurity threats: A comprehensive analysis," 2024.
[8] T. Adewale, "The role of deep learning in cloud-based cybersecurity solutions," 2024.
[9] G. Cuiying *et al.*, "Uncovering and mitigating the impact of code obfuscation on dataset annotation with antivirus engines," in *Proc. 33rd ACM SIGSOFT Int. Symp. Softw. Test. Anal. (ISSTA)*, 2024, pp. 553–565.
[10] S. S. Rajest and R. Regin, "Application of the CatBoost classifier for the detection of Android ransomware," *Central Asian J. Math. Theory Comput. Sci.*, vol. 5, no. 5, pp. 476–486, Nov. 2024.
[11] D. Totham, V. Andersson, H. Thompson, and J. Whitmore, "Dynamic ransomware detection with adaptive encryption pattern recognition techniques," 2024.
[12] M. A. Haq and M. Khuthaylah, "Leveraging machine learning for Android malware analysis: Insights from static and dynamic techniques," *Eng. Technol. Appl. Sci. Res.*, vol. 14, no. 4, pp. 15027–15032, Aug. 2024.
[13] K. Kunku, A. N. K. Zaman, and K. Roy, "Ransomware detection and classification using machine learning," in *Proc. IEEE Symp. Ser. Comput. Intell. (SSCI)*, 2023, pp. 862–866.
[14] G. Mubarak and S. Alasmari, "A framework to analyze OS systems artifacts from Linux machines," *Adv. Appl. Discrete Math.*, vol. 41, no. 8, pp. 603–640, Oct. 2024.
[15] D. Gihavo, O. Ivanovich, A. Harrison, L. Merritt, and V. Schneider, "Automated file trap selection using machine learning for early detection of ransomware attacks," Authorea Preprints, Oct. 2024.
[16] K. Dolesi, E. Steinbach, A. Velasquez, L. Whitaker, M. Baranov, and L. Atherton, "A machine learning approach to ransomware detection using opcode features and k-nearest neighbors on Windows," Authorea Preprints, Oct. 2024.
[17] P. Borah, D. K. Bhattacharyya, and J. K. Kalita, "Malware dataset generation and evaluation," in *Proc. 4th IEEE Conf. Inf. Commun. Technol. (CICT)*, 2020.
[18] A. Alhudhaif, B. Almaslukh, A. O. Aseeri, O. Guler, and K. Polat, "A novel nonlinear automated multi-class skin lesion detection system using soft-attention based convolutional neural networks," *Chaos Solitons Fractals*, vol. 170, p. 113409, May 2023.
[19] F. Ucar, O. F. Alcin, B. Dandil, and F. Ata, "Machine learning based power quality event classification using wavelet-entropy and basic statistical features," in *Proc. 21st Int. Conf. Methods Models Autom. Robot. (MMAR)*, 2016, pp. 414–419.
[20] J. Zhang, "Machine learning with feature selection using principal component analysis for malware detection: A case study," arXiv preprint, Feb. 2019.
[21] D. Ö. Şahin, O. E. Kural, S. Akleylek, and E. Kılıç, "Permission-based Android malware analysis by using dimension reduction with PCA and LDA," *J. Inf. Secur. Appl.*, vol. 63, p. 102995, Dec. 2021.
[22] M. Hadjila, M. Merzoug, W. Ferhi, D. Moussaoui, A. B. Bouidaine, and M. H. Hachemi, "Obfuscated malware detection using deep neural network with ANOVA feature selection on CIC-MalMem-2022 dataset," *Sci. Tech. J. Inf. Technol. Mech. Opt.*, vol. 24, no. 5, pp. 849–857, Sep. 2024.

[23] M. J. Siraj, T. Ahmad, and R. M. Ijtihadie, "Analyzing ANOVA F-test and sequential feature selection for intrusion detection systems," *Int. J. Adv. Soft Comput. Appl.*, vol. 14, no. 2, pp. 185–194, 2022.
[24] C. Cortes and V. Vapnik, "Support-vector networks," *Mach. Learn.*, vol. 20, pp. 273–297, 1995.
[25] S. Buyrukoğlu, "New hybrid data mining model for prediction of Salmonella presence in agricultural waters based on ensemble feature selection and machine learning algorithms," *J. Food Saf.*, vol. 41, no. 4, p. e12903, Aug. 2021.
[26] B. Karakaya, V. Çelik, and A. Gülten, "Chaotic cellular neural network-based true random number generator," *Int. J. Circuit Theory Appl.*, vol. 45, no. 11, pp. 1885–1897, 2017.
[27] O. Güler, "Turbofan motorlarının kestirimci bakımında makine öğrenimi algoritmaları performanslarının karşılaştırılması," *Niğde Ömer Halisdemir Üniv. Müh. Bilim. Derg.*, vol. 13, no. 1, pp. 99–106, Jan. 2024.
[28] R. K. Sheu, M. S. Pardeshi, K. C. Pai, L. C. Chen, C. L. Wu, and W. C. Chen, "Interpretable classification of pneumonia infection using explainable AI (XAI-ICP)," *IEEE Access*, vol. 11, pp. 28896–28919, 2023.
[29] F. Türk, "Investigation of machine learning algorithms on heart disease through dominant feature detection and feature selection," *Signal Image Video Process.*, vol. 18, no. 4, pp. 3943–3955, Jun. 2024.
[30] S. Ahmadov and A. Boyacı, "Multilingual text mining based open source emotional intelligence," *Turkish J. Sci. Technol.*, vol. 17, no. 2, pp. 161–166, Sep. 2022.
[31] H. A. Kwaider and E. Avaroğlu, "Threats detection in IoT network," *Turkish J. Sci. Technol.*, vol. 18, no. 1, pp. 113–122, Mar. 2023.
[32] A. Bilen and A. B. Özer, "Siber saldırılar için rastgele orman algoritması kullanılarak öznitelik seçimi," *Fırat Üniv. Fen Bilim. Derg.*, vol. 34, no. 1, pp. 31–37, Mar. 2022.
[33] A. İmak, "Automatic classification of defective photovoltaic module cells based on a novel CNN-PCA-SVM deep hybrid model in electroluminescence images," *Turkish J. Sci. Technol.*, vol. 19, no. 2, pp. 497–508, Sep. 2024.
[34] İ. Riaz, N. Mushtaq, M. M. Jillani, and U. Navaz, "Performance analysis of Pakistan Super League players using principal component analysis approach," *Sci. J. Mehmet Akif Ersoy Univ.*, vol. 2, no. 4, pp. 127–135, Dec. 2019.
[35] A. Alhogail and R. A. Alharbi, "Effective ML-based Android malware detection and categorization," *Electron.*, vol. 14, no. 8, p. 1486, Apr. 2025.

Fırat Üniversitesi Deneysel ve Hesaplamalı Mühendislik Dergisi

FUJECE

SoC-FPGA Ortamında AXI-DMA ve BRAM Tabanlı Entegrasyon Yöntemlerinde Gecikme ve Kaynak Tüketim Analizi

Güner TATAR[1]*

[1]Elektrik-Elektronik Mühendisliği, Mühendislik ve Doğa Bilimleri Fakültesi, İstanbul Medeniyet Üniversitesi, İstanbul, Türkiye.
[1]guner.tatar@medeniyet.edu.tr

Geliş Tarihi: 23.9.2025
Kabul Tarihi: 22.1.2026

Düzeltme Tarihi: 12.1.2026

doi: https://doi.org/10.62520/fujece.1790038
Araştırma Makalesi

Alıntı: G. Tatar, "SoC-FPGA ortamında AXI-DMA ve BRAM tabanlı entegrasyon yöntemlerinde gecikme ve kaynak tüketim analizi" Fırat Üni. Deny. ve Hes. Müh. Derg., vol. 5, no 1, pp. 316-329, Şubat 2026.

Özet

Bu makale, Xilinx Zynq-7000 SoC üzerinde tasarlanan iki entegrasyon stratejisinin karşılaştırmalı değerlendirmesini sunmaktadır. Araştırmada, Advanced eXtensible Interface Direct Memory Access (AXI-DMA) tabanlı mimari ile Block Read Access Memory (BRAM) tabanlı mimari, performans, kaynak kullanımı ve gecikme açısından ele alınmıştır. Her iki tasarım da aritmetik işlemler için özel olarak geliştirilmiş bir işlem elemanı içermektedir; ancak veri aktarımı ve arabellekleme mekanizmaları bakımından önemli farklılıklar göstermektedir. AXI-DMA tabanlı tasarımda, işlemci sistemi ile programlanabilir mantık (PL) arasındaki iletişim, bir DMA motoru tarafından kontrol edilen AXI4-Stream arayüzü üzerinden sağlanmaktadır. BRAM tabanlı mimaride ise AXI BRAM denetleyicileri aracılığıyla erişilen çift portlu blok bellekler kullanılmakta ve doğrudan veri erişimi mümkün olmaktadır. Uygulama sonuçları, her iki mimarinin de XC7Z020 cihazının kaynak kısıtlarını karşıladığını göstermektedir. Bununla birlikte, AXI-DMA tabanlı tasarımın donanım kaynak tüketiminin, BRAM tabanlı mimariye kıyasla ortalama %54 daha yüksek olduğu belirlenmiştir. Performans analizleri ayrıca gecikme açısından da çarpıcı bir farklılığı ortaya koymaktadır. AXI-DMA mimarisinde işlem başına ortalama 1,19 ms süre gerekmekteyken, BRAM tabanlı yaklaşım yaklaşık 0,10 ms daha düşük gecikme sağlamış ve toplam yürütme süresini 359.919 µs'den 32.487 µs'ye düşürmüştür. Elde edilen bulgular, ölçeklenebilirlik ile gecikme arasında belirgin bir ödünleşim bulunduğunu ortaya koymaktadır. AXI-DMA mimarisi, akış odaklı uygulamalarda esneklik ve yüksek veri aktarım kapasitesi sunarken, BRAM tabanlı mimari daha küçük ölçekli ve düşük gecikme gerektiren senaryolarda daha yüksek verimlilik sağlamaktadır. Çalışma, heterojen bilgi işlem platformlarında Field Programmable Gate Array (FPGA) tabanlı hızlandırıcıların tasarımı için yol gösterici nitelikte sonuçlar sunmaktadır.

Anahtar kelimeler: SoC-FPGA uyum stratejisi, AXI-DMA mimarisi, BRAM tabanlı tasarım, Kaynak kullanımı ve gecikme analizi, FPGA tabanlı heterojen hesaplama

*Yazışılan yazar

İntihal Kontrol: Evet – Turnitin
Şikayet: fujece@firat.edu.tr
Telif Hakkı ve Lisans: Dergide yayın yapan yazarlar, CC BY-NC 4.0 kapsamında lisanslanan çalışmalarının telif hakkını saklı tutar

Firat Univ Jour. of Exp. and Comp. Eng., 5(1), 316-329, 2026

Firat University Journal of Experimental And Computational Engineering

Latency and Resource Trade-off Analysis of AXI-DMA and BRAM Integration Approaches on SoC-FPGA

Güner TATAR[1]*

[1]Electrical-Electronics Engineering, Faculty of Engineering and Natural Sciences, Istanbul Medeniyet University, İstanbul, Türkiye.
[1]guner.tatar@medeniyet.edu.tr

Received: 23.9.2025
Accepted: 22.1.2026
Revision:12.1.2026
doi: https://doi.org/10.62520/fujece.1790038
Research Article

Citation: G. Tatar, "Latency and resource trade-off analysis of AXI-DMA and BRAM ıntegration approaches on SoC-FPGAs", Firat Univ. Jour.of Exper. and Comp. Eng., vol. 5, no 1, pp. 316-329, February 2026.

Abstract

This paper presents a comparative evaluation of two integration strategies for the Xilinx Zynq-7000 System-on-Chip (SoC): an Advanced eXtensible Interface-Direct Memory Access (AXI-DMA)-based architecture and a Block RAM (BRAM)-based architecture. Both designs employ a custom processing element (PE) for arithmetic operations, yet they differ significantly in data transfer and buffering mechanisms. In the AXI DMA design, communication between the processing system (PS) and programmable logic (PL) is achieved via an AXI4-Stream interface controlled by a DMA engine. In contrast, the BRAM-based design uses dual-port block memories via AXI BRAM controllers, enabling direct operand access. Implementation results indicate that both designs comfortably meet the resource constraints of the XC7Z020 device. However, the AXI DMA-based architecture exhibits higher hardware resource utilization, with average consumption approximately 54% greater than that of the BRAM-based design. Performance analysis reveals a pronounced latency difference: the AXI DMA design required an average of ~1.19 ms per operation. In comparison, the BRAM-based approach achieved a reduction of ~0.10 ms, resulting in a total execution time of 32.487 µs compared to 359.919 µs. These findings demonstrate a clear trade-off between scalability and latency. While AXI DMA provides flexibility and throughput for stream-oriented applications, BRAM-based integration delivers superior efficiency in small-scale, low-latency scenarios. The study offers practical insights for guiding the design of Field-Programmable Gate Array (FPGA)-based accelerators on heterogeneous computing platforms.

Keywords: SoC-FPGA integration strategy, AXI-DMA architecture, BRAM-based design, Resource utilization and latency analysis, FPGA-based heterogeneous computing

*Corresponging author

Plagiarism Checks: Yes – Turnitin
Complaints: fujece@firat.edu.tr
Copyright & License: Authors publishing with the journal retain the copyright to their work licensed under the CC BY-NC 4.0

1. Introduction

FPGAs are widely used to accelerate applications that require high computational performance, low power consumption, and design flexibility [1–3]. Unlike general-purpose processors, FPGAs allow designers to implement application-specific hardware pipelines, making them highly efficient for workloads such as digital signal processing, image processing, and cryptography [2–4]. With the emergence of heterogeneous SoC platforms, such as the Xilinx Zynq-7000 family, an ARM-based PS and PL can be integrated on the same chip, enabling tight coupling between software and hardware accelerators [1].

A critical challenge in such SoC-FPGA platforms is the efficient transfer of data between the PS and the PL. The communication mechanism chosen for this interaction has a dominant impact on overall system performance, particularly in terms of latency and resource usage [5-8]. Two widely used integration strategies are AXI-DMA and BRAM-based memory-mapped communication. AXI-DMA provides a scalable, high-throughput streaming interface well-suited for data-intensive, continuous workloads. In contrast, BRAM-based integration relies on on-chip block memories, enabling fast and deterministic access with very low latency, making it attractive for small or control-oriented workloads [6,9-11].

Although both approaches are commonly used, most existing studies focus on either DMA-based streaming accelerators or BRAM-based memory-centric designs in isolation. Works such as [1,5], and [11] demonstrate the advantages of AXI-DMA for high-throughput and large-scale workloads, while studies such as [6] and [13] emphasize the low-latency benefits of BRAM-based architectures. However, these studies do not provide a controlled and fair comparison of AXI-DMA and BRAM-based integration implemented on the same SoC platform using the same processing core. As a result, the practical trade-offs among latency, resource utilization, and architectural overhead remain insufficiently quantified.

This paper addresses this gap by implementing both AXI-DMA-based and BRAM-based integration strategies on the same Xilinx Zynq-7000 SoC using an identical custom arithmetic processing element. By keeping the computation kernel, clock frequency, and experimental conditions fixed, the impact of communication and buffering mechanisms can be isolated and evaluated in a fair, reproducible manner.

1.1. Contribution

The main contributions of this work are summarized as follows:

1. A fair and controlled comparison of AXI-DMA and BRAM-based integration strategies on the same Zynq-7000 SoC using an identical custom arithmetic processing element, eliminating architectural and computational bias.

2. A quantitative evaluation of resource utilization and latency, showing that the BRAM-based design achieves more than an order-of-magnitude reduction in execution latency while consuming significantly fewer hardware resources than the AXI-DMA-based approach.

3. A systematic analysis of the scalability–latency trade-off between streaming-based (AXI-DMA) and memory-mapped (BRAM) accelerator integration, providing practical design guidelines for selecting the appropriate strategy depending on whether an application is throughput-oriented or latency-critical.

2. Background and Related Works

FPGAs have been widely adopted as acceleration platforms for applications requiring high parallelism, low latency, and real-time responsiveness. Their reconfigurable nature and ability to tightly integrate custom hardware with general-purpose processors make FPGA-based SoCs particularly attractive for embedded and heterogeneous computing. In our earlier works [2,4], we demonstrated how reconfigurable MPSoC-FPGA architectures can be exploited for multi-task and multi-learning ADAS, highlighting the effectiveness of pipelined hardware acceleration in safety-critical automotive applications. These studies emphasized the strengths of FPGA-based platforms in achieving both high computational throughput and deterministic real-

time behavior. In contrast, the present work targets more fundamental accelerator kernels. It focuses explicitly on how data transfer mechanisms between the PS and PL influence latency and hardware resource utilization.

Beyond automotive applications, heterogeneous FPGA-based SoC platforms such as the Xilinx Zynq-7000 family have been extensively explored across a wide range of domains. Rios-Navarro et al., [1] investigated hardware/software co-design strategies for CNN accelerators and provided a detailed analysis of memory transfers in SoC-based systems. Their results underline that PS–PL communication efficiency plays a critical role in determining overall system performance and achievable speedup. Although their work focuses on CNN workloads, it demonstrates that communication overhead can significantly limit acceleration gains, motivating more focused investigations into PS–PL data transfer mechanisms independent of application complexity.

When considering communication methods, several studies have highlighted the scalability and throughput advantages of AXI-based and DMA-driven data transfer. Wang et al. [5,12] analyzed scatter–gather DMA performance on SoC-FPGA platforms and showed that AXI-DMA can sustain high throughput for extensive and continuous data streams. Similarly, Canto-Navarro et al. [11] designed an AXI-based FPGA accelerator for cryptographic workloads, demonstrating the effectiveness of AXI-Stream interfaces in bandwidth-intensive applications. However, these studies primarily emphasize throughput and scalability, while per-transaction latency and control overhead receive less attention. As a result, the suitability of AXI-DMA for short, iterative, or latency-critical workloads remains insufficiently explored.

The impact of DMA-induced overhead is further highlighted by Parameshwara et al. [14], who presented an FPGA-accelerated RISC-V architecture with custom ISA extensions for neural network inference on edge devices. Their real-hardware evaluation on a Zynq-based SoC demonstrates that, despite significant computational acceleration, memory transfers and DMA-based communication account for a substantial portion of total execution time. The authors show that data movement overhead can limit achievable speedup, emphasizing that PS–PL communication efficiency is often as critical as the accelerator design itself. While their work focuses on neural network acceleration at the ISA level, it strongly motivates a deeper examination of DMA-related latency in SoC-FPGA systems.

In contrast to DMA-centric approaches, BRAM-based and memory-mapped integration strategies have been widely adopted in latency-sensitive scenarios. Cılasun [6] modeled FPGA memory systems with variable latency and demonstrated that on-chip BRAM access can significantly reduce communication overhead. Likewise, Kieu-Do-Nguyen et al. [13] proposed a low-latency FPGA architecture for post-quantum cryptographic applications, highlighting the benefits of tightly coupled on-chip memory structures. These studies confirm the latency advantages of BRAM-based designs; however, they do not provide a direct comparison with AXI-DMA-based integration under identical hardware and experimental conditions.

A more communication-centric perspective is provided by Irtija et al. [15], who conducted a detailed analysis of digital communication mechanisms in SoC-based systems, focusing on latency, throughput, and reliability of data transfer between processing and programmable logic. Their study evaluates multiple communication approaches, including memory-mapped interfaces and DMA-based transfers, and shows that communication overhead can dominate system-level performance. Although their application domain targets quantum control systems, the reported latency measurements and communication analysis are directly applicable to general-purpose SoC-FPGA platforms.

A complementary, accelerator-oriented study is presented by Axinte et al. [16], who conducted a comprehensive evaluation of embedded streaming hardware-accelerator interconnect architectures on FPGA-based SoCs. Their work compares tightly coupled streaming, FIFO-based adapters, and AXI-DMA-driven architectures, with a particular focus on communication latency and FPGA resource utilization. Experimental results show that while DMA-based streaming can reduce frame-level latency in well-organized streaming scenarios, it incurs substantial hardware overhead and is highly sensitive to data organization and buffer descriptor management. Notably, the authors report that suboptimal DMA data organization can result in a more than 7-fold increase in latency for identical data sizes, highlighting the

inherent trade-off among scalability, flexibility, and latency in AXI-DMA-based communication architectures.

While the aforementioned studies provide valuable insights into PS–PL communication and accelerator integration, most existing work either focuses on application-specific designs or emphasizes throughput-oriented streaming architectures. Direct, fair comparisons between AXI-DMA-based streaming and BRAM-based memory-mapped integration, using identical processing elements and experimental conditions, remain limited in the literature. Addressing this gap, the present work isolates the impact of communication and buffering mechanisms by evaluating both integration strategies on the same Zynq-7000 SoC, with identical clock frequency, processing element, and workload characteristics. This controlled approach enables an application-independent assessment of latency–resource trade-offs and provides practical design guidelines for selecting PS–PL integration strategies based on whether an application prioritizes throughput or low-latency response.

Finally, Berrazueta-Mena and Navas [17] evaluated multiple compute-intensive hardware accelerators on Zynq-based SoCs using an HLS-driven design flow, highlighting performance–resource trade-offs in heterogeneous FPGA-based systems. Their work demonstrates the effectiveness of AXI-based accelerator integration and provides a comprehensive benchmarking framework for Zynq platforms. However, their study relies primarily on AXI-based communication and does not explicitly compare DMA-driven streaming with BRAM-based memory-mapped integration under identical conditions. The present work complements this limitation by focusing explicitly on PS–PL communication mechanisms and their impact on latency and resource utilization, thereby extending existing benchmarking-oriented studies toward communication-aware design analysis.

3. System Design and Methodology

3.1. Overall design flow

The study was conducted on the Xilinx Zynq-7000 SoC platform, utilizing both the PS and PL to implement and test the hardware accelerators. A custom PE was designed to perform basic arithmetic operations (addition, subtraction, and multiplication). The primary distinction between the two approaches lies in how data is transferred and buffered between the PS and PL.

In the BRAM-based design, shown in Figure 1, data exchange between the PS and PL is managed through dual-port block memories accessed via AXI BRAM controllers. The design begins with a BRAM A input, which stores 32-bit data values. These inputs are transferred to the input registers, where operands a, b, and y_in are organized and aligned for arithmetic operations. The PE, specifically developed to support addition, subtraction, and multiply–accumulate operations, performs the core computations. A controller based on a finite state machine (FSM) coordinates the overall flow by generating addresses, managing counters, and signaling data readiness. To guarantee proper synchronization, a start-edge detection module ensures accurate triggering through rising-edge signals. After computation, results are stored in the output register in signed 8-bit format. A sign-extension stage then scales the results to 32-bit to match the BRAM data width, after which the processed values are written into the BRAM output module for efficient storage and later retrieval. This modular organization demonstrates the efficiency of the BRAM-based approach, which minimizes latency by enabling direct operand access while preserving low control complexity.

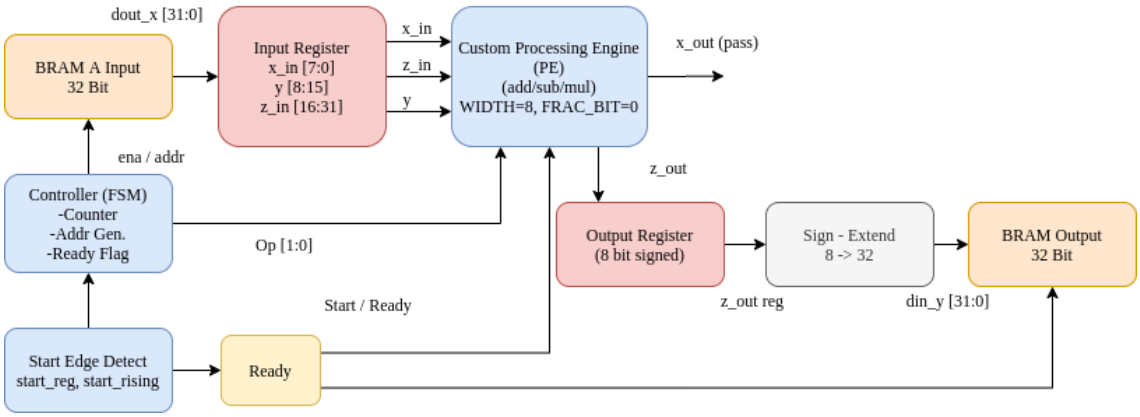


Figure 1. BRAM-based block design for data transfer and buffering between PS and PE

By contrast, the AXI-DMA-based design, illustrated in Figure 2, utilizes direct memory access to transfer data between the PS and PL. In this architecture, the PE is wrapped in an AXI-Stream AXIS interface, where inputs *x_in*, *y*, and *z_in* are received via the slave port and the computed result z_*out* is sent through the master port. The AXI DMA IP handles conversion between memory-mapped transactions (in DDR or other PS memory) and streaming transactions in the PL.

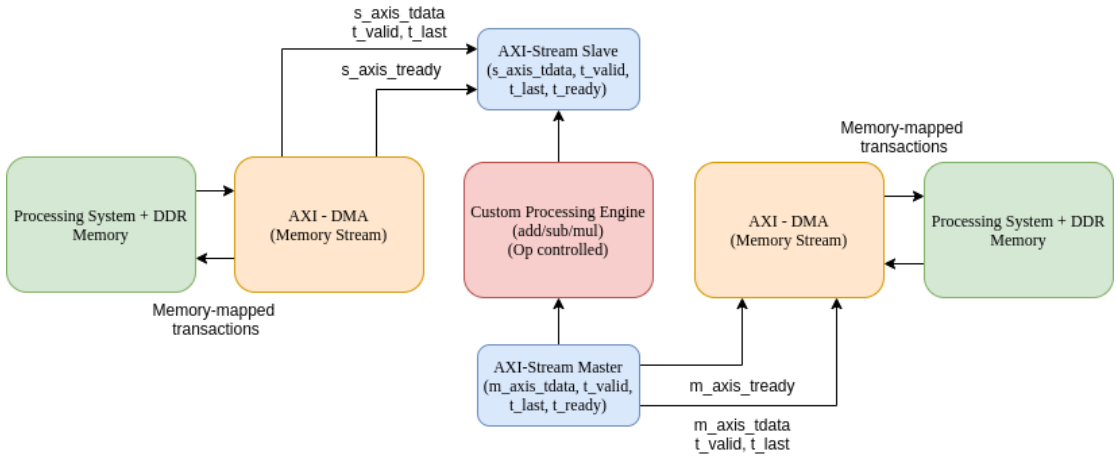


Figure 2. AXI-DMA-based integration architecture with AXI-Stream slave and master interfaces for data transfer between PS and PE

Control and data signals such as *tdata*, *tready*, *tvalid*, and *tlast* participate in protocol handshaking to ensure correct streaming operation. The PS initiates transfers via the AXI DMA, specifying source and destination addresses; DMA moves chunks of data without CPU intervention. This design introduces additional control logic compared to the BRAM-based approach but offers higher throughput and scalability, especially for continuous or burst data streaming.

3.2. AXI-DMA based architecture

In the AXI DMA-based design, data transfer between the PS and the PL is handled through the AXI4-Stream interface, coordinated by the DMA engine. This integration allows operands stored in DDR memory to be efficiently streamed into the custom PE, with results written back to memory via the same mechanism. The PE is implemented as a custom RTL VHDL module, synthesized separately, and packaged as an IP core before being integrated into the block design. The system was created in Vivado Design Suite 2022.1, leveraging the IP Integrator for block-level composition. The Zynq-7000 Processing System block provides the ARM Cortex-A9 subsystem with DDR and peripheral interfaces. An AXI DMA IP core is connected through an AXI Interconnect to enable memory-mapped transactions between DDR and the accelerator. The

axis_pe_0 block, representing the custom PE, is connected to the streaming ports of the DMA (M_AXIS_MM2S for data input and S_AXIS_S2MM for data output). Additionally, AXI GPIO modules were included to configure operation modes (addition, subtraction, multiplication) and control accelerator execution. Reset and clock signals are distributed via the Processor System Reset and FCLK outputs of the PS. The resulting block design, shown in Figure 3, demonstrates the complete AXI DMA-based integration. Here, the PS communicates with the DMA through GP master ports, while high-performance (HP) ports are employed for data movement. The interconnect fabric handles arbitration between master and slave interfaces, ensuring seamless communication between the PS memory subsystem and the accelerator.

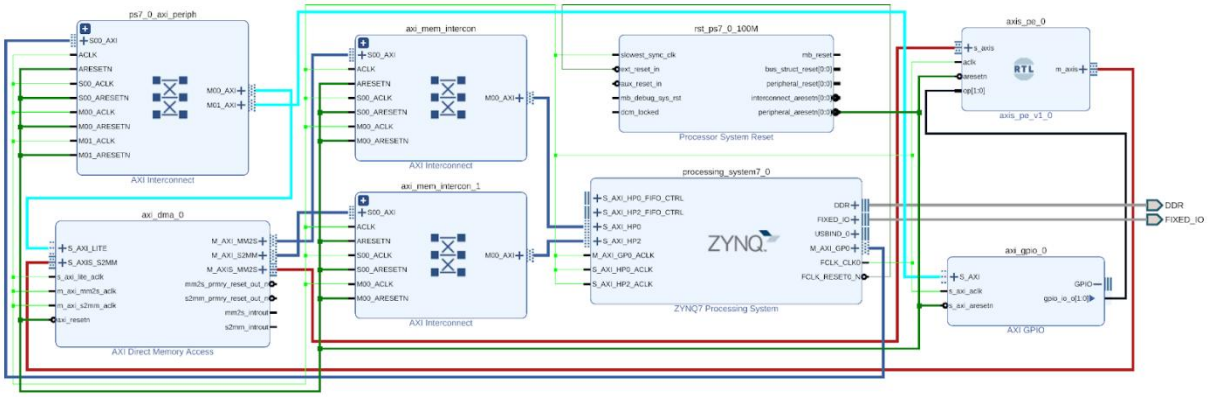


Figure 3. Custom block design of the AXI DMA-based architecture

3.3. BRAM based architecture

The BRAM-based design utilizes dual-port BRAMs interconnected via AXI BRAM controllers. This setup enables direct memory-mapped access for reading and writing operands. The PE is connected directly to BRAMs, eliminating the overhead of streaming interfaces. This architecture is particularly effective for applications where low latency is critical and data size is relatively small. As illustrated in Figure 4, the BRAM-based design enables direct operand access through on-chip block memories with minimal interface complexity.

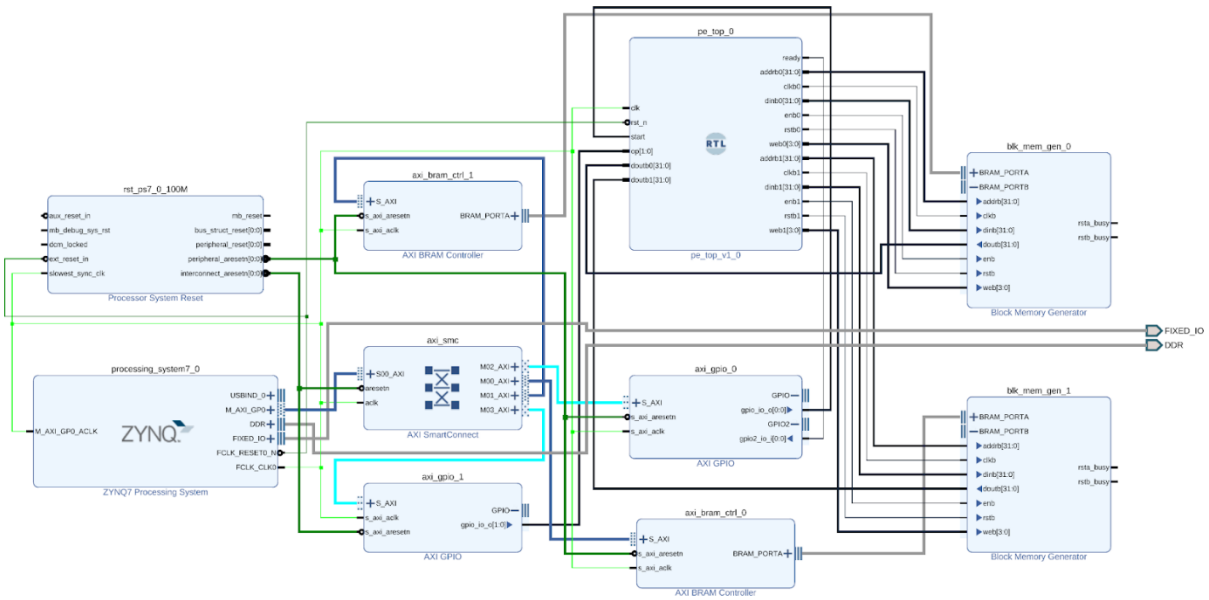


Figure 4. Custom block design of the BRAM-based architecture

3.4. Processing engine (PE)

In both architectures, the core computational unit is a custom PE implemented in VHDL and integrated into the PL. The PE supports three arithmetic operations: addition, subtraction, and multiplication. The desired operation is selected through a 2-bit control signal (op), while two 32-bit operands are provided as inputs. The computed result is then delivered to the output interface, which connects either to the AXI-DMA stream or to the BRAM controller, depending on the architecture. As illustrated in Figure 5, the PE design consists of two operand inputs, an operation selector, and a single result output. The simplicity of this structure ensures minimal hardware overhead while maintaining flexibility in executing different arithmetic tasks.

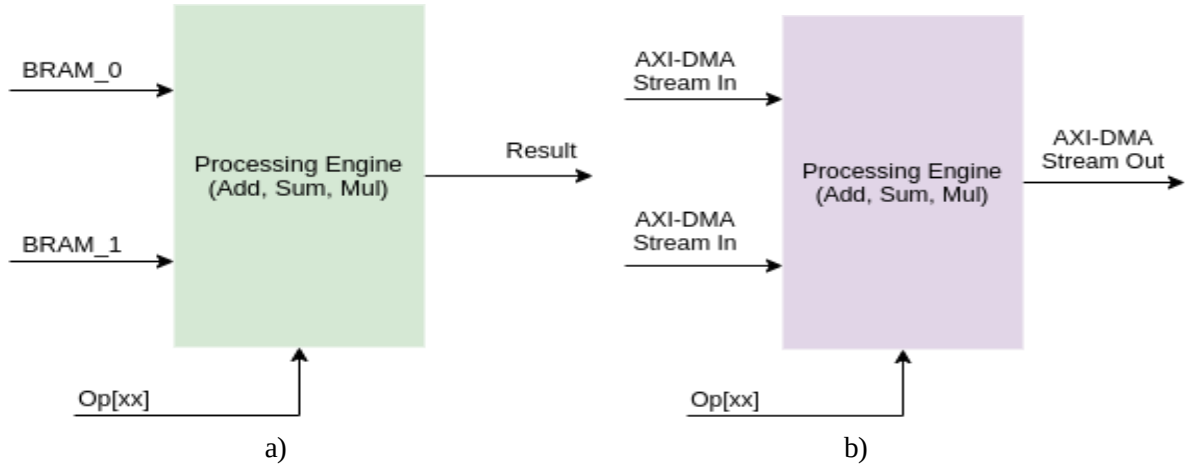


Figure 5. PE structure. a) BRAM-Based PE, b) AXI-DMA-based PE

4. Implementation Details

4.1. Development environment

Both architectures were implemented and tested on the Xilinx Pynq-Z1 development board, which is based on the Zynq-7000 SoC (XC7Z020-1CLG400C). The designs were created using the Vivado Design Suite, with block diagrams generated through the IP integrator. The PE was developed in HDL and integrated as a custom IP core. For software-side control, C/C++ programs were executed on the ARM Cortex-A9 processor within the PS.

4.2. Hardware design integration

The two integration strategies were realized as complete hardware systems. In the AXI DMA-based design, the DMA engine was configured to stream data between DDR memory and the PE via AXI4-Stream connections, as shown in Figure 1. In the BRAM-based design, dual-port block memories were connected to the PE through AXI BRAM controllers, allowing direct operand access, as illustrated in Figure 2. Both systems included GPIO modules for basic control and status monitoring.

4.3. PE implementation

The PE, illustrated in Figure 5, was designed to provide basic arithmetic functionality with minimal hardware overhead while adapting to two different integration strategies. In both cases, the PE accepts 32-bit input words containing operands *a* and *b*, together with an operation code that selects addition, subtraction, or multiplication. Computation is performed in a single clock cycle, and results are written back to the system through either block memories or streaming interfaces, depending on the surrounding architecture.

Algorithm 1: Pseudo-code for BRAM-based PE

```
initialize FSM, counters, and BRAM addresses
loop:
    read operand_a, operand_b, and y_in from BRAM input registers
    latch operands into PE registers
    case (op):
        00 -> result := operand_a + operand_b
        01 -> result := operand_a - operand_b
        10 -> result := operand_a * operand_b
    end case
    extend result from 8 bits to 32 bits
    write result to BRAM output register
    update FSM and counters
end loop
```

In the BRAM-based design, operands are fetched from dual-port block RAMs via AXI BRAM controllers. A finite-state machine supervises address generation, counters, and read/write sequencing, ensuring that operands are correctly aligned before being latched into the datapath. The step-by-step execution of this process is outlined in *Pseudo-code 1*. Arithmetic results are produced in 8-bit format, extended to 32 bits for consistency with the BRAM interface, and written back to memory through output registers. This scheme achieves deterministic operation with low latency by enabling direct operand access without streaming overhead.

Algorithm 2: Pseudo-code for AXI-DMA-based PE

```
loop:
    wait until s_axis_tvalid = '1' and s_axis_tready = '1'
    latch input_word from s_axis_tdata
    extract operand_a, operand_b, and op from input_word
    case (op):
        00 -> result := operand_a + operand_b
        01 -> result := operand_a - operand_b
        10 -> result := operand_a * operand_b
    end case
    store result in result_reg
    set m_axis_tdata := result_reg
    assert m_axis_tvalid
    if m_axis_tready = '1':
        send result word to DMA
        deassert m_axis_tvalid
end loop
```

In the AXI-DMA-based integration, data are transferred between PS memory and the PE through AXI DMA, which converts memory-mapped transactions into AXI4-Stream transfers. Input words arrive at the s_axis interface along with handshake signals (tvalid, tready, tlast), and the corresponding execution steps are summarized in *Pseudo-code 2*. The PE extracts operands from the input word, executes the specified operation in one cycle, and forwards the result through the m_axis interface. Output handshake signals ensure that results are delivered only when the downstream path is ready, while a lightweight buffer prevents data loss during backpressure. This design supports high-throughput streaming with near one-word-per-cycle performance under ideal conditions.

Through these two integration strategies, the same arithmetic kernel can operate either as a memory-centric accelerator or as a stream-oriented processing element. While the BRAM-based organization emphasizes direct access and minimal latency, the AXI-DMA-based version enhances scalability and throughput, thus demonstrating the flexibility of the PE within heterogeneous SoC-FPGA platforms.

4.4. Resource utilization

After the implementation, resource utilization reports were examined for both architectures. Each design fits well within the available resources of the XC7Z020 device. The AXI DMA-based system, however, showed a modest increase in utilization, mainly due to the added interconnect and DMA control logic. This overhead was reflected in higher LUT, FF, and BRAM usage when compared with the BRAM-based alternative. DSP consumption remained identical across both implementations, as the same arithmetic unit was employed in each case. Table 1 summarizes these results, making clear the additional cost of integrating AXI DMA.

Table 1. Resource utilization comparison between AXI DMA and BRAM-based designs

Resource	Available	AXI-DMA based Utilization	Utilization (%)	BRAM-based Utilization	Utilization (%)
LUT	53200	5804	10.91	2354	4.42
LutRAM	17400	861	4.95	202	1.16
FFs	106400	5950	5.59	3186	2.99
BRAM	140	4	2.86	2	1.43
BUFG	32	1	3.13	1	3.13
Power (W)	-	1.466	-	1.408	-

4.5. Experimental setup

The experimental evaluation was carried out on a Pynq-Z1 development board, which integrates a Xilinx Zynq-7000 SoC (XC7Z020) comprising a dual-core ARM Cortex-A9 PS and a PL. The board was connected to a host computer via USB and Ethernet interfaces for programming, configuration, and data exchange. The PS executed C/C++ control software that managed data transfers, triggered the accelerators, and measured execution times.

For both AXI-DMA and BRAM-based designs, identical test conditions were applied to ensure a fair comparison. Input operands were generated and stored in PS memory, and the accelerator was invoked through memory-mapped control registers. In the AXI-DMA-based system, data blocks were transferred between DDR memory and the PE using the AXI DMA engine, while in the BRAM-based system, operands and results were accessed directly through dual-port BRAMs via AXI BRAM controllers.

Each experiment consisted of 100 consecutive iterations of arithmetic operations, including addition, subtraction, and multiplication. The ARM Cortex-A9 timer registers were used to measure the execution time from the moment the accelerator was triggered until the final result was written back to memory. To minimize measurement noise, the results were averaged over all iterations.

Figure 6 illustrates the physical experimental setup, showing the Pynq-Z1 board connected to the host computer. This setup demonstrates the complete hardware–software co-design environment, in which the PS manages data movement and control. At the same time, the PL executes the hardware-accelerated arithmetic operations in real time.

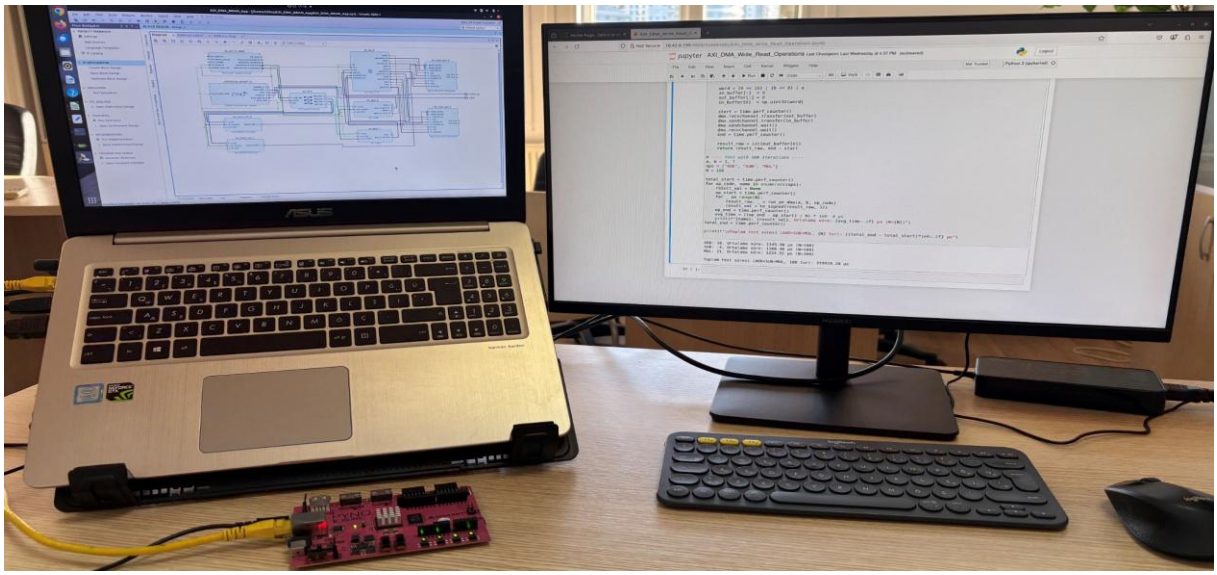


Figure 6. Experimental setup showing the Pynq-Z1 development board connected to the host computer via USB and Ethernet. The ARM-based PS executes the control software and manages data transfers. At the same time, the PL runs the hardware accelerator using either AXI-DMA or BRAM-based integration

5. Performance Evaluation

The performance of both architectures was evaluated on the Pynq-Z1 development board using 100 consecutive iterations of arithmetic operations. The test program, executed on the ARM Cortex-A9 processing system, initialized the operands, triggered the accelerator, and collected timing results. Latency measurements were obtained using ARM-side cycle counters, capturing the total time elapsed from accelerator invocation to result availability in memory. All reported results represent average values over the 100 iterations, reducing the impact of transient effects and ensuring statistically meaningful and reliable performance comparison.

This evaluation methodology allows the communication and control overhead between the PS and PL to be directly reflected in the measured latency, making it well suited for comparing different integration strategies under identical experimental conditions.

.

5.1. Average latency results

The measurements reveal a clear and consistent difference in execution time between the two integration strategies. In the AXI-DMA-based design, the average operation time across all three arithmetic functions (addition, subtraction, and multiplication) was approximately 1.19 ms per iteration. In contrast, the BRAM-based design achieved an average latency of approximately 0.10 ms per iteration.

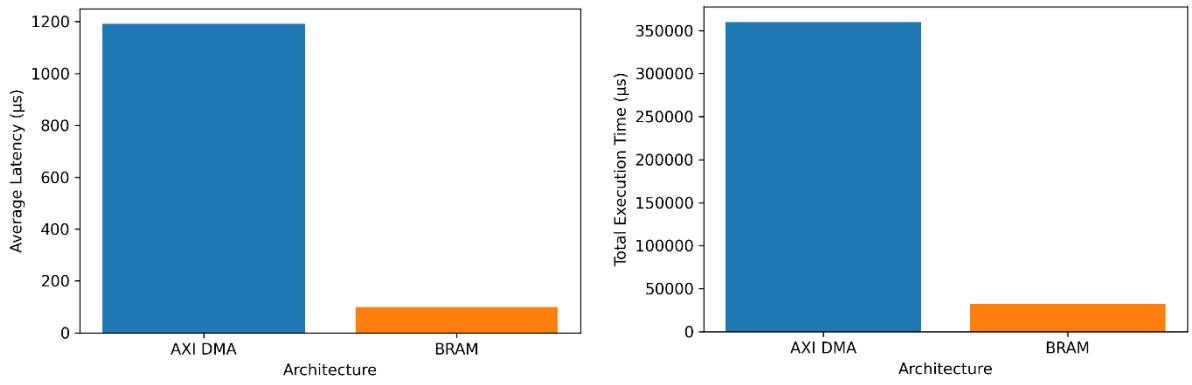
Table 2 summarizes the average latency per operation and the total execution time over 100 iterations for both architectures. The results indicate that the BRAM-based approach reduces the total execution time from 359,919 µs to 32,487 µs, corresponding to more than an order-of-magnitude improvement in latency.

Table 2. Average latency and total execution time over 100 iterations for AXI-DMA and BRAM-based designs

Metric	**AXI-DMA Design**	**BRAM based Design**
Average latency per operation (µs)	~1190.97	~99.79
Total execution time (100 iterations, µs)	359,919.28	32,486.85

To better illustrate this performance gap, Figure 7 presents the experimental results in two forms: (a) average latency per operation and (b) total execution time over 100 iterations. The results clearly demonstrate that

BRAM-based integration significantly outperforms the AXI-DMA-based approach in latency-critical scenarios.



a) b)

Figure 7. Performance comparison between AXI-DMA and BRAM-based designs a) Average latency per operation, b) Total execution time for 100 iterations

6. Discussion of results

The experimental results highlight a fundamental trade-off between AXI-DMA-based and BRAM-based integration strategies in SoC-FPGA platforms. Although both architectures employ the same processing element and operate at the same clock frequency and under identical experimental conditions, their performance characteristics differ substantially due to their data transfer and buffering mechanisms.

The AXI-DMA-based design introduces noticeable communication overhead, resulting in an average latency of approximately 1.19 ms per operation. This overhead arises from several factors, including DMA configuration, memory-to-stream and stream-to-memory transactions, buffer descriptor handling, and AXI protocol handshaking. While these mechanisms enable high throughput and scalability for large data blocks and continuous streaming workloads, they introduce a fixed per-transaction cost that becomes dominant in short, iterative, or latency-sensitive computations.

In contrast, the BRAM-based design achieves a much lower average latency of approximately 0.10 ms per operation. This more than tenfold reduction is primarily attributed to the use of on-chip block memories and direct memory-mapped access, which eliminates the need for DMA setup and streaming handshakes. By allowing the processing element to access operands and store results directly in BRAM, the communication path becomes shorter, simpler, and more deterministic, leading to reduced execution time and lower latency variability.

Resource utilization results further reinforce this observation. The AXI-DMA-based architecture consumes significantly more LUTs, flip-flops, and BRAM resources due to the inclusion of the DMA engine, AXI interconnects, and streaming interfaces. Although this additional hardware provides flexibility and scalability, it increases design complexity and hardware cost. In contrast, the BRAM-based design minimizes control logic and interface overhead, resulting in both lower latency and reduced resource consumption.

Overall, the results indicate that AXI-DMA-based integration is well-suited for throughput-oriented and continuous data-streaming applications, where the communication overhead can be amortized across large data transfers. Conversely, BRAM-based integration is more efficient for small-scale, low-latency, and iterative workloads, where fast response time and deterministic behavior are critical. Therefore, the selection of the integration strategy should be guided by application requirements, particularly the trade-off between throughput scalability and latency sensitivity.

7. Conclusion and Future Work

This paper presented a comparative study of AXI DMA- and BRAM-based accelerator integration on the Xilinx Zynq-7000 SoC. A custom processing element was implemented in both architectures, and the designs were evaluated in terms of resource utilization and performance. The results show that while AXI DMA offers flexibility and scalability for continuous data streaming, BRAM-based integration achieves substantially lower latency and requires fewer hardware resources. The BRAM-based approach achieved over an 11-fold speedup compared to AXI DMA in the tested arithmetic operations.
The contributions of this work are threefold: (1) a detailed implementation of both integration strategies on the same SoC platform, (2) quantitative resource and performance evaluation, and (3) design insights into the trade-offs between throughput-oriented and latency-oriented accelerator architectures.
For future work, several directions can be pursued. First, more complex processing elements could be integrated to evaluate how these strategies scale with increased computational demands. Second, benchmarking with application-level workloads (e.g., digital filters, matrix multiplications, or neural network layers) would provide a broader view of practical performance. Finally, extending the evaluation to include energy consumption and thermal behavior would strengthen the design guidelines for power-sensitive embedded systems.

8. Author Contribution Statement

This study was carried out entirely by a single author. The author contributed to all stages of the work, including developing the research idea, designing the architectures, implementing the systems, collecting and analyzing data, reviewing the relevant literature, and preparing and critically revising the manuscript. No other individuals or institutions contributed to the study.

9. Ethics Committee Approval and Conflict of Interest

“There is no need for an ethics committee approval in the prepared article”
“There is no conflict of interest with any person/institution in the prepared article”

10. Ethical Statement Regarding the Use of Artificial Intelligence

No artificial intelligence-based tools or applications were used in the preparation of this study. The entire content of the study was produced by the author in accordance with scientific research methods and academic ethical principles.

11. References

[1] A. Rios-Navarro, R. Tapiador-Morales, A. Jimenez-Fernandez, M. Dominguez-Morales, C. Amaya, and A. Linares-Barranco, "Performance evaluation over HW/SW co-design SoC memory transfers for a CNN accelerator," *J. Signal Process. Syst.*, vol. 91, no. 9, pp. 999–1012, Sep. 2019.

[2] G. Tatar, S. Bayar, and İ. Çiçek, "Real-time multi-learning deep neural network on an MPSoC-FPGA for intelligent vehicles: Harnessing hardware acceleration with pipeline," *IEEE Trans. Intell. Veh.*, vol. 9, no. 6, pp. 5021–5032, Jun. 2024.

[3] Y. Hao and S. Quigley, "The implementation of a deep recurrent neural network language model on a Xilinx FPGA," in *Appl. Reconfigurable Comput.*, vol. 10216, pp. 67–78, 2017.

[4] G. Tatar and S. Bayar, "Real-time multi-task ADAS implementation on reconfigurable heterogeneous MPSoC architecture," *IEEE Access*, vol. 11, pp. 80741–80760, 2023.

[5] Y. Wang, Z. Li, and H. Liang, "Scatter-gather DMA performance analysis within an SoC FPGA platform," *ACM Trans. Reconfigurable Technol. Syst.*, vol. 17, no. 2, pp. 1–20, Apr. 2024.

[6] H. Cılasun, "FPGA-accelerated simulation of variable latency memory for hardware/software co-design," *ACM Trans. Des. Autom. Electron. Syst.*, vol. 28, no. 1, pp. 1–26, Jan. 2023.

[7] G. Tatar *et al*., "Recent advances in machine learning based advanced driver assistance system applications," *Microprocess. Microsyst.*, vol. 110, p. 105101, 2024.

[8] J. Johnson, "Using the AXI DMA in Vivado," *FPGA Developer*, Aug. 2014.

[9] K. Guerrero-Morejón, A. K. Bhattacharjee, and D. Atienza, "Embedded streaming hardware accelerators interconnect architectures and latency evaluation," *Electron.*, vol. 14, no. 8, p. 1513, Apr. 2025.

[10] D. A. Jiménez-González, J. M. Arnau, and A. González, "Programmable FPGA-based memory controller: Evaluation of resource utilization and performance trade-offs," in *Proc. Int. Conf. Field-Programmable Logic Appl. (FPL)*, Sep. 2021.

[11] E. Canto-Navarro, M. López-García, J. Font-Suñer, *et al*., "AXI hardware accelerator for McEliece on FPGA," *IEEE Trans. Dependable Secure Comput.*, vol. 22, no. 2, pp. 1–14, Feb. 2025.

[12] J. Boudjadar, "Dynamic FPGA reconfiguration for scalable embedded convolutional neural networks," *Future Gener. Comput. Syst.*, vol. 157, pp. 45–61, 2025.

[13] B. Kieu-Do-Nguyen, N. T. Binh, C. Pham-Quoc, H. P. Nghi, N.-T. Tran, T.-T. Hoang, and C.-K. Pham, "Compact and low-latency FPGA-based number theoretic transform architecture for CRYSTALS Kyber post-quantum cryptography scheme," *Information*, vol. 15, no. 7, Art. no. 400, 2024.

[14] P. Arya and S. H. Mokashi, "FPGA-accelerated RISC-V ISA extensions for efficient neural network inference on edge devices," arXiv preprint, 2025.

[15] N. Irtija, J. Plusquellic, E. E. Tsiropoulou, J. Goldberg, D. Lobser, and D. Stick, "Design and analysis of digital communication within an SoC-based control system for trapped-ion quantum computing," *IEEE Trans. Quantum Eng.*, vol. 4, pp. 1–24, Art. no. 5500124, 2023.

[16] C.-T. Axinte, A. Stan, and V.-I. Manta, "Embedded streaming hardware accelerators interconnect architectures and latency evaluation," *Electron.*, vol. 14, no. 8, p. 1513, 2025.

[17] D. Berrazueta-Mena and B. Navas, "AHA: Design and evaluation of compute-intensive hardware accelerators for AMD-Xilinx Zynq SoCs using HLS IP flow," *Computers*, vol. 14, no. 5, p. 189, 2025.

Fırat Üniversitesi Deneysel ve Hesaplamalı Mühendislik Dergisi

FUJECE

Elektrikli Araçlar için Gerçek Trafik Bilgilerini Dikkate Alan Dinamik Fiyatlandırma Tabanlı Enerji Yönetim Modeli

Muhammed Sefa ÇETİN[1]*, Muhsin Tunay GENÇOĞLU[2], İlhan AYDIN[3], Ozan ERDİNÇ[4], Ayşe Kübra ERENOĞLU TATAR[5], Habip SAHIN[6]

[1,2]Elektrik-Elektronik Mühendisliği Bölümü, Mühendislik Fakültesi, Fırat Üniversitesi, Elazığ, Türkiye.
[3]Bilgisayar Mühendisliği Bölümü, Mühendislik Fakültesi, Fırat Üniversitesi, Elazığ, Türkiye.
[4,5]Elektrik Mühendisliği Bölümü, Elektrik-Elektronik Fakültesi, Yıldız Teknik Üniversitesi, İstanbul, Türkiye.
[6]Elektrik ve Enerji Bölümü, Teknik Bilimler Meslek Yüksekokulu, Fırat Üniversitesi, Elazığ, Türkiye.

[1]mscetin@firat.edu.tr, [2]mtgencoglu@firat.edu.tr, [3]iaydin@firat.edu.tr, [4]oerdinc@yildiz.edu.tr, [5]erenayse@yildiz.edu.tr, [6]habipsahin@firat.edu.tr

Geliş Tarihi: 23.11.2025
Düzeltme Tarihi: 29.12.2025
doi: https://doi.org/10.62520/fujece.1828913
Kabul Tarihi: 24.1.2026
Araştırma Makalesi

Alıntı: M. S. Çetin, M. T. Gençoğlu, İ. Aydın, O. Erdinç, A.K. Tatar ve H. Şahin, "Elektrikli araçlar için gerçek trafik bilgilerini dikkate alan dinamik fiyatlandırma tabanlı enerji yönetim modeli", Fırat Üni. Deny. Müh. Derg., vol. 5, no 1, pp. 330-344, Şubat 2026.

Özet

Elektrikli araçların kullanımının yaygınlaşmasıyla birlikte artan şarj talebi, elektrik dağıtım şebekesinde yük dengesizliği, ani yük değişimleri, harmonikler ve gerilim dalgalanmaları gibi negatif etkilere yol açmaktadır. Ayrıca şarj talebinin düzensiz olması elektrikli araç kullanıcı konforunu ve trafik yönetimini de etkileyen negatif bir durumdur. Bu çalışmada, bu negatif durumları ortadan kaldırmak amacıyla şehir içi elektrikli araç şarj altyapısında kullanılmak üzere geliştirilen dinamik fiyatlandırma tabanlı bir enerji yönetim modeli sunulmaktadır. Bu bağlamda önerilen model, fiyatı yalnızca ekonomik bir çıktı olarak değil aynı zamanda şebeke yük dengesini yönlendiren bir kontrol değişkeni olarak ele almaktadır. Modelde dört temel giriş parametresi (trafik, istasyon doluluk oranı, konum ve araç şarj seviyesi) vardır ve her iterasyonda dinamik bir şekilde güncellenmektedir. MATLAB ortamında geliştirilen model, Google Maps API aracılığıyla elde edilen gerçek trafik verileriyle desteklenmiş ve on iterasyon boyunca test edilmiştir. Sonuçlar, geliştirilen modelin düşük şarj seviyesine sahip araçları önceliklendirdiğini ancak bunu yaparken de şebeke yükünü dengeli biçimde gözettiğini göstermektedir. Ayrıca, yüksek doluluk oranına sahip istasyonlarda fiyat artışı gözlenmiş ve bu durumda kullanıcıların daha düşük doluluk oranına sahip istasyonlara teşvik edildiği görülmüştür. Çalışma, fiyatlandırmanın yalnızca ekonomik değil aynı zamanda sistemsel verimlilik açısından da bir karar değişkeni olarak kullanılabileceğini ortaya koymaktadır. Gelecek çalışmalarda model, yapay zekâ ve optimizasyon tabanlı yöntemlerle genişletilebilme ve test sistemleri yardımıyla enerji ve ulaşım sistemlerindeki problemlere çözüm olarak kullanılabilme potansiyeline sahiptir.

Anahtar kelimeler: Elektrikli araçlar, Dinamik fiyatlandırma, Enerji yönetimi, Şebeke, Ulaşım sistemleri

*Yazışılan yazar

İntihal Kontrol: Evet – Turnitin
Şikayet: fujece@firat.edu.tr
Telif Hakkı ve Lisans: Dergide yayın yapan yazarlar, CC BY-NC 4.0 kapsamında lisanslanan çalışmalarının telif hakkını saklı tutar.

Firat University Journal of Experimental and Computational Engineering

Dynamic Pricing-Based Energy Management Model for Electric Vehicles Considering Real Traffic Information

Muhammed Sefa ÇETİN[1]*, Muhsin Tunay GENÇOĞLU[2], İlhan AYDIN[3], Ozan ERDİNÇ[4], Ayşe Kübra ERENOĞLU TATAR[5], Habip SAHIN[6]

[1,2] Department of Electrical-Electronics Engineering, Faculty of Engineering, Fırat University, Elazığ, Türkiye.
[3] Computer Engineering, Faculty of Engineering, Fırat University, Elazığ, Türkiye.
[4,5] Department of Electrical Engineering, Electrical and Electronics Faculty, Yıldız Technical University, İstanbul, Türkiye.
[6]Department of Electricity and Energy, Vocational School of Technical Sciences, Fırat University, Elazığ, Türkiye.

[1]mscetin@firat.edu.tr, [2]mtgencoglu@firat.edu.tr, [3]iaydin@firat.edu.tr, [4]oerdinc@yildiz.edu.tr, [5]erenayse@yildiz.edu.tr, [6]habipsahin@firat.edu.tr

Received: 23.11.2025
Revision: 29.12.2025
Accepted:24.1.2026
doi: https://doi.org/10.62520/fujece.1828913
Research Article

Citation: M. S. Çetin, M. T. Gençoğlu, İ. Aydın, O. Erdinç, A.K. Tatar and H. Şahin, "Dynamic pricing-based energy management model for electric vehicles considering real traffic ınformation", Firat Univ. Jour.of Exper. and Comp. Eng., vol. 5, no 1, pp. 330-344, February 2026.

Abstract

Increasing charging demand with the widespread use of electric vehicles leads to negative effects such as load imbalance, sudden load changes, harmonics and voltage fluctuations in the electricity distribution network. Furthermore, irregular charging demand negatively impacts electric vehicle user comfort and traffic management. This study presents a dynamic pricing-based energy management model developed for use in urban electric vehicle charging infrastructures to address these challenges. The proposed model considers price not only as an economic output but also as a control variable that manages grid load balance. There are four input parameters (traffic, station occupancy rate, location and state of charge) in the pricing model and these parameters are dynamically updated at each iteration. The model was developed in MATLAB environment and was employed real-time traffic data obtained through the Google Maps API. The model tested for ten iterations. The results show that the pricing model prioritizes low charge levels vehicles. But the model maintaining balanced grid load simultaneously. Furthermore, price output increases high occupancy rates charging stations in order to encourage users to choose stations with lower occupancy rates. Results of this study demonstrates that pricing mechanism can be used as a decision variable both economic reasons and system efficiency. In future works, the model might be extended with artificial intelligence and optimization-based methods. Pricing model serves as a potential solution to challenges in energy and transportation networks with the help of test systems.

Keywords: Electric vehicles, Dynamic pricing, Energy management, Grid, Transportation systems

*Corresponging author

Plagiarism Checks: Yes – Turnitin
Complaints: fujece@firat.edu.tr
Copyright & License: Authors publishing with the journal retain the copyright to their work licensed under the CC BY-NC 4.0

1. Introduction

The widespread adoption of electric vehicles (EVs) presents a significant opportunity for the development of sustainable and environmentally friendly transportation systems [1,2]. EVs reduce greenhouse gas emissions and reliance on fossil fuels and they contribute to environmental sustainability by increasing energy efficiency [3,4]. However, there is a quick transition to EV usage in recent years and this has led to increases in energy demand which negatively impacting distribution systems [5,6]. Although the charging infrastructure has been improving recently, the capacity of charging stations remains insufficient to handle the growing EV charging load especially in urban areas [7]. According to the official statistics published by the Energy Market Regulatory Authority (EPDK), as of July 2025 there are 32,682 publicly accessible EV charging sockets in Türkiye, while the total number of registered EVs has reached 291,775, highlighting the increasing pressure on charging station capacity despite the rapid expansion of the infrastructure. [8]. EV charging load can cause technical challenges on the distribution grid such as sudden load changes, harmonics and voltage fluctuations [9-11]. This situation is negatively affecting not only the stability of energy systems but also traffic management systems and user satisfaction [12,13].

The charging load management of EVs is important research area for energy and transportation systems [14,15]. In recent years, studies in the literature focus on several key strategies including charging scheduling algorithms [16,17], routing algorithms [18,19], smart grid-based strategies [20,21], charging demand [22,23] and dynamic pricing mechanisms [24,25]. These strategies are using in order to balance power grid load with affecting EV user behavior in the peak energy demand periods. Dynamic pricing methods is one of the most effective approaches among these key strategies because it integrates variables such as real-time traffic, charging station occupancy rate, locations of station and vehicle and state of charge (SoC) into the pricing process [26]. Dynamic pricing strategy works as a mechanism to both guide user behavior and support grid load balance by managing energy demand and grid load according to real-time conditions [27,28].

In this study, a dynamic pricing-based energy management model was developed. Model evaluates input parameters such as traffic, station occupancy rate, location and SoC. Main purpose of the model is to optimize EV user comfort and the grid balancing objectives of the DSO. In this regard, price parameter is considered both economic outcome and control variable that affects system balance. The model was developed in MATLAB environment. Tests has been made in a simulation-based environment and optimization or artificial intelligence methods were not used. The purpose at this point was show both the basic operation of the price estimation mechanism and the interaction between variables. The model was executed under simple scenarios in order to show the logical consistency of the dynamic pricing system. The model's strong sides are its ability to work with real-time traffic data which received from the Google Maps API and the dynamically changing input parameters. At each iteration traffic, station occupancy rate, location and SoC parameter are dynamically updating and this allow the system to reflect real-time urban conditions.

Although multi parameter pricing models considering factors such as traffic, distance, occupancy and SoC have been investigated in the literature, the proposed model stands out in two main aspects. First, real-time traffic and distance information are directly obtained from the Google Maps API, enabling the pricing mechanism to reflect actual urban mobility conditions rather than synthetic or static data. Second, the price is treated not only as an economic output but also as a control variable to influence charging demand distribution among stations. These allow the model to operate dynamically updated energy management mechanism for urban EV charging infrastructures.

The model aims to balance EV charging demand and load on the distribution grid with the help of dynamic pricing algorithm. Structure of the model, key assumptions and parameters are presented in the Material and Methods section. Performance of the model are evaluated in detail and effects of input parameters on pricing outcomes are presented in the Results and Discussion section. Finally, findings are presented and overall assessment is provided and possible future works (in order to develop model with optimization and artificial intelligence methods) are discussed in the Conclusion section.

2. Material and Methods

In this study, a dynamic pricing-based energy management mechanism was developed for use in urban EV charging infrastructures. The model was designed to simultaneously consider both EV user comfort and the DSO's grid-balancing objectives. In order to achieve this, a real-time model was created in which the input parameters (traffic, station occupancy rate, location and SoC) are dynamically updated, while the output parameter is price.

The model was developed in MATLAB and all calculations, data flow and iterative updates were conducted on this platform. The MATLAB license provided by Fırat University was used. No optimization algorithms or artificial intelligence-based methods were used during model creation or price estimation. MATLAB was chosen due to its flexibility in simulating and numerically modeling multivariable systems. In this study, MATLAB was used both to integrate real-world traffic and location data from the Google Maps API into the system and to calculate dynamically updated parameters at each iteration. As a result, the system extends beyond a random simulation and gain a real-time, data-driven structure.

In the Dynamic Pricing-Based Energy Management Model subsection, the structure of the system, its iterative working principle, interaction with traffic data and the role of price as a control variable are explained. The Model Assumptions section describes elements such as time definition, traffic and charging dynamics, station occupancy rate and system constraints. Finally, the Model Parameters subsection details the influence of each variable on pricing and explains the general operation of the price estimation mechanism. This structure enables the model operates by both monitoring dynamically changing urban transportation conditions and adjusting the load balance of charging stations based on price. Thus, the proposed system has the potential to work as a dynamic, dual-purpose decision support mechanism based on real-time traffic data.

Dynamic pricing-based energy management model

The dynamic pricing-based energy management model developed in this study provides a multi-criteria decision support mechanism designed for urban EV charging infrastructures. The model simultaneously considers both EV user comfort and the DSO's grid-balancing objectives. The input parameters of the model are traffic, station occupancy rate, location and SoC, while the output parameter is price. The structure of the dynamic pricing-based energy management model is presented in Figure 1. The main objective of the model is to develop a real-time price estimation mechanism that enables dynamic evaluation of charging demand based on time-dependent variables. In this approach, price is considered both an economic parameter and control variable that manages the charging load.

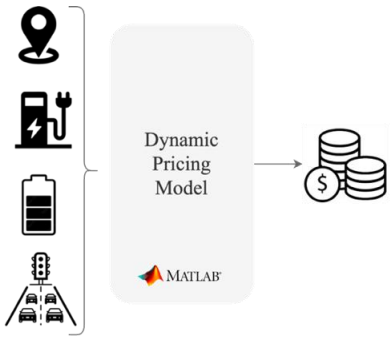


Figure 1. Structure of the dynamic pricing-based energy management model

As illustrated in Figure 1, traffic, station occupancy rate, location and SoC are provided as inputs to the dynamic pricing-based energy management model, where their effects are aggregated through the pricing function. The resulting price output influences the distribution of charging demand among stations, thereby indirectly affecting station occupancy levels in subsequent iterations.

The pricing model is consisting of four charging stations and 16 EVs and it operates on urban charging scenarios. The simulation was run on MATLAB for 10 iterations and the state of the system was evaluated at each step. The starting SoC values of the vehicles are randomly given between 10% and 100%. Vehicles are removed from the system and replaced by new vehicles with new SoC values and location when their SoC values reach %100. This keeps constant the number of vehicles in the system, but traffic, station occupancy rate and energy demand change dynamically.

In the location process of the model, Istanbul was chosen as the study area. Istanbul has high traffic density and large number of charging stations. This makes it a suitable testing city for dynamic pricing scenarios. The locations of the vehicles and charging stations were determined in a realistic latitude–longitude range. This reflects the urban distribution and ensuring that stations were neither too close to each other nor located in inaccessible areas. Thanks to this, model was developed on a geographical scenario which realistically reflects urban mobility and the spatial diversity of the charging infrastructure. For each vehicle, range and traffic time to all stations were received from Google Maps API. This allowed the system operate based on real-time traffic conditions.

One of the input parameters, charging station occupancy rate are dynamically updated between 20% and 100% at each iteration. This rate is a normalized value which representing the density of use relative to the station's capacity. Another input parameter, vehicle locations are also updated sensitively to traffic time. For example, vehicles with light traffic cover more distance in the next iteration, while vehicles with heavy traffic move more limited. Similarly for another input parameter, the SoC parameter increase rate of vehicles is modeled according to a realistic charging curve. For example, fast charging behavior is simulating until 80% and then slow charging behavior is simulating after 80%. Therefore, all input parameters are updated iteratively in consistent and interdependent manner. This ensuring that the pricing model retains its dynamic and realistic structure.

In this section, the dynamic pricing-based energy management model was explained in order to demonstrate the conceptual structure of charging management process. However, its correct operation requires it to be based on some physical and operational assumptions. Thus, basic assumptions of the system were detailed in the following section. Scope and limitations of the model and how the parameters are interpreted was explained. These assumptions important because they both strengthen compatibility of the model with real-world conditions and enhance the understandability of the simulation.

Model assumptions

The accuracy of the model depends not only on the operation of its parameters but also on the physical and operational assumptions on which these parameters are based. These assumptions ensuring both the interpretability of the model and its consistency with real-world conditions by determining the limits of the general system. This section explains the basic assumptions considering time, vehicle movement, station occupancy rate and the overall operation of the system. This provides detailed explanation about the structure of the model and the logic behind its behavior in the simulation.

In this model, time is not defined by a fixed time step in the classical sense. The time is modeled which are dynamically updated according to the current state of the system at each iteration. Each iteration is a decision step and all input parameters (station occupancy rate, location, traffic and SoC) are updated dynamically and simultaneously at each iteration. The model does not work in the constant time step (every 10–15 minutes). Rather, there are its own time dynamics based on the update period of API calls, the variability of traffic data and the rate of SoC increase. This approach allows for both more flexible system operation and dynamic and realistic modeling of charging load management.

In the model, traffic data are received from the Google Maps API. Thus, each iteration becomes not only a series of events where parameters are randomly updated, but also an iterative process where real-world data is reflected in the model. All input parameter was dynamically updated at the beginning of each iteration. Vehicle SoC values are updated, station occupancy rates are dynamically changed by model and real-time

distance and traffic data are obtained for all vehicle-station pairs via API calls. This structure transforms each iteration of the model into a real-time system assessment representing the current state of urban conditions. In the model, locations of vehicles changes related to urban traffic conditions at each iteration. While vehicle displacement is limited in areas with high traffic, vehicles are allowed to travel longer distances in areas with calm traffic. This mechanism allows the model to work both in terms of charging status and price prediction and as an urban mobility simulation encompassing traffic related behaviors. This provides a mobility behavior that is compatible with the dynamic urban mobility and represents the interaction of the charging infrastructure with traffic in a more realistic way.

The station occupancy rate parameter used in this study is not a direct physical quantity, but a normalized indicator representing the current station usage intensity. While this representation does not include physical details of the grid infrastructure (busbar loads, transformer capacities or socket numbers), it is used to analyze the operation of dynamic pricing strategies.

The grid load balancing objective in this study is considered at the charging station demand level rather than at the physical electrical network level. The proposed model does not include an power flow analysis or electrical grid topology. Instead, grid related impacts are interpreted indirectly through changes in charging demand distribution among stations driven by the dynamic pricing mechanism. Therefore, the model focuses on demand side load balancing at the charging infrastructure level. The integration of detailed electrical grid models and power flow analysis is considered as future work.

Since the goal at this stage of the model is to evaluate the relative impact of occupancy on price, stations are assumed to have equivalent service capacity. However, in future studies, this structure can be integrated into platforms or test systems suitable for power flow analysis and occupancy rates can be related to real-time busbar loads. This way, the model can become a comprehensive energy management model that includes not only price prediction but also power flows on the grid.

The occupancy rate is dynamically updated at each iteration and this variable acts as a deterrent or incentive in the price prediction function. High occupancy values reflect situations where the station is more likely to wait, while low occupancy rates represent easy access opportunities. The pricing system increases prices at busy stations while reduces prices at stations with available capacity. With this way, the model directing demand and contributing to a balanced distribution of the charging load.

The primary objective of the model developed in this study is to analyze the operation of the dynamic price estimation mechanism. Therefore, technical differences about to EVs (battery power and charging standards) and charging station types (battery capacity, charging curve, power level and charging standard) are not considered in the model. It is assumed that all vehicles have similar battery capacity and charging characteristics and charging stations have equivalent service capacity. This approach enables the model can operate independently of complex technical differences. This allows for a simple analysis of the basic dynamics affecting the pricing mechanism.

The vehicle profiles in the model can be assumed to represent EVs focused on urban use, with a battery capacity of approximately 50–60 kWh and an average range of approximately 300 km. Thanks to this assumption, charging times and energy consumption patterns in the model is similar to typical real-world user behavior. Fast charging stations are widely used in urban charging infrastructures. That’s why the model is designed with fast charging stations. They allow for realistic representation of changes in occupancy rates, charging curves and charging cycles.

As a result, these assumptions make the model consistent with real-world conditions and enables for analysis of the effects of the dynamic pricing mechanism. After determining the model's physical foundations and behavioral assumptions, it is necessary to define the variables that influence the price estimation mechanism. In this context, input parameters and output parameter are described in the following section.

Model parameters

In the model developed in this study, the dynamic pricing mechanism is considering several variables to operate. This section defines the four input parameters (traffic, station occupancy rate, location and SoC) and the output parameter (dynamic price value) of the model. Every input parameter of the pricing model is important because they play a critical role in representing key components of the urban charging infrastructure. These parameters influence both EV user behavior and the charging load balance of the distribution grid. An overview of the dynamic pricing-based energy management model is provided in this section. The roles of every parameter and their interactions are explained.

In this model, the station occupancy rate is a normalized component which representing availability capacity of the charging station. On the other hand, technical parameters which relate to the charging or electrical infrastructure (number of sockets or transformer load) are not used in the model directly. Instead, charging station occupancy is considered as demand intensity and the grid managing potential. Station occupancy rate is not modeled based on socket type or busbar load. Rather on the percentage usage rate. This rate shows the current usage situation of the charging station and it allows to be evaluated those stations of different capacities and standards on a common scale. As charging station occupancy rate increases the price value also rises because of the model dynamics. With this, the model can encourage EV users to choose most available stations and can support to balance load distribution across the grid. This parameter is important because it can directly affect both user experience and grid efficiency. Furthermore, charging station occupancy rate parameter has the highest weight among the input parameters of the dynamic pricing-based energy management model. Therefore, the pricing model consider this parameter more than the others while making price estimation.

One of the input parameters of the model, the location parameter is important because it represents the actual driving distance between a vehicle's current position and the target charging station, based on real road routes. As the distance increases, transportation costs, time losses and energy consumption are expected to increase, leading to an increase in price. Thus, the model considers not only traffic density but also the overhead created by distance. Distances are measured in kilometers at each iteration and information from API data is normalized and incorporated into the price function. Distance serves two fundamental roles in the system. First, as a physical quantity that indirectly affects transportation costs and energy consumption and second, as an optimization variable that increases price sensitivity in demand management. Thus, the model considers distance as a strategic input for energy efficiency and user guidance.

One of the primary strengths of the dynamic pricing-based energy management model is its use of real-time traffic data. Vehicle access conditions to charging stations are calculated based on current traffic density within the urban transportation network. Thus, the model considers the actual travel time between two geographical locations, rather than synthetic or hypothetical values. This allows the price estimation mechanism to have a dynamic and realistic structure that responds to the urban traffic, unlike static approaches. Traffic duration is defined as a time-varying environmental variable in the model. This parameter represents the travel time between vehicle-station pairs in minutes and is updated via the Google Maps API at each iteration. Thus, the model acquires a stochastic structure dependent on external inputs. Traffic duration is used as a weighting factor in the price function, affecting the dynamic state of the system. High traffic periods are the situation which directly increase the price function. This situation direct EV users to alternative charging stations and contribute to demand balancing.

SoC parameter expresses the current battery charge rate as percentage (%) of the EV. The model updates SoC parameter at each iteration by considering the charging curve. In the model, SoC parameter is important both vehicle prioritization and price function personalization for each EV user. The model is thinking high priority charging requests vehicles with low SoC levels, while vehicles with high SoC levels reduce demand elasticity. Among the input parameters the SoC is the only parameter which represent EV user behavior in the pricing model. Thanks to this representation, the model considers both infrastructure factors and individual demand dynamics based on energy requirements.

Variables such as traffic, station occupancy, location and SoC can cause real-time fluctuations in charging demand. In order to manage this situation, dynamic pricing is used to balance demand and optimize energy distribution. In this study, pricing is designed not only as an economic value but also as a control mechanism that guides user behavior. The pricing model normalizes all input parameters and gives them weights with λ values. Then, it produces a dynamic price estimate from the combination of these parameters as the output. As a result, the price is sensitive not only to the measured conditions but also to the λ values that determine the importance of each parameter. This approach enables the model can update itself with dynamically changing conditions. Thus, pricing model balances distribution of charging demand and supports grid load management. The price estimation mechanism is developed using λ weights. These weights representing the influence of four main variables:

- ✓ λ_1: Charging station occupancy rate,
- ✓ λ_2: Location,
- ✓ λ_3: Traffic,
- ✓ λ_4: State of charge (SoC).

The initially determined λ values (λ_1=0.5, λ_2=0.2, λ_3=0.3, λ_4=0.2) represent the initial sensitivities of the parameters relative to each other. At each iteration, these parameters are normalized and considered in the price estimation function, producing price values in the 0–1 range.

The weighting coefficients (λ_i) were selected based on heuristic considerations reflecting the relative importance of each parameter in urban charging scenarios. In particular, charging station occupancy was assigned a higher weight due to its direct impact on congestion, bus load and waiting time, while distance and traffic duration were assigned moderate weights. The SoC related term was included to prioritize low charge vehicles without dominating the pricing mechanism. The primary objective of this study is to demonstrate the operational behavior and internal consistency of the proposed dynamic pricing-based energy management model rather than to optimize the weighting coefficients. A systematic sensitivity analysis and data driven optimization of the λ values will be addressed in future studies.

Restricting the resulting price value to a range of 0–1 prevents both negative and excessively high price values, ensuring the system operates in balance. The purpose of the normalization process is to ensure that all parameters are evaluated on the same scale. The price parameter must be calculated to represent both user comfort and grid balancing objectives of the DSO. These parameter weights allow this. Normalized weights are calculated as shown in Equation 1 and used as shown in Equation 2.

$$\omega_i = \frac{\lambda_i}{\lambda_1 + \lambda_2 + \lambda_3 + \lambda_4} \tag{1}$$

$$\omega_1 + \omega_2 + \omega_3 + \omega_4 = 1 \tag{2}$$

This method is based on the principle of producing a single result by weighting the effects of different criteria using λ weights. Here, ω_i shows the normalized weights.

Following the normalization of the weighting coefficients given in Equation 1 and 2, the input parameters of the dynamic pricing-based energy management model are normalized in order to ensure comparability among variables with different physical units.

The charging station occupancy rate, expressed as $L_s(t)$, represents the percentage utilization of charging station s at iteration t. This parameter is normalized using min–max normalization as:

$$\tilde{L}_s(t) = \frac{L_s(t) - L_{min}(t)}{L_{max}(t) - L_{min}(t) + \varepsilon} \tag{3}$$

where $L_{min}(t)$ and $L_{max}(t)$ represent the minimum and maximum station occupancy rates at iteration t, respectively and ε is a small positive constant introduced to avoid division by zero.

The driving distance between vehicle v and charging station s, expressed as $D_{v,s}(t)$ (km), represents the actual road distance obtained from real-time traffic data. This parameter is normalized using logarithmic scaling as:

$$\widetilde{D}_{v,s}(t) = \frac{log(1 + D_{v,s}(t))}{log(1 + D_{max}(t))} \tag{4}$$

where $D_{max}(t)$ represents the maximum distance value observed at iteration t.

Similarly, the traffic-based travel time v and charging station s, expressed as $T_{v,s}(t)$ $(minutes)$, represents the real-time travel duration under current traffic conditions. This parameter is normalized using logarithmic scaling as:

$$\widetilde{T}_{v,s}(t) = \frac{log(1 + T_{v,s}(t))}{log(1 + T_{max}(t))} \tag{5}$$

where $T_{max}(t)$ represents the maximum travel time observed at iteration t.

The state of charge of vehicle v, expressed as $SoC_v(t)$, represents the current battery level of the vehicle expressed as a percentage. The SoC related priority term is defined as:

$$\tilde{S}_v(t) = \frac{SoC_{max} - SoC_v(t)}{SoC_{max}} \tag{6}$$

where SoC_{max} represents the maximum state of charge value and is set to 100%.

Using the normalized input parameters defined in Equations 3-6 and the normalized weighting coefficients ω_i defined in Equaitons 1 and 2, price score is calculated for each vehicle-station pair as:

$$Score_{v,s}(t) = \omega_1 \tilde{L}_s(t) + \omega_2 \widetilde{D}_{v,s}(t) + \omega_3 \widetilde{T}_{v,s}(t) + \omega_4 \tilde{S}_v(t) \tag{7}$$

In order to reflect congestion related price adjustments, an occupancy-based price adjustment factor, expressed as $\phi_s(t)$, is introduced and defined as:

$$\phi_s(t) = \begin{cases} 1.2, & L_s(t) > 90 \\ 0.8, & L_s(t) < 40 \\ 1, & otherwise \end{cases} \tag{8}$$

Finally, the dynamic price value assigned to vehicle v at charging station s is calculated as:

$$p_{v,s}(t) = min(1, max(\varepsilon_p, \phi_s(t) \cdot Score_{v,s}(t)) \tag{9}$$

where ε_p represents a small positive constant ensuring that the resulting price remains in the interval $0 < p_{v,s}(t) \leq 1$.

3. Results and Discussion

In this section, the iterative structure of the developed dynamic pricing-based energy management model and the time-dependent variation of its input parameters are demonstrated. The model was executed for ten iterations, though only selected iterations are presented here as representative examples. These iterations effectively illustrate the typical behavior of the model and the operational mechanism of the price estimation process.

At each iteration, the input parameters are dynamically updated. For instance, in the second iteration, the occupancy rate of Station 3 was 57%, which increased to 64% in the third iteration. This increase was caused

by the inclusion of new vehicles in the system and the transition to the charging process. Similarly, in the fourth iteration, the occupancy rate of Station 1 was 72%, but it decreased to 63% in the fifth iteration, indicating that some vehicles completed charging and left the station. Additionally, in the seventh iteration, the traffic duration between Vehicle 1 and Station 3 was 14.6 minutes, which decreased to 10.1 minutes in the eighth iteration. This change demonstrates that the model operates in accordance with the natural flow of urban traffic conditions. Furthermore, the SoC and location parameters also change dynamically with each iteration. These examples demonstrate that the system parameters change consistently and in a physically significant manner with each iteration and that the model's input parameters change dynamically.

The output values (prices) of the model change dynamically at each iteration because the input parameters of the model change dynamically. Table 1 presents the results of the third iteration to illustrate how the dynamic pricing mechanism behaves across different vehicle profiles. The third iteration is presented as a representative example to illustrate the model's operating mechanism. However, consistent and expected pricing behavior is observed across all ten iterations, indicating that the proposed model functions as intended during the simulation. The dynamic pricing-based energy management model produced different prices for 16 vehicles at 4 charging stations due to different input parameters for each vehicle, as shown in Table 1.

Table 1. Dynamic price values.

Vehicles	Station-1	Station-2	Station-3	Station-4
1	0.81847	0.35402	0.83262	0.49114
2	0.80702	0.32253	0.83375	0.44734
3	0.69606	0.17904	0.74583	0.36931
4	0.52061	0.20738	0.73732	0.38899
5	0.74776	0.26865	0.74417	0.34095
6	0.76736	0.31154	0.7794	0.44812
7	0.78503	0.29956	0.7829	0.37308
8	0.61158	0.22301	0.75785	0.39568
9	0.81776	0.32941	0.84225	0.45394
10	0.7442	0.13662	0.74939	0.36893
11	0.67238	0.23524	0.59895	0.38093
12	0.83834	0.3472	0.86313	0.47221
13	0.72092	0.2455	0.79798	0.43455
14	0.72973	0.25547	0.7263	0.3262
15	0.71988	0.24598	0.77744	0.41291
16	0.73109	0.26439	0.73929	0.33956

For the analysis of the model results, Vehicle 1 (with a SoC of 65.13%) and Vehicle 12 (with a SoC of 23.91%) were selected, representing two different charge levels. The purpose of this selection is to comparatively examine how the model adjusts its price estimation under high and low SoC conditions. Both vehicles were evaluated under the same set of charging stations, where the station occupancy rates were 63% (Station 1), 20% (Station 2), 64% (Station 3) and 35% (Station 4), respectively.

Vehicle 1 has a high SoC level (65.13%), which allows the model to evaluate its charging priority in a balanced manner. As shown in Table 1, the price values for this vehicle were calculated as 0.818 (Station 1), 0.354 (Station 2), 0.833 (Station 3) and 0.491 (Station 4). For example, the high price at Station 3 results from its high occupancy rate (64%) and long traffic duration (14.6 minutes). In contrast, the lowest price was observed at Station 2 (0.354), which has the lowest occupancy rate (20%). These findings clearly demonstrate the model's sensitivity to charging station occupancy and traffic parameters.

Vehicle 12 has a low SoC value (23.91%), representing the highest priority charging demand in the system. The calculated prices for this vehicle were 0.838 (Station 1), 0.347 (Station 2), 0.863 (Station 3) and 0.472 (Station 4). The higher price at Station 3 can be attributed to its high occupancy (64%) and long traffic duration (10.9 minutes), emphasizing the dominant influence of λ_1 (station occupancy rate) and λ_3 (traffic)

weights in the price function. Conversely, the price decreases to 0.34 at Station 2, which has a low occupancy rate, reflecting the model's tendency to direct users to stations with more available conditions.

Although Vehicle 12's charge level is low, the model appears to assign the lowest price not to the nearest station, but to the station with more favorable traffic and occupancy conditions. This is because the λ_1 (station occupancy rate) parameter in the price function has a higher weight than the λ_4 (weights of SoC) parameter. However, this does not mean that the model only considers grid load. The system assumes the vehicle can reach the station with its current SoC level and performs pricing accordingly. In other words, vehicles with lower SoC are evaluated among the stations within reach and are directed to those with more favorable traffic and occupancy conditions. Thus, vehicles with lower SoC are prioritized but are routed in a way that maintains overall system balance.

Figure 2 presents the dynamic evolution of the price values assigned to a single vehicle at four different charging stations over successive iterations. The results clearly demonstrate that the proposed pricing mechanism produces time varying and station specific price signals rather than static values. While Stations 1 and 3 exhibit relatively higher price levels and moderate fluctuations, Station 2 consistently offers lower prices, demonstrating relatively favorable operating conditions throughout the simulation. In contrast, station number 4 shows significant price variability, reflecting its higher sensitivity to changes in density-related parameters such as occupancy and traffic conditions. Overall, these results confirm that the proposed dynamic pricing-based energy management model is capable of generating adaptive and differentiated price signals in response to evolving system conditions.

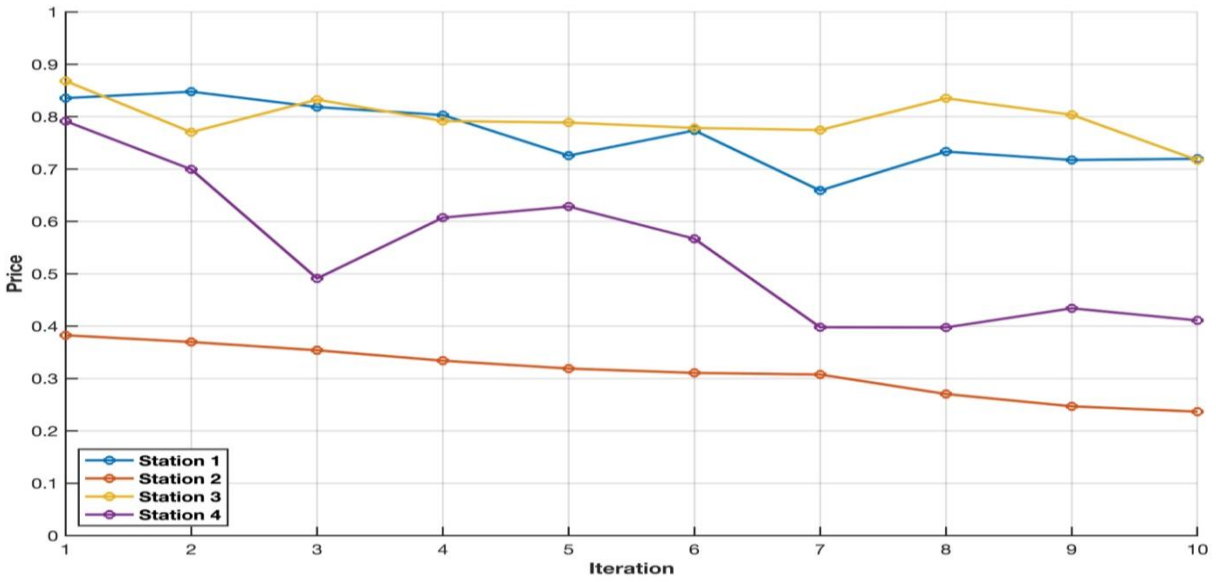


Figure 2. Dynamic prices generated for Vehicle 1 at four different charging stations over ten iterations

The model's dynamic pricing approach considers not only infrastructural factors (traffic, location, occupancy) but also user priorities. This priority is represented by the SoC parameter. Vehicles with low SoC values are considered by the system to be users with urgent charging needs. Therefore, the low SoC-high price relationship is the result of a routing strategy based on user behavior. The goal here is to prioritize the charging needs of low SoC vehicles while preventing this demand from overloading the system. Setting a high price, based on demand separation logic, encourages low SoC vehicles to charge only in truly urgent situations. Low SoC vehicles tend to target the same stations. The price increase also acts as a balancing factor for this congestion.

In the model, some vehicles were included in the system despite having high SoC values. In the real-world, a vehicle with a high SoC value is unlikely to request charging. However, because the aim of this study was to analyze how the model's price estimation mechanism behaves in all possible situations, vehicles were not restricted to a specific SoC range. This allows the system to test both the realistic charging demand behavior

of vehicles with low charge levels and the sensitivity of the price function to vehicles with high SoC values. This approach was preferred to observe the consistency of the price variable at different energy levels.

These findings demonstrate that the developed dynamic pricing-based energy management model has a structure that simultaneously evaluates both user behavior and grid load. Within the same city network and station set, differences in vehicle's traffic, station occupancy rate, location and SoC created significant changes in the price. Therefore, the model works both as an economic outcome but also as a dynamic decision support mechanism which balances grid load and affect user demands.

4. Conclusion

A dynamic pricing-based energy management model was developed in this study for EV charging infrastructure. The model is considering four input parameters (traffic, station occupancy rate, location and SoC) which influencing EV charging demand in order to estimate price dynamically. The model was developed in the MATLAB environment and it was supported with real-time traffic data received from the Google Maps API. This makes the simulation dynamic structure reflecting urban conditions.

It was seen from the findings that the developed price prediction model demonstrates beneficial results for both EV users and the DSO. The input parameters and price values were updated dynamically at each iteration. Pricing model was able to balance the grid load while maintaining the charging priority of vehicles with low SoC. The model is reducing system congestion by increasing prices at stations with high occupancy rates and directing users to stations with more available conditions. On the other hand, the decrease was observed in prices at stations with low occupancy rates. This showed that the pricing-based demand balancing mechanism was working successfully on the grid.

The results show that the pricing mechanism produces the lowest prices at charging stations with low occupancy rates. This is because, this input parameter (station occupancy rates) is given the highest weight among all parameters at the input of the model. The pricing model prioritizes both user comfort and the grid balancing objectives of the DSO. However, it was observed that the model produces low prices primarily at stations with low occupancy and to direct EV users to these charging stations unless there are critical SoC levels.

It was seen that the model is sensitive to dynamic urban conditions. The weights employed in the input of the pricing model provide flexibility for the system’s behavior different scenarios behavior of system because they defined the relative importance of each parameter. The weights employed in the price function defined the relative importance of each parameter, making the system's behavior flexible to different scenarios. The results clearly demonstrate the potential of such dynamic pricing systems to improve both user experience and energy management, particularly in urban areas.

This model, created in the MATLAB environment, is a basic model designed to test the structure of the dynamic price estimation process. No optimization or artificial intelligence algorithms were used at this stage. The aim of this model is only to observe the relationship between the price variable and the input parameters and the system's dynamic responses.

In future works, the proposed dynamic pricing-based energy management model has the potential to be integrated into power flow platforms, where charging station occupancy indicators can be associated with real-time busbar loading conditions. Moreover, the current heuristic weighting strategy can be strengthened through systematic sensitivity analysis and data-driven tuning of the λ coefficients. Finally, the framework has the potential to be expanded with artificial intelligence and optimization-based approaches to support more adaptive pricing under diverse operational conditions.

5. Acknowledgements

The authors confirm that this work was supported by The Scientific and Technological Research Council of Türkiye (TÜBİTAK) under grant number 124R072. Muhammed Sefa ÇETİN was supported by TÜBİTAK

within the scope of Directorate of Science Fellowships and Grant Programmes (BİDEB) 2211-A National PhD Scholarship Program.

6. Author Contribution Statement

In the conducted work Author 1 contributed to the formation of the idea, literature review, the writing and the development of the model; Author 2 contributed to analysis of the results, the writing and content review; Author 3 contributed to the development of the model, literature review and analysis of the results; Author 4 contributed to formation of the idea, conceptual design of the research and analysis of the results; Author 5 contributed to analysis of the results, the writing and literature review. Author 6 contributed to literature review and the writing.

7. Ethics Committee Approval and Conflict of Interest

"There is no need for an ethics committee approval for the prepared manuscript."
"There is no conflict of interest with any individual or institution in the prepared manuscript."

8. Ethical Statement Regarding the Use of Artificial Intelligence

No artificial intelligence-based tools or applications were used in the preparation of this study. The entire content of the study was produced by the authors in accordance with scientific research methods and academic ethical principles.

9. References

[1] A. A. Arefin, S. T. Meraj, M. H. Lipu, M. S. Rahman, T. Rahman, K. Hasan and K. M. Muttaqi, "Societal, environmental and economic impacts of electric vehicles towards achieving sustainable development goals," *Results Eng.*, p. 107060, 2025.

[2] S. R. Mekapati and N. B. D. Choudhury, "An overview of sustainable transportation: Solar modules integrated electric vehicles," *J. Power Sources*, vol. 659, p. 238424, 2025.

[3] M. A. Abdelkareem, A. G. Olabi, M. N. AlMallahi, M. Mahmoud and M. Elgendi, "Contributions of electric vehicles towards the sustainable development goals," *Energy Convers. Manag. X*, p. 101170, 2025.

[4] M. S. Çetin, M. T. Gençoğlu and A. Dobrzycki, "Investigation of charging technologies for electric vehicles," *Turk. J. Sci. Technol.*, vol. 19, no. 1, pp. 97–106, 2024.

[5] J. Sarda, N. Patel, H. Patel, R. Vaghela, B. Brahma, A. K. Bhoi and P. Barsocchi, "A review of the electric vehicle charging technology, impact on grid integration, policy consequences, challenges and future trends," *Energy Rep.*, vol. 12, pp. 5671–5692, 2024.

[6] L. Sun, J. Teh, W. Liu, C. M. Lai and L. R. Chen, "Impact of electric vehicles on power system reliability and related improvements: A review," *Electr. Power Syst. Res.*, vol. 247, p. 111838, 2025.

[7] P. Arulkumar, R. Karthick, R. Saravanan and K. Balamurugan, "Design of adaptive control framework for collaborative electric vehicle charging to improve hosting capacity in constrained distribution networks," *J. Energy Storage*, vol. 140, p. 118980, 2025.

[8] EPDK, "Şarj hizmeti piyasası aylık istatistikleri – Temmuz," [Online]. Available: https://www.epdk.gov.tr/Detay/Icerik/4-16153/sarj-hizmeti-piyasasi-aylik-istatistikleri-temmuz. [Accessed: Jan. 10, 2025].

[9] A. Dobrzycki, L. Kasprzyk, M. S. Çetin and M. T. Gençoğlu, "Analysis of the influence of the charging process of an electrical vehicle on voltage distortions in the electrical installation," *Appl. Sci.*, vol. 14, no. 17, p. 7691, 2024.

[10] S. Torres, I. Durán, A. Marulanda, A. Pavas and J. Quirós-Tortós, "Electric vehicles and power quality in low voltage networks: Real data analysis and modeling," *Appl. Energy*, vol. 305, p. 117718, 2022.

[11] A. Dobrzycki, M. S. Çetin and M. T. Gençoğlu, "Harmonics generated during the electric vehicle charging process," in *Proc. 2nd Int. Conf. Adv. Innov. Eng. (ICAIE)*, Elazığ, Turkey, 2023, pp. 173–178.

[12] N. Aung, W. Zhang, K. Sultan, S. Dhelim and Y. Ai, "Dynamic traffic congestion pricing and electric vehicle charging management system for the Internet of Vehicles in smart cities," *Digit. Commun. Netw.*, vol. 7, no. 4, pp. 492–504, 2021.

[13] W. Gan, J. Wen, M. Yan, Y. Zhou and W. Yao, "Enhancing resilience with electric vehicles charging redispatching and vehicle-to-grid in traffic-electric networks," *IEEE Trans. Ind. Appl.*, vol. 60, no. 1, pp. 953–965, 2023.

[14] M. S. Çetin, M. T. Gençoğlu and H. Şahin, "A review of electric vehicles: Their impact on the electricity grid and artificial intelligence-based approaches for charging load management," *Int. J. Energy Smart Grid*, vol. 9, no. 1, pp. 51–59, 2024.

[15] Z. Ding, Y. Lu, K. Lai, M. Yang and W. J. Lee, "Optimal coordinated operation scheduling for electric vehicle aggregator and charging stations in an integrated electricity-transportation system," *Int. J. Electr. Power Energy Syst.*, vol. 121, p. 106040, 2020.

[16] M. A. Gharibi, H. Nafisi, H. Askarian-Abyaneh and A. Hajizadeh, "Deep learning framework for day-ahead optimal charging scheduling of electric vehicles in parking lot," *Appl. Energy*, vol. 349, p. 121614, 2023.

[17] J. Jin and Y. Xu, "Optimal policy characterization enhanced actor-critic approach for electric vehicle charging scheduling in a power distribution network," *IEEE Trans. Smart Grid*, vol. 12, no. 2, pp. 1416–1428, 2020.

[18] M. Tang, W. Zhuang, B. Li, H. Liu, Z. Song and G. Yin, "Energy-optimal routing for electric vehicles using deep reinforcement learning with transformer," *Appl. Energy*, vol. 350, p. 121711, 2023.

[19] R. Basso, B. Kulcsár, I. Sanchez-Diaz and X. Qu, "Dynamic stochastic electric vehicle routing with safe reinforcement learning," *Transp. Res. Part E Logist. Transp. Rev.*, vol. 157, p. 102496, 2022.
[20] A. Ahmadian, K. Sedghisigarchi and R. Gadh, "Empowering dynamic active and reactive power control: A deep reinforcement learning controller for three-phase grid-connected electric vehicles," *IEEE Access*, vol. 12, pp. 66068–66084, 2024.
[21] Y. Zhang, Q. Yang, D. An, D. Li and Z. Wu, "Multistep multiagent reinforcement learning for optimal energy schedule strategy of charging stations in smart grid," *IEEE Trans. Cybern.*, vol. 53, no. 7, pp. 4292–4305, 2022.
[22] S. Shahriar, A. R. Al-Ali, A. H. Osman, S. Dhou and M. Nijim, "Prediction of EV charging behavior using machine learning," *IEEE Access*, vol. 9, pp. 111576–111586, 2021.
[23] T. Lan, K. Jermsittiparsert, S. T. Alrashood, M. Rezaei, L. Al-Ghussain and M. A. Mohamed, "An advanced machine learning based energy management of renewable microgrids considering hybrid electric vehicles' charging demand," *Energies*, vol. 14, no. 3, p. 569, 2021.
[24] J. Zhong, J. Liu and X. Zhang, "Charging navigation strategy for electric vehicles considering empty-loading ratio and dynamic electricity price," *SSRN Electron. J.*, Art. no. 4203560, 2023.
[25] Z. Zhao and C. K. Lee, "Dynamic pricing for EV charging stations: A deep reinforcement learning approach," *IEEE Trans. Transp. Electrif.*, vol. 8, no. 2, pp. 2456–2468, 2021.
[26] H. Lin, Y. Zhou, Y. Li and H. Zheng, "Aggregator pricing and electric vehicles charging strategy based on a two-layer deep learning model," *Electr. Power Syst. Res.*, vol. 227, p. 109971, 2024.
[27] M. B. Rasheed, A. Llamazares, M. Ocana and P. Revenga, "A game-theoretic approach to mitigate charging anxiety for electric vehicle users through multi-parameter dynamic pricing and real-time traffic flow," *Energy*, vol. 304, p. 132103, 2024.
[28] B. Palaniyappan and T. Vinopraba, "Dynamic pricing for load shifting: Reducing electric vehicle charging impacts on the grid through machine learning-based demand response," *Sustain. Cities Soc.*, vol. 103, p. 105256, 2024.

Fırat Üniversitesi Deneysel ve Hesaplamalı Mühendislik Dergisi

FUJECE

U-Net ile Derin Steganografi: Video içerisine Metni Gizleme ve Yeniden Elde Etme

Mahmut SİNECEN [1]*

[1] Bilgisayar Mühendisliği Bölümü, Mühendislik Fakültesi, Adnan Menderes Üniversitesi , Aydın, Türkiye.
[1]mahmut@adu.edu.tr

Geliş Tarihi: 09.9.2025
Kabul Tarihi: 27.01.2026

Düzeltme Tarihi: 23.12.2025

doi: https://doi.org/10.62520/fujece.1780558
Araştırma Makalesi

Alıntı: M. Sinecen, "U-Net ile derin steganografi: video içerisine metni gizleme ve yeniden elde etme", Fırat Üni. Deny. ve Hes. Müh. Derg., vol. 5, no 1, pp. 345-362, Şubat 2026.

Öz

Video tabanlı steganografi, görüntü tabanlı yaklaşımlara kıyasla sunduğu yüksek veri taşıma kapasitesi ve gelişmiş görsel algılanamazlık özellikleri nedeniyle son yıllarda artan bir ilgi görmektedir. Bu çalışmada, U-Net mimarisi kullanılarak video içeriği içerisine metinsel bilgilerin gizlenmesi ve geri elde edilmesi amacıyla derin öğrenmeye dayalı bir steganografik yöntem önerilmektedir. Geleneksel en düşük anlamlı bit (LSB) tabanlı tekniklerden farklı olarak, önerilen yaklaşım; dayanıklılığı ve görsel kaliteyi artırmak amacıyla ilgi alanı (ROI) seçimi ve yama (patch) tabanlı yerleştirme stratejilerini kullanmaktadır. Metinsel veriler öncelikle görüntü tabanlı yamalara dönüştürülmekte ve eğitilmiş bir gizleme ağı aracılığıyla video karelerinin seçilen bölgelerine gömülmektedir. Gizlenen bilginin geri elde edilmesi için karşılık gelen bir çıkarım ağı kullanılmakta ve ardından metnin çıkarımı optik karakter tanıma (OCR) yöntemi ile gerçekleştirilmektedir. Deneysel sonuçlar, stego videolarda yüksek görsel bütünlük korunurken karakter geri kazanım doğruluğunun %81 ile %88 arasında değiştiğini göstermektedir. Önerilen ROI güdümlü U-Net tabanlı çerçeve, video akışlarında güvenli ve algılanamaz metin gizleme için etkili ve ölçeklenebilir bir çözüm sunmaktadır.

Anahtar kelimeler: Derin stenografi, U-Net, Video gizleme, Metin çıkarımı, OCR

*Yazışılan yazar

İntihal Kontrol: Yes – Turnitin
Şikayet: fujece@firat.edu.tr
Telif Hakkı ve Lisans: Dergide yayın yapan yazarlar, CC BY-NC 4.0 kapsamında lisanslanan çalışmalarının telif hakkını saklı tutar.

Firat University Journal of Experimental and Computational Engineering

Deep Steganography with U-Net: Hiding and Revealing Text in Video

Mahmut SİNECEN [1]*

[1] Computer Engineering Department, Engineering Faculty Adnan Menderes University, Aydın, Türkiye.
[1]mahmut@adu.edu.tr

Received: 09.9.2025
Accepted: 27.01.2026
Revision: 23.12.2025
doi: https://doi.org/10.62520/fujece.1780558
Research Article

Citation: M. Sinecen "Deep steganography with U-Net: hiding and revealing text in video", Firat Univ. Jour.of Exper. and Comp. Eng., vol. 5, no 1, pp. 345-362, February 2026.

Abstract

Video-based steganography has attracted increasing attention due to its high payload capacity and improved imperceptibility compared to image-based approaches. In this study, a deep learning–based steganographic framework is proposed to embed and recover textual information within video content using the U-Net architecture. Unlike traditional least significant bit (LSB)–based techniques, the proposed method utilizes region-of-interest (ROI) selection and patch-based embedding to enhance robustness and visual quality. Textual data are first encoded into image patches and embedded into selected regions of video frames via a trained hiding network. A corresponding revealing network is employed to recover the hidden information, followed by an optical character recognition (OCR) pipeline for text extraction. Experimental results demonstrate character recovery accuracies between 81% and 88% while preserving high visual fidelity in the stego videos. This ROI-guided U-Net framework provides an effective and scalable solution for secure and imperceptible text hiding in video streams.

Keywords: Deep steganography, U-Net, Video hiding, Text recovery, OCR

*Corresponging author

Plagiarism Checks: Yes – Turnitin
Complaints: fujece@firat.edu.tr
Copyright & License: Authors publishing with the journal retain the copyright to their work licensed under the CC BY-NC 4.0

1. Introduction

Steganography refers to the practice of hiding secret information within innocuous digital carriers such as images, audio, or video files in a manner that conceals the very existence of communication. The growing demand for secure and covert communication channels has renewed interest in steganography as an effective method for embedding sensitive data into unobtrusive media [1]. Unlike cryptography, which protects information by transforming it into an unintelligible form, steganography focuses on concealing the presence of the message itself within a cover object [2, 3]. Although both techniques aim to safeguard information, they differ fundamentally in their objectives and operational principles. This distinction underscores steganography's unique capability to provide plausible deniability, making it particularly suitable for covert information exchange [4, 5].

Rooted in the broader field of information hiding, steganography exploits various multimedia formats including images, audio, and video as cover media while striving to preserve imperceptibility against unauthorized observers [6, 7]. Historically, steganographic techniques have been employed in applications ranging from secure communication to digital watermarking; however, their dual-use nature also raises concerns due to potential misuse in illicit activities [8]. The primary objective of effective steganography is imperceptibility, ensuring that the embedded data remains undetectable not only to the human visual system but also to advanced computational steganalysis tools [9, 10]. Consequently, the continuous evolution of steganographic methods has been accompanied by parallel advances in steganalysis, giving rise to an ongoing arms race between data hiding and detection techniques [11, 12].

In recent years, deep learning has significantly influenced both steganography and steganalysis by enabling data-driven feature learning and improved modeling of complex patterns in multimedia content. Deep neural networks have facilitated more adaptive and robust embedding strategies, while simultaneously enhancing the accuracy of steganalytic detection methods, particularly in forensic analysis scenarios [13, 14]. Within this framework, the present study proposes a U-Net–based approach for embedding textual information into video data and subsequently recovering it. The remainder of this paper is organized as follows. Section 2 reviews related work, Section 3 describes the proposed methodology, Section 4 presents the experimental results, and Section 5 discusses the findings and concludes the study.

2. Literature Review

Steganography encompasses methods for storing and transmitting data by embedding it into different carriers. While early approaches often favored spatial-domain techniques, contemporary methods have shifted toward transform-domain and deep learning–assisted techniques [10, 11]. Video steganography presents unique challenges due to the dynamic structure of frames, requiring the preservation of confidentiality and robustness against various video compression standards.

The Least Significant Bit (LSB) technique, a classical method, has been widely used for a long time thanks to its simplicity. However, because it is vulnerable to statistical analysis, modern studies tend to employ a more complex and reliable approach [15, 16]. In this context, the use of deep neural networks has provided significant progress; combined with adaptive embedding techniques, researchers have developed systems more resistant to steganalysis [17].

In recent years, approaches based on Generative Adversarial Networks (GANs) have stood out. GAN-based methods can produce content statistically very similar to the cover media, thereby making the detection of hidden messages more difficult [18]. Moreover, neural networks are heavily utilized not only in steganography but also in steganalysis, with new detection algorithms being developed to discriminate between original and embedded content [19, 20].

Although the roots of steganography date back to ancient times, multimedia steganography has gained prominence in modern digital applications. The high-dimensional and complex nature of multimedia data, including images and videos, enables imperceptible embedding while offering improved robustness against

various manipulations and statistical steganalysis techniques [21, 22]. In this context, recent deep learning–based approaches aim to distribute secret information across multiple learned representations and, in the case of video data, across temporal frames to enhance imperceptibility and maintain robustness under compression or degradation.

Additionally, the literature highlights several strategies to improve the reliability and imperceptibility of steganographic systems, including controlling embedding rates, exploiting perceptual limitations of the human visual system, and leveraging learned feature representations through deep neural networks [4, 9]. In parallel, increasingly sophisticated analysis techniques developed for detecting hidden information continue to fuel the ongoing "arms race" between steganography and steganalysis [2, 17].

In conclusion, deep learning–based steganographic approaches have demonstrated improved imperceptibility and adaptive embedding capabilities compared to classical techniques, particularly using generative and encoder–decoder architectures [23]. While most prior studies focus on reconstructing image-based secrets, the present work extends this paradigm by incorporating an OCR-based post-processing stage, enabling direct textual information recovery from the reconstructed secret images.

Unlike existing learned or generative steganography approaches that primarily focus on image carriers such as encoder–decoder hiding/revealing networks, GAN-based formulations, reversible secret-to-image transformations, and diffusion-based generative schemes [10, 17, 23, 24] the proposed approach introduces an ROI-guided, patch-based U-Net architecture tailored specifically for video data. By embedding text-encoded image patches only into visually complex regions, the method enhances imperceptibility while maintaining reliable recovery performance. Moreover, integrating an OCR pipeline enables direct textual information retrieval, which is not the primary objective in most prior deep or generative steganography studies (Table 1).

Table 1. Comparison of deep learning–based generative/learned steganography approaches

Study	Carrier	Learning paradigm	Payload type	ROI-guided	Retrieval mechanism	Scope/Notes
Baluja (2017)	Image	CNN-based hiding + reveal networks (trained as a pair)	Image	No	Direct reconstruction (reveal network)	Image-in-image hiding; not designed for text extraction
Volkhonskiy et al. (2020)	Image	GAN-based (DCGAN/SEGAN-style) container generation and/or learned embedding	Binary secret message (and key)	No	Decryption/extraction network ("Bob")	Focus on image carriers; emphasizes (anti-) steganalysis via generative containers
Zhou et al. (2022)	Image (generated)	Flow-based generative steganography (Glow), reversible secret-to-image transformation (S2IRT)	Secret message	No	Reversible (inverse) transformation for message extraction	Coverless/generative formulation; high-capacity + high extraction accuracy reported
Wei et al. (2023)	Image	Diffusion-based generative steganography	Secret data	No	Diffusion-based generation with implicit message recovery	Diffusion-based generative steganography; message is embedded/recovered through the diffusion generation process
Proposed method	Video	ROI-guided patch-based U-Net hiding/revealing networks	Text (image-encoded patches)	Yes	Revealer network + OCR pipeline	Video carrier + explicit text retrieval; embedding constrained to visually complex ROIs (high imperceptibility with recoverable text)

3. Materials and Methods

The study focuses on embedding textual information into a video file and subsequently recovering the hidden text in a readable form. The input text is first converted into an image-based representation, where individual characters or character groups are encoded as small image patches. In parallel, the input video is decomposed into individual frames. For each selected frame, visually complex regions are identified and used as regions of interest (ROIs). Text-encoded image patches are then embedded into these ROIs using a deep learning–based hiding network, while preserving the perceptual quality of the video frames. After processing all selected frames, the resulting stego frames are recombined to form the final stego video. During the retrieval stage, a corresponding revealing network extracts the embedded patches from the stego frames, and the

recovered image patches are subsequently processed using an optical character recognition (OCR) pipeline to reconstruct the original text (Figure 1).

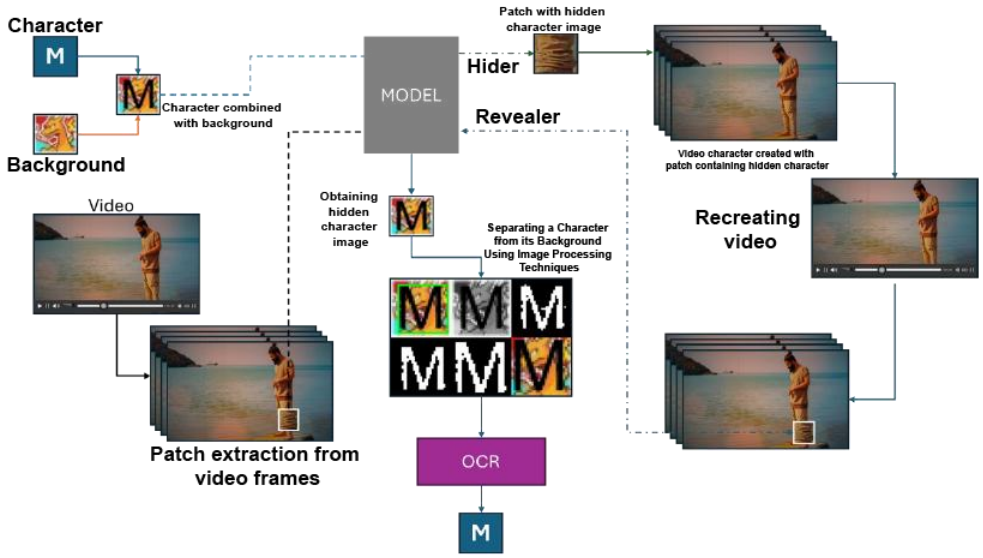


Figure 1. Overview of the proposed video-based steganography framework, including text-to-image encoding, ROI-guided patch embedding using hiding and revealing networks, and OCR-based text reconstruction

3.1. Materials

The experimental setup was constructed using a single publicly available video source downloaded from YouTube. The original video has a resolution of 1920 × 1080 pixels and a frame rate of 30 frames per second. The content of the video includes natural scenes with moderate motion and texture variations, making it suitable for evaluating imperceptible data embedding in realistic conditions.

From the complete video stream, a total of 4.500 frames were extracted, out of which 150 frames were selectively used for training and evaluation. This selection was performed to balance computational cost while maintaining experimental consistency and representative visual diversity. The selected frames were processed individually within the proposed steganographic pipeline.

Textual information was encoded into image-based payloads prior to embedding. Uppercase English characters (A–Z) were rendered using a fixed font configuration and converted into grayscale image patches. To analyze the impact of payload size on embedding performance and visual quality, three different patch sizes were employed: 32 × 32, 48 × 48, and 64 × 64 pixels. These patches were embedded into visually complex regions of selected video frames identified through region-of-interest (ROI) analysis.

All experiments were conducted on a workstation equipped with an NVIDIA RTX 3090 GPU and an AMD Ryzen 9 5950X CPU, providing sufficient computational power for deep learning–based training and inference. The software environment was configured using Python 3.10 and the PyTorch deep learning framework (version 2.3.1) with CUDA 11.8 support. Auxiliary libraries were utilized for image and video processing, numerical computation, visualization, and evaluation, including OpenCV, NumPy, Matplotlib, and Pandas. For perceptual quality assessment, the PyTorch-MSSSIM library was employed. Optical Character Recognition (OCR) experiments for text recovery were conducted using EasyOCR and Tesseract. Video decoding and frame extraction were handled using ImageIO and FFmpeg-based tools.

3.2. Method

3.2.1. Video frame extraction

This subsection describes the preprocessing steps applied to the carrier video prior to embedding. Using the yt-dlp library, a publicly available video is downloaded from YouTube at 1080p (1920×1080 pixels) and 30 frames per second. Each input video is decomposed into individual frames using OpenCV. Frames are converted to RGB color space and normalized to the [0,1] range.

3.2.2. ROI (Region of Interest) Selection

Regions with high spatial complexity are initially identified using Sobel edge detection, followed by thresholding and morphological operations to suppress noise and enhance prominent structures. Based on the resulting edge magnitude map, bounding boxes with sufficient texture density are selected as candidate embedding regions, since visually complex areas are less sensitive to subtle modifications.

In the proposed framework, this region-of-interest (ROI) selection strategy is directly integrated into the patch-based hiding process. When combining the secret text images with the video frames, a cover patch is extracted from the selected ROI, and the ROI is constrained to have the same spatial dimensions as the corresponding secret text image. The ROI location is determined by evaluating the magnitude of horizontal and vertical gradient responses obtained from the Sobel edge detector. By selecting the region with the highest gradient energy, the most visually complex area of the frame is chosen, thereby making the embedded text significantly more difficult to perceive in the resulting stego video.

To compute the gradient magnitude used for ROI selection, each grayscale frame is convolved with the Sobel operator using 3×3 kernels that approximate first-order derivatives in the horizontal and vertical directions (Eqs. 1–2).

$$K_x = \begin{bmatrix} -1 & 0 & +1 \\ -2 & 0 & +2 \\ -1 & 0 & +1 \end{bmatrix}, K_y = \begin{bmatrix} -1 & -2 & -1 \\ 0 & 0 & 0 \\ +1 & +2 & +1 \end{bmatrix} \quad (1)$$

$$G_x = K_x * I, \quad G_y = K_y * I \quad (2)$$

Here "*" denotes 2-D convolution. These kernels can be seen as a separable combination of smoothing with (1, 2, 1) and differencing (derivative) with (−1, 0, 1), which makes them more robust to noise [25, 26].

The per-pixel gradient vector, the magnitude and the direction were calculated using Eqs. 3-4-5.

$$\nabla I = [G_x, G_y] \quad (3)$$

$$M = \sqrt{G_x^2 + G_y^2} \quad (4)$$

$$\theta = atan2(G_y, G_x) \quad (5)$$

With this method, the patch extracted from the frame is detected after passing through successive stages as illustrated in Figure 2.

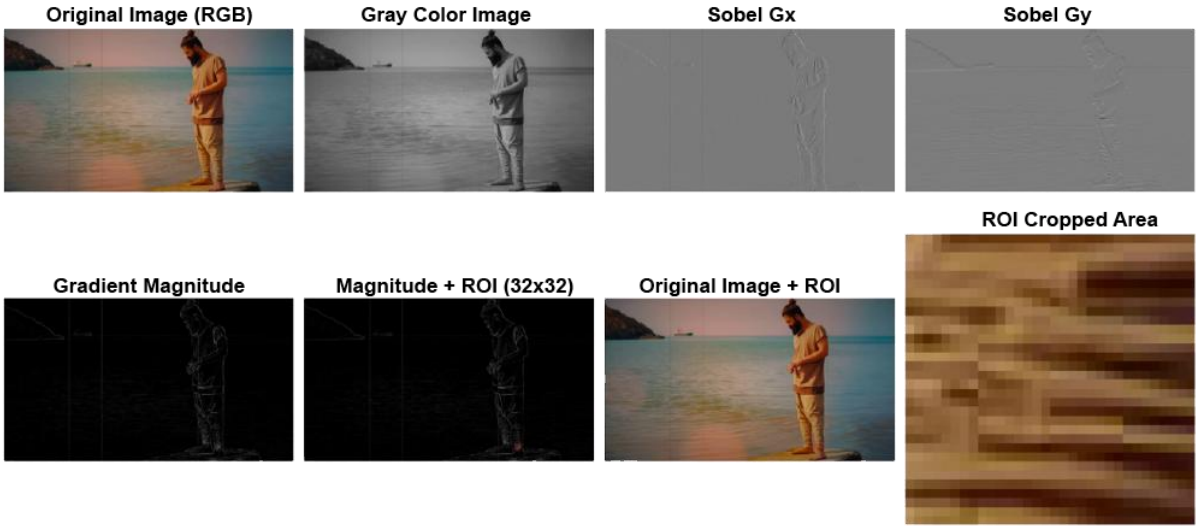


Figure 2. ROI detection process using the Sobel operator. The gradient magnitude map is thresholded and post-processed to identify visually complex regions. The selected ROI (x = 1400, y = 968, w = 32, h = 32) is used as the cover patch for text embedding

The primary motivation for using gradient magnitude in ROI detection is that it effectively measures the strength of local intensity variations, producing high responses at object boundaries and textured regions. This property is well suited for identifying visually complex areas that can better mask embedding distortions. In addition, the gradient magnitude is invariant to edge orientation, enabling robust ROI selection without prior knowledge of dominant directions [27]. Due to the inherent smoothing effect of the Sobel operator, the method is less sensitive to high-frequency noise, allowing thresholding and adaptive thresholding strategies to operate more reliably [28]. Finally, the sequential application of thresholding, morphological merging, and connected component analysis enables efficient extraction of bounding boxes, yielding a simple and computationally efficient ROI selection pipeline.

3.2.3. Text-to-ımage encoding

Text strings are rendered into grayscale image patches using a fixed font type and size, and these patches are used as payload inputs to the hiding network. Each character in the input text is first converted into an individual image, referred to as a secret image.

A predefined background image with moderate visual complexity is combined with each character image prior to embedding. Empirical observations during preliminary experiments indicated that character-only images (i.e., images containing only foreground text on a uniform background) tend to suffer from severe degradation or partial disappearance after the embedding and recovery process. This effect is attributed to the low structural and intensity variation in such images, which makes them more vulnerable to distortion during deep feature transformation and reconstruction.

To mitigate this issue, a background image is introduced to provide additional spatial texture and intensity variation, thereby stabilizing the learning and reconstruction of character features. The character is rendered in the center of the background image, ensuring consistent alignment across samples.

Character image sizes of 32×32, 48×48, and 64×64 pixels were evaluated independently to analyze the impact of payload size on embedding performance and recovery accuracy. As illustrated in Figure 3, the secret text “MAHMUTSINECEN” was rendered using the Arial font and placed centrally on the background

image, with the font size occupying approximately 80% of the image area. This process resulted in 13 individual character images, each stored as a separate secret patch.

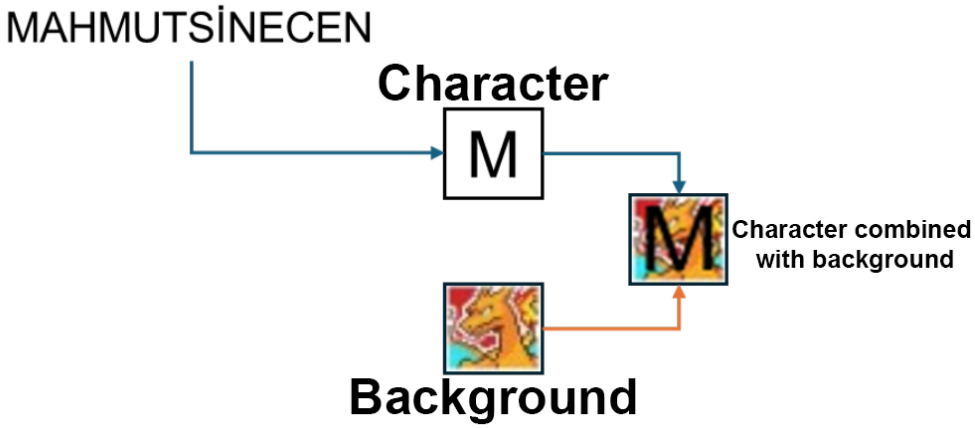


Figure 3. Generation of secret image patches by combining individual text characters with a predefined background image prior to embedding

3.2.4. U-Net-based hiding and revealing networks

The proposed framework consists of two complementary deep learning components: a hiding network and a revealing network. The hiding network takes a cover video frame together with an encoded text patch as input and generates a stego frame in which the secret information is imperceptibly embedded. Conversely, the revealing network operates on the stego frame to reconstruct the hidden text patch. To effectively capture both global contextual information and fine-grained spatial details during these processes, skip connections are employed to enable multi-scale feature fusion.

Accordingly, a U-Net–based architecture is adopted due to its proven capability to preserve spatial resolution while modeling high-level contextual representations. The contracting and expanding paths of the U-Net architecture allow the network to learn robust hierarchical features, which is particularly beneficial for localized, patch-scale information hiding tasks. Building upon the standard encoder–decoder U-Net structure [29], the network is further enhanced with residual convolutional blocks, Group Normalization, and SiLU (Swish) activation functions to improve training stability and convergence behavior. In addition, Squeeze-and-Excitation (SE) blocks are incorporated to emphasize informative inter-channel dependencies, enabling adaptive allocation of embedding capacity to textured and edge-rich regions while restricting modifications in visually smooth areas [30].

This architectural configuration yields a computationally efficient and stable backbone for both hiding and revealing operations, making it well suited for localized, patch-based steganographic embedding and recovery [30-32]. During the retrieval phase, the revealing network receives not only the stego patch (containing both cover and embedded information) but also multi-scale high-pass and Laplacian feature summaries. These inputs, resulting in a total of 12 channels (RGB stego patch concatenated with residual feature maps), are included to amplify subtle embedding traces distributed over fine textures. Such high-pass

residual–based representations are commonly adopted in steganalysis and have been shown to facilitate more accurate recovery of hidden information by enhancing weak signal components [33].

The internal structure of the proposed network, including the residual convolutional block (GroupNorm + SiLU + SE with residual connections) and the U-shaped downsampling and upsampling paths, is illustrated in Figure 4.

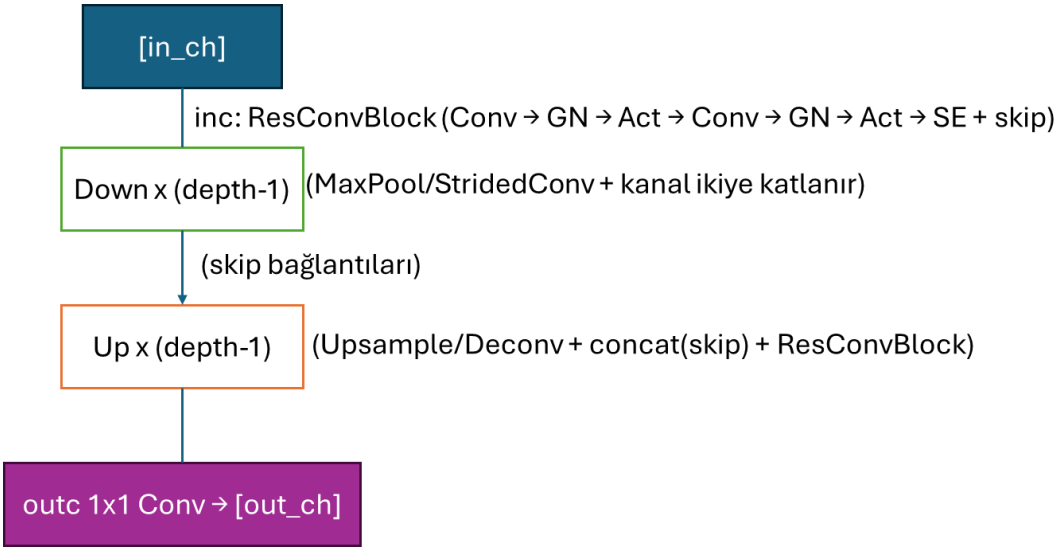


Figure 4. Internal architecture of the proposed U-Net–based hiding and revealing networks, illustrating the residual convolutional blocks, skip connections, and downsampling/upsampling paths

Training strategy

The training procedure is designed to ensure stable convergence and balanced optimization of both hiding and revealing tasks. To this end, a two-stage training strategy is employed.

In the first stage, a warm-up phase is applied in which only the revealing network is trained using stego–secret pairs. This partial supervision allows the revealing network to learn a reliable stego-to-secret mapping before being exposed to the joint optimization process. Such pre-training stabilizes subsequent training and prevents early-stage error amplification when both networks are optimized simultaneously.

In the second stage, the hiding and revealing networks are trained jointly in an end-to-end manner. Optimization is performed using the AdamW optimizer with decoupled weight decay, combined with a ReduceLROnPlateau learning rate scheduler to adaptively adjust the learning rate based on validation performance. This strategy enables stable convergence while mitigating overfitting.

To enhance robustness against common video distortions and post-processing operations, data augmentation techniques are applied during training. These include additive color noise, mild Gaussian blur, JPEG compression artifacts, and gamma correction. Such augmentations encourage the network to learn invariant embedding patterns that remain recoverable under realistic degradation scenarios.

In addition, channel masking is employed during embedding. Specifically, secret patches are embedded into a single-color channel (e.g., the blue channel) using a Modified RGB (MRGB) representation. This constraint reduces perceptual distortion in luminance-sensitive channels and further improves visual imperceptibility.

Training losses

The overall training objective is formulated as a multi-component loss function that jointly balances visual fidelity of the stego frames and accurate recovery of the embedded secret content.

To preserve the visual quality of the cover frames, a cover reconstruction loss is defined as a combination of the L1 loss and the Structural Similarity Index Measure (SSIM). This loss encourages the generated stego frames to remain perceptually close to the original cover frames while penalizing pixel-level deviations[34].

For secret recovery, a weighted L1 loss is employed, where higher weights are assigned to darker regions of the secret patches to improve character legibility after extraction. In addition, a gradient-based L1 loss is introduced to preserve edge structures and character contours, which are critical for successful OCR-based text recognition. SSIM is further incorporated to enforce structural consistency between the original and recovered secret patches.

To improve robustness, a residual-energy regularization term is added to penalize excessive high-frequency embedding artifacts. Moreover, controlled Gaussian noise is injected into the stego representations during training. This noise injection acts as a regularizer, encouraging the revealing network to recover secret information under slight perturbations and enhancing resilience against compression and signal degradation.

Hider (Embedding)

U-Net (6→4): the 6-channel input (cover + secret) yields 3 residual channels + 1 mask. The mask uses sigmoid, the residual uses tanh, and with a color-channel constraint and factor α, the residual is added onto the cover (Figure 5). The color-channel constraint (e.g., write only to the B channel) and α are set parametrically. Formal definitions and Eqs. (6–10) follow the paper; the mask limits writing to a single channel and α is a small mixing coefficient (in this study, the B channel was used with a small α).

$$X = [C, S] \in \mathbb{R}^{6xsxs} \tag{6}$$

$$Y = UNet(X) \tag{7}$$

$$m = \sigma(Y_4) \tag{8}$$

$$r = \tanh(Y_{1:3}) \odot m \odot M_{rgb} \tag{9}$$

$$\hat{C} = clip(C + \alpha\, r, 0,1) \tag{10}$$

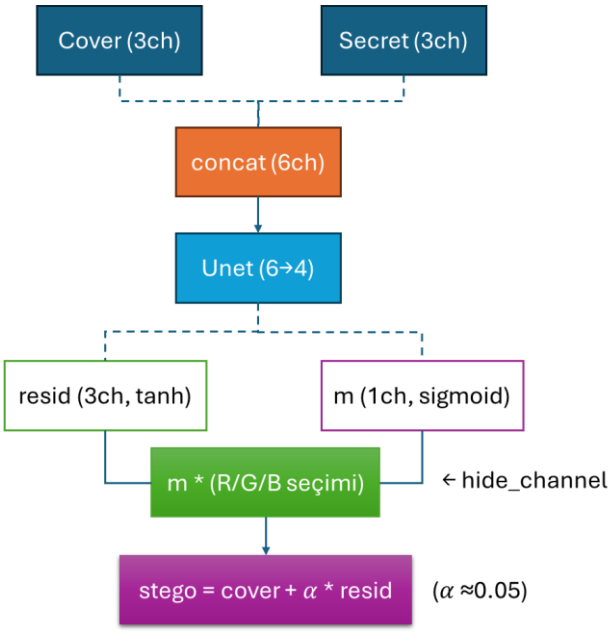


Figure 5. Hider (Embedder) diagram

Revealer (Recovery)

Using multi-scale high-pass (HP) emphasizes faint traces of the hidden signal distributed over fine textures [33]. In this study, three-scale high-pass summaries (two different HP + Laplacian) were produced and concatenated as 9 channels (Figure 6). U-Net (12→3) with a sigmoid output performs recovery, taking the stego patch plus its multi-scale HP/Laplacian derivatives as input (Eqs. 11–12).

$$U = concat\left(\hat{C}, HP_1(\hat{C}), HP_2(\hat{C}), Lap(\hat{C})\right) \in \mathbb{R}^{12xsxs} \tag{11}$$

$$\hat{S} = \sigma\left(UNet(U)\right) \tag{12}$$

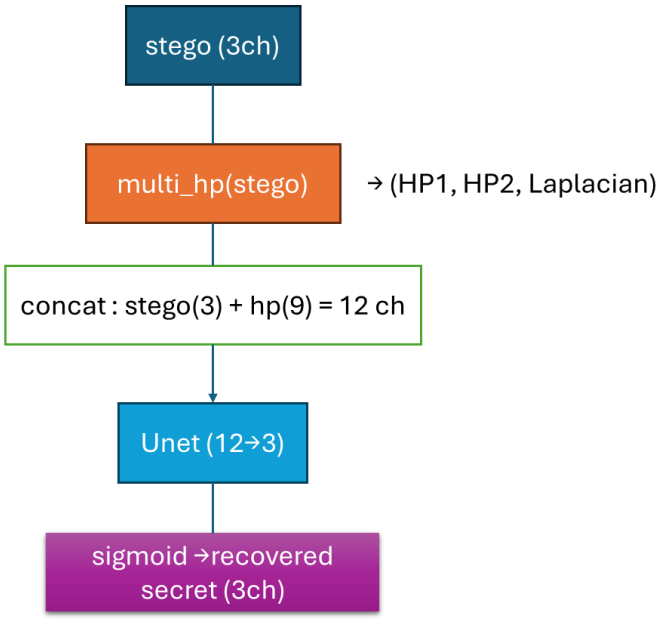


Figure 6. Revealer (Extractor) diagram

3.2.5. Loss functions and training

SSIM is used to maintain a perceptual balance for both cover and secret. Optimization uses AdamW [35] and the ReduceLROnPlateau scheduler, which lowers the learning rate when a monitored metric (e.g., validation loss or accuracy) stops improving for a period, allowing the model to proceed with smaller steps when it gets "stuck" [36-39]. Training proceeds in two stages: a short revealer pre-training, then joint training. The components include a cover loss limiting visual distortion (Eq. 13), a secret loss promoting accurate recovery and quality (Eq. 14) with brightness-aware weighting (Eq. 15), a residual energy term that accentuates visible traces for the stego image (Eq. 16), and the total loss (Eq. 17).

$$\mathcal{L}_{cover} = \left\|\hat{C} - C\right\|_1 + \lambda_{ssim}\left(1 - SSIM\left(\hat{C}, C\right)\right) \tag{13}$$

$$\mathcal{L}_{secret} = \left\|\omega \odot \left(\hat{S} - S\right)\right\|_1 + \mu\left\|\nabla\hat{S} - \nabla S)\right\|_1 + \eta\left(1 - SSIM\left(\hat{S}, S\right)\right) \tag{14}$$

$$\omega = 0.3 + 0.7\left(1 - Gray(S)\right)^2 \tag{15}$$

$$\mathcal{L}_{resid} = \|r\|_2^2 \tag{16}$$

$$\mathcal{L} = \lambda_1\mathcal{L}_{cover} + \beta\mathcal{L}_{secret} + \rho\mathcal{L}_{resid} \tag{17}$$

The total loss function is defined as:

$$L_{total} = \lambda_{loss}L_{hide} + (1 - \lambda_{loss})L_{reveal} \tag{18}$$

Where L_{hide} represents reconstruction loss and L_{reveal} denotes cover reconstruction loss.

The complete set of training parameters used during the optimization process is provided in Table 2.

Table 2. Training parameters

Parameter	Value
Epochs	100
Batch size	8
Learning rate	0.0001
Optimizer	AdamW
Loss weight (λ_{loss})	0.75
Input size	256 × 256

3.3. Constructing the video with hidden text

Using the proposed U-Net–based hiding network, stego patches containing the embedded character information were generated for each selected video frame. These stego patches were subsequently placed back into their corresponding regions of interest (ROIs) at the original spatial locations from which the cover patches were extracted. This ensured spatial consistency and prevented any unintended distortion outside the embedding regions.

After all selected frames were processed, the modified frames were reassembled to reconstruct the final stego video. Video encoding was performed using OpenCV with an FFmpeg-based codec, while preserving the original spatial resolution and frame rate of the input video. Maintaining identical encoding parameters ensured that any observed distortions were attributable solely to the embedding process rather than to re-encoding artifacts.

No additional post-processing or compression was applied beyond standard video encoding, allowing a fair assessment of the embedding-induced distortions.

4. Results

Figure 7 shows the histogram changes in each color channel for (i) the patch from the video frame, (ii) the backgrounded character image to be hidden, and (iii) the embedded and recovered images produced by the U-Net model. Only minor distortions were observed in images; the recovered images carrying the secret message largely represent the original character. As seen in Figure 7, the frequency distributions of the Red, Green, and Blue channel pixels in the original image do not change significantly, and as a result there is no perceptible visual degradation.

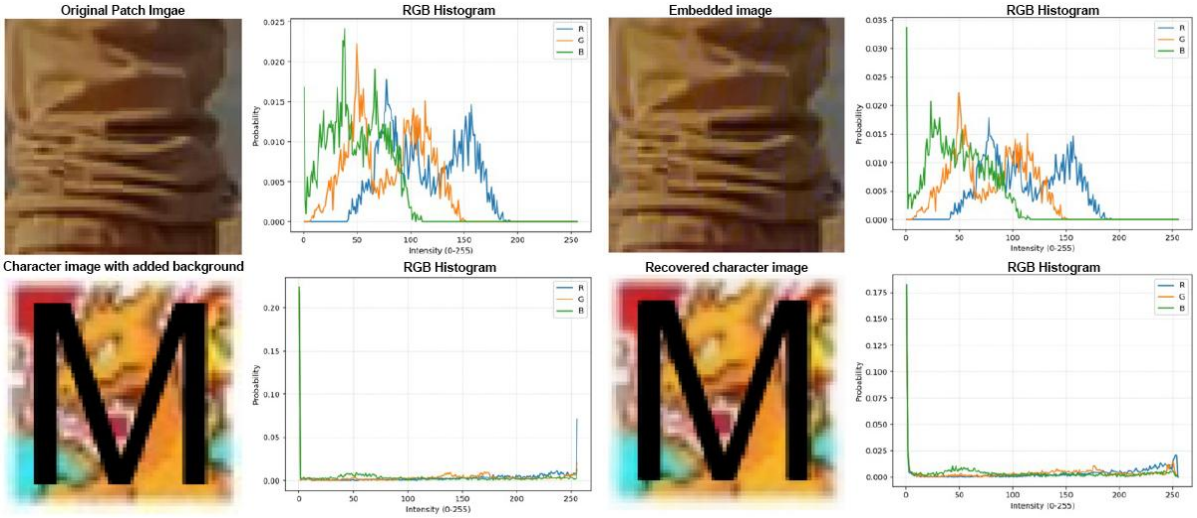


Figure 7. Illustrates the RGB histogram distributions for (i) the original patch extracted from the video frame, (ii) the character image combined with a background prior to embedding, and (iii) the corresponding embedded and recovered character images generated by the proposed U-Net–based framework

The results indicate that the embedding process introduces only minimal alterations to the pixel intensity distributions across the Red, Green, and Blue channels. In particular, the histogram profiles of the embedded patches remain closely aligned with those of the original cover patches, suggesting that the statistical properties of the video content are largely preserved. This behavior is essential for maintaining imperceptibility and reducing the risk of detection by both human observers and histogram-based steganalysis methods.

The recovered character images exhibit histogram distributions that closely resemble those of the original character images with background, demonstrating that the revealing network successfully reconstructs the embedded information with minimal loss. Despite slight smoothing effects introduced by the embedding and recovery stages, the character structures remain visually intact and sufficiently distinguishable, which directly supports the high OCR-based character recovery accuracies reported in subsequent evaluations.

4.1. Quantitative evaluation

To convert the recovered character images back into meaningful text, the character must be separated from its background and recognized via OCR. Different preprocessing variants were tested before OCR to assess their impact on performance. The methods used for these variants are listed in Table 3. For each variant, an index string is generated (e.g., thr40_adnone_mopen_k1_ma10_pad2_easy), and the recognition accuracy is computed by comparing the OCR output with the ground truth. Table 4 shows sample index values among the 288 variants. Figure 8 plots accuracies for 32/48/64-pixel images by variant index. The top-performing OCR results are summarized in Table 5.

Table 3. Methods and variants used to separate the character from the background prior to OCR

Process	Variations
Threshold	[40, 80, 120]
Adaptive Thresholding	[“none”, “gauss”]
Morphological Operation	[“none”, “open”, “close”]
Kernel	[0, 1]
Noise Elimination	[5, 10]
Pad	[1, 2]
OCR	[“Tesseract”, “EasyOCR”]

Table 4. Example variant index values

Variation	Variation Index
thr80_adnone_mclose_k1_ma10_pad2_easy	1
	. . .
thr80_adnone_mclose_k1_ma10_pad1_easy	20
	. . .
thr40_adgauss_mopen_k0_ma5_pad1_easy	96
	. . .
thr120_adgauss_mopen_k1_ma10_pad1_tess	126
	. . .
thr120_adnone_mclose_k1_ma5_pad2_tess	256
	. . .
thr40_adgauss_mclose_k1_ma5_pad1_tess	288

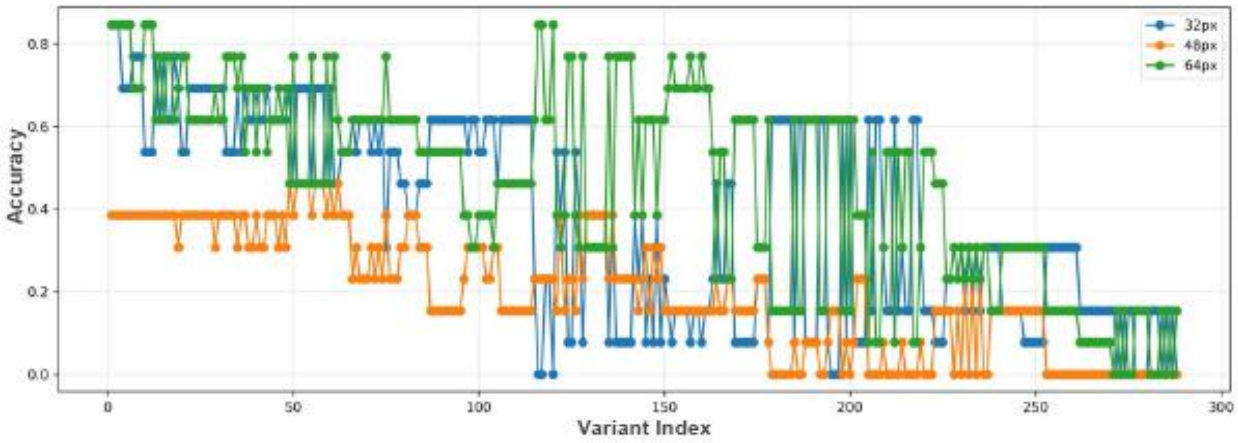


Figure 8. Accuracy of 32/48/64-pixel images by variant index

Table 5. OCR accuracy results

Pixel Size	Variant	Accuracy (%)
64	thr40_adnone_mopen_k1_ma10_pad2_easy	0.88
48	thr80_adnone_mclose_k0_ma10_pad2_easy	0.81
32	thr40_adnone_mclose_k0_ma10_pad2_easy	0.83

The error matrix of the highest accuracy results found because of hiding and retrieving the "MAHMUTSİNECEN" text used within the scope of the study is shown in Figure 9.

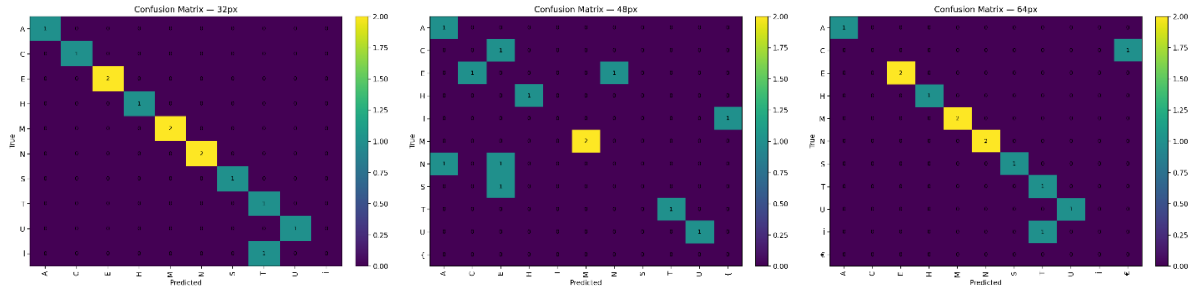


Figure 9. Confusion matrices for the recovered secret text at 32/48/64-pixel image sizes

4.2. Ablation study

The ablation study demonstrates the importance of ROI selection and high-pass feature extraction. Removing ROI selection significantly reduces both recovery accuracy and visual quality, confirming its effectiveness in preserving imperceptibility. As shown in Table 6, these results quantitatively confirm that ROI-guided embedding and high-pass–assisted recovery are critical components of the proposed framework, jointly contributing to both imperceptibility and reliable text reconstruction.

Table 6. Ablation study results

Configuration	Accuracy (%)	SSIM
Full model	87.9	0.94
No ROI	79.3	0.89
No HP filters	82.1	0.91
RGB embedding	80.7	0.88

5. Discussion

Steganography aims to conceal the existence of secret communication by embedding information within an innocuous carrier while preserving the carrier's perceptual integrity. From this perspective, video-sharing platforms that are publicly accessible worldwide provide a particularly suitable medium for steganographic applications, as videos can be distributed and consumed without arousing suspicion. Without specialized analysis tools and knowledge of the embedding mechanism, hidden messages remain indistinguishable from benign visual content.

Motivated by these considerations, the present study proposes a deep learning–based framework for embedding and retrieving textual information from video data. Unlike classical least significant bit (LSB)–based methods, which rely on direct bit-level replacement and are vulnerable to statistical steganalysis, the proposed approach leverages a U-Net–based architecture combined with ROI-guided embedding. This design enables the secret information to be adaptively distributed within visually complex regions of video frames, thereby improving imperceptibility and resistance to detection. Moreover, restricting access to the hidden content through a trained neural network further increases the difficulty of unauthorized recovery.

One practical challenge observed in the experiments is the trade-off between payload resolution and computational cost. Increasing the resolution of embedded character patches significantly raises the computational burden during training and inference, as model complexity and memory consumption grow accordingly. In this study, patch sizes of 32×32, 48×48, and 64×64 pixels were selected to balance recovery accuracy, processing time, and visual quality. While higher resolutions could mitigate the impact of video compression artifacts, they may also increase the risk of perceptible distortions within the carrier frames.

Although the experiments in this study were conducted on uppercase English characters, extending the pipeline to diacritics commonly used in Turkish (e.g., ğ, ö, ü, and dotted i) remains challenging due to OCR

and preprocessing sensitivity. These errors stem primarily from binarization, morphological filtering, and OCR model limitations, rather than from the embedding process itself. As a result, OCR accuracy constitutes a bottleneck in the end-to-end system performance.

Compared to GAN-based steganography approaches, this ROI-guided U-Net framework demonstrates improved training stability and reduced computational complexity, as it avoids adversarial optimization and mode-collapse issues commonly associated with GANs. The encoder–decoder structure with skip connections enables effective multi-scale feature fusion while maintaining stable convergence. Nevertheless, the dependency on OCR for final text recovery remains a limitation of the current implementation.

Future research will focus on enhancing robustness against video compression artifacts introduced by different codecs and extending the framework to support multilingual text. Additional investigations will explore alternative deep learning architectures, parameter optimization strategies, and hardware configurations to reduce training time and enable real-time or near-real-time text retrieval. Furthermore, improving OCR robustness—particularly for low-resolution characters, diacritics, and punctuation—will be a key objective to ensure accurate sentence-level reconstruction.

6. Author Contribution Statement

In the study, Author 1 contributed to the idea, design, literature review, experimental study and writing of the article.

7. Ethics Committee Approval and Conflict of Interest

Ethics committee approval is not required for this study. “There is no conflict of interest with any person/institution in the prepared article.”

8. Ethical Statement Regarding the Use of Artificial Intelligence

No artificial intelligence-based tools or applications were used in the preparation of this study. The entire content of the study was produced by the author in accordance with scientific research methods and academic ethical principles.

9. References

[1] M. A. Idakwo, M. B. Muazu, A. E. Adedokun and B. O. Sadiq, "An extensive survey of digital image steganography: State of the art," arXiv:2404.19548, 2024.
[2] I. I. Araujo and H. Kazemian, "Vulnerability exploitations using steganography in PDF files," *Int. J. Comput. Netw. Appl.*, vol. 7, no. 1, p. 10, 2020.
[3] F. Nabi and M. M. Afzal, "Image steganography: Critical findings through some novel techniques," *Int. J. Innov. Technol. Explor. Eng.*, vol. 9, no. 5, pp. 878–890, 2020.
[4] H. Li *et al*., "Smaller is bigger: Rethinking the embedding rate of deep hiding," 2023.
[5] K. Koptyra and M. R. Ogiela, "Distributed steganography in PDF files—Secrets hidden in modified pages," *Entropy*, vol. 22, no. 6, p. 600, 2020.
[6] A. D. Wiranata and R. T. Aldisa, "Aplikasi steganografi menggunakan least significant bit (LSB) dengan enkripsi Caesar Chipper dan Rivest Code 4 (RC4) menggunakan bahasa pemrograman JAVA," *J. JTIK (J. Teknol. Inf. dan Komun.)*, vol. 5, no. 3, pp. 277–281, 2021.
[7] M. A. Ali Khodher and T. W. Aldeen Khairi, "Review: A comparison steganography between texts and images," *J. Phys.: Conf. Ser.*, vol. 1591, no. 1, p. 012024, 2020.
[8] J. Kose, O. B. Chia and V. Baboolal, "Review and test of steganography techniques," 2020.
[9] Q. Li *et al*., "A novel grayscale image steganography scheme based on chaos encryption and generative adversarial networks," *IEEE Access*, vol. 8, pp. 168166–168176, 2020.
[10] P. Wei, Q. Zhou, Z. Wang, Z. Qian, X. Zhang and S. Li, "Generative steganography diffusion," 2023.
[11] A. K. Sahu and M. Sahu, "Digital image steganography and steganalysis: A journey of the past three decades," *Open Comput. Sci.*, vol. 10, no. 1, pp. 296–342, 2020.
[12] J. Fridrich, *Steganography in Digital Media: Principles, Algorithms, and Applications*. Cambridge, U.K.: Cambridge Univ. Press, 2012.
[13] L. Zeng, W. Lu, W. Liu and J. Chen, "Deep residual network for halftone image steganalysis with stego-signal diffusion," *Signal Process.*, vol. 172, p. 107576, 2020.
[14] J. Wang *et al*., "Fighting malicious media data: A survey on tampering detection and deepfake detection," 2022.
[15] S. Rahman *et al*., "A novel and efficient digital image steganography technique using least significant bit substitution," *Sci. Rep.*, vol. 15, no. 1, p. 107, 2025.
[16] B. Chen, W. Luo, P. Zheng and J. Huang, "Universal stego post-processing for enhancing image steganography," *J. Inf. Secur. Appl.*, vol. 55, p. 102664, 2020.
[17] D. Volkhonskiy, I. Nazarov and E. Burnaev, "Steganographic generative adversarial networks," in *Proc. 12th Int. Conf. Mach. Vis. (ICMV 2019)*, SPIE, 2020, p. 97.
[18] J. Liu *et al*., "Recent advances of image steganography with generative adversarial networks," *IEEE Access*, vol. 8, pp. 60575–60597, 2020.
[19] S. Rahman *et al*., "A comprehensive study of digital image steganographic techniques," *IEEE Access*, vol. 11, pp. 6770–6791, 2023.
[20] R. Chaganti, V. Ravi, M. Alazab and T. D. Pham, "Stegomalware: A systematic survey of malware hiding and detection in images, machine learning models and research challenges," 2021.
[21] R. Apau, M. Asante, F. Twum, J. Ben Hayfron-Acquah and K. O. Peasah, "Image steganography techniques for resisting statistical steganalysis attacks: A systematic literature review," *PLoS One*, vol. 19, no. 9, p. e0308807, 2024.
[22] Y. Sanjalawe, S. Al-E'mari, S. Fraihat, M. Abualhaj and E. Alzubi, "A deep learning-driven multi-layered steganographic approach for enhanced data security," *Sci. Rep.*, vol. 15, no. 1, p. 4761, 2025.
[23] Z. Zhou, Y. Su, Q. M. J. Wu, Z. Fu and Y. Shi, "Secret-to-image reversible transformation for generative steganography," 2022.
[24] M. Shukor, B. B. Damodaran, X. Yao and P. Hellier, "Video coding using learned latent GAN compression," in *Proc. 30th ACM Int. Conf. Multimedia*, New York, NY, USA: ACM, 2022, pp. 2239–2248.
[25] R. C. Gonzalez and R. E. Woods, *Digital Image Processing*, 4th ed. New York, NY, USA: Pearson, 2018.

[26] I. Sobel and G. Feldman, "A 3×3 isotropic gradient operator for image processing," 1968.
[27] *scikit-image: Image processing in Python*. [Online]. Available: https://scikit-image.org/
[28] *OpenCV documentation index*. [Online]. Available: https://docs.opencv.org/
[29] O. Ronneberger, P. Fischer and T. Brox, "U-Net: Convolutional networks for biomedical image segmentation," 2015.
[30] J. Hu, L. Shen and G. Sun, "Squeeze-and-excitation networks," in *Proc. IEEE Conf. Comput. Vis. Pattern Recognit. (CVPR)*, 2018, pp. 7132–7141.
[31] Y. Wu and K. He, "Group normalization," in *Proc. Eur. Conf. Comput. Vis. (ECCV)*, 2018, pp. 3–19.
[32] P. Ramachandran, B. Zoph and Q. V. Le, "Searching for activation functions," in *Proc. Int. Conf. Learn. Represent. (ICLR), Workshop Track*, 2018.
[33] J. Fridrich and J. Kodovsky, "Rich models for steganalysis of digital images," *IEEE Trans. Inf. Forensics Security*, vol. 7, no. 3, pp. 868–882, 2012.
[34] Z. Wang, A. C. Bovik, H. R. Sheikh and E. P. Simoncelli, "Image quality assessment: From error visibility to structural similarity," *IEEE Trans. Image Process.*, vol. 13, no. 4, pp. 600–612, 2004.
[35] S. Baluja, "Hiding images in plain sight: Deep steganography," in *Proc. Adv. Neural Inf. Process. Syst. (NeurIPS)*, 2017, pp. 1–11.
[36] I. Loshchilov and F. Hutter, "Decoupled weight decay regularization," 2019.
[37] *ReduceLROnPlateau — PyTorch documentation*. [Online]. Available: https://docs.pytorch.org/docs/stable/generated/torch.optim.lr_scheduler.ReduceLROnPlateau.html
[38] *ReduceLROnPlateau — Keras API documentation*. [Online]. Available: https://keras.io/api/callbacks/reduce_lr_on_plateau/
[39] I. Goodfellow, Y. Bengio and A. Courville, "Optimization for training deep models," in *Deep Learning*. Cambridge, MA, USA: MIT Press, 2016, pp. 271–325.

Fırat Üniversitesi Deneysel ve Hesaplamalı Mühendislik Dergisi

FUJECE

Burdur Havzası'nda Kara Yüzey Sıcaklığı (LST) ve Spectral İndekslerin (NDVI, NDBI, NDBaI) Mekansal-Zamansal Dinamikleri

Erkan KARAKOYUN[1]*

[1]Mühendislik Mimarlık Fakültesi, Muş Alparslan Üniversitesi, Muş, Türkiye.
[1]e.karakoyun@alparslan.edu.tr

Geliş Tarihi: 01.1.2026
Kabul Tarihi: 02.2.2026

Düzeltme Tarihi: 24.1.2026

doi: https://doi.org/10.62520/fujece.1854048
Araştırma Makalesi

Alıntı: E. Karakoyun,'' Burdur havzası'nda kara yüzey sıcaklığı (LST) ve spectral indekslerin (NDVI, NDBI, NDBaI) mekansal-zamansal dinamikleri '', Fırat Üni. Deny. ve Hes. Müh. Derg., vol. 5, no 1, pp. 363-381, Şubat 2026.

Öz

Son yıllarda iklim değişikliği, artan kentleşme, ormansızlaşma ve arazi kullanım-arazi örtüsü değişikliği gibi çeşitli çevresel parametreler farklı çevresel sorunlara yol açmıştır. Bu etkileri değerlendirmek ve gözlemlemek için, bu çalışma 2014-2025 yılları arasında Burdur Havzası'ndaki Kara Yüzey Sıcaklığı (LST) ve Normalleştirilmiş Fark Bitki Örtüsü İndeksi (NDVI), Normalleştirilmiş Fark Çıplaklık İndeksi (NDBaI) ve Normalleştirilmiş Fark Yapılaşma İndeksi (NDBI) gibi bazı spektral indeksleri incelemiştir. Coğrafi Bilgi Sistemi (GIS) ve Uzaktan Algılama teknolojileri, çok zamanlı Landsat uydularından elde edilen görüntüler kullanılarak Burdur Havzası üzerindeki bu çalışmada kullanılan indekslerin korelasyon analizi, zamansal değişimleri ve mekansal dağılımını hesaplamak için entegre edilmiştir. Bu çalışmanın sonuçlarına göre, LST değerleri özellikle havzanın kuzeydoğu ve orta kesimlerinde 2016 ve 2019 yıllarında artış göstermiştir. Çalışma döneminde NDBI ve NDBaI değerlerinde önemli bir değişiklik görülmemesine rağmen, 2018 yılında kısmen hafif yukarı yönlü değişimler gözlemlenmiştir. NDVI değerleri -0,36 ile 0,68 arasında değişmiş olup, bu değerler yıllar boyunca çoğunlukla istikrarlı kalmıştır. LST ve NDVI arasında çok zayıf pozitif bir korelasyon analizi tespit edilmiştir. Ayrıca, LST ile NDBI ve NDBaI arasındaki ilişki, 2014-2025 yılları arasında orta derecede pozitif bir korelasyon göstermiştir. Sonuçlar, kentsel ve çıplak toprak alanlarının genişlemesinin LST değerlerinde artışa neden olduğunu göstermiştir. Buna karşılık, bitki örtüsünün varlığı yüzey sıcaklığını düşürmeye yardımcı olabilir. Sonuç olarak, bu çalışma, bitki örtüsünün varlığı, kentleşme ve arazi kullanımı ve arazi örtüsü özelliklerinin Burdur Havzası üzerindeki LST değerleri üzerinde etkili olduğunu kanıtlamıştır. Dahası, bu çalışma, CBS ve uzaktan algılama teknolojilerinin entegrasyonunun, zamansal ve mekansal çevresel değişiklikleri değerlendirmek için değerli bir teknik olduğunu göstermiştir.

Anahtar kelimeler: LST, NDVI, NDBI, NDBaI, Uzaktan algılama

*Yazışılan yazar

İntihal Kontrol: Evet – Turnitin
Şikayet: fujece@firat.edu.tr
Telif Hakkı ve Lisans: Dergide yayın yapan yazarlar, CC BY-NC 4.0 kapsamında lisanslanan çalışmalarının telif hakkını saklı tutar.

Firat University Journal of Experimental and Computational Engineering

Spatiotemporal Dynamics of Land Surface Temperature (LST) and Spectral Indices (NDVI, NDBI, NDBaI) in the Burdur Basin

Erkan KARAKOYUN[1]*

[1]Faculty of Engineering and Architecture, Muş Alparslan University, Muş Türkiye.
[1]e.karakoyun@alparslan.edu.tr

Received: 01.1.2026
Accepted: 02.2.2026
Revision: 24.1.2026
doi: https://doi.org/10.62520/fujece.1854048
Research Article

Citation: E. Karakoyun, "Spatiotemporal dynamics of land surface temperature (LST) and spectral ındices (NDVI, NDBI, NDBaI) in the Burdur basin", Firat Univ. Jour.of Exper. and Comp. Eng., vol. 5, no 1, pp. 363-381, February 2026.

Abstract

In recent decades, several environmental parameters such as climate change, expanding urbanization, deforestation, and land use land cover change resulted in various environmental issues. To evaluate and observe these impacts, this study indicated the Land Surface Temperature (LST), and some spectral indices including Normalized Difference Vegetation Index (NDVI), Normalized Difference Bareness Index (NDBaI), and Normalized Difference Built-Up Index (NDBI) in the Burdur Basin for the years between 2014-2025. Geographical Information System (GIS) and Remote Sensing technologies were integrated by using the images obtained from multi-temporal Landsat satellites to calculate correlation analysis, temporal changes, and spatial distribution of indices used in this study over the Burdur Basin. Based on the results of this study, LST values increased especially in the northeastern and central parts of the basin in 2016 and 2019. Although no significant variation was seen for NDBI and NDBaI values during the studied period, slight upward changes were partly observed in 2018. NDVI values varied between -0.36 and 0.68 while those values were observed mostly stable over years. A very weak positive correlation analysis was indicated between LST and NDVI. Additionally, the relationship between LST and NDBI, and NDBaI produced a moderately positive correlation between 2014-2025. The results indicated that, expanding urban and bare soil areas, resulted in increased LST values. In contrast, presence of vegetation can help to reduce surface temperature. To conclude, this study proved that, the presence of vegetation, urbanization, and land use and land cover properties has an impact on LST values over the Burdur Basin. Furthermore, this study indicated that integrating GIS and Remote Sensing technologies are valuable technique to evaluate temporal and spatial environmental changes.

Keywords: LST, NDVI, NDBI, NDBaI, Remote sensing

*Corresponging author

Plagiarism Checks: Yes – Turnitin
Complaints: fujece@firat.edu.tr
Copyright & License: Authors publishing with the journal retain the copyright to their work licensed under the CC BY-NC 4.0

1. Introduction

In recent years, Land Use and Land Cover Change (LULCC) methods and their associated techniques have been extensively utilized in different areas. In addition, numerous mapping techniques have been developed to analyse changes in land properties in a particular region using the LULCC technique [1,2]. Because of this, LULCC in specific basins is very important parameter for monitoring environmental impacts and anthropogenic base changes. With the development of computer technologies in recent years and the consequences of improvements in remote sensing methods and satellite technologies researchers have conducted studies in various regions using different techniques to observe LULCC [3]. Obtaining current and accurate data is necessary to determine the effect of such changes on water resources, surface temperature, and vegetation in the basin. This is because evaluating the environmental impact of the watershed based on a single parameter change may not be sufficient. In addition to traditional land use and land cover classification algorithms, various spectral indices including Normalized Difference Vegetation Index (NDVI), Normalized Difference Water Index (NDWI), Normalized Difference Built-up Index (NDBI), Normalized Difference Bareness Index (NDBaI), and Land Surface Temperature (LST) are utilized in literature to determine particular land properties. These indices are used for numerous purposes all over the world in many different fields, such as mapping environmental changes in a specific region over time, as well as correlating changes in these indices with each other.

Land Surface Temperature (LST) is a parameter that can be generated using several GIS techniques and collected from many remote sensing data. It is mostly used when defining Urban Heat Island (UHI) zones. Additionally, UHI calculations often use the LST values derived from meteorological stations. However, these estimations may be inadequate due to the stations' limited coverage of most of the region. However, satellite imagery and its integration with remote sensing and GIS tools can overcome these constraints.

Especially in recent decades, the population in most cities is growing [4]. Because of these situations, researchers are investigating how environmental properties and building patterns are changed over time [5,6]. In parallel, the increasing population and urbanization have an adverse effect on environmental factors and have caused changes in LULC over time [7-11]. Therefore, it is essential for researchers to investigate LULCC and related spectral indices to evaluate them in terms of environmental properties in specific regions [12].

In order to determine LULC classification for a particular region, the percentage of different LULC are utilized. Besides, numerous spectral indices are also used to define land properties [13]. At this point, remote sensing techniques and GIS methods have become the most suitable methods to determine LULCC, land surface temperature, and other indices. In order to do that, it requires comprehensive studies integrating scientific methods, remote sensing, and GIS technologies with spatial correlation, regression, and temporal variation models [14]. Observing LST and LULC dynamics over long periods using multi temporal imagery from satellites such as Landsat, Sentinel, and MODIS over a specific area is an effective method for these studies. Integrating this satellite imagery with GIS platforms provides a fundamental environment for the analysis, classification, and interpretation of these datasets, generating spatial outputs that support decision-making processes [9].

The Normalized Difference Vegetation Index (NDVI) is the most common technique that determines the vegetation changes over time, and is particularly integrated with the studies related to surface temperature [15,16,17]. Besides, NDVI is an important part of LST calculations. Several studies related to LST-NDVI correlation have been conducted in the literature to define LST models. Because LST and NDVI indices are closely related and affect each other mutually [5]. In addition, numerous studies have examined the relationship between NDVI and different climate variables over time. But studies show an especially emphasis on the relationship between LST and NDVI [10,18,19]. Researchers assessed the environmental impacts of changes by examining land based modifications and various indicators in addition to key indices like LST and NDVI. For example, in studies related to LULC and LST, the Normalized Difference Water Index (NDWI) is a commonly used index that determines water bodies

[20-23]. Normalized Difference Bareness Index (NDBaI) is another index that is commonly used in the literature. The NDBaI is utilized to define bare areas and generally uses the studies related to LST and LULC indices in different areas [23]. For example, [24] studied the relationship between LST and NDBaI in Raipur City, India. Their results indicate that LST and NDBaI have a positive moderate relationship. Another spectral index, Normalized Difference Built-Up Index (NDBI) is commonly used in literature to detect built up areas, and is mostly used with LST studies [25]. The studies that investigate the relationship between LST and NDBI have produced mostly positive results. However, this relationship can be effected by numerous parameters including vegetation, meteorological parameters, and soil condition [5].

Many researchers have investigated environmental changes in different regions by using several spectral indices and determining their relationship. For example, [26] studied with the indices including LST, NDVI, and LULC as well as the correlation with topographic parameters in Pakistan. Their results indicate that NDVI values increased with altitude, while LST values decreased with altitude. Besides, they found that surface temperature values are higher where built-up and bare soil areas. In addition, the study conducted by [22] determined the seasonal changes in LST and LULC with the indices NDVI, NDBI, NDWI, and NDBaI in Hong Kong. Their findings revealed that LULC types are the primary indicator of LST. Besides, a negative correlation was observed between NDVI and NDWI, while a positive correlation was observed between NDBI and NDBaI. In addition to studies around the world, many researchers have revealed temporal variation in land properties also in different regions in Türkiye by using different indices such as LST, NDVI, NDBI, NDBaI, and NDWI [9,18,27]. For example, [29] investigated spatiotemporal variability in LST for Zonguldak, Türkiye. Their results indicated that the temperature has been steadily increasing, and the expansion of the urban area has resulted in increased LST. [29] used LST and NDVI in Salt Lake Basin Area, Türkiye, to monitor drought. Another study of [30] was used to detect the temporal changes of NDVI and NDBI in Bursa, Türkiye. Their findings showed that NDVI is an effective method for monitoring changes, particularly in urban areas. Besides, details of some of the studies in the literature reviewed for this study, as well as the current study, are given in Table 1.

Table 1. Detailed list of previous studies

Authors	Published Journal	Study Area	Data Used	Method Used
Anbazhagan and Paramasivam (2016)	International Journal of Advanced Earth Science and Engineering	India	Landsat 5, Landsat 7	LST, NDVI
Değerli and Çetin (2022)	Turkish Journal of Agriculture - Food Science and Technology	Samsun, Türkiye	Landsat 7, Landsat 8	NDVI, NDBI
Karakoyun (2024)	MAUN Journal of the Faculty of Engineering and Architecture	Muş, Türkiye	Landsat 8	LST, NDVI
Guha and Govil (2021)	Environment, Development and Sustainability	Raipur City, India	Landsat 5, Landsat 7, Landsat 8	LST, NDVI
Guha et al (2020)	Geomatics, Natural Hazards and Risk	Raipur City, India	Landsat 5, Landsat 7, Landsat 8	LST, NDWI
Siqi and Yuhong (2020)	Urban Climate	Hong Kong	Landsat 8, Sentinel 2	LST, NDBI, NDBaI, NDVI, NDWI
Guha and Govil (2022)	International Journal of Engineering and Geosciences	Raipur City, India	Landsat 5, Landsat 7	LST, NDBaI
Alademomi et al. (2022)	Applied Geomatics	Lagos, Nigeria	Landsat 7, Landsat 8	LST, NDVI, NDBI
Garai et al (2022)	Safety in Extreme Environments	West Bengal, India	MODIS	LST, NDVI
Ullah et al. (2023)	Heliyon	Himalayan Region, Pakistan	Landsat 8	LST, NDVI
Altıner and Bingöl (2025)	Sustainability	Balıkesir, Türkiye	Landsat 4, Landsat 5, Landsat 8, Landsat 9	LST, NDVI, NDBI
This study		Burdur Basin, Türkiye	Landsat 8, Landsat 9	LST, NDVI, NDBI, NDBaI

The integrated application of remote sensing and geographic information systems (GIS) offers robust methodologies for monitoring long-term environmental changes using vegetation indices and land surface temperature (LST) data. This study aims to investigate the spatio-temporal relationship between LST and selected spectral indices, including NDVI, NDWI, NDBI, and NDBaI, within the Burdur Basin over recent decades. To address this aim, remote sensing–based indices derived from multi-temporal satellite imagery are analyzed, and correlation analyses are performed to assess the interactions between LST and other spectral indices. Additionally, the spatial distribution of these indices is mapped to facilitate the interpretation of environmental changes in this semi-arid region.

2. Material and Method

2.1. Study area and data

The Burdur Basin is located in the mid-southwest of Türkiye. The basin covers a total area of 627,378 hectares and constitutes 0.8% of Türkiye's total surface area. Burdur Basin is also called the lakes region. Burdur Lake, Acı Lake, Salda Lake, and Karatas Lake are located within the basin boundaries. The basin location is shown in Figure 1.

In this study, the primary datasets consist of time-series Landsat imagery obtained from the United States Geological Survey website (https://earthexplorer.usgs.gov/), captured by Landsat 8 and Landsat 9 satellites. An image covering the study area and consisting of two different paths for each year was downloaded, and its specifications are given in Table 2. Before proceeding with the calculation of spectral indices, some procedures should be done. ArcGIS Pro software was used for all spectral indices obtained during the study. First, two images covering the study area were combined using the mosaic function in ArcGIS Pro. Then, the resulting image was clipped using the extracted-by-mask function to obtain the necessary bands for the specified study area.

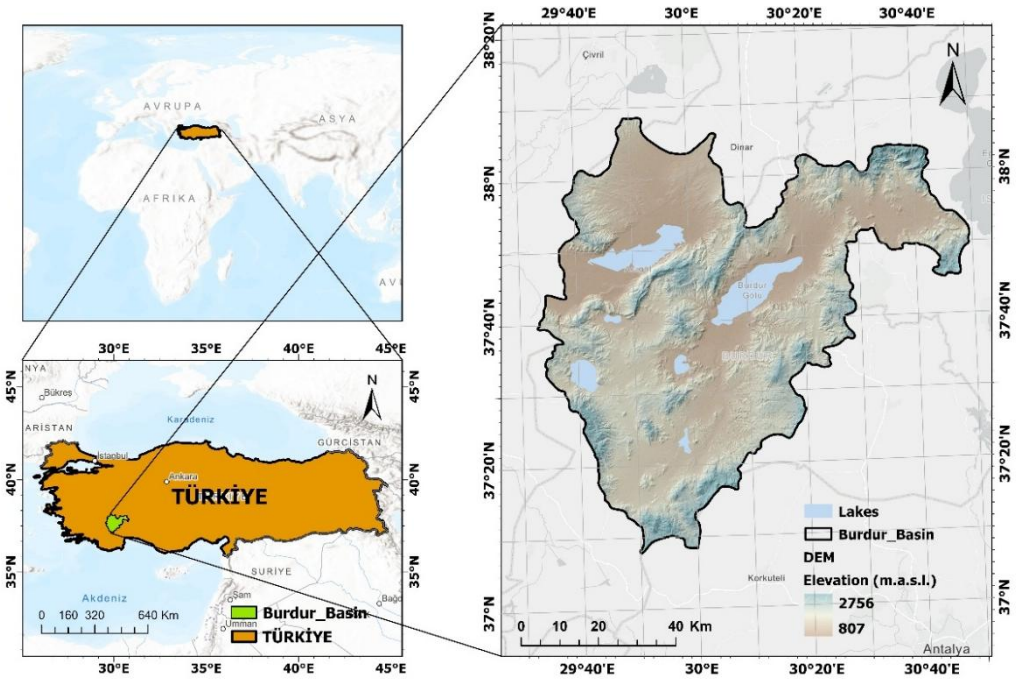


Figure 1. Location of study area

Table 2. Specifications of landsat images

Year	Sensor	Path/Row	Date of acquisition
2014	Landsat 8	178/34	7/3/2014
	Landsat 8	179/34	7/10/2014
2015	Landsat 8	178/34	7/22/2015
	Landsat 8	179/34	7/13/2015
2016	Landsat 8	178/34	7/24/2016
	Landsat 8	179/34	7/15/2016
2017	Landsat 8	178/34	7/11/2017
	Landsat 8	179/34	7/2/2017
2018	Landsat 8	178/34	7/14/2018
	Landsat 8	179/34	7/5/2018
2019	Landsat 8	178/34	7/1/2019
	Landsat 8	179/34	7/8/2019
2020	Landsat 8	178/34	7/19/2020
	Landsat 8	179/34	8/11/2020
2021	Landsat 8	178/34	7/22/2021
	Landsat 8	179/34	7/29/2021
2022	Landsat 8	178/34	7/25/2022
	Landsat 9	179/34	7/24/2022
2023	Landsat 8	178/34	7/12/2023
	Landsat 8	179/34	7/19/2023
2024	Landsat 8	178/34	8/15/2024
	Landsat 9	179/34	8/14/2024
2025	Landsat 8	178/34	8/9/2025
	Landsat 9	179/34	8/10/2025

2.2. Method

2.2.1. Calculation of LST and NDVI

LST represents the surface temperature estimated from thermal-band imagery. The formulas used to compute LST (Eq. 1-6), which rely on satellite-derived inputs, are given below. The initial step in deriving LST for Landsat images involves converting the digital number (DN) to spectral radiance (Lλ), as shown in Equation 1.

$$L_\lambda = RadianceMultiBand * Digital\ Number + Radiance\ Add\ Band \quad (1)$$

where L_λ is spectral radiance.

$$T_b = \frac{K_2}{\ln\left(\frac{K_1}{L_\lambda}+1\right)} \quad (2)$$

where T_b is the sensor of brightness temperature, K_2 and K_1 are the calibration constants for Bands 10 and 11.

$$F_v = \left(\frac{NDVI-NDVI_{min}}{NDVI_{max}-NDVI_{min}}\right)^2 \quad (3)$$

where $NDVI_{min}$ and $NDVI_{max}$ refer to the minimum and maximum values of NDVI.

$$NDVI = \left(\frac{Band5-Band4}{Band5+Band4}\right) \quad (4)$$

where Band 4 (red) and Band 5 (Near infrared) are for Landsat 8 and Landsat 9 images.
Next, land surface emissivity is determined using Equation 5.

$$\varepsilon = 0.004 * P_v + 0.986 \quad (5)$$

Subsequently, the LST can be calculated as given in equation 6.

$$LST = \frac{T_b}{1+\left(\lambda*\frac{T_b}{\rho}\right)*\ln(\varepsilon)} \quad (6)$$

Where, λ is the thermal band wavelength, ρ is the value derived from physical constants such as Planck's constant and the speed of light.

2.2.2. Calculation of NDBI and NDBaI

NDBI is calculated by getting the difference between the SWIR and NIR reflectance values and dividing it by their sum. It is commonly used to define built-up areas. Built-up surfaces—such as concrete, asphalt, and roofing materials—generally show strong reflectance in the SWIR bands and comparatively low reflectance in the NIR bands. Urban and built-up areas typically yield positive NDBI values, while vegetation and water surfaces produce negative values. The NDBI formula is given in equation 7.

$$NDBI = \frac{SWIR-NIR}{SWIR+NIR} \quad (7)$$

A bareness index, referred to as NDBaI, distinguishes among bare land, and semi-bare land, and other land-use/land-cover types. NDBaI is obtained by taking the difference between the SWIR and TIR reflectance values and dividing it by their sum. For Landsat 8 and 9 data, SWIR is defined by band 6, and TIR is defined by band 10, and its formula is provided in equation 8.

$$NDBaI = \frac{SWIR-TIR}{SWIR+TIR} \quad (8)$$

3. Results and Discussion

In this study, different spectral indices, including LST, NDVI, NDBI, and NDBaI, were analyzed using a GIS platform over the last decade (2014-2025) in the Burdur Basin. The descriptive statistics, spatial distribution, and correlation analysis of the spectral indices used in this study are given in the following section.

3.1. Descriptive statistics of LST, NDVI, NDBI, and NDBaI

To determine the results of the indices retrieved from the map, some processes were applied. First, fishnet maps were created using a 10x10 grid, resulting in 100 points. Then, the fishnet maps were clipped by the study area, and 41 points remained withinthe study area. The image of these 41 points obtained in the study area is given in Figure 2. Next, all the points were determined for all the spectral indices with the function "extract multi values to points" in the ArcGIS Pro software. The descriptive statistics of the spectral indices used in this study are given in Table 3.

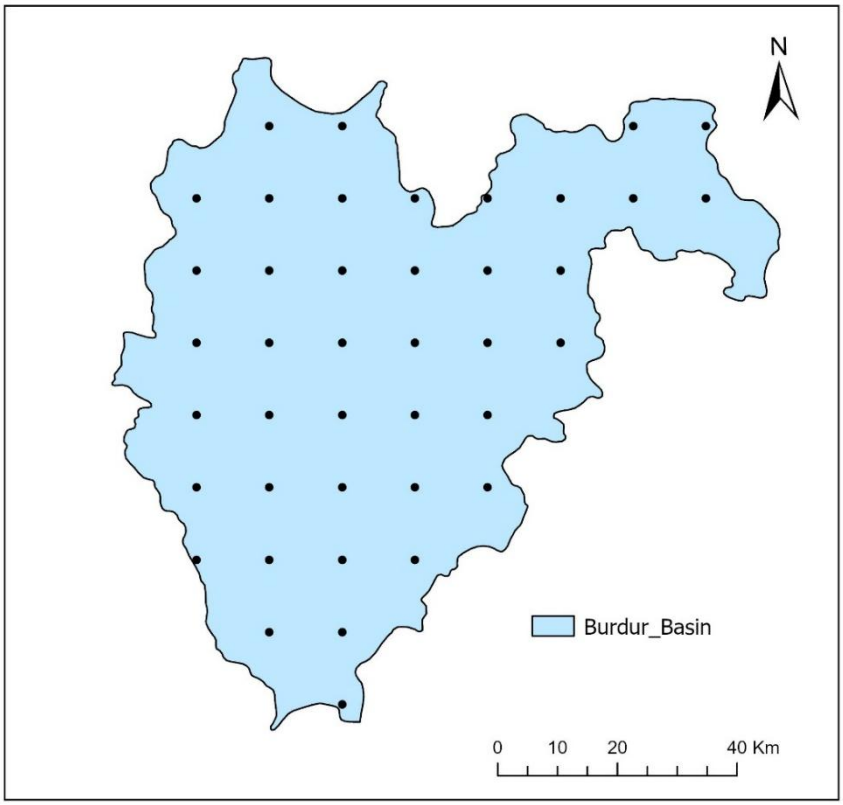


Figure 2. The created fishnet points over the study area

Table 3 shows that the minimum LST values, obtained from 41 points, were observed in 2022 at 11.90 ºC, while the maximum value was observed in 2017 at 48.11 ºC. In addition, the minimum NDBI value in 2019 was -0.34, while the maximum value was observed in 2024 at 0.14. Similarly, the minimum NDVI value was observed in 2020 with -0.26, while the highest value was observed in 2019 with 0.51. Besides, the minimum and maximum values were obtained in 2017 and 2019, respectively, at -0.70 and -0.01.

Table 3. Descriptive statistics of indices used

Year	LST			NDBI			NDVI			NDBal		
	Min	Max	Avg	Min	Max	Avg	Min	Max	Avg	Min	Max	Avg
2014	22.34	46.08	34.95	-0.16	0.08	-0.01	-0.13	0.35	0.17	-0.67	-0.10	-0.35
2015	20.68	38.74	29.77	-0.18	0.13	-0.02	-0.13	0.39	0.19	-0.66	-0.05	-0.33
2016	22.60	47.86	38.37	-0.19	0.09	0.00	-0.20	0.37	0.16	-0.70	-0.04	-0.36
2017	24.53	48.11	38.71	-0.24	0.08	-0.02	-0.21	0.41	0.18	-0.70	-0.10	-0.37
2018	21.51	39.81	31.38	-0.17	0.10	-0.01	-0.17	0.38	0.18	-0.67	-0.06	-0.33
2019	17.14	41.91	33.42	-0.34	0.07	-0.03	-0.24	0.51	0.19	-0.68	-0.01	-0.35
2020	21.19	44.01	34.14	-0.17	0.09	-0.01	-0.26	0.34	0.16	-0.68	-0.09	-0.33
2021	19.43	40.48	32.54	-0.22	0.10	0.01	-0.15	0.31	0.15	-0.66	-0.08	-0.31
2022	11.90	38.07	26.04	-0.16	0.08	-0.01	-0.13	0.33	0.17	-0.64	-0.06	-0.28
2023	21.38	38.68	32.36	-0.24	0.07	-0.04	-0.22	0.44	0.19	-0.68	-0.09	-0.35
2024	14.69	40.10	29.18	-0.13	0.14	0.02	-0.16	0.55	0.18	-0.65	-0.13	-0.29
2025	15.15	35.61	28.92	-0.24	0.09	-0.01	-0.07	0.43	0.18	-0.69	-0.03	-0.29

3.2. Spatial Distribution of LST, NDVI, NDBI, and NDBaI

LST distributions from 2014 to 2025 reveal notable interannual and spatial variations in surface temperatures within the study area (Figure 3). The maps show that the northern, northeastern, and central parts of the basin consistently have high LST values. On the other hand, wetlands and water surfaces showed lower LST values. The warmest years of the research period were 2016, 2017, 2018, and 2019. In these years, temperatures approached or even exceeded 50°C in many regions. In particular, as shown in the 2018 LST maps, the extent of warming zones reached its peak. A detailed examination of the maps shows a significant warming trend in the basin in 2023, 2024, and 2025. Specifically, it has been defined that higher LST values in the northern and northeastern regions are expected to expand through 2025.

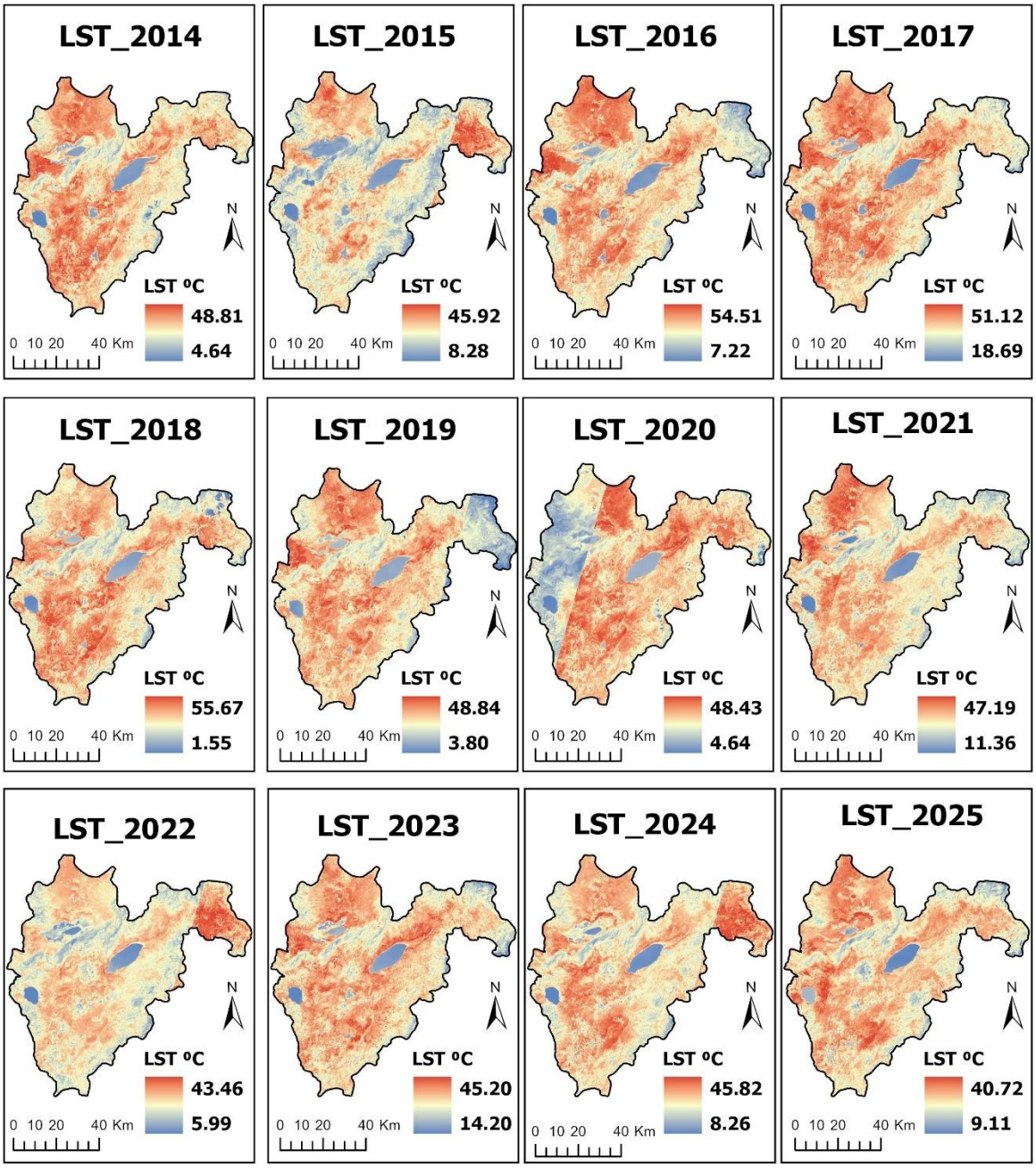


Figure 3. Spatial Distribution of LST over Burdur Basin

The distribution of NDVI values across the basin from 2014 to 2025 shows that vegetation density generally does not change much, but significant fluctuations are observed during specific periods (Figure 4). NDBI shows the size of settlements or urban areas, whereas NDVI shows the density and health of vegetation at the time of measurement. The values of both indices range from −1 to +1. Smaller values represent less vegetation and built-up, while higher values represent more vegetation and built-up [6]. NDVI values broadly indicate moderate to high vegetation cover. However, notable changes have occurred over the years. NDVI values were particularly high in 2017, 2022, and 2025, indicating healthier and denser vegetation during those years. In general, NDVI values did not show a significant deterioration trend during the 2014–2025 period. Still, declines, especially in 2020 and 2024, indicate that the ecosystem's sensitivity in the region persists and remains sensitive to climatic changes.

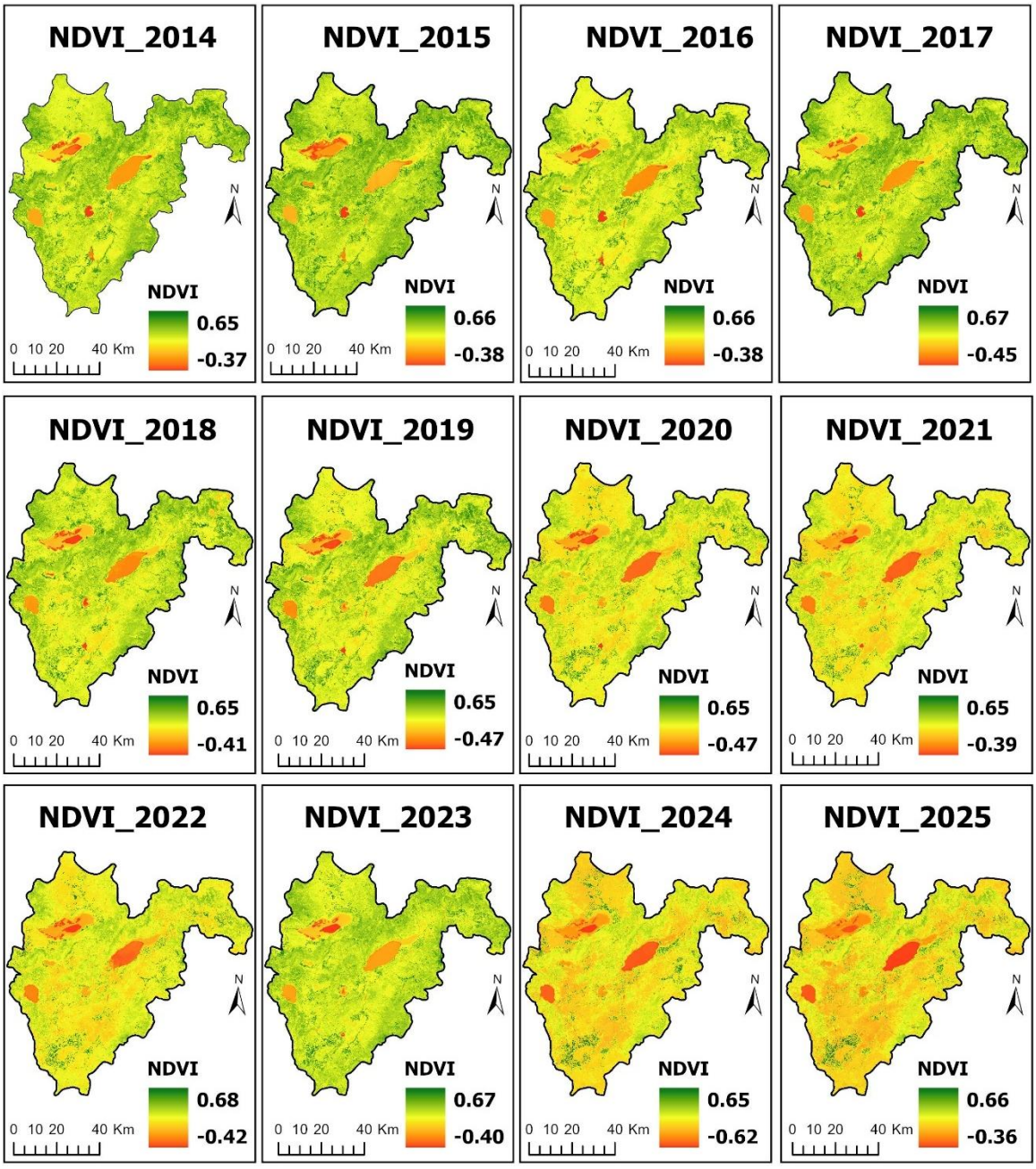


Figure 4. Spatial Distribution of NDVI over Burdur Basin

NDBI distributions from 2014 to 2025 show a similar pattern in the spatial distribution of urban areas and bare-soil surfaces across the study area over the years (Figure 5). However, some specific periods exhibit limited increasing or decreasing trends. In all years, higher NDBI values were observed in the northern and eastern parts of the basin. This indicates a greater density of construction or a higher proportion of bare land in these areas compared to others. Conversely, regions dominated by agricultural lands, water surfaces, and natural vegetation exhibited lower NDBI values. The concentration of NDBI values, mainly within the range 0.35–0.45, suggests a moderate level of construction and bare soil in the study area. It is observed that 2016, 2017, 2018, and 2019 had the highest positive NDBI values. The lower NDBI values in 2020 and 2021 suggest that vegetation cover increased or that bare land areas decreased during this period. In urban areas, NDBI values are consistently positive, which indicates that settlements are either steady or growing modestly over time. Overall, the NDBI values show slight variation between 2014 and 2025, indicating that there hasn't been a significant change in the urban areas in the research region.

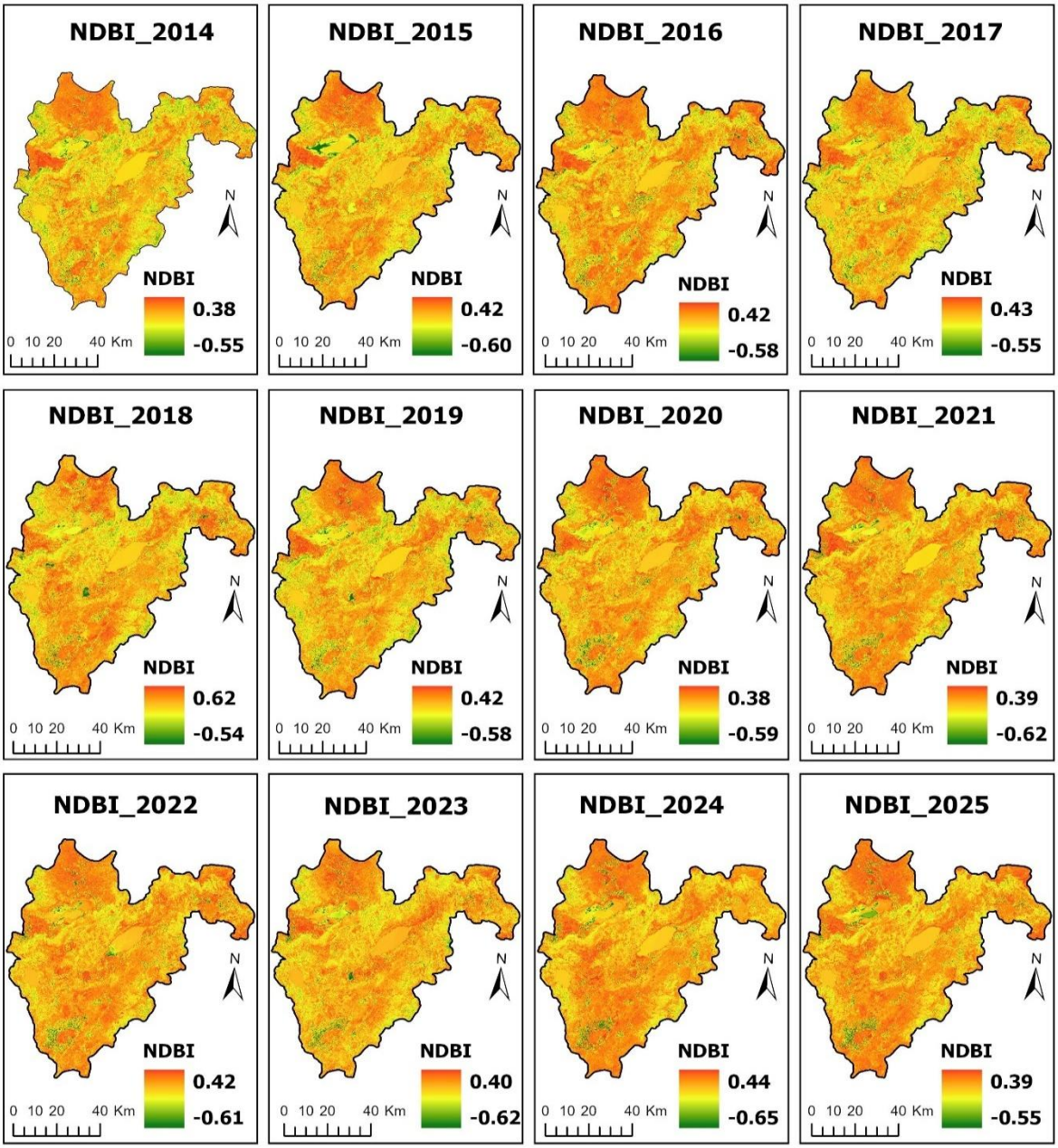


Figure 5. Spatial Distribution of NDBI over Burdur Basin

The NDBaI results from 2014 to 2025 are given in Figure 6. The results indicated that bare soil surface area produces both spatial and temporal variation over the study area. The NDBaI values are mostly moderate across the basin, which means these results are associated with soil moisture and vegetation density. This is because NDBaI values are expected to be lower at water surfaces, while they are expected to be higher in bare soil and sparse vegetation. This trend confirms that NDBaI values increase with decreasing surface moisture and increasing bare soil proportion. The years 2015, 2018, 2022, 2024, and 2025 were periods when relatively higher NDBaI values were observed, indicating that surface moisture decreased or the bare-soil ratio increased in these years. In contrast, NDBal values were relatively low in 2017 and 2019, indicating that those years were either more humid or that vegetation density had increased. The analysis of the NDBal distribution from 2014 to 2025 indicates that seasonal changes driven by climatic conditions have a greater impact on the basin's soil moisture and bare soil conditions than any long-term decline. However, the increasing trend observed after 2022 suggests that water stress and drought pressures are becoming more significant in some regions of the basin.

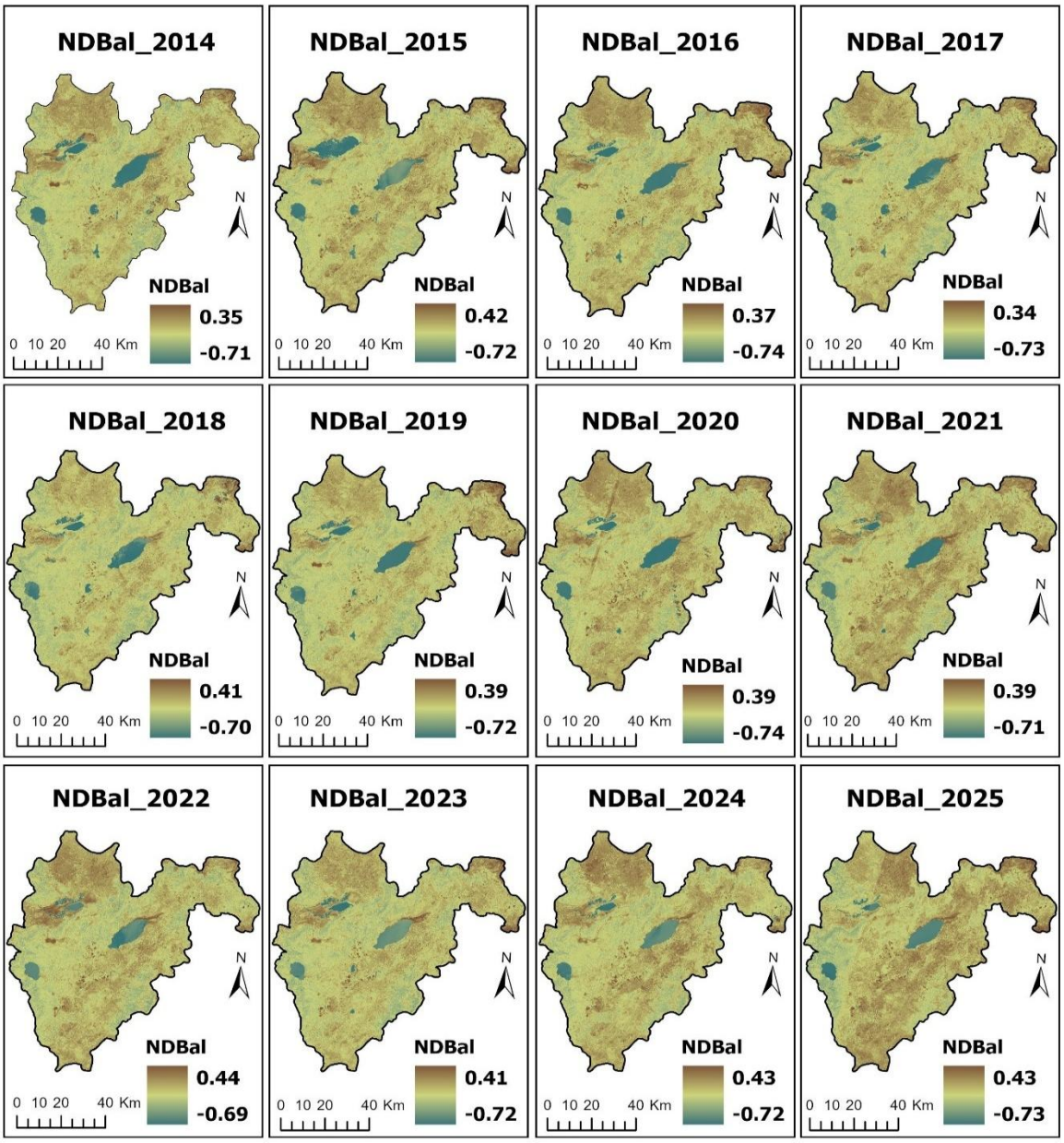


Figure 6. Spatial distribution of NDBaI over Burdur basin

3.3. Correlation analysis of LST, NDVI, NDBI, and NDBaI

The scatter plots of the mean values of LST-NDVI, LST-NDBI, and LST-NDBaI are illustrated in Figure 7. The correlation matrix indicates that LST and NDBaI are negatively associated, whereas LST-NDBI and LST-NDVI have a weak correlation.

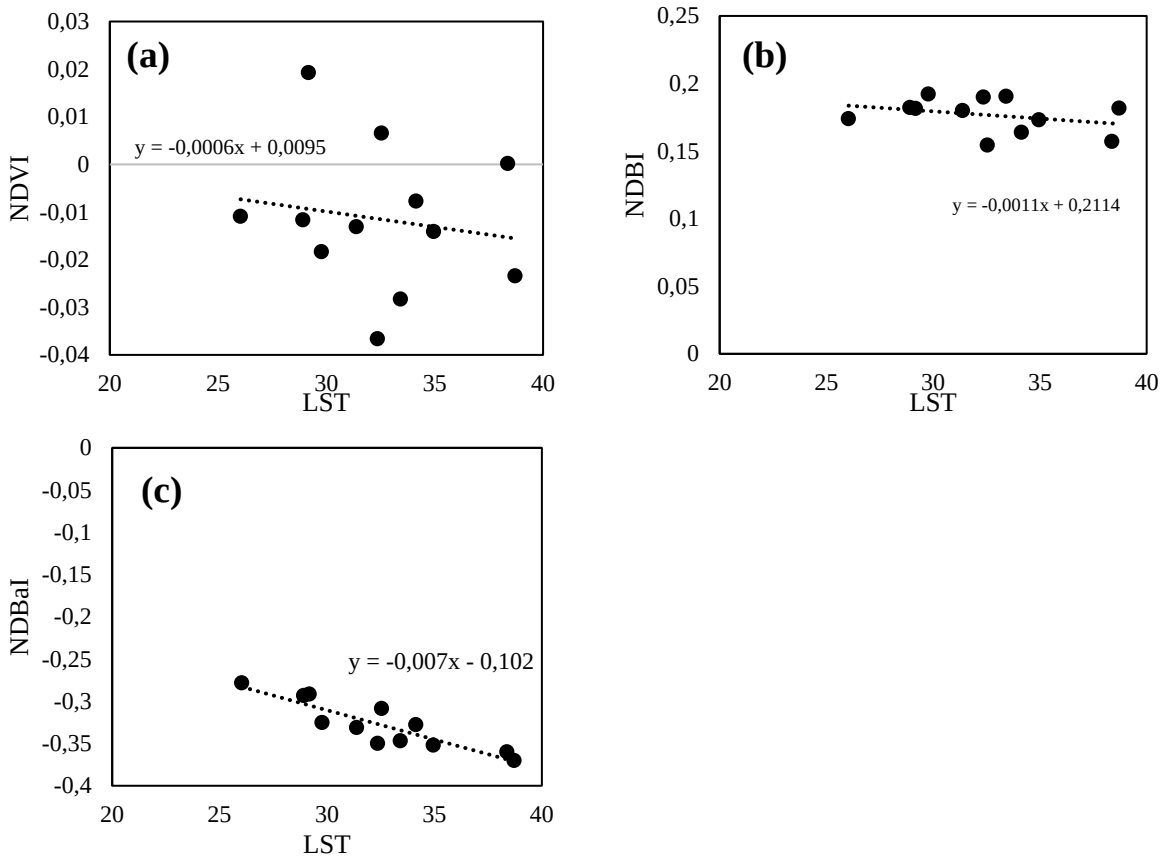


Figure 7. The scatter plot of mean values of (a) LST-NDVI, (b) LST-NDBI, and (c) LST-NDBaI

The results of the annual correlation analysis of LST, NDVI, NDBI, and NDBaI indices between 2014 and 2025 are given in Figure 8. According to these results, a positive correlation is generally observed between LST and NDBaI, and the highest correlation was obtained in 2014 with r=0.63. These results indicate that LST values are higher in dense urban areas. In addition, in terms of the results of annual correlation between LST and NDBI, the highest correlation was observed in 2014 with r = 0.63 while the lowest value was observed in 2025 with r = 0.28. Similarly, it was observed that the correlation between LST and NDBI was positive and moderate between 2014 and 2025, with the highest correlation value in 2021 (r = 0.62) and the lowest value in 2025 (r = 0.25). Similar findings were indicated by [5,9] which also presented positive LST responses to built up and bare soil. According to these results, the effects of the density of urban areas were observed on LST. These results indicate the impact of the density of urban areas on surface temperature. Similar results were also found in the study of [22]. According to their results, LST is positively related to NDBI and NDBaI.

As expected, NDVI, an indicator of vegetation health, showed negative correlations with both building density indices and surface temperature. While the correlation between NDVI and NDBI was -0.48 in 2024, only a very weak positive (0.05) relationship was observed in 2021. The study conducted by [22] also supported the results of this study. Their findings revealed that LST has a positive correlation with NDBI and NDBaI, while a negative correlation with NDVI and NDWI.

A weak but positive correlation has been observed between LST and NDVI. The correlation coefficient ranges from 0.14 in 2019 to 0.41 in 2023. These results may be attributed to several factors, such as seasonal variations in NDVI and LST, or different land use and land cover types. Similar findings have been reported in previous studies. For example, [13] found a similar weak positive correlation in their study conducted in Pakistan. Spatially, higher LST values are particularly observed in urban and sparsely vegetated areas. These results are observed similarly from other studies indicated in Türkiye [18,28] and globally [26] and compared with their findings.

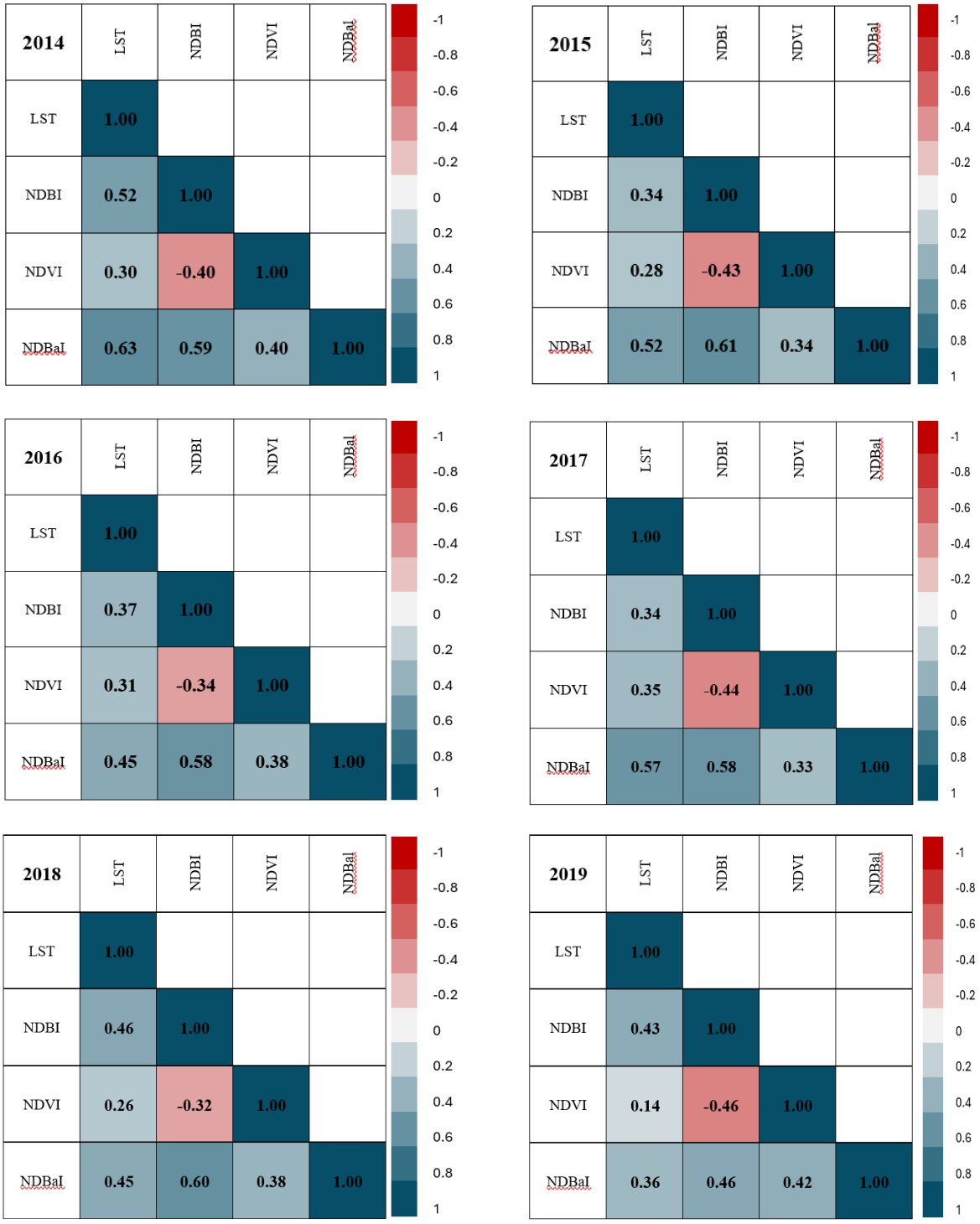


Figure 8. Correlation matrix of spectral indices for the years 2014-2025

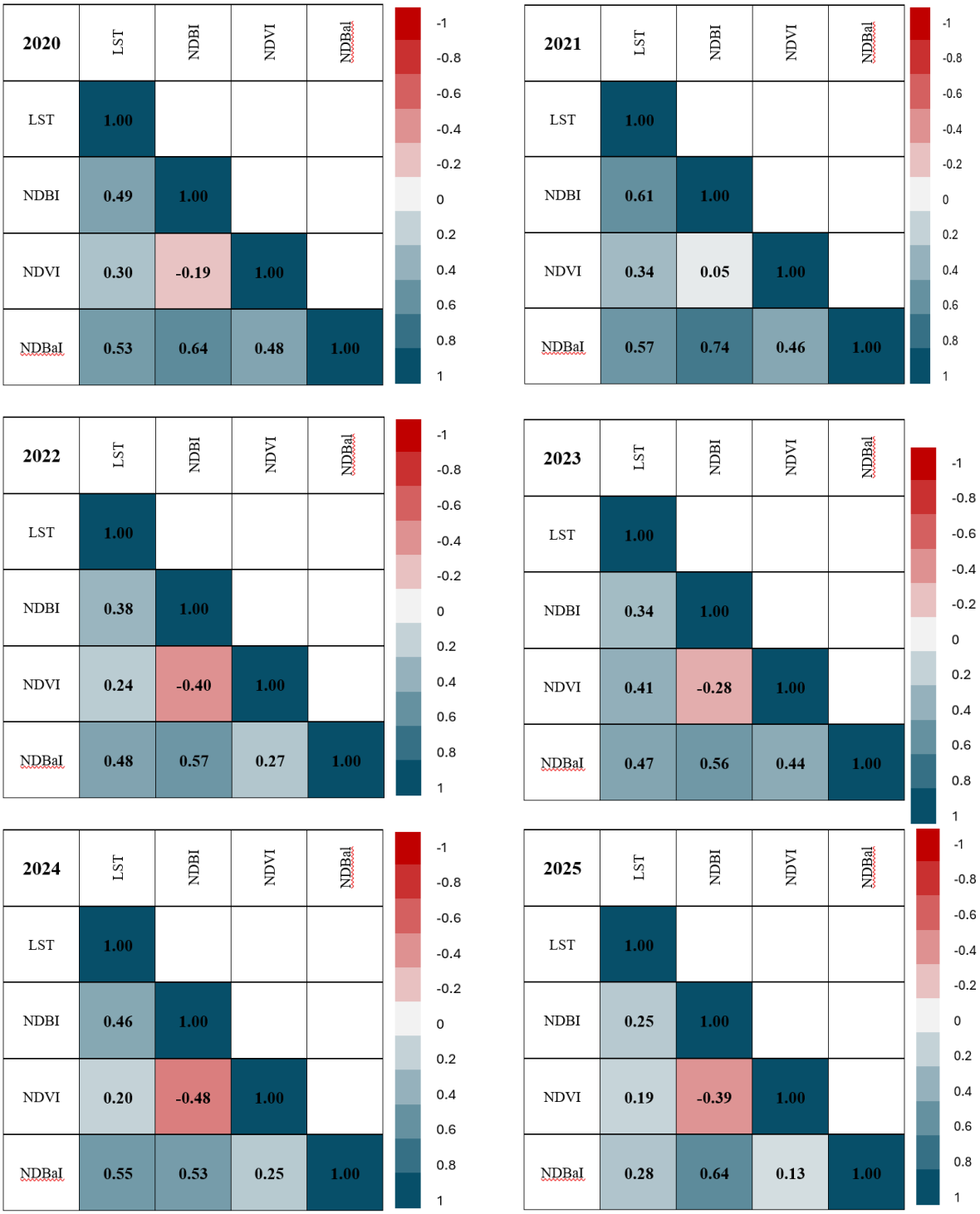


Figure 8. (continued) Correlation matrix of spectral indices for the years 2014-2025

A comprehensive assessment of NDVI, NDBI, NDBaI, and LST changes from 2014 to 2025 clearly reveals the annual dynamics of land cover and surface temperature in the study area (Figure 9). As can be seen in Figure 9, NDVI values remained between 0.15 and 0.20 throughout the period, indicating that vegetation conditions did not change significantly. Although partial decreases in NDVI values were seen, especially in 2015 and 2020, NDVI values generally remained stable during the study period. However, the NDBI values mostly varied between -0.05 and 0.02. This is because the study area has limited urban areas. Although slight increases in urban areas are seen in 2021, these results did not effect the significant variation on the regional scale. Based on the annual NDBaI results, the values ranged between -0.38 and -0.28. It can be concluded

from these results that bare soil areas are limited and that the trend of change in these areas during the study period is not upward. The result of LST values has mostly fluctuated between 27 ºC and 36 ºC. between the years 2014-2025. Although LST values decreased significantly in 2022, a partial increase was observed in 2016 and 2023. Besides, an investigation of the relationship between LST and NDVI over the years reveals a negative correlation between these two indices, indicating that surface temperatures tend to decrease over time along with dense vegetation. In contrast, it is expected that LST would increase with less vegetation areas. All these inferences proved that there is a significant effects of vegetation on LST.

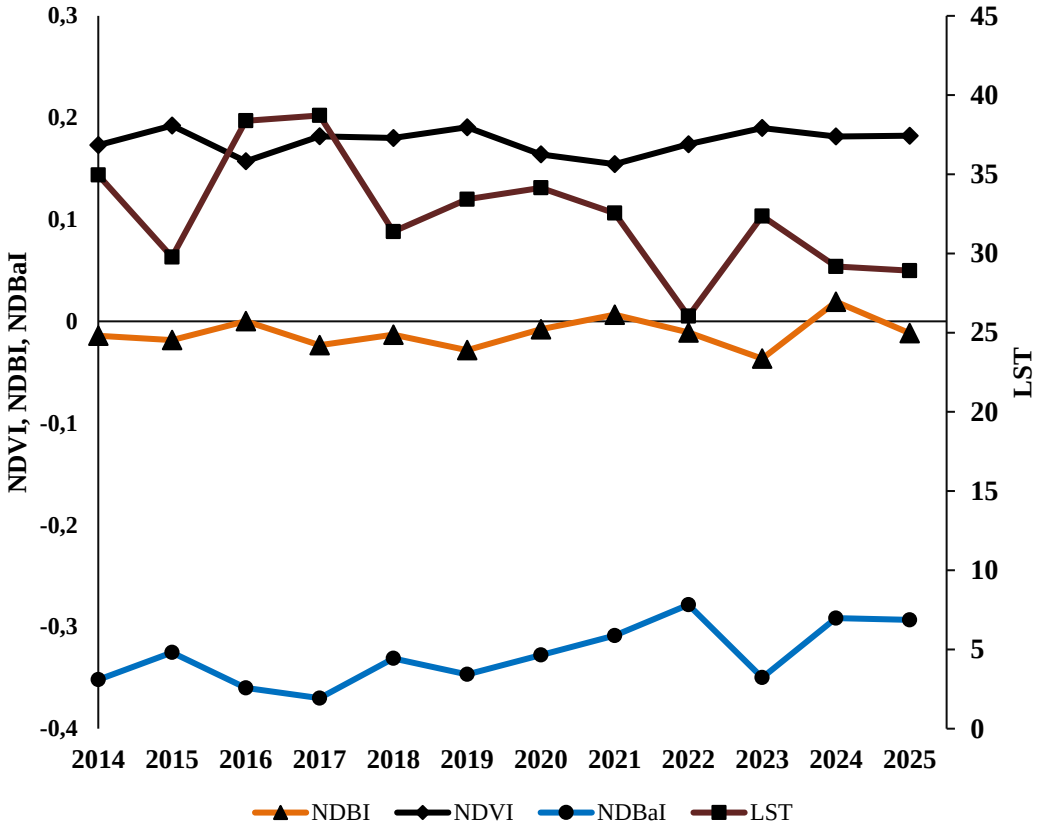


Figure 9. Temporal analysis using the mean values of NDBI, NDVI, NDBaI, and LST

4. Conclusion

This study aimed to investigate the changes and correlations between the spectral indices including LST, NDVI, NDBI, and NDBaI, which are commonly used in literature, in the Burdur Basin using multi temporal Landsat satellite imagery between the years 2014 and 2025. Based on the results, an important variation of LST values was observed in the Burdur Basin during the study period. Spatially, the highest value of LST was seen in the northeastern and central zones of the basin, particularly from 2016 to 2019. In contrast, as expected, the wetland and water surface areas produced the lowest LST values. Besides, during the study period, the NDVI values have not shown any significant changes, but have particularly decreased in the years 2020 and 2024. These could be the reason of the basin can be vulnerable to climate variation. Although NDBI and NDBaI have not shown an important variation during the years, and mostly observed moderate positive correlation with LST, the values were particularly increased in some regions. From these results, it can be concluded that urban and bare soil areas tend to increase LST. The weak and positive relationship between the LST and NDVI in some years can be inferred from seasonal fluctuating and complex land use and land cover change. To conclude, the results of this work revealed that, the climate variables significantly effects the LST values. In order to reduce the adverse effects of climate change, it is crucial to preserve vegetation, mitigate bare land areas, and control the expansion of urban areas in the Burdur Basin. Additionally, this

study has shown that GIS and remote sensing methods are dependable and efficient means of tracking long-term environmental changes in semi-arid basins.

5. Author Contribution Statement

The entire work was undertaken solely by the author.

6. Ethics Committee Approval and Conflict of Interest

There is no conflict of interest with any person/institution in the prepared article.

7. Ethical Statement Regarding the Use of Artificial Intelligence

During the writing process of this study, the artificial intelligence tool "ChatGPT," developed by "OpenAI," and “Grammarly” were used only for limited purposes of linguistic editing and translation. The scientific content, analyses, and results belong entirely to the authors.

8. References

[1] R. Thapa *et al*., "Examining the spatio-temporal relationship between LST, NDVI, NDBI and LULC change of Pachhua Dun, Dehradun, Uttarakhand (India)," *J. Geospatial Inf. Sci. Eng.*, vol. 6, no. 2, pp. 136–152, Nov. 2023.

[2] B. Guo, Y. Zhou, S. X. Wang, and H. P. Tao, "The relationship between normalized difference vegetation index (NDVI) and climate factors in the semiarid region: A case study in Yalu Tsangpo River Basin of Qinghai–Tibet Plateau," *J. Mt. Sci.*, vol. 11, no. 4, pp. 926–940, May 2014.

[3] N. You, J. Meng, and L. Zhu, "Sensitivity and resilience of ecosystems to climate variability in the semi-arid to hyper-arid areas of Northern China: A case study in the Heihe River Basin," *Ecol. Res.*, vol. 33, no. 1, pp. 161–174, Dec. 2018.

[4] J. Peng, J. Jia, Y. Liu, H. Li, and J. Wu, "Seasonal contrast of the dominant factors for spatial distribution of land surface temperature in urban areas," *Remote Sens. Environ.*, vol. 215, pp. 255–267, Sep. 2018.

[5] S. Guha and H. Govil, "A long-term monthly analytical study on the relationship of LST with normalized difference spectral indices," *Eur. J. Remote Sens.*, vol. 54, no. 1, pp. 487–512, Aug. 2021.

[6] Shahfahad *et al*., "Longitudinal study of land surface temperature (LST) using mono- and split-window algorithms and its relationship with NDVI and NDBI over selected metro cities of India," *Arab. J. Geosci.*, vol. 13, Art. no. 1040, pp. 1–19, Sep. 2020.

[7] D. Sun and R. T. Pinker, "Estimation of land surface temperature from a geostationary operational environmental satellite (GOES-8)," *J. Geophys. Res. Atmos.*, vol. 108, no. D11, Jun. 2003.

[8] K. Deilami, M. Kamruzzaman, and Y. Liu, "Urban heat island effect: A systematic review of spatio-temporal factors, data, methods, and mitigation measures," *Int. J. Appl. Earth Obs. Geoinf.*, vol. 67, pp. 30–42, May 2018.

[9] F. Altıner and F. Bingol, "Spatio-temporal assessment of land surface temperature, vegetation cover, and built-up areas using LST, NDVI, and NDBI in Balıkesir, Türkiye (1985–2025)," *Sustainability*, vol. 17, Art. no. 9245, pp. 1–25, Oct. 2025.

[10] S. Garai *et al*., "Assessing correlation between rainfall, normalized difference vegetation index (NDVI) and land surface temperature (LST) in Eastern India," *Saf. Extrem. Environ.*, vol. 4, pp. 119–127, Jun. 2022.

[11] B. Naga, K. Naidu, and F. Ahmed, "Assessing LULC changes and LST through NDVI and NDBI spatial indicators: A case of Bengaluru, India," *GeoJournal*, vol. 88, pp. 4335–4350, Apr. 2023.

[12] P. E. Zope, T. I. Eldho, and V. Jothiprakash, "Impacts of land use–land cover change and urbanization on flooding: A case study of Oshiwara River Basin in Mumbai, India," *CATENA*, vol. 145, pp. 142–154, Oct. 2016.

[13] A. Ali *et al*., "Examining the landscape transformation and temperature dynamics in Pakistan," *Sci. Rep.*, vol. 15, Art. no. 2575, pp. 1–16, Jan. 2025.

[14] M. S. A. Salan and M. A. H. Bhuiyan, "Estimating impacts of micro-scale land use/land cover change on urban thermal comfort zone in Rajshahi, Bangladesh: A GIS and remote sensing based approach," *Urban Clim.*, vol. 58, Art. no. 102187, Nov. 2024.

[15] X. Yuan *et al*., "Vegetation changes and land surface feedbacks drive shifts in local temperatures over Central Asia," *Sci. Rep.*, vol. 7, no. 1, pp. 3–10, Jun. 2017.

[16] S. Anbazhagan and C. R. Paramasivam, "Statistical correlation between land surface temperature (LST) and vegetation index (NDVI) using multi-temporal Landsat TM data," *Int. J. Adv. Earth Sci. Eng.*, vol. 5, no. 1, pp. 333–346, Apr. 2016

[17] B. Ç. Değerli and M. Çetin, "Evaluation from rural to urban scale for the effect of NDVI-NDBI indices on land surface temperature in Samsun, Türkiye," *Turkish J. Agric. Food Sci. Technol.*, vol. 10, no. 12, pp. 2446–2452, Oct. 2022.

[18] E. Karakoyun, "Evaluating the correlation between land surface temperature (LST) and normalized difference vegetation index (NDVI)," *MAUN J. Fac. Eng. Archit.*, vol. 5, no. 1, pp. 15–25, May 2024.

[19] S. Guha and H. Govil, "An assessment on the relationship between land surface temperature and normalized difference vegetation index," *Environ. Dev. Sustain.*, vol. 23, no. 2, pp. 1944–1963, Jan. 2021.

[20] S. Guha, H. Govil, and M. Besoya, "An investigation on seasonal variability between LST and NDWI in an urban environment using Landsat satellite data," *Geomatics Nat. Hazards Risk*, vol. 11, no. 1, pp. 1319–1345, Jul. 2020.
[21] M. Jothimani, J. Gunalan, and R. Duraisamy, "Study the relationship between LULC, LST, NDVI, NDWI and NDBI in Greater Arba Minch area, Rift," in *Proc. 3rd Int. Conf. Integr. Intell. Comput. Commun. Security (ICIIC)*, 2021, pp. 183–193.
[22] J. Siqi and W. Yuhong, "Effects of land use and land cover pattern on urban temperature variations: A case study in Hong Kong," *Urban Clim.*, vol. 34, p. 100693, Dec. 2020.
[23] H. Zhao and X. Chen, "Use of normalized difference bareness index in quickly mapping bare areas from TM/ETM+," in *Proc. IEEE Int. Geosci. Remote Sens. Symp. (IGARSS)*, vol. 3, pp. 1666–1668, 2005.
[24] S. Guha and H. Govil, "Estimating the seasonal relationship between land surface temperature and normalized difference bareness index using Landsat data series," *Int. J. Eng. Geosci.*, vol. 7, no. 1, pp. 9–16, Jan. 2022.
[25] A. S. Alademomi *et al*., "The interrelationship between LST, NDVI, NDBI, and land cover change in a section of Lagos metropolis, Nigeria," *Appl. Geomatics*, vol. 14, pp. 299–314, Apr. 2022.
[26] W. Ullah *et al*., "Analysis of the relationship among land surface temperature (LST), land use land cover (LULC), and normalized difference vegetation index (NDVI) with topographic elements in the lower Himalayan region," *Heliyon*, vol. 9, no. 2, p. e13322, Feb. 2023.
[27] E. Kilic and S. Arslan, "Uzaktan algılama teknikleri ile altyapı sistemlerinin konumsal analizi: Burdur Havzası örneği," *Turkish J. For.*, vol. 23, no. 2, pp. 146–155, Jun. 2022.
[28] A. Sekertekin and S. H. Kutoglu, "Evaluation of spatio-temporal variability in land surface temperature: A case study of Zonguldak, Turkey," *Environ. Monit. Assess.*, vol. 188, no. 30, pp. 1–15, Jan. 2016.
[29] O. Orhan, S. Ekercin, and F. Dadeser-Celik, "Use of Landsat land surface temperature and vegetation indices for monitoring drought in the Salt Lake Basin area, Turkey," *Sci. World J.*, vol. 2014, pp. 1–11, Jan. 2014.
[30] A. Unver and Z. Baskaya, "NDVI, NDBI ve UI analizleriyle yapılaşma yoğunluğu değişimi analizi (1999–2022): Yıldırım İlçesi (Bursa) örneği," *J. Geogr.*, vol. 49, pp. 65–81, Oct. 2024.